NASA/TM–2011-217059

Alternative Aviation Fuel Experiment (AAFEX)

B. E. Anderson, A. J. Beyersdorf, C. H. Hudgins, J. V. Plant, K. L. Thornhill, E. L. Winstead, and L. D. Ziemba
NASA Langley Research Center, Hampton, Virginia

R. Howard
ATA, Arnold Engineering Development Center, Arnold AFB, Tennessee

E. Corporan
Air Force Research Laboratory, Wright Patterson AFB, Ohio

R. C. Miake-Lye, S. C. Herndon, M. Timko, and E. Woods
Aerodyne Research, Inc., Billerica, Massachusetts

W. Dodds
General Electric Aircraft Engines, Cincinnati, Ohio

B. Lee and G. Santoni
Harvard University, Cambridge, Massachusetts

P. Whitefield, D. Hagen, and P. Lobo
Missouri University of Science and Technology, Rolla, Missouri

W. B. Knighton
Montana State University, Bozeman, Montana

D. Bulzan, K. Tacina, and C. Wey
NASA Glenn Research Center, Cleveland, Ohio

R. Vander Wal
Pennsylvania State University, University Park, Pennsylvania

A. Bhargava
Pratt and Whitney, East Hartford, Connecticut

J. Kinsey
U.S. EPA, Research Triangle Park, North Carolina

D. S. Liscinsky
United Technologies Research Center, East Hartford, Connecticut

February 2011

NASA STI Program . . . in Profile

Since its founding, NASA has been dedicated to the advancement of aeronautics and space science. The NASA scientific and technical information (STI) program plays a key part in helping NASA maintain this important role.

The NASA STI program operates under the auspices of the Agency Chief Information Officer. It collects, organizes, provides for archiving, and disseminates NASA's STI. The NASA STI program provides access to the NASA Aeronautics and Space Database and its public interface, the NASA Technical Report Server, thus providing one of the largest collections of aeronautical and space science STI in the world. Results are published in both non-NASA channels and by NASA in the NASA STI Report Series, which includes the following report types:

- TECHNICAL PUBLICATION. Reports of completed research or a major significant phase of research that present the results of NASA programs and include extensive data or theoretical analysis. Includes compilations of significant scientific and technical data and information deemed to be of continuing reference value. NASA counterpart of peer-reviewed formal professional papers, but having less stringent limitations on manuscript length and extent of graphic presentations.

- TECHNICAL MEMORANDUM. Scientific and technical findings that are preliminary or of specialized interest, e.g., quick release reports, working papers, and bibliographies that contain minimal annotation. Does not contain extensive analysis.

- CONTRACTOR REPORT. Scientific and technical findings by NASA-sponsored contractors and grantees.

- CONFERENCE PUBLICATION. Collected papers from scientific and technical conferences, symposia, seminars, or other meetings sponsored or co-sponsored by NASA.

- SPECIAL PUBLICATION. Scientific, technical, or historical information from NASA programs, projects, and missions, often concerned with subjects having substantial public interest.

- TECHNICAL TRANSLATION. English-language translations of foreign scientific and technical material pertinent to NASA's mission.

Specialized services also include creating custom thesauri, building customized databases, and organizing and publishing research results.

For more information about the NASA STI program, see the following:

- Access the NASA STI program home page at *http://www.sti.nasa.gov*

- E-mail your question via the Internet to help@sti.nasa.gov

- Fax your question to the NASA STI Help Desk at 443-757-5803

- Phone the NASA STI Help Desk at 443-757-5802

- Write to:
  NASA STI Help Desk
  NASA Center for AeroSpace Information
  7115 Standard Drive
  Hanover, MD 21076-1320

NASA/TM–2011-217059

Alternative Aviation Fuel Experiment (AAFEX)

B. E. Anderson, A. J. Beyersdorf, C. H. Hudgins, J. V. Plant, K. L. Thornhill, E. L. Winstead, and L. D. Ziemba
NASA Langley Research Center, Hampton, Virginia

R. Howard
ATA, Arnold Engineering Development Center, Arnold AFB, Tennessee

E. Corporan
Air Force Research Laboratory, Wright Patterson AFB, Ohio

R. C. Miake-Lye, S. C. Herndon, M. Timko, and E. Woods
Aerodyne Research, Inc., Billerica, Massachusetts

W. Dodds
General Electric Aircraft Engines, Cincinnati, Ohio

B. Lee and G. Santoni
Harvard University, Cambridge, Massachusetts

P. Whitefield, D. Hagen, and P. Lobo
Missouri University of Science and Technology, Rolla, Missouri

W. B. Knighton
Montana State University, Bozeman, Montana

D. Bulzan, K. Tacina, and C. Wey
NASA Glenn Research Center, Cleveland, Ohio

R. Vander Wal
Pennsylvania State University, University Park, Pennsylvania

A. Bhargava
Pratt and Whitney, East Hartford, Connecticut

J. Kinsey
U.S. EPA, Research Triangle Park, North Carolina

D. S. Liscinsky
United Technologies Research Center, East Hartford, Connecticut

National Aeronautics and
Space Administration

Langley Research Center
Hampton, Virginia 23681-2199

February 2011

Available from:

NASA Center for AeroSpace Information
7115 Standard Drive
Hanover, MD 21076-1320
443-757-5802

Table of Contents

1.00 Project Description and Executive Summary

The rising cost of oil coupled with the need to reduce pollution and dependence on foreign suppliers has spurred great interest and activity in developing alternative aviation fuels. Although a variety of fuels have been produced that have similar properties to standard Jet A, detailed studies are required to ascertain the exact impacts of the fuels on engine operation and exhaust composition. In response to this need, NASA acquired and burned a variety of alternative aviation fuel mixtures in the Dryden Flight Research Center DC-8 to assess changes in the aircraft's CFM-56 engine performance and emission parameters relative to operation with standard JP-8. This Alternative Aviation Fuel Experiment, or AAFEX, was conducted at NASA Dryden's Aircraft Operations Facility (DAOF) in Palmdale, California, from January 19 to February 3, 2009 and specifically sought to establish fuel matrix effects on: 1) engine and exhaust gas temperatures and compressor speeds; 2) engine and auxiliary power unit (APU) gas phase and particle emissions and characteristics; and 3) volatile aerosol formation in aging exhaust plumes. A secondary goal of the study was to evaluate the role of ambient conditions in regulating volatile aerosol emissions. Managed by the Combustion sub-element of NASA's Subsonic Fixed-Wing Program, AAFEX received additional sponsorship from the U.S. Air Force, the Federal Aviation Administration (FAA) and the U.S. Environmental Protection Agency (EPA). Groups from Air Force Research Lab at Wright-Patterson, Air Force Arnold Engineering Development Center, Aerodyne Research Inc., Carnegie-Mellon University, Harvard University, Missouri University for Science and Technology, Montana State University, NASA Langley and Glenn Research Centers, and the University of California at San Diego provided support and measurement expertise. Measured engine parameters included N1, N2, fuel flow, and exhaust gas temperature. Gas phase measurements included the standard ICAO certification species (CO_2, CO, NO_x, and THC) along with SO_2, HONO, methane isotopes, speciated hydrocarbons, hazardous air pollutants (HAPS), and oxygenated compounds. Measured particle parameters included smoke number; number density, size distribution and total and nonvolatile mass; black carbon morphology, composition and total mass; volatile aerosol speciation and mass; and particle cloud-forming tendency. Participants made duplicate measurements of many aerosol and trace-gas species, which facilitated an assessment of the relative differences in emission data sets collected by the different groups in separate test venues.

During AAFEX, the aircraft was parked in an open-air run-up facility and complete sets of gas and particle emission measurements were made as a function of engine thrust. To delineate fuel-matrix related changes in emissions from those caused by variations in ambient conditions, samples were alternately drawn from the exhaust of the left inboard engine (#2), which always burned JP-8, and the right inboard engine (#3), which burned either standard JP-8 or one of the four test fuels: a Fischer/Tropsch (FT) fuel prepared from natural gas; an FT fuel made from coal; and 50:50 blends of each FT fuel with JP-8. To examine plume chemistry and particle evolution in time, samples were drawn from inlet probes positioned 1 and 30 m downstream of the aircraft's engines. To sample more aged plumes, instruments were also placed in trailers parked on the northeastern edge of the ramp to measure aerosol and gaseous properties in air drawn from a common inlet mounted ~145 m behind the aircraft. At ground idle thrust conditions, a mobile laboratory vehicle periodically profiled the exhaust plume from 30 to 300 m downstream to examine temperature/time-dependent changes in particle and reactive gas composition and concentration. In addition, the 1-m rakes included multiple gas and aerosol

inlet tips, which allowed emissions to be mapped across the breadth of the engine exhaust plane to establish the extent of the core-flow region within the near-field plume. Taking advantage of the broad diurnal variation in air temperature in the Mojave Desert, tests were conducted in the early morning and at mid-day to examine the effect of ambient conditions on gas phase and volatile aerosol emissions.

From detailed analyses presented in the attached appendices and observations made in the field, the following general conclusions can be drawn.

Aircraft Performance and Maintenance Issues

- Burning FT fuel did not appreciably affect the DC-8's CFM-56 engine performance. Once corrected for density and heating values, the fuel flow rates required to produce any particular N1 (low fan speed) setting were almost identical for JP-8 and the tested FT fuels, suggesting that the alternative fuels offer no advantage or penalty in terms of fuel economy.
- The FT fuels exhibited higher combustion efficiencies than JP-8 at low power settings indicating that they are in general less polluting.
- The aromatic-free FT fuel caused fuel-system seals to shrink, which resulted in fuel leaks in the aircraft #3 main tank and the two tanker trucks that were used to store/deliver the pure Shell and Sasol fuels. The leaks went away after introduction of JP-8 or blended fuel.
- Exhaust samples drawn from within 20 cm of the #3 engine centerline at mid-power settings were contaminated with volatile aerosol formed from engine oil emanating either from the engine's central vent tube or from a leaky turbine seal; appreciable amounts of oil were not seen in 1-m samples collected 15 cm off the #2 engine centerline or at high engine thrust levels.

Exit plane engine emissions when burning standard JP-8 Fuel

- CO and THC emissions from the DC-8's two inboard engines were somewhat elevated above ICAO certification values at idle, whereas NOx emissions were within the acceptable range at all thrust settings.
- At mid to high power settings, the DC-8's port-side (#2) engine produced higher levels of NO_x and nonvolatile particulate matter (PM) number and mass emissions than the starboard (#3) engine. Detailed analysis showed that at thrust settings above idle, the #2 engine exhaust gas temperatures were significantly higher and that when plotted as functions of exhaust gas temperature (EGT), emission parameters from the two engines collapsed onto single curves. The higher EGTs produced by the #2 engine are possible signs of engine component aging.
- The DC-8's #3 engine emitted higher levels of CO, hydrocarbons and nonvolatile aerosols during AAFEX compared to the Aircraft Particle Emission Experiment (APEX-1), which was conducted during spring 2004, just after the aircraft's engines had been overhauled to repair damage incurred during a volcanic plume encounter. This, along with the observation that the engine's EI_{CO} at 7% idle greatly exceeded the ICAO certification value, suggests the engines' emission performance had degraded during the period between the two experiments.
- CO and hydrocarbon emission indices were highly sensitive to throttle setting at low engine powers, as values often increased by a factor or two or more in going from 7% (the ICAO certification setting) to 4% idle. Since engines are operated at the lowest possible fuel flows

when the aircraft are not in motion, this finding has implications for modeling air quality in airport terminal areas.

- The engines emitted log-normally distributed nonvolatile (soot) particles with mean diameters that ranged from about 15 nm at idle to 35 nm at takeoff thrust. Number emission indices (EI_n) varied from 0.3 to 1 x 10^{15} kg^{-1} and were a maximum at the ground idle and takeoff thrust and a minimum at 30 to 45% power. Black carbon mass emission indices (EI_{bc}) varied from about 10 mg kg^{-1} for mid-power settings to over 100 mg kg^{-1}at takeoff thrust.
- Engine gas phase and nonvolatile PM emissions decreased significantly with increasing ambient temperature. Indeed EI values for many hydrocarbon species decreased by a factor of two as temperatures warmed from 0 to 15^{o}C. PM number and black carbon EIs exhibited temperature coefficients (dEI/dT) that respectively ranged from -2 to -6 x 10^{13} $kg^{-1}{}^{o}C^{-1}$ and -0.4 to -2 mg $kg^{-1}{}^{o}C^{-1}$. As a percentage of the mean value, temperature coefficients were largest at idle and declined with increasing engine power.

Fuel Effects on nonvolatile PM and Gas-Phase Emissions

- Relative to JP-8, burning alternative fuels generally reduced engine CO, THC and NOx emissions. The reductions were greatest for FT-1, which decreased NOx and CO EIs by up to 10% at high power and idle, respectively. At low power settings, THC emissions from FT-2 fuels were slightly higher than from JP-8.
- HAPS emissions were significantly lower for FT fuels. For example, at idle EI-benzene was about five times smaller for FT-1 compared to JP-8.
- Burning 50% blends of JP-8 and the FT fuels did not produce significant reductions in certification gas species emissions.
- Engine PM emissions were substantially reduced when burning the FT fuels. The effects were greatest for FT-1, where nonvolatile EI_n and EI_{bc} values were factors of 200 and 20 lower at idle than corresponding JP-8 values, but were also quite notable for FT-2, which exhibited EI_n and EI_{bc} that were factors of 35 and 20 lower than JP-8 at mid power settings.
- The blended fuels produced similar, but disproportionally large PM emission reductions. Ratios of JP-8 to Blend EIs varied from 2 to 9 for nonvolatile number and 2 to 22 for black carbon. Reduction benefits were greatest at 45% power and a minimum at idle and takeoff thrust.
- The reduction benefits of burning FT fuels decreased with increasing power so that the JP-8 to FT-1 EI ratios for nonvolatile number and black carbon mass were respectively 4 and 7 at the 85% thrust setting. Smoke numbers at takeoff power were two to three times lower for the FT fuels than JP-8.
- Nonvolatile particles produced from burning the FT fuels were noticeably smaller and more compact than those generated by JP-8 combustion. For example, at 85% power, respective geometric mean diameters for FT-1, FT-2 and JP-8 were about 50, 55, and 75 nm, and corresponding densities were 1.45$\pm$0.1 g cm^{-3}, 1.2$\pm$0.15 g cm^{-3}, and 0.92$\pm$0.08 g cm^{-3}.
- Concurrent lab studies show that the FT particles contain more oxygenated species than those generated by burning JP-8, which suggests they would form more active cloud condensation nuclei.
- Considering all fuels burned:
  - The range between idle and high thrust nonvolatile number EIs decreased considerably with increasing fuel end point and aromatic content and decreasing hydrogen content.

- At any given power setting, EI_n and EI_{bc} linearly increased with aromatic content and decreased with hydrogen content.
- Correlation coefficients with fuel properties were greater for EI_n than for EI_{bc}, suggesting that the variability in EI_n was better captured by variability in fuel composition than was the variability in EI_{bc}.
- For both EI_n and EI_{bc}, the best correlations with all examined fuel properties were observed at idle (4 %) and takeoff (100 %) thrust settings.

Volatile Aerosols

- Low-volatility species condensed in the cooling exhaust plume to form nucleation mode aerosols with mean diameters in the 10 to 25 nm size range, so that at 30-m downstream, EI_n values were more than an order of magnitude greater than measured at the engine exit plane, regardless engine power setting or fuel composition.
- Results from AAFEX and other recent studies indicate that the volatile aerosols are composed of sulfate, lube oil and lube-oil related substances, hydrocarbons, and aromatics species.
- Because of the greater amounts of organic aerosol precursors emitted and lower relative plume temperatures, volatile mass emissions were largest at idle, accounting for more than 90% of EI_m under most conditions
- For JP-8, volatile aerosol emissions decreased with power, but still dominated total number EIs and represented a significant fraction of total mass EIs at take-off thrust.
- Volatile aerosol EI_n and EI_m values at idle were an order of magnitude or more lower for the FT fuels than JP-8, which suggests that the combustion emissions, not lube oil, are the primary source of volatile aerosol precursors.
- The propensity of low volatility gas-phase species to form new aerosols (nucleate) or to deposit onto the surface of existing soot particles depended on both plume soot concentrations and ambient conditions, with cold temperatures and low soot loading favoring nucleation and warm temperatures and high soot loading favoring soot surface deposition.
- Volatile aerosol formation was heavily dependent on ambient temperature, as EI_m values typically deceased by a factor of two when temperatures warmed from 0 to 15^{o}C.
- The mean size of nucleation mode particles depended on engine thrust, ambient temperature, and plume age, with sizes increasing with downstream distance and decreasing temperature and engine power.
- Volatile aerosol number EIs varied according to fuel sulfur content so that under the same engine and ambient conditions, JP-8 > Blends > FT-1~FT2.
- Volatile aerosol mass emissions varied according to fuel sulfur content and hydrocarbon complexity so that JP-8 > Blend-2 > Blend-1 > FT-2 > FT-1.

Plume Chemistry

- The DC-8's CFM-56 engines were a weak source and sink of CH_4 at low (<15% of maximum thrust) and high (>30%) power settings, respectively. AAFEX results suggest that for a typical flight profile, the aircraft would destroy significantly more CH_4 than it created.
- N_2O emissions were relatively constant with power and typically in the 50 to 100 g hr^{-1} in mode range.

- Greenhouse gas emissions (CO_2, CH_4, and N_2O) were not significantly influenced by fuel composition.
- In downstream sampling, HONO EIs increased by a factor of six in going from idle to takeoff power and were not sensitive to ambient temperature, solar insolation or fuel composition. The results suggest that HONO is primarily created within the combustor, not in the downstream plume.
- H_2O_2 was observed for the first time in an engine plume. EIs were 0.43 ± 0.31 g kg^{-1} at idle, but decreased to below detection limits at higher power settings.
- Ozone production was observed for the first time in a fresh (< 60 s old) engine exhaust plume.
- Net conversion of NO to NO_2 was observed in some cases and chemical circumstances suggest that this occurred through reaction with peroxy radicals, which in turn are formed through reactions of OH and VOCs
- A detailed chemical analysis suggests that exhaust plume OH concentrations were ~2×10^7 molecules cm^{-3}, which, when compared to typical background values, suggests VOC oxidation rates were elevated during the first minute of plume evolution.

APU Emissions

- When both were operated at low power, the DC-8's APU emitted about 25 times more black carbon mass per kg of fuel burned that one of its CFM-56 engines.
- Unlike for the engine, APU gas and PM emissions decreased with increasing engine power as indicated by exhaust gas temperature. For JP-8, EI_n and EI_{bc} respectively dropped from ~5×10^{15} kg^{-1} and ~500 mg kg^{-1} at minimum load (cockpit power) to $2.5\ 10^{15}$ kg^{-1} and 200 mg kg^{-1} at maximum load (full air conditioning and bleed air). Similarly CO and THC emissions also declined by respective factors of 2 and 7 as power was increased from minimum to maximum.
- Burning FT-2 fuel did not significantly affect NO_x emissions, but lowered CO and THC EIs by averages of 9 and 37%, respectively, when compared to JP-8 emissions.
- Compared to JP-8, FT-2 fuel drastically reduced the APU's PM emissions. Indeed, average EI_n and EI_{bc} values were respectively factors of 6 and 13 lower when burning the alternative fuel.
- APU FT-2 nonvolatile PM emissions were smaller and had higher mass densities compared to JP-8 emissions.

Sampling and Measurement Observations

- At low engine powers, FT-fuel nonvolatile PM number and black carbon emissions were very low and presented a measurement challenge for the SMPS and MAAP sensors.
- THC measurements made using standard FID sensors don't accurately measure oxygenated species, which account for a significant fraction of VOCs at low engine powers. It is thus not possible to obtain closure between THC and summated hydrocarbon measurements.
- The transmission efficiency of PM sampling lines degrade with use and can appreciably alter measured emission parameters
- Although volatile aerosol number EIs quickly reached equilibrium in fresh exhaust plumes, low volatility species continued condense in time so that 30-m EI_m values increased during sample transport through sampling long lines.

- Nonvolatile PM EIs were sensitive to sample dilution, possibly because of inertial enrichment of large particles at low inlet tip velocities.
- Exhaust plume gaseous and PM emissions were homogeneously distributed within ~10 cm of the engine centerline.
- Nonvolatile PM number and mass EIs measured at 30-m were always larger than 1-m values, possibly because of thermophoretic and turbulent eddy impaction losses occurring within the 1-m inlet probes.
- Nonvolatile PM EI measurements performed on 1-m aerosol-probe samples diluted at the inlet tip and gas probe samples diluted 1.5-m downstream were essentially identical, which suggests that existing sampling equipment used in engine certification tests can be modified to yield representative particle number and mass EI data.

2.00 INTRODUCTION

Since 1970, the U.S. has had to import oil from other countries to meet its energy production needs. This situation often places our country in a weak position when negotiating political and diplomatic agreements and forces us to do business with unstable or totalitarian regimes. It leaves us economically vulnerable to fluctuations in supply and open to the threat of embargoes. Shortages of oil may also constrain the growth of some economic sectors, with the aviation industry being a case in point. These factors, coupled with recent oil price increases and the heightened awareness that global fossil fuel production may be at or near its peak, has spurred significant interest in developing alternative, domestically-produced fuels for the nation's transportation sector. A wide variety of alternative liquid fuels are now being tested or used for powering internal combustion engines, with ethanol being the most popular and, because of the food vs. fuel debate, the most controversial.

For the aviation industry, the options for "drop-in" replacement fuels are more limited because of the narrow energy density (i.e, Joules/Liter), viscosity, thermal stability and corrosion property standards that must be met for economically powering the existing aircraft fleet. Alcohol-based fuels are unsuitable for aviation because of their low energy density and potential for corroding fuel system components. Research and development is presently focusing on converting hydrocarbon feedstocks into kerosene using the Fischer-Tropsch (FT) process, which is the basis for the Sasol fuels produced in South Africa. Plants are now operating that convert either natural gas or coal into synthetic fuels that meet Jet A standards but have improved viscosity and thermal stabilities. These properties extend the fuels' use to lower temperatures, result in lower fuel system deposits, and allow them to be stored for long periods of time. In addition, FT fuels are essentially aromatic-hydrocarbon and sulfur free, which means their use results in much lower soot and sulfate aerosols emissions, making them particularly attractive for use in mitigating aircraft impacts on local air quality and climate. The downside to these fuels is that they are not sustainable in the long term (natural gas and coal deposits are limited) and their manufacture produces significant amounts of CO_2 (about 1.8 times more than standard jet fuels), which must be captured or permanently sequestered to circumvent possible climate impacts. Also, there are presently no U.S.-based manufacturers that produce these fuels.

The search for renewable aviation fuels that have essentially no direct impact on atmospheric CO_2 levels has focused on bio-oils such as those produced naturally by palm trees, soybeans,

corn, and algae. These products are already being used to power diesel vehicles, but they have a number of drawbacks for use in aircraft engines, including a tendency to gel at relatively high temperatures, poor thermal stability, and the fact that they are grown in competition with food crops (i.e., recent increases in ethanol fuel production within the U.S. has caused corn prices to more than double in the last two years). Researchers have found that hydro-treated bio-fuels or 80:20 blends of Jet A and biofuel meet current fuel standards (a Virgin Airlines aircraft recently made a well-publicized flight fueled by such a mixture), but Daggett et al. (2004) and others warn that sufficient land is not available to support large-scale biofuel production from standard farm crops and that an efforts to increase acreage may come at the sacrifice of rainforests and other ecosystems that are critical in maintaining the Earth's climate system. This factor has led the European Union to abandon programs to develop "fuels from food" and for the U.S. to place more emphasis on bio-fuels that can be produced from saltwater plants. Supporting this effort, NASA Glenn Research Center in Cleveland, OH has initiated a pilot program to investigate, refine, and optimize techniques for growing saltwater algae and halocytes and work with commercial partners on procedures to efficiently convert these plants into biostocks suitable for jet fuel production. Researchers estimate that large-scale production of algae-based bio-jet fuels may commence within the next 10 years.

In tandem with research on sources and manufacturing of alternative aviation fuels, engine and aircraft manufacturers along with the federal government have conducted tests to assess the impact of alternative fuels on engine performance and emissions. Because of its interest in gaining fuel security, stable sources of supply, and emission reductions at bases located within U.S. EPA non-attainment areas, the U.S. Department of Defense (DOD) has taken a lead this work, conducting ground-based and in-flight tests on stand- and wing-mounted military aircraft engines. However, the bulk of these tests have been conducted on older engine technologies, such as those that power helicopters and the B-52 bomber (Corporan et al., 2007), and the results may not be particularly applicable to modern commercial engines. And while engine manufacturers have investigated the effects of alternative fuels on performance and emissions of selected engines, results of the tests are proprietary and thus not available for public use. Clearly, additional alternative fuel tests on modern commercial engines are required to produce an open-access data set that can be used, for example, to guide technology development, refine fuel specifications, and assess environmental impacts.

In addition to uncertainties in alternative fuel impacts, other important questions related to commercial aircraft emissions and their effect on air quality and climate remain unanswered. Through tests conducted during EXCAVATE (Anderson, 2003), the APEX series (i.e., Wey et al., 2007), and UNA-UNA (Lobo, 2008), a fairly good understanding of gas-turbine soot emissions and how they vary with combustor design and thrust setting has been gained. Data gathered in these studies also suggest that sulfur and organic compounds condense very rapidly within aging exhaust plumes to form volatile aerosols or coatings on soot particle surfaces and that the formation of new particles can be suppressed by reducing fuel-sulfur content. However, the fraction of fuel sulfur that is oxidized to sulfuric acid and the exact sources and composition of the volatile organic species are highly uncertain. Data detailing how ambient conditions influence volatile aerosol formation as well as primary pollutant (i.e., soot, hydrocarbons, CO, and NOx) emissions is also scarce. In addition, a recent study shows that airports may be significant sources of hazardous gas-phase air pollutants, such as benzene, formaldehyde, and

naphthalene—very few data are available to assess the aircraft contribution to this potential problem.

The knowledge gap regarding aircraft particle emissions may inhibit expansion and construction of airport facilities in EPA non-attainment areas because the impacts of these activities on local PM2.5 levels cannot be accurately assessed. In an attempt to bridge this gap, the FAA correlated available soot emission data with engine-specific smoke numbers from the ICAO archives to develop a "First Order Approximation" (FOA, Wayson et al. 2007), which provides an estimate of aircraft soot mass emissions at standard engine thrust settings. Terms to estimate the mass of volatile emissions arising from fuel sulfur, unburned hydrocarbons and engine oil have been incorporated in recent FOA versions, but the magnitudes of these contributions are highly speculative, possibly over-conservative, and certainly need to be verified through comparison with careful measurements of aged exhaust plumes sampled under a variety of ambient conditions.

To address the needs outlined above, NASA conducted the Alternative Aviation Fuel Experiment (AAFEX) at NASA Dryden Flight Research Center Aircraft Operations Facility (DAOF) in Palmdale, CA during between January 20 and February 4, 2009. AAFEX used the NASA DC-8 to test the effects of coal- and natural gas-derived FT fuels and ambient conditions on the aircraft's CFM56 engines' emissions and performance. The tests focused on the aircraft's right inboard engine, which was sampled extensively during the spring 2004, NASA-sponsored Aircraft Particle Emission Experiment (APEX-1; see Wey et al., 2007 for details), and thus has a well-documented performance and emission profile. Although the CFM56 is of somewhat older vintage, it is the most widely used engine within the current commercial fleet (almost all B737 use some versions of this engine) and is likely representative of the combustor technology that will be used for at least the next decade. We thus anticipate that the acquired data set will have broad relevance to current studies of air quality and engine technology.

The purpose of this document is to provide an overview of the AAFEX experiment as an introduction to the more detailed reports contributed by the individual investigative groups that are attached as appendices. We describe the test objectives, source aircraft, fuels, test setup, the exhaust sampling system, and ambient conditions. A sample test run is described and a summary of the test schedule provided. We briefly describe the contents of each of the attached appendices and conclude by providing recommendations for future research.

3.00 PROJECT DESCRIPTION

3.01 Project Objectives

The AAFEX science team was established several months ahead of the field deployment, which provided the opportunity for mission objectives and experiment plans to be thoroughly vetted by a panel of experts. After much discussion, the experiment plan was optimized to:

- Evaluate whether and how the alternative fuels affect engine performance or produce any notable degradation of engine or fuel system components
- Determine the effects of alternative fuels and ambient conditions on black carbon and gas phase emission indices (EIs) and characteristics as measured within 1 m of the engine's exhaust plane.

- Establish the composition, origin, and temperature-dependent concentrations and formation rates of the volatile aerosols that condense in the engine's exhaust plume as it ages and mixes with background air; determine how fuel composition influences these processes.
- Establish emission factors for the aircraft's auxiliary power unit (APU) and determine how these factors change with ambient conditions and fuel composition
- Evaluate the performance of new black carbon-measuring instruments relative to that of more proven techniques.
- Compare particle number, size, and mass emission measurements made by separate groups to ascertain the expected range of relative uncertainty in EI values in data sets collected in previous test venues.

3.02 Aircraft Engines and APU

The NASA Dryden DC-8 was used as the AAFEX emissions source. This aircraft was originally built by McDonell Douglas, and NASA purchased it from Eastern Airlines in the mid-1980s to use as a flying laboratory to support Earth science research and satellite validation activities. The aircraft is typically flown < 1000 hrs/year, which means it has a relatively low number of hours on the engines and airframe. The DC-8 is equipped with four CFM56-2C1 gas-turbine engines, which are certified at 22,000 pounds thrust; the nominal operating characteristics of selected CFM56 engines are provided in Table 1.

The DC-8's engines were totally re-built in 2000 when turbine damage was detected after the aircraft flew through a thick cloud of volcanic dust during the SOLVE mission, which was based in Kiruna, Sweden. Emissions from the DC-8's right inboard engine were documented in detail during the spring 2004, NASA Aircraft Particle Emission Experiment (APEX; Wey et al., 2006). Gas phase EIs recorded at 7, 30, 85, and 100% of maximum thrust during APEX were consistent with those archived by ICAO from certification tests, suggesting that the DC-8 engines were operating within the manufacturers specifications and also that ground based tests of this nature can provide broadly representative results.

Table 1. Operating Characteristics of CFM56 Engines

Engine Parameters	CFM56 engine models		
	2-C1	2A-2&3	2-B1
TAKEOFF CONDITIONS (sea level)			
Max. takeoff (lb)	22,000	24,000	22,000
Airflow (lb/sec)	788	817	784
Bypass ratio	6.0	5.9	6.0
IN-FLIGHT PERFORMANCE (installed) (35,000 ft-Mach = 0.80-ISA)			
Max. climb thrust (lb)	5,400	5,760	5,450
Overall pressure ratio at max. climb	31.3	31.8	30.5
Max. cruise thrust (lb)	4,980	5,760	4,970
Cruise SFC (Bucket)(lb/lb hr).	0.671	0.657	0.648

During APEX, the DC-8 engines were run for over 30 hours while the aircraft was in a parked/chocked position without encountering any significant problems. However to prevent

undue stress on the aircraft wings and brakes, runtimes at 85 and 100% thrust were restricted to about 4 and 2 minutes, respectively, and to avoid compressor stalls, power levels were maintained below 40% when winds exceeded 5 mph from directions 90 to 270 degrees off the aircraft heading. These same limitations were in effect during AAFEX.

Sometime after its original manufacture, the DC-8 was retrofitted with a Honeywell Model GTCP85-98CK APU to provide power for stand-alone, ground-based operation. This APU delivers a portion of its compressor (bleed) flow to the combustor and the rest to the aircraft for environmental control, generator operation, engine start, etc. Essentially a low bypass gas-turbine engine, the APU is located in the forward baggage compartment and exhausts out the starboard side, just ahead of the wing spar. It has the following specifications:

- Single can combustor
- Two-stage centrifugal compressor
- Single stage radial inflow turbine
- Bleed air flow: 58 kg/min at 220 °C exhaust gas temperature (EGT) and 0 kW shaft work
- Maximum shaft work: 149.2 kW
- Maximum EGT: 621 °C

The APU draws fuel from the aircraft #2 main tank, which is also the principle supply for the #3 engine. Fuel flow to the APU varies according to the work demands of the aircraft systems and is not a parameter that can be monitored or adjusted by the operator. For this reason, the APU emissions were tested at several different load settings and the emissions was assessed as a function of exhaust gas temperature, which is known to be proportional to fuel air ratio.

3.03 Fuels

Five different fuels were tested during AAFEX: a standard JP-8 (or baseline) fuel obtained from the fuel dump at Dryden Air Force Base; a Fischer-Tropsch (FT) fuel synthesized from natural gas (FT1) by Shell corporation and provided by the Air Force Research Lab (AFRL); an FT fuel prepared from coal by Sasol (FT2), also supplied by AFRL; and 50:50 blends of FT1 and FT2 with JP-8. A 25,000 gal aliquot of the JP-8 was obtained before the mission and stored in on-site tankers so that a single batch of baseline fuel could be used throughout the tests. The FT fuels were shipped to the Dryden Aircraft Operations Facility (DAOF) and stored on-site in rented tankers. DOAF tankers that were subsequently used to store, transfer and blend the fuels were drained and steam cleaned prior to use. A lubricity additive was added to each FT fuel to ensure that their use would not cause any issues with the aircraft or tanker fuel pumps. Fuel samples were drawn from the right inboard-engine drain line before and after each test run and were analyzed for a variety of properties, including sulfur and aromatic content, by the Air Force Research Lab (AFRL), Wright-Patterson fuels lab.

The properties of the five fuels as determined from the AFRL tests are summarized in Table 2; carbon spectra for FT1 and JP-8 fuels are exhibited in Figure 1 to emphasize the significant differences in hydrocarbon composition of the two fuels. Table 2 results indicate that the two FT fuels are essentially sulfur free, the minor amounts of contamination (~20 ppm) probably being introduced from residual JP-8 in the fuel pumps or transfer lines. The FT fuels also contain zero (FT1) or only minor amounts (FT2) of aromatic hydrocarbons, which is reflected in their higher

hydrogen contents and H/C ratios as compared to JP-8. Their low aromatic, olefinic, and long-chain hydrocarbon (i.e., Figure 2) contents also lead the FT fuels to have much lower specific gravities than JP-8. The heats of combustion for the FT fuels are slightly higher (~2%) than for JP-8, but this advantage is offset by the much lower FT fuel specific gravities. The physical and compositional properties of the blended fuels are, to within measurement precision, averages of those for the JP-8 and FT fuels.

Table 2. Fuel Properties

TEST	JP-8	FT1	FT1 Blend	FT2	FT2 Blend
Sulfur (ppm)	1148	19	699	22	658
Aromatics (%vol)	18.6	0	8	0.6	9.1
Distillation, deg C					
IBP	158	157	156	160	158
10%	176	162	166	167	170
20%	184	164	170	170	175
50%	207	170	183	180	190
90%	248	186	232	208	233
EP	273	206	264	231	263
Residue (%vol)	0.8	0.9	1	1	0.8
Loss (%vol)	0.8	0.9	1	0.9	0.9
Flash Point, deg C	46	41	43	42	46
API Gravity	41.9	60.2	50.5	54	47.9
Freezing Point, deg C	-50	-54	-60	<-80	-60
Viscosity, mm^2/s	4.7	2.6	3.3	3.6	4.1
Cetane Index	41	58	46	51	45
H Content (%mass)	13.6	15.5	14.5	15.1	14.3
Naphtalenes (%vol)	1.6	0	0.8	0	0.8
Heat of Combustion (MJ/kg)	43.3	44.4	43.8	44.1	43.8
Olefins (%vol)	0.9	0	0.6	3.8	3.3
Fuel H/C ratio	1.88	2.19	2.02	2.12	1.99
Specific Gravity	0.816	0.738	0.777	0.763	0.789

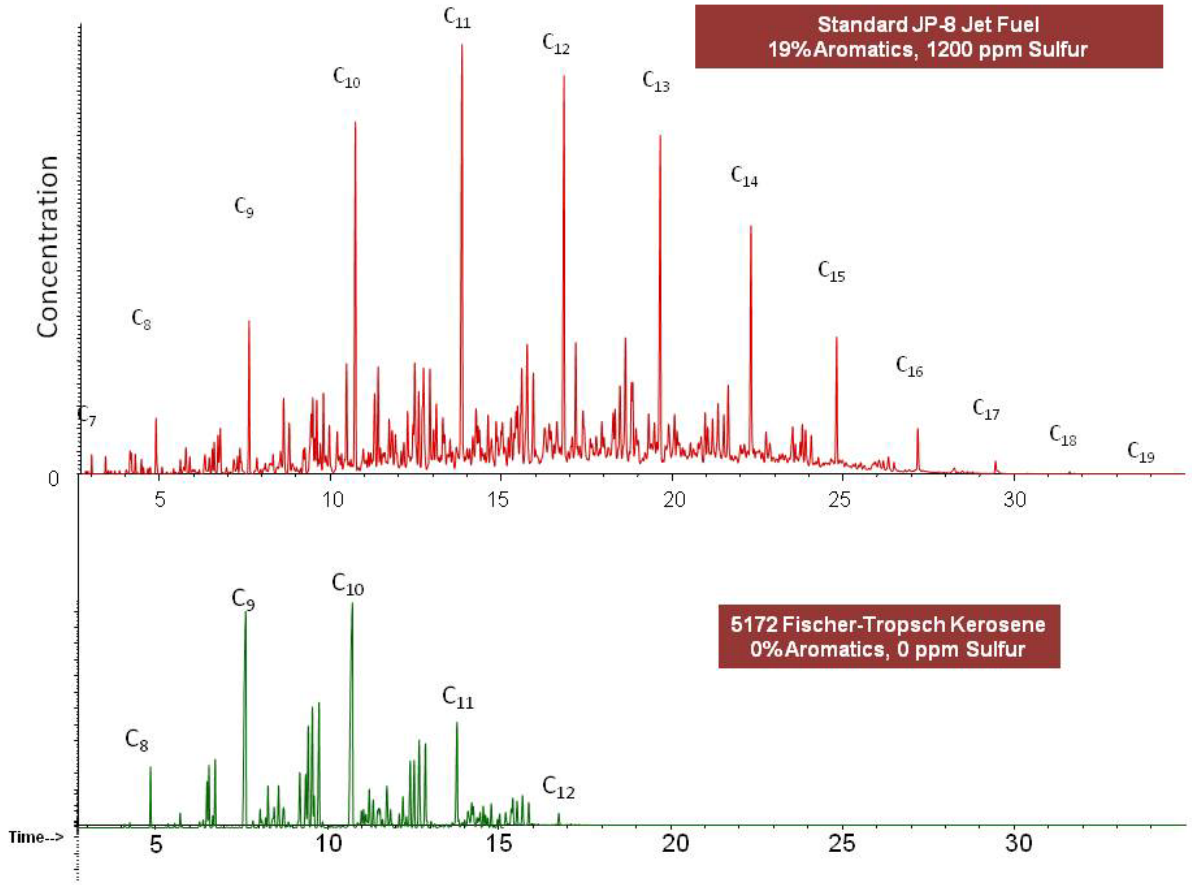

Figure 1 Analysis of standard JP-8 and FT-1, the natural gas fuel that was used during AAFEX.

3.04 Experiment Site

AAFEX was conducted at the Dryden Aircraft Operations Facility (DAOF), which is operated by NASA's Dryden Flight Research Center and is located in Palmdale, Calif., about 70 miles northeast of downtown Los Angeles. The leased facility is adjacent to the Palmdale Regional Airport and consists of 210,000 square feet of hanger space and an equivalent amount of space for offices, labs, conference rooms and storage for spare equipment, flammables, and hazardous chemicals. While some laboratory tests and instrument checkouts were conducted in the hanger, actual engine test runs were performed on the large outdoor aircraft test facility located just north of DOAF, which is accessed via a seldom-used taxiway (Figure 2). This facility was used in previous years for conducting on-wing tests of military aircraft engines; it is at least 300 m and typically cross-wind from the access road and parking lot, so that automobile pollution and exhaust from other aircraft is not a problem for emission characterization studies. The concrete staging area associated with the facility is approximately 150 m wide by 300 m long and is equipped with three sets of office buildings/control rooms along with stadium-style lighting, water hydrants, and a variety of power outlets.

Figure 2. Aerial photograph of the NASA DAOF Hanger and engine run-up area at the Palmdale Regional Airport.

3.05 Participants

Table 3 lists the principle investigators and consultants that contributed either measurements or analysis support to AAFEX. These participants were supported by NASA (AEDC, DFRC, LaRC, GRC, Penn State, and UTRC); FAA (ARI, MST, MSU); U. S. Air Force (WPAFB) or their own parent organizations (Boeing, EPA, GE, and Pratt and Whitney).

Table 3. AAFEX Participants

Organization	POC	Role
AEDC	Robert Howard Robert.Howard@arnold.af.mil	Project Engineer, Sampling probes and heated lines; Smoke Number
ARI	Rick Miake-Lye rick@aerodyne.com	NOx, CO, Hydrocarbons, aerosol composition, BC mass
Boeing	Steve Baughcum Steven.L.Baughcum@boeing.com	Science advisor, observer
Carnegie Mellon University	Allen Robinson alr@andrew.cmu.edu	Hydrocarbon volatility and speciation
EPA	John Kinsey kinsey.john@epamail.epa.gov	Aerosol Mass and Composition
GE	Willard Dodds Willard.Dodds@ae.ge.com	Engine Performance/Operation Advisor
Missouri S&T	Phil Whitefield pwhite@mst.edu	Aerosol Physical Properties
Montana State U	Berk Knighton Knighton@msu.edu	Speciated Hydrocarbons
NASA DFRC	Frank Cutler frank.w.cutler@nasa.gov	Aircraft Operations
NASA GRC	Changlie Wey changlie.wey@nasa.gov	Certification gases, SO2, O2, H2O, NMHCs; Black Carbon
NASA GRC	Dan Bulzan Dan.L.Bulzan@nasa.gov	Project Manager, Test Conductor
NASA LaRC	Bruce Anderson bruce.e.anderson@nasa.gov	Project Scientist, Bulk Aerosol Composition/Physical Properties, Black Carbon Mass
Penn State U	Randy Vander Wal	Black Carbon Morphology and Composition
Pratt and Whitney	Anuj Bhargava anuj.bargava@pw.utc.com	Science advisor, instrument/group inter-comparison lead
U. California San Diego	Terri Jackson tjackson@ucsd.edu	Sulfate Aerosol Isotopes
UTRC	David Liscinsky LiscinDS@utrc.utc.com	Aerosol Physical Properties; instrument comparisons
AFRL/WPAFB	Edwin Corporan edwin.coporan@wpafb.af.mil	Aerosol Physical Properties, BC Mass, Smoke Number, PAH

Notes: AEDC=Arnold Engineering Development Center, Tullahoma, TN; ARI=Aerodyne Research, Inc., Bedford MA; AFRL=Air Force Research Lab at Wright Patterson AFB, OH; EPA=U.S. Environmental Protection Agency at Research Triangle Park, NC; GE=General Electric Commercial Aircraft Engines, Cincinnati, OH; MST=Missouri University for Science and Technology, Rolla MO; DFRC=Dryden Flight Research Center; GRC= Glenn Research

Center; LaRC=Langley Research Center; Pratt and Whitney Commercial Engines, East Hartford, CT; UTRC=United Technologies Research Center, East Hartford, CT.

Primary project leadership was provided by Bruce Anderson (science), Robert Howard (engineering), Dan Bulzan (management), and Frank Cutler (aircraft operations). However, the final objectives, experiment plan, and operational procedures were established in consultation with science team members, project stakeholders, and the aircraft support team. Input from GE and Boeing was particularly valuable in test planning, as these companies provided proprietary information on engine, fuel, and airframe issues and helped to define engine-operating parameters for the alternative fuels and for changing ambient conditions. The contributions of many other groups were critical to the success of AAFEX: AEDC designed, constructed and installed the 1-m aerosol and gas sampling probes and rakes and the 30-m instrument enclosure; Missouri University for Science and Technology (MST) designed, constructed, installed, and operated the sample selection system; WPAFB supplied the FT fuels and performed the post-mission fuel analyses; and the DC-8 ground crew, headed by Mike Bereda, provided timely and enthusiastic support in installing the sampling systems and operating the aircraft engines during the extensive test runs.

AAFEX investigators included groups that had participated in EXCAVATE (Anderson et al., 2003), APEX-1 (Wey et al., 2007), APEX-2, APEX-3, the PW308 alternative fuel experiment and a variety of other previous engine emissions tests. Their participation guaranteed that the emissions would be thoroughly characterized and documented. However, note that AFRL, MST, NASA LaRC, and the United Technologies Research Center (UTRC) provided similar measurements of particle number and size, while ARI, LaRC, and UTRC use the same techniques to measure BC mass. This overlap provided an opportunity to inter-compare measurement results and to help establish the expected range of uncertainty between data sets collected by the individual investigators in separate test programs.

3.06 Measurements

A comprehensive suite of measurements was required to address the very challenging objectives outlined in section 3.01. Listed in tables 4 and 5, these included detailed measurements of gas and aerosol parameters on samples drawn from inlets placed at 1, 30 and 145 m behind the aircraft engines as well as onboard the Aerodyne Research, Inc (ARI) mobile laboratory as it profiled the engine plumes during a number of low power engine tests. The measurements are divided into those linked to specific fixed sites or moving vehicles (Table 4) and ones made on the common aerosol sampling manifold and 1-m gas sampling probes (Table 5). Table 4 also lists a variety of ancillary measurements, which were needed to establish links between engine thrust and emission characteristics, to elucidate plume dynamics, and to evaluate the impact of alternative fuels on engine performance. Key among these was the aircraft operating parameters. To acquire these data and because the aircraft avionics lacked digital outputs, the test conductor sat in a jump seat behind the aircraft operator, read the analog displays, mentally averaged values during stable operating periods, and manually recorded the key parameters during each of the 411 test points conducted during AAFEX. The resulting data set includes for each engine: fan speed (N1), core speed (N2), fuel flow rate (WF), and exhaust gas temperature (EGT). Similarly, APU EGT was recorded during the fuel tests involving that emission source. Ambient temperature and pressure data provided by a portable weather station erected and operated

continuously at the site were used to correct N1, N2 and WF to standard day conditions. The weather station additionally logged relative humidity and wind speed/direction; this information was relayed through wireless transmission to the DC-8 cockpit and where it was both hand-recorded by the test conductor and used in real time by the aircraft operators to determine whether crosswinds exceeded the range for safe engine operation. Other ancillary measurements included temperature and pressure on the left and right 1-m rakes and the right 30-m sampling inlet and temperature and winds on the ARI van. These data were subsequently used to calculate plume mach number and velocity as a function of downstream distance from the engine exit planes.

A variety of detailed aerosol and gas phase measurements were performed on samples collected using individual sampling probes/inlets. Carnegie Mellon University (CMU) used a large-bore probe mounted on the R1 stand to collect sample on filters for offline determination of organic compounds using a technique that involves slowing ramping the sample temperature and identifying the evaporating compounds using a GC/MS system. The resulting data can be coupled with a model to predict the partitioning of the VOCs between the gas and aerosol phase at any prescribed plume age and ambient condition. UCSD used the nearby "button-hook" probe (see section 3.08) to supply exhaust flow to a high-volume sampler to collect quartz-fiber filters for sulfur isotope analysis, with the hope that sulfate formed from fuel sulfur contaminants would have distinctly different isotopic ratios than background aerosols and thus be a powerful tool for delineating aircraft from other sulfate aerosol sources in complex urban airsheds.

As in APEX-1, 2 and 3, the U.S. EPA approached AAFEX as an opportunity to establish engine emission profiles for dilute exhaust plumes as a function of engine power, ambient conditions and, this time, fuel composition. To address this objective, they made measurements exclusively on samples collected using a matched pair of inlets/sampling lines positioned 30 m behind the #2 and #3 engine exit planes (see section 3.08 for details). Their instrument suite included capability for determining particle number, size, total mass, black carbon mass and sulfate aerosol mass.

To investigate sample line effects and plume chemistry or to provide longer integration times for slower responding sensors, small suites of instruments were set up to make continuous measurements on the R30 and R145 inlets and inside the UTRC deathbox. A primary focus was measurements aerosol number and size, since these are useful indicators of particle formation and growth. Black carbon was also measured on R30 and R145 samples to provide a second means (other than CO_2) of normalizing plume dilution. Filter samples for isotopic analysis were collected as were data from a portable CCN counter, the latter to examine how the solubility of the soot particles varied with power, fuel composition, and plume age. A pair of Particle-Into-Liquid Samplers (PILS) attached to a total organic carbon (TOC) analyzer and liquid sample collection drew sample from R30 to provide 4-min resolution measurements of water-soluble organic carbon and ion species concentration, respectively. Instruments to determine aerosol volatility, hygroscopic properties and sulfate aerosol loading were additionally deployed to sample from R145. Gas phase measurements were also emphasized at this location, in particular those of methane isotopes and species such as HONO and H_2O_2 that are important for characterizing oxidative processes in the engine exhaust plume. The UTRC EEPS was the critical instrument inside the deathbox: its output was compared to an identical instrument

located in the NASA truck to investigate the impact that long sample-line residence times on aerosol number, size and total volume.

As mentioned in section 3.08, the ARI van had a portable power source and was often disconnected from the primary aerosol sampling manifold during extended ground-idle operation periods to profile the chemical and aerosol characteristics of the right engine exhaust plume as a function of distance behind the aircraft. On a few occasions, the van was parked >0.5 km downwind of the aircraft to sample the aged plume at high engine thrust levels during JP-8 runs. The van carried a comprehensive suite of chemical and aerosol sensors that included a single particle aerosol mass spectrometer (AMS) to determine volatile aerosol composition, a proton-transfer reaction mass spectrometer for non-methane hydrocarbons, and a tuneable diode laser spectrometer for CO, formaldehyde and other tracer species. The van payload was, at times, supplemented with the UTRC EEPS to provide more detailed information on particle formation and growth in the expanding/cooling plume. The van instruments were connected to an external inlet through a short length of sample line so that the resulting measurements were relatively free of sampling-system induced biases. Thus the van's measurements were also valuable in establishing the effects of line losses and chemistry on observations recorded on samples drawn through much longer lengths of tubing.

Table 4. Measurements made at individual locations, single probes or on moving vehicles.

Location/sample	Parameter	Instrument	Group
Aircraft	N1, N2, Fuel Flows, EGT	Cockpit Displays	NASA
Experiment Site	T, P, winds, humidity	Weather station	NASA
1 m Rakes	Temperature	Thermocouple	AEDC
	Total Pressure	Pressure Transducer	AEDC
	Volatile Organics	Filter/offline analysis	CMU
	Sulfate Isotopes	Filter/offline analysis	UCSD
30 m EPA inlets	Particle Number, Size	CPC, SMPS, APS	EPA
	Aerosol Mass	QCM	EPA
	Sulfate Mass	TECO Sulfate Analyzer	EPA
	Black Carbon	MAAP	EPA
	Surface PAH	PAS 2000	EPA
	SO_2	Pulsed Fluorescence	EPA
	CO_2	NDIR	EPA
Right 30-m Probe and Deathbox	T, dP	Thermocouple, pitot tube	NASA
	Particle Number, Size	CPC, EEPS	UTRC, NASA
	Sulfate Isotopes	Filter/offline analysis	UCSD
	Black Carbon	EC/OC	NASA
	Cloud Condensation Nuclei	DMT CCN	NASA
	Bulk Aerosol Composition	PILS/TOC, PILS/IC	NASA
	CO_2	NDIR	NASA
145 m inlet	Particle Number, Size	CPC, SMPS, DMS-500, OPC	NASA, UTRC, MST
	Nonvolatile Number, Size	CPC, SMPS, OPC	NASA, UTRC
	Black Carbon	MAAP	UTRC
	Sulfate Mass	TECO Sulfate Analyzer	NASA
	Cloud Condensation Nuclei	DMT CCN	NASA
	Particle Hygroscopicity	SMPS/Humidifier	MST
	Sulfate Isotopes	Filter/offline analysis	UCSD
	CO_2	NDIR	ARI
	HONO, HOHO, CH_4	TILDAS	ARI/Harvard
Aerodyne Van	T, P, winds, humidity	weather station	ARI
	Particle Number, Size	CPC, SMPS, EEPS	ARI, UTRC
	Black Carbon	MAAP	ARI
	Single Particle Composition	AMS	ARI
	CO_2	NDIR	MST
	CO, NO, NO_2, O_3, etc.	TILDAS, TECO	ARI
	Hydrocarbons, HAPS	PTRMS	ARI/MSU

Table 5 measurements were recorded by instruments located in the equipment trailers parked off the aircraft's right wing from exhaust samples drawn through sampling systems depicted in Figures 3 and 4. On the gas lines, certification gas measurements (NOx, CO, CO2, and THC) were made using ICAO accepted sampling techniques and instruments; these were important for evaluating engine operation and establishing how emissions changed with fuel composition and ambient conditions. The sulfur dioxide and O_2 measurements were included to allow real-time fuel sulfur content and fuel-air-ratio determinations. Fourier-transform, infrared spectrometer-type, multi-gas analyzers provided additional information on speciated hydrocarbon concentrations, whereas smoke numbers were determined by both AEDC and AFRL using conventional sample collection and analysis techniques. Total aerosol and black carbon masses were measured in the more concentrated samples using a tapered-element oscillating microbalance (TEOM) and laser-induced incandescence instrument, respectively. Polyaromatic hydrocarbon (PAH) concentrations were assayed using the conventional filter-collection/extractive analysis method well as with an online instrument that purports to measure surface bound PAH using an UV ionization/electrometer technique (ECO 2000).

The most comprehensive set of gas-phase and aerosol measurements were made on samples provided by the "aerosol" sampling system. These included multiple determinations of particle number, size, and black carbon content as well as unique measurements of particle composition, PAH content, surface area, and black carbon morphology. Note that several BC sensing instruments were deployed, mainly to determine whether they are straightforward to use, provide reliable and consistent data, and are insensitive to changes in soot morphology and coatings. The Multi-Angle Aerosol Absorption Photometer (MAAP) instrument was the primary black carbon standard as it was specified for use in characterizing BC emission from Joint-Strike Fighter engines (PW135) by the "Interim Test Method," which has subsequently been approved by the EPA as a substitute for "Method 5" determinations of aircraft particle emissions.

However, the MAAP calibration is not well established for aircraft emissions and its response is known to vary as particles accumulate surface coatings. AAFEX measurements at multiple sampling distances allowed us to determine the severity of this problem and to evaluate whether any of the new instruments yielded better results. Three different types of instruments were also used to establish particle size distributions: SMPS, EEPS and DMS-500. In this case, the SMPS was assumed to be the "standard" while the EEPS and DMS-500 instruments were used to provide fast response measurements for the exhaust mapping and plume chemistry experiments.

Table 5. Measurements made on multi-source sampling manifolds.

Sample Line	Parameter	Instrument	Group
Aerosol (1R, 1L, 30R, 30L)	Dilution flow, sample pressure	Misc.	MST
	Particle Number, Size	CPC, SMPS, EEPS, DMS	AFRL, MST, NASA, UTRC
	Nonvolatile Number, Size	Heated CPC, SMPS	MST, NASA
	Black Carbon Mass	MAAP	ARI, NASA, UTRC
		EC/OC	NASA
		PASS-3	NASA
	Black Carbon Morphology	Electron Microscope	Penn State
	Surface PAH	PAS 2000	AFRL, NASA
	Single Particle Composition	AMS	ARI
	Cloud Condensation Nuclei	CCN counter	NASA
	Surface Area	TSI EAD	NASA
	CO2	NDIR	AFRL, ARI, MST, NASA, Navy
	CO, NO, NO2, etc.	TILDAS	ARI
	Hydrocarbons, HAPS	PTRMS	ARI/MSU
Gas (1L, 1R)	CO2, CO, NOx, THC, SO2, O2	Conventional Gas Analyzers	NASA
	Certification Gases, NMHCs	MGA	AFRL, NASA
	Smoke Number	Filter, reflectance meter	AFRL
	Particle Mass	TEOM	AFRL
	PAH	Filter/offline analysis; ECO 2000	AFRL
	Black Carbon Mass	EC/OC	AFRL
		Artium LII	NASA

3.07 Site Layout

Figure 3 is an aerial photograph of the test site taken on January 30, during the middle of the mission. During initial setup, the aircraft was parked and chocked on the western edge of the B-1 bomber test area (see Figure 2 for a large-scale view), facing into the prevailing winds. Afterward, the equipment vehicles were driven onto the ramp and carefully positioned off the aircraft's right wingtip to minimize sampling line lengths between the diagnostic instruments and the right inboard engine.

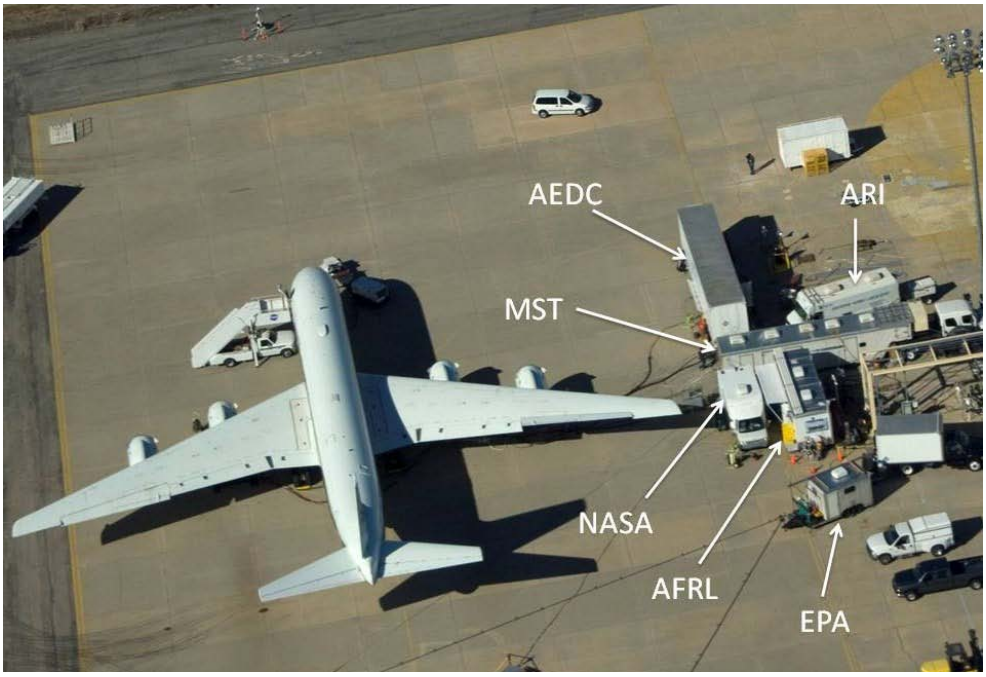

Figure 3. Aerial photograph of the experiment site with the equipment trailers for each of the participating groups indicated. Note the portable weather station located ~50 m ahead of the aircraft, on the far edge of the pad. Photo taken on January 30, 2009 by the DC-8 pilots while flying the DFRC King Air.

The aerosol sample selection box and sample dilution controls were located in the MST trailer, hence it was positioned on a line extending perpendicular from the inboard engine exhaust plane; the other trailers were arranged to either side of the MST trailer to minimize the lengths of tubing connecting the individual investigator's aerosol instruments to the common sampling manifold (see section 3.08 below). Similarly, the primary gas-phase monitoring instruments were located in the AEDC trailer, thus it was situated so as to minimize the gas sample line lengths.

Power was supplied to the trailers from 440 VAC, 3-phase outlets and a bank of 120 VAC outlets located on the superstructure of bomber test station 1 (Figure 2). A portable "skid" was supplied by the USEPA to divide the 3-phase power into the single-phase, 208 VAC needed by many of the experimenters (i.e., NASA, MST, AFRL, and ARI). Water for cooling the 1-m sampling rakes was obtained from a high-pressure outlet also located on the test pad. A wireless weather station was erected on the edge of the ramp, upwind of the aircraft to monitor wind direction and other meteorological parameters. For convenience, portable toilets were installed behind the row of vehicles. Light for nighttime operations was provided by banks of "stadium" lights located along the north edge of the test area. Communications between the aircraft and equipment shelters was provided by a wired, centrally located intercom system provided by Missouri University for Science and Technology. One person in each group was required to wear a headset during the tests so that changes in the test plan or notification of emergency situations could be quickly communicated.

3.08 Sample Probes and Inlets

To prevent placing excessive torque on the DC-8 airframe, both inboard engines are operated at approximately the same fuel flow rates at all times. Thus, under the assumption that both engines exhibited approximately the same emission characteristics and taking advantage of the independent fuel delivery systems onboard the plane, it was possible to burn a baseline fuel (standard JP-8) in the non-test engine and sample its exhaust periodically to assess the effects of changing ambient conditions on emissions characteristics and to provide a "calibration" standard for judging alternative fuel impacts on the exhaust composition of the test engine. Figure 4 provides a coarse schematic of the sampling system that was installed behind the DC-8 to facilitate this test procedure. Important components included: four sample inlet rakes/probes that were bolted to the concrete pad at 1 and 30 m behind each engine; fire valve boxes that were used to select sample from the different probe tips on the 1-m rakes; a sample selection valve box located in the MST trailer; and various lengths of tubing that transported sample to diagnostic instruments located in experimenter trailers.

The multi-probed sample inlet rakes were the most complex and costly elements of the sampling system. Shown in Figures 5 and 6, these were positioned behind each of the two inboard engines, about 10 cm off the center lines (to avoid drawing sample from the crankcase vent) and within 1 exhaust diameter downstream of the exhaust plane. Both rakes contained vertical arrays of gas and aerosol probes mounted in alternate slots on 3.2 cm spacing. The left (#2) engine rake (L1, Figure 5), identical to those deployed during APEX-1, was mounted at a 45^{o} angle to provide additional clearance below the engine-mounting pylon. The L1 rake stand was bolted to the tarmac so that the probes were about 4 inches off the centerline and 1 m downstream of the crankcase vent tube. L1 was populated with water-cooled inlet probes (Figure 7) and sensors of the style used during APEX-1 (Wey et al., 2006); these were designed by Robert Hiers and Robert Howard of the Air Force's Arnold Engineering Development Center (AEDC) for use in sampling emissions from military aircraft engines.

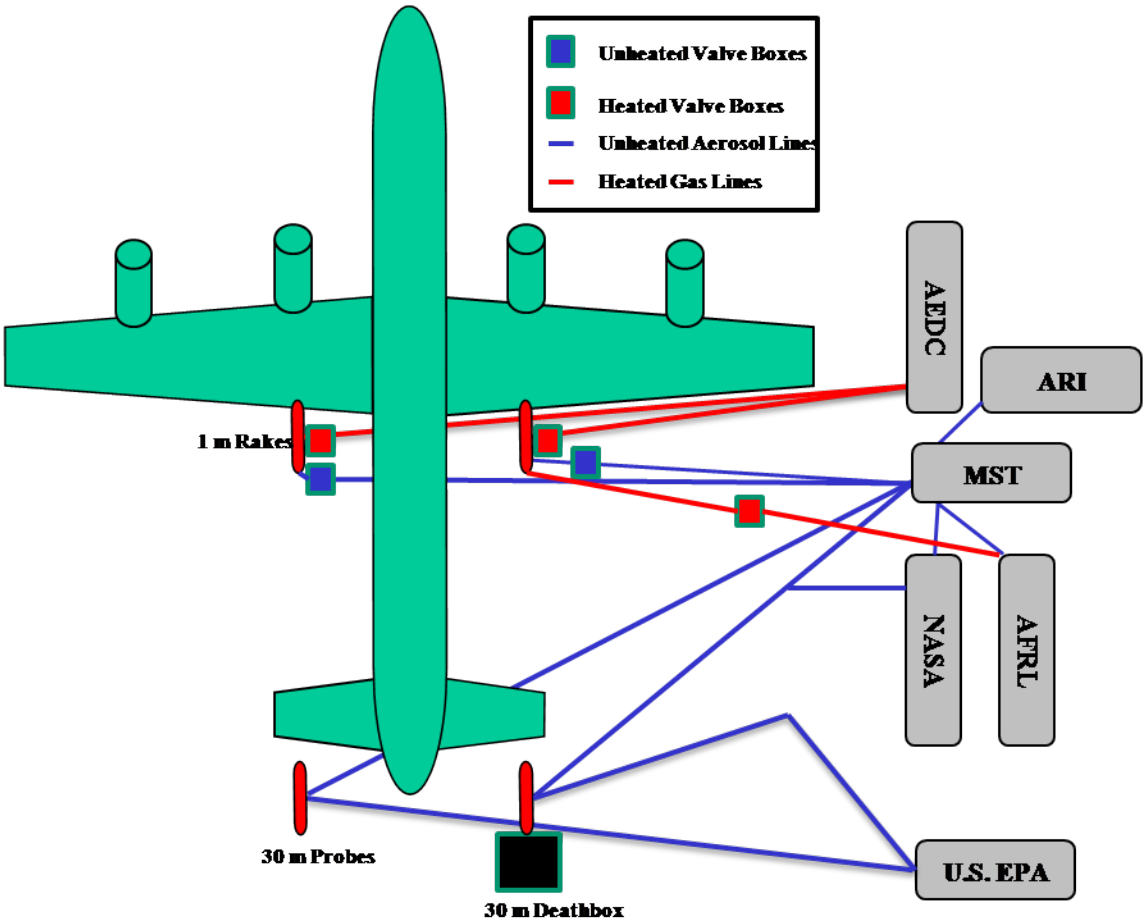

Figure 4. Diagram of the near-field gas and aerosol sampling systems. The heated gas sample transport tubes are indicated in red, the unheated aerosol in blue.

The inset in Figure 5 shows the L1 probe/sensor layout, with a thermocouple mounted in the top slot, followed in descending order by two particle probes, four gas probes, two more particle probes, a fifth gas probe, a second thermocouple and a ram pressure tap. The particle probes were designed to allow introduction of a concentric flow of dilution gas just downstream of the tip (see Figure 7) to prevent water and volatile aerosol condensation and suppress particle coagulation processes within the sample flow. The aerosol probes have 1-mm inlet diameters and the flow is gradually expanded into 8.5-mm or 9.5-mm O.D. tubing downstream of the dilution zone. The "gas" probes have 1.27-mm diameter tip openings, which rapidly expands to the internal diameter of thin-walled tubing a few inches back from the inlet tip. The probes and rakes are constructed from 316 Stainless Steel and were found to maintain integrity throughout the many hours of testing conducted during APEX-1. Subsequent tests have shown that the aerosol probes transmit particles with 80% or better efficiency over the size range (10 to 300 nm) typically associated with aircraft particle emissions. The gas probes were installed in positions near the engine centerline with the intent of collecting samples of essentially identical composition for analysis by the two gas-phase measurement groups (NASA and AFRL). The four particle probes were connected to a valve box and were alternately sampled during the exhaust mapping experiment to examine the variability of emission parameters across the #2 engine exit plane.

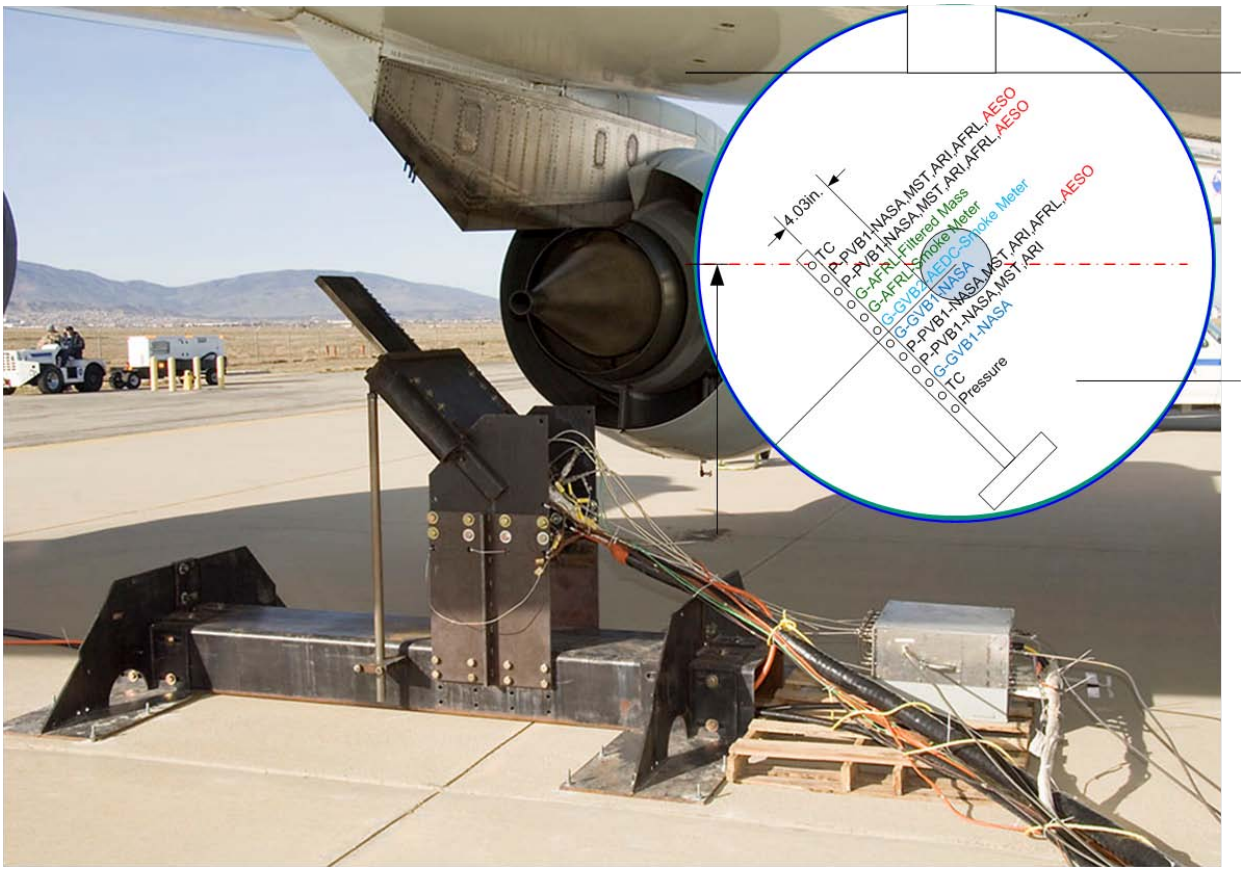

Figure 5. Sampling stand and inlet rake used behind the left inboard (#2) engine; inset shows arrangement of gas (G) and particle (P) probes and sensors (thermocouple and pressure tap) in the water-cooled rake.

The more complex right engine rake (R1) was developed by AEDC with support from the Strategic Environmental Research and Development Program (SERDP) for use in characterizing emissions from the Joint-Strike Fighter, a military aircraft with afterburner capability. Pictured in Figure 6, this rake has a very small frontal profile (i.e., low drag) and was mounted on a traversing table, which made it possible to move the rake in discrete horizontal increments across the exhaust plane to examine crank-case emissions emanating from the center vent tube as well as to establish the variability of emission parameters across the breadth of the engine.
A close-up photograph and probe/sensor placement diagram for R1 is shown in Figure 8. The R1 rake body had multiple channels in the leading edge to allow circulation of cooling water. Note that R1 supported eight gas probes and six dilution probes, with the gas probes being divided between NASA, AFRL and ARI. The R1 probes were internally similar to the L1 probes, but lacked outer jackets for cooling water circulation. A vertical bar was attached to the translation stage just outboard of R1 to support three additional large-diameter, "gas"-type inlet probes. These were used to supply high flows of undiluted air directly to the UCSD and CMU teams for filter sample collection.

Figure 6. The traversing rake (R1) used to sample emissions behind the right inboard (#3) engine.

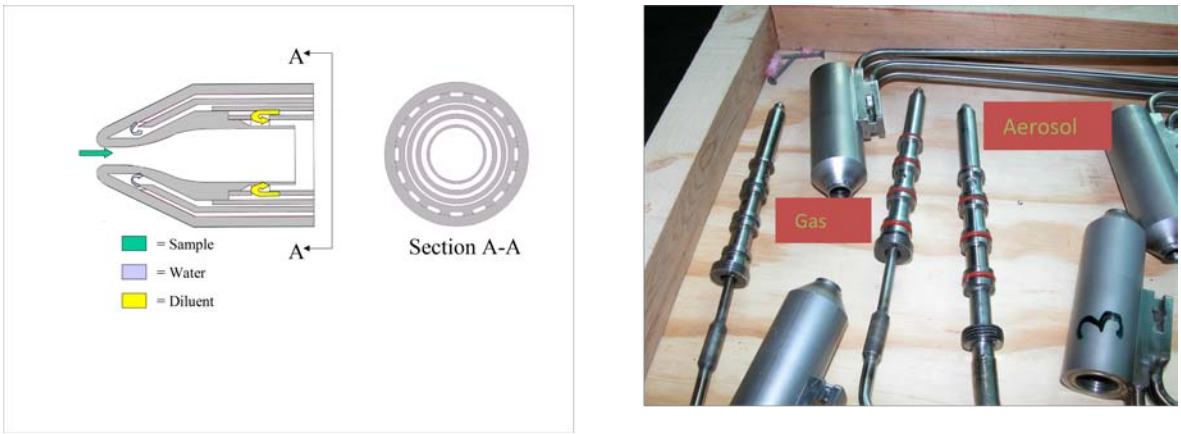

Figure 7. At left, cross-sectional diagram of AEDC dilution probe showing the sample, water and diluents flow paths around the inlet tip. APEX-1 style gas and aerosol inlet probes used in L1 shown at right.

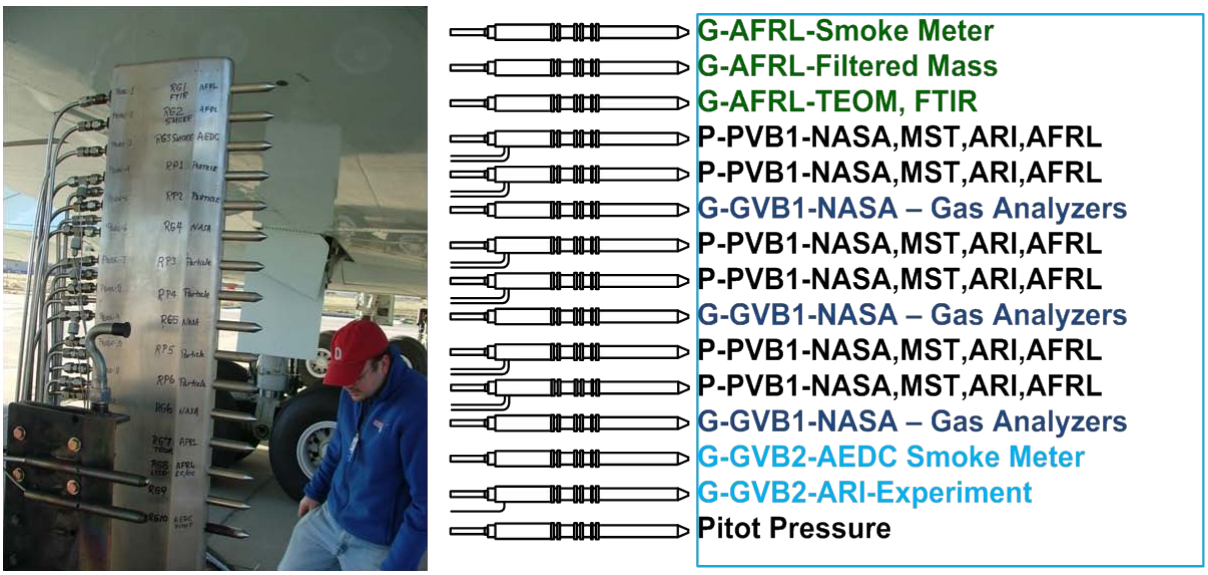

Figure 8. Closeup of R1 showing the "button-hook" and two, large-diameter inlet probes mounted adjacent to the multi-probe rake in the lower left-hand corner. The diagram at right shows the placement of gas (G) and particle (P) probes in the primary rake.

Thermocouples were affixed to the outside of R1 to record exhaust gas temperatures; impact pressure was measured on the R1 pitot tube as well as on the individual gas probes when they were valved-off from the sample flow line. These data were used to estimate plume velocity and, in conjunction with co-located CO2 measurements, to determine which of the probes were located within the core flow exhaust flow. The R1 traversing stand was bolted to the tarmac such that the probe tips were about 1 m behind the center-body of the engine—this gave more than 30 cm clearance between the top of the rake and the lowest point of the engine-mounting pylon.

Figure 9. At left, the identical inlet probes and tripod stands used to sample exhaust emissions at 30-m behind the DC-8's #2 and #3 engines. The image at right shows the 1.9- and 5-cm inlet tubes used to deliver sample to the community aerosol sample manifold and EPA trailer, respectively.

Pictured in Figure 9, the left and right 30-m sample inlets, L30 and R30 respectively, were attached to heavy-duty steel tripods, which were in turn bolted to the concrete pad using lag screws and lead anchors. Two separate inlets were used on each stand: the EPA inlet which was constructed of 5-cm diameter stainless steel sanitary tubing and the community aerosol inlet, which used 1.9-cm seamless, electro-polished, stainless steel tubing. Because R30 was used to sample emissions from the primary test engine, it was instrumented with a pitot tube and a thermocouple to allow determination of plume velocity and temperature. It also was equipped with a port for introducing of dry N2 dilution gas near the probe tip to investigate sample line chemistry, moreover to address the question of whether a majority of the volatile aerosol mass forms during sample transport through the long sample lines.

Figure 4 shows the layout of the gas and aerosol sample transport systems. As can be seen in the diagrams of Figures 5 and 6, separate gas inlet probes were used to supply sample to NASA and AFRL instruments. The NASA probes on the 1-m rakes were connected with 2-3 m long, insulated 6.3-mm stainless tubing to heated valve boxes located at the base of the stands; the boxes were designed to force a small amount of purge gas out of each non-selected probe tip. Sample flow from the two valve boxes was transported through heated 9.5-mm stainless temptrace tubing to heated sample selection valves located ~1-m from the diagnostic instruments housed in the AEDC trailer. Total line lengths for the L1 and R1 sampling probes were less than the 70-ft limit specified for ICAO certification tests. Flow from the AFRL sampling probes was transported through 6.3-mm stainless temptrace line to a 6-port, heated valve box located near the Aircraft's right wing tip, then through additional 6.3-mm heated lines to gas and aerosol sensors located in the AFRL trailer.

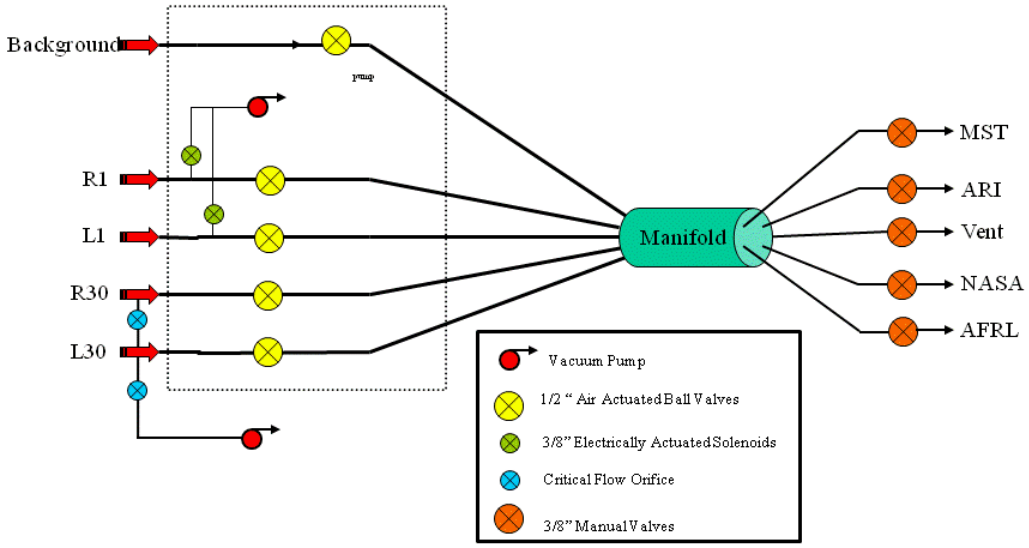

Figure 10. Aerosol selection and distribution system located in the MST trailer. Critical flow orifices were teed off the 30-m sampling lines and plumbed to a vacuum pump to draw a continuous flow through the lines to reduce stagnation problems and the time necessary to establish equilibrium concentrations.

Exhaust air collected using L1 and R1 particle probes was transported through 2 to 3 m of 9.5-mm stainless tubing to unheated, 6-port valve boxes located at the base of the rake stands. These boxes also directed dilution air to the individual probes through 6.3-mm stainless tubing and contained bypass flow valves, which delivered purge-gas flow to the probe tips that were not in use. Sample flow from the two 6-port valve boxes was transported through 1.9-cm stainless tubing to a multiport automated sampling manifold located in rear of the MST trailer (Figure 10). Overall transport tubing lengths were about 40 m for the #2 engine and 23 m for #3; this yielded sample residence times that, depending on sample line pressure and dilution flow rates, varied from about 5 to 15 seconds. The 30-m community inlets were connected to the sample manifold using a combination of unheated 1.9-cm stainless and 1.9-cm, conductive PTFE tubing; the lines were attached to the concrete pad in areas where it passed beneath the engine plume with adel clamps and lead anchors. Transport line lengths for L30 and R30 were 46 m and 38 m, which resulted in nominal sample residence times of 12 to 20 seconds. The 30-m EPA inlets were connected with 5-cm diameter stainless steel, sanitary tubing to an electrically-actuated selection valve located just outside the group's trailer. A high volume (1.1 m^3/min) of sample was drawn through the selected inlet using a Roots blower attached to the terminal end of the sample line; a 9.5-cm stainless tube inserted into the 5-cm sanitary tubing just ahead of the blower was used to deliver sample flow to the EPA instrument suite.

All lines, valves, and inlet probes were thoroughly cleaned and inspected prior to use. Pressure and vacuum leak checks were performed on both the gas and aerosol systems with the goal of reducing the leakage rate to < 0.1% of total flow. In addition, integrity of the aerosol transport system was checked by placing High Efficiency Particulate Air (HEPA) filters on the inlet probes and counting the number of particles in flow drawn from the downstream manifold; values <10 cm^{-3} are generally acceptable, assuming ambient counts are on the order of 10^4 cm^{-3}.

3.09 Downstream Sampling

To study the effects of sampling lines on volatile aerosol formation and nonvolatile aerosol characteristics, instruments were placed in a sturdy enclosure that was bolted to the tarmac immediately behind R30. Nicknamed the "death box" because of its precarious position within the engine exhaust plume, the enclosure shown in Figure 11 was designed and constructed by AEDC and consisted of a 5-cm aluminum angle framework with 6.3-mm aluminum sides and top. Its components were screwed together with ¼-20 bolts spaced about 20-cm apart on the top and sides. Lock washers were installed on the bolts after many of those holding down the top backed out and were blown down the tarmac during the initial engine tests. The Deathbox instruments (see Table 3) drew samples through a 1-m long, 9.5-mm diameter stainless tube that faced forward and was affixed to the side of R30. Power cables and RS232 signal wires were run out to the box from the NASA truck; data from the instruments were monitored and recorded by an operator sitting in this location.

Figure 11. R30 with the "Death-box" instrument enclosure bolted to the tarmac immediately downstream.

Figure 12 shows that trailers and inlets that were set up about 145 m behind the DC-8 engine exhaust plane to examine the composition of engine exhaust as it further aged and mixed with background air. The trailer shown on the right of the figure was supplied by MST and contained gas phase instruments fielded by ARI and Harvard; the left-hand "toy-hauler" trailer was provided by NASA Dryden and used to house aerosol instruments operated by MST, NASA, and UTRC. Aerosol samples were collected from the exhaust plume using a 5-cm sanitary-pipe inlet provided by the EPA. A small blower was attached to the distal end of the 5-cm stainless-steel line to draw a continuous flow of sample through a section of tubing positioned just below the toy-hauler window that contained a number of 9.5-mm Swagelok fittings for withdrawing samples from the primary flow. Short lengths of 9.5-mm or 13.2-mm OD stainless tubing were connected to the fittings and used to deliver sample to the suite of aerosol instruments (see Table 4 for a list) housed in the toy-hauler and to a small set of conventional gas analyzers located in the other trailer. A separate inlet was used to collect gas samples for the more sensitive, Harvard/ARI diode-laser spectrometer instruments. Shown in the inset within Figure 12, this

probe was designed to deliver calibration gases near the inlet tip and to reduce sample pressure to better preserve reactive gas species such as HONO and H_2O_2 during transport through the long sampling lines.

Figure 12. Downstream equipment trailers with the 145-m inlet shown in the foreground and inset photo.

Additional downstream exhaust composition measurements were made during a number of the engine tests using the ARI mobile laboratory. Shown in Figure 13, the lab drew air samples through a 1.9-cm Swagelok chassis fitting mounted just above the windshield on the driver's side. Power was supplied power by a portable diesel generator hitched behind the van. Carrying the instruments listed in Table 3, the van was de-coupled from the main aerosol sampling system during the "intermission" idle runs and used to perform a series of plume penetrations starting as far down stream as possible and gradually closing to within a few meters behind L30 and R30. The van operators were careful to avoid sampling the van and generator exhaust plumes and were required to move the van out of the near-field exhaust plume once the high-engine-power testing resumed.

Figure 13. ARI mobile laboratory with diesel generator hitched to the back.

3.10 APU Sampling

As described above, the APU is located in the forward baggage compartment and is essentially a small, low-technology, gas-turbine engine. When powered, its exhaust is mixed with bleed air and blown out through a shuttered port on the starboard side of the aircraft, just ahead of the wing spar. The APU exhaust duct is angled downward so that the blast hits the tarmac about 10 m out from the aircraft fuselage. The inlet probes shown in Figure 14 take this into consideration and were designed and positioned to collect sample in the center of the exhaust plume. As can be seen in the photo, the inlets were constructed on site and consisted of stainless steel tubing strapped to a vertical stand with hose and adel clamps. The gas sample inlet was constructed from an insulated 1.9-cm diameter, insulated stainless steel "Y" (with one leg capped) that connected to a heated sample line <1-m downstream of the tip. The heated tubing transported sample to the NASA gas-instrument rack in the AEDC trailer and met the length, diameter, and temperature requirements for engine-emission certification tests. Community aerosol samples were also collected using a 1.9-cm diameter stainless "Y", but here dilution gas was injected into the leg of the "Y" facing away from the exhaust port to prevent particle coagulation and water condensation. The diluted sample was transported through unheated, 1.9-cm diameter flexible PTFE and stainless tubing to the aerosol sample distribution manifold located in the MST trailer. The EPA collected aerosol samples through a separate ½-in diameter, unheated stainless tube that ran directly to their instrument suite; a Swagelok "T" was placed in the tube near to the base of the inlet stand and used to inject dry N2 dilution gas to reduce condensable gas concentrations and prevent particle coagulation.

Figure 14. The photo on the right shows the inlet probes used for sampling exhaust from the DC-8 APU. On the left, members of the AAFEX science team erect the inlet stand and adjust its position to align the probes with the exhaust flow.

3.11 Aircraft Fueling

Figure 15 shows a diagram of the DC-8 fuel system. The fuel capacities for the tanks are: 1 and 4 mains, 3100 gals each; 1 and 4 alternates, 1740 gals; 2 and 3 mains, 4700 gals; center auxiliary, 4400 gals; and forward auxiliary, 2100 gals. Valves isolate the tanks from one another so that it is possible to run each engine from a separate fuel tank. During AAFEX, JP-8 was loaded in the center and #2 main tanks and the test fuel was pumped into the #3 main tanks, which allowed us to burn JP-8 in the #2 engine and alternative fuel in #3. This made it possible to contrast the emissions from the two engines to more accurately delineate ambient- from fuel-related changes in emission characteristics.

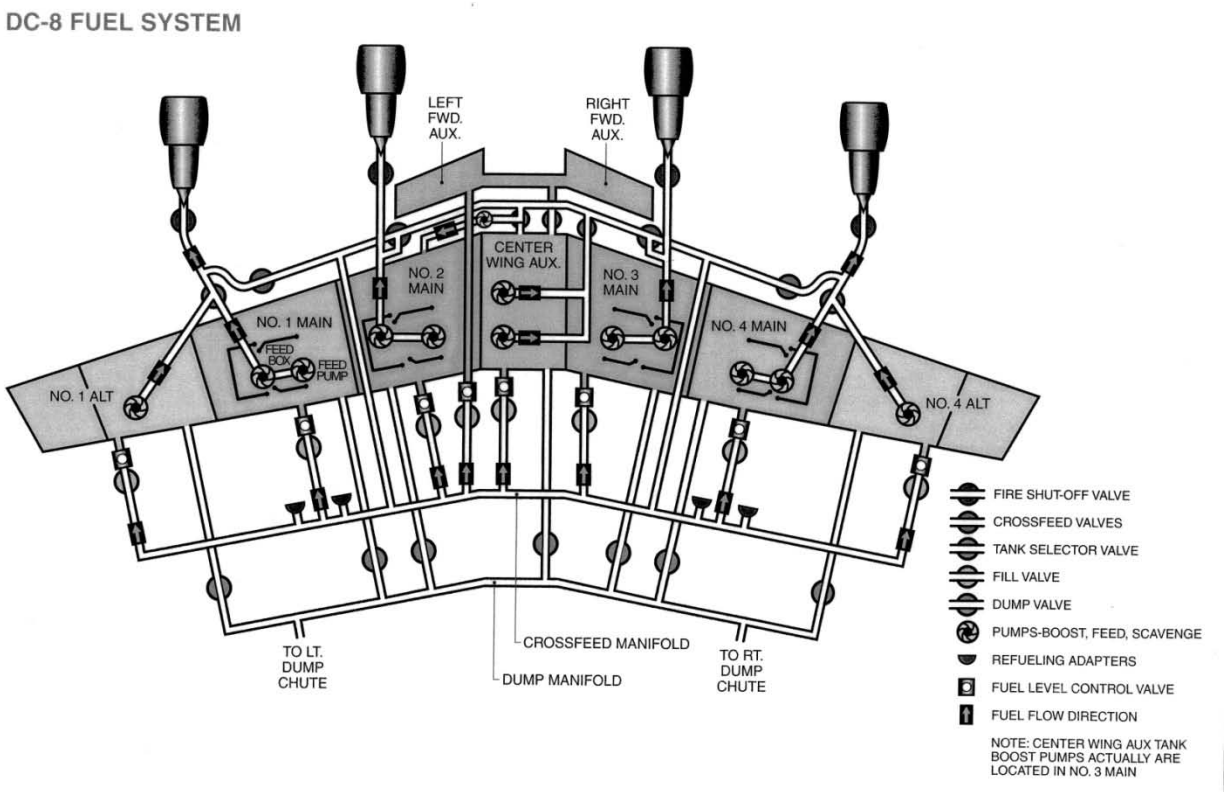

Figure 15. DC-8 fuel system.

Aircraft fueling was accomplished using the following available fuel tanker assets:

- FT1 tank truck (Air Force)
- FT2 tank truck (Air Force)
- Truck A, Fueling capable with 5,000 gal volume, 4,500 usable (NASA – K&A)
- Truck B – Fuel/defuel capable with 5,000 gal volume, 4,500 usable (NASA – K&A)
- Truck C – Fuel/defuel capable with 5,000 gal volume, 4,500 usable (NASA – K&A
- 8,000 gallon Tanker (NASA – K&A)
- 1,000 gallon Fuel Bowser (NASA – K&A) – all fuel in Bowser handled as waste fuel
- 4,000 gallon Waste Fuel Truck (NASA – Health & Safety)

Prior to the AAFEX, Air Force tanker trucks arrived on site carrying the FT1 and FT2 fuels; these stayed on site for the duration of the mission. Fuel remaining in the aircraft tanks from previous operations was drained into the 8,000-gallon tanker to be reused after AAFEX. Fuel trucks A, B, and C were drained and cleaned and had their fuel filters replaced. Dryden purchased 20,000 gallons of a single batch of JP-8 fuel from Air Force Plant 42 at Edwards AFB. Using truck A to pick the fuel, 15,000 gallons of the JP-8 was transferred into the DC-8 center- and #2 main tanks. Transferring directly from the Air Force tanker trucks, 3,500 gallons of the FT1 and FT2 fuels were loaded onto fuel trucks B and C, respectively. Neither of the FT fuels were loaded onto the aircraft prior to test initiation because of concern (justified) that long exposure to the aromatic-hydrocarbon-free fuels would cause fuel system seals to shrink and create leaks.

Fuel samples were collected from the #3 main fuel drain before and after each of the test runs listed in Table 6 below. The samples were subsequently shipped to the AFRL fuels lab at Wright Patterson AFB and analyzed for the parameters listed in Table 2 above.

At the conclusion of the initial JP-8 tests (runs 1-4 in Table 6), fuel was transferred from the #3 main into the outboard main and alt fuel tanks and residual fuel in the pumps and fuel lines was drained into the bowser truck, which was subsequently dumped into the waste fuel truck. Next, 3,000 gallons of FT1 was transferred into the #3 main from fuel truck B. To prepare for the upcoming "blended" fuel test, 800 gallons of FT1 was transferred into the truck B from the AF tanker and was topped off with 1,300 gallons of JP-8 from truck A and was circulated for 15 minutes to create a 50:50, FT1:JP-8 mixture.

At the end of the FT1 tests (5 and 6), the residual fuel in #3 main was drained into the bowser truck and was replaced with blended fuel from truck B. When the blended fuel run (7) was complete, the residual fuel was transferred to aboard tanks and the fuel pumps and lines were drained into the bowser truck for disposal.

Just prior to test 9, 3,000 gallons of FT2 fuel was transferred from truck C into the #3 main tank. Afterward, 500 gallons of FT2 from the AF tanker and 1,300 gallons of JP-8 from truck A were added to truck C to create the 50:50 blend. After test 10 was aborted due to a fuel leak on #3 main, residual FT2 fuel was drained into the bowser truck for disposal and was replaced with 3,000 gallons of the FT2-JP-8 blend.

During tests 12 and 13, JP-8 fuel was burned in the #3 engine. To balance the fuel load and provide enough fuel to complete the tests, an additional 1,500 gallons of the same batch of JP-8 was purchased from the Edwards AFB and loaded into the #3 tank from fuel truck A. During test 13, blended fuel from one of the alt tanks was burned in the #2 engine to reduce waste and conserve JP-8.

The DC-8 APU draws fuel from the #2 main tank. After APU emission test 15, it was thus necessary to transfer JP-8 from the #2 tank to an outboard tank, drain the sumps into the bowser truck, and load the #2 main with ~500 gallons of FT2.

At the conclusion of all tests, fuel trucks B and C were drained into the waste truck, cleaned, and then had their filters replaced. All FT or blended fuel remaining on the DC-8 was drained into the waste truck and replaced with JP-8 from truck A. Afterward, the engines and APU were run at idle for 15 minutes to purge the fuel lines and pumps of residual FT and blended fuel.

3.12 Engine Test Runs

About 30 minutes prior to engine start, a short briefing was held to review the test objectives, test matrix and safety procedures. The crew and test conductor (Dan Bulzan) then boarded the aircraft and established communications with the distributed investigators via headset. Once all participants were ready, the crew started the APU, which was subsequently used to motor the #2 engine. Once both inboard engines were stable at ground idle, the test conductor announced the beginning of the overall test point and recorded engine fuel flows, temperatures, fan speeds, etc.

As operators of the community aerosol sampling manifold, MST selected the aerosol sampling probe, adjusted sample dilution flow (if necessary), announced when aerosol concentrations were stable, and logged the start time of the data point. After two minutes of sampling time, the project scientist (PS) polled the investigators to determine whether their sampling requirements had been satisfied. When all agreed, the MS requested that engine power be adjusted to that required for the next data point and the process described above was repeated. If at any time a safety issues arose, testing was halted and the engines were shut down as quickly as possible.

Table 6 lists the engine and APU test runs that were conducted during AAFEX; Table 7 and Figure 14 provide the meteorological context of the tests. In all, 16 separate tests were performed between January 27 and February 2, with 13 focusing on engine emissions and 3 sampling exhaust from the APU as it burned either JP-8 or FT-2. The tests required almost 35 hours of DC-8 engine operations and just over 3 hours of separate APU runtime.

As indicated in the Table 6, test 1 was a "shakedown" run to assess the integrity of the sampling system and to check for problems with the sampling protocol, dilution procedures, etc. During this and all subsequent tests, observers were stationed at strategic locations to quickly identify and communicate to the aircraft operators any problems that arose with either the engines or sampling system installation. Video cameras were also used to monitor the integrity of the rakes and inlet probes from within the AEDC equipment truck. Any time loose or vibrating equipment were spotted, the engine was shutdown as quickly as possible and potential remedies were discussed and implemented.

After a installing additional tie-downs on sampling lines that either came loose or showed excessive movement during the shakedown test, test 2 was conducted to examine the distribution of emissions across the #2 and #3 engine exhaust planes to establish which of the aerosol and gas probes resided within the core region of exhaust and to determine which locations were susceptible to engine oil contamination. Aerosol and gas phase measurements were made on samples drawn from each of the L1 and R1 probe tips at power settings of 4, 30, and 65% of maximum rated thrust. In addition, R1 was translated laterally to characterize emissions to the left and right of the #3 engine center. As expected, results indicated that core flow extended out to ~10 in from the engine axis and that positions near the central vent tube were often contaminated engine oil. Oil contamination was particularly notable near the #3 engine centerline, possibly because the engine had a leaky seal that produced a slow drip of oil when it wasn't in use. In any case, based on results of this mapping test, R1 and L1 were positioned 4 in to the left of engine center and probe tips 3 and 4 of each rake were selected for use in the subsequent emission characterization studies.

Test runs 3-6 and 8-13 focused on characterizing the DC-8 engine emissions as a function of fuel composition and ambient temperature. Duplicate tests of the pure fuels (JP-8, FT-1, and FT-2) were conducted under warm and cold conditions to observe plume chemistry over the broadest temperature range possible. In addition, engine #2 burned JP-8 throughout the emissions characterization tests, which provided the opportunity to examine exhaust composition and plume chemistry under a wide variety of ambient conditions.

Table 6. Aircraft Engine and APU Test Runs

Test No.	Test Date	Test Objective	Aircraft Engine	Engine Fuel	Engine Start	Engine Shutdown	Sampled Thrust Levels (%)
1	26-Jan	Equipment Shakedown	#2	JP-8	14:01	15:00	4, 45
			#3	JP-8	14:03		4, 7, 30, 45, 65, 85, 100
2	26-Jan	Exhaust Mapping	#2	JP-8	16:02	19:20	4, 7, 30, 45, 65, 85
			#3	JP-8	16:04		4, 7, 30, 45, 65, 85, 100
3	27-Jan	JP-8, warm conditions	#2	JP-8	12:38	15:46	4, 7, 30, 45, 65, 85
			#3	JP-8	12:43		4, 7, 30, 45, 65, 85, 100
4	28-Jan	JP-8, cold conditions	#2	JP-8	5:59	9:28	4, 7, 30, 45, 65, 85
			#3	JP-8	6:03		4, 7, 30, 45, 65, 85, 100
5	28-Jan	FT-1, warm conditions	#2	JP-8	12:35	15:54	4, 7, 30, 45, 65, 85
			#3	FT1	12:39		4, 7, 15, 30, 45, 65, 85, 100
6	29-Jan	FT-1, cold conditions	#2	JP-8	5:41	8:36	4, 7, 30, 45, 65, 85
			#3	FT1	5:45		4, 7, 15, 30, 45, 65, 85, 100
7	29-Jan	APU, JP-8 Fuel	APU	JP-8	12:34	13:57	EGT = 350, 610 °C
8	30-Jan	FT-1/JP-8 Blend	#2	JP-8	6:14	9:38	4, 7, 30, 45, 65, 85
			#3	FT1/JP-8	6:19		4, 7, 15, 30, 45, 65, 85, 100
9	30-Jan	FT-2, warm conditions	#2	JP-8	10:48	13:41	4, 7, 30, 45, 65, 85
			#3	FT2	10:51		4, 7, 15, 30, 45, 65, 85, 100
10	31-Jan	FT-2, cold conditions	#2	JP-8	5:57	7:03	4, 7, 30, 45, 65, 85
			#3	FT2	5:42		4, 7, 15, 30, 45, 65, 85, 100
11	31-Jan	FT-2/JP-8 Blend	#2	JP-8	8:28	10:59	4, 7, 30, 45, 65, 85
			#3	FT2/JP-8	8:31		4, 7, 15, 30, 45, 65, 85, 100
12	31-Jan	JP-8, warm conditions	#2	JP-8	12:49	15:18	4, 7, 30, 45, 65, 85
			#3	JP-8	12:52		4, 7, 15, 30, 45, 65, 85, 100
13	2-Feb	JP-8, cold conditions	#2	JP-8	7:12	8:38	4, 7, 30, 45, 65, 85
			#3	JP-8	7:14		4, 7, 15, 30, 45, 65, 85, 100
14	2-Feb	Sampling System Tests	#2	FT/JP-8	9:37	12:07	4, 7, 30, 45, 65, 85
			#3	JP-8	9:40		4, 7, 15, 30, 45, 65, 85, 100
15	2-Feb	APU, JP-8	APU	JP-8	14:12	15:23	EGT = 345, 365, 475, 550, 555, 610 °C
16	2-Feb	APU, FT2	APU	FT2	15:40	16:37	EGT = 360, 475, 550, 555, 620 °C

Table 7. Meteorological Conditions during the AAFEX Test Runs

			Start	End	Ambient T (deg F)			Ambient %RH			WSPD KNTS			WDIR	Solar Rad (W/m2)			P (mB)
Test #	Test Objective	Date	Time	Time	Med	Min	Max	Med	Min	Max	Med	Min	Max	Med	Med	Min	Max	Med
1	Shakedown	26-Jan	13:52	15:00	8.7	8.1	9.3	48.0	45.6	51.6	15.3	12.6	21.9	292	528	266	650	925
2	Mapping	26-Jan	15:57	19:15	4.7	3.4	7.5	58.6	51.2	64.1	20.6	12.0	31.7	282	0	0	250	927
3	JP-8 Warm	27-Jan	12:34	15:34	9.3	8.6	10.2	22.9	18.6	28.0	5.8	1.4	14.0	45	609	343	738	939
4	JP-8 Cold	28-Jan	5:53	9:25	-1.0	-4.1	4.2	62.4	53.1	69.8	3.9	1.2	8.7	246	128	0	485	938
5	FT1-Warm	28-Jan	12:35	15:49	13.9	11.3	15.2	23.6	20.8	27.8	3.9	0.8	6.7	321	580	286	726	935
6	FT1-Cold	29-Jan	5:34	8:34	0.9	-0.9	5.3	60.9	53.8	69.7	6.7	0.7	12.2	316	14	0	325	937
7	APU-JP8 Test 1	29-Jan	12:58	13:50	17.4	16.8	17.7	14.7	11.9	18.9	12.7	9.8	16.3	58	677	608	729	936
8	FT1/JP-8 Blend	30-Jan	6:07	9:36	3.4	-0.9	9.4	47.8	30.3	57.3	4.6	1.1	10.3	222	182	0	529	938
9	FT2-Warm	30-Jan	10:45	13:45	16.8	12.7	18.2	22.2	18.3	28.9	6.6	1.9	12.4	57	734	656	755	937
10	FT2-Cold	31-Jan	5:35	7:05	-1.2	-2.6	0.3	70.5	65.1	79.4	2.6	0.5	5.9	209	0	0	18	932
11	FT2/JP8	31-Jan	8:25	11:00	10.9	7.1	14.6	38.9	30.6	54.3	4.4	0.5	9.3	318	554	304	717	933
12	JP-8 Warm/Mapping	31-Jan	12:55	15:20	18.9	17.5	20.1	20.0	17.2	23.7	2.9	0.7	5.8	175	616	405	740	930
13	JP8 Cold	2-Feb	7:10	8:36	5.5	0.9	6.6	45.4	41.8	54.7	3.1	0.5	7.3	241	198	39	351	938
14	Dilution/Probe Comp	2-Feb	9:40	12:10	12.8	9.6	16.3	29.3	22.5	34.1	6.3	3.0	10.9	330	720	555	773	938
15	APU-JP8	2-Feb	14:11	15:25	20.1	19.5	20.6	8.1	6.9	9.5	7.5	5.3	9.9	60	520	403	621	934
16	APU-FT2	2-Feb	15:35	16:40	19.6	19.2	20.0	9.4	7.8	12.0	5.6	4.0	8.4	54	252	133	368	934

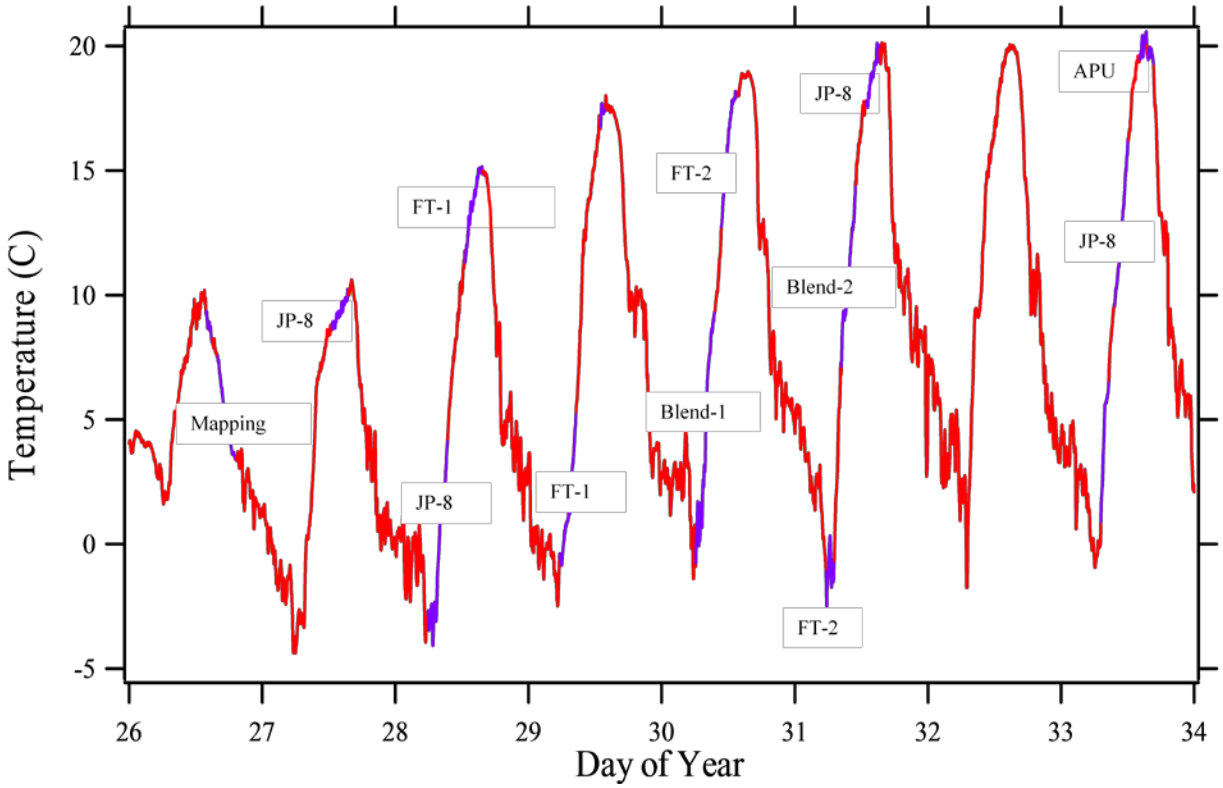

Figure 16. Ambient temperature recorded by the portable weather station that was deployed to the AAFEX experiment site. The blue trace corresponds to the times during which the indicated experiments were being conducted.

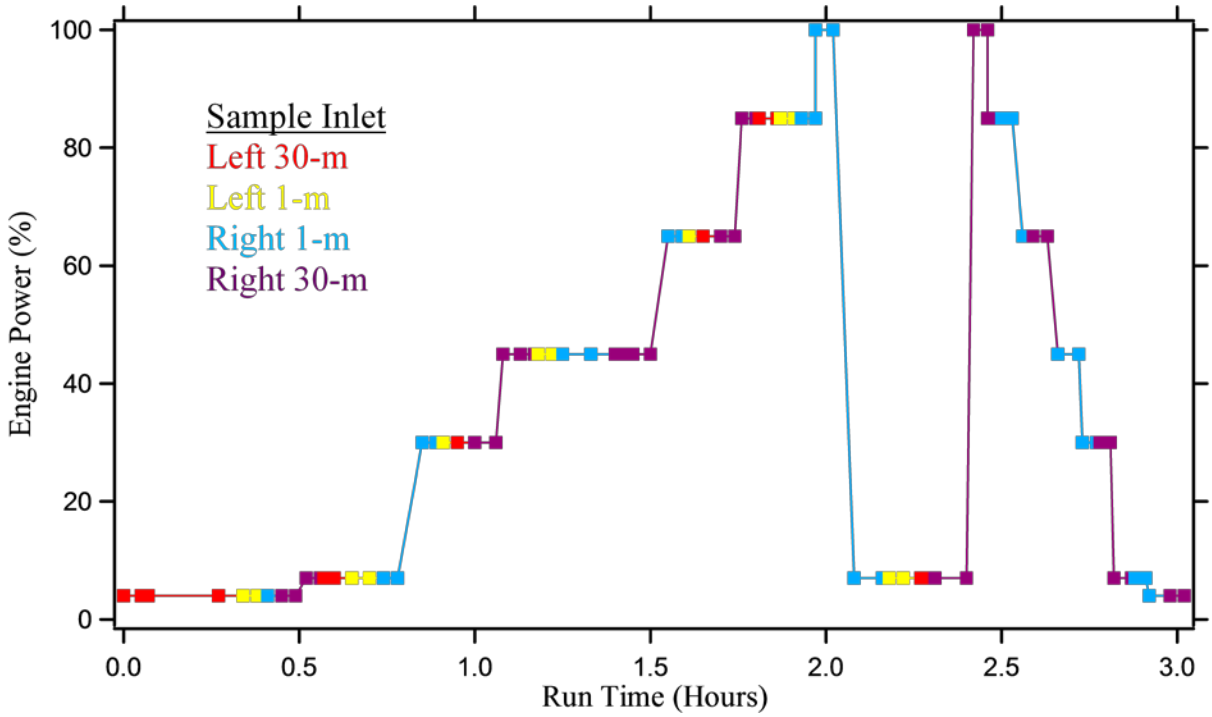

Figure 17. Typical test matrix for the fuel characterization studies.

Figure 15 shows a typical experiment matrix for the fuel characterization tests. The power settings followed an up and down stair-step pattern with idle runs at the start, middle and end to assess variations in the engine's emission characteristics over time and with changing ambient conditions. In cases where the #3 engine fuel was changed just before testing, a 5-min run at 30% power was included just after engine start to clear the fuel pumps and supply lines of fuel from the previous test. Exhaust concentrations of SO_2 were monitored in these cases to determine the engines emission exhibited characteristics of the new fuels.

Aerosol sample was typically drawn from L30 during engine start-up (because as noted in table 6, the #2 engine was started first) while purge air was expelled out each of the 1-m rake tips. Once the engines were stable at 4% thrust, sample was alternately drawn for ~3 min from each of the inlet probes. Samples from the 1-m rake tips were diluted with dry nitrogen to achieve a dilution ratio of about 10:1 as judged from sample CO_2 mixing ratio. Once satisfactory measurements had been acquired from each sampling probe/rake, engine thrust was increased to the next power setting and the sampling process was repeated. Power settings of 4, 7, 15, 30, 45, 65, 85 and 100% of maximum rated thrust were typically included in test matrix and were accessed in the stair-step pattern shown in Figure 15. After a brief "intermission" at 7% power to allow participants to adjust equipment and take a comfort break, the power progression was repeated in reverse, but only allowing time to sample from R30 and R1. Note also that the 2-min limit on operating the engines at takeoff thrust only allowed time to drawn sample from R1 and R30 during the two high power engine runs.

As shown in Table 6, the fuel characterization tests typically required about 3 hours to complete. The exceptions were test 10, where the fuel system developed a leak and testing was suspended after the first set of power settings was complete, and test 13, where sampling was restricted to L30 and R30 to examine plume chemistry under cold conditions.

During AAFEX and previous engine emissions tests, a number of questions arose regarding sampling system design, the effects of the sampling probes on gas and particle concentrations and properties, and the source of differences between various measurement teams. Test run 14 and a portion of run 13 were designed to address some of these questions including:

- Is it necessary to dilute aerosol samples near the probe tip (i.e., use a special "particle" probe), or can dilution gas be injected into sample collected by a standard gas probe at some point downstream?
- Does anisokinetic sampling affect large particle concentrations at high engine powers?
- Can the differences between the NASA and AFRL gas phase measurements be attributed to differences in probe location?

To address the gas vs. aerosol probe question, prior to run 14 gas probe #3 on R1 was re-plumbed to introduce a stream of dry N2 about 1 m downstream of the inlet tip. Sample and dilution lines were then plumbed into seldom-used ports on the 6-port aerosol sample selection box at the base of the probe stand. During the subsequent engine test, MST switched back and forth between the gas probe 3 and the adjacent particle probe 3 to obtain comparative particle number, size, and composition measurements.

Isokinetic sampling issues were addressed during run 14 by measuring particle size distributions on R1 at 65 and 85% thrust as the dilution flow was varied. Increasing dilution flow reduces the differential pressure across the inlet tip, resulting in a greater mismatch between the exhaust plume and inlet flow velocities. Sample dilutions were varied by factors of 4 and 8 at 65 and 85% power, respectively.

The initial part of test 12 explored whether the systematic differences seen between NASA and AFRL measurements could be caused by differences in probe location coupled with inhomogeneous distributions of species across the engine exhaust plume. The test involved making emission measurements from R1 probes as the rake was translated 20, 10, 5, and 0 cm off the #3 engine centerline. Data were recorded over the same stair-step power sequence shown in Figure 15.

Tests 7, 15 and 16 were conducted to determine emission factors for the DC-8 APU and to examine how those factors changed with fuel composition. Because the APU fuel flow could not be changed in a systematic manner, different power settings were accessed by changing the APU workload and monitoring the EGT as a measure of engine thrust. Four operating modes were selected that yielded EGTs of approximately 360, 475, 550 and 660^{o}C: 1) idle or generator mode; 2) minimum air conditioning (A/C) pack; 3) medium A/C pack; and 4) motor engine. For a variety of reasons, only test modes 1 and 4 could be implemented during test 7. Tests 15 and 16 included sampling in all modes as the APU burned JP-8 and FT-2 fuels, respectively. Full sets of aerosol measurements were recorded by all groups, but because of plumbing limitations, gas phase sampling was only performed by NASA and AEDC. Sampling procedures and protocols were similar to those employed in the aircraft engine tests. The test conductor coordinated load settings with APU operator, MST controlled sample dilution and called out the start of each run when CO_2 mixing ratios had stabilized, and the PS monitored progress of the experiment groups in meeting measurement objectives and issued requests for new power settings to the test conductor.

3.13 Engine Power Settings

The NASA DC-8 has an analog cockpit without readouts of the various pressures and temperatures that control the combustion process. The test point thrust settings therefore had to be set based on cockpit instrumentation, which limited the options to fuel flow and fan speed. If PM are primarily formed in the combustor, we ideally would have set fuel flows to replicate exactly the same combustor pressure, inlet temperature, fuel air ratio, airflow, and humidity each time we wanted to characterize emissions at a certain engine thrust setting. If ambient temperature, pressure, and humidity were always the same, either fuel flow or fan speed would be equally effective to set the points. However, there were big swings in ambient temperature during the test and combustor inlet conditions (pressure, temperature, fuel flow, and fuel air ratio) could not be exactly replicated as the ambient temperature changed. We note that as temperature increases, the air is less dense, so more airflow, pumped to a higher pressure and temperature, is needed to achieve a given level of thrust. These effects are not huge, but experience from fuels tests at GE indicate that changes in emissions due to variation in ambient temperature can be of the same magnitude as changes due to fuel properties.

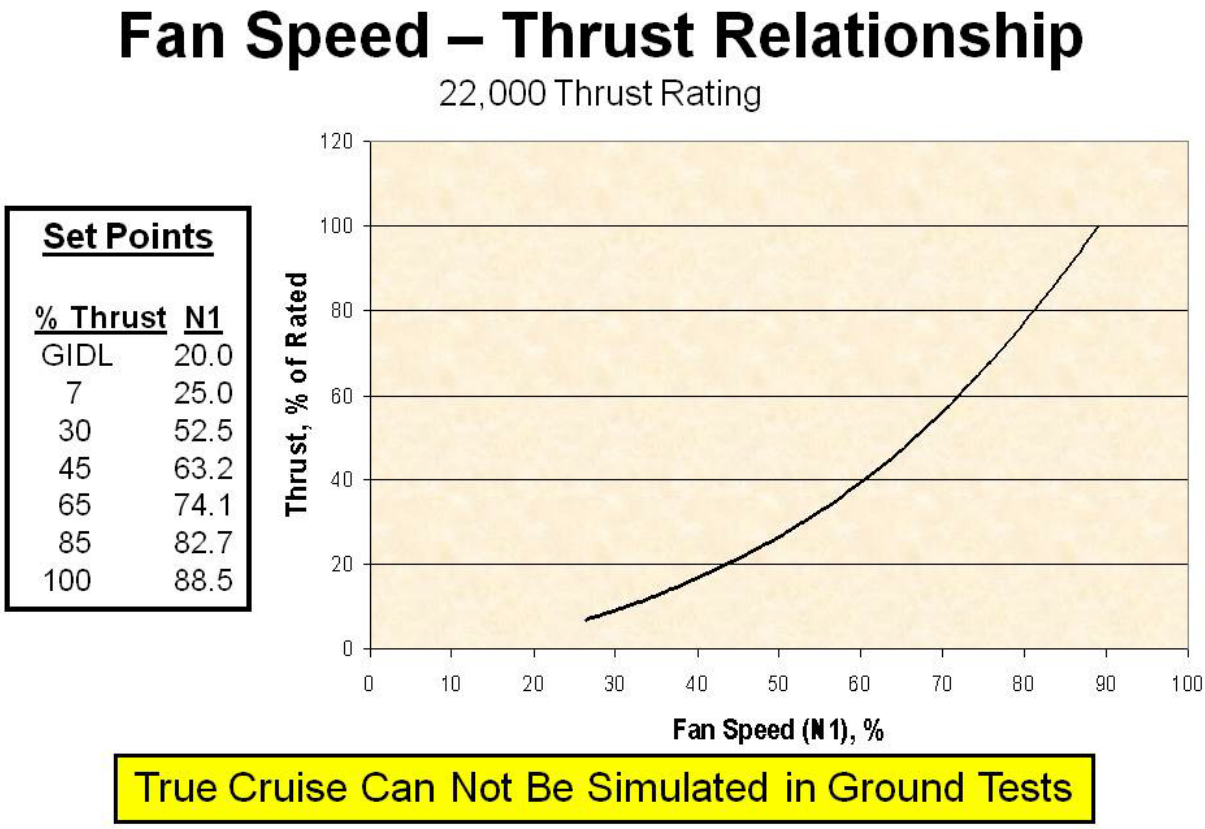

Figure 18. Engine power as a function of first-stage, fan speed. The vales displayed in the box at left were used to set thrust levels during AAFEX.

On a warm day, if thrust level is set with fuel flow, combustor inlet pressure and fuel flow will be close to ISA levels, but combustor inlet temperature and fuel air ratio will be higher than ISA levels. If fan speed is used as the controlling parameter, fuel flow and combustor inlet pressure will be low, but combustor inlet temperature and fuel air ratio will be closer to ISA levels. Based on an analysis of APEX-1 test results which showed that fan speed came closest to replicating combustor inlet temperature and fuel air ratio and because the cockpit gauge could be read more accurately, AAFEX adopted the approach of setting thrust as a function of N1, the low-pressure compressor fan speed. This approach also allowed thrust settings to be set without considering how the different fuel density and heating values of the FT fuels affected fuel flow rate.

Figure 17 provides a plot of thrust as a function of N1 and shows the values that were selected to access thrust settings of 4 (ground idle), 7, 30, 45, 65, 85, and 100% of maximum RPM; a value of N1=37.5 was used for the 15% power point that was included in some of the test runs.

4.00 OVERVIEW OF RESULTS

Measurement results obtained by AAFEX participants are included in the attached appendices. The sections below summarize important findings from these reports in a variety of areas including fuel and ambient temperature effects on engine performance and emissions, the effects of the sampling system on the emission measurements, and instrument performance.

4.01 Engine Performance and Certification Gas Emissions

Appendix A, contributed by Wey and Bulzan from NASA GRC, describes the engine operating data that was recorded in the aircraft cockpit and examines fuel effects on both standard-day, heating value-corrected engine performance parameters and certification gas emissions as measured with a conventional instrumentation suite. As shown in Figure 19, very little difference was observed in the levels of JP-8 and FT fuels required to produce the N1 (low speed fan) settings that corresponded to 4, 7, 30, 45, 65, 85 and 100% power points, suggesting that the alternative fuels offer no advantage or penalty in terms of fuel economy. However, the FT fuels exhibited higher combustion efficiencies at low fuel flow rates (Figure 19, right panel), indicating they are in general less polluting. Moreover, the only problem found in using the aromatic-hydrocarbon-free FT fuels is that they caused fuel system seals to shrink, which resulted in fuel leaks; the leaks went away soon after blended fuel was introduced to the tanker or aircraft fuel tanks.

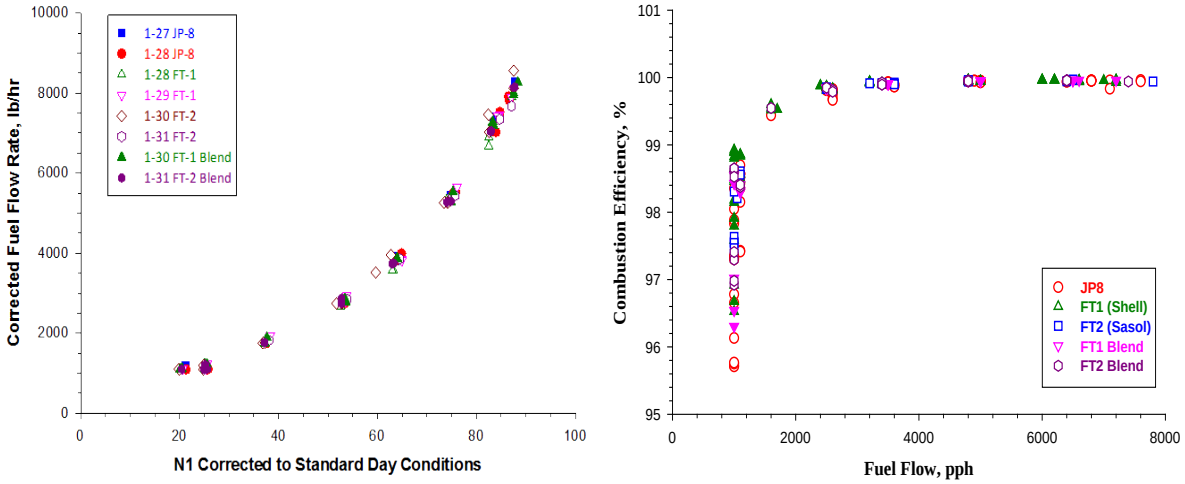

Figure 19. Fuel flow rate corrected to standard day conditions and fuel heating value versus N1 (left) and fuel combustion efficiency as a function of corrected fuel flow rate (right). Data are for the DC-8, right inboard engine and are presented and discussed more thoroughly in appendix A.

Appendix A goes on to note that the FT fuels reduced NOx, CO, and total hydrocarbon (THC) emissions. As shown in Figure 20, the reduction in NOx is quite notable, especially for the FT1 fuel at high engine powers.

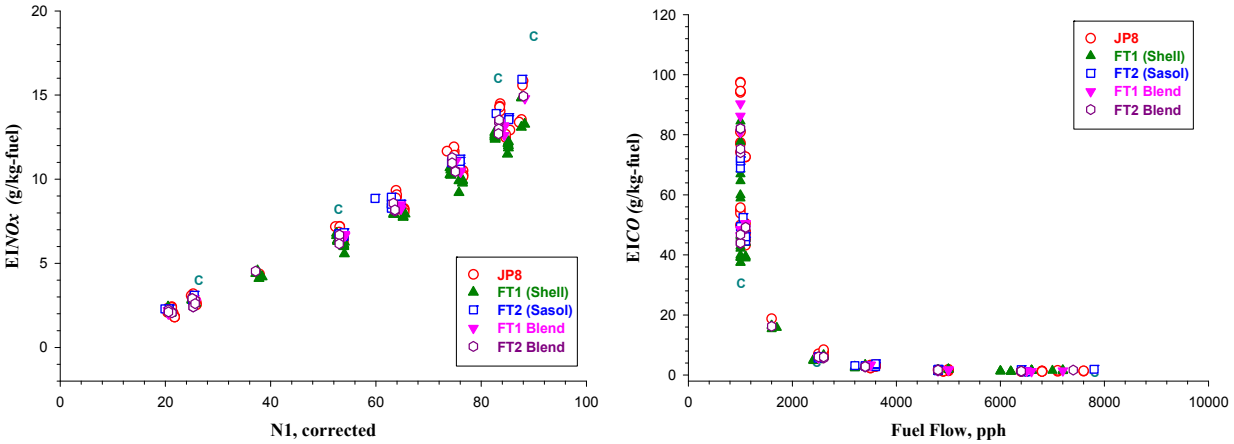

Figure 20. NOx emission index plotted versus corrected N1(right) and CO emission index plotted versus corrected fuel flow rate (left). The "C" points correspond to ICAO certification values for the CFM56-2C engine.

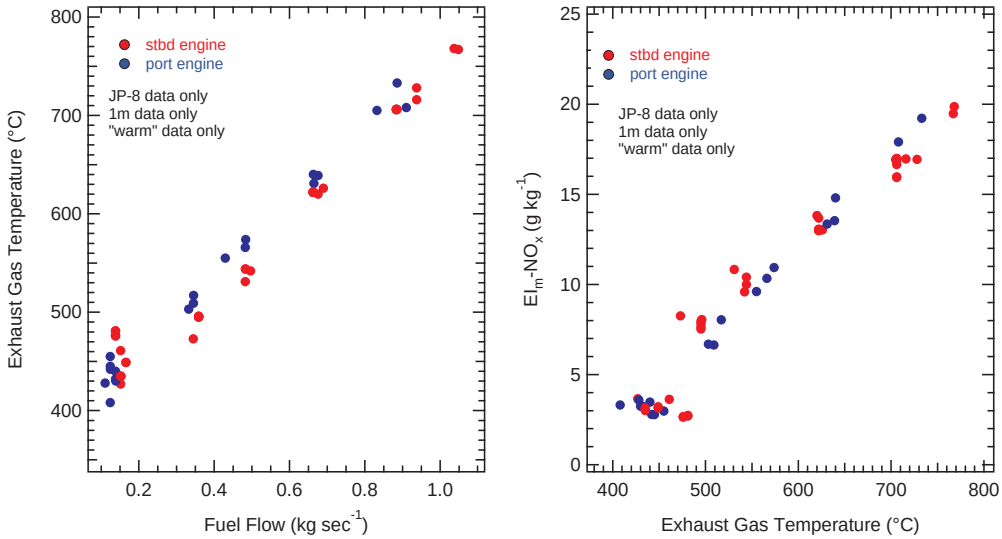

Figure 21. Exhaust gas temperature as a function of fuel flow rate (left panel) and EI_m-NOx as a function of exhaust gas temperature (right panel) for the port and starboard engines studied during AAFEX. Plot taken from appendix B.

Appendix B, contributed by Aerodyne Research Inc., also examines fuel effects on the CO and NO_X emissions data measured using quantum cascade laser and chemiluminescence instruments, respectively. After developing a protocol for analyzing emissions performance data for combustion of alternative jet fuels that accounts for fuel energy differences compared to JP-8, the authors found that, compared to JP-8 combustion, combustion of the FT fuels reduced EI_m-NO_X by 5-10% at high power and reduced EI_m-CO by as much as 10% at idle. Further analysis showed, however, that the pollution reduction benefit of FT1 was significantly greater than that of FT2. The authors also note that for engine powers greater than 30%: NOx emissions increase with ambient temperature; EI_m-NOx has similar slopes with respect to ambient temperature for

the various fuels; and at any given temperature, the EI_m-NOx value for FT1 was always less than for JP-8. The ambient temperature dependence of EI_m-CO was similar for all fuels studied and was strongest for 4% thrust and nearly absent for power settings greater than 30%. Appendix B also notes that when both engines burned JP-8 fuel, the portside engine generated greater NOx and less CO emissions than the starboard engine. By examining simultaneous engine operating parameter measurements, the authors show that the differences in emissions were caused by the propensity of the portside engine to have higher exhaust gas temperatures (EGT) than the starboard engine at fuel flow rates above idle (see appendix B). They further observe that the two engines operated at different fuel flow rates and fan speeds (N1 and N2) to achieve the same nominal thrust level and suggest that the overall differences in emissions and operational characteristics are consistent with predictions from an aircraft engine aging model described in recently published literature.

4.02 Trace Gas Emissions

Aircraft are a significant source of hydrocarbon species and hazardous air pollutants that can impact local air quality. To evaluate the effect of alternative fuels and ambient conditions on these emissions, Montana State University and ARI deployed a tunable infrared laser differential absorption spectrometer (TILDAS) and highly sensitive proton transfer reaction mass spectrometer (PTR-MS) to assay a large suite of VOCs including formaldehyde, acetaldehyde, methanol, ethene, propene, benzene, toluene, phenol, styrene and naphthalene that together account for about 50% of the total nonmethane hydrocarbon emissions from a typical engine burning JP-8. Results of these measurements are presented in **appendix C**.

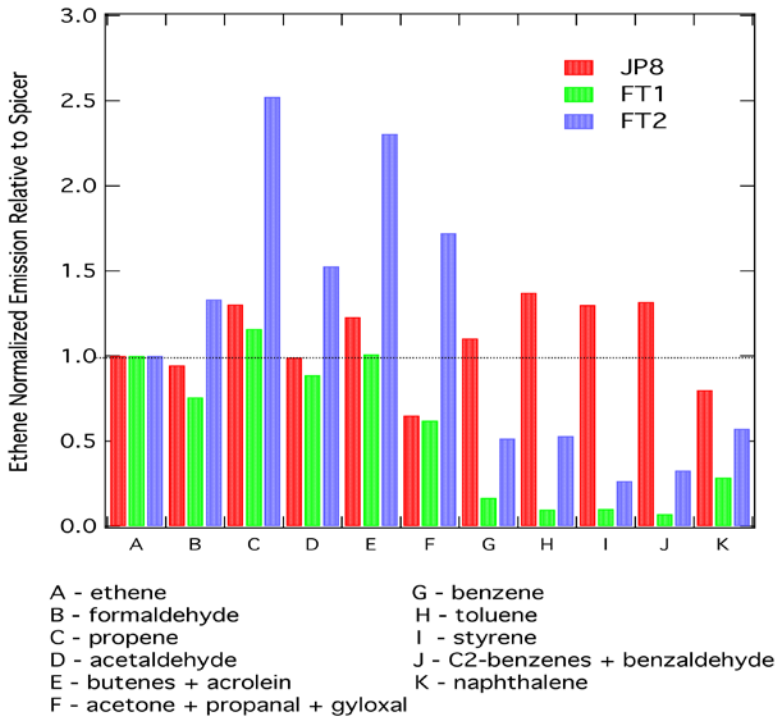

Figure 22. Comparison of ethene-nomalized EIs measured at AAFEX with respect to those reported by Spicer et al. (1994). Plot taken from appendix C**.**

Figure 22 summarizes the fuel dependencies for a number of important species; the values are normalized to EIs for a similar engine as reported by Spicer et al. (1994). The authors indicate that ethene EIs were fortuitously similar for the three different fuels and that for JP-8, AFFEX values for all species were within $\pm$35% of those reported in the earlier work. They further indicate that FT1 and FT2 engine exhaust had very different composition and that aromatic emissions are reduced, but not eliminated during FT1 fuel combustion, which, because FT1 was devoid of aromatic components, indicates that aromatic compounds were being formed during the combustion process. The discussion indicates that C1-C3 species (principally formaldehyde, ethene, propene and acetaldehyde) account for >70% of the measured mass emissions for all fuels. The authors further observe that a significant fraction of the emissions were contributed by carbonyl species (i.e., formaldehyde), which are not effectively measured by the instruments used for THC emission certification. In addition, they note that the EIs for all measured species were lower for FT1 than FT2, which is consistent with the lower relative THC EI reported for FT1 in Appendix A. FT2 emissions of C3 and C4 hydrocarbons species are noted to be substantially higher than for JP-8, and partially offset the reduced aromatic emissions for that fuel. A more detailed analysis shows that the total measured hydrocarbon emission ratios in units of ppbC/ppmCO_2 for JP-8, FT1 and FT2 were 2.79, 2.17, and 3.74, respectively, which indicates that for total VOC emission the fuels rank FT1 < JP-8 < FT2, a surprising result since both the alternative fuels were anticipated to burn much cleaner than JP-8.

Appendix C also examines the temperature dependencies of the hydrocarbon emissions and finds that for all measured species and at low power settings, EIs always increased with decreasing ambient temperature. As an example, Figure 23 shows plots of ethene and formaldehyde (and total particle mass) emissions versus ambient temperature constructed from data acquired during AAFEX and several previous missions; values are normalized to the EI measured at 288 K. For both species, values increased by about a factor of two in going from 288 to 273 K; similarly, normalized values declined by ~50% as temperature increased from 288 to 303 K. These observations underscore the need for specifying the ambient temperature range when reporting aircraft engine hydrocarbon emission parameters.

DC-8 starboard engine hydrocarbon emissions measurements from AAFEX and APEX-1 are additionally compared in appendix C. The authors note that the ratio of ethene emissions at 4% and 7 percent power was about 2 during AAFEX and 3 to 5 during APEX-1. They suggest that differences in actual power settings between the two experiments could explain the dissimilarity in the emission ratios. However, the authors also note that the DC-8 engines were re-built just prior to the 2004 APEX-1 mission whereas they had been in service for five years prior to AAFEX. A more detailed analysis shows that total hydrocarbon emissions at 7% power and 288 K and in terms of ppbC/ppmCO2 was ~2.79 during AAFEX as opposed to ~1.8 during APEX-1. This, along with the observation that AAFEX 7% EI_{CO} values were substantially higher than ICAO certification values (58.5 versus 30.7 gkg^{-1}, respectively), indicates that the starboard engine emissions performance had substantially degraded during the period between the two experiments.

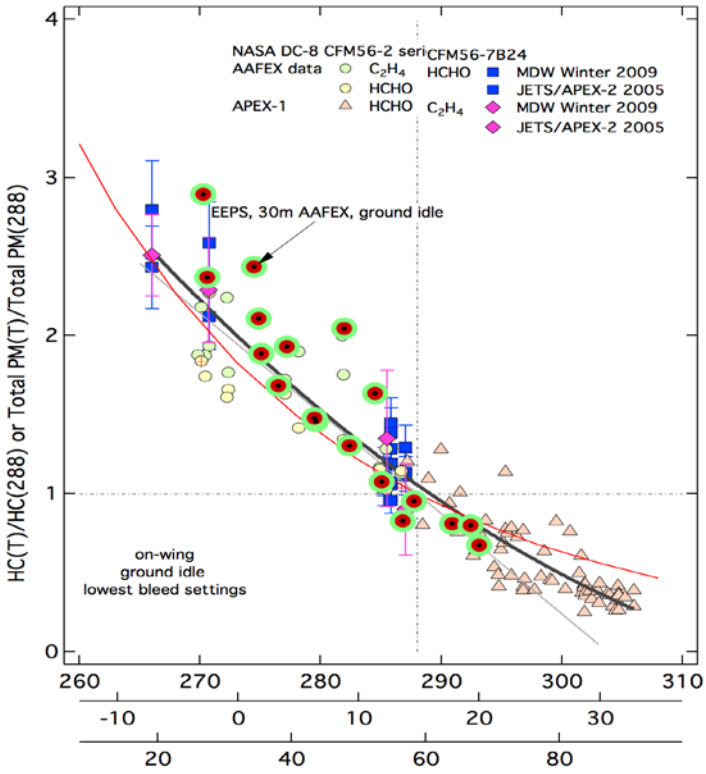

Figure 23. Plot of normalized (to corresponding EIs measured at 288 K) emissions versus ambient temperature take from appendix C. The units to the three x-axes starting from bottom are F [not U], C, and K. The large green points with red cores represents aerosol mass emissions as measured with an Electrical Exhaust Particle Sizer (EEPS). Plot is from appendix C.

4.03 Plume Chemistry

Appendix D, contributed by Harvard and ARI, examines nitrous acid (HONO) and nitrogen oxides (NO_x) emissions measured approximately 140 m downwind of the grounded aircraft using an advance quantum cascade-laser spectrometer and chemiluminescence instruments, respectively. They found that HONO EIs increased approximately six-fold from idle to take-off conditions, but leveled off between 60 and 100% engine power reflecting the point at which HONO production (reaction between NO and OH) and loss (reaction with OH and HONO self-reaction) reached equilibrium. The authors note that HONO EIs observed at the 140 m trailer showed no particularly dependence on fuel type regardless of engine power setting, and unlike NOx emissions, did not vary with ambient temperature. A suggested explanation for the temperature independence is that the dominant HONO production and loss mechanisms (reactions with OH) are insensitive to temperature, which may be the case if the OH radical was the limiting reactant and its production had no temperature dependence. HONO EIs were also found to be invariant with solar insolation, which indicates insignificant photochemical loss or production within the exhaust plume. To the authors, this, along with a lack of dependence on wind speed or direction (factors that effect plume age), suggests that HONO was produced primarily within the engine, a result that is consistent with previous investigations.

The speciation of NO_y within the exhaust plume at 140 m is also examined in appendix D (see Figure 23). The authors found that HONO to NO_x ratios increased from 3% at idle to 7% at mid-power settings before decreasing to less than 4% at maximum thrust. They note these observations are at odds with results from previous studies which report ratios of around 7% at idle that monotonically decrease to values that are a factor of 3 lower than AAFEX ratios at maximum thrust. In addition to the simple explanation that these differences could be due to differences in engine types or ages, the authors suggest that problems with the previous data sets caused by sampling losses due to thermal dissociation, adsorption on metal probe/tubing surfaces, HONO self-reaction at high mixing ratios or poor thermal control leading to cis to trans conversion, or incomplete HONO formation linked to sampling near the engine exit plane could account for the disparity in the observations.

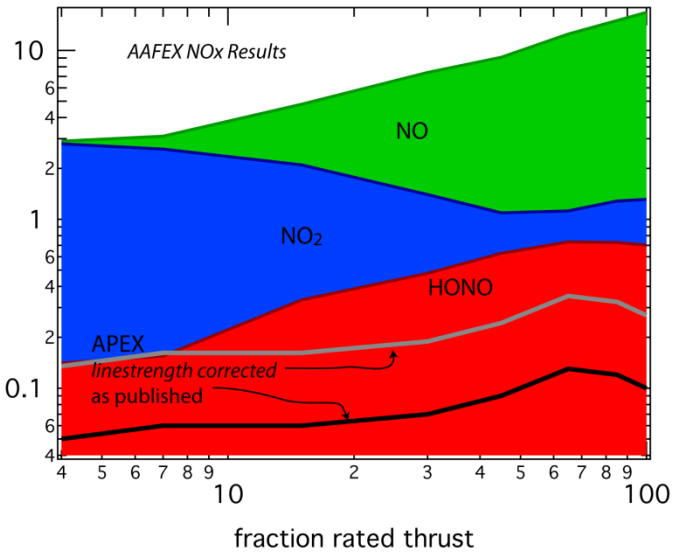

Figure 24. HONO EIs from the Aircraft Particle Experiment 3 (APEX-3, black), corrected for linestrength (grey), overlaid on top of observations from AAFEX (red). Emission indices for NO_2 (blue) and NO (green) from APEX3 are added on top of that of HONO. Taken from appendix D.

A bonus feature of appendix D is the first reported measurements of H_2O_2 EIs in an aircraft exhaust plume. During AAFEX, the investigators serendipitously discovered absorption lines for this species in TDL spectra and quickly devised a calibration scheme to allow for quantitative measurements. Although offering a variety of caveats regarding the precision and accuracy of the measurement, they report EIs of 0.43 ± 0.31 (2s) g H_2O_2 kg fuel burned at idle and that values decrease to below detection limits at power settings greater than 20% of maximum rated thrust. From the observed power dependency and other AAFEX gas-phase specie observations, the authors suggest that HO_2 not OH is the primary H_2O_2 precursor in aircraft exhaust, which is an important finding that validates a proposed mechanism for HOx production in combustion plumes.

Appendix E, contributed by ARI, Harvard and MSU, further explores plume chemistry using a variety of measurements recorded in the ARI Moble Laboratory (AML) as it made multiple

plume penetrations at downwind locations. The investigators note that, unlike most combustion sources, idling aircraft emit NO_x primarily in the form of NO_2, which can lead to greater ambient levels of both O_3 and NO_2 than primary NO emissions. Drawing from the AML AAFEX data set, they provide several examples (see Figure 25) that show O_3 production in aged idle plumes and O_3 depletion in high thrust plumes where NO dominates the NO_x budget. Although anticipated, these were, to the investigators' knowledge, the first observations of O_3 generation in a fresh aircraft engine exhaust plume.

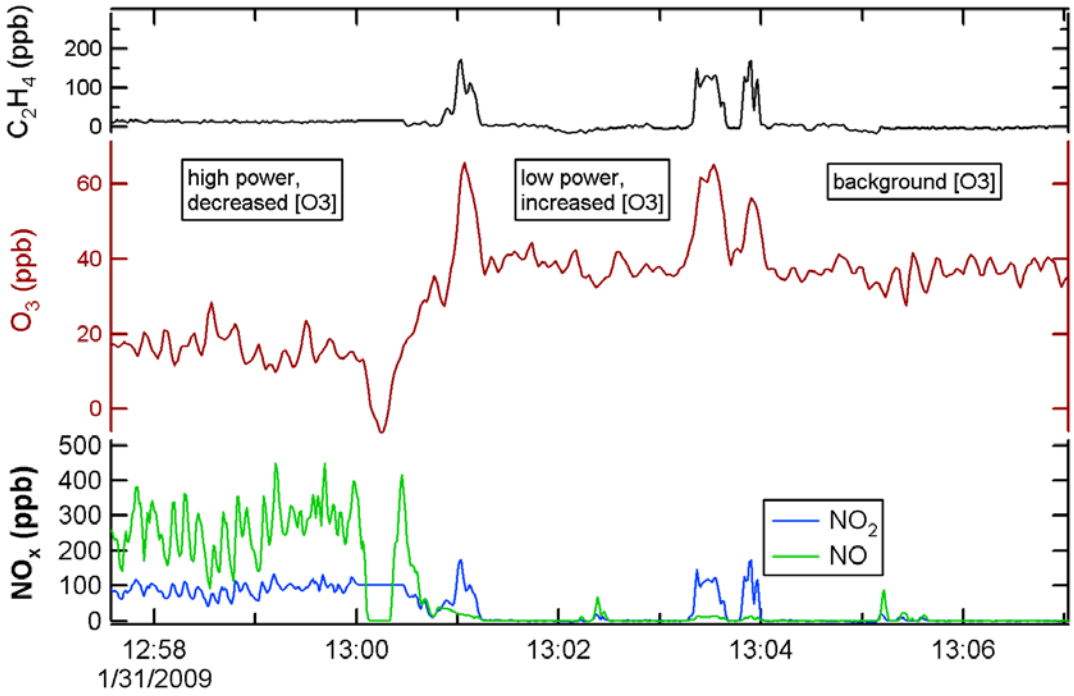

Figure 25. Time series of C_2H_4, O_3, NO, and NO_2 measured downwind of the NASA DC-8 during high engine power (up until 13:01) and low engine power (after 13:01). Taken from appendix E.

From the slope of a $[NO_2]+[O_3]$ versus [NOx] plot the investigators also infer there was net conversion of NO to NO_2 in some of the fresh exhaust plumes and suggest this occurs through NO reaction with HO_2 and RO_2 (peroxy) radicals, which in turn are formed through the reactions of OH and VOCs with OH radicals. It is noted that H_2O_2, which is formed primarily by HO_2 self-reaction, is elevated at idle, consistent with the observed net oxidation of NO to NO_2 at low engine power settings. The investigators then present a detailed analysis of peroxy radical sources in the exhaust plume, which concludes by suggesting that inclusion of these species within air pollution models is important for making accurate predictions of aircraft operations on local air quality. AAFEX AML observations are also used to assess the concentration of OH within aging exhaust plumes. Because OH was not directly measured, the authors infer its concentration by examining the ratios of highly reactive VOC species whose OH reaction rates are very well established. Examining plumes ~60 second in age, they calculate OH concentrations of ~2 x 10^7 molecules cm^{-3}, which, when compared to nominal daylight

background OH concentrations of 1 to 10 x 10^6 molecules cm^{-3}, indicates that the rate of VOC oxidation was elevated within the first minute of plume evolution.

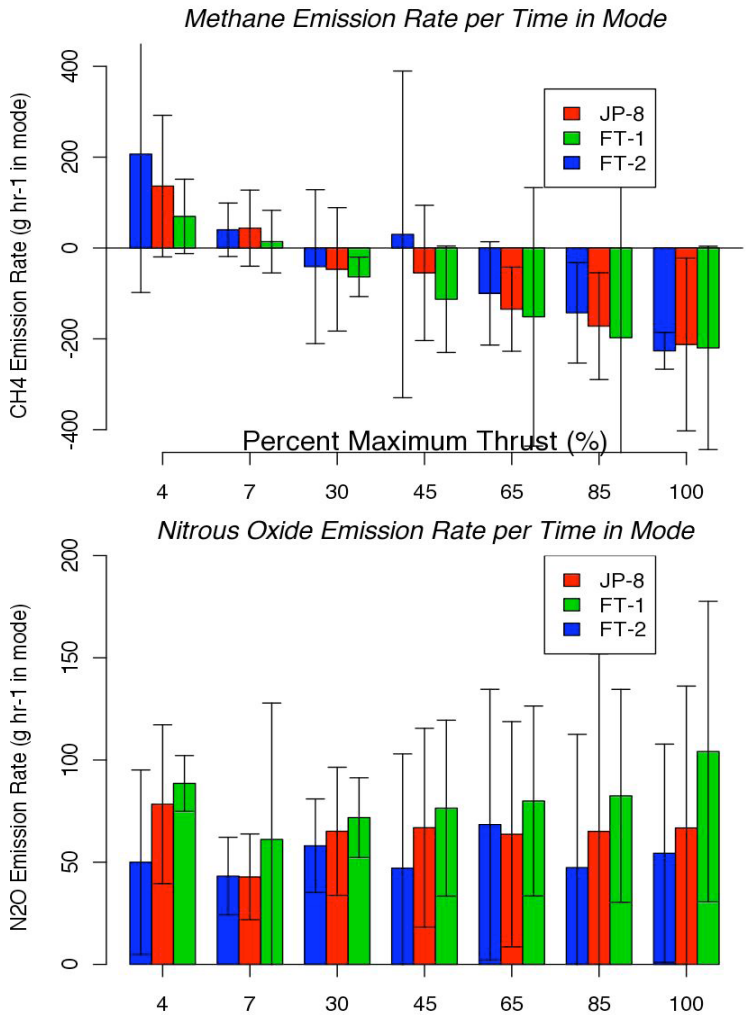

Figure 26. Emission indices in terms of mass per unit time in mode for methane (top) and nitrous oxide (bottom) as functions of engine power and time in mode. Taken from appendix F.

4.04 Greenhouse Gas Emissions

Engine emission indices for the green house gases methane (CH_4) and nitrous oxide (N_2O) are reported in **appendix F** and were determined by investigators from Harvard and ARI using advanced diode-laser spectrometer systems sampling aged exhaust through a special, low pressure inlet positioned 143 m behind the aircraft. These measurements are important because non-CO_2 gases, primarily CH_4 and N_2O, but also including trace quantities of other halocarbons, together represent roughly 60% of the total forcing due to carbon dioxide (CO_2) alone. Results of the AAFEX measurements are shown in Figure 26. The investigators note that for JP-8 combustion at idle (4% and 7% of maximum thrust) the DC-8 engines emit both CH_4 and N_2O at a rate of 168 $\pm$ 155 $mgCH_4(kgFuel)^{-1}$ and 114 $\pm$ 47 $mgN_2O(kgFuel)^{-1}$, respectively. Variability in the CH_4 EIs is attributed to differences in engine operation history, background variability, and limited plume sampling cases as a result of unfavorable winds. At higher thrust levels, i.e.

operational modes corresponding to greater fuel flow rates and higher engine combustion temperatures, they report that exhaust methane concentrations were lower than ambient concentrations (shown as negative EIs in Figure 26). Average emission indices for JP-8 fuel combusted with engine thrusts greater than 30% of maximum were -53.8 $\pm$ 33.2 $mgCH_4(kgFuel)^{-1}$ and 32.2 $\pm$ 17.5 $mgN_2O(kgFuel)^{-1}$, where the negative sign for methane indicates consumption of atmospheric methane in the engine. Methane and nitrous oxide EIs for the FT fuels are noted as being statistically indistinguishable from those for JP-8. For a typical flight profile (includes taxi, takeoff, cruise, et cetera), the investigators calculate that aircraft destroy significantly more methane than they create. From the AAFEX observations, they further conclude that an airline industry shift in fuel usage (i.e., from petroleum to synthetic fuels) will not affect global CH_4 and N_2O budgets.

4.05 Nonvolatile Particle Emissions

Appendix G, contributed by the Air Force Research Laboratory (AFRL), and appendix H, from the NASA Langley Research Center (LaRC), summarize the characteristics and concentrations of particulate matter emitted from the DC-8's CFM56 engines as they burned each of the five test fuels under varying atmospheric conditions. Appendix G also presents gas phase emission measurement results and a discussion of the JP-8 and FT fuel properties as determined from analyses of samples collected during the AAFEX campaign. Appendix I, from Missouri University of Science and Technology (MST), examines the effect of ambient temperature on nonvolatile particle emission indices. Results presented in these Appendices are based on measurements provided by CN counters, SMPS-type instruments, a smoke meter, and thermal-optical filter analysis. Appendix J**,** contributed by Penn State University (PSU), discusses results of electron microscope analyses of black carbon particles captured on impactors during AAFEX.

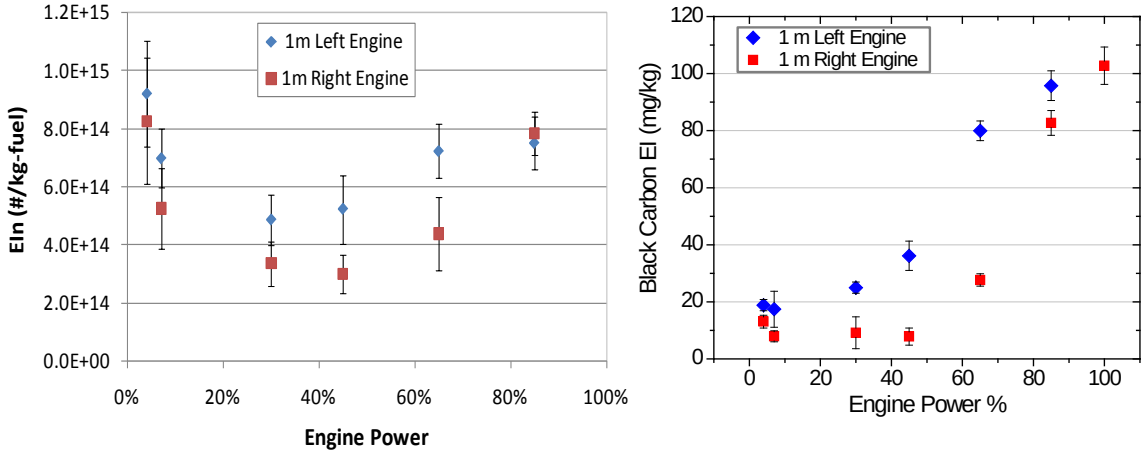

Figure 26. Nonvolatile particle number (left) and black carbon mass (right) emission indices for the port and starboard inboard engines on the DC-8 as they burned JP-8 fuel. Left panel from appendix G, right panel adapted from appendix H.

Appendices G and H first examine JP-8 emissions and note that the DC-8's left (#2) engine emitted higher PM number and mass emissions than the right (#3) inboard engine (see Figure 26). The differences were particularly apparent at medium thrust settings (30 to 65%), where the

left engine emitted two to five times more PM mass than the right engine. Noting the wide spatial variation in PM emissions observed behind the #3 engine during the emission mapping test, the appendix H authors suggest the observed emission differences could be caused by having the inlet probes placed in different relative positions behind the two engines. However, they acknowledge that left engine black carbon emissions were also enhanced relative to the right engine in samples collected 30-m downwind, which contradicts the theory that spatial variations contributed to the observed emission differences. Appendix H authors also note the differences in EGT readings between the engines and show that the EI_n and EI_{bc} values collapse onto a single curves when plotted as functions of EGT; this finding is consistent with appendix B results, which suggest that higher combustor temperatures may have caused the left engine to produce greater amounts of black NO_x at any particular power condition than the right engine. Regardless of the explanation, all investigators agree that the #2 engine was more polluting of the two from both a gas-phase and aerosol standpoint.

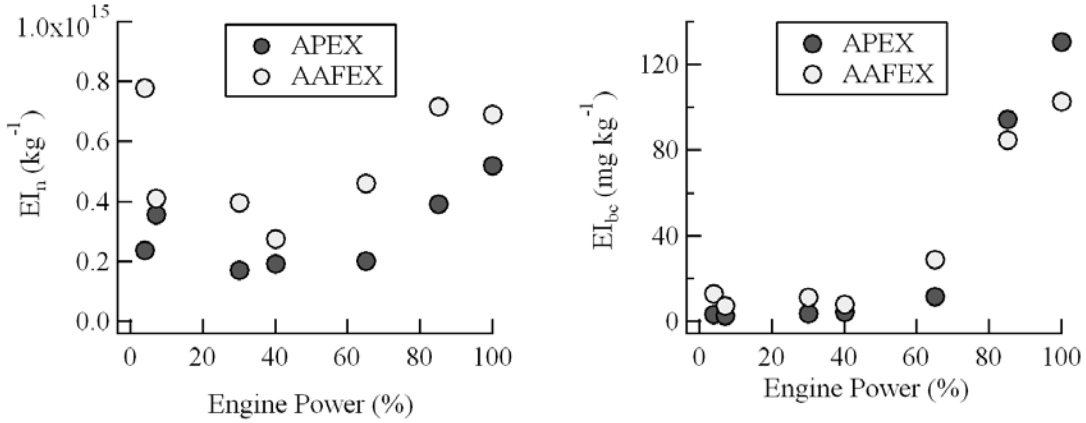

Figure 27. Comparison of nonvolatile particle emission parameters for DC-8's #3 engine burning JP-8 fuel as measured during APEX-1 and AAFEX. Adapted from Appendix H.

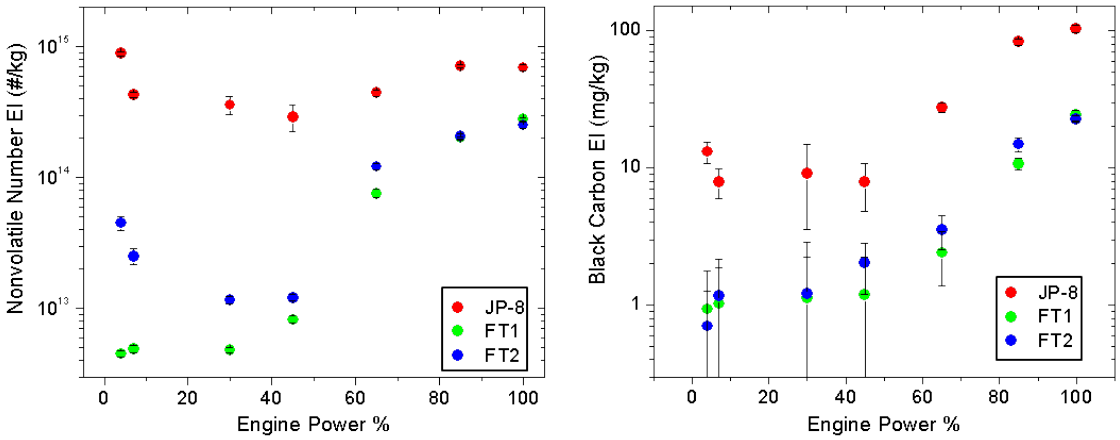

Figure 28. Nonvolatile particle number (left) and black carbon mass (right) emission indices as functions of percent maximum thrust for the starboard engine as it burned each of the indicated fuels. Adapted from Appendix H.

Appendix H also compares AAFEX starboard engine PM emission observations with corresponding measurements made during the spring 2004, APEX-1 study; results are shown in Figure 27. The investigators note the similarity in emission trends between the two campaigns, but point out that EI_n values were higher at all power settings during AAFEX. They propose that a portion of the enhancements could be caused by differences in the 50% cut sizes (7 vs. 10 nm) of the two particle counters deployed to the experiments. Ambient temperatures differences are also considered to be a factor as it was about 10°C warmer during APEX, which, as discussed below, would tend to reduce PM emissions. Differences in instrument characteristics (PSAP vs. MAAP) and ambient temperatures are also suggested as possible factors contributing to the disagreement in EI_{bc} measurements. In the end, however, the report recognizes the possibility that the AAFEX soot emissions were higher simply because the engines had aged almost five years between the two missions.

Fuel effects on engine nonvolatile PM number and mass emissions are examined in detail within appendices G and H. Results from the two investigations are in good agreement and indicate that burning alternative fuels greatly reduced PM emissions from the DC-8's starboard engine (see Figure 28). To exemplify the reductions more clearly, appendix H introduces an "emissions benefit" value, which is simply the ratio of the JP-8 to alternative fuel emission index for any particular emission parameter and power condition; for example, an emission benefit of 10 for PM number emissions means that EI_n was reduced by a factor of 10 by burning the selected test fuel as opposed to JP-8. Figure 29 shows the power dependent emission benefits for PM number and black carbon mass emissions associated with burning each of the tested fuels. As pointed out in both appendices, FT1 provided the greatest PM reductions; indeed at idle, EI_n was about 200 times lower for FT1 than Jp-8. Its relative number reduction benefit deceased monotonically with power to about 4 at 85% of maximum thrust. FT2 showed similar, but slightly lower emission reductions, but its number emission benefit peaked around 50 at medium-thrust levels and deceased to around 20 and 4 at 4% and 85% power, respectively.

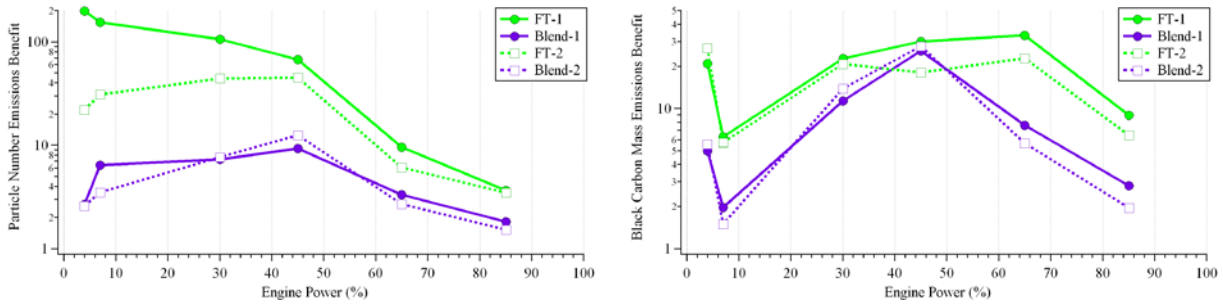

Figure 29. Relative reduction in PM number (left) and black carbon mass (right) emissions from burning each of the alternative fuels in the DC-8's right inboard engine. Adapted from appendix H.

As shown in Figure 29, mass emission benefits of the two pure alternative fuels peaked at around 30 in the 45 to 65% power range and exhibited relative minima at 7 and 85% power. PM number and mass emission benefits of the blended fuels also varied with power, but for unexplained reasons, were seldom 50% of the values calculated for the pure FT fuels.

Appendix G takes a close look at fuel impacts on elemental carbon (EC) emissions and smoke numbers at climb and takeoff thrust settings (Figure 30). The authors note that at 85% power, there was no significant difference between the FT1 and FT2 EC EIs, but that both were substantially lower than JP-8 values. Surprisingly, EC EIs for the blended fuels were only slightly higher than the FT-fuel values. The investigators also derived volatile organic carbon (OC) aerosol emission indices from analysis of collected filter samples and found values at 85% power that were 60% lower for the FT fuels than JP-8. For smoke numbers, FT1 values were consistently lower than those for FT2 and values for both fuels doubled in going from 85 to 100% thrust. At 85% thrust, smoke numbers were respectively reduced by ~83 and 72% when burning FT1 and FT2 as opposed to JP-8.

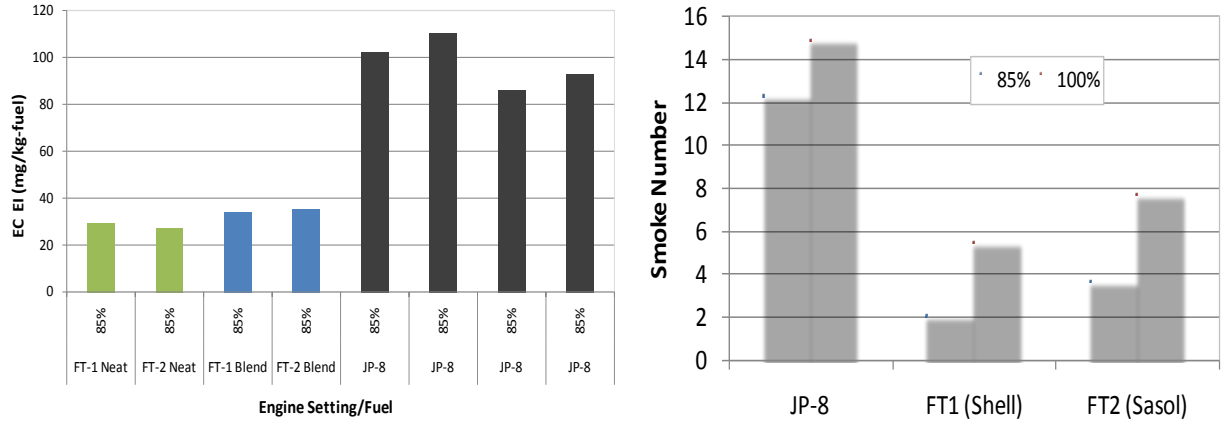

Figure 30. Elemental carbon emission indices (left) and smoke numbers (right) for the various fuels and high engine powers. From appendix G.

Appendices G and H independently examine fuel effects on nonvolatile PM size and conclude that, in general, the FT particles were smaller than those generated when burning JP-8. The two reports differ, however, regarding fuel-size effects in the 4 to 30% power range. The authors of appendix G indicate that FT geometric mean diameters were larger in the 4 to 30% power range than JP-8 values, which contradicts findings from their earlier studies. In contrast, appendix H investigators observed 5 to 10% and 15 to 20% smaller FT GMD values at idle and takeoff thrust levels, respectively, and note that volume mean diameters (VMD) were 20 to 40% smaller for the FT fuels across the entire power envelope. They explain that at low power settings, measured FT PM emissions were very low and potentially contaminated with background particles; background particle impacts were reduced by limiting the size range over which emission parameters were calculated. This approach, coupled with lower transmission line losses and the removal of nucleation mode particles and surface coatings by use of a thermal denuder, perhaps explains why LaRC (appendix H) GMD values were systematically 5 to10 nm lower than those reported by AFRL (appendix G).

The appendix H authors also point out that black-carbon mass densities were greater for the FT fuels than for JP-8. Over the 65 to 100% thrust range, they report effective density values derived from ratio of black carbon to nonvolatile particle volume of 1.45 ± 0.1 g cm^{-3} for FT-1, 1.2 ± 0.15 g cm^{-3} for FT-2, 1.1 ± 0.1 g cm^{-3} for Blend-1, 1.05 ± 0.15 g cm^{-3} for Blend-2, and 0.92 ± 0.08 g cm^{-3} for JP-8. These results are consistent with previous work and suggest that the

black carbon particles generated from FT fuel combustion are much more spherical and compact than particles produced by burning JP-8.

The temperature dependence of JP-8 black carbon emissions is examined in detail within appendix H. The authors indicate that, similar to CO and THC emissions (see appendices A-C), nonvolatile PM number and mass decrease monotonically with increasing temperature at all power settings. They further perform a linear regression analyses between the PM emission parameters and temperature and find good correlations in most cases (for example, see Figure 31). The regression slopes vary with engine power and range from about -0.6 x 10^{-14} $kg^{-1}{}^{o}C^{-1}$ at ground idle to -0.2 x 10^{-14} $kg^{-1}{}^{o}C^{-1}$ at takeoff thrust for EI_n and from 0.4 mg $kg^{-1}{}^{o}C^{-1}$ at taxi to -2 mg $kg^{-1}{}^{o}C^{-1}$ at climb. Thus at ground idle, the nominal EI_n value of 20 x 10^{-14} kg^{-1} would increase by 33% (6 x 10^{-14} kg^{-1}) if ambient temperature dropped by 10^{o}C. Similarly, the nominal EI_{bc} of ~100 mg kg^{-1} for 85% power would increase by 20% (20 mg kg^{-1}) if temperatures dropped by the same amount.

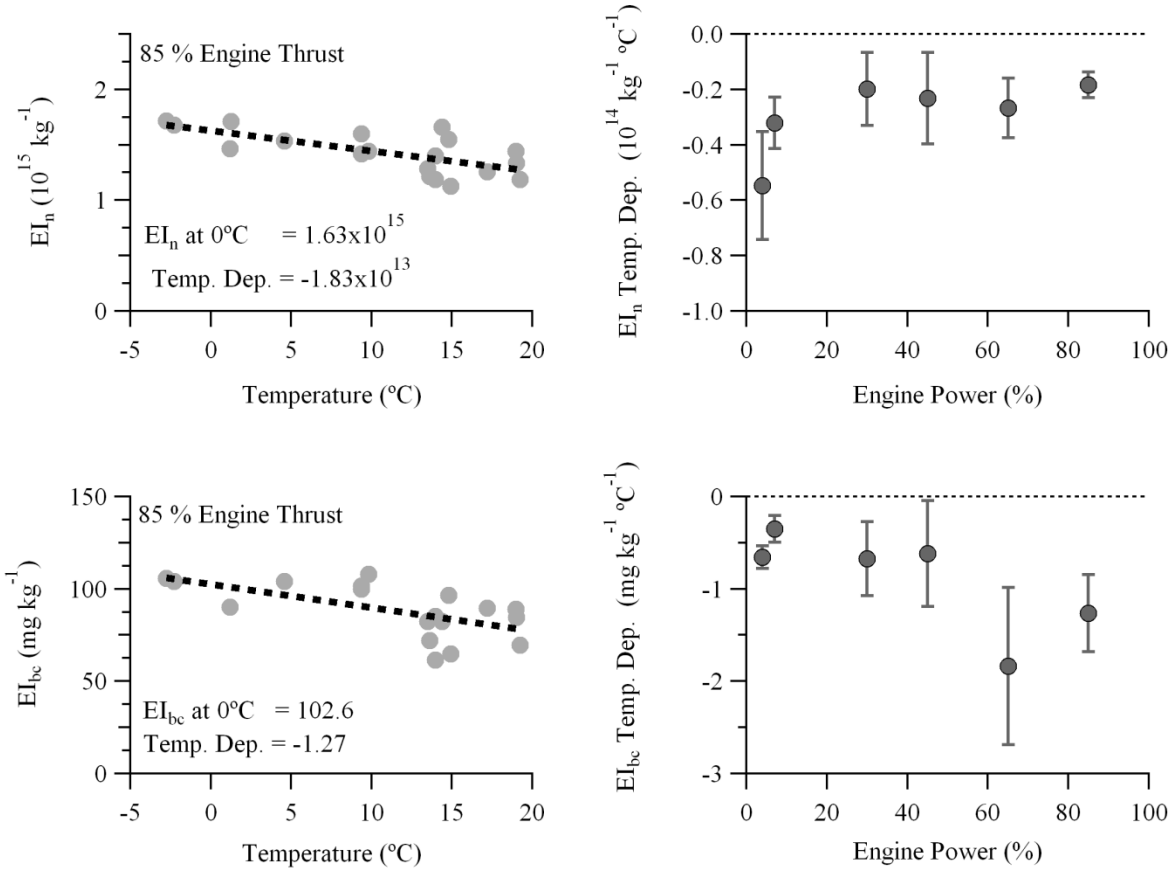

Figure 31. EI_n (top left) and EI_{bc} (bottom left) at 85% power plotted as functions of ambient temperature. Power-dependent slopes derived from regression of EI_n and EI_{bc} on temperature are shown in the right top and bottom panels, respectively. Error bars are the 1sigma standard deviation of the linear fits. The temperature dependence for 100% power is not shown because there too few data points.

Appendix I also examines ambient temperature effects on nonvolatile PM emission indices and mean particle size. By examining the mean ratio changes at widely separated temperatures, they show that the JP-8 and FT-1 emission parameters exhibited statistically significant changes with temperature in over 90% of the cases studied. They further note that the FT1 emission parameters appeared to vary more strongly with temperature than did the JP-8 parameters, but additional analyses fail to provide statistical support for this observation.

Appendices G and H explore possible causes for the fuel-dependent differences in nonvolatile PM emissions. The AFRL investigators examine the range in PM number emissions as a function of fuel end point (EP, defined as the temperature at which all distilled fuel is recovered) and find, as indicated in Figure 32, that the range between idle and high thrust EIs decreased considerably with increasing EP—there was no correlation between EP and the EIs at any particular power setting.

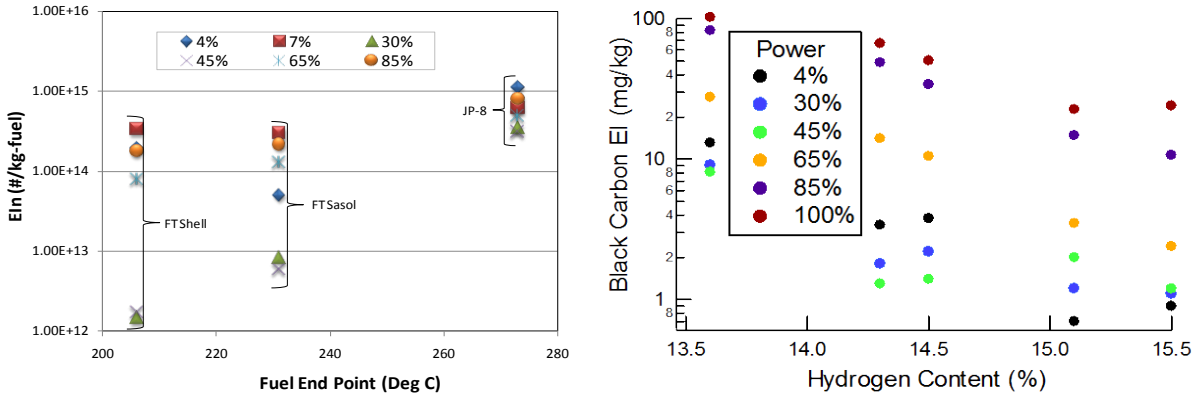

Figure 32. Nonvolatile particle number EI as a function of fuel end point (left) and black carbon EI as a function of fuel hydrogen content (right). Plots adapted from appendices G (left) and H (right).

Based on a results from modeling studies of gas turbine soot emissions, the Langley investigators assess the relationships between fuel components and PM number (EI_n) and black carbon (EI_{bc}) and find very high linear correlations ($r2 > 0.7$ in most cases) between the emission parameters and fuel hydrogen (see Figure 32), aromatic and naphthalene contents, and H/C ratios. They also note the following (abstracted from appendix H):

- At all power settings, EI_n and EI_{bc} increased with aromatic content and decreased with hydrogen content.
- The variability in EI_n decreased with increasing aromatic content and decreasing hydrogen content. For example, EI_n for JP-8 (highest aromatics, lowest hydrogen) varied about 60% between idle and takeoff thrust whereas those for FT-1 (lowest aromatics, highest hydrogen) varied by almost two orders of magnitude.
- In general, correlation coefficients with fuel properties were greater for EI_n than for EI_{bc}, suggesting that the variability in EI_n was better captured by variability in fuel composition than was the variability in EI_{bc}.
- For both EI_n and EI_{bc}, the best correlations with all examined fuel properties were observed at idle (4 %) and takeoff (100 %) thrust settings; correlation coefficients were a minimum at 30 and 45 % power.

- Slopes for EI_n linear regressions were greatest at the 4 % thrust setting, suggesting that absolute EI_n values were most sensitive to variable fuel properties at aircraft idle.
- Slopes for EI_{bc} linear regressions were greatest at the 100 % thrust setting, suggesting that absolute EI_{bc} values were most sensitive to variable fuel properties at aircraft takeoff.
- EI_n and EI_{bc} appear to be better correlated with fuel aromatic than hydrogen content at all thrust settings, however the fuel components did not vary independently so these results are only suggestive of observed relationships.

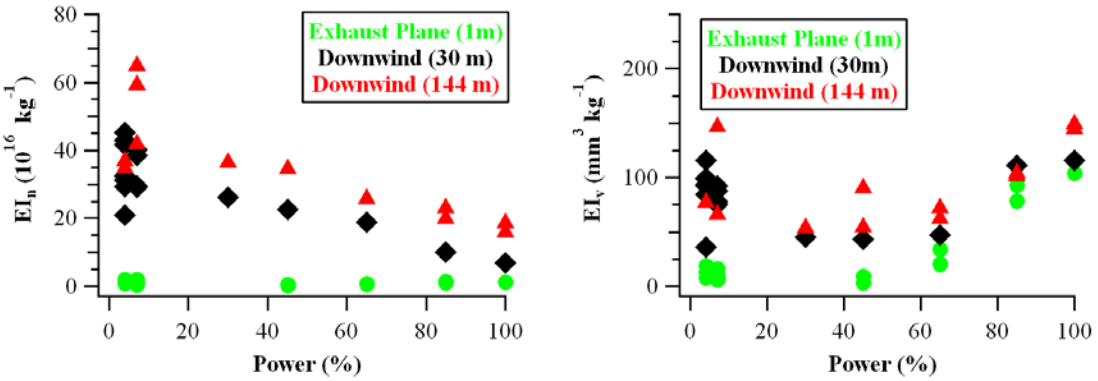

Figure 33. Results from afternoon JP-8 engine test showing EI_n (left) and EI_v (right) as functions of distance behind the aircraft. Taken from appendix H; similar plots for EI_n are shown and discussed within appendices G and I.

4.06 Volatile Particle Emissions

As aircraft engine exhaust plumes cool and mix with background air, low volatility species such as sulfuric acid, engine oil, and unburned hydrocarbons condense to either form new aerosols though homogeneous nucleation or to coat the surface of existing soot or background aerosol particles. Gaining a better understanding of the composition and the factors that control the formation and growth of these volatile aerosols was a major AAFEX objective. The fuel and temperature-dependent physical characteristics and concentrations of the volatile aerosols in aged exhaust plumes as measured with particle counting-type instruments are discussed in appendices G and H. Results of ARI, aerosol mass spectrometer-based, volatile aerosol composition studies are presented in appendices K and L.

All AAFEX reports agree that volatile aerosols formed very rapidly within diluting exhaust plumes and that, for JP-8 fuel (which contained ~1200 ppm sulfur), EI_n values were at least a factor of five greater at the downstream sampling inlets than observed in the hot exhaust directly behind the engines. For example, Figure 33 shows 1-, 30- and 145-m PM emission measurements plotted as functions of engine power. Although the data were recorded on a relatively warm afternoon, EI_n values increased by factors of 10 to 20 in going from 1 to 30 m; Aerosol volume EIs (EI_v) also increased significantly, particularly at low thrust settings. As described in appendix H, the downwind-increases in EI_n and EI_v are attributed to volatile aerosol formation and are the greatest at low power when emissions of gaseous precursors are greatest and plume temperatures are the lowest. As shown in Figure 34, at the exhaust plane the particles are comprised of a single soot mode, while an additional nucleation mode, peaking at

15 to 25 nm in the volume (10 to 20 nm in number) distribution is only observed downwind. At low power, this nucleation mode dominates the PSD in downstream samples. As power increases the nucleation mode decreases and the soot mode increases with the soot mode dominating at high power. Very little variation is observed in the soot mode volume between each distance. In contrast, significant variability is observed for the nucleation-mode, as the peak-diameter and integrated volume each increase with increasing distance (from 30 m to 145 m, Figure 34), suggesting that gas-to-particle conversion and particle growth is also occurring. This is also evident from Figure 33, as EI_v is greater at 145 m than at 30 m. Differences in EI_n are most significant between 1 m and 30 m, as the exhaust plume is cooling and particle nucleation is most prevalent. The difference between 30-m and 145-m EI_n is much less, suggesting that nucleation processes are still occurring but are less significant after 30 m.

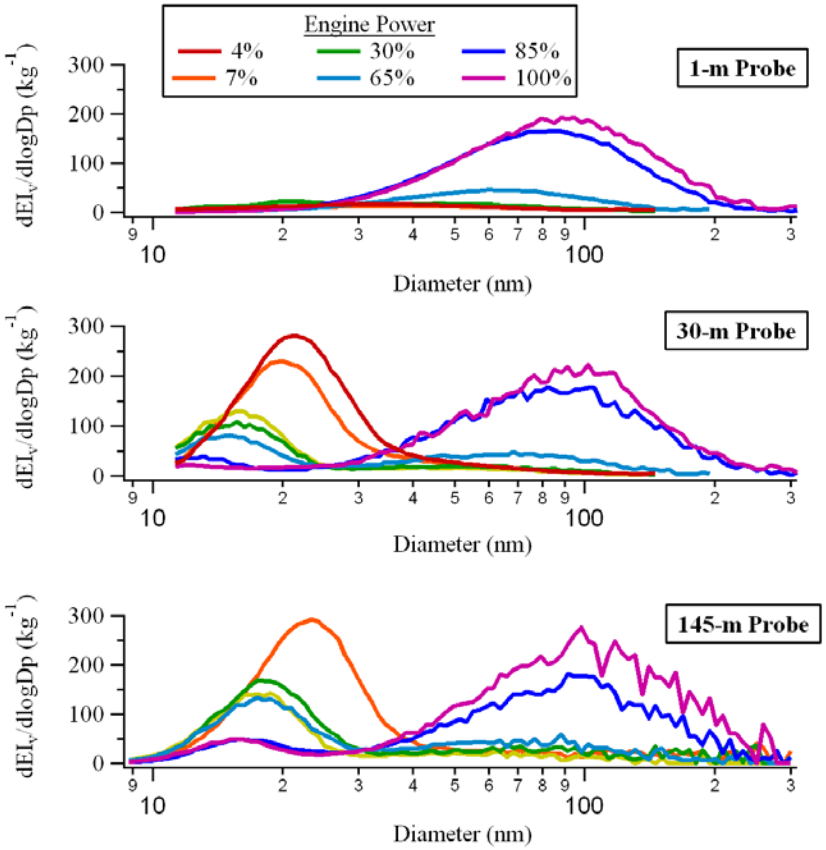

Figure 34. Size distributions ($dEI_v/dlogDp$, mg kg^{-1}) as a function of sampling probe and engine power setting for JP-8 fuel. More uncertainty is observed with increasing probe distance due to increasing dilution correction factors. Figure taken from Appendix H; similar PSD plots are presented and discussed within Appendices G and I.

AAFEX investigators note that volatile aerosol formation and growth was heavily dependent ambient temperature. Figure 35 from appendix H shows JP-8, 30-m EI_n and EI_v values for the 7% power setting plotted as functions of temperature; also included are plots of power-dependent, temperature coefficients for the two emission parameters derived from the slopes of

linear regression analyses. At all power settings, the volatile PM EIs decreased monotonically with increasing temperature. Temperature coefficients (dEI/dT) were greatest at ground idle (where the largest amount of condensable material was available in the plume) and generally larger for volatile PM volume than number. For example, at 4% power, a 10°C change in temperature produced ~30 and ~60% changes in EI_n and EI_v, respectively. This observation is consistent with the idea that volatile aerosol number populations quickly reach an equilibrium between formation and coagulation while total volatile aerosol mass continues to grow through nucleation, coagulation and direct gas-phase condensation on existing particles. This concept may also explain why EI_n values in the aged JP-8 high thrust plumes were relatively high (compared to idle plumes), despite there being less material available for condensation.

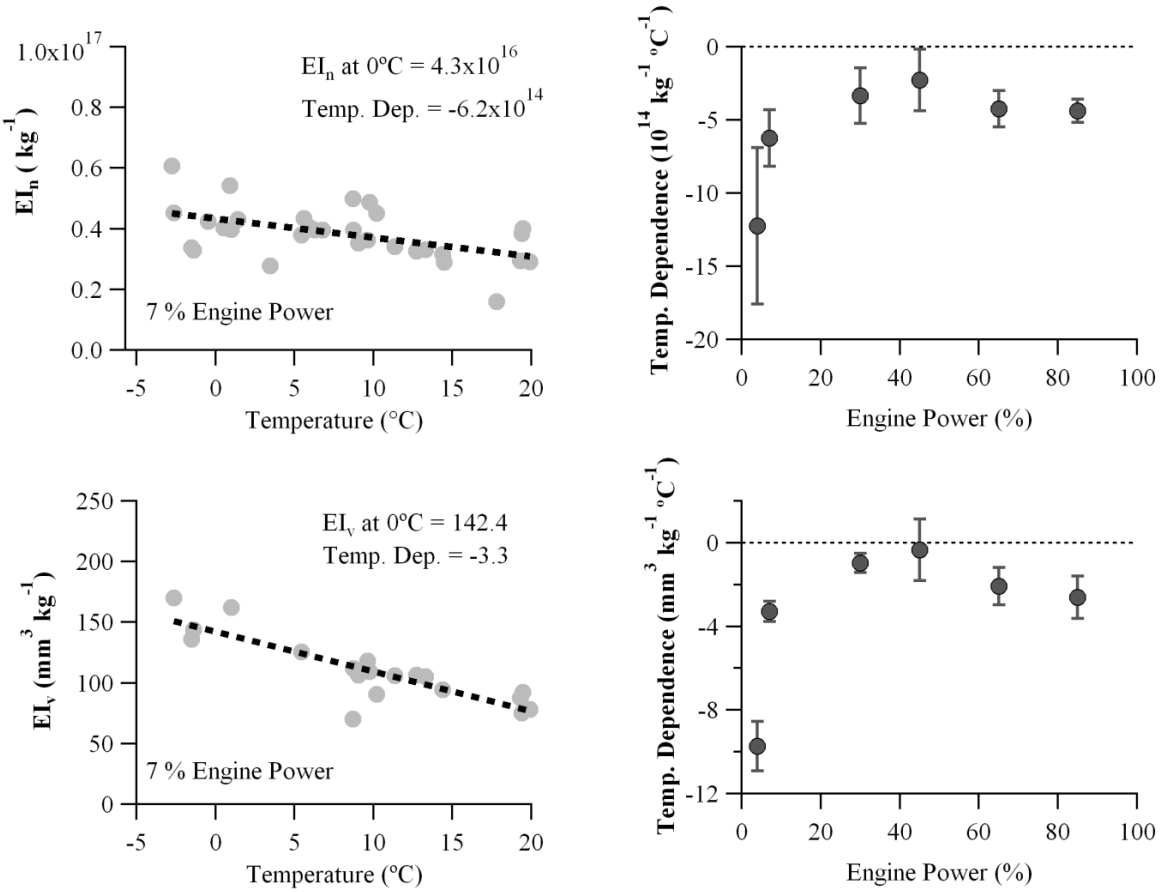

Figure 35. Total aerosol number (top left) and volume (bottom left) emission indices for JP-8 as functions of ambient temperature. Plots at right display the power dependent temperature coefficients for EI_n (top) and EI_v (bottom). Adapted from appendix H.

The temperature and age dependent growth of the volatile aerosols is further exemplified in Figure 36, which is extracted from appendix L and exhibits mean particle diameter data recorded in the ARI mobile laboratory during multiple downwind penetrations of a JP-8, ground-idle exhaust plume. The size distribution mode is seen to increase both with distance downstream (which is equivalent to plume age) and with decreasing temperature. The authors note that the larger sizes associated with colder temperatures may be caused by more rapid volatile aerosol

nucleation and growth or by enhanced concentrations of condensable material in exhaust or by some combination of the two.

Appendix H examines fuel effects on volatile aerosol concentrations and characteristics in exhaust plumes sampled at 30 m behind the aircraft. The authors state that at low power, FT-1 total EI_n (and EI_m) values were an order of magnitude lower than from JP-8, but still were enhanced above 1-m values. They suggest that this may be due to the slight sulfur contamination or to nucleation of semi-volatile hydrocarbons at the relatively cold ambient temperatures. They further note that Blend-1 total EI_n values were similar to JP-8 values despite the factor of two difference in sulfur content between the fuels. By way of explanation, they cite a study by Timko et al. (2010) which used modeling analysis to show that the reduced availability of soot surface area in the blended fuel exhaust causes new particle formation to be favored over condensation of volatile material onto soot mode particles. They propose that during AAFEX volatile particle populations reached equilibrium between formation by nucleation and loss through coagulation that made the overall particle number densities vary independently from fuel sulfur content. To support this contention, the authors note that JP-8 nucleation-mode mean diameters were significantly larger than corresponding Blend-1 diameters in the 30-m samples at all power settings. Additional analysis shows that FT-2 and its blend formed considerably more volatile aerosol in aging exhaust plumes than FT-1; this is consistent with the comparatively higher total hydrocarbon emissions associated with the FT-2 fuel.

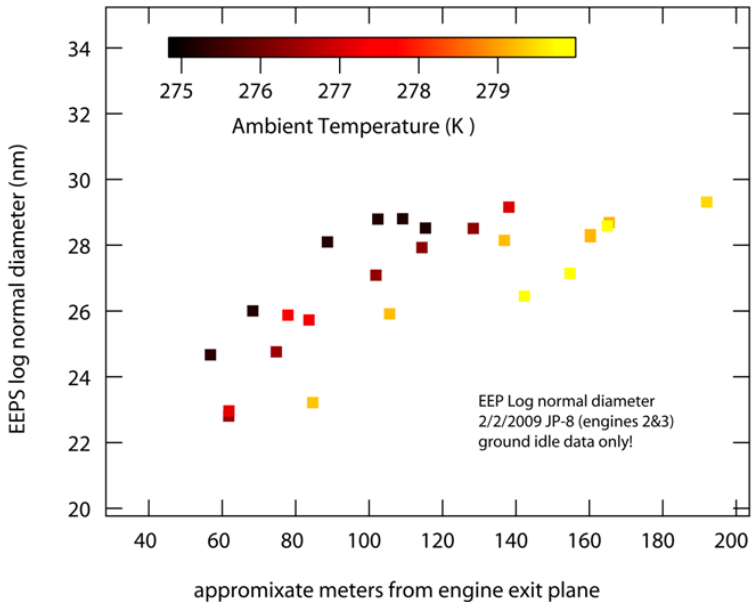

Figure 36. EEPS number density-based, nucleation mode diameter data obtained during early morning idle plume penetrations. The "X" axis represents meters downstream of the engine exit plane and indicates that the subject data were recorded between 50 and 200 m behind the aircraft. Plot taken from appendix L.

Appendices K and L, contributed by Aerodyne, discuss the composition of volatile exhaust particles as measured using an Aerodyne, time-of-flight, Aerosol Mass Spect (AMS), which is capable of determining the size-dependent concentrations of both sulfate and organic aerosols.

Both appendices couple AAFEX results with measurements from previous field experiments to provide a broader and more substantiated interpretation of the observations. Appendix L additionally includes results from mass spectral analyses conducted on vaporized JP-8 and FT-2 fuels and from AMS studies of the PM generated when the fuels were combusted at ambient pressure in a laboratory diffusion flame burner.

In appendix L, the authors note observing that: 1) for aged plumes (>100 sec), EI_m-organic ranges from 50 – 150 mg kg_{-1} (idle conditions, 275 K); 2) the aromatic signature identified at 30 m perseveres or even increases at 50 m and beyond; and 3) EI_m-organic scales with EI-CO. They acknowledge that the larger EI_m-organic values are partly due to recent improvements in AMS sensitivity to nucleation mode particles, but point out that growth of nucleation mode particles during aging also leads to increased instrument sensitivity and, in turn, higher EI_m-organic. They finally note that the more recent EI_m-organic values are in much better agreement with volatile aerosol mass EIs inferred from volatile aerosol size distribution measurements and indicate that further analyses are needed to identify whether particular organic species preferentially condense in the plume and to evaluate the effects of dilution and processing time on EI_m-organic values.

Appendix K takes a comprehensive look at volatile aerosol composition and how fuel composition, engine technology, combustion conditions, and ambient temperature influence organic aerosol partitioning and mass emission indices. From mass spectral analysis, the investigators note that the JP-8 and FT fuels were fundamentally much different and that JP-8 contained much higher concentrations of large aromatics and heavy hydrocarbons that are likely to be PAH precursor species. Their diffusion flame studies showed that pyrene was the predominant PAH species emitted when burning all fuels under relatively lean conditions, but that PAH emissions in general were substantially lower from FT-2 than JP-8. The authors observed that, in addition to fuel composition, PAH emissions for all fuels were highly dependent on fuel air ratio. In rich flames, all fuels produced PM with relatively higher oxygen content, but on a percentage basis, FT-2 levels were greater than JP-8 (16% versus 11% of total organic aerosol emissions). The authors indicate that because of its higher oxygen content, the FT-2 volatile aerosols would likely be more soluble than JP-8 PM emissions and hence make better cloud condensation nuclei.

To gain insight into the composition and characteristics of gas turbine PM emissions, appendix K authors performed a positive matrix factorization (PMF) analysis on recent AMS data sets. They found that the organic aerosol emissions could be grouped into five basic types: lube oil, siloxane (from sampling system out-gassing), hydrocarbons, aromatics, and an unknown category that scaled with lube oil. They found that at all power settings lube oil dominated total organic PM emissions from RB211 engines, but that hydrocarbons and aromatics (incomplete combustion products) accounted for 60% or more of EI_m-organic for a CJ6108A turbojet engine (an example of 50-year-old engine technology). For a CFM56-3B1, which is similar to the engine tested during AAFEX, lube oil and the lube-oil-like compounds composed between 50 and 70% of EI_m-organic across the power range, whereas products of incomplete combustion accounted for about 45 and 30% of the organic PM emissions at idle and high thrust levels, respectively. The ratio of hydrocarbon to aromatic PM emissions varied between engines and power settings, but was typically lowest at idle and greatest at medium to high thrust settings.

Appendix K also presents and discusses AAFEX EI_m-sulfate and EI_m-organic values derived from AMS measurements. Figure 37, adapted from the report, shows how these two parameters varied as functions of engine power, fuel composition and ambient temperature. As the authors note, the dependence of the EIs on fuel composition is readily apparent. For JP-8, EI_m-sulfate varied from about 1 mg kg^{-1} at idle to nearly 4 mg kg^{-1} at take-off. In contrast, EI_m-sulfate for both pure FT fuels was below detection limits (0.2 mg kg^{-1} for these tests) regardless of power or ambient conditions. EI_m-sulfate for the blended FT fuel was intermediate to the pure FT fuels and JP-8, though closer to the FT data. Increasing power increased EI_m-sulfate, most likely because of the power dependence of EI_{bc} and the better ability of the AMS to quantify soot sized particles (and/or their coatings) than nucleation/growth mode particles. Temperature was also important. As temperature increased, so too did EI_m-sulfate. This counter-intuitive finding is likely due to the competition between nucleation (favored at low temperature) and soot coating (favored at high temperature) – and the relative sensitivity of the AMS to nucleation particles (low) and soot particles (high). Consistent with these observations, EI_m-sulfate for the port engine is greater than the starboard engine just as EI_m-soot for the port engine is greater than for the starboard engine.

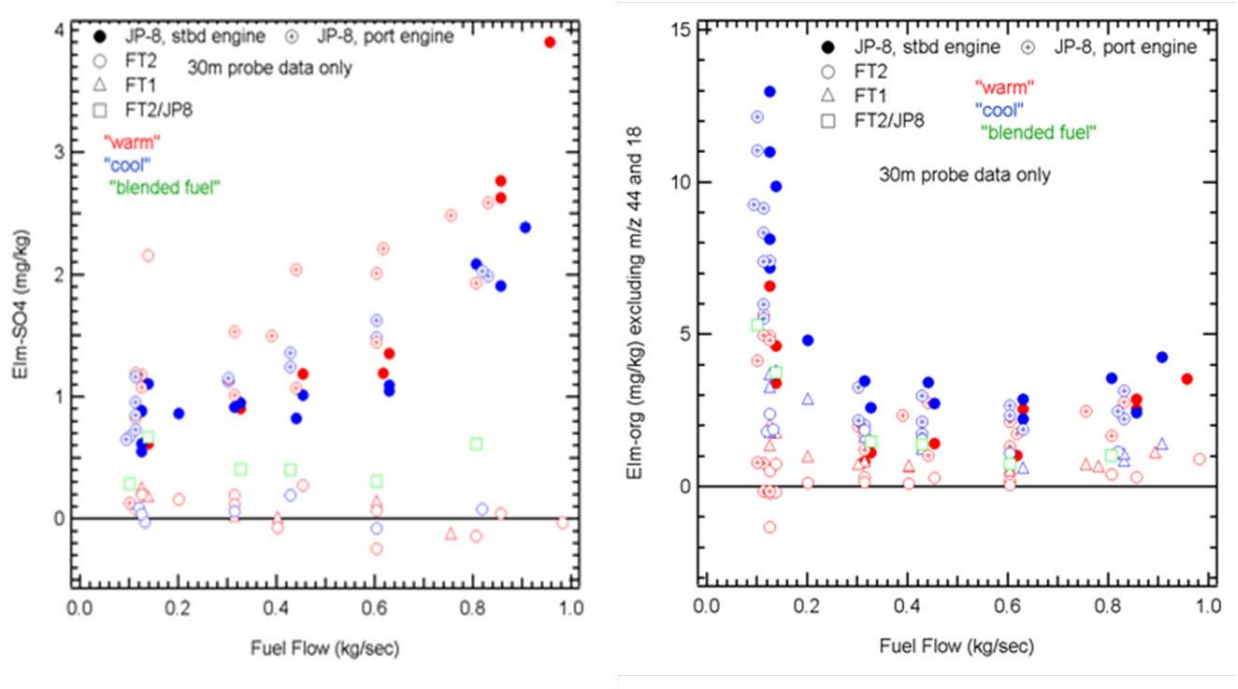

Figure 37. Sulfate (left) and organic (right) aerosol emission indices plotted as functions of fuel flow rate. Adapted from appendix K.

For organic PM emissions, the authors point out that EI_m-organic depends on fuel composition, engine power, and ambient conditions (see right panel of Figure 37). The dependence of EI_m-organic on the engine (port or starboard) is weaker than for EI_m-sulfate. Taking the other three variables in turn: 1) fuel: EI_m-organic is greater at all power conditions for JP-8 than for the FT fuels or the blended fuel; 2) temperature: EI_m-organic increases with decreasing ambient temperature; 3) power: consistent with APEX results, EI_m-organic decreases from 0-15%

(plotted as fuel flows ranging from 0 to 0.3 kg sec^{-1}) and then increases from 65-100% (0.6 to 1 kg sec^{-1}). Quantitatively, EI_m-organic for JP-8 fuel at idle and low ambient temperature reaches a value of nearly 15 mg kg^{-1}; the authors attribute this large value to the low ambient temperature of the test and the relatively low efficiency of the CFM56-2C1 combustor when operated near idle.

To explore the mechanisms responsible for regulating the partitioning of the volatile aerosol species between the nucleation and soot modes, appendix K examines the ratio of EI_m-sulfate to EI_m-organic as a function of engine power and ambient temperature. For JP-8, the ratio exhibits an increasing trend with power under both cold and warm ambient conditions. At idle, the volatile PM is dominated by organic material, which constitutes more than 90% of the total mass. At take-off thrust in warm conditions, the ratio of organic to sulfate PM is nearly 1:1. The authors note that at power settings greater than 4%, the ratio of sulfate to organic depends on ambient temperature. They further indicate that higher ambient temperatures favor EI_m-sulfate and correspondingly lower EI_m-sulfate to EI_m-organic ratios. Two explanations are proposed: 1) lower ambient temperatures decrease combustion efficiency, thereby increasing the amount of organic precursors available to form organic PM or 2) decreasing temperature shifts sulfate material preferentially to the nucleation mode (and away from the soot mode) where it is not detected efficiently by the AMS. The investigators present a series of compositionally-resolved size distributions that support these explanations and note that the observation that the nucleation mode may have a different ratio of sulfate to organic material than the soot mode is new and potentially important for understanding aircraft emissions at cruise altitude conditions.

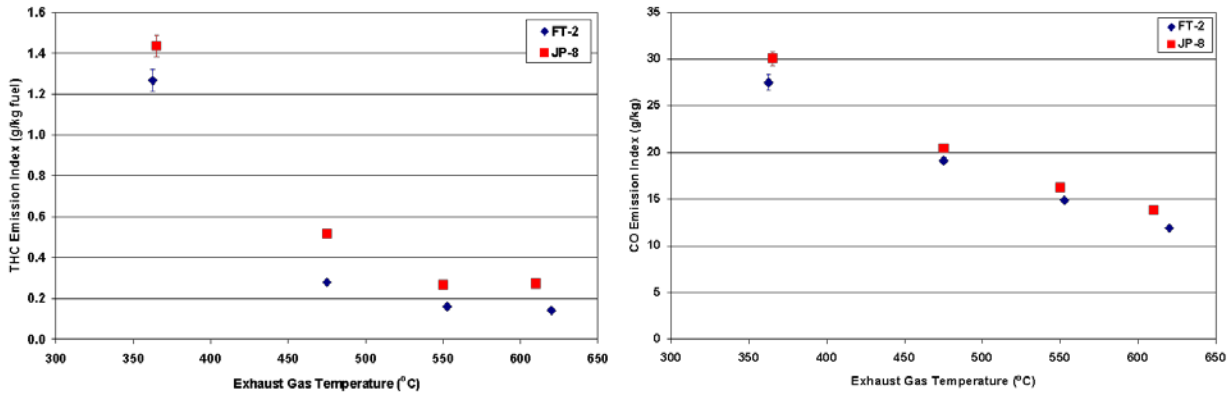

Figure 38. Total hydrocarbon (left) and CO (right) emission indices for JP-8 (red squares) and FT-2 (blue diamonds) for the APU plotted as functions of exhaust gas temperature. Adapted from appendix M.

4.07 Auxiliary Power Unit (APU) Gaseous and PM Emissions

Emissions from the DC-8's APU were also characterized during AAFEX and are discussed in appendices H and M. As noted above, the APU is essentially an old-technology, turbo-jet engine that operates at relatively low combustion temperatures. Because it was not equipped with fuel flow meters, emission parameters are examined as functions of exhaust gas temperature, which was varied by adjusting the generator, air handling or bleed air demands of the aircraft. Nominal EGT set point values were 360 (idle), 475, 550 and 620°C (full load); for

comparison, EGT for the DC-8's starboard engine varied from approximately 400°C at idle to 716°C at takeoff thrust. Fuel composition effects on APU emissions were evaluated by alternately burning either standard JP-8 or the FT-2 fuel. Ambient conditions were relatively constant and essentially the same during the three APU test runs, so it is not possible to assess temperature effects on the APU emissions.

Appendix M summarizes results from APU gas phase emission measurements conducted by EPA, NASA, AFRL, and ARI. The investigators found that EI-SO_2 was relatively constant with APU load and that JP-8 values were significantly greater than those from FT-2; this is not surprising, because the JP-8 contained ~1200 ppm sulfur impurities as opposed to the FT-2's 22 ppm. Actual values ranged from 1.5-1.8 g kg^{-1} for JP-8 fuel and 0.13-0.15 g kg^{-1} for FT-2. It is noted that use of the alternative fuel reduced SO_2 emissions by an average of 92%. The authors further report that total hydrocarbon (THC) emission indices (Figure 38, left plot) decreased exponentially with EGT from about 1.4 g kg^{-1} (for JP-8) at idle (EGT = 350^{o}C) to ~0.25 g kg-1 at full APU load (EGT = 610^{o}C). FT-2 EI-THC values were an average of 37% lower than those calculated for JP-8. Carbon monoxide EIs (Figure 38, right plot) were also found to decrease with power from ~30 g kg-1 at idle to 12 g kg-1 at full APU load; observed FT-2 EI-CO values were on average 9% lower than corresponding JP-8 values. NOx emission indices varied only slightly around a central value of 4.5 g kg-1 and were relatively insensitive to fuel type and operating conditions.

The characteristics and concentrations of APU PM emissions receive considerable attention in both appendix H and M. Figure 39 summarizes the overall observations. For both fuels, EI_n and EI_{bc} values were a maximum at idle and decreased with increasing APU load.

As noted in appendix H, from a PM standpoint, the APU was much more polluting than the DC-8's CFM-56 engines. For JP-8 at idle, APU EI_n and EI_{bc} values far exceeded those from the DC-8's starboard engine and, unlike for the high-pass engines on the DC-8, APU PM emissions decreased with increasing power (see Figure 39). Indeed, both EI_n and EI_{bc} values declined by more than a factor of two as the APU load was increased from minimum (cabin lights and avionics only) to maximum (air handler operation plus providing bleed air to spin the DC-8 control engine). Since the APU fuel-air-ratio increased with thrust (similar to the aircraft engine), the decreasing emissions can't be attributed to rich combustion conditions at idle. Improved combustion efficiency or increased combustor pressure with thrust are other factors that could influence the emission behavior of the APU.

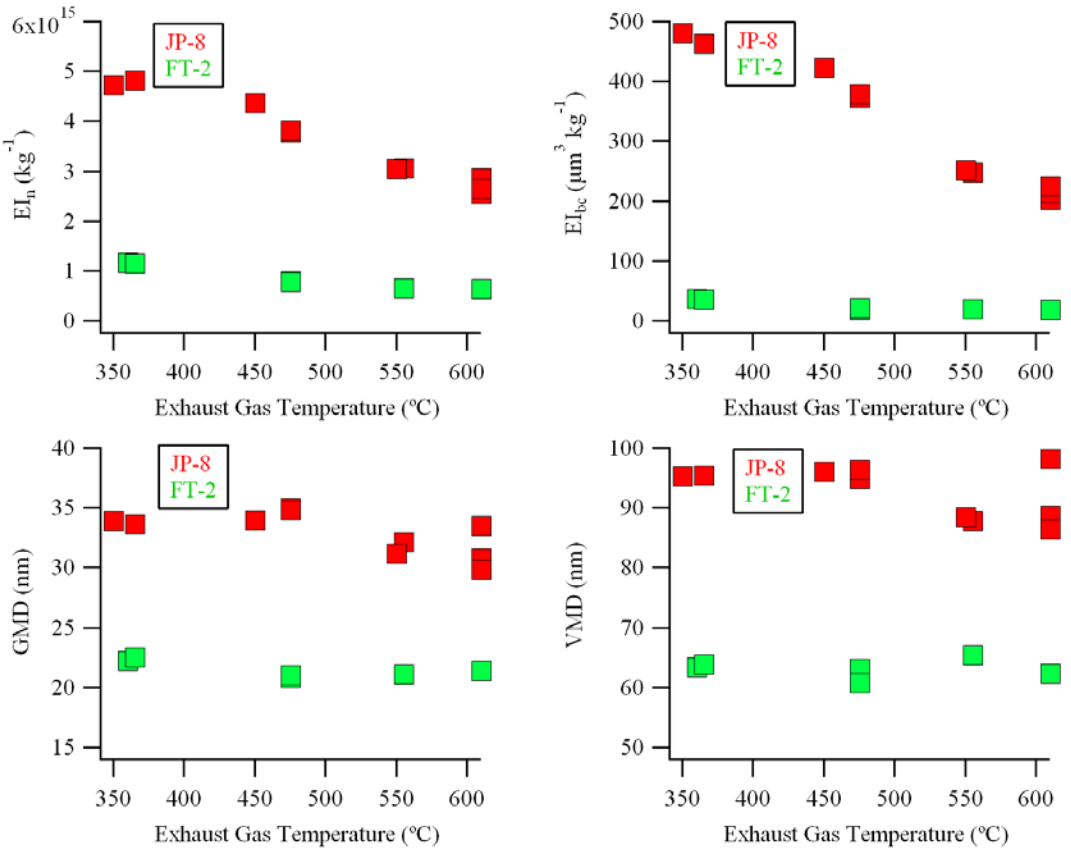

Figure 39. APU nonvolatile PM EI_n (top left), EI_{bc} (top right), geometric mean diameter (bottom left) and volume mean diameter (bottom) right for JP-8 (red squares) and FT-2 (green squares) plotted as functions of exhaust gas temperature. Taken from appendix H.

Regarding PM size, appendix H notes that for JP-8 at idle, GMDs and VMDs were respectively 32.9 versus 21.2 nm and 92.8 versus 57.0 nm for the APU compared to DC-8's starboard engine. Similar to then engines, FT-2 particles were smaller compared to PM emissions from JP-8. Overall, particle size varied with EGT such that APU GMD and VMD values decreased slightly with increasing load (Figure 38), which is opposite to the trends exhibited by the DC-8's engines. However, even at the highest load/thrust settings, APU particles were still 20 to 30% larger, on a volume-basis, than those emitted by the DC-8 engines. Appendix H authors also point out that the APU particles were more fractal and less dense than those emitted by the engines. For example, density values for JP-8 fuel combustion obtained by taking the ratio of EI_{bc} (from the MAAP) to EI_v (from an SMPS) averaged 0.51±0.02 g cm^{-3} for APU compared to 0.92±0.08 g cm^{-3} for the engines at thrust settings greater than 65 %. It also notes that FT-2 particles were smaller compared to emissions from JP-8. APU PM emissions are likely more similar in size, density and fractal nature to soot emissions from older, turbo-jet aircraft engines.

Both appendices emphasize the remarkable reduction in APU PM emissions associated with burning the FT-2 fuel. Appendix H points out that average FT-2 EI_n and EI_{bc} values were respectively factors of 6 and 13 lower than those for JP-8, but were still significant and comparable to JP-8 EI_n and EI_{bc} from the DC-8 engines. APU FT-2 combustion also produced significantly smaller particles compared to JP-8; at idle GMD was 32.9 and 21.5 nm for JP-8 and

FT-2, respectively, and VMD was 92.8 and 63.2 nm, respectively. APU FT particles were more dense than APU JP-8 particles with average density values of 0.60±0.06 g cm^{-3} as opposed to 0.51±0.02 g cm^{-3} for JP-8.

Appendix N, contributed by Penn State University, examines the morphology and detailed chemistry of soot particles generated by the APU. The author notes that synthetic fuels composed of paraffinic species delay the onset of particle formation and growth by absence of dehydrogenated species and aromatics. This permits increased fuel-air mixing, increased formation of oxygenated intermediates and production of alkyl intermediates containing an odd number of carbon atoms, in addition to dehydrogenated molecules and aromatics. He further states that these species will increase the concentration of cyclopentadienyl radicals and aromatics incorporating them, such as naphthalene. Such compounds incorporated into graphene segments give rise to curvature and result in fullerenic nanostructure. The degree or content of fullerenic structure is here postulated to correlate with level of partial premixing. Nanostructure comparisons as a function of engine power supports this postulate as increased fuel concentration with increased (required) power decreases the level of partial premixing, both local and global. The result is a lesser content of fullerenic nanostructure, as observed by HRTEM. Comparisons between the FT and JP-8 fuels provides further support in that for the same power level, soot from the JP-8 fuel contains less fullerenic nanostructure, reflecting its substantial aromatic content, that accelerates soot formation which minimizes the impact of partial premixing. Differences in aggregate size between the two fuels at each power level are consistent with this interpretation. Therein soot nanostructure preserves a record of the gas phase species contributing to its formation and growth and can be used as an in situ tracer of the early combustion chemistry within the engine.

4.08 Sampling System Assessments

Appendix O examines the variability of PM emissions across the starboard engine exhaust plane to address the question of whether single point sampling can yield EI values equivalent to multipoint averages.

Appendix P summarizes AAFEX efforts to assess the impact of the sampling lines and inlet probes on measured particle emission parameters. The report examines results from focused experiments and conducts analyses to: determine size-dependent sampling line transport efficiencies; evaluate particle formation and growth within the 30-m sampling lines; determine PM spatial variability across the engine exhaust plane; evaluate particle losses in the 1-m inlet probes; and examine whether samples collected with modified gas inlet probes yield representative PM emission measurements.

Loss of particles to sampling system components is always a concern in aircraft engine emission tests. To assess these losses, the last official day of AAFEX was devoted to evaluating the size-dependent transmissions efficiencies of the four primary sampling lines. Appendix Q presents the results and notes that after 35 hours of engine testing, up to 50% of particles of all sizes were lost in some of the long sample transport lines (see Figure 40). It states that the losses were greatest in the lines that had been used the most, which suggests that the reduced transmission efficiencies were caused by build-up of material on the tubing walls. An analysis of the port

engine black carbon emissions measured downstream from the 30-m inlet indicate the losses were modest initially, but increased in time as soot and other contaminants accumulated on tubing walls; the analysis further suggests that for the left, 30-m inlet line's efficiency dropped ~5%/day over the course of the experiment. A variety of physical processes are explored as possible causes for the significant losses of particles in the 100 to 300 nm diameter particles in the sampling lines. The most reasonable explanation is that the accumulated material increased surface roughness, essentially creating a surface-filter effect that enhanced particle losses through interception and turbulent impaction.

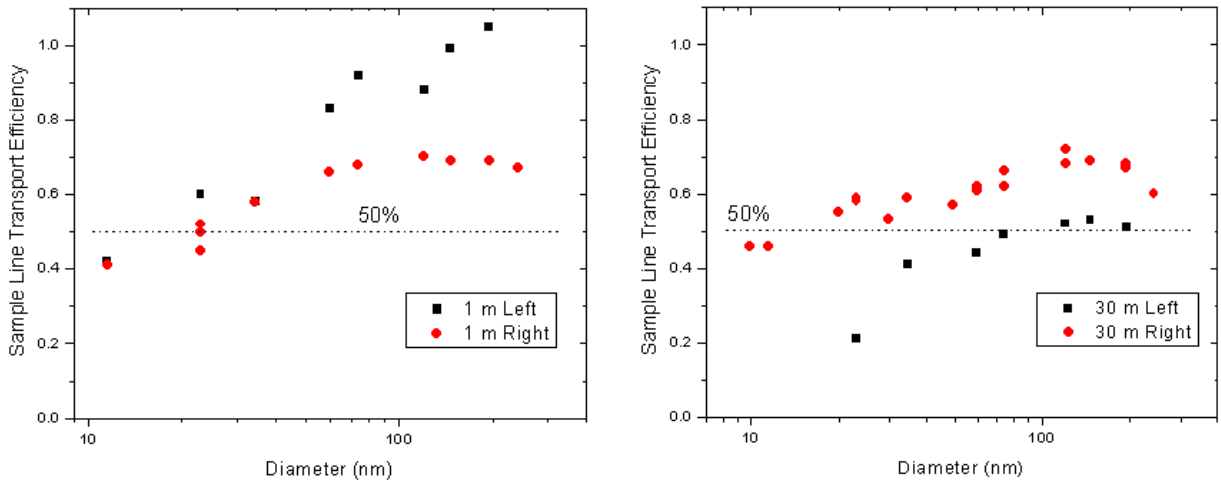

Figure 40. Transmission efficiencies for the 1 (left) and 30 m sampling lines as determined after the engine tests were complete. Taken from appendix P.

Appendix P examines results from the "Deathbox" experiment to address the question of whether a majority of the volatile aerosols seen at 30 m condense in the exhaust plume or during transport through the long sampling lines. The authors note that under relatively cold conditions (~0^{o}C), volatile particle nucleation within the aging exhaust plume typically reached equilibrium between formation and coagulation before entering the 30-m inlet probe. However, volatile particle mass continued to form during the subsequent 16-second transport time within sampling lines, potentially increasing calculated mass emission indices by 50 to 75% at high engine powers.

Appendices P and Q address the question of whether point measurements of PM emissions are representative of the engine PM emissions as a whole. Appendix O investigators examine data acquired throughout the mission to assess the PM emission variability across the engine exit plane. They note that the spatial homogeneity was power dependent, with minimum PM parameter variability at the highest power and maximum variability at mid power. They also found that measured emission indices showed more variability than the size distribution shape parameters and note that overall, normalized PM emissions varied from 6 to 70% across the limited span of engine exit plane explored in the study. To eliminate the effects of changing ambient temperatures and sampling system characteristics, appendix P authors restrict their spatial variability assessment to data recorded within a single test, wherein the sampling rake was translated in 5-cm increments from 0 to 20-cm off centerline at power settings ranging from idle to 85% of maximum thrust. The investigators indicate that non-volatile PM mass and

number EIs were fairly stable and equivalent within 10 cm of centerline, suggesting that single point sampling in that region would yield emission parameters broadly representative (within 20%) of the entire engine.

Results from a study in which sample dilution ratios were systematically increased to reduce inlet tip velocity are also examined in appendix P to evaluate the impact of non-isokinetic sampling on calculated PM emission parameters. The authors note that at high engine thrust, PM emissions generally increased with freestream to sample inlet velocity ratio, U_0/U, suggesting that particle populations were being enhanced by virtual impaction. However, the enrichment trends did not faithfully follow sub-isokinetic flow predictions and were thus possibly caused by other mechanisms.

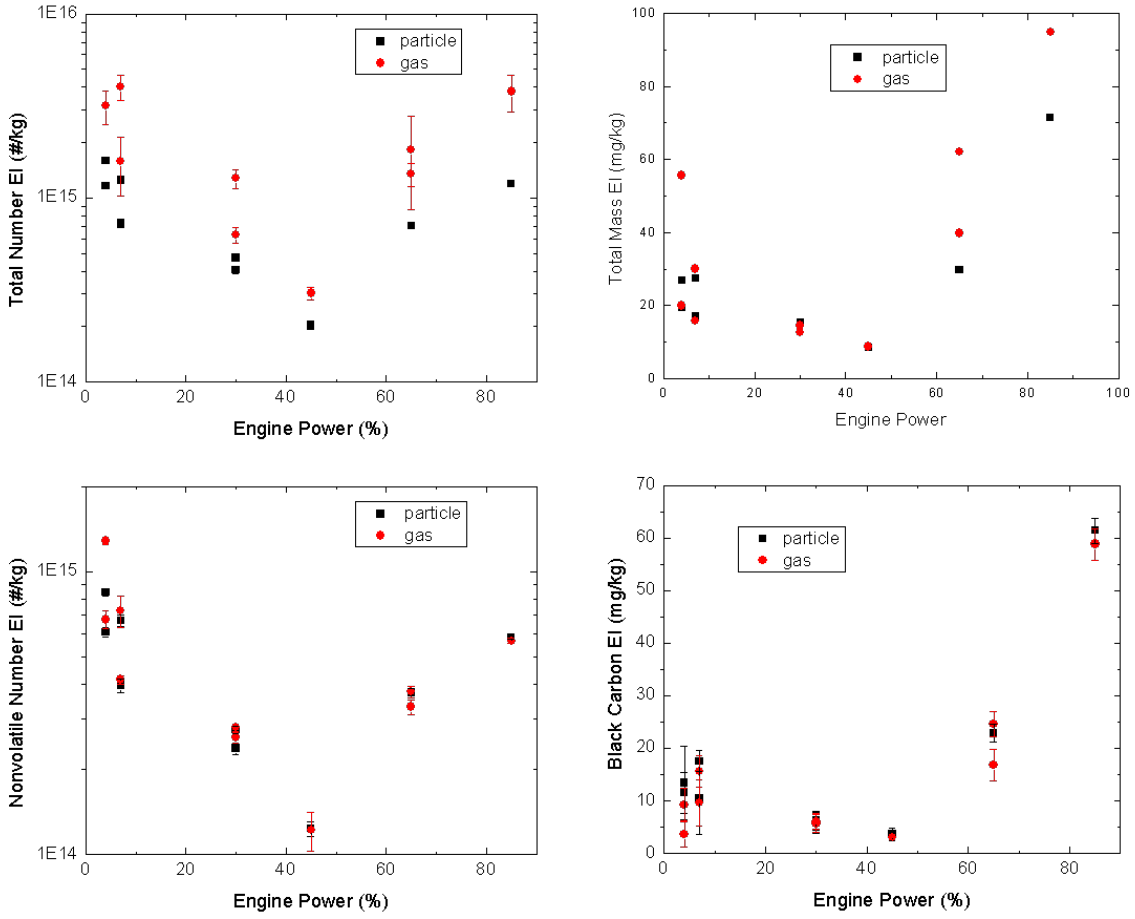

Figure 41. Total number (top left) and mass (top right) along with nonvolatile number (bottom left) and black carbon (bottom right) emission indices plotted as functions of engine power and as measured in samples froma particle dilution probe (black squares) and gas probe with dilution gas introded 1.5 m downstream of the inlet tip. Taken from appendix P.

Loss of particles within inlet probes and sampling lines is of great concern when sampling hot, high-velocity engine exhaust 1 m downstream of the engine exit plane. To evaluate the losses, appendix P compares PM emission measurements from the 1- and 30-m inlet probes. The

investigators found that 30-m, non-volatile EI_n and EI_m were systematically higher for both engines than those measured at 1 m, indicating possible particle loss in the 1-m inlets or transport tubes; thermophoretic deposition and turbulent eddy impaction are suggested to be possible mechanisms that account for these losses.

A portion of one of the later JP-8 test runs conducted during AAFEX addressed the question of whether it is possible to make representative PM measurements from standard gas inlet probes. The experiment involved comparing PM number and mass EIs measured from adjacent gas and particle probes mounted near the engine centerline in the starboard 1-m rake; dry dilution gas was introduced concentrically to the particle probes at the inlet tip (see section 3 discussion) and to the gas probe samples about 1.5 meters downstream, near the base of the rake stand. Results are presented in appendix P and shown in Figure 41. The investigators found that volatile aerosols formed in the gas probe samples which cause total PM number and mass EIs to be somewhat enhanced in comparison to the particle probe measurements (see top panels in Figure 41). However, samples first routed through a thermal denuder upstream of the diagnostic instruments yielded nonvolatile EI_n and EI_{bc} data from the two probes that agreed to within 10%, suggesting that existing gas certification sampling probes used by engine manufacturers may be modified to yield representative particle number, mass and PSD measurements.

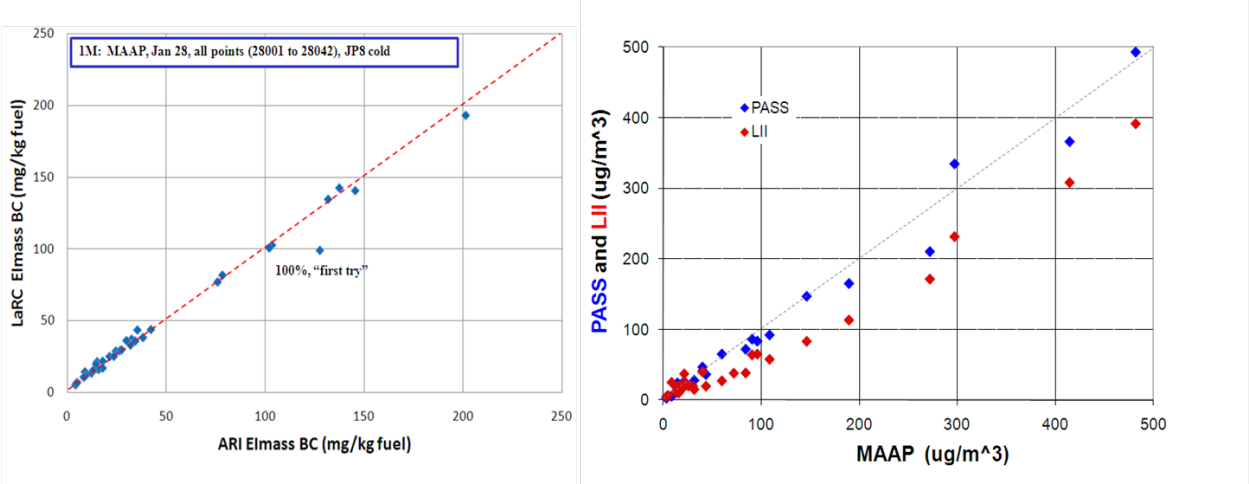

Figure 42. Instrument comparison data acquired during tests that used a CAST diffusion burner as a black carbon source. Figure adapted from appendix R.

4.08 Instrument Comparisons

Appendix Q reports results from a collaborative study performed at the conclusion of AAFEX, wherein a portable soot generator was used as an engine surrogate to assess the agreement between a variety of instruments used to characterize aircraft PM emissions. A separate objective was to evaluate the soot generator as a possible calibration source for field measurements. In the test, soot samples of varying concentration were distributed to a number of different instruments so that simultaneous measurements could be performed. Although the suite of instruments provided the capability of measuring particle concentration, size distribution, and mass, the focus of the experiment was to compare instruments that measure BC mass because factors other than instrument performance (e.g., line loss) were expected to affect measurements of the other parameters. Tested instruments included: (1) several ThermoElectron Multi Angle

Absorption Spectrometer (MAAP) model 5012, (2) an Artium LII-200 Laser Induced Incandescence instrument, (3) a Droplet Measurement Technologies Photo-Acoustic Soot Spectrometer (PASS-3), (4) a standard Smoke Number instrument, (5) Scanning Mobility Particle Sizers (SMPS), and (6) Condensation Particle Counters (CPC). The report notes that intra-instrument comparisons of the MAAP (see Figure 42) for the measurement of black carbon mass showed that as expected the same instrument analyzing the same sample produces the same result. Inter-instrument comparisons (right panel in Figure 42) showed that particle properties and instrument factors can influence the results. The removal of volatile particles is a key to compare mass and number datasets. The authors note that instrument efficacy can be obtained; however, without established instrument calibration methods, traceability is lacking and measurement uncertainty remains. They also point out that the commercially available portable particle generator based on a well-controlled propane diffusion flame that was used in the test produced results which encourage its further assessment as a source for field measurement of line loss and instrument calibration.

5.00 FINAL REMARKS AND RECOMMENDATIONS

By all accounts, AFFEX was highly successful in that participants acquired extensive engine performance and emissions observations that addressed all test objectives and provide valuable insight into the factors that control gas turbine gaseous and PM emissions. Indeed mission data are unparalleled in detail and quality and will be particularly useful in developing models to predict soot emissions based on fuel composition and for validating both photochemical and microphysical models of engine exhaust plume evolution.

Moreover, AAFEX results are consistent with previous studies and indicate that engines and aircraft support equipment burning synthetic fuels generate substantially less PM and HAPS emissions than those burning standard petroleum-based fuels. Thus, provided aircraft fuel system leak problems can be solved, the tested fuels can be used as drop-in replacements that impose no penalty on engine performance, but significantly reduce local air quality and health impacts.

AAFEX success was greatly enabled by experience gained in previous ground-based, on-wing engine emission tests including the summer 1999 NASA aerosol instrument workshop (Cofer et al., 2000), EXCAVATE (Anderson et al., 2005), and the APEX test series (i.e., Wey et al., 2007). However, despite being cognizant of the knowledge gained in these experiments, additional lessons were learned that could potentially improve future emissions test plans and procedures. These primarily relate to exhaust sampling and are listed below.

- Be cautious when using non-metallic aerosol sampling lines. Long lengths of conductive PTFE were used in some of the AAFEX sampling lines and are suspected to have accumulated surface contamination more quickly than the polished stainless steel.
- Carefully design sample flow systems to minimize tubing exposure to concentrated exhaust sample. A large amount of exhaust flow was drawn continuously through the 30-m sampling lines at all times during engine runs; this was potentially a cause of the large transmission losses observed in the lines at the conclusion of the mission.

- Perform frequent sample line leak tests. Several hours of data were partially compromised by having small leaks in and around the sample selection valves. Sample systems should also be designed to include a minimum of valves and fittings.
- Perform sample line PM transmission tests at frequent intervals; have a procedure in place for cleaning lines if losses become excessive. Line loss tests were conducted after all the engine emission tests were complete and suggested that up to 50% of PM mass was lost to the walls in some cases. Since this would not be the case for clean lines, the question arose: when did the losses become evident? An attempt to clean the lines by flushing with water appeared to be ineffective.
- Design sample dilution systems to minimize dry N_2 requirements. To avoid line contamination it is recommended that a small flow (~2 lpm) be blown out unused inlet tips rather than drawing large dry N_2 flow through unused lines with a vacuum pump.
- When sampling with a single set of probes, be sure to survey emissions across the exhaust plume so that areas contaminated with oil leaks or associated emissions can be avoided. The DC-8's #3 engine had an oil leak that apparently produced volatile aerosols in the region within 10 cm of its centerline. Several tests were conducted before the source of the volatile aerosols was recognized and the sample rake was repositioned to avoid the contaminated flow.
- When using cold sampling lines or diluting samples downstream of the inlet tip, a thermal denuder should be used to remove volatile aerosols before PM emission parameters are measured. On cold mornings, exit plane PM samples sometimes exhibited nucleation mode particles formed by condensation of low-volatility species within the cold tubing.
- When sampling emissions from engines burning alternative fuels, make frequent measurements of background PM and gas species concentrations. Emissions from these fuels are very low, particularly at idle, and 30-m measurements must be corrected for background contributions.
- Use large (400 L), high-pressure LN2 tanks to provide dilution gas; the small tanks cannot provide adequate flow for 10-fold sample dilution at high engine thrust settings.
- Be cautious in conducting downstream sampling with mobile vehicles; personnel should be exposed to the noxious gases in the exhaust plume for only brief periods of time to avoid toxic reactions (headaches, nausea, etc.)

AAFEX measurements and data analysis activities have greatly advanced our understanding of fuel and ambient-condition effects on engine black carbon emissions and volatile aerosol formation and growth in aging exhaust plumes. The project also brought to light several areas where additional research is needed.

- Improved measurements of volatile aerosol nucleation mode mass and composition are required to further develop and validate aerosol microphysical models. The AMS instrument used in AAFEX and previous studies is not sensitive to aerosols in this size range and thus in many cases it only "sees" a small fraction of the volatile aerosols inferred to be present from SMPS-type measurements.
- Direct measurements of engine-exhaust black carbon mass density are needed to better characterize the fractal nature of the particles and how it varies with combustor technology, fuel composition, and combustion conditions. In AAFEX, bulk density values were calculated from the ratio of MAAP black carbon mass to SMPS volume. A much better

approach is to use an Aerosol Particle Mass instrument, which are now available commercially, to measure the mass of monodisperse particles selected by an SMPS.

- Measurements of the soluble components of aged aircraft exhaust plumes are needed to evaluate the impact of aircraft emissions on local water quality and clouds. Instruments are available for performing these measurements and should be deployed during the next suitable engine test or to an airport for an advected plume study.
- Detailed measurements of exhaust plume chemistry for a variety of engine types over a broad range of ambient conditions. AAFEX measurements indicate that CFM-56-2C engine emission performance is highly dependent on ambient temperature. Additional studies are needed to verify that this sensitivity is common and of the same magnitude for all engine types. Effects of relative humidity and background aerosol loading should also be explored.
- Better characterization of particle losses in near-field sampling probes. AAFEX results suggest that PM number and mass measurements are significantly reduced by particle losses occurring within the 1-m inlet probes, possibly by thermophoretic or turbulent eddy impaction processes. AAFEX observations also suggest that PM measurements are influenced by mismatched freestream and inlet tip velocities. Carefully designed experiments are needed to characterize these losses/uncertainties and develop procedures for minimizing their effects.
- Non-proprietary design for an efficient thermal denuder that operates at high sample flow (up to 10 lpm) rates. Volatile aerosols form in aircraft exhaust samples for a variety of reasons. Commercially available thermal denuders remove these aerosols but only at low flow rates (~1.5 lpm) and for relatively low-volatile aerosol loadings. A high-flow device that both evaporates and removes aerosol precursors would be a greatly advance our ability to characterize black carbon particles within aged plumes or samples acquired with gas probes and diluted a few seconds after entering the sample transport system.
- A simpler, more robust, and standardized exhaust sampling system. The AAFEX aerosol sampling system was a plumbing nightmare of fittings, valves, pumps, and tubing that took three days of intensive work by three or more technicians to install. Trade studies should be conducted to evaluate the relative sacrifice in PM measurement fidelity associated with employing much simpler sampling systems. Emissions researchers should collaborate with the SAE E-31 committee that is developing an Aerospace Recommended Practice (ARP) for exhaust PM sampling to establish an acceptable system design that capitalizes on existing facilities and ensures reproducible results between test venues.
- Calibration standards for particle concentration and black carbon mass. At present, there are no direct means of calibrating the instruments used to measure PM number and mass. Such calibration standards are critically needed before regulations on engine PM emissions can be established.

6.00 ACKNOWLEDGEMENTS

The authors gratefully acknowledge the significant contributions of NASA Dryden personnel to AAFEX, particularly the excellent project management provided by Frank Cutler and Ron Wilcox and the excellent aircraft and technical support provided by the DC-8 crew, Mike Bereda, chief. AAFEX was sponsored by the NASA Fundamental Aeronautics, Subsonic Fixed Wing program. Any opinions, findings or conclusions expressed with this report are those of the authors and do not necessarily reflect the views of NASA.

7.00 REFERENCES

Anderson, B. E. et al., 2005; Experiment to Characterize Aircraft Volatile Aerosol and Trace Species Emissions (EXCAVATE), NASA/TM-205-213783.

Timko, M. T., Z. Yu, T. B. Onasch, H.-W. Wong, R. C. Miake-Lye, A. J. Beyersdorf, B. E. Anderson, K. L. Thornhill, E. L. Winstead, E. Corporan, M. J. DeWitt, C. D. Klingshirn, C. Wey, K. Tacina, D. S. Liscinsky, R. Howard, A. Bhargava, 2010; Particulate emissions of gas turbine engine combustion of a Fischer-Tropsch synthetic fuel, in review.

Wey, C.C. et al. 2006; Aircraft Particle Emission Experiment, NASA/TM-2006-214382.

Wey, C. C., B. E. Anderson, C. Wey, R. C. Miake-Lye, P. Whitefield, and R. Howard (2007), Overview on the aircraft particle emissions experiment, Journal of Propulsion and Power 23, 898-905.

8.00 LIST OF APPENDICES

APPENDIX A: Engine Performance and Gaseous Emissions (NASA GRC)

APPENDIX B: Effects of Alternative Fuels on CO and NO_X Emissions Performance: A Summary of AAFEX Field Mission Data (Aerodyne)

APPENDIX C: VOC Emissions from Jet Aircraft Engines Burning Alternative Fuels: A Summary of the Alternate Aviation Fuel Experiment (AAFEX, MSU/ARI)

APPENDIX D: Measurements of Nitrous Acid in Commercial Aircraft Exhaust (Harvard/ARI)

APPENDIX E: Investigations of plume chemistry during AAFEX (ARI)

APPENDIX F: Aircraft Emissions of Methane and Nitrous Oxide during the Alternative Aviation Fuel Experiment (Harvard/ARI)

APPENDIX G: Gaseous and Non-volatile Particulate Matter Emissions Measurements in CFM56 Engines – AAFEX project (AFRL)

APPENDIX H: Concentrations and Physical Properties of Particles within the Exhaust of Aircraft Engines burning Standard and Synthetic Fuels: AAFEX Results (LaRC)

APPENDIX I: Influence of Ambient Temperature on the PM Emissions at the Engine Exit (MST)

APPENDIX J: Soot Particle Morphology and Composition (PSU)

APPENDIX K: Composition of Gas Turbine Engine Combustion Volatile Particle Material (ARI)

APPENDIX L: Microphysical Evolution of Gas Turbine Engine Combustion Particles (ARI)

APPENDIX M: Determination of the Emissions from an Aircraft Auxiliary Power Unit (APU) during the Alternate Aviation Fuels EXperiment (AAFEX)

APPENDIX N: Insights Into The Combustion Chemistry Within a Gas-Turbine Driven Auxiliary Power Unit as a Function of Fuel Type and Power Level Using Soot Nanostructure as a Tracer (PSU)

APPENDIX O: Spatial Variation of PM Emissions at the Engine Exit (MST)

APPENDIX P: Sampling System Effects on Particle Emission Measurements (LaRC)

APPENDIX Q: Instrument Inter-comparison (UTRC)

APPENDIX A: Engine Performance and Gaseous Emissions

Changlie Wey
ASRC Aerospace Corporation
And
Dan Bulzan
NASA Glenn Research Center

During the Alternative Aviation Fuels EXperiment (AAFEX) test series, engine performance was measured by collecting data from the cockpit instrument readouts during the experimental tests. Engine speed (N1), fan speed (N2), exhaust temperature, and fuel flow readouts were recorded by hand for each of the test points. Nominal engine power settings were obtained by adjusting the throttle until the desired value of N1 was obtained. Care was taken to make sure that the engine had reached a steady operating condition before the data was recorded.

Since the test series was designed to investigate "cold" and "warm" ambient conditions, fairly large variations in ambient, inlet temperature were encountered. In order to compare engine performance under all conditions, fuel flows and N1 were corrected to standard day conditions of temperature and pressure using data from the weather station according to the following [1]:

(1) N1 STD = N1/$\sqrt{\theta}$, where $\theta = (Tamb, °F + 459.7)/(59. + 459.7)$

(2) Fuel Flow STD = Fuel Flow/(Delta $*$ $\sqrt{\theta}$) , where Delta = Barometric Pressure(mbar)/1013.25.

The engine performance data is provided in tables 1-5 for the JP-8, FT-1, FT-2, FT-1/JP-8 blend, and FT-2/JP-8 blend. Fuel flows to the engines were measured with analog, mass-flow meters, which have an estimated accuracy of plus or minus 1 to 2 % at cruise flow rates and reduced accuracy at lower power conditions [2]. Readout of the fuel flow could only generally be read in 100 lb/hr increments. For the very low-power conditions, 4% and 7%, fuel flow readings for some of the test points were the same, however, the engine throttle setting had been reduced slightly. Differences in fuel flow readings at these very low-power settings should therefore be viewed with caution. Adjustments in fuel flow rate were calculated to account for higher fuel heating values of the Fischer-Tropsch fuel and are also provided in the data tables. For these adjustments, the fuel flow was multiplied by the ratio of the heating value of the Fischer-Tropsch fuel divided by the heating value of the JP-8 fuel to provide an equivalent JP-8 fuel flow rate. Columns labeled with Fuel Flow STD-HV adjust the heating value corrected fuel flow rates to standard operating day conditions. Ambient conditions as well as calculated values for Theta and Delta are provided.

A comparison of engine rotor speed, N1, versus fuel flow rate is provided in figure 1 for the left inboard engine, engine #2, and the right inboard engine, engine #3, for operation

on JP-8 fuel at cold ambient conditions. As shown in figure 1, there is a slight difference at lower engine power settings between the engines with engine #2 achieving requiring slightly less fuel than engine #3. At higher engine power settings, the two engines appear to be almost identical. Figure 2 shows the same comparison for both engines operating on JP-8 but the data was obtained during operation under warm ambient conditions. The results are similar to those previously shown for the cold ambient conditions with engine #2 requiring slightly less fuel than engine #3 at lower power conditions.

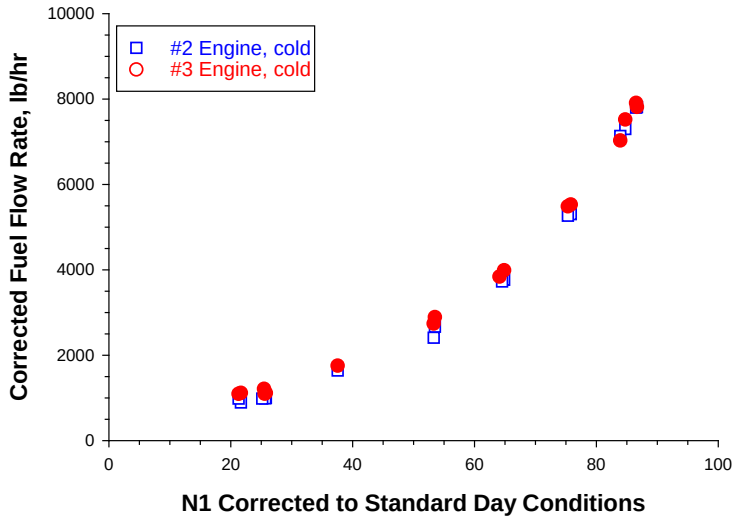

Figure 1. Comparison of Engine #2 and Engine #3 performance operating on JP-8 fuel at cold ambient conditions.

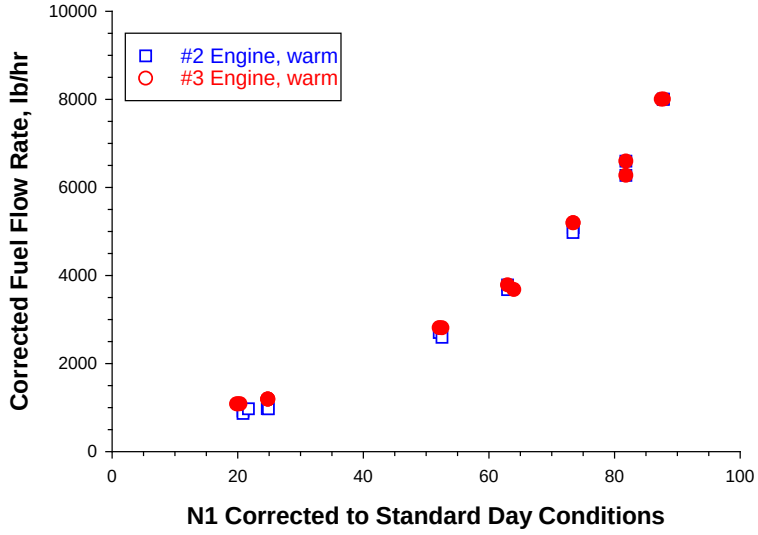

Figure 2. Comparison of Engine #2 and Engine #3 performance operating on JP-8 at warm ambient conditions.

Engine performance for all of the fuels is presented in Figure 3 for engine #3. Only engine #3 was operated with the various test fuels during the experimental testing. The testing required operation of both engines, however, engine #2 was always operated on JP-8. Data from engine #3 for all of the fuels tested is shown and plotted for each date of testing so it includes data under both warn and cold ambient conditions for all of the fuels except the blends where only one ambient condition was run. All data was corrected to standard day conditions, but no adjustments for fuel heating value were made in this figure. The increased scatter in the data for the FT-2 fuel on January 30 was probably caused by very high tail winds, which were encountered during testing on that day.

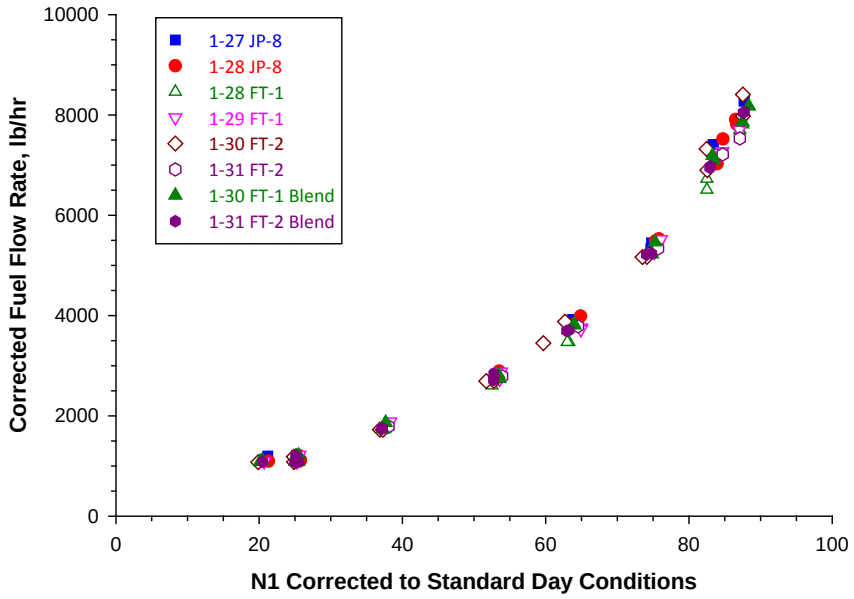

Figure 3. Corrected N1 versus corrected fuel flow rate for all fuels.

Figure 4 presents engine performance data for all of the fuels but the fuel flow rate has been corrected for fuel heating value and then corrected to standard day operating conditions. As shown in figure 4, the correction for heating value decreases the scatter in the data slightly compared to figure 3 and shows very similar results for all of the fuels within the accuracy of the speed and fuel flow measurements. Again, the increased scatter evident for the FT-2 fuel on January, 30 is probably due to the very strong tailwinds encountered during the testing.

Gaseous emissions measured 1 m downstream of the #3 right inboard main engine are illustrated in figures 5-13 for all of the fuels tested. Results are shown for NO_x, CO, unburned hydrocarbons (HC), combustion efficiency, and SO_2. NO_x emissions are presented in figure 5 as a function of fuel mass flow rate for all of the fuels. No corrections have been applied to the measured fuel flow rate in figure 5.

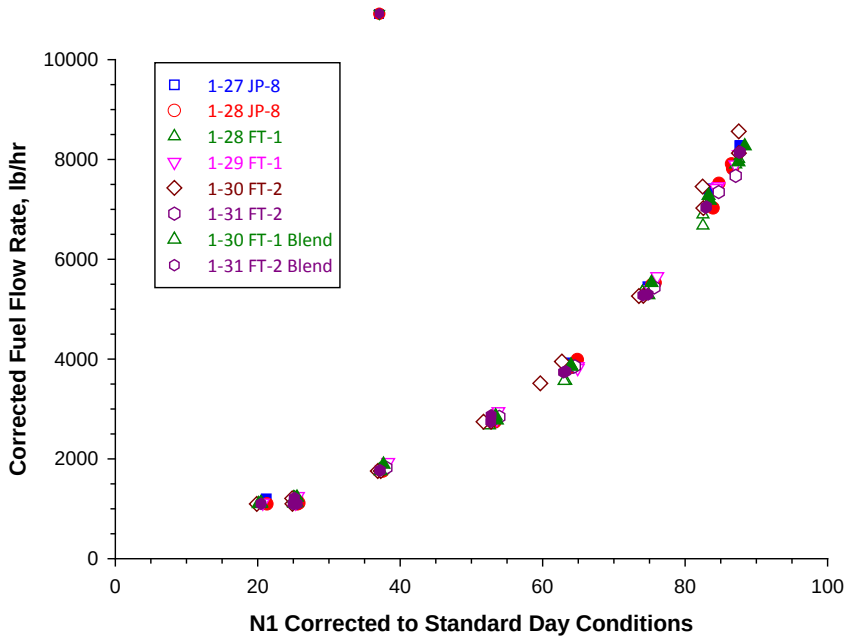

Figure 4. Corrected N1 versus heating value corrected fuel flow rate for all fuels.

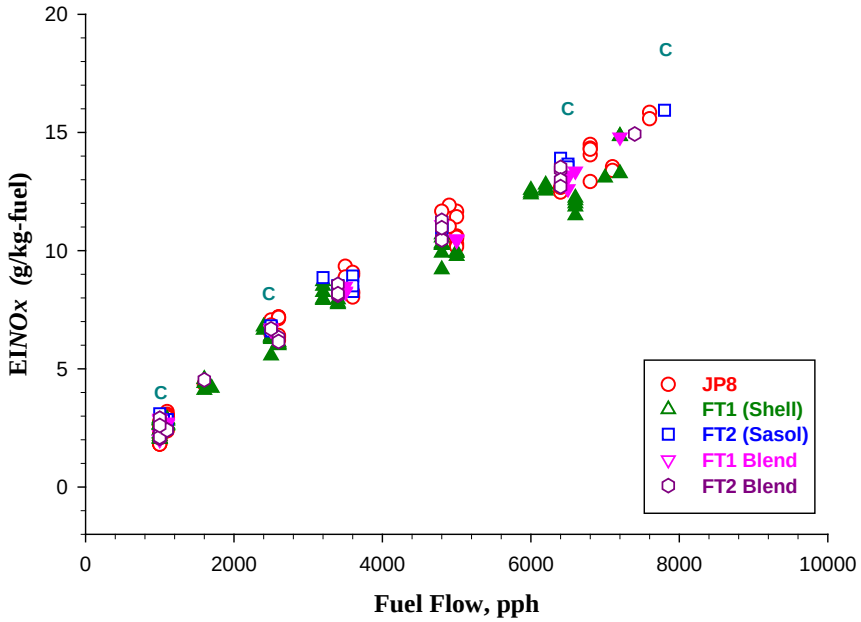

Figure 5. NOx emissions versus measured fuel flow

Also indicated on the figure with a "C" are International Civil Aviation Organization (ICAO) certification values for the engine thrust levels corresponding to idle, descent, takeoff, and climbout. As shown in figure 5, measured NOx emissions for all of the fuels were slightly below the certification values but fairly similar for all of the fuels. There is

some scatter in the NOx data due to differences in engine operating conditions. At higher fuel flowrates, the FT-1 and FT-1/JP-8 blend had slightly lower NO_x emissions.

NOx emissions plotted as a function of corrected engine speed N1 are presented in figure 6. Engine speed was corrected to standard day conditions using equation (1).

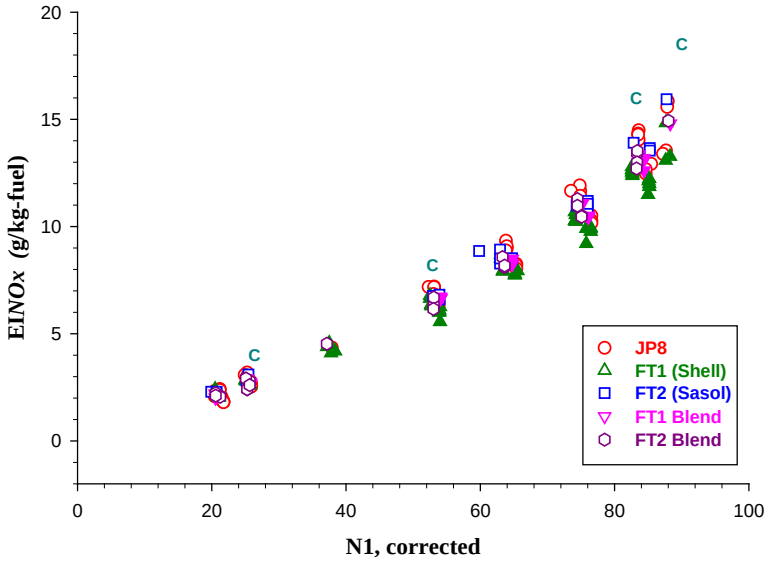

Figure 6. NOx emissions for all fuels versus corrected N1

This correction improves the agreement with the certification values, especially at the higher power conditions. A slight decrease in NOx emissions with the FT1 fuel and FT-1 Blend at higher power conditions is evident.

Results for CO and unburned hydrocarbons are presented in figures 7 and 8. Fuel flowrates have not had any corrections applied. Results are quite similar for both and indicate very low levels at all higher power conditions with sharply increasing values at the low-power conditions. The large amount of scatter in the data at lower power conditions is caused by inaccuracies in the measured fuel flow rate. In many cases, there was no measured difference in fuel flowrate for engine power settings of 7% and 4%. Plots of CO and HC versus corrected N1 using equation (1) correlate much better at the lower power conditions and this is illustrated in figures 9 and 10. CO and unburned hydrocarbon emissions for the F-T fuels are reduced at lower power levels compared to JP-8.

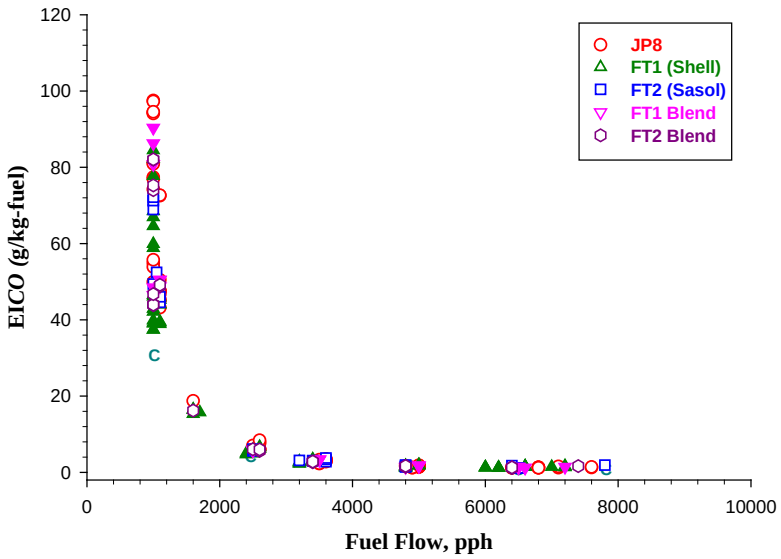

Figure 7. CO emissions for all fuels versus fuel flow

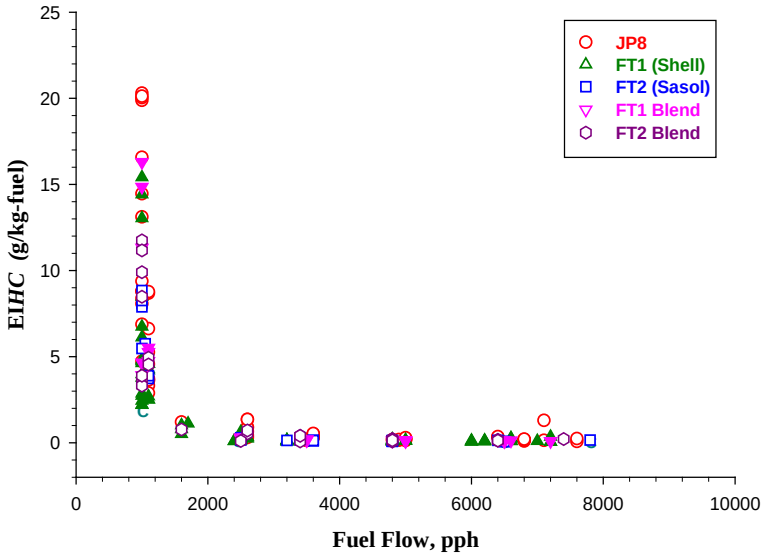

Figure 8. Unburned hydrocarbon emissions for all fuels versus fuel flow

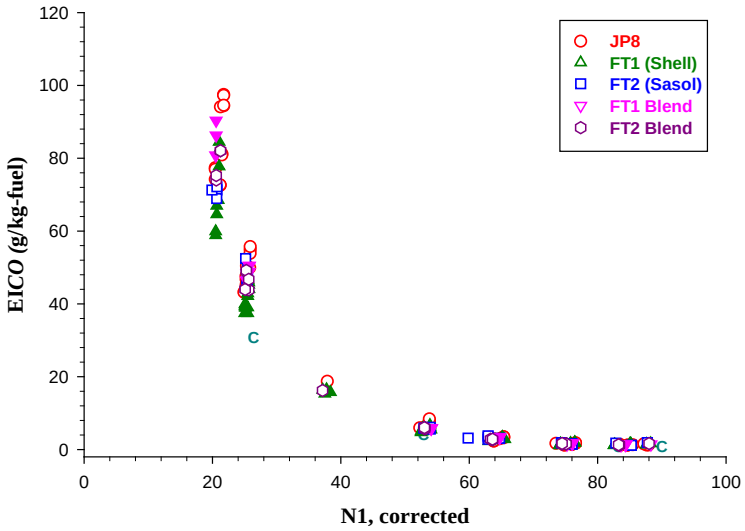

Figure 9. CO emissions versus corrected N1

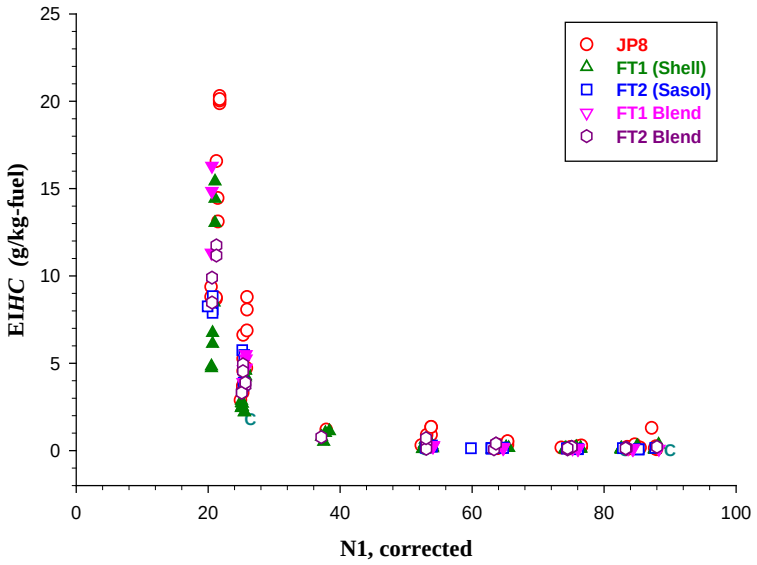

Figure 10. Unburned hydrocarbon emissions versus corrected N1

Combustion efficiency measurements are presented in figures 11 and 12 for engine #3 operating on all of the various fuels. Since combustion efficiency is derived from CO and unburned hydrocarbon emissions, it is greater than 99.9% for all engine power levels above 7%. Results at low-power conditions are similar to those previously discussed for CO and HC emissions with higher combustion efficiencies for the F-T fuels at lower power conditions compared to the JP-8 fuel. As expected, the blends ended up in between the two neat fuels in terms of combustion efficiency.

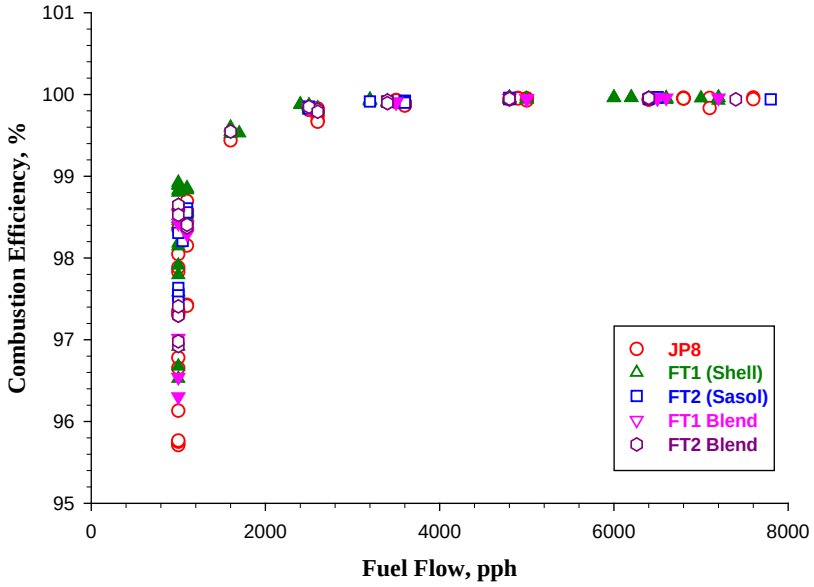

Figure 11. Combustion efficiency for all fuels versus fuel flow

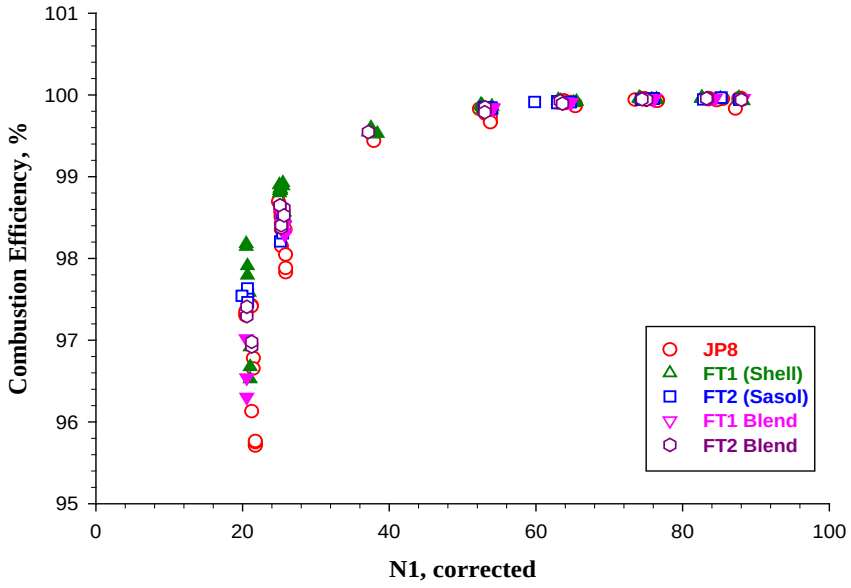

Figure 12. Combustion efficiency measurements versus corrected N1

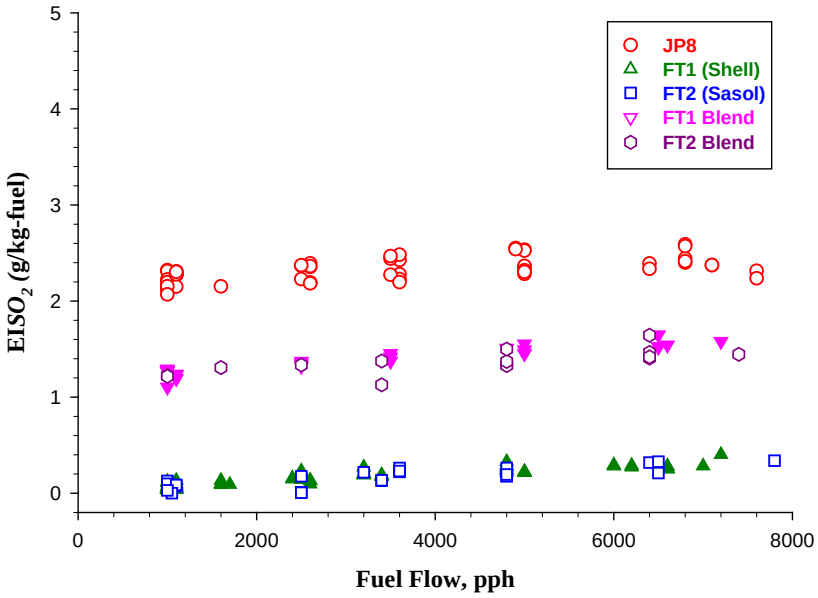

Figure 13. SO_2 emissions for all fuels versus fuel flow

Sulfur dioxide (SO_2) emissions are presented in figure 13. As expected, SO_2 emissions are directly proportional to the amount of sulfur in the fuel. The JP8 fuel had 1148 parts per million of sulfur while the neat F-T fuels had essentially no sulfur. This is reflected in the SO2 emissions data with the pure fuels having very low levels of SO2 emissions and 50/50 blends having about half the SO2 emissions of the pure JP-8. The SO2 emissions that were measured from the pure F-T fuels are attributed to contamination issues associated with fuel handling.

APPENDIX A

Table 1. JP-8 engine performance data for engines #2 and #3

JP-8 Cold Ambient																	
	Nom.	# 2 Engine						# 3 Engine						Ambient Conditions			
Date	Engine Power	N1	EGT deg C	N2	Fuel flow lb/hr	N1-STD	Fuel Flow STD	N1	EGT deg C	N2	Fuel flow lb/hr	N1-STD	Fuel Flow STD	Tamb-deg F	BP mBar	Theta	Delta
1/28/09	4%	21	418	58	800	21.7	892	21	447	58	1000	21.7	1115	27	938	0.939	0.926
1/28/09	7%	25	406	62	900	25.8	1002	25	426	62	1000	25.8	1114	28	938	0.941	0.926
1/28/09	30%	52	479	81	2400	53.5	2668	52	472	81	2600	53.5	2890	30	938	0.945	0.926
1/28/09	45%	63.2	538	83	3400	64.9	3766	63.2	525	83	3600	64.9	3988	33	939	0.949	0.927
1/28/09	65%	74	605	89	4800	75.8	5306	74	600	89	5000	75.8	5527	35	939	0.953	0.927
1/28/09	85%	82.7	693	91	6600	84.7	7298	82.7	689	91	6800	84.7	7519	34	939	0.952	0.927
1/28/09	100%	85	740	93	7100	86.7	7813	85	730	93	7100	86.7	7813	39	939	0.962	0.927
1/28/09	7%	25.2	397	62	900	25.7	989	25	413	62	1100	25.5	1209	40	939	0.963	0.927
1/28/09	100%	85	728	92	7100	86.5	7799	85	723	92	7200	86.5	7908	41	939	0.965	0.927
1/28/09	85%	82.5	695	91	6500	83.9	7136	82.5	688	91	6400	83.9	7026	41	939	0.966	0.927
1/28/09	65%	74.1	599	89	4800	75.3	5266	74.1	593	89	5000	75.3	5485	42	939	0.967	0.927
1/28/09	45%	63.5	526	83	3400	64.5	3728	63.1	519	83	3500	64.1	3838	43	939	0.969	0.927
1/28/09	30%	52.5	469	81	2200	53.3	2411	52.5	463	81	2500	53.3	2739	43	939	0.970	0.927
1/28/09	15%	37	412	77	1500	37.6	1643	37	415	77	1600	37.6	1752	44	939	0.971	0.927
1/28/09	7%	24.8	395	62	900	25.2	985	25.2	416	62	1000	25.6	1095	44	939	0.971	0.927
1/28/09	4%	21	417	58	900	21.3	985	21	447	58	1000	21.3	1094	45	939	0.973	0.927
JP-8 Fuel Warm Ambient																	
	Nom.	#2 engine						#3 engine						Ambient Conditions			
Date	Engine Power	N1	EGT deg C	N2	Fuel Flow lb/hr	N1 STD	Fuel Flow STD	N1	EGT	N2	Fuel Flow lb/hr	N1 STD	Fuel Flow STD	T amb deg F	BP mBar	Theta	Delta
1/31/09	4%	21	465	58	850	20.9	921	20.5	488	58	1000	20.4	1083	66	929	1.014	0.917
1/31/09	7%	24.9	455	62	900	24.7	974	25	472	62	1100	24.8	1191	67	929	1.015	0.917
1/31/09	30%	52.5	522	81	2500	52.1	2706	52.5	503	81	2600	52.1	2814	67	929	1.016	0.917
1/31/09	45%	63.5	572	87	3500	63.0	3785	63.5	556	87	3500	63.0	3785	68	929	1.017	0.917
1/31/09	65%	74	640	91	4700	73.4	5086	74	632	91	4800	73.4	5195	67	929	1.016	0.917
1/31/09	85%	82.5	719	96	6100	81.8	6597	82.5	723	96	6100	81.8	6597	68	929	1.017	0.917
1/31/09	100%	88.5	775	98	7400	87.8	8006	88.5	772	98	7400	87.8	8006	68	929	1.016	0.917
1/31/09	4%	21	457	58	800	20.8	866	20.2	475	58	1000	20.0	1083	67	929	1.015	0.917
1/31/09	7%	25	449	62	1000	24.8	1082	25	468	62	1100	24.8	1190	67	929	1.016	0.917
1/31/09	30%	53	514	81	2400	52.5	2595	53	495	81	2600	52.5	2811	68	929	1.018	0.917
1/31/09	45%	63.5	569	88	3400	63.0	3677	64.5	582	88	3400	64.0	3677	68	929	1.017	0.917
1/31/09	65%	74	645	91	4600	73.4	4976	74	631	91	4800	73.4	5192	68	929	1.017	0.917
1/31/09	85%	82.5	719	96	5800	81.8	6273	82.5	731	96	5800	81.8	6273	68	929	1.017	0.917
1/31/09	100%	88.5	786	98	7400	87.7	8002	88.2	779	98	7400	87.4	8002	68	929	1.017	0.917
1/31/09	7%	25.1	434	62	900	24.9	973	25	449	62	1100	24.8	1190	68	929	1.017	0.917
1/31/09	4%	21.9	459	58	900	21.7	973	20	479	58	1000	19.8	1081	68	929	1.017	0.917

Table 2. FT-1 performance data for engine #3

FT-1 Cold Ambient													
		#3 engine								Ambient Conditions			
Date	Nom. Engine Power	N1	EGT deg C	N2	Fuel flow lb/hr	Fuel Flow HV-C	N1 STD	Fuel Flow STD	Fuel Flow STD-HV	T amb deg F	BP mBar	Theta	Delta
1/29/09	4%	20.5	451	56	1000	1025	21.0	1109	1137	34	937	0.951	0.925
1/29/09	7%	25	430	62	1100	1128	25.6	1220	1251	34	937	0.951	0.925
1/29/09	15%	37.4	422	75	1700	1743	38.3	1883	1931	34	937	0.953	0.925
1/29/09	30%	52.5	479	80	2600	2666	53.8	2877	2950	35	938	0.953	0.926
1/29/09	45%	63.5	535	85	3400	3486	64.9	3756	3852	36	938	0.956	0.926
1/29/09	65%	74.5	610	89	5000	5127	76.1	5516	5656	38	938	0.959	0.926
1/29/09	85%	83	695	94	6600	6768	84.7	7273	7458	39	938	0.961	0.926
1/29/09	100%	85.4	717	95	7000	7178	87.0	7699	7895	40	939	0.963	0.927
1/29/09	7%	24.9	405	64	1000	1025	25.4	1099	1126	41	939	0.965	0.927
1/29/09	100%	86.1	744	95	7200	7383	87.5	7899	8099	42	939	0.968	0.927
1/29/09	85%	83	701	94	6600	6768	84.4	7239	7423	42	939	0.968	0.927
1/29/09	65%	74	594	90	4800	4922	75.2	5261	5395	43	939	0.969	0.927
1/29/09	45%	64	516	85	3400	3486	64.9	3722	3816	44	939	0.972	0.927
1/29/09	30%	52.9	464	80	2500	2564	53.6	2732	2801	46	939	0.975	0.927
1/29/09	15%	37	414	76	1600	1641	37.4	1746	1791	47	939	0.978	0.927
1/29/09	7%	25	422	64	1000	1025	25.3	1091	1119	48	939	0.978	0.927
1/29/09	4%	20.5	447	58	1000	1025	20.7	1090	1117	49	939	0.980	0.927
FT-1 Warm Ambient													
		# 3 Engine								Ambient Conditions			
Date	Nom. Engine Power	N1	EGT deg C	N2	Fuel Flow lb/hr	Fuel Flow HV-C	N1 STD	Fuel Flow STD	Fuel Flow STD-HV	T amb deg F	BP mBar	Theta	Delta
1/28/09	4%	20.5	477	58	1000	1025	20.5	1086	1114	56	935	0.995	0.923
1/28/09	7%	25	450	64	1100	1128	25.0	1194	1224	57	935	0.996	0.923
1/28/09	15%	37	446	76	1600	1641	37.1	1739	1783	57	934	0.996	0.922
1/28/09	30%	52.5	496	82	2500	2564	52.6	2716	2785	58	934	0.997	0.922
1/28/09	45%	63.2	547	86	3200	3281	63.2	3473	3561	59	934	0.999	0.922
1/28/09	65%	74	627	91	4800	4922	74.0	5207	5339	59	934	1.000	0.922
1/28/09	85%	82.5	709	94	6000	6152	82.5	6509	6675	59	934	1.000	0.922
1/28/09	100%	87.5	768	96	7200	7383	87.5	7811	8009	59	934	1.000	0.922
1/28/09	7%	25	439	64	1000	1025	25.0	1085	1112	59	934	1.000	0.922
1/28/09	100%	87.1	779	95	7100	7280	87.1	7703	7898	59	934	1.000	0.922
1/28/09	85%	82.5	712	94	6200	6358	82.5	6727	6898	59	934	1.000	0.922
1/28/09	65%	74	614	91	4800	4922	74.0	5209	5341	59	934	0.999	0.922
1/28/09	45%	63	534	86	3200	3281	63.0	3472	3560	59	934	1.000	0.922
1/28/09	30%	52.5	476	82	2400	2461	52.5	2604	2671	59	934	0.999	0.922
1/28/09	15%	37.5	435	78	1600	1641	37.5	1736	1780	59	934	0.999	0.922
1/28/09	7%	25.5	447	64	1000	1025	25.5	1086	1113	58	934	0.999	0.922
1/28/09	4%	20.5	478	58	1000	1025	20.5	1086	1114	58	934	0.997	0.922

Table 3. FT-2 performance data for engine #3.

FT-2 Cold Ambient													
		#3 Engine								Ambient Conditions			
Date	Nom. Engine Power	N1	EGT deg C	N2	Fuel Flow	Fuel Flow HV-C	N1 STD	Fuel Flow STD	Fuel Flow STD-HV	T amb deg F	BP mBar	Theta	Delta
1/31/09	4%	20	459	58	950	968	20.6	1063	1083	30	932	0.944	0.920
1/31/09	7%	24.5	436	62	1050	1069	25.2	1175	1197	30	932	0.944	0.920
1/31/09	15%	37	429	76	1600	1630	38.1	1789	1822	31	932	0.945	0.920
1/31/09	30%	52.5	485	81	2500	2546	53.9	2791	2842	32	932	0.948	0.920
1/31/09	45%	63	532	84	3400	3463	64.5	3786	3856	35	932	0.953	0.920
1/31/09	65%	74	600	89	4800	4889	75.7	5337	5436	36	932	0.956	0.920
1/31/09	85%	83	692	93	6500	6620	84.7	7213	7347	38	932	0.960	0.920
1/31/09	100%	85.5	706	94	6800	6926	87.1	7532	7671	40	932	0.963	0.920
1/31/09	7%	24.8	408	64	1000	1018	25.2	1106	1127	41	932	0.966	0.920
FT-2 Warm Ambient													
		#3 Engine								Ambient Conditions			
Date	Nom. Engine Power	N1	EGT deg C	N2	N1 STD	Fuel Flow lb/hr	Fuel Flow HV-C	Fuel Flow STD	Fuel Flow STD-HV	Tamb deg F	BP mBar	Theta	Delta
1/30/09	4%	20.6	479	58	20.5	1000	1018	1078	1098	62	937	1.005	0.925
1/30/09	7%	25.3	456	64	25.2	1100	1120	1186	1208	63	937	1.007	0.924
1/30/09	15%	37	454	76	36.9	1600	1630	1725	1757	63	936	1.008	0.924
1/30/09	30%	53	506	82	52.8	2500	2546	2694	2744	64	936	1.009	0.924
1/30/09	45%	63	544	86	62.7	3600	3667	3878	3950	64	936	1.010	0.924
1/30/09	65%	74.5	632	92	74.1	4800	4889	5170	5266	64	936	1.010	0.924
1/30/09	85%	83	733	95	82.6	6400	6518	6899	7026	65	935	1.011	0.923
1/30/09	100%	88	763	98	87.5	7400	7537	7978	8126	64	935	1.010	0.923
1/30/09	7%	25	442	64	24.9	1000	1018	1078	1098	64	935	1.010	0.923
1/30/09	100%	88	803	96	87.5	7800	7944	8407	8563	65	935	1.011	0.923
1/30/09	85%	83	746	95	82.5	6800	6926	7322	7457	66	935	1.013	0.923
1/30/09	65%	74	639	92	73.5	4800	4889	5167	5263	66	935	1.013	0.923
1/30/09	45%	60	534	86	59.7	3200	3259	3449	3513	65	935	1.011	0.923
1/30/09	30%	52	486	82	51.7	2500	2546	2694	2743	65	935	1.012	0.923
1/30/09	15%	37.5	442	78	37.3	1600	1630	1724	1755	65	935	1.012	0.923
1/30/09	7%	25	454	64	24.8	1100	1120	1185	1206	66	935	1.013	0.923
1/30/09	4%	20	485	58	19.9	1000	1018	1077	1096	66	935	1.013	0.923

Table 4. FT-1/JP-8 engine performance data for engine #3.

FT-1/JP-8 Blend													
		#3 Engine								Ambient Conditions			
Date	Nom. Engine Power	N1	EGT	N2	Fuel flow lb/hr	Fuel Flow HV-C	N1 STD	Fuel Flow STD	Fuel Flow STD-HV	T amb deg F	BP mBar	Theta	Delta
1/30/09	4%	20	460	58	1000	1012	20.4	1104	1117	37	938	0.957	0.926
1/30/09	7%	25	430	62	1100	1113	25.5	1213	1227	38	938	0.960	0.926
1/30/09	15%	37	431	78	1700	1720	37.7	1867	1888	41	939	0.966	0.927
1/30/09	30%	52.7	483	81	2500	2529	53.6	2743	2774	42	939	0.967	0.927
1/30/09	45%	63.1	532	83	3500	3540	64.0	3829	3874	45	939	0.973	0.927
1/30/09	65%	74.3	617	90	5000	5058	75.3	5466	5529	46	939	0.974	0.927
1/30/09	85%	82.5	699	93	6500	6575	83.5	7097	7179	47	939	0.977	0.927
1/30/09	100%	86.5	738	95	7200	7283	87.5	7858	7949	47	939	0.978	0.927
1/30/09	7%	24.9	416	62	1000	1012	25.2	1091	1103	48	939	0.979	0.927
1/30/09	4%	20.2	456	58	1000	1012	20.4	1090	1103	48	939	0.980	0.927
1/30/09	100%	87.5	767	93	7500	7587	88.4	8174	8269	49	939	0.980	0.927
1/30/09	85%	82.5	699	91	6600	6676	83.3	7190	7274	49	939	0.981	0.927
1/30/09	65%	74.2	602	90	4800	4855	74.9	5225	5285	50	939	0.983	0.927
1/30/09	45%	63.5	540	85	3500	3540	64.0	3807	3851	51	939	0.984	0.927
1/30/09	30%	53	477	81	2600	2630	53.4	2827	2859	51	939	0.985	0.927
1/30/09	15%	37	427	78	1600	1618	37.3	1738	1758	52	939	0.986	0.927
1/30/09	7%	25	435	62	1100	1113	25.2	1194	1208	53	939	0.988	0.927
1/30/09	4%	20	456	58	1000	1012	20.1	1086	1098	53	939	0.988	0.927

Table 5. FT-2/JP-8 engine performance data for engine #3.

FT-2/JP-8 Blend													
		#3 Engine								Ambient Conditions			
Date	Nom. Engine Power	N1	EGT deg C	N2	Fuel Flow lb/hr	Fuel Flow HV-C	N1 STD	Fuel Flow STD	Fuel Flow STD-HV	T amb deg F	BP mBar	Theta	Delta
1/31/09	4%	21	467	58	1000	1012	21.1	1094	1106	52	933	0.986	0.921
1/31/09	7%	25	443	64	1100	1113	25.2	1202	1216	53	933	0.988	0.921
1/31/09	15%	37	436	76	1600	1618	37.2	1747	1768	53	933	0.989	0.921
1/31/09	30%	52.5	489	82	2600	2630	52.8	2838	2871	54	933	0.990	0.921
1/31/09	45%	63	539	86	3400	3439	63.3	3708	3751	55	933	0.991	0.921
1/31/09	65%	74.5	620	90	4800	4855	74.8	5234	5294	55	933	0.992	0.921
1/31/09	85%	82.7	702	94	6400	6474	83.0	6976	7056	55	933	0.993	0.921
1/31/09	100%	87.5	747	96	7400	7485	87.7	8059	8152	56	933	0.994	0.921
1/31/09	7%	25.5	428	65	1000	1012	25.5	1088	1100	57	933	0.997	0.921
1/31/09	100%	87.5	761	96	7400	7485	87.6	8044	8137	58	933	0.998	0.921
1/31/09	85%	82.9	701	94	6400	6474	82.9	6950	7031	59	933	1.000	0.921
1/31/09	65%	74.1	605	90	4800	4855	74.1	5215	5276	60	932	1.001	0.920
1/31/09	45%	63	529	86	3400	3439	62.9	3693	3735	60	932	1.002	0.920
1/31/09	30%	52.8	478	82	2500	2529	52.7	2713	2745	61	932	1.003	0.920
1/31/09	15%	37	428	76	1600	1618	37.1	1746	1766	55	932	0.993	0.920
1/31/09	7%	25	440	64	1000	1012	24.9	1085	1097	61	932	1.004	0.920
1/31/09	4%	20.5	472	58	1000	1012	20.4	1086	1098	62	931	1.005	0.919

APPENDIX A

References

[1] Yechout, T., Morris, S., Bossert, D. and Hallgren, W., "*Introduction to Aircraft Flight Mechanics: Performance, Static Stability, Dynamic Stability, and Classical Feedback Control*, AIAA Education Series, 2003

[2] Willard Dodds, General Electric Aircraft Engines, personal communication

APPENDIX B: Effects of Alternative Fuels on CO and NOX Emissions Performance

A Summary of AAFEX Field Mission Data

Michael T. Timko, Scott C. Herndon, Ezra C. Wood, W. Berk Knighton, Richard C. Miake-Lye

Aerodyne Research, Inc.
45 Manning Road
Billerica MA 01821

Abstract

We report CO and NO_X emissions measurements for gas turbine engine combustion of JP-8 and two Fischer-Tropsch (FT) synthetic fuels. Compared to JP-8 combustion, combustion of the FT fuels reduces EI_m-NO_X by 5-10% at high power and reduces EI_m-CO by as much as 10% at idle. Increasing temperature increases EI_m-NO_X at high power and decreases EI_m-CO at low power. We outline a protocol for analyzing emissions performance data for combustion of alternative jet fuels that accounts for fuel energy differences compared to JP-8.

Introduction

The cost and availability of petroleum-based transportation fuels and the environmental impacts of petroleum fuel combustion motivate a search for alternatives. Because of the demanding requirements of air transportation, replacing petroleum jet fuels (Jet-A, JP-8, and similar) is a particular challenge that will require better characterization of many different aspects of fuel supply and usage.[1] Alternative fuel combustion products is one area that requires greater attention. Previous studies have shown dramatic decreases in particulate material (PM) emissions when petroleum jet fuels are replaced with synthetic jet fuels synthesized via the Fischer-Tropsch (FT) process. A primary objective of the Alternative Aviation Fuels EXperiment (AAFEX) was to document the emissions performance for a CFM56 engine for both petroleum jet fuel (JP-8) and two FT fuels – one derived from a natural gas feedstock (termed FT1) and the other derived from coal (termed FT2). Additional components of the AAFEX test were to characterize physical and chemical evolution of the exhaust plume and to quantify the effects of ambient temperature on emissions performance.

In total, six teams contributed to the experimental effort and a comprehensive suite of measurements was performed. In this report, we summarize our findings on NO_X and CO emissions performance. Additional reports summarize hydrocarbon emissions and speciation, exhaust plume evolution, and NO_X speciation.

Data Collection Method and Experimental Protocol

The port (engine #1) and starboard (engine #2) CFM56-2C1 engines mounted on the NASA DC-8 aircraft served as the test engines. The complete test matrix included

measurements at 1 m and 30 m from the engine exit plane, under "cold" (270-280 K) and "warm" (280-295 K) ambient conditions, and for five different fuels. Different ambient temperature conditions were sampled by performing tests at night and during the afternoon. Coincidentally, the relative humidity of the "cold" tests was much higher than during the "warm" tests, and we took steps, outlined below, to remove the influence of humidity on NO_X emissions performance. Additionally, measurements were routinely made at 143m from the engine exit plane and occasionally using the Aerodyne Laboratory as a mobile platform. Here, we summarize data collected at the 1 m and 30 m locations only; the Aerodyne Laboratory was disengaged from the sampling manifold during the FT1/JP-8 blended fuel tests, therefore we do not report data for that fuel here. Table 1 provides NASA fuel analysis summary data for the five fuels tested. Standard data collection methods and experimental protocol were followed during the AAFEX test. Wey et al.[2] summarize the methods used for a previous emissions study and no substantial differences were introduced into the Wey et al.[2] testing and sampling protocol.

Table 1. Summary of Relevant Fuel Properties.

Fuel	Source	Density[a] (g cm^{-3})	Heat of Combustion[a] (MJ kg^{-1})	EI_m-CO_2[b] (g kg^{-1})
JP-8	petroleum	0.815 (1)	43.3 (1)	3160
FT1	Shell, natural gas	0.768 (0.942)	44.4 (1.025)	3090
FT1/JP-8		0.793 (0.972)	43.8 (1.011)	3130
FT2	Sasol, coal	0.761 (0.933)	44.1 (1.018)	3110
FT2/JP-8		0.789 (0.967)	43.8 (1.011)	3140

[a]density and heat of combustion data reported by NASA GRC personnel.
[b] EI_m-CO_2 calculated using Air Force Research Lab fuel analysis data.

Data Analysis Method

Figure 1 provides EI_m-NO_X data measured at 30 m for the five different fuels for both "warm" and "cold" test conditions. Clear but minor (<20%) effects of both ambient temperature and fuel composition are apparent in Figure 1. However, we caution that Figure 1 has not been corrected for differences in fuel energy content and ambient conditions. Additionally, detailed analysis (reported below) revealed some discrepancies between the port and starboard engines and the 1- and 30-m sample probes. Therefore, Figure 1 must be interpreted with care. Although the observed effect is minor, it was sufficiently large to motivate a more careful analysis of NO_X emissions.

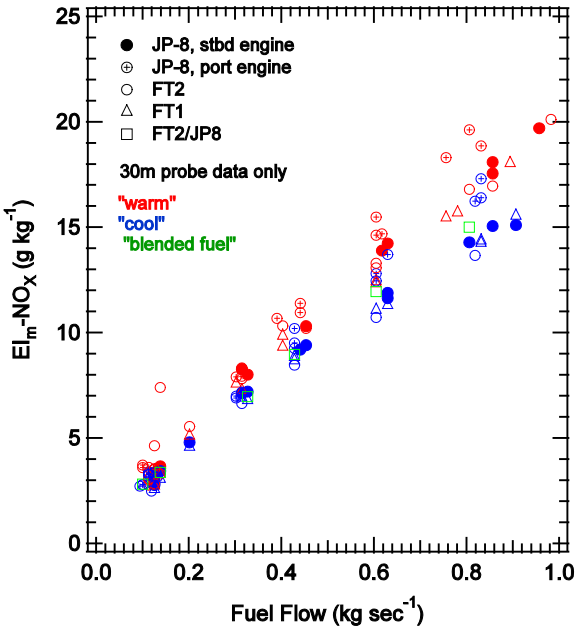

Figure 1. EI_m-NO_X data for the test fuels measured at 30 m.

Making quantitative comparisons of emissions performance for different fuels requires careful analysis to remove the effects of fuel energy content differences, ambient conditions, etc. The data plotted in Figure 1 have already been corrected for combustion differences resulting from differing carbon/hydrogen ratios of the various fuels using the EI_m-CO_2 values provided in Table 1. In addition, we used the following data analysis refinements to attempt to bring the emissions performance of the test fuels to the same baseline:

1. Fuel flow data were normalized by fuel energy content (provided in Table 1) using the equation:

$$\text{energy normalized fuel flow} = \text{measured fuel flow}\,\frac{\Delta H_{\text{combustion, fuel X}}}{\Delta H_{\text{combustion, JP-8}}}$$

2. EI_m data were converted into "energy" EIs using the equation:

$$\text{energy} - \text{EI}(\text{species Y}) = \frac{\text{EI}(\text{species Y})}{\Delta H_{\text{combustion, fuel X}}}$$

We note that the units of energy-EIs are pollutant mass per fuel energy content – rather than pollutant mass per fuel mass.

3. NO_X data were corrected for differences in ambient humidity using the relationship recommended by Wey et al. (2007) following the advice of GE technical staff:

$$\text{EI}_m - \text{NO}_X(\text{humidity corrected}) = \text{EI}_m - \text{NO}_X(\text{measured})\exp\left[19(h_s - 0.00629)\right]$$

where h_s is the specific humidity of ambient air measured as kg of water per kg of dry air. A NASA meteorology data station, located less than 50 m from the test engines, collected ambient temperature, pressure, and relative humidity data that were used to make the ambient humidity correction.

4. During data analysis, we recognized that 1 m and 30 m EI data sometimes exhibited systematic biases. We provide additional information in the Appendix documenting the effect. At this time, the source of the bias is unclear. Potential contamination of the 30-m sampling line or improper determinations of ambient trace gas concentrations may both play a role. In any event, NO_X and CO have typically been observed to depend marginally – if at all – on sampling location. Since our current hypotheses implicate only the accuracy of the 30-m data taken during AAFEX, we restrict our data report for NO_X and CO to the 1-m rake.
5. The emissions performance of the port and starboard engines was very different throughout the test. Since the port engine was used only for JP-8 and the starboard engine was used for both JP-8 and the FT fuels, we restrict our analysis to the starboard engine. The Appendix provides more details on the emissions performance differences in the port and starboard engines.
6. To improve interpretability, "warm" emissions performance data were retained in plots of EIs vs. fuel flow rates. When EIs are plotted vs. ambient temperature, all available data are retained.

With the exception of the humidity refinement, we have treated NO_X and CO data identically. In all cases, we have not at this time corrected for ambient temperature and/or humidity using the standard Boeing Fuel Flow Method (BFFM). Continuing work will focus on resolving the discrepancy between the 1m and 30 m and applying the BFFM correction factor.

NO_X Emissions Performance

The left panel of Figure 2 is a plot of NO_X emissions performance as a function of energy normalized fuel flow rate. The corrections and refinements described previously make interpretation of the general features of the NO_X performance data straightforward. First, FT1 fuel combustion reduces EI_m-NO_X by about 10% for fuel flow rates greater than 0.6 kg sec^{-1} (i.e., >65% power). The NO_X reduction associated with FT1 fuel is less than 5% for fuel flow rate less than 0.6 kg sec^{-1}. Second, the NO_X reduction associated with FT2 fuel is smaller than for FT1 fuel and the difference is smaller than our estimated limits of experimental uncertainty and reproducibility (±5%). Third, as documented by the right panel of Figure 2, increasing ambient temperature increases EI_m-NO_X for power greater than 30%. At a given temperature, EI_m-NO_X has similar slopes with respect to ambient temperature for the various fuels and EI_m-NO_X for the FT1 fuel was always less than for JP-8.

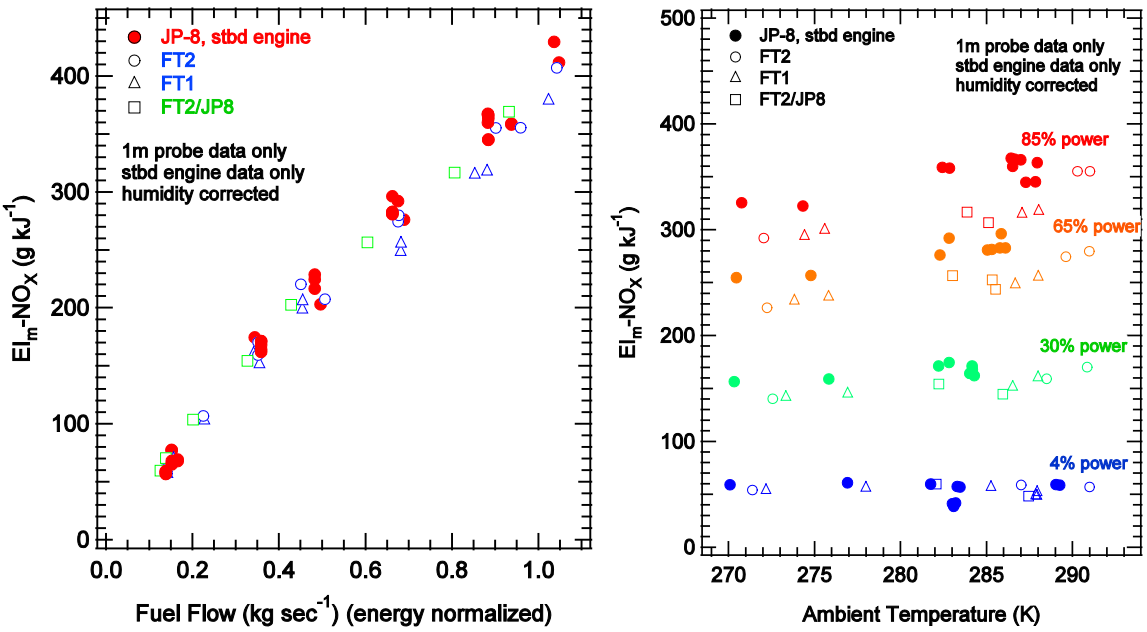

Figure 2. NO_X emissions performance corrected for fuel energy content and ambient relative humidity as a function of fuel flow rate (left panel) and ambient temperature (right panel).

The 5-10% NO_X reduction that we observed during AAFEX is consistent with two previous tests of natural-gas FT fuels emissions performance: 1) Pratt & Whitney on a PW308 engine (Florida) and 2) GE on a CFM56-7 engine (Ohio). While operating at 85% power, EI_m-NO_X for the PW308 engine was reduced by about 7% for FT fuel combustion (Shell, natural gas) relative to JP-8. Interestingly, EI_m-NO_X at idle was greater for the FT fuel tested for the PW308 engine, though the difference may be due to experimental noise. During the CFM56-7 test, EI_m-NO_X was reduced by 11% for FT fuel combustion (natural gas, Syntroleum) relative to Jet-A1. No previous tests examined combustion of the coal-based FT fuel (FT2) studied during AAFEX.

CO Emissions Performance

Figure 3 provides plots of EI_m-CO as a function of energy content fuel flow rate (left panel) and ambient temperature (right panel) for 4%, 7%, and 30% power. The left panel of Figure 4 indicates roughly a 10% decrease in EI_m-CO for FT1 fuel combustion relative to either JP-8 or the FT2 fuel. The left panel of Figure 3 shows the expected dependence of EI_m-CO on ambient temperature and supports the conclusion that EI_m-CO is greater for JP-8 and FT2 fuel combustion than FT1 fuel at all ambient temperatures studied during AAFEX. Just as was the case for EI_m-NO_X (see Figure 2), the ambient temperature dependence of EI_m-CO is similar for all the fuels studied. The temperature dependence of EI_m-CO is strongest for 4% thrust and is nearly absent (to within our measurement capability) for powers greater than 30%.

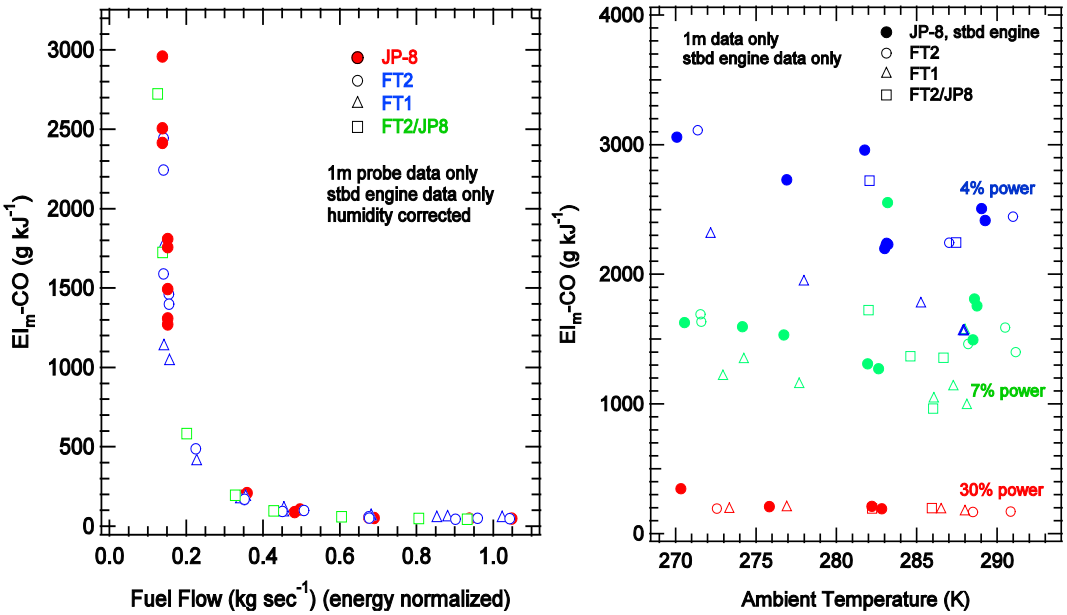

Figure 3. CO emissions performance corrected for fuel energy content as a function of fuel flow rate (left panel) and ambient temperature (right panel).

Previous measurements of EI_m-CO emissions performance for FT fuels conflict. During the PW308 test, EI_m-CO at 7% was 30% lower for combustion of the Syntroleum natural gas FT fuel compared to JP-8. During the CFM56-7 tests, EI_m-CO was 30% lower for Shell natural gas FT fuel combustion compared to Jet-A; however, EI_m-CO was the same for FT fuel and Jet-A1, making interpretation of the CFM56-7 EI_m-CO data ambiguous. In summary, the AAFEX data indicate that EI_m-CO may be reduced slightly for FT1 fuel combustion relative to JP-8 and we therefore conclude that the AAFEX data are more consistent with the PW308 test data.

Appendix

The discrepancies between 1-m and 30-m and port- and starboard-engine data are provided here.

Sample Rake Discrepancy

Figure A1 contains corrected EI_m-NO_X plotted as a function of energy normalized fuel flow rate for the 1 m and 30 m sampling locations. The 1 m EI_m-NO_X data are systematically lower than the 30 m data. To simplify interpretation, Figure A1 is restricted to the port engine. We attribute the discrepancy to one of two phenomena: 1) improper accounting of the ambient background or 2) contamination of the 30-m sampling line.

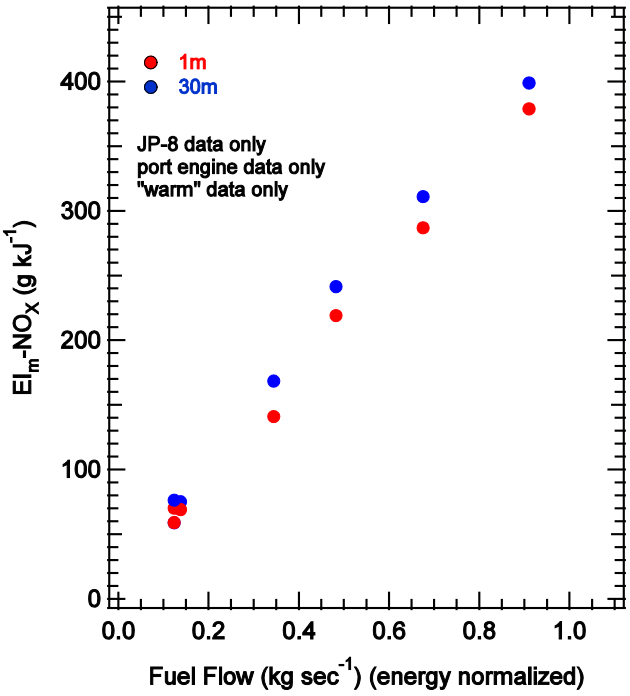

Figure A1. Sample rake discrepancy for EI_m-NO_X observed at AAFEX. Data restricted to JP-8 combustion on the port engine.

For the 30-m samples – but not the 1-m samples – ambient background air influences the measured trace gas concentrations. If trace gas concentrations in the ambient air were not recorded accurately, then a systematic error might be expected in the 30-m data. Standard operating procedure is to sample ambient air just prior to and just following the engine test and to average these measurements to provide the ambient trace gas concentrations. During AAFEX, this method of ambient air sampling was not always possible because of a range of factors not in our control. We will continue to work to identify suitable periods of ambient air sampling to remove the potential for biases introduced into the EI calculations.

In terms of contamination, the sample lines were exposed to differing levels of soot and other emissions during the tests. As a result, chemical processing that may have occurred in the sampling lines may have been different in the 1 m and 30 m sample lines. To remove potential contaminants, the sample lines were flushed with water midway through the test. Water flushing may have inadvertently introduced additional discrepancies because of retained moisture and/or differences in cleaning efficiency. At this time, we can neither conclusively confirm nor deny potential contamination during transport through the sample lines and will continue to evaluate the data to arrive at the firmest conclusion possible.

Port and Starboard Engine Discrepancy

The left panel of Figure A2 plots EI_m-NO_X as a function of energy content normalized fuel flow rate. The port engine consistently has higher EI_m-NO_X than the starboard engine; the difference is greatest for flow rates greater than 0.6 kg sec^{-1} (power > 65%). Likewise, EI_m-CO was lower for the port engine than the starboard engine (data not shown here). The difference between the two engines will not likely ever be known; however, in the right panel of Figure A2 we provide a plot that may provide some clues. Figure A2 is a plot of EI_m-CO as a function of EI_m-NO_X in log-log space. When plotted in as in Figure A2, the NO_X/CO behavior of the two engines collapses onto a universal curve – at least to within the limits of experimental uncertainty and reproducibility.

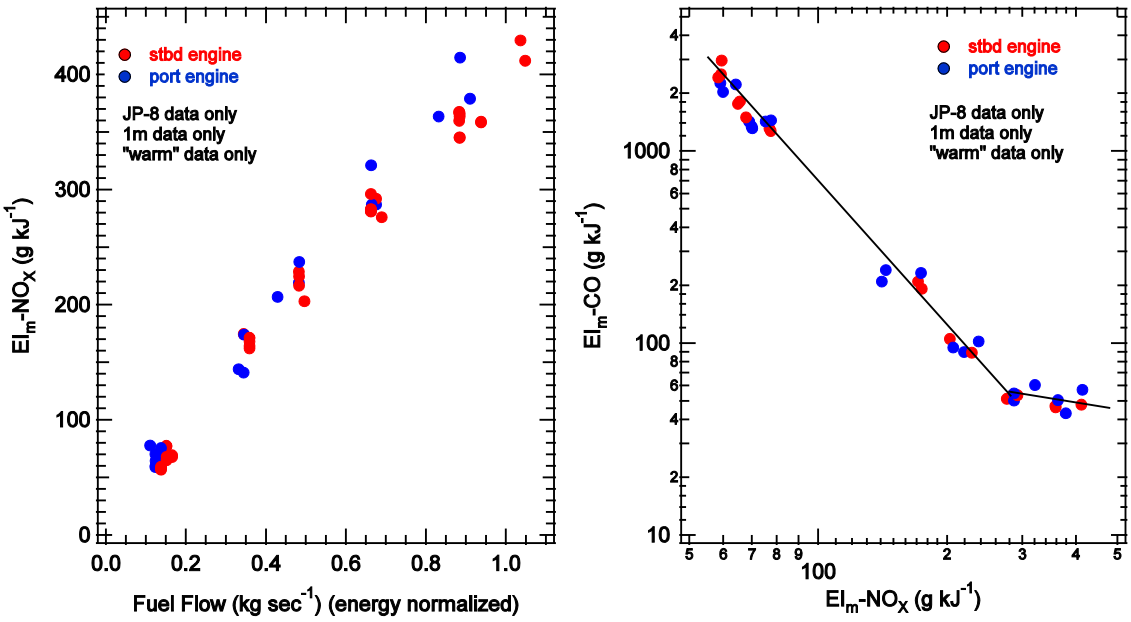

Figure A2. EI_m-NO_X as a function of energy normalized fuel flow rate (left panel) and EI_m-CO as a function of EI_m-NO_X (right panel).

The right panel of Figure A2 implicates combustion temperature as the difference between the port and starboard engines. CO emissions are expected to decrease with increasing combustion temperature, whereas NO_X emissions should increase with increasing combustion temperature – all other factors being held equal. We did not have the capability to measure combustion temperatures during AAFEX, but we did measure exhaust gas temperatures. Consistent with our hypothesis, the left panel of Figure A3 shows that the port engine exhaust gas temperature was always greater than the starboard engine. The right panel of Figure A3 is a plot of 1-m EI_m-NO_X data as a function of exhaust gas temperature for the port and starboard engines. Interestingly, Figure A3 indicates that the port engine emits slightly more NO_X than the starboard engine for

exhaust gas temperatures greater than 700 °C and that the starboard engine emits more for exhaust gas temperatures less than 600 °C. In addition to systematic differences in exhaust gas temperature, the two engines also operated at different fuel flow rates and fan speeds (N1 and N2) to achieve the same nominal thrust level. These additional factors are consistent with the aicraft engine aging model proposed by Lukachko and Waitz[3] and may explain the ambiguous trends captured in the right panel of Figure A3. Therefore based on Figures A2 and A3, we conclude that differences in combustion temperature may play a role in the CO and NO_X emissions differences observed for the port and starboard engines. Additional analysis is required to determine whether differences in combustion temperature alone can explain the different CO and NO_X emissions behavior.

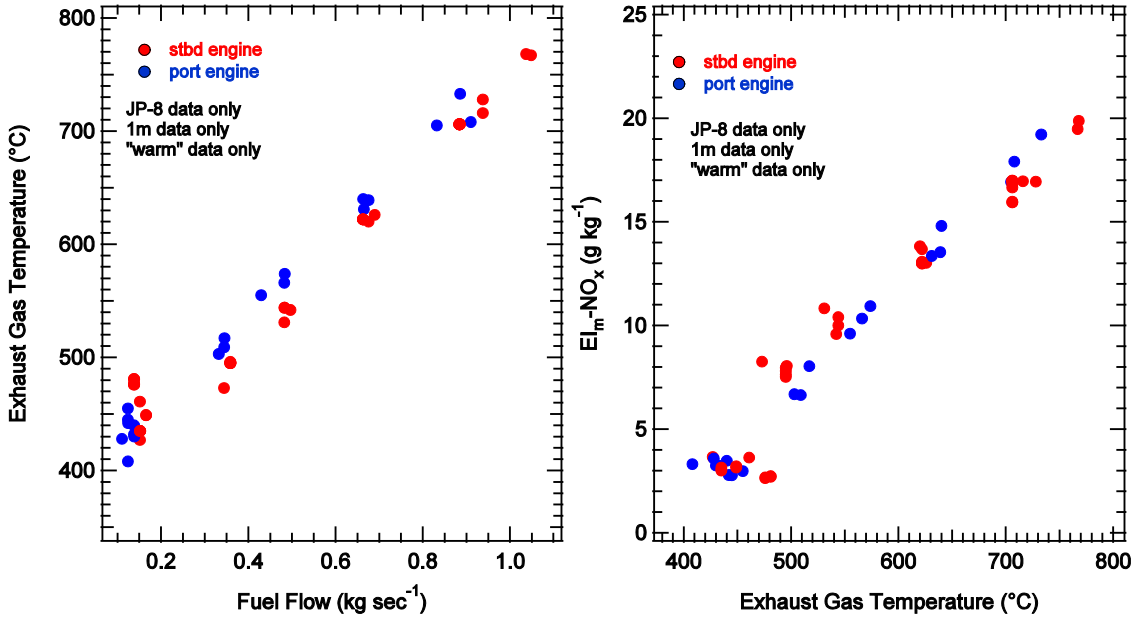

Figure A3. Exhaust gas temperature as a function of fuel flow rate (left panel) and EI_m-NO_X as a function of exhaust gas temperature (left panel) for the port and starboard engines studied during AAFEX.

References

1. Rye, L.; Blakey, S.; Wilson, C. W., *Energy & Environmental Science* 3, (1), 17-27.
2. Wey, C. C.; Anderson, B. E.; Wey, C.; Miake-Lye, R. C.; Whitefield, P.; Howard, R., *Journal of Propulsion and Power* **2007,** 23, (5), 898-905.
3. Lukachko, S. P.; Waitz, I. A. In *Effects of engine aging on aircraft NOx emissions*, International Gas Turbine Exhibition, Orlando, FL, 1997; Orlando, FL, 1997.

APPENDIX C: VOC Emissions from Jet Aircraft Engines Burning Alternative Fuels
A Summary of the Alternate Aviation Fuel Experiment (AAFEX)

W. B. Knighton,[a] S. C. Herndon,[b] E. C. Wood,[b] M. T. Timko[b] and R. C. Miake-Lye[b]

[a]Department of Chemistry and Biochemistry
Montana State University
Bozeman, MT 59717
[b]Aerodyne Research Inc.
Billerica, MA 01821

Introduction

Instabilities in the cost and supply of crude oil has spurred interest in developing liquid fuels from alternative feed stocks, including biomass, natural gas and coal. Alternate aviation fuels have been produced from coal and natural gas using the Fischer-Tropsch (FT) process. The chemical composition of these FT fuels is substantially different than conventional aviation fuel (kerosene) in that they are essentially free of sulfur and aromatic hydrocarbons. Previous studies have demonstrated that these FT fuels result in substantially lower particulate matter (PM) emissions, which makes them attractive for reducing the impact of aviation emissions on the environment. Less is known about the gaseous emissions from these alternative fuels. The Alternative Aviation Fuels EXperiment (AAFEX) was conducted to characterize the PM and gaseous combustion emission products from FT fuels in aviation gas turbine engines.

This report focuses on the VOC emissions performance related to fuel type and ambient temperature. Other teams contributed to this experimental effort and a comprehensive suite of gaseous and PM measurements were performed. Those results are summarized in other reports.

Experimental

The AAFEX measurement campaign was conducted in January 2009 at the Dryden Flight Research Center using the CFM56-2C1 engines mounted on the NASA DC-8 aircraft. A primary objective of this test was to document the changes in the combustion exhaust emissions between conventional JP-8 fuel and two FT fuels; one derived from natural gas (FT1) and another derived from coal (FT2). To delineate the influence of ambient conditions on the exhaust emissions, the port inboard engine burned JP-8 fuel while the starboard engine burned one of the alternative fuels. Exhaust samples were alternatively drawn from either engine from dedicated probes located at 1m and 30m from the engine exit. The VOC measurements discussed in this report were made using the 1m dilution probe. The desert location experiences wide diurnal variations in ambient temperature and tests were conducted early in the morning (cold 270-280K) and again in the afternoon (warm 280-295K) to examine the influence of ambient conditions.

A suite of VOCs including formaldehyde, acetaldehyde, methanol, ethene, propene, benzene, toluene, phenol, styrene, and naphthalene were measured. Formaldehyde and ethene were measured by tunable infrared laser differential absorption spectroscopy (TILDAS). The remaining species were measured by chemical ionization spectrometry using a proton transfer reaction mass spectrometer (PTR-MS). A complete description of the TILDAS and PTR-MS techniques and their application to measurement of VOCs in jet engine exhaust is provided in our previous papers.[1,2] Additional information regarding the quantification details of the PTR-MS can be found in Appendix I. VOC measurements were continuously recorded, TILDAS (1-hz), PTR-MS (0.3-hz), throughout the testing. The times series concentration data is then averaged over the appropriate time intervals that are defined when the engines were under stable operations. These averaged VOC concentrations were converted to emission ratios (ER) by dividing them by their appropriately averaged CO_2 concentrations. Emission indices are computed via Eq. 1:

$$EI_X\left(g_x/kg_{fuel}\right) = ER_X\left(mole_x/mole_{CO_2}\right)\left[MW_x/MW_{CO_2}\right]EI_{CO_2}\left(g_{CO_2}/kg_{fuel}\right) \qquad (1)$$

Where MW_x and MW_{CO_2} are the molecular weights of the component (X) and CO_2, respectively. EI_{CO_2} is the emission index of CO2, which is 3160 g/kg, 3090 g/kg and 3110 g/kg for JP-8, FT1 and FT2 fuels, respectively.

Results and Discussion

VOC emissions scaling – decoupling fuels effects from the influence of engine power and ambient temperature

VOC emissions from jet aircraft engines exhibit a strong inverse non-linear dependence with engine power.[1-4] Ambient temperature also exerts a strong influence with colder temperatures leading to higher emissions. Under static ambient conditions, constant pressure, temperature, and relative humidity, combustor inlet conditions (combustor pressure, inlet temperature, fuel flow, and fuel air ratio) could be set to provide reproducible engine operating conditions. In practice, ambient conditions are not constant and these changes make it impossible to replicate combustor inlet conditions. To a first order approximation, the variations in the emissions due to variability in engine power, ambient temperature, and fuel structure are all about the same order of magnitude. This is demonstrated in Figure 1, where the EIs for ethene and formaldehyde are plotted as a function of engine power. This figure illustrates that all of the emissions decrease rapidly with increasing power and that colder temperatures generally lead to higher emissions. It is not immediately obvious from the data shown in these figures how to quantify the changes in emissions that are related to fuel composition. Our previous work on VOC emissions has shown that we can delineate exhaust composition changes from the effects of temperature and engine power through a normalization process. We call this normalization process "emission scaling", because we have observed that virtually all of the VOC exhaust emission components scale in a near-linear relationship with respect to one another.[1] This emission scaling relationship is demonstrated in

Figure 2, where we have taken the EI data in Figure 1 for formaldehyde and ethene and plotted the formaldehyde EIs versus the ethene EIs. The marker styles in Figure 2 indicate the different fuels and are colored to reflect ambient temperature conditions. This figure nicely illustrates that the emissions of these two components scale linearly and that the different fuels produce different amounts of formaldehyde relative to that of ethene.

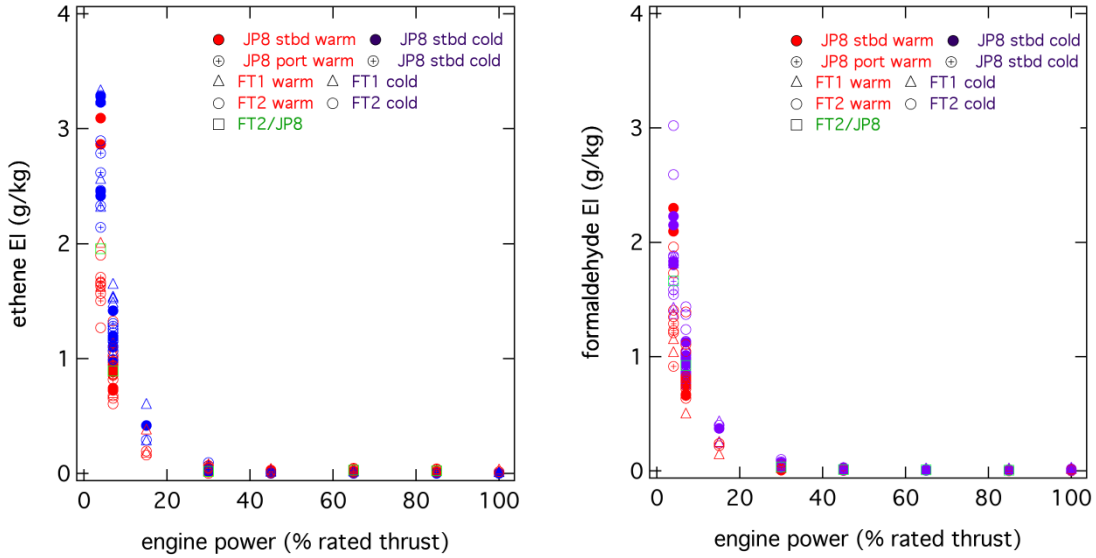

Figure 1. Variation of ethene and formaldehyde emissions with engine power. Marker styles indicate fuel type and marker colors reflect ambient temperature.

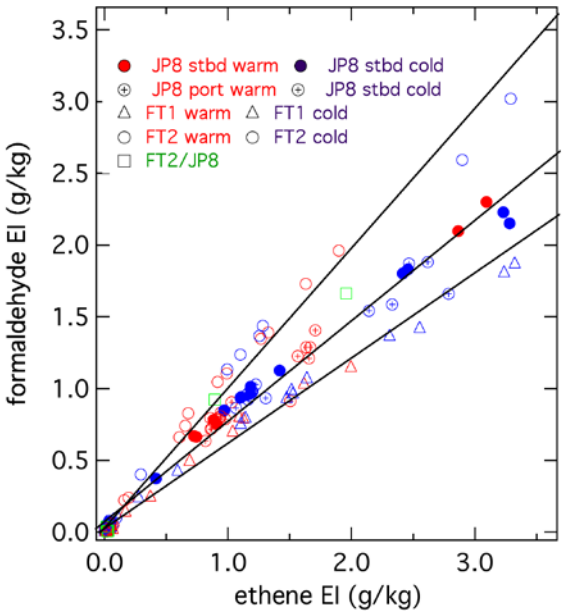

Figure 2. Emissions scaling plot of formaldehyde versus ethene.

We use the slopes of the lines fitted to the data shown in Figure 2 to quantify the amount of formaldehyde emitted per unit of ethene. This same procedure has been applied to all of the other measured VOCs. These normalized emissions can then be used to build a chemical speciation profile for each fuel. These ethene normalized emissions and the correlation coefficients, R, from the linear regressions are summarized in Table 1.

Table 1. Compound EIs normalized to ethene for the three fuels used at AAFEX.

	JP8		FT 1		FT 2	
Compound	$\frac{EI_x}{EI_{C_2H_4}}$	R	$\frac{EI_x}{EI_{C_2H_4}}$	R	$\frac{EI_x}{EI_{C_2H_4}}$	R
ethene	1	------	1	------	1	------
formaldehyde	0.752	0.996	0.602	0.998	1.06	0.998
methanol	0.112	0.996	0.087	0.996	0.158	0.993
propene	0.382	0.996	0.34	0.993	0.74	0.998
acetaldehyde	0.274	0.993	0.245	0.987	0.422	0.998
butenes + acrolein	0.351	0.997	0.289	0.996	0.659	0.999
acetone + propanal + glyoxal	0.135	0.997	0.129	0.985	0.358	0.994
[a]mass 71	0.229	0.999	0.18	0.998	0.504	0.996
benzene	0.12	0.996	0.018	0.941	0.056	0.994
[a]mass 85	0.106	0.998	0.089	0.998	0.259	0.993
toluene	0.057	0.999	0.004	0.931	0.022	0.997
C_8H_{10} + C_7H_6O	0.093	0.997	0.005	0.803	0.023	0.986
C_9H_{12} + C_8H_8O	0.101	0.991	0.0045	0.114	0.017	0.868
$C_{10}H_{12}$ + $C_9H_{10}O$	0.061	0.986	0.0058	0.547	0.012	0.549
$C_{11}H_{14}$ + $C_{10}H_{12}O$	0.032	0.983	0.0036	0.423	0.0074	0.655
naphthalene	0.028	0.951	0.01	0.935	0.02	0.911
methyl-naphthalenes	0.012	0.83	0.014	0.976	0.018	0.8
dimethyl-naphthalenes	0.009	0.518	0.017	0.982	0.019	0.892
styrene	0.026	0.994	0.002	0.681	0.0053	0.94
phenol	0.051	0.975	0.013	0.823	0.028	0.842

[a] GC/PTR-MS analysis indicates that mass 71 and mass 85 represent multiple compounds which include the isomeric alkenes C_5H_{10} and carbonyls C_4H_6O, C_6H_{12} and C_5H_8O respectively. Specific identities have not been determined.

VOC Exhaust Emission Speciation versus Fuel Type

The normalized emissions reported in Table 1 can be examined in relation to other data sets, such as Spicer[3] or our previous APEX results[1,2], provided that ethene has been

measured. Figure 3 shows a comparison of the present JP8 measurements with those reported by Spicer. In this figure, a value of 1 indicates that our ethene-normalized emissions are equal to those computed from Spicer. Inspection of this figure shows that the present JP8 measurements are within +/- 35% of those reported by Spicer, which we consider to be excellent agreement.

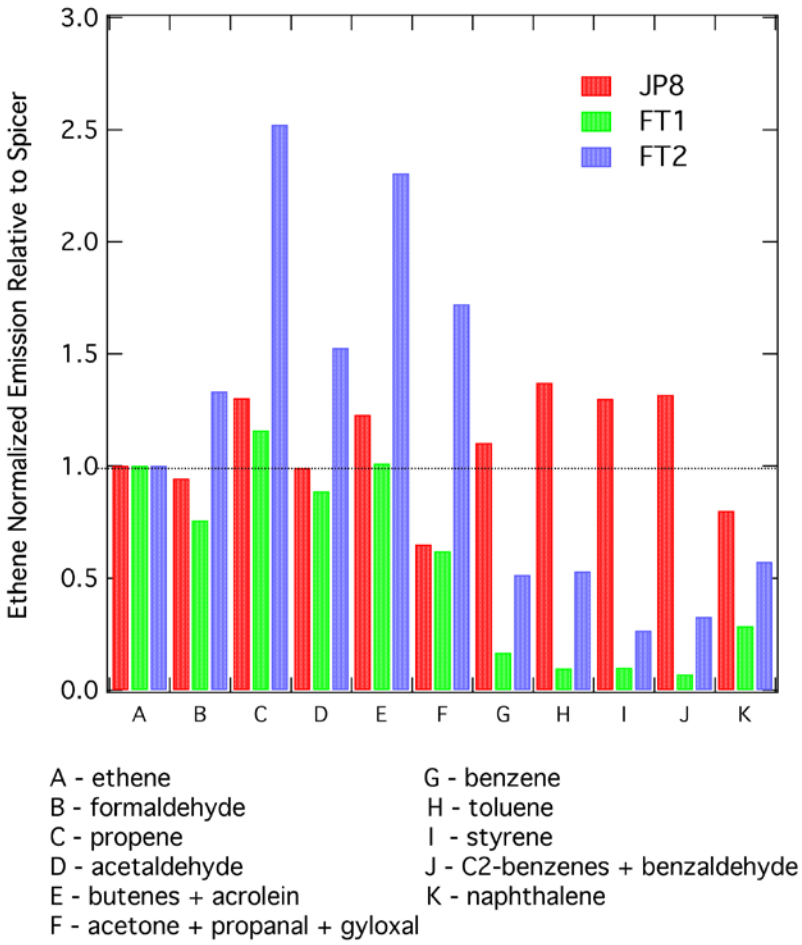

Figure 3. Comparison of ethene normalized EIs measured at AAFEX with respect those reported by Spicer et al.[3] for JP-5.

Figure 3 shows that there are some striking differences in the chemical composition of the exhaust produced with the different fuels: 1) The two FT fuels appear to have very different exhaust compositions. 2) The aromatic emissions from the FT fuels are reduced but not eliminated. Before we proceed further with our discussion on these fuel effects, we note that direct comparison of normalized emissions can be misleading if the absolute magnitude of the compound (ethene) to which the other compounds are scaled to changes significantly with the different fuels. As will be shown later, the ethene EIs are roughly equivalent for all of the fuels. This fortunate consequence allows us to use the results shown in Figure 3 to highlight the differences in the chemical speciation between the different fuels.

An obvious difference between the alternate fuels and JP8 is the significant reduction in the emission of aromatic compounds with the FT fuels. This result might have been anticipated since the liquid FT fuels have very low aromatic contents. What might not have been expected is that the aromatic emissions are not eliminated in the FT1 fuel, which is essentially devoid of any aromatic compounds in the liquid fuel. This result indicates that these aromatic compounds are being formed during the combustion process. A broad range of literature exists regarding the formation of aromatic compounds in engines and flames with respect to fuel structure (e.g. Zhang et al.[5], Schulz et al.[6]) and discussion of that literature is beyond the scope of this report. What can be concluded is that the aromatic emissions don't scale in direct proportion to the aromatic content of the liquid fuel.

Figure 3 indicates that the chemical speciation profiles are very different for the two FT fuels. The VOC emissions from the FT1 fuel are lower than those for the FT2 fuel for all of the measured compounds. The FT1 emissions are also lower than those measured for JP8. In contrast, the reduction in the aromatic emissions in the FT2 fuel appears to be offset by enhanced emissions of C3 and C4 compounds. These results suggest, but do not prove, that the total VOC emissions are lowest for FT1 fuel and greatest for FT2 fuel.

Because only a limited subset of the measured VOCs are shown in Figure 3, we now examine the chemical speciation profiles from the perspective of all of the data reported in Table 1. The exhaust composition for each fuel displayed as a pie chart in Figures 4-6. In these charts, mass57 represents the sum of butenes + acrolein, mass59 represents the sum of acetone + propanal + glyoxal, and other aromatics represents the sum of all of the aromatic compounds excluding benzene and naphthalene. These charts assume that the VOC emissions reported in Table 1 sum to 100%, a condition that is clearly not met. For JP5 fuel, Spicer reports that they were able to identify approximately 70% of the non-methane carbon in the exhaust. We estimate that the components listed in Table 1 represent approximately 75% of carbon identified by Spicer. We note that there are compounds in Table 1 such as methanol and most of the larger aromatics (mass121, mass135 and mass149) that are not included in Spicer's list of identified compounds. Conservatively, we estimate that the chemical components listed in Table 1 represent better than 50% of total non-methane organic carbon within the exhaust produced by JP8. The bulk of remaining mass is presumed to be from alkanes, which are not measured by either the TILDAS or PTR-MS. The relative distributions are useful and will remain valid provided that the emissions measured in Table 1 reflect a near constant fraction of the actual total.

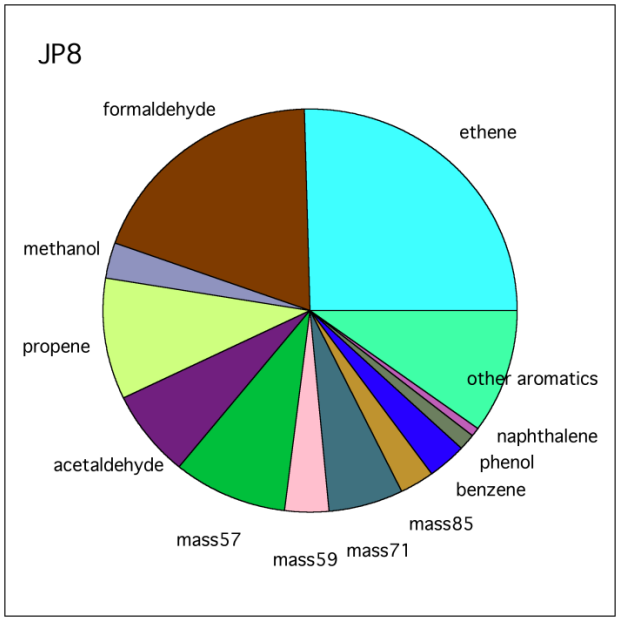

Figure 4. Distribution of the measured exhaust components for JP8 fuel.

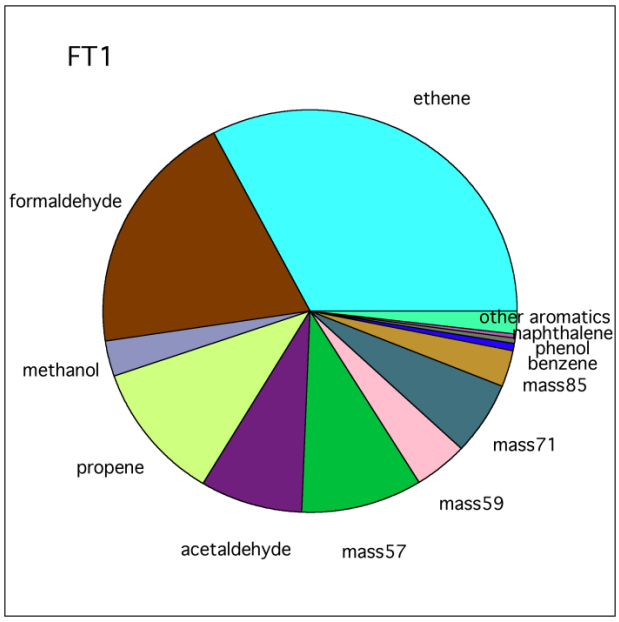

Figure 5. Distribution of the measured exhaust components for FT1 fuel.

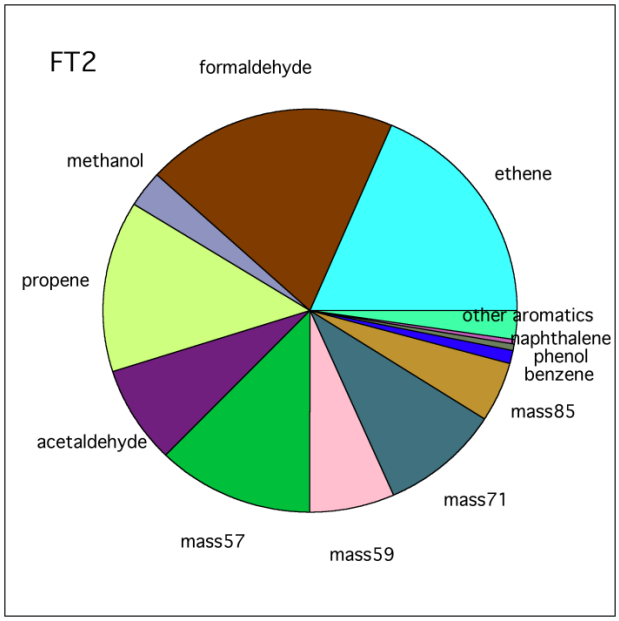

Figure 6. Distribution of the measured exhaust components for FT2 fuel.

Figures 4-6 clearly indicate that small molecular weight components (C1-C3) constitute the majority (>70%) of the measured mass emissions for all fuels. The distribution of these emissions is roughly equally divided between alkenes (fuel cracking products) and carbonyl compounds (partially oxidized products). Exhaust produced from FT2 fuel contains a greater proportion of carbonyls to alkenes (1.05), FT1 fuel (0.76) favors alkene production, while JP8 fuel (0.86) falls between the two alternate fuels. The significant presence of carbonyl compounds in the exhaust has several important consequences. One is that the aldehydes such as formaldehyde and acetaldhyde are important air toxics. Second, total hydrocarbon (HC) emissions are typically measured using a flame ionization detector (FID), which essentially "counts carbon atoms", but does not count carbons to which an oxygen is attached. Thus the FID is essentially blind to formaldehyde and methanol and only records about half of the carbon from acetaldehyde. This result has important consequences with respect to comparing total HC emissions to total VOC emissions.

Absolute VOC Emissions – Influence of fuel type, engine power and ambient temperature

A major objective of the AAFEX campaign was to determine how the VOC emissions from the alternative fuels compare to those produced from conventional JP8 fuel. In this section we will examine in detail how the ethene emissions are influenced by fuel type, engine power and ambient temperature. Figure 7 shows plots of the ethene EIs versus ambient temperature for the three fuels under two power conditions.

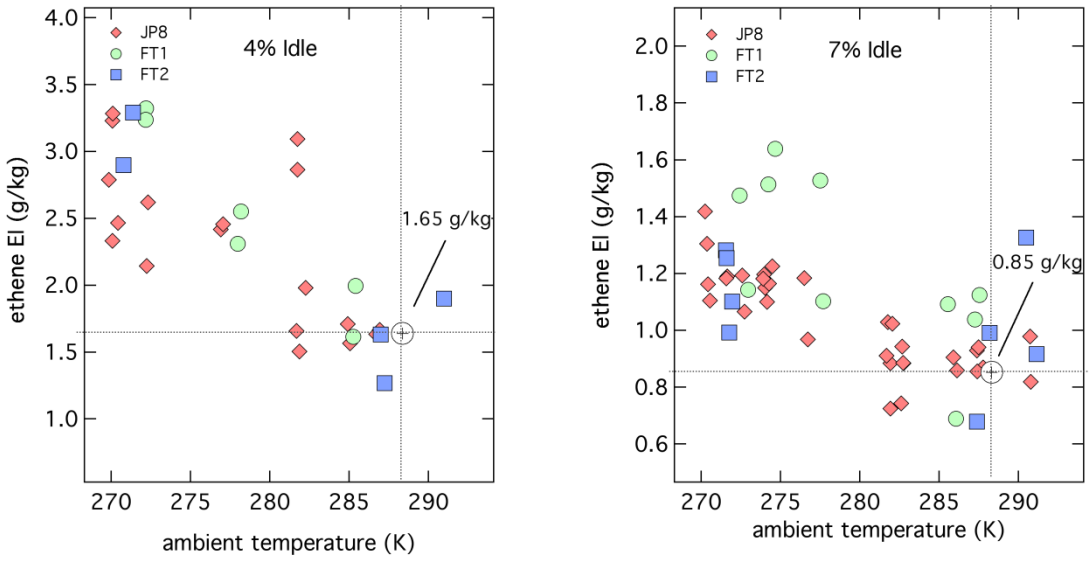

Figure 7. Effect of ambient temperature on the ethene EI under two low-power conditions. Highlighted point represents the average ethene EI at 288K.

Temperature Dependence

Figure 7 shows that EI of ethene is strongly dependent on engine power and ambient temperature, but it exhibits a weaker dependence on fuel type. The effects of engine power and temperature are similar in magnitude such that the low temperature (270K) 7% power points overlay with the high temperature (290K) 4% power points. To aid in the discussion of the power and fuel dependencies, we will address the temperature dependence first. Lower ambient temperatures lead to higher emissions. The temperature effect is strongest at 4% power where the ethene EI's change by about a factor of two over the ambient temperature range of 270 – 290 K. The temperature dependence appears to be slightly less pronounced under the higher 7% power condition. The strong temperature dependence makes it difficult to directly compare measurements made at different temperatures. Thus we need to create a standard temperature condition to which we can normalize all of our data sets. We have set 288K as our standard temperature. Different data sets are normalized to 288K by dividing each EI by the EI value measured at 288K. The 288K EIs for ethene are labeled in Figure 7. Figure 8 shows a plot of these temperature-normalized EIs versus temperature for AAFEX and several other measurement campaigns. This figure shows that the present measurements made at 270 – 290 K merge with our previous measurements made at 287 – 305 K during APEX. The inclusion of both formaldehyde and ethene measurements is allowed because the emissions scaling phenomena demonstrates that all VOCs have the same temperature dependence.

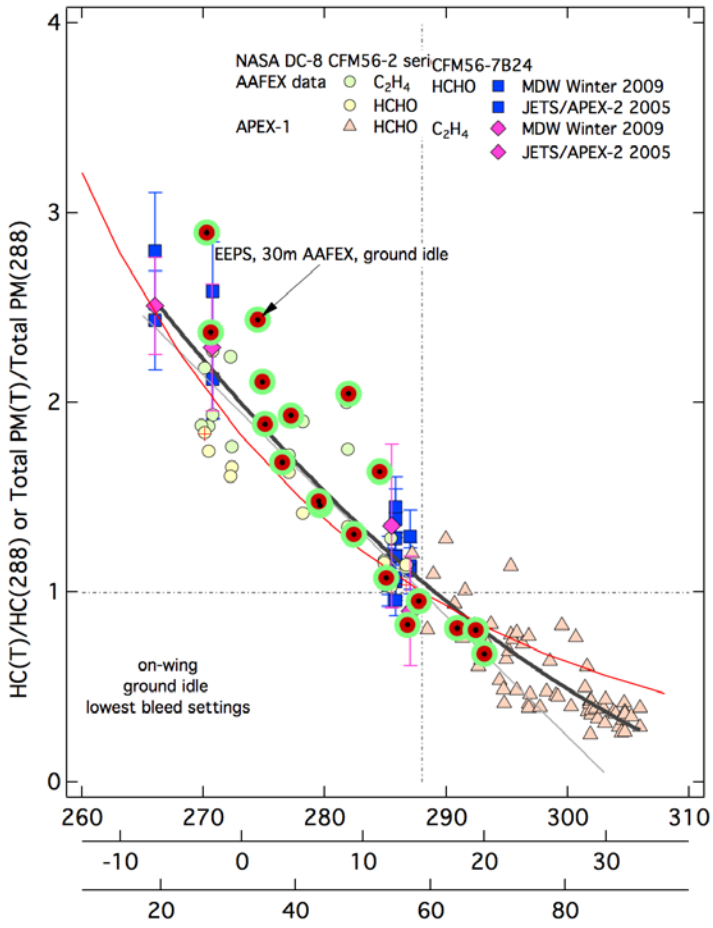

Figure 8. Plot of temperature normalized emissions versus ambient temperature. The units to the three x-axes starting from bottom are F [not U], C, and K.

Engine Power Dependence

VOC emissions are known to have a strong non-linear dependence on engine power.[2-4] This dependence is clearly demonstrated in Figure 1. In Figure 7 we observe that the AAFEX ethene EI at 4% power (1.65 g/kg) is approximately two times larger than the 7% power (0.85 g/kg) condition. We note that this power dependence is substantially reduced from what was observed at APEX. At APEX the EIs of ethene and the other VOCs generally decreased by a factor of 3x-5x when the power was increased from 4% to 7%.[2] Our preliminary analysis suggests that this difference may be due to the differences in the actual power conditions, although we can't rule out the effect of engine age. At APEX the engines had just been rebuilt and so these engines had been in-service for five years prior to the testing at AAFEX.

To further address the power dependence anomaly, we examine in greater detail how emissions measurements made at AAFEX for JP8 fuel compare with those made at APEX and with ICAO engine certification data. One can't directly compare VOC EI values to total HC EI's because the VOC EI's include the mass of oxygen while the total HC EI value expresses the HC emissions in terms of gram-equivalents of CH_4 per kg of

fuel. To alleviate this problem, we have converted the data in Table 1 and the total HC EI's to carbon emission ratios (ER_C) expressed as ppbC per ppm CO_2 at 288K. The conversion from EI_x to ER_C is accomplished via Eq 2. Note that the ER_C are not equal for all of the fuels because they have different EI_{CO_2} values.

$$ER_C = \left[EI_X\left(g_x/kg_{fuel}\right)\right/ EI_{CO_2}\left(g_{CO_2}/kg_{fuel}\right)\left][MW_{CO_2}/MW_X\right][Carbon\#][1000\ mmole/mole] \quad (2)$$

Table 2. Carbon emission ratios (ppbC/ppmCO_2) computed at 7% power from data shown in Table 1 assuming the 288K EI_m-Ethene = 0.85 g/kg

Compound	JP8 ER_C	FT1 ER_C	FT2 ER_C
ethene	0.850	0.865	0.859
formaldehyde	0.297	0.243	0.425
methanol	0.041	0.033	0.059
propene	0.323	0.294	0.636
acetaldehyde	0.147	0.135	0.231
butene + acrolein	0.260	0.219	0.495
acetone + propanal + gyloxal	0.065	0.064	0.176
mass71	0.194	0.156	0.433
benzene	0.109	0.017	0.052
mass 85	0.090	0.077	0.222
toluene	0.051	0.004	0.020
C_8H_{10} + C_7H_6O	0.083	0.005	0.021
C_9H_{12} + C_8H_8O	0.090	0.004	0.015
$C_{10}H_{14}$ + $C_9H_{10}O$	0.054	0.005	0.011
$C_{11}H_{16}$ + $C_{10}H_{12}O$	0.028	0.003	0.007
naphthalene	0.026	0.009	0.019
methylnaphthalene	0.011	0.013	0.017
dimethylnaphthalene	0.008	0.016	0.018
styrene	0.024	0.002	0.005
phenol	0.039	0.010	0.021
sum	2.79	2.17	3.74

The data for JP8 fuel in Table 2 was computed at 7% power so that we can our measurements to ICAO database emissions and to the measurements reported by Yelvington et al. at APEX. Yelvington reports a similar list of exhaust components to that shown in Table 2 and compares the sum (ER_C-VOC) to total HC (ER_C-HC) measurements made using a continuous FID instrument. The ICAO database lists the

total HC emission index for the CFM56-2-C5 engine at 1.83 g/kg, which represents an ER_C of 1.59 ppbC/ppmCO_2. Table 3 summarizes the relevant ER_C data from the AAFEX, APEX and ICAO data sets and includes EI_m-CO from AAFEX and ICAO. The data in Table 3 for ER_C-VOC and ER_C-HC at APEX was taken directly from Yelvington et al. and has not been normalized to 288K. The APEX data set represents an average and was collected at higher ambient temperatures (287 – 305 K).

Table 3. Carbon emission ratios and EIm-CO for CFM56-2-C5 engine at 7% power from different sources.

AAFEX ER_C-VOC	APEX ER_C-VOC	APEX ER_C-HC	ICAO ER_C-HC	AAFEX EI_m-CO	ICAO EI_m-CO
2.79	1.31	1.16	1.59	58.5	30.7

Some initial discussion of the APEX data set is warranted. We note that APEX ER_C-VOC and ER_C-HC values are quite similar and that the VOC value is actually greater than total HC measurement. This similarity must be considered as accidental because the VOC measurements don't include any of the alkane exhaust component. The FID, however, only records the HC component of the exhaust and does not accurately account for components containing oxygen. Apparently the reduction in the FID response due to the presence of compounds like formaldehyde or methanol in the exhaust offsets the omission of the alkanes from the VOC sum. The difference between the APEX ER_C-HC and the corresponding ICAO measurement is primarily due to a temperature effect, since the ICAO value is determined at a lower temperature (288K). Normalizing the APEX ER_C-HC to the ICAO value would suggest a 288K temperature corrected APEX ER_C-VOC value of 1.80.

The ER_C-VOC measurement taken at AAFEX is substantially larger than that observed at APEX. The differences in exhaust chemical composition and temperature between the AAFEX and APEX data sets cannot account for this disparity. Examining the CO emission observed at AAFEX with the ICAO value also shows a large discrepancy. Scaling our AAFEX ER_C-VOC number by the ratio (30.7/58.5) leads to a corrected VOC ER_C of 1.46. This corrected value is now in line with our previous APEX measurement. While this discussion does not identify the source, engine power variations, or engine age, it certainly suggests that the difference is real and is not a measurement artifact.

Fuel Dependence

The sums in Table 2 for the different fuels provide a direct estimate of how the total VOC emissions vary between fuels. These estimates assume that the ethene emissions are similar for all three fuels and that the chemical composition of the exhaust shown in Table 2 accounts for a constant fraction of the actual exhaust emissions. The latter assumption cannot be interrogated fully in the absence of a full chemical speciation profile. The first assumption can be addressed by examining the data shown in Figure 7. The ethene EIs for the different fuels generally overlap with one another, particulary in the case of the JP8 and FT2 fuels. The ethene emissions from the FT1 at 7% power do appear to be generally higher, by maybe 20%. If we assume that the ethene EIs are the same for all of the fuels, then the VOC emissions from FT1 fuel are 28% lower than JP8

fuel and FT2 fuel is 34% higher than JP8. Allowing the ethene EI in FT1 fuel to increase by 20% would increase the VOC emissions to 2.6 ppbC/ppmCO_2, which is only 7% lower than the JP8 fuel. The FT2 288K ethene EI would need to be 0.65 g/kg to make its VOC emissions equivalent to that of JP8. The data in Figure 7 does not support such a reduction. In light of additional information we can conclude that the total VOC emissions rank in the order FT1 < JP8 < FT2.

Sample Line Perturbations

Reliable sampling of engine exhaust gas matrix represents one of the most important and difficult challenges. APEX style emissions tests require the use of extensive sample lines in order to transport and deliver a common sample to all of the participants. A consequence of this sampling strategy is that exhaust gas is exposed to long lengths of stainless steel tubing. Organic compounds, particularly those with low vapor pressures, interact with the walls of the sample line, which affects the delivery efficiency of these compounds to the measurement instrumentation. These sample wall interactions lead to poor temporal correlation between the affected substrate and other exhaust gas components, such as CO_2 the primary combustion tracer, that are efficiently transported through the sample system. An example of this is shown in Figure 9, where the naphthalene signal has been overlaid onto the ethene time series. In this figure the naphthalene response lags behind the ethene response during the transition between test points and then slowly approaches to a steady state concentration.

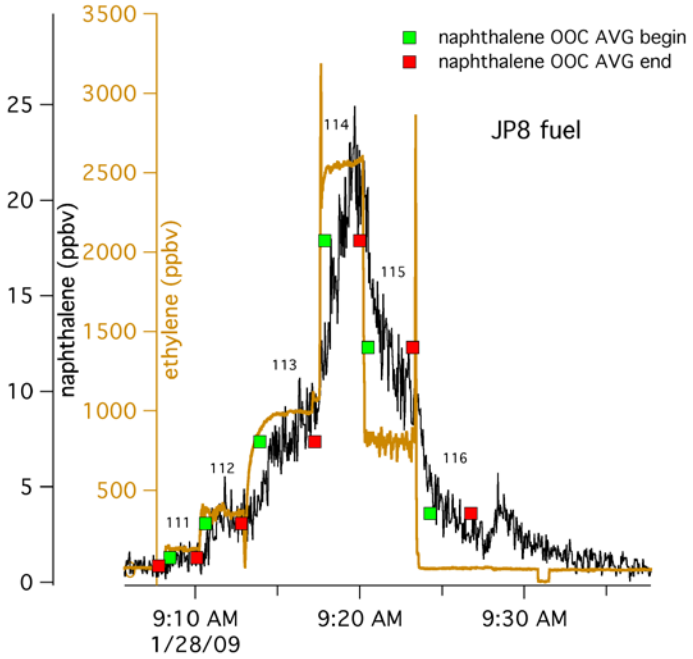

Figure 9. Naphthalene time series illustrating temporal distortion due to its retention in the sample lines.

For this illustrated case, the naphthalene signal nearly reaches its equilibrium value by the end of the test point. With respect to other compounds, we have found that the extent of this phenomenon is related to the components vapor pressure. Compounds having lower vapor pressures have more pronounced temporal distortion. A consequence of this effect is that the measurements exhibit a dependence on the previous sample history. Measurements are affected any time the sample concentration changes dramatically but are most apparent when the sample concentration goes from a high value to a low value. To help reduce the bias of these sample line interactions on the final data product, we have employed a new algorithm to compute the average test point concentration, which is described in Appendix II.

Improvements in sampling strategy are needed if we want to understand the role low volatility compounds have on the formation and growth of aerosol particles. In this section we examine how the measurement of low volatility compounds might be improved. An obvious first thought would be to increase the duration of the test points. Increasing the time will improve the precision of the measurements by ensuring that the gas phase concentrations achieve a true steady state value. Unfortunately, the steady state concentration reflects an equilibrium between gas phase and condensed or adsorbed naphthalene and this equilibrium condition is dependent on the surface composition of the sample line and temperature. Control of these variables may not be entirely possible in an APEX style test. Even if control of these variables could be achieved, it is unlikely that we would be able to ascertain how surface composition and temperature affects the results. The only reliable way to eliminate sample line perturbations is to eliminate the sample line. While this can’t be accomplished explicitly, these sample line effects can be reduced by moving the instruments to the exhaust plume rather moving the exhaust sample to the instruments. Techniques such as the EEPS "death box" and the Aerodyne mobile laboratory demonstrated this sample strategy during AAFEX. The improvement in time response for naphthalene measured while the Aerodyne mobile lab was deployed downrange of the aircraft is shown in Figure 10. In this mode of operation the sample line is a short 3-m section of 0.5" OD Teflon line. The reduction in sample line length leads to a time response of naphthalene of ~10 seconds as compared with ~100 seconds in the main sampling system. While these downrange measurements become challenging because of the low sample concentrations, the improvements achieved due to improved sampling integrity provide the best conditions to study gas-to-particle processes.

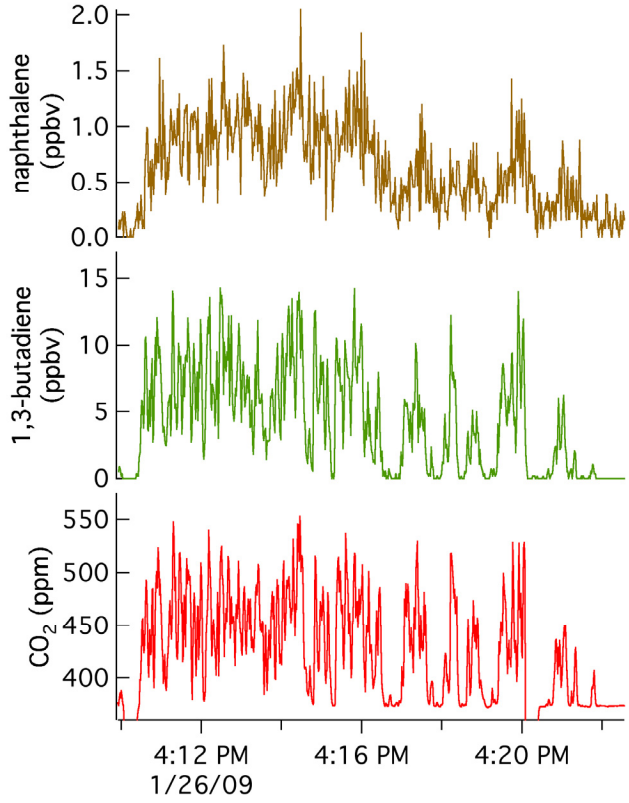

Figure 10. Downrange measurement of naphthalene showing the improvement in time response due to the reduction of sample line perturbations.

References

(1) Knighton WB, Rogers TM, Anderson BE, Herndon SC, Yelvington PE, Miake-Lye RC. *Journal of Propulsion and Power* 2007; **23**, 949.

(2) Yelvington PE, Herndon SC, Wormhoudt JC, Jayne JT, Miake-Lye RC, Knighton WB, Wey C. *Journal of Propulsion and Power* 2007; **23**, 912.

(3) Spicer CW, Holdren MW, Riggin RM, Lyon TF. *Ann. Geophys.-Atmos. Hydrospheres Space Sci.* 1994; **12**, 944.

(4) Wey CC, Anderson BE, Wey C, Miake-Lye RC, Whitefield P, Howard R. *Journal of Propulsion and Power* 2007; **23**, 898.

(5) Zhang HR, Eddings EG, Sarofim AF. *Environmental Science & Technology* 2008; **42**, 5615.

(6) Schulz H, De Melo GB, Ousmanov F. *Combustion and Flame* 1999; **118**, 179.

Quantification using the PTR-MS

The concentrations of the VOC exhaust emission components, R, are deduced from measured ion intensities using relationships derived either from reaction kinetics or calibrated response factors. The methods used to quantify the concentrations of VOCs in jet engine exhaust have been previously described in detail by Knighton et al.[1] A brief overview of these methods is provided here along with a tabulation of the pertinent quantification information relevant to the measurements made at AAFEX. Sensitivity response factors are derived from calibration experiments performed using a certified multicomponent gas standard that were conducted periodically throughout the campaign. Compounds for which gas standards were not available were quantified using reaction rate constants taken from Zhao and Zhang.[2]

Compounds quantified from calibrated response factors utilize Eq. 1, which describes the relationship between the volumetric mixing ratio (VMR) expressed in ppbv and the response factors.

$$VMR_R = \left(\frac{1}{S_R}\right)\left(\frac{I_{RH^+}}{I_{H_3O^+} + X_R \bullet I_{H_3O^+(H_2O)}}\right)\left(\frac{T}{300}\right)^2\left(\frac{2}{P}\right)^2 \quad (1)$$

I_{RH^+}, $I_{H_3O^+}$, and $I_{H_3O^+(H_2O)}$ represent the measured ion intensities in counts per second (cps). S_R represents the calibrated response factor expressed as cps/ppbv per 1-million reagent ions, which is referred to as ncps. X_R is a correction factor that compensates for differences in the detection and reaction efficiency of the $H_3O^+(H_2O)$ versus the H_3O^+ reagent ion. The drift tube temperature (T) and drift tube pressure (P) are included in this expression to account for small changes in the reaction time and gas number density that occur when we operate outside the standard conditions of 300K and 2 mbar.

For compounds where calibration standards were not available, concentrations were calculated from an expression derived from standard reaction kinetics, Eq. 2.

$$VMR_R = \left(\frac{I_{RH^+} / BF}{\left(I_{H_3O^+} + I_{H_3O^+(H_2O)}\right) k_c t}\right)\left(\frac{10^9}{N_{tot}}\right) \quad (2)$$

In the case of Eq. 2, I_{RH^+}, $I_{H_3O^+}$, and $I_{H_3O^+(H_2O)}$ represent transmission corrected ion intensities. BF is the product ion fraction fraction, t is reaction time, defined by the drift time of the reagent ions, k_c is the reaction rate constant, 10^9 is the conversion factor to ppbv and N_{tot} is the total number density of the sample within the drift tube reaction region.

Table 1 provides a compilation of the response factors, reaction rate constants and product ion branching fractions used quantify the reported VOC concentrations. Quantification notes provide more specific information on which quantification equation

was employed and other relevant details. Some compounds are reported as sums, because they exist in a variety of structural isomers and/or there are other compounds present that possess the same nominal molecular weight (isobars) that cannot be resolved using a quadrupole mass spectrometer. The quantification notes indicate whether a weighted average or single compound response factor or reaction rate constant is assumed. The rational for these choices has been discussed previously in Knighton et al.[1]

Table 1 Compounds monitored within the engine exhaust and pertinent quantification information

Compound	Ions formed (abundance)	Quantification Note	S_R (ncps)	X_R	reaction rate constant (ml/s) x10^9
methanol	33(100%)	Eq, 1	19.6	0.18	2.33
propene	41(23%) 43 (77%)	Eq. 1 – see text	12.4	-0.12	1.58
acetaldehyde	45(100%)	Eq. 1	33.8	0.34	3.36
butenes	57(100%)	Eq. 2 – weighted average rate constant summed with acrolein	-	-	1.73
acrolein	57(100%)	Eq. 2 – weighted average rate constant summed with butenes	-	-	3.35
acetone	59(100%)	Eq. 1 - weighted average response factor summed with propanal and glyoxal	36.4	0.48	3.00
propanal	59(100%)	Eq. 1 - weighted average response factor summed with acetone and glyoxal	36.4	0.48	3.44
glyoxal	59(100%)	Eq. 1 - weighted average response factor summed with actone and glyoxal	36.4	0.48	1.34
acetic acid	43(34%) 61(66%)	Eq. 2 m/z 61 BF = 0.66	-	-	2.27
benzene	79(100%)	Eq. 1	25.2	-0.21	1.97
toluene	93(100%)	Eq. 1	33.3	0.05	2.12
phenol	95(100%)	Eq. 2	-	-	2.52
styrene	105(100%)	Eq. 1	36.9	0.35	2.33
o,m,p-xylene	107(100%)	Eq. 1 p-xylene calibration summed with ethylbenzene and benzaldeyhde	36.9	0.33	2.26-2.32
ethylbenzene	79(12%)107(88%)	Eq. 1 p-xylene calibration summed with xylenes and benzaldehyde	36.9	0.33	2.25
benzaldehyde	107(100%)	Eq. 1 p-xylene calibration summed to xylenes and ethylbenzene	36.9	0.33	4.12
C_9H_{12} isomers + C_8H_8O isomers	121 (100% assumed)	Eq. 1 1,2,4 trimethylbenzene calibration	37.8	0.37	2.4 – 3.9

naphthalene	129(100%)	Eq. 2	-	-	2.59
$C_{10}H_{14}$ isomers + $C_9H_{10}O$ isomers	135 (100% assumed)	Eq. 2 $C_{10}H_{14}$ reaction rate constant	-	-	2.5
methylnaphthalenes	143(100%)	Eq. 2	-	-	2.7
$C_{11}H_{16}$ isomers + $C_{10}H_{12}O$ isomers	149(100% assumed)	Eq. 2 $C_{11}H_{16}$ reaction rate constant	-	-	2.6
dimethylnaphthalenes	157(100%)	Eq. 2	-	-	2.9

Aircraft engine exhaust also contains a number of other known compounds, which are detectable using PTR-MS, but can't be specifically quantified due to the presence of other compounds within the exhaust matrix whose identities have not yet been confirmed. In effort to retain as much information as possible about the total mass balance, it is desirable to be able to estimate the amount of material present in the exhaust beyond what is accounted for in Table 1. For ion masses where their respective neutral precursors can't be identified, these ions are quantified using Eq. 2 assuming a reaction rate constant of $2x10^{-9}$ ml molecule^{-1} sec^{-1}. Contributions from these ion masses are designated by their respective mass number. Two ion masses, m/z 71 and m/z 85, contain a significant amount a spectral intensity and are quantified assuming that their molecular weights are 70g/mole and 84 g/mole respectively.

Interpreting the PTR-MS mass spectrum relies heavily on knowing what compounds are present in the exhaust matrix and their ion chemistry, because ion mass is not a unique indicator of compound identity. In our initial paper, we utilized the exhaust composition reported by Spicer et al.[3] to predict which compounds could be quantified. The accuracy of compound identities reported in Table 1 depends on how well we know both the chemical composition and the ion chemistry associated with each compound. For example, does the ion intensity measured at m/z 57 reflect only the presence of the butenes (C_4H_8) and acrolein (C_3H_4O)? To address this question and others, we have interfaced a gas chromatograph to the PTR-MS. Chromatograms are recorded for a specified ion (single ion chromatograms). These single ion chromatograms help us determine how many different compounds contribute to the spectral response. All compounds present in the engine exhaust matrix are not amenable to GC analysis, i.e. acetic acid, and any interpretation of the ion signals must remain cognizant of this fact. Below we discuss our GC/PTR-MS results for most of the ion mass assignments listed in Table 1. The information provided in this discussion is restricted to exhaust measurements made from engines burning conventional fuels. Most of measurements discussed were taken from a F-100 engine although a limited number were taken from CFM56-2 engine at AAFEX. An implicit assumption is that the exhaust composition in not affected by differences in engine technology. The body of our work[1,4-6] suggests strongly that this is the case.

Summary of GC/PTR-MS analyses

Mass 43

Propene is quantified from the signal measured at m/z 43. Acetic acid and larger alkenes produce fragment ions that are detected at this mass. In our previous work we estimated

that 68% of the ion signal measured at m/z 43 was attributable to propene.[1] We have an improved understanding on how to quantify propene. We now directly correct for the acetic acid contribution. Under our experimental conditions acetic acid expresses 52% of its m/z 61 signal at m/z 43 allowing us to directly adjust the total m/z 43 signal by this amount. GC/PTR-MS analysis of the m/z 43 signal reveals that 85% of peak area in the chromatogram is due to propene. Two other peaks are observed in the m/z 43 chromatogram account for the remaining 15% of the peak area. Acetic acid does not elute off of the column and thus is not observed in the chromatogram. Propene is quantified from the adjusted m/z 43 response: $I_{propene}^{m/z43} = \left(I_{total}^{m/z43} - 0.52 * I^{m/z61}\right) \bullet 0.85$.

Mass 45
Acetaldehyde produces the only peak observed in the m/z 45 single ion chromatogram.

Mass 57
Single ion chromatograms obtained for m/z 57 indicate that 1-butene and acrolein are the predominate engine exhaust products (>90%) detected at this mass. The chromatogram suggests that only 1-butene is present, but the chromatographic resolution is poor enough that the isomeric 2-butenes could be unresolved and contained within the 1-butene peak. Quantification of these peak area responses confirms that the butenes and acrolein are present in roughly equimolar proportions. This result is consistent with results reported by Spicer et al.[3]

Mass 59
The single ion chromatogram obtained for m/z 59 produces a single broad peak. Given that all three compounds detected at this ion mass have similar boiling points; glyoxal 323K, propanal 322K and acetone 329K, it seems likely that our chromatographic column does not provide sufficient resolution to resolve these components. This is essentially a null result and we treat ion signal at m/z 59 as if all three compounds are present in the proportions reported by Spicer et al.[3]

Mass 71
The single ion chromatogram for m/z 71 generally produces 4-5 distinct peaks. Based on comparison of retention times obtained with known standards, one of these peaks has been indentified as methacrolein. There is one peak that elutes prior to methacrolein, which suggests the presence of one of pentene isomers. The remaining peaks all elute after methacrolein. Crotonaldehyde, a known exhaust emission component[3], has a higher boiling point than methacrolein and is most likely responsible for one of the other peaks.

Mass 79
Benzene is the only peak significant peak observed in the m/z 79 single ion chromatogram. The single substituted alkyl benzenes, ethyl, propyl, and butyl etc. all produce m/z 79 as fragment ion[7], but their contributions to the overall m/z 79 are very small <5%.

Mass 85
The single ion chromatogram for m/z 85 produces a number of distinct peaks ranging from 5 – 6 with a number of smaller features. None of these peaks have been definitively identified, but by analogy with the interpretation of mass 71 suggests a mixture of alkenes and aldehydes.

Mass 93
The single ion chromatogram for m/z 93 reveals that toluene is the dominant component detected at this mass. The toluene peak accounts for at least 80 – 90% of the total peak area. The other peaks in this chromatogram have much longer retention times, which suggests that they are fragment ions produced from larger alkylated toluenes. These GC results provide a reasonable explanation for why our previous measurements of toluene have typically been larger than that reported by Spicer et al.[3] No correction has been applied to our toluene data to date.

Mass 105
The single ion chromatogram for m/z 105 indicates that only styrene is detected at this mass.

Mass 107
The single ion chromatogram for m/z 107 shows 4 peaks. Three of these peaks reflect the presence of the 4 C_8H_{10} isomers; ethylbenzene and the three xylene isomers. Note that the meta- and para-xylene isomers can't be resolved and are detected as single chromatographic peak. The 4^{th} peak in the chromatogram has a significant longer retention time, and we ascribe the presence of this peak to benzaldehyde.

Mass 121 and Mass 135
The single ion chromatograms for these ion masses show a mixture of semi-distinct peaks and unresolved humps, which reflects the presence of a significant number of compounds. Mass 121 is attributed to both the C_9H_{12} and C_8H_8O compounds, which can exist as up to 8 alkyl-substituted aromatics and 5 substituted aromatic carbonyls. While Mass 135, which we attribute to both $C_{10}H_{14}$ and $C_9H_{10}O$ compounds can exist as more than 30 different aromatic compounds. One does not expect to see all of the possible isomeric forms expressed nor is there great value in identifying all of the specific isomers. There would be value of separating the aromatic hydrocarbons from their oxygenated isobars. Our chromatographic system cannot do this as it lacks the capability to efficiently transfer these large relatively low volatility compounds onto the chromatographic column. We note for these compounds that we have significant retention and loss of material in the sample valve. This leads to peak broadening, loss of chromatographic resolution and ultimately the total loss of signal. Lower volatility compounds, such as naphthalene, cannot be successfully analyzed by GC using our existing interface.

NO^+ MS

The PTR-MS can be adapted to employ NO^+ as the reagent ion by switching the reagent ion source gas from water to dry air. The full details on this mode of operation are provided in Knighton et al.[8] The instrument was configured to operate in the NO^+ mode during the first two days of the AAFEX campaign. NO^+ reacts via a charge transfer reaction, Eq. 3, with compound having ionization energies lower than 9.26 eV:

$$NO^+ + R \xrightarrow{k} R^+ + NO \tag{3}$$

This technique provides greater measurement specificity as only the diene and aromatic hydrocarbon exhaust components fit this criterion. This technique was designed specifically for the measurement of 1,3-butadiene, an important air toxic.

Calibration and quantification of the ion signals of the NO^+ MS are similar to that described above for the PTR-MS. Compound response factors are provided in Table 2. Volumetric mixing ratios (VMR) expressed as ppbv are computed using Eq. 4:

$$VMR_R = \left(\frac{I_{R^+}}{I_{NO^+}}\right)\left(\frac{10^6}{S_R}\right)\left(\frac{T}{300}\right)^2\left(\frac{2.1}{P}\right)^2 \tag{4}$$

Where I_{R^+} and I_{NO^+} represent the measured ion intensities and S_R is the sensitivity factor expressed in ncps. The drift tube temperature (T) and drift tube pressure (P) are included to account for changes in the reaction time and gas number density that occur when we operate outside of these standard conditions.

Table 2. Compounds monitored within the engine exhaust using the NO+ MS. Ion products and compound response factors measured at E/N = 104 Td.

Compound	Ions formed (abundance)	S_R (ncps)
1,3-butadiene	54 (~100%)	12.3
benzene	78 (100%)	12.7
toluene	92 (100%)	19.6
styrene	104 (100%)	22.1
C2-benzenes (sum of o,m,p-xylene and ethylbenzene	106 (100%)	23.5
naphthalene	128 (100%)	22.5[a]

[a] calibration factor calculated assuming a reaction rate constant of $2x10^{-9}$ ml molecule^{-1} sec^{-1}

GC/PTR-MS has been used to examine the single ion chromatograms at m/z 54, m/z 78, m/z 92, m/z 104 and m/z 106. The C2-benzenes (m/z 106) show 3 peaks corresponding to o-xylene, m,p-xylene and ethylbenzene while other masses only show one peak. These results confirm the mass assignments made in Table 2. The purity of the m/z 128 ion signal has not been established for naphthalene. While there is no doubt that naphthalene reacts with NO^+ to form an ion at m/z 128, there are potential interferences to this measurement. NO^+ can react with alkenes via an insertion mechanism to produce ions of the type $C_2H_{2n-1}HNO$.[9] 1-heptene is a known jet engine exhaust component and could

possibly interfere with the measurement of naphthalene. We intend to investigate this potential interference.

(1) Knighton WB, Rogers TM, Anderson BE, Herndon SC, Yelvington PE, Miake-Lye RC. *Journal of Propulsion and Power* 2007; **23**, 949.
(2) Zhao J, Zhang RY. *Atmospheric Environment* 2004; **38**, 2177.
(3) Spicer CW, Holdren MW, Riggin RM, Lyon TF. *Ann. Geophys.-Atmos. Hydrospheres Space Sci.* 1994; **12**, 944.
(4) Herndon SC, Rogers T, Dunlea EJ, Jayne JT, Miake-Lye R, Knighton B. *Environmental Science & Technology* 2006; **40**, 4406.
(5) Herndon SC, Wood EC, Northway MJ, Miake-Lye R, Thornhill L, Beyersdorf A, Anderson BE, Dowlin R, Dodds W, Knighton WB. *Environmental Science & Technology* 2009; **43**, 1730.
(6) Yelvington PE, Herndon SC, Wormhoudt JC, Jayne JT, Miake-Lye RC, Knighton WB, Wey C. *Journal of Propulsion and Power* 2007; **23**, 912.
(7) Warneke C, De Gouw JA, Kuster WC, Goldan PD, Fall R. *Environmental Science & Technology* 2003; **37**, 2494.
(8) Knighton WB, Fortner EC, Herndon SC, Wood EC, Miake-Lye RC. *Rapid Communications in Mass Spectrometry* 2009; **23**, 3301.
(9) Diskin AM, Wang TS, Smith D, Spanel P. *Int. J. Mass Spectrom.* 2002; **218**, 87.

APPENDIX D: Measurements of nitrous acid in commercial aircraft exhaust

Ben H. Lee[1], Greg W. Santoni[1], Ezra C. Wood[2], Scott C. Herndon[2], Richard C. Miake-Lye[2], J. William Munger[1], Steven C. Wofsy[1], J. Barry McManus[2], David D. Nelson[2], Mark S. Zahniser[2]

[1] Harvard University, Cambridge, Ma
[2] Aerodyne Research, Inc., Billerica, Ma

Abstract

The Alternative Aviation Fuels Experiment (AAFEX), conducted in January of 2009 in Palmdale, California evaluated aerosol and gaseous emissions from a DC-8 aircraft equipped with CFM56-2C1 engines alternating between traditional and synthetic fuels. This study examines the emissions of nitrous acid (HONO) and the sum of nitrogen oxides (NO_x) measured approximately 140 m downwind of the grounded aircraft. The emission index (EI) for HONO increases approximately six-fold from idle to take-off conditions but plateaus between 60% and 100% engine power setting, as opposed to that of NO_x, which increases continuously. HONO EI did not exhibit a dependence on fuel type (traditional, synthetic, synthetic blend), ambient temperature, relative humidity, or presence of sunlight, while NO_x EI showed a positive dependence on ambient temperature at maximum rated engine thrust. Additionally, hydrogen peroxide (H_2O_2) was identified in exhaust plumes emitted during idle conditions. Chemical reactions responsible for emissions and comparisons to previous studies are discussed.

Introduction

Exhaust emissions from aircraft are pertinent to global climate change and air quality [1]. This is a particularly pressing concern given the projected increase in air travel over the coming decades [2]. While the International Civil Aviation Organization (ICAO) monitors the emissions of many trace gases including nitrogen oxides (NO_x) from every class of commercial aircraft, nitrous acid (HONO) specifically is not one of these gases. Moreover, while the impact of aircraft NO_x (= NO + NO_2) emissions on regional ozone levels and NO_x burden has been studied [3-5], the effects of aircraft HONO emissions on atmospheric chemistry particularly on the HO_x (= OH + HO_2) budget are not well known.

HONO emitted from aircraft is a reservoir for HO_x and NO_x as it photo-dissociates to nitric oxide (NO) and the hydroxyl radical (OH), the main atmospheric oxidant. In the upper atmosphere, where the OH number density is low, HONO emitted from aircraft may influence the local oxidative capacity along flight corridors. In the lower troposphere, nighttime buildup and subsequent photolysis of HONO is the dominant OH source in the early morning. Recent daytime ground-level measurements in urban, rural and even remote environments have shown levels far exceeding those expected under photo-stationary state, indicating a yet-unidentified HONO source, which may significantly contribute to daytime HO_x budgets. In order to determine OH contribution from HONO photolysis, the strengths of all HONO sources including homogeneous, heterogeneous, photo-induced reactions and direct emissions need to be accurately quantified and their controlling factors characterized.

The Fischer-Tropsch process – though highly energy- and cost-intensive – can reduce the need for foreign oil because the main ingredients are readily available feedstock, such as coal, natural gas and bio-oils. In addition, FT-derived fuels do not contain aromatic-hydrocarbon and sulfur, resulting in emissions that are lower in soot and sulfate aerosols. However, few studies have looked at emissions from the combustion of these fuels by typical commercial aircraft engines. We present here the emission indices of HONO, NO_x and H_2O_2 determined through reference to emitted carbon dioxide (CO_2).

Methods

During AAFEX, a DC-8 aircraft was chocked on the runway at NASA's Dryden Flight Research Center in Palmdale, California. Two engines – one on either side of the aircraft – were fired for each experiment, lasting a few hours during which the engine power was varied to simulate idle to take-off conditions. The left inboard engine was supplied with traditional JP8 fuel, while the right inboard engine alternated between traditional, two different synthetic Fischer-Tropsch fuels and blends of both. Experiments were conducted from before sunrise to late afternoon over a span of a week to utilize the wide range in ambient conditions to test their impact on emission characteristics. Composition and mixing ratios of particles and various trace gases were measured at 1 m and 30 m behind both engines [*Anderson et al.*, 2010, in preparation], and also 140 m downwind, which is the focus of the present study.

Mixing ratios of HONO, H_2O_2, nitrous oxide (N_2O) and methane (CH_4) were measured simultaneously by a tunable infrared laser differential absorption spectrometer (TILDAS) utilizing a single continuous-wave mode quantum cascade laser operating near the 1275 cm^{-1} spectral region [6, 7]. Figure 1 shows typical one-second spectra observed while sampling plumes emitted during 7% (a, b) and 85% (c, d) rated engine thrusts. For AAFEX, the scanning window was less than 0.2 cm^{-1} and repeatedly tuned at just over 3 kHz. The laser linewidth was less than 0.002 cm^{-1}, hence not the limiting factor in determining the lineshape. Sampled air flowed through an astigmatic multi-pass absorption cell in which infrared laser beam traversed a total path of 210 m [8]. An absorbance precision of less than 6×10^{-6} $Hz^{-1/2}$ in one second was achieved in the field, which translated to detection limits (S/N = 3) of 450 ppt (pmol/mol), 1200 ppt and 900 ppt for HONO, H_2O_2 and N_2O, respectively, in one second. Complete details regarding the instrument and HONO linestrength quantification are provided by *Lee et al.* [manuscript in preparation]. Results for N_2O, along with $^{12}CH_4$ and $^{13}CH_4$ isotopologues measured by a second TILDAS instrument connected in series with this system are presented by *Santoni et al.* [manuscript in preparation].

Special attention was paid to the sampling procedure to minimize attenuation and artifact formation on inlet and tubing surfaces for reactive species such as HONO and H_2O_2. A siloxyl-coated quartz inlet – used previously by *Herndon et al.* [9] to measure formic acid and formaldehyde – with a built-in critical orifice with a 0.04'' (1 mm) diameter immediately reduced the sample pressure by at least a factor of two. The sample subsequently traveled through approximately 40 feet (12.2 m) of 3/8'' OD PFA Teflon tubing to a siloxyl-coated 5.0 L glass multi-pass sampling cell in which the pressure was

maintained at around 30 torr. The sample residence times in the inlet, tubing and cell were calculated to be on average 0.3, 0.2 and 1.2 seconds, respectively, given a volumetric flow-rate of ~10 liters per minute. It was determined from introducing HONO along with CH_4 (an inert gas) at the end of the eight-day campaign that there was undetectable loss or interaction of HONO with the inlet/tubing/cell surfaces. Figure 2 shows the time responses (e-folding time determined by an exponential fit of the rise and fall of HONO and CH_4 mixing ratios during injection tests) of the two gases were virtually identical, indicating that HONO response time was determined only by physical mixing and was not affected by chemistry. Gaseous HONO was generated using hydrochloric acid vapor passed over sodium nitrite powder as described by *Febo et al.* [10].

A similar test for H_2O_2 could not be conducted because a steady source was not available. However, it is not inconceivable that there was some loss of H_2O_2 given that the Henry's law constant for HONO is 50 atm M^{-1} compared to 82,000 atm M^{-1} for H_2O_2 [11, 12]. In addition, the near overlap between HONO and H_2O_2 absorption lines at around 1275.82 cm^{-1} (figure 1a, 1c) resulted in artificial enhancement of the retrieved H_2O_2 mixing ratios in the presence of high HONO absorbance. This was not observed when H_2O_2 was scanned near the 1275.98 cm^{-1} region (figure 1b, 1d), where its absorption lines were free of overlap. These effects, as a result, limit the accuracy of H_2O_2 measurements during AAFEX. We observed no evidence of H_2O_2 significantly affecting HONO mixing ratios.

Routine calibrations were not performed in the field, but instead measurements relied on the accuracy of linestrengths. Peak positions for mid-infrared HONO absorption were obtained from high-spectral resolution Fourier Transform Infrared Spectroscopy [*Herman*, personal communication]. The effective linestrengths – referring to the total (*cis* + *trans*) HONO absorption given by the absorption by one isomer – were obtained by calibrating measurements of *cis* (1660 cm^{-1}) and *trans*-HONO (1275 cm^{-1}) individually by TILDAS against measurements of NO by ozone chemiluminescence following the complete reduction of HONO to NO by heated molybdenum catalyst [*Lee et al.*, in prep]. Preliminary results show that previous measurements used linestrengths that were high by a factor of about 2.5 (discussed below). The linestrengths for N_2O, CH_4, H_2O_2 and water vapor were obtained from the High Resolution Transmission (HITRAN) molecular absorption database [13].

NO_x mixing ratio – defined here as the sum of NO and NO_2 – was measured using molybdenum catalysis ozone chemiluminescence (ThermoElectron 42i). We assume negligible amounts of other reducible nitrogen oxide species such as HONO and nitric acid to which this technique is sensitive, partly based on observations and assuming sampling loss due to use of particle filters and long sampling tubing at ambient pressures. The mixing ratio of CO_2 was measured using a non-dispersive infrared absorption spectrometer (Li-Cor 6262). The flowrate through both instruments was approximately 0.5 liters per minute, resulting in a time response (1/e) less than one second for both instruments.

We report emission indices (g of species per kg of fuel consumed) calculated as the slope of the linear fit relative to CO_2 corrected for the average mass of CO_2 emitted per mass of the fuel consumed. This method is more robust in downwind plumes with highly variable mixing ratios than the background-subtracted ratio of the average mixing ratio to CO_2 [14]. Note that the EI for HONO and H_2O_2 are scaled by their respective molecular masses, while EI for NO_x is reported using the molecular mass of NO_2.

$$EI = ER_X \times \frac{MW_X}{MW_{CO_2}} \times 3160 \frac{gCO_2}{kg\,fuel}$$

ER_x is the emission ratio of species X defined as the correlation slope with respect to CO_2 and 3,160 g CO_2 per kg fuel is the CO_2 emission index of JP8 fuel [reference].

Figure 3 (a, b) shows 1 hertz time-series of HONO, NO_x, H_2O_2 and CO_2 mixing ratios measured in the 140 m downwind trailer. Note that all gases co-vary together in time. This is also reflected in the correlation of that same plume of HONO, NO_x and H_2O_2 versus CO_2 mixing ratios (figure 3c).

Results and Discussion

HONO, NO_x and HONO/NO_x

Figure 4 (a, b) shows the emission indices for NO_x and HONO plotted as a function of rated engine thrust for each of the 12 experiments conducted during AAFEX. Whereas the EI for NO_x increases continuously from idle to 100% rated engine thrust, the EI for HONO levels off between 60% and 100% reflecting the point at which HONO production (reaction between NO and OH) and loss (reaction with OH and HONO self-reaction) become balanced.

Emission indices of HONO observed at the 140 m trailer show no sufficient evidence of fuel type dependence regardless of engine setting (figure 5). The EI for NO_x likewise did not exhibit a dependence on the type of fuel consumed (figure 5), which is in contrast to observations made at the 30 m location where EI values for FT fuels were lower than those for JP8 fuels by as much as 10% [*Timko et al.*, manuscript in preparation]. This was likely due to a combination of limited instrument precision and the difference in the EI due to fuel type being less than experimental reproducibility. Note that the variability in the emission indices of individual plumes observed for a particular experiment exceeds 10% (figure 5). It is also possible, though unlikely, that exhaust from only the left engine fueled with JP8 was sampled at the downwind site for the entire duration of AAFEX.

EI for NO_x exhibits a positive dependence on ambient temperature (negative on relative humidity) only at the highest rated engine thrusts (figure 6), consistent with the ICAO database [reference]. The emission indices for HONO do not show the same dependence (figure 6), but may be masked by instrument precision. It is also possible that the dominant HONO production and loss processes (reactions with OH) are insensitive to ambient temperatures, which may be the case if the OH radical was the limiting reactant and its production had no temperature dependence. Moreover, HONO EI is not affected by the presence of sunlight, which is indicative of insignificant photochemical loss or

production during transport from engine to the downwind sampling location. Likewise, wind speed or wind direction had no effect on HONO EI, all suggesting that production took place predominantly within the engine as also observed by *Tremmel et al.* [15], which found much of the HONO formation occurs prior to engine exit. However, we note that the ambient variables could not be adjusted in a controlled manner, hence, it is possible, though unlikely, that some effects could counteract one another.

Figure 4d shows HONO to NO_x ratios ranging from 3% to 7% depending on engine setting during AAFEX. Tunnel studies of on-road vehicles show HONO to NO_x ratios typically range between 0.29% (California, USA) and 0.80% (Wuppertal, German), with diesel-powered engines emitting a higher ratio than their gasoline-powered counterparts [16, 17]. Similarly at AAFEX, the HONO to NO_x ratio of a plume emitted from a diesel-powered generator was 0.82% (figure 7). Previous field studies have inferred in situ photochemical production of HONO in the atmosphere from observing urban HONO to NO_x ratios in excess of 0.8%, assuming the NO_x signatures are predominantly vehicle emission derived. These results from AAFEX, along with observations of HONO to NO_x emission ratios from biomass burning ranging from 3% to 20% [reference], suggest direct combustion sources need to be better constrained in order to apportion HONO source strengths in the atmosphere.

HONO in aircraft exhaust has been previously measured [18-24]. In two dedicated engine tests measuring HONO and NO_x from similar engine types, the observed HONO to NO_x ratios were within range of those observed during AAFEX [23, 24]. However, in those studies the ratios consistently decreased from as high as 7% at engine idle to 0.5% at maximum thrust, whereas at AAFEX the HONO to NO_x ratios increase from 3% at idle to as high as 7% around cruise setting where it begins to decrease with increasing engine thrust (figure 4). Moreover, emission indices of HONO from those two previous studies agree well (after correcting for linestrengths) at low idle thrust to those observed here but are lower by a factor of about three at higher engine settings (figure 8). The discrepancies may simply be explained by difference in engine type and age, both of which can influence aircraft NO_x emissions [25]. However, the good agreement under certain circumstances (figure 6) suggests that previous campaigns suffered from sampling loss at high engine thrust because of thermal dissociation, adsorption on metal probe/tubing surface, HONO self-reaction at high mixing ratios, or poor temperature control leading to a *cis* to *trans* conversion. Another possible reason for the differing observations may be incomplete HONO formation. If a significant amount of aircraft HONO is produced post engine exit from the reaction between NO and OH, it may explain the lower HONO to NO_x ratio and HONO EI at high engine thrust in the previous campaigns when measurements were made close to the engine. This, however, is inconsistent with our findings here and in previous reports [15].

H_2O_2

Hydrogen peroxide was identified in aircraft exhaust emitted during low idle thrust (figure 1). As observed for NO_x and HONO, there is no evidence of EI dependence on ambient temperature, presence of sunlight, or fuel type. The AAFEX averaged emission index at idle thrust is 0.43 +/- 0.31 (2σ) g H_2O_2 per kg fuel and decreases to below

detection limit at rated engine thrusts greater than 20% (figure 4c). The first ten experiments during AAFEX, however, exhibit a finite EI at higher engine thrusts because of spectroscopic interference from HONO absorbance, as mentioned above. Plans for future deployments call for measuring H_2O_2 in a more optimal spectral location or operating at lower sampling pressures to minimize spectral overlap at the expense of instrument precision. Though this was the first spectroscopic measurement of H_2O_2 in aircraft exhaust, the reported values for H_2O_2 from AAFEX should be qualified because of the yet uncharacterized potential for attenuation during sampling.

However, we can still comment qualitatively on our observations. Gaseous H_2O_2 can be formed by the self-reactions of HO_2 and OH. That the emission index trend with respect to rated engine thrust observed during AAFEX follows that of CO (produces HO_2 from reaction with OH and O_2) and is opposite to that of HONO (formed by the reaction between NO and OH), strongly suggests HO_2 and not OH is the H_2O_2 precursor in aircraft exhaust, as proposed by *Wood et al.* and *Arnold et al.* [23, 26]. *Tremmel et al.* considered the sum of the enhancements of OH, HONO and nitric acid (HNO_3) measured downwind in an aircraft exhaust plume as the lower limit of the total HO_x generated in an engine, neglecting all other OH loss pathways [15]. Our findings at AAFEX suggest the reaction between OH and CO and subsequent HO_2 self-reaction to generate H_2O_2 represents an additional HO_x loss at low engine thrust. H_2O_2 is, however, a HO_x reservoir species like HONO thus will photo-dissociate once emitted to release two OH molecules.

Summary

We report here the emission indices for gaseous HONO, NO_x and H_2O_2 from the AAFEX campaign, a dedicated engine experiment measuring emissions from a DC-8 aircraft utilizing two CFM56-2C1 engines fueled by traditional and synthetic fuels. The emission indices for HONO and NO_x increase with rated engine thrusts, while that of H_2O_2 decrease to below detection limit at engine settings greater than 20%. We did not observe at the downwind sampling location strong evidence to support an EI dependence on fuel type (tradition, synthetic or blends of the two) for any of the gases, but this may not have been discernible with current instrument precision and experiment setup given the mixing of plumes of different origins. Changes in ambient temperatures (270 to 293 K) or presence of sunlight, likewise, did not have an influence on emission indices of HONO and H_2O_2. HONO EI observed at AAFEX are higher by at least a factor of 2.5 than those previously reported because of incorrect linestrengths. Moreover, HONO EIs at the higher engine settings in those studies were underestimated by another factor of three, likely because of sampling losses. We also report for the first time spectroscopic measurements of H_2O_2 in aircraft exhaust, however, the values reported here represent lower limits because of possible sampling losses.

These observations from AAFEX were made from one particular aircraft equipped with one engine type. Although HONO EI and HONO to NO_x ratios measured at cruise altitude from completely different airframes and engine types fall in the range observed during AAFEX [15, 27], emissions are likely to vary depending on numerous factors such as engine type, age, aircraft payload and certainly engine thrust. Consequently, scaling up using EI observed from one experiment is an unrealistic representation of real-

world scenarios, which calls for additional measurements under widely varying conditions at ground as well as at altitude to better model the impact of these emissions on the oxidative capacity of the atmosphere.

Acknowledgements
This research was funded by the Partnership for AiR Transportation Noise and Emissions Reduction (PARTNER) Center of Excellence (jointly sponsored by the FAA, NASA and Transport Canada) via Missouri University of Science and Technology, the National Science Foundation (Atmospheric Chemistry, proposal number 0813617) and by the Transportation Research Board Graduate Research Award. The authors greatly acknowledge W. Berk Knighton of Montana State University and Michael T. Timko and Zhenhong Yu of Aerodyne Research Inc.

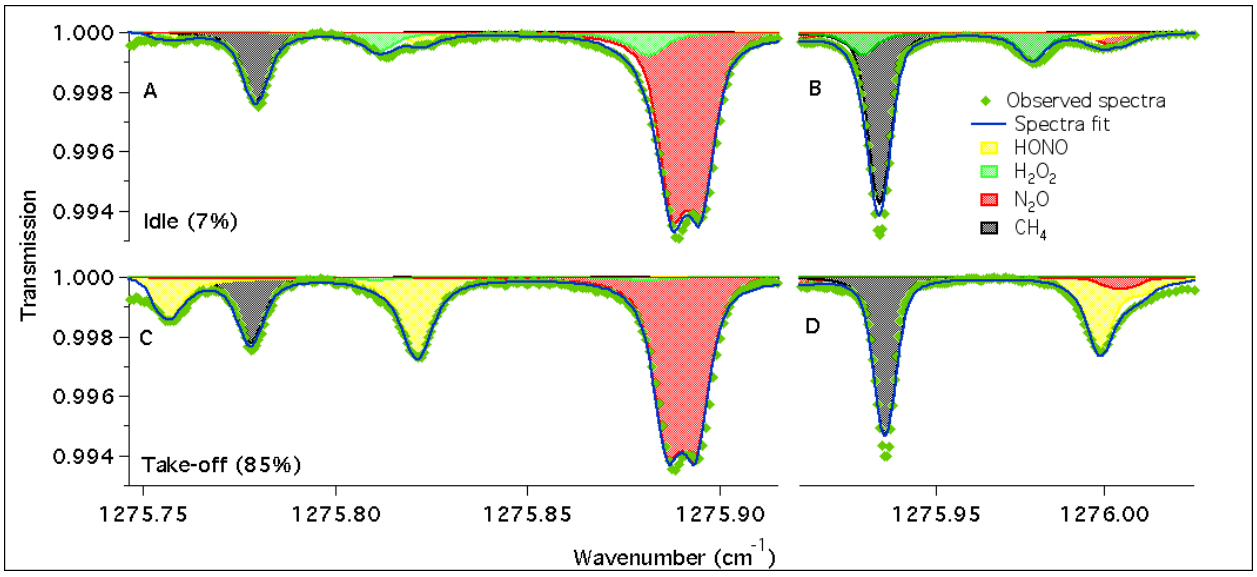

Figure 1. One-second spectra observed in aircraft exhaust emitted during 7% (a, b) and 85% (c, d) rated engine thrust. The above snapshots at idle and take-off conditions represent CH_4, N_2O, HONO and H_2O_2 values of 2000, 335, 10, 35 ppb and 1875, 325, 75, 5 ppb, respectively. For most of AAFEX, the spectral window shown in a) and c) was scanned, save for one day when the window in b) and d) was scanned. The filled-in color areas are simulations of the retrieved mixing ratios.

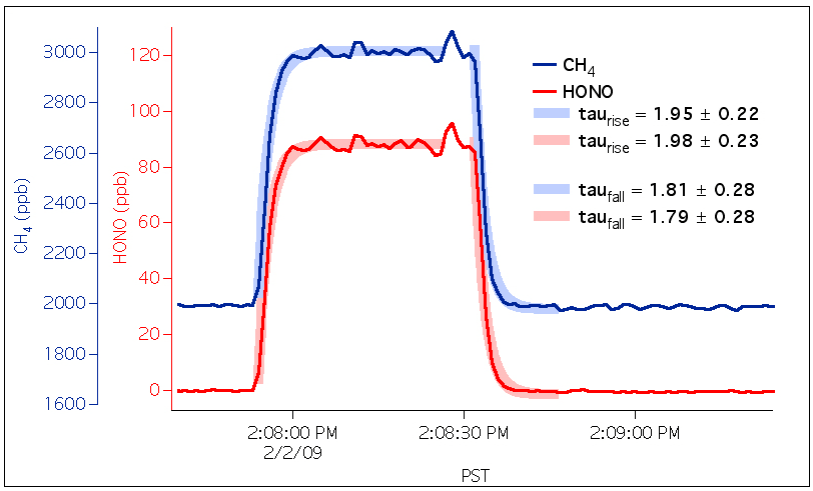

Figure 2. Mixing ratios of CH_4 and HONO observed during a typical injection of calibration gas. Time response (1/e) – determined by an exponential fit of the increase and decrease of the mixing ratios versus time – are averages of six injection tests.

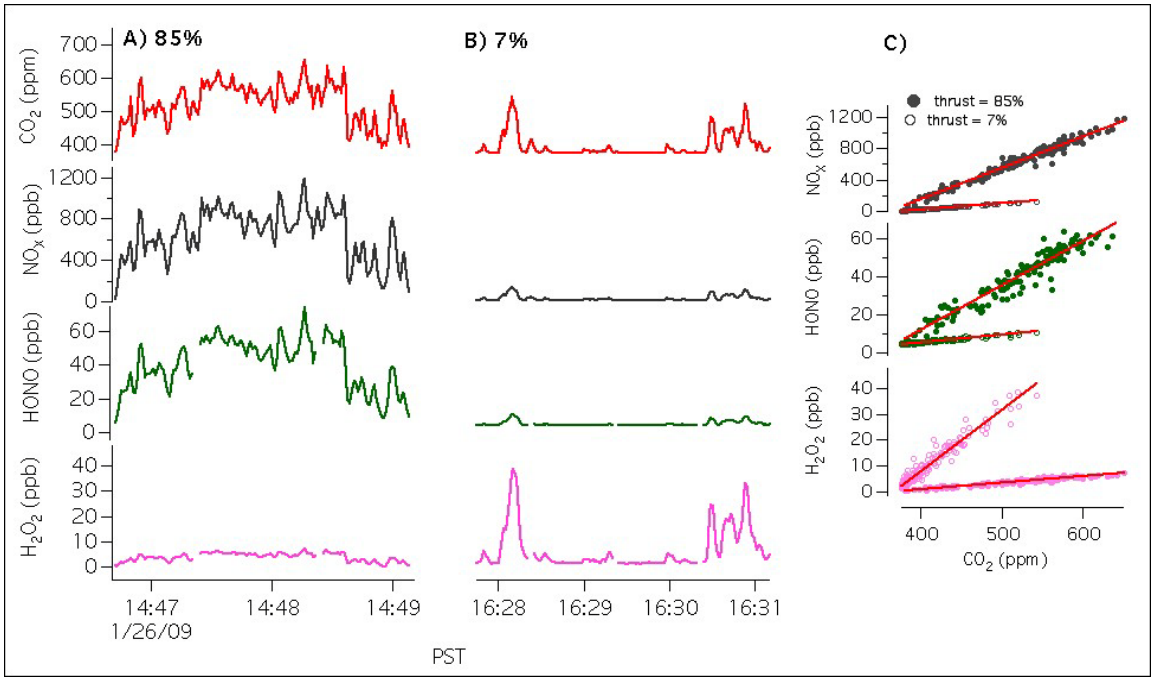

Figure 3. Mixing ratios of CO_2, NO_x, HONO and H_2O_2 measured 140 m downwind of the aircraft in plumes emitted during 85% (a) and 7% (b) rated engine thrust. Correlation plots (c) of NO_x, HONO and H_2O_2 versus CO_2 for the same time periods from (a) and (b).

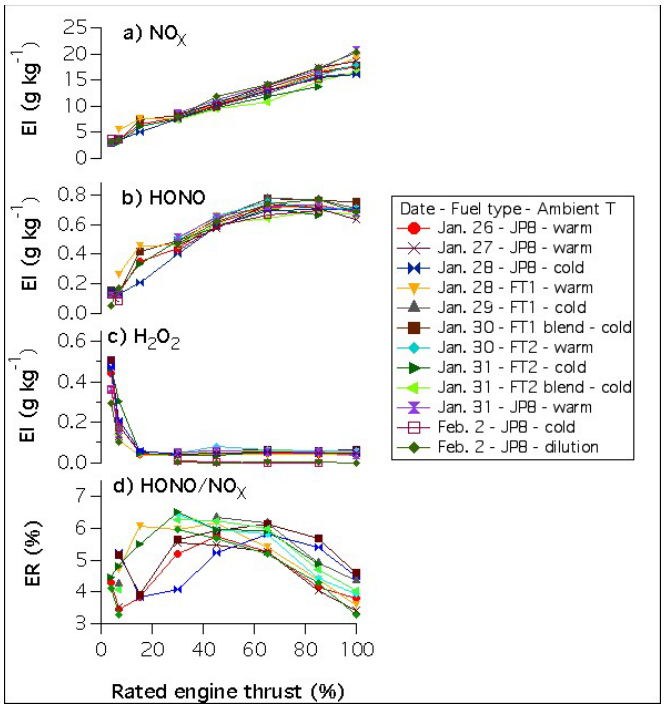

Figure 4. Emission indices (EI = g per kg of fuel) for NO_x (a), HONO (b) and H_2O_2 (c) are plotted against rated engine thrust, along with HONO to NO_x ratio (d). Each colored plot, totaling 12 in all, represents a single experiment conducted with JP8, Fischer-Tropsch (FT) or blends of fuels under warm or cold conditions. Each marker represents the experiment average at that particular engine setting.

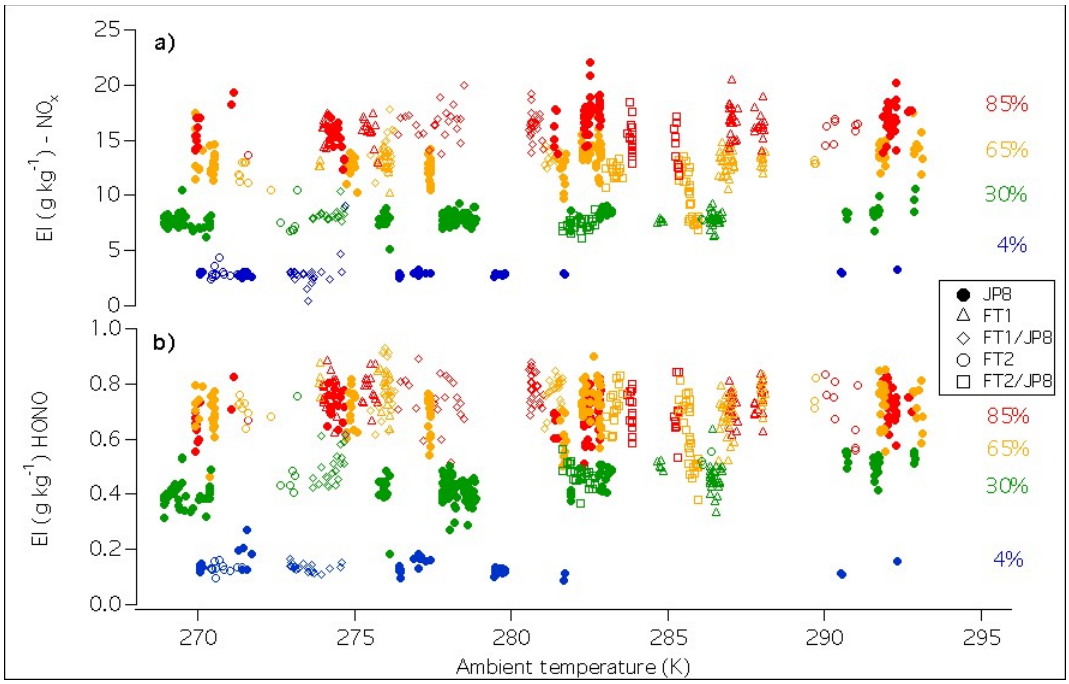

Figure 5. Emission indices of individual plumes for NO_x (a) and HONO (b) parsed by rated engine thrust (color: blue = 4%, green = 30%, orange = 65%, red = 85%) and fuel type (symbols), plotted against ambient temperature.

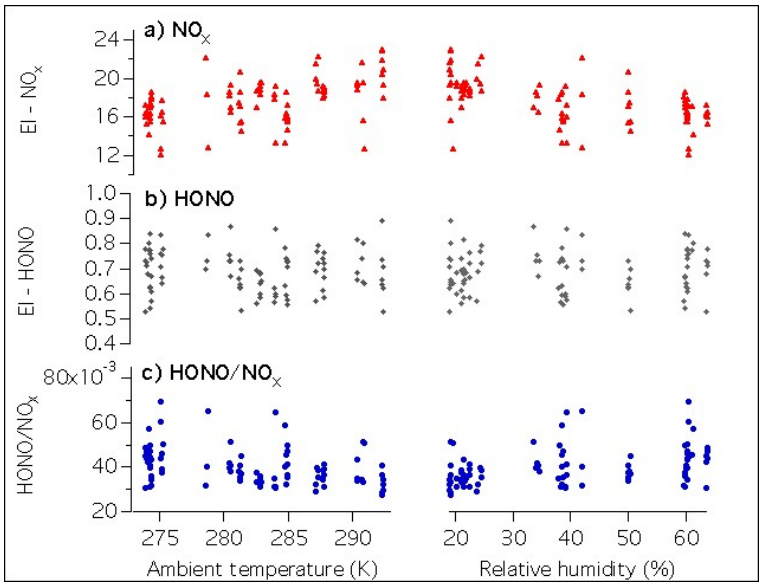

Figure 6. Emission indices of individual plumes for all of AAFEX sampled at 100% rated engine thrust for NO_x (a), HONO (b) and HONO to NO_x ratio (c).

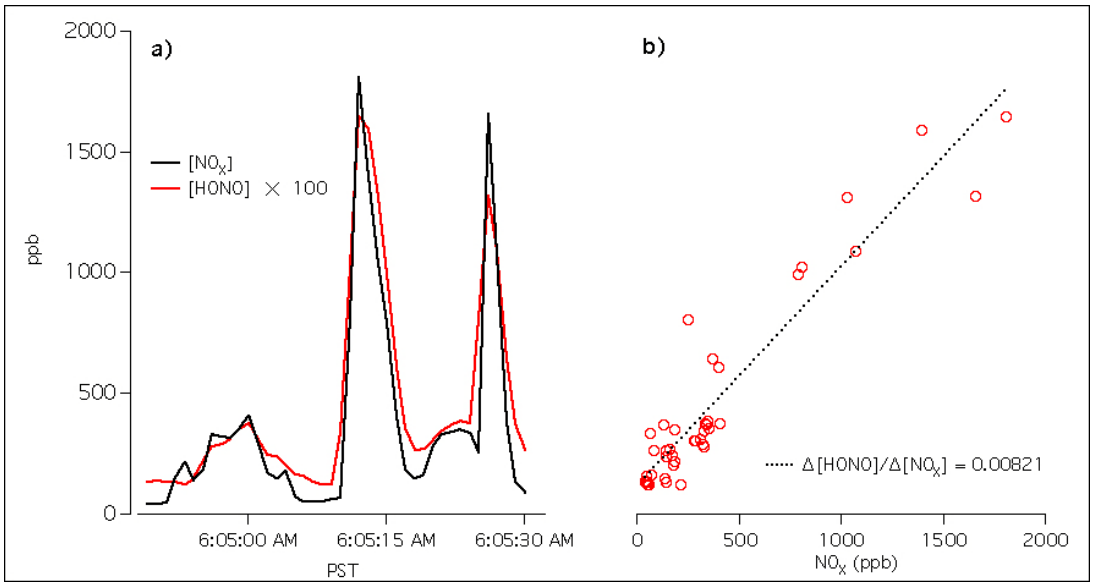

Figure 7. A time-series of HONO and NO_x measured a) from a diesel-powered generator during AAFEX. Scatter plot b) between HONO and NO_x shows an emission ratio of 0.82%.

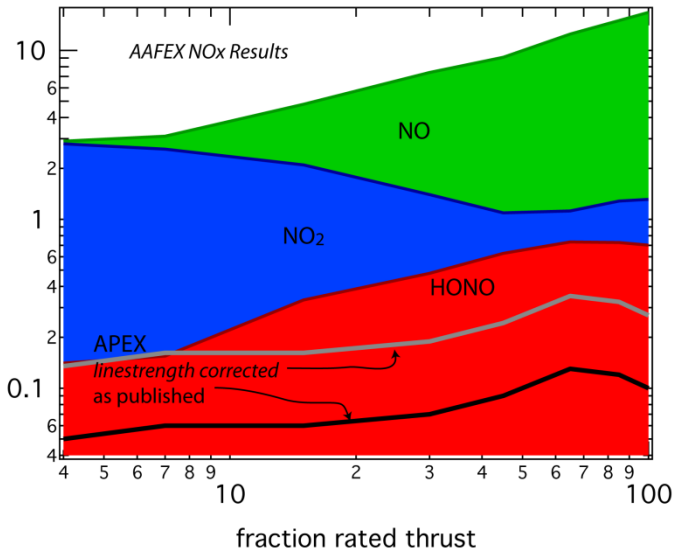

Figure 8. Observed emission indices of HONO observed at the Aircraft Particle Experiment 3 (black), corrected for linestrength (grey), overlaid on top of observations from AAFEX (red). Emission indices for NO_2 (blue) and NO (green) from APEX3 are added on top of that of HONO.

References

1. Forster, P.; Ramaswamy, V.; Artaxo, P.; Berntsen, T.; Betts, R.; Fahey, D. W.; Haywood, J.; Lean, J.; Lowe, D. C.; Myhre, G.; Ngana, J.; Prinn, R.; Raga, G.; Schulz, M.; Van Dorland, R., Changes in atmospheric constituents and in radiative forcing. Fourth Assessment Report of Working Group I of the Inter-governmental Panel on Climate Change. In: Climate Change. In Cambridge Univsersity Press, UK: 2007.
2. Lee, D. S.; Fahey, D. W.; Forster, P. M.; Newton, P. J.; Wit, R. C. N.; Lim, L. L.; Owen, B.; Sausen, R., Aviation and global climate change in the 21st century. *Atmospheric Environment* **2009,** *43*, (22-23), 3520-3537.
3. Dameris, M.; Grewe, V.; Kohler, I.; Sausen, R.; Bruhl, C.; Grooss, J. U.; Steil, B., Impact of aircraft NOx emissions on tropospheric and stratospheric ozone. Part II: 3-D model results. *Atmospheric Environment* **1998,** *32*, (18), 3185-3199.
4. Grewe, V.; Dameris, M.; Hein, R.; Kohler, I.; Sausen, R., Impact of future subsonic aircraft NOx emissions on the atmospheric composition. *Geophysical Research Letters* **1999,** *26*, (1), 47-50.
5. Kohler, I.; Sausen, R.; Reinberger, R., Contributions of aircraft emissions to the atmospheric NOx content. *Atmospheric Environment* **1997,** *31*, (12), 1801-1818.
6. Zahniser, M. S.; Nelson, D. D.; McManus, B.; Herndon, S. C.; Wood, E. C.; Shorter, J.; Lee, B. H.; Santoni, G. W.; Jimenez, R.; Daube, B. C.; Park, S.; Kort, E. A.; Wofsy, S. C., Infrared QC laser applications to field measurements of atmospheric trace gas sources and sinks in environmental research: enhanced capabilities using continuous wave QCLs. *Proceedings of SPIE* **2009,** *7222, 72220H*.
7. Horii, C. V.; Zahniser, M. S.; Nelson, D. D.; McManus, B.; Wofsy, S. C., Nitric Acid and Nitrogen Dioxide Flux Measurements: a new Application of Tunable Diode Laser Absorption Spectroscopy. *Proceedings of SPIE* **1999,** *3758*, 152-161.
8. McManus, J. B., Paraxial matrix description of astigmatic and cylindrical mirror resonators with twisted axes for laser spectroscopy. *Applied Optics* **2007,** *46*, (4), 472-482.
9. Herndon, S. C.; Zahniser, M. S.; Nelson, D. D.; Shorter, J.; McManus, J. B.; Jimenez, R.; Warneke, C.; de Gouw, J. A., Airborne measurements of HCHO and HCOOH during the New England Air Quality Study 2004 using a pulsed quantum cascade laser spectrometer. *Journal of Geophysical Research-Atmospheres* **2007,** *112*, (D10), -.
10. Febo, A.; Perrino, C.; Gherardi, M.; Sparapani, R., Evaluation of a High-Purity and High-Stability Continuous Generation System for Nitrous-Acid. *Environmental Science & Technology* **1995,** *29*, (9), 2390-2395.
11. Becker, K. H.; Kleffmann, J.; Kurtenbach, R.; Wiesen, P., Solubility of nitrous acid (HONO) in sulfuric acid solutions. *Journal of Physical Chemistry* **1996,** *100*, (36), 14984-14990.
12. OSullivan, D. W.; Lee, M. Y.; Noone, B. C.; Heikes, B. G., Henry's law constant determinations for hydrogen peroxide, methyl hydroperoxide, hydroxymethyl hydroperoxide, ethyl hydroperoxide, and peroxyacetic acid. *Journal of Physical Chemistry* **1996,** *100*, (8), 3241-3247.
13. Rothman, L. S.; Jacquemart, D.; Barbe, A.; Benner, D. C.; Birk, M.; Brown, L. R.; Carleer, M. R.; Chackerian, C.; Chance, K.; Coudert, L. H.; Dana, V.; Devi, V. M.;

Flaud, J. M.; Gamache, R. R.; Goldman, A.; Hartmann, J. M.; Jucks, K. W.; Maki, A. G.; Mandin, J. Y.; Massie, S. T.; Orphal, J.; Perrin, A.; Rinsland, C. P.; Smith, M. A. H.; Tennyson, J.; Tolchenov, R. N.; Toth, R. A.; Vander Auwera, J.; Varanasi, P.; Wagner, G., The HITRAN 2004 molecular spectroscopic database. *Journal of Quantitative Spectroscopy & Radiative Transfer* **2005,** *96*, (2), 139-204.
14. Herndon, S. C.; Shorter, J. H.; Zahniser, M. S.; Nelson, D. D.; Jayne, J.; Brown, R. C.; Miake-Lye, R. C.; Waitz, I.; Silva, P.; Lanni, T.; Demerjian, K.; Kolb, C. E., NO and NO2 emission ratios measured from in-use commercial aircraft during taxi and takeoff. *Environmental Science & Technology* **2004,** *38*, (22), 6078-6084.
15. Tremmel, H. G.; Schlager, H.; Konopka, P.; Schulte, P.; Arnold, F.; Klemm, M.; Droste-Franke, B., Observations and model calculations of jet aircraft exhaust products at cruise altitude and inferred initial OH emissions. *Journal of Geophysical Research-Atmospheres* **1998,** *103*, (D9), 10803-10816.
16. Kurtenbach, R.; Becker, K. H.; Gomes, J. A. G.; Kleffmann, J.; Lorzer, J. C.; Spittler, M.; Wiesen, P.; Ackermann, R.; Geyer, A.; Platt, U., Investigations of emissions and heterogeneous formation of HONO in a road traffic tunnel. *Atmospheric Environment* **2001,** *35*, (20), 3385-3394.
17. Kirchstetter, T. W.; Harley, R. A.; Littlejohn, D., Measurement of nitrous acid in motor vehicle exhaust. *Environmental Science & Technology* **1996,** *30*, (9), 2843-2849.
18. Anderson, B. E.; Branham, H.-S.; Hudgins, C.; Plant, J.; Ballenthin, J.; Miller, T. M.; Viggiano, A.; Blake, D. R.; Boudries, H.; Canagaratna, M. R.; Miake-Lye, R.; Onasch, T.; Wormhoudt, J.; Worsnop, D. R.; Brunke, K. E.; Culler, S.; Penko, P.; Sanders, T.; Han, H.-S.; Lee, P.; Pui, D. Y. H.; Thornhill, K. L.; Winstead, E. H., Experiment to Characterize Aircraft Volatile Aerosol and Trace-Species Emissions (EXCAVATE). In NASA: Aug. 2005; Vol. TM-2005-213783.
19. Anderson, B. E.; Winstead, E. H.; Hudgins, C.; Plant, J.; Branham, H.-S.; Thornhill, L.; Boudries, H.; Canagaratna, M. R.; Miake-Lye, R.; Wormhoudt, J.; Worsnop, D. R.; Miller, T.; Ballenthin, J.; Hunton, D.; Viggiano, A.; Pui, D.; Han, H.-S.; Blake, D.; McEchern, M. *Overview of Results from the NASA Experiment to Characterize Aircraft Volatile Aerosol and Trace Species Emissions (EXCAVATE)*; European Commission: Luxembourg, Germany, 2004; pp 27-36.
20. Boudries, H.; Wormhoudt, J.; Worsnop, D. R.; Canagaratna, M. R.; Onasch, T.; Miake-Lye, R.; Anderson, B. E. *Aerosol and Gas Chemistry of Commericial Aircraft Emissions Measured in the NASA EXCAVATE Program*; European Commission: Luxembourg, Germany, 2004; pp 85-90.
21. Brundish, K. D.; Clague, A. R.; Wilson, C. W.; Miake-Lye, R. C.; Brown, R. C.; Wormhoudt, J.; Lukachko, S. P.; Chobot, A. T.; Yam, C. K.; Waitz, I. A.; Hagen, D. E.; Schmid, O.; Whitefield, P. D., Evolution of Carbonaceous aerosol and aerosol precursor emissions through a jet engine. *Journal of Propulsion and Power* **2007,** *23*, (5), 959-970.
22. Whitefield, P. D.; Hagen, D. E.; Wormhoudt, J. C.; Miake-Lye, R. C.; Wilson, C. W.; Brundish, K. D.; Waitz, I.; Lukachko, S. P.; Yam, C. K., NASA/QinetiQ Collaborative Program: Final Report. In NASA: Sept. 2002; Vol. CR2002-211900.
23. Wood, E. C.; Herndon, S. C.; Timko, M. T.; Yelvington, P. E.; Miake-Lye, R. C., Speciation and chemical evolution of nitrogen oxides in aircraft exhaust near airports. *Environmental Science & Technology* **2008,** *42*, (6), 1884-1891.

24. Wormhoudt, J.; Herndon, S. C.; Yelvington, P. E.; Miake-Lye, R. C.; Wey, C., Nitrogen oxide (NO/NO2/HONO) emissions measurements in aircraft exhausts. *Journal of Propulsion and Power* **2007,** *23*, (5), 906-911.
25. Lukachko, S. P.; Waitz, I. A.; Miake-Lye, R. C.; Brown, R. C., Engine design and operational impacts on particulate matter precursor emissions. *Journal of Engineering for Gas Turbines and Power-Transactions of the Asme* **2008,** *130*, (2), -.
26. Arnold, F.; Scheid, J.; Stilp, T.; Schlager, H.; Reinhardt, M. E., Measurements of Jet Aircraft Emissions at Cruise Altitude-I - the Odd-Nitrogen Gases No, No2, Hno2 and Hno3. *Geophysical Research Letters* **1992,** *19*, (24), 2421-2424.
27. Hanisco, T. F.; Wennberg, P. O.; Cohen, R. C.; Anderson, J. G.; Fahey, D. W.; Keim, E. R.; Gao, R. S.; Wamsley, R. C.; Donnelly, S. G.; DelNegro, L. A.; Salawitch, R. J.; Kelly, K. K.; Proffitt, M. H., The role of HOx in super- and subsonic aircraft exhaust plumes. *Geophysical Research Letters* **1997,** *24*, (1), 65-68

APPENDIX E: Aircraft Emissions of Methane and Nitrous Oxide during theAlternative Aviation Fuel Experiment

Gregory W. Santoni[1], Ben H. Lee[1], Ezra C. Wood[2], Scott C. Herndon[2], Richard C. Miake-Lye[2], Steven C. Wofsy[1], J. Barry McManus[2], David D. Nelson[2], Mark S. Zahniser[2]

[1] Harvard University, School of Engineering and Applied Sciences and Department of Earth and Planetary Sciences, Cambridge, Ma
[2] Aerodyne Research, Inc., Center for Aero-Thermodynamics and the Center for Atmospheric and Environmental Chemistry, Billerica, Ma

Abstract

The radiative forcing of non-CO_2 greenhouse gases, primarily methane (CH_4) and nitrous oxide (N_2O) but also including trace quantities of other halocarbons, together represent roughly 60% of the total forcing due to carbon dioxide (CO_2) alone. Given the concerns over anthropogenic impacts on climate change and the predicted growth of the aviation industry, quantifying methane and nitrous oxide emission factors from aircraft is important for assessing future impacts of aviation on the Earth's radiative balance. The contribution of methane to total organic compound emissions is also of interest, as mass conservation during combustion requires carbon balance. Given recent developments of new alternative aviation fuels, comparing emission factors and speciation of total organic compounds in aircraft exhaust is necessary to benchmark these new fuels and their potentially distinct emissions characteristics against traditional kerosene-based fuel. Fuel-based emission indices for CH_4 and N_2O were quantified from the CFM56-2C1 engines aboard the NASA DC-8 aircraft during the Alternative Aviation Fuel EXperiment (AAFEX), conducted in early 2009. The measurements of JP-8 fuel combustion indicate that at low thrust engine states (idle and taxi, or 4% and 7% maximum thrusts) the engines emit both CH_4 and N_2O at a rate of 168 ± 155 $mg\ CH_4\ (kgFuel)^{-1}$ and 114 ± 47 $mg\ N_2O\ (kgFuel)^{-1}$, respectively. At thrust levels higher than idle and taxi, the modes corresponding to greater fuel flow rates and higher engine combustion temperatures, methane concentrations in engine exhaust were lower than ambient concentrations. Average emission indices for JP-8 fuel combusted with engine thrusts greater than 30% of maximum were -53.8 ± 33.2 $mg\ CH_4\ (kgFuel)^{-1}$ and 32.2 ± 17.5 $mg\ N_2O\ (kgFuel)^{-1}$, where the negative sign for methane indicates consumption of atmospheric methane in the engine. Emission indices for the alternative aviation fuels, including two synthetic Fischer-Tropsch fuels with varying sulfur content, were statistically indistinguishable from those for JP-8.

Introduction

Methane is a radiatively active gas in Earth's emission spectrum, roughly 25 times more effective on a per-molecule level than CO_2 in terms of its integrated greenhouse effect at hundred-year timescales (Lelieveld et al. 1998). Nitrous oxide has an even larger per-molecule global warming potential, roughly 300 times higher than CO_2 on these timescales. This is partly because its atmospheric lifetime is ~120-years, compared to the

~9-year methane lifetime (Denman et al. 2007). The concentration of these two species in the atmosphere is determined primarily by a balance between surface sources and atmospheric losses. The atmospheric destruction of methane is dominated by reaction with the hydroxyl radical (Quay et al. 1999) while loss of atmospheric nitrous oxide mostly proceeds via stratospheric photodissociation (Prather 1998). Since 1750, when atmospheric methane concentrations hovered around 700 nmol /mol , anthropogenic activities have increased methane abundances to 1850 nmol /mol (Denman et al. 2007). Methane growth rates leveled off in the mid-1980s and early part of the 21st century (Lassey et al. 2007), but recent studies have shown renewed growth (Lelieveld 2006; Rigby et al. 2008). In that same time period, the atmospheric abundance of nitrous oxide has increase from 270 nmol /mol to its present value of 320 nmol /mol (Fluckiger et al. 1999).

Quantifying the impact of the airline industry on climate change must include accurate accounts of CH_4, N_2O, and CO_2, given their radiative importance and long atmospheric lifetimes. Many studies have quantified the emission of CO_2 in aircraft engines (Brasseur et al. 1998), but fewer have examined methane and nitrous oxide emissions. Direct aircraft emissions of these species have the potential to affect global budgets. Nitrogen oxide emissions also indirectly decrease the lifetime of methane in the atmosphere via chemical feedbacks involving ozone and the hydroxyl radical (OH) (Denman et al. 2007). A competing effect exists with carbon monoxide emissions, as feedbacks with CO and OH can increase methane's atmospheric lifetime (Prather 1996). Aircraft emissions are also noteworthy in that they affect chemical composition at altitude. This is readily apparent in cloud contrails, but is also of interest given atmospheric dynamics and known loss mechanisms.

Previous studies have highlighted the large variability of methane concentrations seen at the exit of engines operating at different conditions. Spicer et al. (1992, 1994) were among the first to give detailed aircraft exhaust emission concentrations for a variety of organic species in military and commercial aircraft engines. Wiesen et al. (1994) examined methane and nitrous oxide emissions from different commercial jet engines using different fuels during the AERONOx campaign. The finding emphasized in these studies was the consumption of atmospheric methane at high engine thrust conditions, the production of methane at low-power conditions, and the production of N_2O irrespective of engine mode. The findings suggested that aircraft emissions had negligible impacts on the global CH_4 budget. They also found that N_2O emissions were smaller than those of lower-temperature combustion power plants (Laird and Sloan 1993) and concluded that aircraft emissions of N_2O also had a negligible impact on the global N_2O budget.

Methane emissions at idle and taxi conditions, however, varied by 500%. The general trend was that methane was produced at these modes, but estimates varied based on engines and fuels consumed. Spicer et al. (1994) showed enhancements of upwards of 9 µmol /mol in undiluted exhaust, roughly five times ambient concentrations, whereas Spicer et al. (1992) measured methane concentrations of 1.8 µmol /mol in the exhaust, most of which was presumably from the ambient air flushed through the turbine engines. Currently, the ambient concentration of methane is approximately 1.8 µmol /mol, though

it was closer to 1.7 µmol /mol in 1992 (Dlugokencky et al. 1998).

While there has been a consensus on the overall trends, a more complete quantitative assessment of methane emission factors as a function of engine thrust has remained poorly constrained. AAFEX provided a means to quantify non-CO_2 greenhouse gases emission data, in addition to other gaseous and particulate pollutants, for a variety of fuels, engine operating powers, and ambient conditions. Analysis of the AAFEX dataset is intended to guide the aviation industry in addressing the most important emission issues associated with alternative fuels.

Isotopic information is potentially useful in answering questions about methane consumption and production in the aircraft. Methane sources can be categorized as bacterial, biomass burning, or thermogenic (Quay et al. 1999). Each of these sources has a characteristic isotopic composition that differs from the isotopic composition of ambient methane: $\delta^{13}C_{CH4}$ = -47.5 ‰ relative to vienna pee dee belemnite (VPDB). Bacterial methanogenesis is dominated by two pathways: methylated substrate methanogenesis and CO_2 reduction. Carbon reduction by hydrogen fractionates according to its kinetic isotope effect (KIE) that discriminates against ^{13}C leading to $\delta^{13}C_{CH4}$ as low as -110 ‰ (Whiticar 1999). Fermentation of methylated substrates has a lower KIE fractionation depending on the substrate, leading to $\delta^{13}C_{CH4}$ on the order of -50 ‰ -60 ‰. The $\delta^{13}C_{CH4}$ observed in samples is very much dependent on the $\delta^{13}C$ of the methylated substrate and CO_2 precursors, which are in turn dependent on the cumulative fractionation associated with prior reactions. Thermogenic sources, primarily associated with fossil carbon combustion, are more enriched in ^{13}C and have isotopic compositions around -20 ‰ to -30 ‰.

Advances in laser and detector technology have allowed for greater sensitivity in high-resolution absorption spectroscopy (Nelsonet al. 2008; Tuzsonet al. 2008). Zahniseret al. (2009) provide a description of the spectrometer used at AAFEX to measure $^{12}CH_4$ and $^{13}CH_4$ at two distinct spectral lines with precisions of 0.6 nmol/mol and 6 nmol/mol, respectively. A similar instrument operating at a different spectral region was used to measure N_2O and HONO, with precisions of 0.3 nmol/mol and 0.15 nmol/mol, respectively. With a high duty cycle due to continuous wave operation and a relatively small sampling cell volume operated at low pressure, these instruments provided high frequency measurements of methane, nitrous oxide, and the isotopic composition of that methane.

Methods

AAFEX was a comprehensive test of the effects of synthetic Fischer-Tropsch (FT) fuels on the trace gas and particle emissions of gas turbine engines. The tests were performed in Palmdale, California on the same CFM56-2C1 engine studied during APEX-1(Wey et al. 2006). AAFEX included three chemically distinct fuels: JP-8, a Fischer-Tropsch (FT-1) fuel derived from a natural gas feedstock and synthesized by Shell, and a second Fischer-Tropsch (FT-2) fuel derived from a gasified coal feedstock and synthesized by Sasol. The JP-8 fuel contained 1200 ppm sulfur, while the sulfur contents of the two Fischer-Tropsch fuels were 20 ppm (Sasol) and less than 17 ppm (Shell). In addition to

the pure fuels, 50/50 (by volume) blends of the fuels were tested. During all tests, engines 2 and 3 (the two engines closest to the fuselage) were active and were sampled at 1 m and 30 m probes. Engine 2 (inboard left engine) served as a reference as it burned JP-8 for the entire test duration while engine 3 (inboard right engine) burned either JP-8 or the synthetic fuel depending on the test day. Advected plumes of emissions were sampled downwind of the plane at the 150 m probe. Figure 1 shows the layout of the sampling trucks, trailers and inlets relative to the aircraft. The daily AAFEX test activities are summarized in Table 1.

The majority of instrumentation at AAFEX was located on the starboard side of the plane. In Figure 1, the top left insert shows the NASA DC-8 which was chocked on the runway. The downwind trailers housed instrumentation to measure CH_4, CO_2, O_3, NO_x, HONO, N_2O, and particulates, and were positioned 150 m away from the engine output in the direction of the predominant wind. This positioning was critical to measure advected plumes of engine exhaust at low-power conditions when exit velocities of engine emissions did not have sufficient momentum to reach the downwind trailer inlets. The lower-left insert of the figure shows the inlet in relation to the aircraft and lower-right insert shows the configuration of the particulate and gas phase inlets mounted to a 1-meter tripod. The inlet was designed to eliminate the need of a filter which is critical for the HONO measurement, but it also eliminated potential contamination of the CH_4 and N_2O measurements. These precisions for the $^{12}CH_4$ and $^{13}CH_4$ measurements were 50% worse than lab performance because of alignment instabilities from the lack of trailer conditioning and the requirement of keeping the trailer closed during aircraft engine operation. Simultaneous measurements of CO_2 were made using a commercially available Licor LI-6262 infrared gas analyzer. By making highly time-resolved measurements of methane and CO_2, the concentrations of each are quantified in both the exhaust plume and in the background air unaffected by the exhaust. This measurement technique was particularly important during early morning measurements before atmospheric convection fully mixed the planetary boundary layer. Strong methane sources nearby resulted in ambient mixing ratios on the order of 2.5 µmol /mol during night-time inversions, as measured overnight during the AAFEX day off (tTable 1).

Results

Figure 2a shows time series data from January 26, 2009 showing the different correlations between carbon dioxide, methane, and nitrous oxide concentrations. During idle conditions, CH_4 plumes of 30 nmol /mol correspond to 70 µmol /mol CO_2 plumes. At 30% thrust conditions, this relation changes noticeably, with larger 200 µmol /mol CO_2 plumes corresponding to methane depletions of 20 nmol /mol . Fuel-based emission ratios in units of nmol /mol CH_4 per µmol /mol CO_2 can be calculated by regressing CH_4 against CO_2 in individual plumes, as shown in Figure 2b. Fuel-based emission indices can be calculated according to Herndon et al. (2004):

$$EI_{CH_4} = \left(\frac{3160\ g\ CO_2}{kg\ Fuel}\right) \cdot \frac{16\ g\ CH_4}{44\ g\ CO_2} \cdot \frac{\Delta CH_4}{\Delta CO_2} \qquad (1)$$

The factor of 3160 g CO_2 (kgF uel) $^{-1}$ represents the stoichiometric calculation of CO_2 produced per kilogram of JP-8 fuel consumed assuming complete combustion given a

particular hydrogen to carbon ratio. This ratio is 13.7% hydrogen by weight for JP-8 (Vay et al. 1998; Brasseur et al. 1998). Corresponding fuel analyses were carried out for FT-1 and FT-2 fuels, resulting in CO_2 emissions ratios of 3090 and 3110 g CO_2 (kgF uel)$^{-1}$, respectively. An identical calculation is carried out for nitrous oxide by substituting N_2O in the place of methane and accounting for the molecular mass differences. These emission indices of methane and nitrous oxide were calculated for 1480 plumes at various engine thrust modes, of which only the plumes with a variance on the regression smaller than 0.2 were used (n= 1103) in subsequent analysis.

Figure 3 shows the individual plume distributions of emission indices binned by fuel type for each of engine power conditions along with ambient temperature values for each plume. It is immediately apparent that the number of plumes observed at low-power conditions is much fewer than those at higher engine thrusts. This is not surprising for two reasons: a) advection of the plumes of engine exhaust was facilitated by the wind velocities generated at higher thrusts, and b) the prevailing winds were not favorable on all but the first day of AAFEX when only JP-8 fuel was measured. Figure 3 also illustrates the broader distributions observed at idle and taxi conditions in comparison with those at higher engine thrusts. Figure 4 shows box and whisker plots for methane and nitrous oxide emission indices as well as undiluted carbon dioxide concentrations observed at the engine exhaust plane (EEP) (Yelvington et al. 2007). Two sample T-tests were performed between each fuel (JP-8 vs FT-1, JP-8 vs FT-2, and FT1 vs FT2) at each of the 7 engine thrust conditions. Of the 21 population comparisons for methane, 5 were significant at the p=0.05 level, but the mean p-value was 0.30. For nitrous oxide, 10 of the 21 tests had p-values below .05, but the mean p-value was 0.15.

An explanation of the greater range of emission indices at idle and taxi conditions is further illustrated with subsamples of aircraft exhaust taken during each test flight and analyzed with the same instrumentation while the aircraft engines were off. Aircraft exhaust from the 1 m probe was flushed into 2-L steel canisters during each test flight and then diluted down with ultra-high purity helium. These subsamples were then overblown across the inlet of the spectrometers to validate the emission ratios calculated from the advected plume data. Figure 4 shows the emission indices calculated from these subsamples. Only cans where the carbon dioxide and methane values reached a steady value were used, as these represented the mixing ratios of those compounds in the can. Corrections were made for the dilution by multiplying the methane values with the ratio of CO_2 values observed at the EEP to the concentrations measured while overblowing the inlet. Emission indices could then be calculated for these subsamples by dividing the corrected methane exhaust values by the CO_2 EEP values from Figure 4. The corresponding emission indices are shown in Figure 5 for the 11 canisters collected in this way. We focused the measurements on idle conditions and high-power conditions because these were where previous studies have dissagreed. Canisters 1 and 2 were both sampled from the same inlet at 7% engine thrusts, the first being sampled while the engine was starting from a cold state, and the latter was sampled after the engine had operated for 40 minutes at higher thrusts. The engine history, therefore, has an important effect on methane emission indices, and this in part explains the variability seen in advected plume derived emission indices, similar to other hydrocarbon emissions. Figure

4 also includes the 1-m subsample data superimposed on the range of advected plume data observed. Canisters 2 and 3 are outside the range of this plot, however. Additionally, the emission indices at 100% thrust calculated from subsamples could never be less than zero, as the subsamples at 100% thrust contain no methane, and the methane measured in those samples from the QCLS is within the detection limit of methane. The plume EIs are negative only because the engine is consuming atmospheric methane, and in the absence of atmospheric methane, these EIs would also be zero.

Figure 6 shows emission rates for N_2O and CH_4 at percentage maximum thrusts that correspond to the main operational modes - idle, approach, climb-out, cruise, and take-off. The measured, fuel-based emission indices (g N_2O (kgFuel)$^{-1}$) have been converted to an absolute emission rate (gN_2Ohr^{-1}) using the fuel flow rates noted from the cockpit during the test. The analysis for JP-8 fuel is representative of the Jet-A fuels currently used throughout the world. Emission rates for FT-1 and FT-2, which are also shown in Figure 6 were indistinguishable from those for JP-8 fuel, though we note that N_2O emission indices for FT-1 are consistently higher than JP-8 while those of FT-2 are lower. No apparent trend is present in the methane emission data. Since the aircraft test was conducted on the ground, the cruise mode measurement may not be completely representative of in-flight emissions because of the reduced pressure and temperature at cruising altitude.

The total amount of methane emitted or consumed during a hypothetical landing take-off cycle or an entire flight can be calculated by multiplying the above emission rates by the time-in-mode for each segment of a flight. Table 2 shows this calculation using the time-in-modes for a standard International Civil Aviation Organization (ICAO) landing take-off cycle and one hour of cruise. These times, and their corresponding thrusts, are subject to significant variability that can affect the results for an actual landing take-off cycle. The results indicate that there are net methane emissions during this hypothetical flight, but that even just 1-hour of cruise conditions (65% thrust) leads to far more atmospheric methane destruction. Accounting for the variability of the inputs to these calculations (e.g., ICAO idle vs. ground idle, time spent in cruise, etc), it is evident that the aircraft operations have a net negative direct impact on atmospheric methane concentrations. A more accurate calculation would require methane emission indices measured from aircraft at actual cruise altitude rather than at the surface as measured during AAFEX. Even for a relatively short flight, however, consumption at cruise is much larger than production at idle.

Conclusions about the isotopic composition of methane produced in jet-engines are difficult because of the range of observed methane values typically seen 150 m downwind of the source. Taking the isotopic composition of JP-8 fuel to be -40% and assuming no fractionation during methane production means resolving a 7% shift over a range from 0 to 1/1800 nmol /mol on an inverse scale, as is typically used with Keeling plots (Pataki et al. 2003). This corresponds to resolving a 0.115% shift over a 30 nmol/mol range in advected plumes which are typically observed on the order of seconds. With in-field 1-sec instrument precision of 3%, isotopic interpretations are difficult to make because of the sampling. Fewer diluted plumes sampled closer to the aircraft engine

combined with better temperature control would have allowed for better measurements of the $^{13}CH_4$ absorption line. Similarly, isotopic analysis of the subsamples taken at the 1-m probe and diluted with He were impossible because a) subsamples taken at high engine powers had no methane in them and b) subsamples taken at low engine powers were diluted by a factor of ~70 such that the mixing ratios present in the subsamples were all below 500 nmol /mol, well outside of the dynamic range of calibrated $^{13}CH_4$ concentrations for this instrument.

Future aircraft measurements of the isotopic composition of methane emitted in aircraft exhaust could help answer several questions about the chemistry occurring in the engine, potentially distinguishing methane produced in the engine from background atmospheric methane. A closer probe sampling location to ensure a larger range of observed methane mixing ratios would be necessary. The mean engine exhaust plane methane concentration at idle and taxi conditions was 8.3 µmol /mol, calculated from dilution corrections of the CH_4 emission ratios using the EEP CO_2 distributions in Figure 4.

Discussion

A discussion of this work in context of previous studies is helpful. Wiesen et al. (1994) and Heland and Schafer (1998) are the only studies to our knowledge to present nitrous oxide emissions data, while methane emission data has been characterized by a total of 7 studies to date. The results of past studies and the present AAFEX work are summarized in Tables 3 and 4. Mean engine exhaust concentrations of methane and nitrous oxides determined in these studies are shown in Figure 5. These different methods of presenting emissions observations can be compared by normalizing the concentrations with CO_2 data according to Equation 1.

Nitrous oxide aircraft emissions data is limited. Wiesen et al. (1994) presented a mean nitrous oxide emission index of 0.11 g N_2O (kg fuel)$^{-1}$ ± 0.0098 across all thrust settings. This was not corrected for ambient nitrous oxide concentrations, which, if accounted for, would decrease the average emission index by ~30\% to a value closer to .077 g N_2O (kg fuel)$^{-1}$, still slightly higher than the value of 0.064 g N_2O (kg fuel)$^{-1}$ ± 0.0035 in the present study. The trend of increasing nitrous oxide emissions with increasing thrust appeared to be reversed at AAFEX. Beyond the obvious differences attributed to the fuel and engines used, nitrogen oxides (NO_x) can convert to N_2O in these engine plumes, especially in the presence of acid aerosols (Wiesen et al. 1994). This might affect advected plume data but the present agreement with Wiesen et al. (1994), which measured nitrous oxide offline from exhaust filled cylinders, suggests that these effects are small. NO_x data was not presented in the Wiesen et al. (1994) study, so it is impossible to compare those effects. Such a mechanism could explain the differences in emission indices at lower thrusts seen at AAFEX, as these plumes had longer lifetimes than those sampled at higher powers, when advection was aided by larger engine exit velocities.

Heland and Schafer (1998) were the only other study to present data on nitrous oxide emissions of aircraft exhaust. They measured using an passive FTIR spectrometer that relies heavily on good spectroscopic parameters for the various absorbers present,

calibration of blackbody emission spectra, and good background spectra to normalize out the absorption due to molecules present in the instrument aperture but not in the plume. They reported an emission index for higher-thrust levels of 1.3 g N_2O (kg fuel)$^{-1}$ a full order of magnitude greater than those of Wiesen et al. (1994) and this study, but also state that nitrous oxide mixing ratios were below the detection limit at idle power conditions. The engine probed in this study is the same as that of AAFEX, and therefore the large discrepancy between the emission ratios reported, as well as the lack of data at idle conditions when nitrous oxide emissions have been shown not significantly different from other power conditions, call into question the instrument precisions of nitrous oxide possible with a passive spectrometer.

Other studies mention nitrous oxide aircraft emissions but do not report data. Vay et al. (1998) measured contrail plumes behind a T-39 and a B-757 aircraft but did not report the nitrous oxide data. They claim that N_2O was found not to be an important exhaust constituent. Zheng et al. (1994) examined 20 plumes of NO_y, 5 of which correlated to CO_2 spikes seen during the Airbone Arctic Stratospheric Expedition. Of those five plumes, they found no significant increases for either nitrous oxide or methane.

Nitrous oxide emission indices during AAFEX most closely resemble those measured by Wiesen et al. (1994) despite being consistently lower at higher thrusts, and provide another constraint on the nitrous oxide budget. Scaling up the emission rate of nitrous oxide from the ~20 billion gallons of fuel consumed by the airline industry annually, results in a yearly N_2O flux of ~4 GgN_2Oyr^{-1} roughly .025 % of the total source term of 17.7 $TgNyr^{-1}$ (Denman et al. 2007).

Methane, in contrast to N_2O, is a net atmospheric sink term, consuming roughly 3.5 $GgCH_4yr^{-1}$, completely negligible in terms of the global source and sink terms, each on the order of 580 $TgCH_4yr^{-1}$ (Denmanetal.2007). Spicer et al. (1992) were among the first to report detailed organic species as well as CO, CO2, and nitrogen oxides for aircraft engine emissions. The 1992 paper published data using JP-4 fuel in F-101 and F-110 engines used primarily on the B1-B and F-16 airplanes, respectively. The 1994 paper focused on engines used in more commercial transport aircraft such as the Boeing 737, the CFM-56 and TF-39. Interestingly, the core engine of the CFM-56 is the same as that of the F101 engine used in the 1992 study, but it seemingly produced very different methane emissions, particularly at idle. This could be explained by the differences in methane emissions observed between idle conditions on a recently started engine, versus those from an engine in the same idle power condition after having run at high-power conditions.

Wiesen et al. (1994) report positive emission indices at all powers but also present exhaust concentrations. Their emission indices are positive at high thrusts only because CH_4 is present in the air used in the aircraft engines. Background atmospheric concentrations of species must be used when determining emission ratios. This was not possible given their extractive sampling technique, but their emission indices are misleading because background air samples were never characterized. Only the exhaust concentrations are used in the study comparisons presented in Figure 7.

The NASA EXperiment to Characterize Aircraft Volatile Aerosol and Trace-species Emissions (EXCAVATE) sought to further expand the sparse data set of organic emissions from roughly 300 commercial aircraft engines in use. Anderson et al. (2006) measured methane to a 1-sec precision of 1 nmol /mol on the Rolls Royce RB211-535E4 engine using JP-5 fuel with two sulfur contents (810 and 1820 µmol /mol S) and reported methane emission concentrations as well as upper limits of emission indices. They chose not to report possibly negative emissions indices, as these represent consumption of methane, but present exhaust concentrations of methane that are similar to ambient values around 1.8 µmol /mol . Their emissions indices are dependent on the instrumental accuracy, which they report as 1% (as opposed to precision of .1%) meaning that nearly all of their reported exhaust methane concentrations are within 20 nmol /mol of ambient methane concentrations. In contrast with this direct exhaust canister sampling, the advected plume method employed in this study relies only on the instrument precision, as it is the relative changes in methane that determine emission indices, once normalized to CO_2 values. Our instrument precision is .027%. The emission indices during low power of JP-8 fuel during the AAFEX mission were higher by an order of magnitude than during the EXCAVATE mission,
most likely attributable to the different engine, fuel, ambient operating conditions, and engine history before sampling. EXCAVATE low-power findings most closely resemble those of Spicer (1992), while AAFEX low-power results are more similar to those of Spicer (1994).

One research question that persists in many of these studies is whether the findings were representative of actual flight conditions. Vay et al. (1998) sought to answer this during the SUCCESS (Subsonic Aircraft: Contrail and Cloud Effects Special Study) campaign by sampling CO, CH_4, N_2O, and H_2O from inlets aboard the NASA DC-8 (the same plane used as the emission source in AAFEX) flying behind a T-39 and B-757 aircraft. Both high and low sulfur content fuel (675 and 75 µmol /mol S) exhaust was sampled and the reported 1-sec precision of their methane analyzer was 1 nmol /mol . They reported that 81% of the plume crossings observed showed anticorrelation with the CO_2 data, showing that atmospheric methane was being consumed during in situ observations.

Their reported emission indices ranged from -1.6 to 1.2 g CH_4 /kg fuel, with the positive values attributed to transient engine conditions (i.e. changing from 65% to 85% maximum thrust). The range of values observed at AAFEX were much smaller in magnitude than the -1.6 value, though we note that only 12 plumes were quantified in Vay et al. (1998). Their findings further validate previous ground based methane exhaust emission studies. Furthermore, Wiesen et al. (1994) showed that methane depletion at high power was observed from aircraft both at a ground-level test facility and at a special altitude-simulation test cell. It is important to note that aviation NO_x emissions at altitude have a greater potential to impact global methane budgets than the levels of methane emissions quantified in these various studies, whether positive or negative (Denman et al. 2007).

The results from the Aircraft Particle Emissions eXperiment (APEX) reported positive

methane emission indices at higher engine power (Wey et al. 2006). Methane was measured with a multi-gas analyzer. Because of its relatively broad spectroscopic resolution, this instrument does not have the specificity to methane that other measurement techniques have, and may have been subject to interference from other species present in the exhaust. The data from APEX does not agree with that reported by Spicer et al. (1992), Spicer et al. (1994), Vay et al. (1998), Anderson et al. (2006), Wiesen et al. (1994), or the current results from AAFEX.

Spicer et al. (2009a) also present methane emission indices for both a C-130 aircraft and a F-15 aircraft. The corrigendum to the study (Spicer et al. 2009b) that noted an error in the algorithm used to calculate emissions factors decreased the methane emission factors by ~15% for the C-130 and changed the sign on the F-15 factors. Only the F-15 emission indices are presented in Figure 7 as the emission factors for the C-130 aircraft are so high that corresponding methane exhaust concentrations at all power settings would be on the order of 20-30 µmol /mol well beyond the range of the figure. Pure exhaust concentrations can be calculated by multiplying emissions ratios (Equation 1) by the difference between CO_2 values at the EEP and ambient values, and adding ambient concentrations to those values. We also note that their equation for determining emission factors effectively removes the CO_2 concentrations measured from the emission factor calculation by assuming that all of the fuel carbon is converted to either CO_2, CO or other hydrocarbons. Because the equation then depends on the emission factors of other chemical species, many of which have much lower measurement precisions, these values are not directly comparable to other methane emission indices, which may be an additional reason why the C-130 values are completely beyond the range of expected emission indices and exhaust concentrations.

Although low-power emissions of methane seem to vary by almost an order of magnitude, with the exception of Spicer et al. (2009b), these studies agree on the methane consumption at power conditions greater than idle and taxi, by far the predominate mode of engine operation. Data presented here further confirms methane emission results from previous aircraft exhaust studies, and highlights the lack of effects alternative fuels will have on these greenhouse gases. We observe methane depletion during engine operating states higher than 7% maximum thrust and conversely methane production at ground idle and taxi conditions when aircraft engines are less efficient at combusting fuel. Canisters taken from the 1 m inlets further suggest that, similar to other hydrocarbon emissions, methane production efficiency can vary based on the history of the engine, with a colder engine producing more methane than a warmer one at equal thrusts.

Conclusion

This AAFEX study, in context with previous methane and nitrous oxide exhaust studies, provides another robust constraint on long-lived, greenhouse-gas emissions of commercial aircraft engines in operation today. Furthermore, the quantification of methane emissions is important for understanding the speciation of organic emissions at low powers. Because engine certification for hydrocarbon emissions requires uses of Flame Ionization Detector which measures a wide variety of hydrocarbons without speciation detail, relating this certification hydrocarbon data to speciated measurements

must take into account the contribution of methane. Proper accounting of speciated hydrocarbons help inform the correct proportions of individual compounds that contribute the most risk to human health and welfare. The measurement precisions of both methane and nitrous oxide presented in this study are the best to date; more than two times better than previous studies. By considering a representative flight profile, the net contributions to global methane from aviation due to direct methane emissions are negative, indicating a net methane consumption. However, the role of NO_x emissions at altitude have a greater potential to affect the global methane budget than direct methane emissions, whether positive or negative, at the levels quantified in studies to date. Analysis of the different fuels used at AAFEX also shows that the global methane and nitrous oxide budgets will not be affected by an airline industry shift in fuel usage.

Acknowledgements
Parts of this reasearch are supported by the Department of Energy, Small Business Innovation Research Award DE-FG02-07ER84889, the PARTNER Center of Excellence (jointly sponsored by the FAA, NASA and Transport Canada) via Missouri University of Science and Technology, and the National Science Foundation Graduate Research Fellowship Program. The authors also greatly acknowledge W. Berk Knighton of Montana State University, Michael T. Timko and Zhenhong Yu of Aerodyne Research Inc., and Changlie Wey of ASRC Aerospace Corp.

References

Anderson, B., G. Chen, and D. Blake, 2006: Hydrocarbon emissions from a modern commercial airliner. Atmospheric Environment, 40, 3601–3612.

Brasseur, G. P., R. A. Cox, D. Hauglustaine, I. Isaksen, J. Lelieveld, D. H. Lister, R. Sausen, U. Schumann, A. Wahner, and P. Wiesen, 1998: European scientific assessment of the atmospheric effects of aircraft emissions. Atmospheric Environment, 32, 2329–2418.

Denman, K., G. Brasseur, A. Chidthaisong, P. Ciais, P. Cox, R. Dickinson, D. Hauglustaine, C. Heinze, E. Holland, D. Jacob, U. Lohmann, S. Ramachandran, P. da Silva Dias, S. Wofsy, and X. Zhang, 2007: Couplings Between Changes in the Climate System and Biogeochemistry. In: Climate Change 2007: The Physical Science Basis. Contribution of Working Group I to the Fourth Assessment Report of the Intergovernmental Panel on Climate Change. Cambridge University Press, Cambridge, United Kingdom and New York, NY, USA.

Dlugokencky, E. J., K. A. Masarie, P. M. Lang, and P. P. Tans, 1998: Continuing decline in the growth rate of the atmospheric methane burden. Nature, 393, 447–450.

Fluckiger, J., A. Dallenbach, T. Blunier, B. Stauffer, T. F. Stocker, D. Raynaud, and J. M. Barnola, 1999: Variations in atmospheric n2o concentration during abrupt climatic changes. Science, 285, 227–230.

Heland, J. and K. Schafer, 1998: Determination of major combustion products in aircraft

exhausts by ftir emission spectroscopy. Atmospheric Environment, 32, 3067–3072.

Herndon, S., J. Shorter, M. Zahniser, D. Nelson, J. Jayne, R. Brown, R. C. Miake-Lye, I. Waitz, P. Silva, T. Lanni, K. Demerjian, and C. Kolb, 2004: NO and NO2 emission ratios measured from in-use commercial aircraft during taxi and takeoff. Environ. Sci. Tech., 38, 6078–6084.

Laird, C. K. and S. A. Sloan, 1993: Nitrous-oxide emissions from uk power-stations. Atmospheric Environment Part a-General Topics, 27, 1453–1457.

Lassey, K. R., D. M. Etheridge, D. C. Lowe, A. M. Smith, and D. F. Ferretti, 2007: Centennial evolution of the atmospheric methane budget: what do the carbon isotopes tell us? Atmospheric Chemistry and Physics, 7, 2119–2139.

Lelieveld, J., 2006: Climate change - a nasty surprise in the greenhouse. Nature, 443, 405–406.

Lelieveld, J., P. J. Crutzen, and F. J. Dentener, 1998: Changing concentration, lifetime and climate forcing of atmospheric methane. Tellus Series B-Chemical and Physical Meteorology, 50, 128–150.

Nelson, D. D., J. B. McManus, S. C. Herndon, M. S. Zahniser, B. Tuzson, and L. Emmenegger, 2008: New method for isotopic ratio measurements of atmospheric carbon dioxide using a 4.3 mu m pulsed quantum cascade laser. Applied Physics B-Lasers and Optics, 90,301-309.

Pataki, D. E., J. R. Ehleringer, L. B. Flanagan, D. Yakir, D. R. Bowling, C. J. Still, N. Buchmann, J. O. Kaplan, and J. A. Berry, 2003: The application and interpretation of keeling plots in terrestrial carbon cycle research. Global Biogeochemical Cycles, 17.

Prather, M. J., 1996: Time scales in atmospheric chemistry: Theory, gwps for ch4 and co, and runaway growth. Geophysical Research Letters, 23, 2597–2600.

Prather, M. J., 1998: Time scales in atmospheric chemistry: Coupled perturbations to n2o, noy, and o-3. Science, 279, 1339–1341.

Quay, P., J. Stutsman, D. Wilbur, A. Snover, E. Dlugokencky, and T. Brown, 1999: The isotopic composition of atmospheric methane. Global Biogeochemical Cycles, 13, 445–461.

Rigby, M., R. G. Prinn, P. J. Fraser, P. G. Simmonds, R. L. Langenfelds, J. Huang, D. M. Cunnold, L. P. Steele, P. B. Krummel, R. F. Weiss, S. O'Doherty, P. K. Salameh, H. J. Wang, C. M. Harth, J. Muhle, and L. W. Porter, 2008: Renewed growth of atmospheric methane. Geophysical Research Letters, 35, 6.

Spicer, C., M. Holdren, R. Riggin, and T. Lyon, 1994: Chemical composition and

photochemical reactivity of exhaust from aircraft turbine engines. Annales Geophysicae, 12, 944–955.

Spicer, C., M. Holdren, D. Smith, D. Hughes, and M. Smith, 1992: Chemical composition of exhaust from aircraft turbine engines. Journal of Engineering for Gas Turbines and Power, 114, 111–117.

Spicer, C. W., M. W. Holdren, K. A. Cowen, D. W. Joseph, J. Satola, B. Goodwin, H. Mayfield, A. Laskin, M. L. Alexander, J. V. Ortega, M. Newburn, R. Kagann, and R. Hashmonay, 2009a: Rapid measurement of emissions from military aircraft turbine engines by downstream extractive sampling of aircraft on the ground: Results for c-130 and f-15 aircraft. Atmospheric Environment, 43, 2612–2622.

Spicer, C. W., M. W. Holdren, K. A. Cowen, D. W. Joseph, J. Satola, B. Goodwin, H. Mayfield, A. Laskin, M. L. Alexander, J. V. Ortega, M. Newburn, R. Kagann, and R. Hashmonay, 2009b: Rapid measurement of emissions from military aircraft turbine engines by downstream extractive sampling of aircraft on the ground: Results for c-130 and f-15 aircraft (vol 43, pg 2612, 2009). Atmospheric Environment, 43, 6120–6120.

Tuzson, B., J. Mohn, M. J. Zeeman, R. A. Werner, W. Eugster, M. S. Zahniser, D. D. Nelson, J. B. McManus, and L. Emmenegger, 2008: High precision and continuous field measurements of delta c-13 and delta o-18 in carbon dioxide with a cryogen-free qclas. Applied Physics B-Lasers and Optics, 92, 451–458.

Vay, S., B. Anderson, G. W. Sachse, J. E. Collins, J. R. Podolske, C. H. Twohy, B. Gandrud, K. R. Chan, S. L. Baughcum, and H. A. Wallio, 1998: Dc-8-based observations of aircraft co, ch4, n2o, and h2o(g) emission indices during success. Geophysical Research Letters, 25, 1717–1720.

Wey, C. C., B. E. Anderson, C. Hudgins, C. Wey, X. Li-Jones, E. Winstead, L. K. Thornhill, P. Lobo, D. Hagen, P. Whitefield, P. E. Yelvington, S. C. Herndon, T. B. Onasch, R. C. Miake-Lye, J. W. Wormhoudt, B. Knighton, R. Howard, D. Bryant, E. Corporan, C. Moses, D. Holve, and W. Dodds, 2006: Aircraft particle emissions experiment (apex). NASA/TM-2006-214382.

Whiticar, M. J., 1999: Carbon and hydrogen isotope systematics of bacterial formation and oxidation of methane. Chemical Geology, 161, 291–314.

Wiesen, P. J., J. Kleffmann, R. Kurtenbach, and K. Becker, 1994: Nitrous oxide and methane emissions form aero engines. Geophysical Research Letters, 21, 2027–2030.

Yelvington, P. E., S. C. Herndon, J. C. Wormhoudt, J. T. Jayne, R. C. Miake-Lye, W. B. Knighton, and C. Wey, 2007: Chemical speciation of hydrocarbon emissions from a commercial aircraft engine. Journal of Propulsion and Power, 23, 912–918.

Zahniser, M. S., D. D. Nelson, J. B. McManus, S. C. Herdon, E. C. Wood, J. H. Shorter,

B. H. Lee, G. W. Santoni, R. Jimnez, B. C. Daube, S. Park, E. A. Kort, and S. C. Wofsy, 2009: Infrared qc laser applications to field measurements of atmospheric trace gas sources and sinks in environmental research: enhanced capabilities using continuous wave qcls. SPIE, 7222.

Zheng, J., A. J. Weinheimer, B. A. Ridley, S. C. Liu, G. W. Sachse, B. E. Anderson, and J. E. Collins, 1994: An analysis of aircraft exhaust plumes from accidental encounters. Geophysical Research Letters, 21, 2579–2582.

Day #	Date	Experiment	Fuel	Start	End	T (K)	RH (%)	ARI Activities	Notes
Prep	1/25	Mini-CAST Line Loss	N/A	N/A	N/A	280	60	MAAP, AMS, SMPS, CPC on line	
0	1/26	Shakedown	JP8	13:50	15:00	282	50	ARI downstream	EEPS
		Mapping	JP8	16:00	19:20	278	60	ARI downstream	EEPS
1	1/27	JP8 warm	JP8	12:40	15:30	283	30	ARI connected, MP at 2nd 7%	
		JP8 cold	JP8	6:00	9:30	270	75	ARI connected	
2	1/28	FT1 warm	FT1	12:30	15:40	283	30	ARI connected, MP at 2nd 7%	
		FT1 cold	FT1	5:40	8:30	273	60	ARI connected	
3	1/29	APU	JP8					ARI connected	high winds
4	1/30	FT1 blend	Mix	6:15	9:40	275	55	ARI downstream	
		FT2 warm	FT2	10:50	13:40	287	25	ARI connected	
		FT2 cold	FT2	5:45	7:00	273	75	ARI connected	
5 "Triple Saturday"	1/31	FT2 blend	Mix	8:30	10:40	287	30	ARI connected,	
		JP8 warm	JP8	12:40	15:30	290	20	MP on 2nd half	EEPS
								ARI downstream	
DAY OFF	2/1								
7	2/2	JP8 cold	JP8	7:11	9:00	275	60	ARI downstream	EEPS
		Dilution	JP8	9:30	12:10	285	25	ARI connected	
		APU	JP8	14:10	15:40	293	10	ARI connected	
		APU	JP8	15:40	16:40	290	15	ARI connected	
8	2/3	Mini-CAST Line loss	N/A	N/A	N/A			ARI travel day	

Table 1: *Summary of the daily AAFEX activities for the Aerodyne Research Inc. team*

Figure 1: *AAFEX sampling layout and the 145 m "advected-plume" trailer positioning relative to the aircraft*

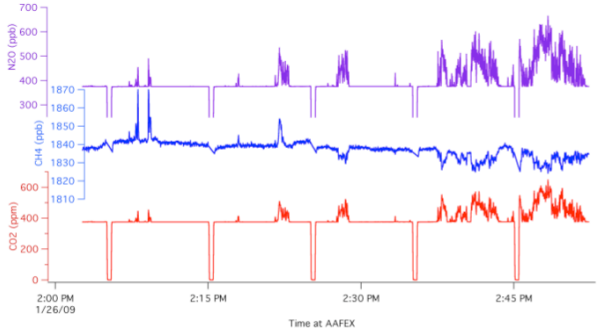

(a) AFEX sampling data illustrating positive correlation between methane and carbon dioxide at idle conditions, and negative correlation at higher thrusts. Nitrous oxide is generally positively correlated with carbon dioxide. Zero CO_2 and N_2O data correspond to ultra-zero-air additions into the sampling lines to calculate baseline spectra for the Methane Isotope QCLS. Methane data is not collected during these intervals.

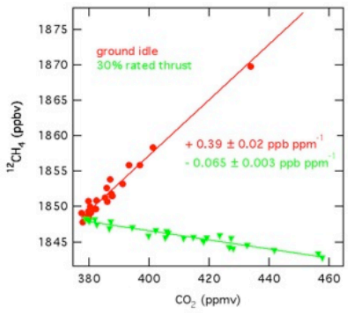

(b) Illustration of fitting to solve for emission ratios at idle and 30% thrust for methane. Similar regressions are carried out for nitrous oxide.

Figure 2: *Time Series of Ambient Plume Measurements along with Methane Emission Ratio Regression Examples from two Plume Samples*

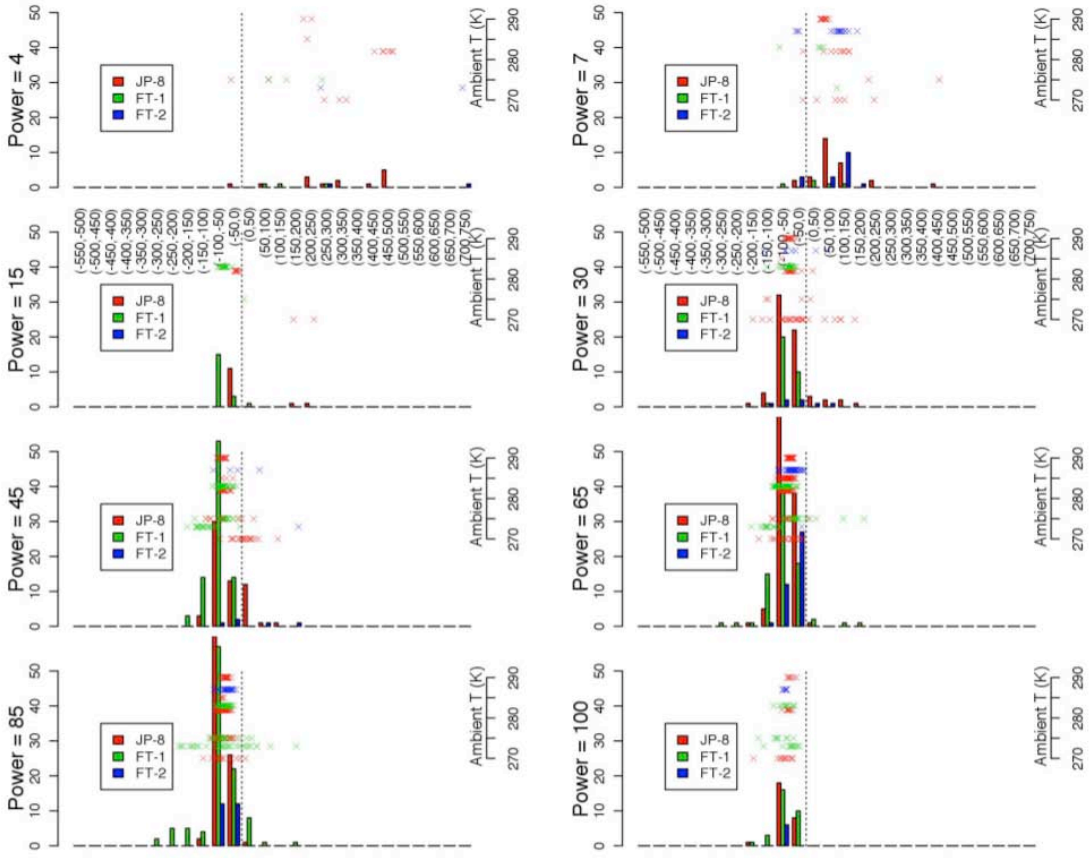

Figure 3: *Histogram of Individual Methane Emission Index Calculations Grouped by Power Setting*

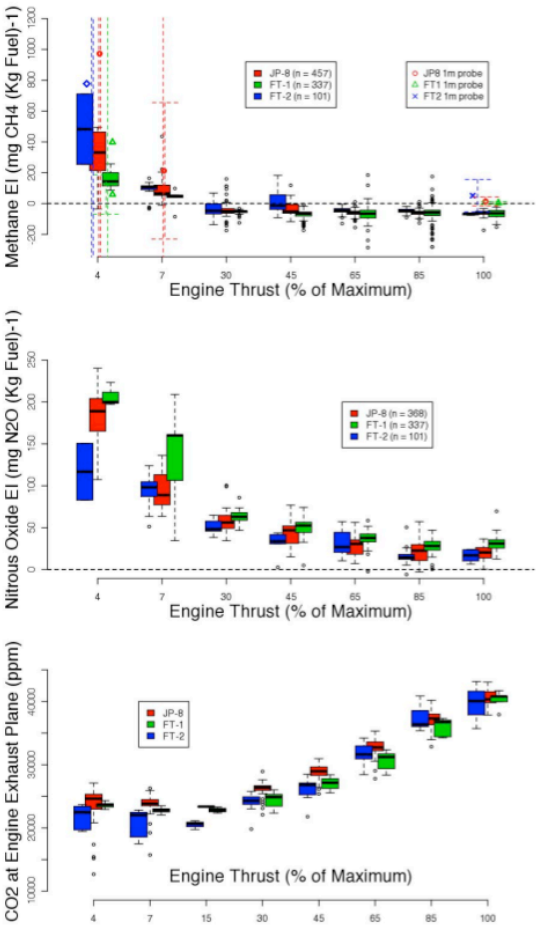

Figure 4: *Methane and nitrous oxide emission indices by power setting binned by fuel with outliers shown as circles. Also shown are CO2 at EEP values courtesy of Changlie Wey. Black bars represent the median, boxes extend from the first to the thirst quartile, and whiskers represent 1.5 times the inter-quartile range. Also shown superimposed on the methane data are canister samples from the 1-m probe.*

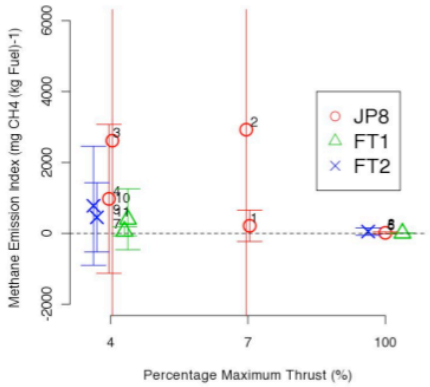

Figure 5: *Subsamples from the 1-m probe showing large distribution of methane emission indices possible. Error bars indicate 1σ and are much larger at low powers because of both the variance of CO_2 seen at the engine exhaust plane as shown in Figure 4 and the higher methane concentrations measured in the canisters.*

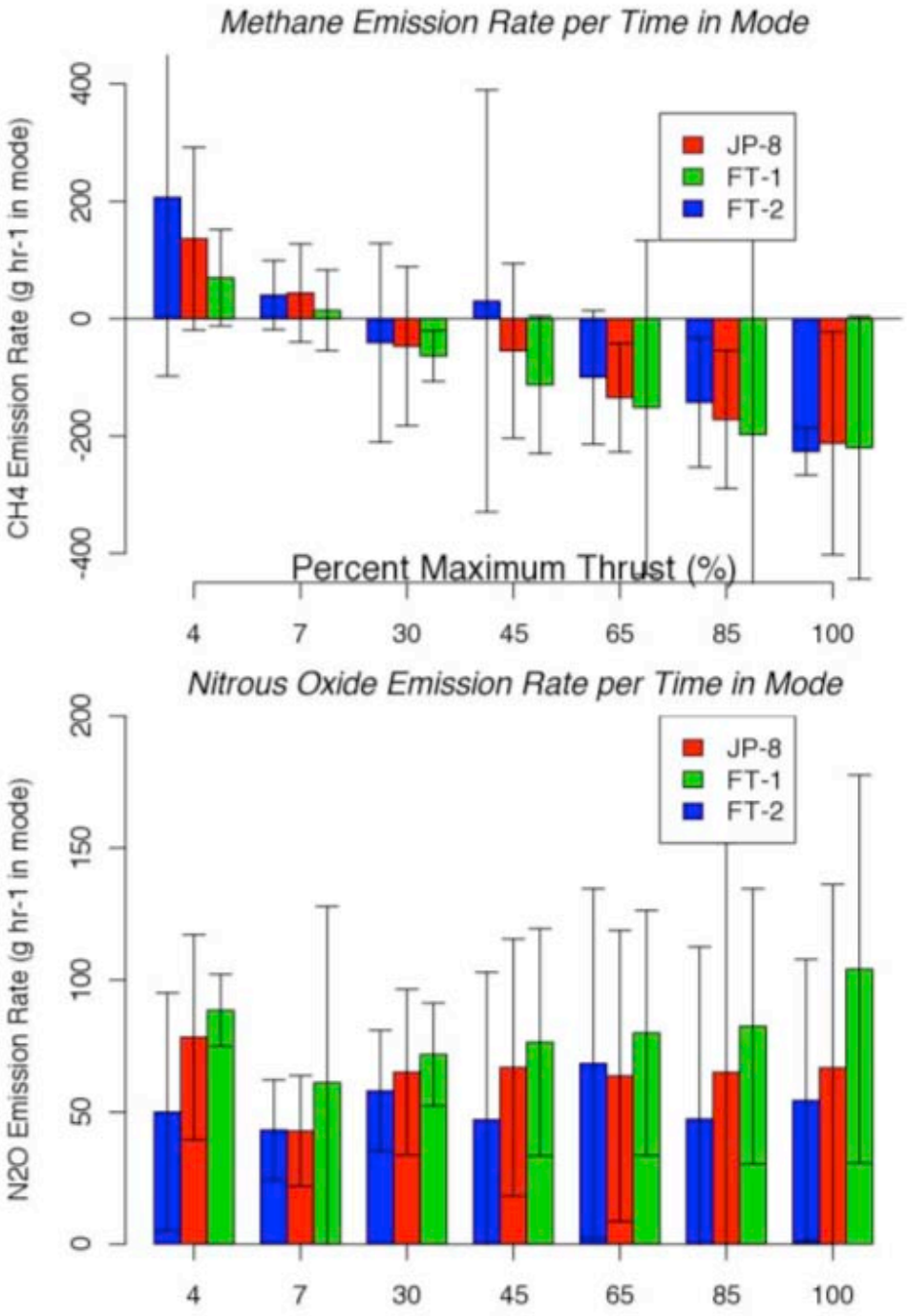

Figure 6: *CH_4 and N_2O Emission Rates per unit time in mode*

APPENDIX E

Mode	Methane emission/consumption rate (g/hr)	Nitrous Oxide emission rate (g/hr)	Time in mode (hrs)	Total methane emitted/consumed (g)	Total nitrous oxide emitted/consumed (g)
Landing (30% thrust)	-67.8	+87.1	0.067	-4.5	+5.8
Idle (7%)	+39.7	+60.0	0.433	+17	+26
Take-off (100%)	-234	+80.3	0.012	-2.8	+0.96
Climb-out (85%)	-177	+67.3	0.037	-6.5	+2.5
Total for ICAO LTO				+3.3	+35
Cruise (65%)	-148	+81.4	1	-148	+81.4
Total for flight				-145	+116

Table 2: *Estimates of Total Emissions of Methane and Nitrous Oxide for a Simulated 1-hour Flight*

Study	Engine	Fuel	Ground or Flight based	Methane Emission Index (g CH_4/kg fuel) or exhaust concentration (ppm). Engine condition noted (percent thrust)
Spicer et al. 1992	F101 F110	JP-4	Ground	$[CH_4]$ = 1.85 (idle) 1.5 (44%) 1.4 (75%) $[CH_4]$ = 1.76 (idle) 1.5 (38%) 1.1 (63%)
Wiesen et al. 1994	PW 305	NA	Ground and altitude test cells	Ground: $[CH_4]$ = 2.97 (5.5%), 1.05 (23.5%), 0.76 to 0.22 (33% to 96% thrust) Altitude: $[CH_4]$ = 0.18 to 0.58 (89% to 100%)
Wiesen et al. 1994	RB 211	NA	Altitude test cell	1.3 – 1.54 ppm *in diluted exhaust* (core + bypass air) (0.5 to 1.4 kg/s fuel flow rate)
Spicer et al. 1994	TF-9 CFM-56	JP-5	Ground	$[CH_4]$ = 9.42 (idle) 1.63 (30%) 1.09 (80%) $[CH_4]$ = 5.58 (idle) 0.58 (30%) 0.44 (80%)
Vay et al. 1998	B-757 T-39	Jet A high/low S	Flight	$EI(CH_4)$ = -1.6 to 1.19 (plume n=6) $EI(CH_4)$ = -1.1 to -0.37 (plume n=6)
Anderson et al. 2006	RR211-535E4	JP-5 high/low S	Ground	$[CH_4]_{(S=810\ ppmw)}$ = 1.95 (idle) 2.60 (26%) 1.80 (47%) 2.41 (61%), $EI(CH_4)_{(S=810\ ppmw)}$ < 0.050, 0.042, 0.026, 0.020 $[CH_4]_{(S=1820\ ppmw)}$ = 2.16, 2.32, 1.40, 1.39 $EI(CH_4)_{(S=1820\ ppmw)}$ < 0.071, 0.044, 0.026, 0.019
APEX-1 Wey et al. 2006	CFM-56-2C	JP-8	Ground	$EI(CH_4)$ = 0.17 (4%), 0.08 (7%), 0.04 (30%), 0.02 (65%), 0.01 (85 – 100%)
AAFEX This study	CFM-56-2C	JP-8 FT-1 FT-2	Ground	$EI(CH_4)$ = 0.319 (4%), 0.096 (7%), -0.042 (30%), -0.059 (85%) $EI(CH_4)$ = 0.166 (4%), 0.031 (7%), -0.057 (30%), -0.068 (85%) $EI(CH_4)$ = 0.490 (4%), 0.089 (7%), -0.036 (30%), -0.049 (85%)

Table 3: *Comparison of Studies Presenting Methane Aircraft Emission Data*

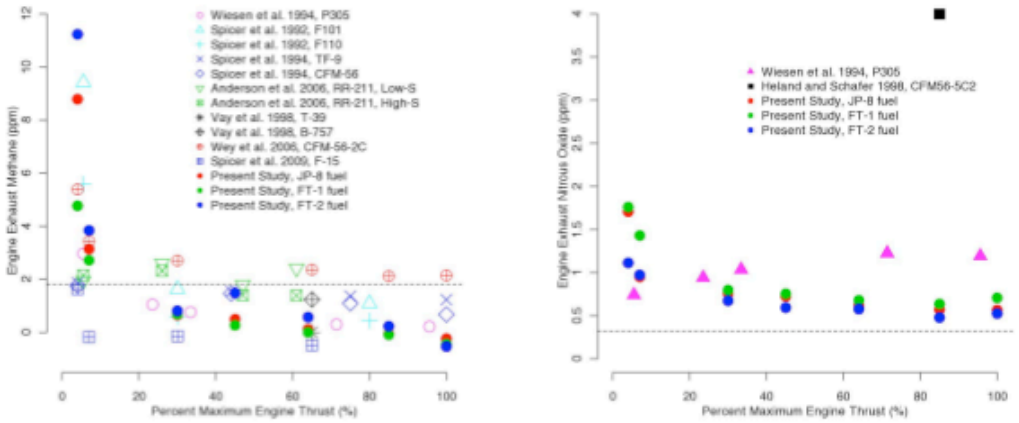

(a) Mean engine exhaust methane concentrations at percent maximum engine thrust

(b) Mean engine exhaust nitrous oxide concentrations at percent maximum engine thrust

Figure 7: *Mean Engine Exhaust Concentrations of Non-CO_2 Greenhouse Gasess*

APPENDIX F: Investigations of Plume Chemistry during AAFEX

Ezra C. Wood[1], Scott C. Herndon[1], H. Ben Lee[2], Michael Timko[1], Zhenhong Yu[1], W. Berk Knighton[3], Richard C. Miake-Lye[1]

[1] Aerodyne Research, Inc., Billerica MA
[2] School of Engineering and Applied Sciences, Harvard University, Cambridge MA
[3] Department of Chemistry, Montana State University, Bozeman MT

Introduction

Understanding the chemistry of aircraft exhaust plumes is important in order to understand the transformations of VOCs/HAPs from the engine exhaust plane to the airport fence line and beyond, the timescale of formation of "secondary" particles that require oxidation to form (e.g., formation of sulfate aerosol from SO_2), and the formation and/or destruction of ozone (O_3) in the plume.

During the AAFEX campaign, various aspects of plume chemistry were investigated with the Aerodyne mobile laboratory (AML). The focus was on chemistry in the plume of exhaust while the engines were operated at low thrust (idle) because of the potential to identify observable changes in the VOC speciation and NO_x-ozone chemistry.

Methods

In order to address plume chemistry, the Aerodyne mobile laboratory (AML) detached from the probe sampling system several times and sampled the exhaust plume approximately 60- to 200-m downwind of the DC-8. At high powers (above 15% rated thrust), the AML remained stationary and at least 150 m downwind of the engines. When the engines were operated at ground idle thrust, the AML drove on the tarmac and intercepted the exhaust plume at various locations. An example map of the mobile lab's measurements are shown below, colored by the formaldehyde concentration:

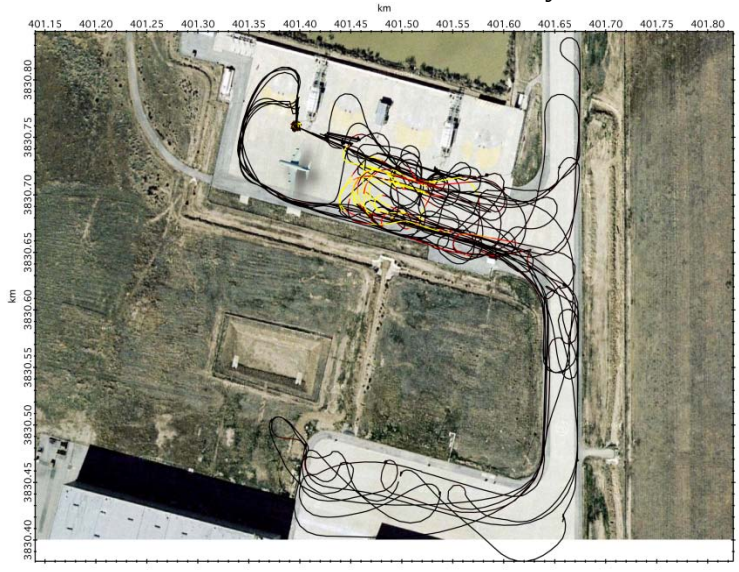

Figure 1. Downwind measurements with the truck were performed on 1/26/2009, 1/30/2009 (05:25 – 10:14), 1/31/2009 (11:42 – 15:18), and 2/2/2009 (07:00 – 08:45).

The instrumentation onboard the AML are described in companion reports. The key measurements aboard the AML for these studies are listed below:

Table 1. Instrumentation aboard the AML used for the measurements in this report.

Species	**Instrument**	**Time response (sec)**
Ozone (O_3)	2B-Tech UV absorbance sensor at 254 nm	2
Nitric oxide (NO)	Thermoelectron 42i chemiluminescence sensor	1
Nitrogen dioxide (NO_2)	QC-TILDAS (quantum cascade – tunable infared laser differential absorption spectrometer)	1
Ethene (C_2H_4)	QC-TILDAS	1

Additionally, hydrogen peroxide (H_2O_2) and nitrous acid (HONO) were measured at the "150 m" trailer using the QC-TILDAS described in the companion report by Lee et al.

Results and Discussion

The main findings from the plume studies are summarized below.

1. O_3 is formed in ground idle exhaust plumes

Most NO_x is emitted in the form of NO. For example, NO_x emissions from fossil-fuel fired power plants and vehicular traffic in the US consist of over 95% NO (Ban-Weiss et al. 2008; Ryerson et al. 2001), with the remainder NO_2. NO_x emissions from idling aircraft engines are an exception; depending on engine type and thrust level, the NO_x emitted consists of 70% to over 95% NO_2 (Wood et al. 2008; Wormhoudt et al. 2007). This has ramifications for both ozone and NO_2 pollution emitted from aircraft, since primary NO_2 emissions lead to greater ambient concentrations of both O_3 and NO_2 than do primary NO emissions. We examined NO_x-O_3 chemistry in fresh exhaust plumes from the NASA DC-8 CFM56-2C engine using the downwind measurements.

Primary NO emissions lead to decreases in ambient O_3 because of the reaction

$$NO + O_3 \rightarrow NO_2 + O_2. \quad (1)$$

Primary NO_2 emissions lead to net formation of O_3 because of the photolysis of NO_2:

$$NO_2 + light + O_2 \rightarrow NO + O_3 \quad (2)$$

Since NO_x is emitted primary in the form of NO at high engine power (~climb-out to take-off), ambient O_3 that is entrained into the exhaust plume reacts rapidly with the NO,

leading to decreased O_3 concentrations. Conversely, the primary NO_2 emissions from low-power engine operation lead to increases in [O_3]. Both of these cases are shown in figure 1 below. From 12:58 to 13:00, the mobile lab intercepted exhaust from the engine operating at high power and observed O_3 concentrations that were ~20 ppb lower than the background concentration of 38 ppb. From 13:01 to 13:04, occasional exhaust plumes from the engine operating at low engine thrust (idle) were sampled by the mobile laboratory. In these low-power plumes, O_3 was elevated up to 20 ppb above the background concentration.

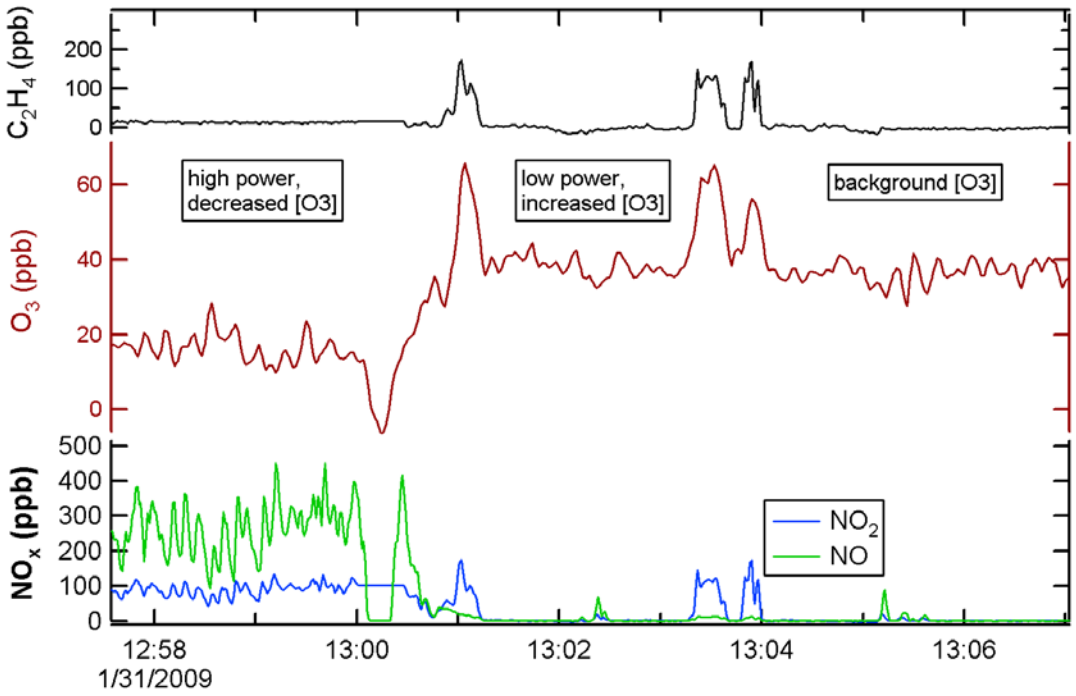

Figure 1. Time series of C_2H_4, O_3, NO, and NO_2 measured downwind of the NASA DC-8 during high engine power (up until 13:01) and low engine power (after 13:01).

The ethene concentrations are shown because they are a good indication of when the engines were operated at low thrust. Although the above results are expected based on the known emission indices of NO and NO_2 and basic atmospheric chemistry, the formation of O_3 in a fresh (aged less than minutes) combustion plume is unique to our knowledge. A second example is shown in figure 2.

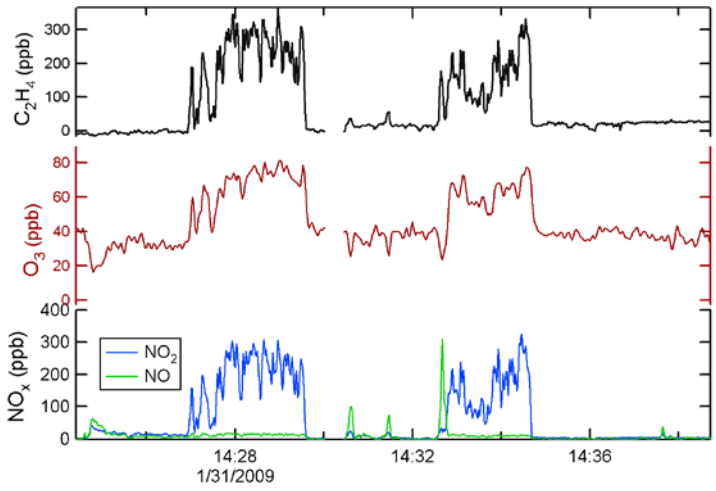

Figure 2. Formation of O_3 in idle exhaust plumes.

Ozone sensors based on the absorption of UV light at 254 nm are known to suffer from interferences because of other species (gas or particle) that absorb or scatter in the same spectral region (Dunlea et al. 2006). Figure 3 below demonstrates that for the measurements at AAFEX, such interferences were not a significant problem. Figure 3 plots O_3 vs. C_2H_4, which is an indicator of low-power engine exhaust (along with all VOCs; the choice of C_2H_4 is mostly arbitrary). The data are color-coded by time of day. Data taken after 6:00 pm show no correlation between O_3 and C_2H_4, which is expected because in the absence of sunlight O_3 cannot form in the plume. Since enhanced O_3 was only observed while there was still daylight (around 4:00 pm in Figure 3), we conclude that under the conditions sampled, interferences in the O_3 measurement were negligible.

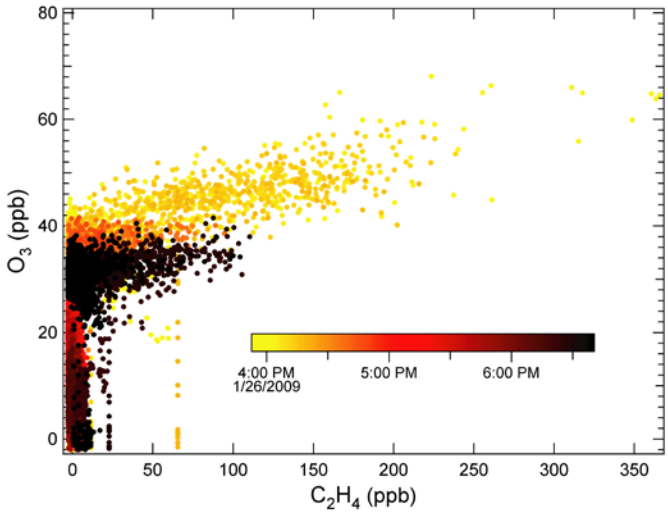

Figure 3. Enhanced O_3 concentrations in the exhaust plumes were only observed during daylight, indicating that the O_3 signal recorded by the 2B-tech O_3 sensor were actually from O_3 and not interfering species.

2. Peroxy radical chemistry is active in low thrust plumes

If the initial NO_2/NO_x ratio is 1 and the only transformations that occur in the plume are the photolysis of NO_2 and subsequent formation of ozone, then any O_3 formed in the plume would be at the expense of NO_2. That is, the quantity $([NO_2]+[O_3])/[NO_x]$ would always equal 1, since an increase in O_3 would correspond to an equal decrease in NO_2. For the time period shown in Figure 2, the correlation between $[NO_2] + [O_3]$ and NO_x is graphed in figure 4:

.

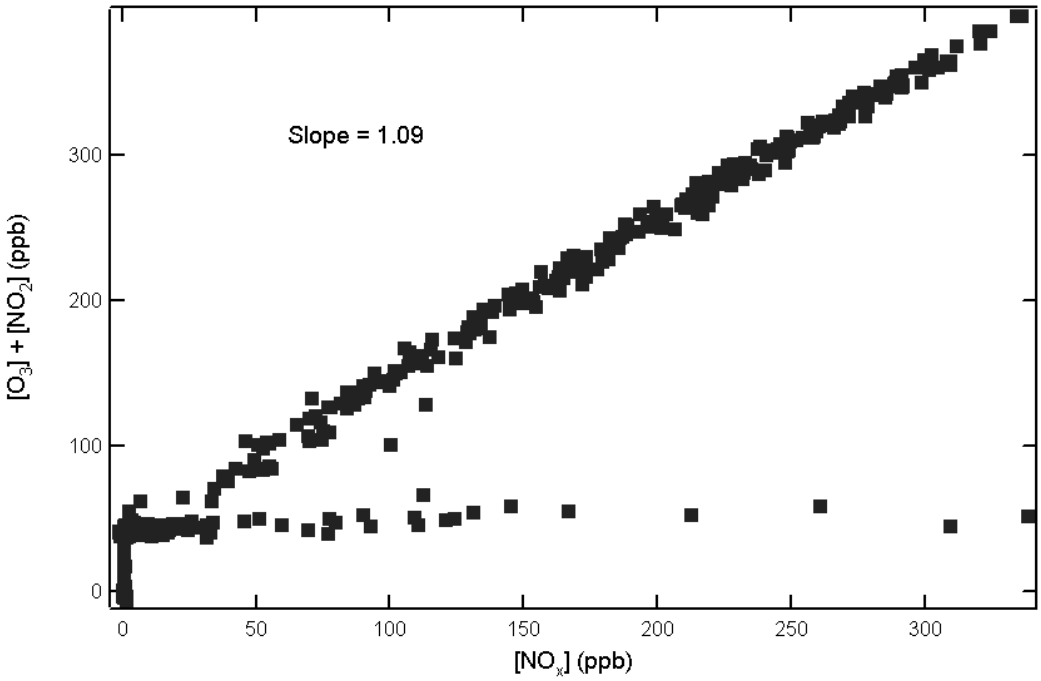

Figure 4. Correlation of $([O_3] + [NO_2])$ with NO_x. The high slope infers intraplume oxidation of NO to NO_2 by peroxy radicals.

Since the slope actually exceeds 1 (and is equal to 1.09), it is evident that there was net conversion of NO to NO_2 in the plume, as inferred from one limited idle plume observed at night during APEX3 (Wood et al., 2008). The NO oxidation is mostly likely from the following reactions:

$NO + HO_2 \rightarrow NO_2 + HO$ (3)
$NO + RO_2 \rightarrow NO_2 + RO$ (4)

Where "RO_2" represents an organic peroxy radical (e.g., CH_3OO). These organic peroxy radicals are formed from the oxidation of VOCs by reaction with the hydroxyl radical (OH):

$RH + OH \rightarrow R\cdot + H_2O$ (5)
$R\cdot + O_2 + M \rightarrow RO_2 + M$ (6)

This VOC oxidation (i.e., combustion) is most rapid in the combustor of the engine, of course, but continues into the plume.

Figure 5 shows the correlation of $[O_3] + [NO_2]$ with $[NO_x]$ for all downwind sampling:

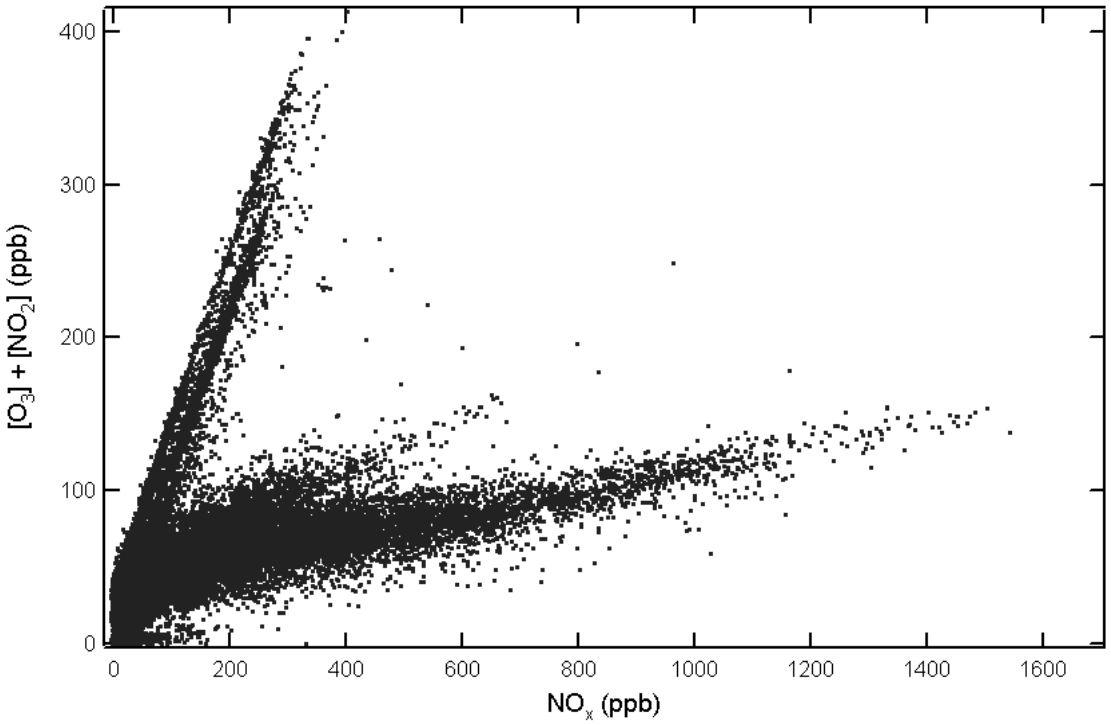

Figure 5. Correlation of ($[O_3] + [NO_2]$) with NO_x for all downwind observations during AAFEX

The lower slopes (0.06 to 0.09) correspond to observations at high engine power. These slopes are very similar to the initial NO_2/NO_x emission ratio observed during probe tests. This indicates that the reactive peroxy radical chemistry is limited to low-power operation.

3. Formation of H_2O_2 in the plume

The measurements of H_2O_2 at the 150 m trailer represent, to our knowledge, the first ever measurements of H_2O_2 in the exhaust plume of any type of combustion source. The H_2O_2 observed can have two sources: direct emissions from the engine and plume chemistry. In both cases, the dominant formation reaction is likely to be self reaction of HO_2:

$$HO_2 + HO_2 \rightarrow H_2O_2 + O_2 \qquad (7)$$

This reaction is hastened by water vapor. The emission indices observed for the entire AAFEX campaign are shown in figure 6:

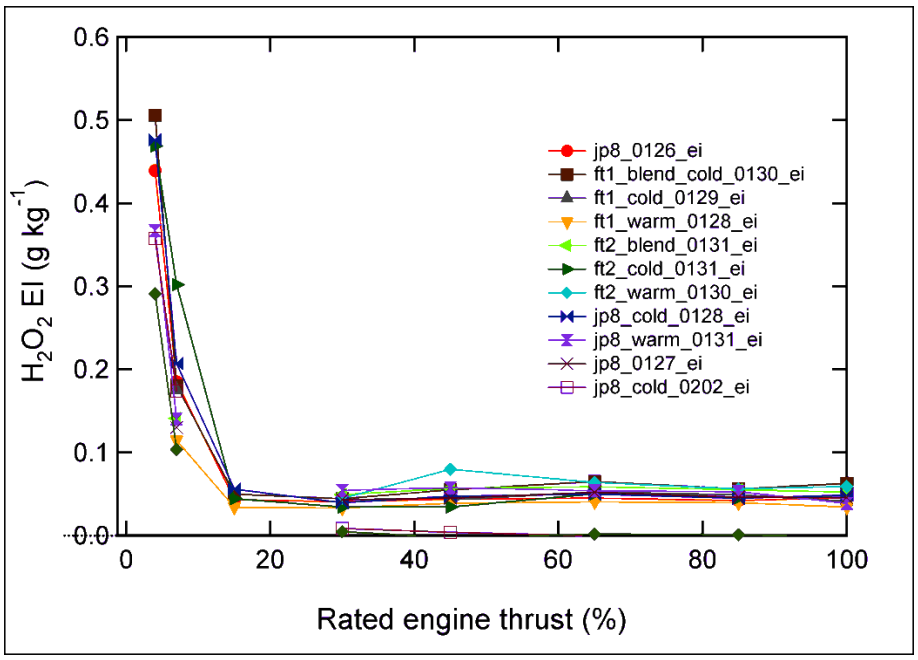

Figure 6. Dependence of H_2O_2 emission indices on engine power (from Lee et al. 2010).

The most noticeable trend is the decrease of H_2O_2 EI with engine power. There is no discernable trend of H_2O_2 emission indices with fuel type or ambient temperature. That H_2O_2 EIs are highest at low-power is consistent with the intraplume conversion of NO to NO_2 described earlier, which is largely a result of the reaction of HO_2 with NO. The combustion model described in Wood et al. (2008) predicts H_2O_2 EIs of 0.036 g/kg fuel at 7% thrust – several times lower than the observed values (0.1 to 0.3 g/kg). This result suggests that either the model is not describing the combustion processes adequately or that a large portion of the H_2O_2 observed was formed in the plume itself.

4. HO_x sources in the plume

The data presented above suggest that the concentrations of peroxy radicals (organic "RO_2" radicals and the hydroperoxy radical HO_2) in the plume are highly elevated above ambient values. Radical concentrations depend on the radical initiation rates, the propagation rates, and the termination rates. In this section we investigate the overall radical initiation rate and the propagation of the central OH radical. Calculations of the propagation and termination rates of the HO_2 and RO_2 radicals are more complicated because they require knowledge of the absolute radical concentrations. This is a topic for further study.

A. Radical initiation rates

The radical initiation rates (HO_x production rate; "$P(HO_x)$") are plotted in figure 7. The following reactions are included. Radical species (not counting NO which is a relatively stable species) are colored in red:

$HONO + h\nu \rightarrow HO + NO$
$HCHO + h\nu \rightarrow H + CHO$ (which forms 2 HO_2 radicals)
$CH_3CHO + h\nu \rightarrow CH_3 + CHO$

alkenes + O_3 → products + OH + R/HO_2

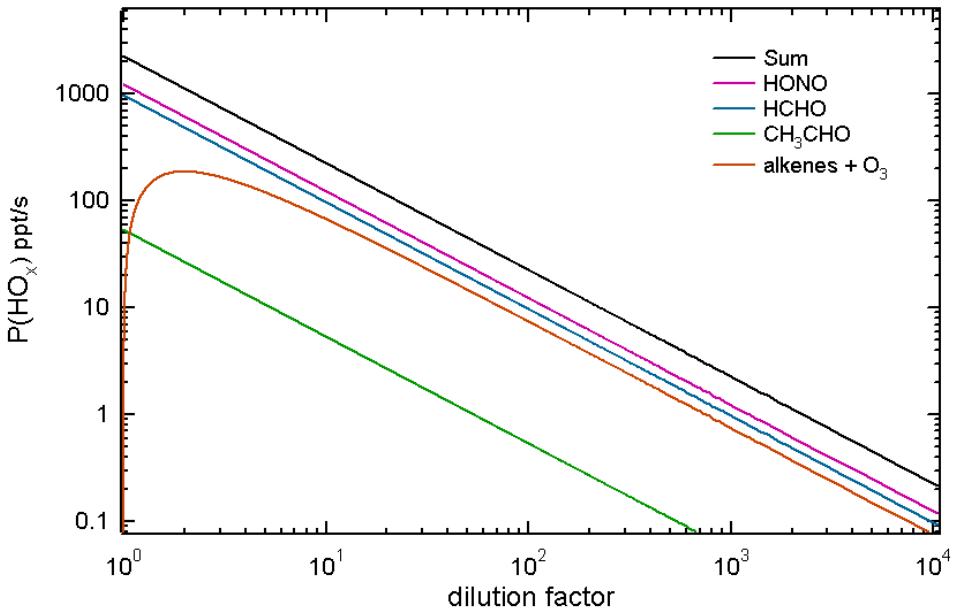

Figure 7. HO_x sources in the exhaust plume at low engine power as a function of dilution.

Conditions for these calculations:
solar zenith angle = 30°
HCHO EI = 0.4 g/kg (corresponds to ~20° C operation for the CFM56-2C1 engine)
HONO EI = 0.1 g/kg
$[O_3]_{ambient}$ = 50 ppbv

Typical ambient $P(HO_x)$ values vary from 0.1 to 2 ppt/s. The total calculated value of $P(HO_x)$ does not decrease to 1 ppt/s until the exhaust has diluted by a factor of 2000. $P(HO_x)$ is several orders of magnitude higher than ambient before the exhaust is diluted by a factor of 100.

B. Propagation and termination of the OH radical

Reactions of the highly reactive OH radical either count as radical propagation or radical termination reactions. Reaction of OH with closed-shell molecules such as VOCs leads to further radicals (HO_2, RO_2), whereas reactions with other radicals (including NO and NO_2) terminate the cycle. The overall OH reactivity is defined by the following equation:

$$\text{OH reactivity} = \sum_i [X_i] k_{OH+Xi}$$

where X is the concentration of each species with which it reacts and $k_{OH + X}$ are the reaction rate constants. Figure 8 shows the absolute OH reactivity values and the wedges of the pie chart represent the species that dominate reaction with OH. Of the main

wedges, the only reaction that is a radical termination is reaction with NO_2, which forms HNO_3. All other reactions propagate the radical chain cycle. The relative size of the NO_2 reaction increases with dilution because of the inverse dependence of the reaction rate with ambient temperature.

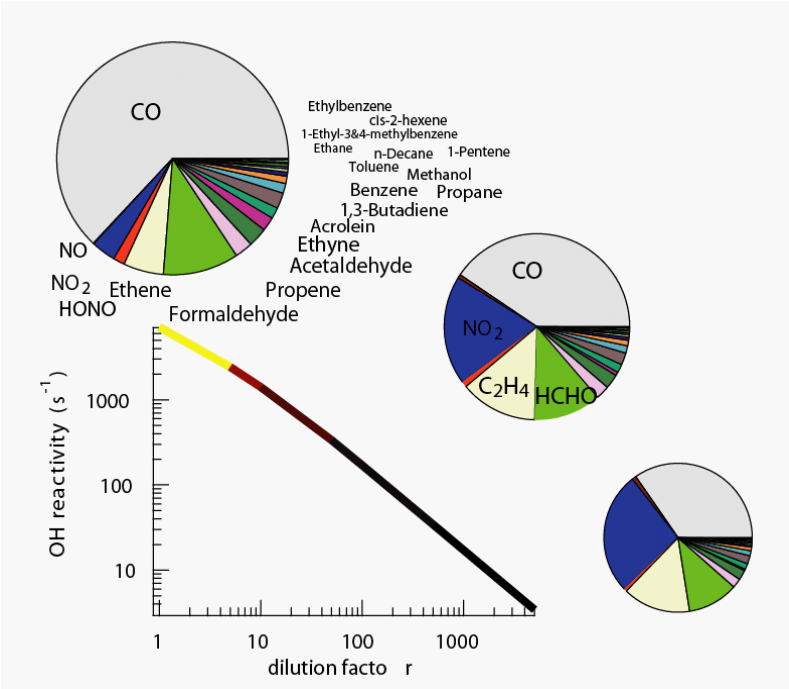

Figure 8. OH reactivity of exhaust (ground idle) as a function of dilution.

Overall, the reactions of OH favor propagation rather than termination. For comparison, the highest OH reactivities observed in ambient air are ~100 s^{-1}, observed only during a small time window of the morning in Mexico City (Shirley et al. 2006) – an exceptionally polluted place. These calculations by themselves do not quantitatively predict HO_2 or RO_2 concentrations, but when combined with the O_3 and H_2O_2, observations do indicate that such chemistry cannot be ignored by air pollution models for accurate predictions of the impact of airports on air quality.

5. The concentration of OH in the plume

While a direct measurement of OH in the diluted exhaust plume is elusive, it is possible to estimate the product of the OH concentration and the reaction time by investigating the reactions of VOCs with different OH reactivities. Consider ethene (C_2H_4) and 1,3-butadiene (C_4H_6). The rate constant for the reaction of OH with benzene (1.2×10^{-12} cm^3 $molecule^{-1}$ s^{-1}) is 56 times slower than the rate constant for the reaction of OH with 1,3-butadiene (6.7×10^{-11} cm^3 $molecule^{-1}$ s^{-1}). Thus as the plume reacts, the ratio of 1,3-butadiene to benzene is expected to decrease as both species react with OH (making the safe assumption that neither VOC is formed by other reactions). The ratio of the two compounds is quantitatively related to the integrated OH exposure time $\Delta t[OH]$ by the following equation:

$$\ln([C_4H_6]_t/[C_6H_6]_t) = \ln([C_4H_6]_o)/[C_6H_6]_o) + (k_{C_4H_6+OH} - k_{C_6H_6+OH})\Delta t[OH]$$

where the k values are the rate constants for reaction with OH. At ground idle, the molar $[C_4H_6]/[C_6H_6]$ ratio was 1.51 observed using the probe sampling but only 1.37 observed downwind when the AML detached and sampled exhaust downwind. At 7% idle, the two ratios were 0.95 (probe) and 0.87 (downwind). Both sets of values, when plugged into the above equation, give a value of $\Delta t[OH]$ of $\times 10^{8}$ molecules OH · s/cm^3. With an estimate of 60 seconds for the total reaction time (Δt), this gives an estimate for the average OH concentration of 2×10^7 molecules/cm^3. For comparison, ambient OH concentrations during daytime are usually in the range 1×10^6 molecules/cm^3 to 1×10^7 molecules/cm^3. This indicates that the rate of VOC oxidation is elevated within the first minute of plume evolution.

References

Ban-Weiss, G. A., McLaughlin, J. P., Harley, R. A., Kean, A. J., Grosjean, E., and Grosjean, D. (2008). "Carbonyl and Nitrogen Dioxide Emissions from Gasoline- and Diesel-Powered Motor Vehicles." *Environ Sci Technol*, 42, 3944-3950.

Dunlea, E. J., Herndon, S. C., Nelson, D. D., Volkamer, R. M., Lamb, B. K., Allwine, E. J., Grutter, M., Ramos Villegas, C. R., Marquez, C., Blanco, S., Cardenas, B., Kolb, C. E., Molina, L. T., and Molina, M. J. (2006). "Technical note: Evaluation of standard ultraviolet absorption ozone monitors in a polluted urban environment." *Atmos. Chem. Phys.*, 6(10), 3163-3180.

Ryerson, T. B., Trainer, M., Holloway, J. S., Parrish, D. D., Huey, L. G., Sueper, D. T., Frost, G. J., Donnelly, S. G., Schauffler, S., Atlas, E. L., Kuster, W. C., Goldan, P. D., Hubler, G., Meagher, J. F., and Fehsenfeld, F. C. (2001). "Observations of ozone formation in power plant plumes and implications for ozone control strategies." *Science*, 292(5517), 719-723.

Shirley, T. R., Brune, W. H., Ren, X., Mao, J., Lesher, R., Cardenas, B., Volkamer, R., Molina, L. T., Molina, M. J., Lamb, B., Velasco, E., Jobson, T., and Alexander, M. (2006). "Atmospheric oxidation in the Mexico City Metropolitan Area (MCMA) during April 2003." *Atmos. Chem. Phys.*, 6, 2753-2765.

Wood, E. C., Herndon, S. C., Timko, M. T., Yelvington, P. E., and Miake-Lye, R. C. (2008). "Speciation and Chemical Evolution of Nitrogen Oxides in Aircraft Exhaust near Airports." *Environ Sci Technol*, 42, 1884-1891.

Wormhoudt, J., Herndon, S. C., Yelvington, P. E., Miake-Lye, R. C., and Wey, C. (2007). "Nitrogen Oxide (NO/NO_2/HONO) Emissions Measurements in Aircraft Exhausts." *Journal of Propulsion and Power*, 23(5), 906-911.

APPENDIX G: Gaseous And Non-Volatile Particulate Matter Emissions Measurements In CFM56 Engines – AAFEX Project

Edwin Corporan[1], Matthew J. DeWitt[2], Christopher Klingshirn[2]
[1]Air Force Research Laboratory, Fuels and Energy Branch
Wright-Patterson AFB, OH 45433 USA. edwin.corporan@wpafb.af.mil

[2]University of Dayton Research Institute, 300 College Park, Dayton, OH 45469 USA

Abstract
Gaseous and particulate matter emissions were measured from a CFM56 engine burning two Fischer-Tropsch (FT) alternative (non-petroleum) jet fuels derived from coal and natural gas, and blends at 50% by volume of each fuel with JP-8. Detailed chemical analysis of the fuels was performed to provide insight into their performance and to infer potential impacts on engine emissions. Chemical analyses show that the alternative fuels were comprised of mostly paraffinic compounds (synthetic paraffinic kerosenes – SPKs) at varying relative concentrations and contained negligible heteroatom content and were mostly aromatic free. Engine tests demonstrated that the SPKs (neat and blended with JP-8) produced significantly lower non-volatile particulate matter (soot) and had negligible effects on gaseous emissions relative to baseline JP-8 fuel. Measurement of the downstream exhaust plume showed a nucleation mode for particle formation, which increased the relative particle emission index. Initial analyses show a potential impact of fuel end-point temperature on particulate emissions at several low-power engine conditions. It was observed that the FT fuel with the higher end-point temperature produced significantly higher non-volatile particulate emissions; however, further research is warranted to verify this impact as only two fuels were evaluated.

Introduction
The growing demand and reduced supply of petroleum products combined with the instability in petroleum-rich countries results in high uncertainties and volatility in the cost of energy, particularly transportation fuels. As a result, efficient energy technologies and the development of alternative energy options, such as fuels from domestic alternative sources, have become a national priority. Alternative transportation fuels are desirable both from an energy security and environmental perspective as the preponderance of imported oil is converted to liquid transportation fuels. In the United States, liquid fuel production is roughly 200 billion gal/year, with gasoline, diesel, and jet fuel being produced in approximately a 70/20/10 ratio. Thus, domestically-produced alternative fuels could increase energy security. Domestic alternatives for gasoline (ethanol) and diesel (biodiesel) exist, but no operational alternative jet fuels are currently being produced in the United States. Alternative aviation fuels are also of interest for mitigating environmental impacts of fuel use, both on the global (climate change) and local (airport) air quality level. Although aviation contributes only 2% to global CO_2 emissions[1], the U.S. Air Force (USAF) and the aviation industry are committed to contributing to potential solutions. Alternative aviation fuels are being sought as "drop-

in" replacements for current aircraft, requiring no modification to equipment, aircraft operations, handling, or transportation. This rules out ethanol (due to safety, performance, handling, and material compatibility issues) and biodiesel (due to low temperature and combustion performance, and storage stability issues).

Initial U.S. efforts in developing alternative aviation fuels focused on Fischer-Tropsch (FT) fuels produced from coal, biomass, and/or natural gas. Coal-derived "iso-paraffinic kerosene" (IPK) produced by Sasol in South Africa was approved for aviation use in blends up to 50% in Jet A-1 (on a producer-specific basis) in 1999. Generic FT "synthetic paraffinic kerosene" (SPK) was approved for use in blends up to 50% by vol. with JP-8 in MIL-DTL-83133F[2] in 2008 and in blends with Jet A in ASTM D7566 ("Specification for Aviation Turbine Fuels Containing Synthesized Hydrocarbons")[3] in August 2009 (supported by a Research Report outlining the properties of SPK[4]). The USAF has been very active in the evaluation, demonstration, and certification of FT fuel blends from natural gas and coal. To date, U.S. military aircraft such as the B-52, C-17, and B-1B have been certified for use of a 50/50 (by volume) JP-8/FT blend. Other aircraft (i.e., F-22, KC-135, F-15, C-5, T-38) have already undergone flight tests and are scheduled to be certified on the FT blend in the near future. The next alternative fuel being studied for military/commercial certification is "hydrotreated renewable jet" (HRJ), which is a hydrocarbon aviation fuel produced from animal fat/vegetable oils (triglycerides) by hydroprocessing. This fuel has also been called bio-SPK and "green jet." The ASTM D7566 specification is structured to support various classes of alternative fuels (in Appendices), with HRJ anticipated to be added in the near future as more data become available. It is anticipated that fuel produced from ligno-cellulosic feedstocks will also be added at a future date.

∫Techniques For Chemical And Physical Analysis

The chemical composition and physical properties of the alternative fuels were evaluated to provide improved insight into their performance and to infer potential behavior during implementation. The analyses included evaluation of JP-8 specification properties and non-standard analysis such as Gas Chromatography/Mass Spectrometer (GC/MS), Gas Chromatography with a Flame Ionization Detector (GC/FID), and High Pressure Liquid Chromatography (HPLC).

Emissions Evaluations

Emissions Instrumentation

PM and gaseous emissions were sampled from the engine exit plane using water-cooled probes and transported to the analytical instruments via unheated lines. PM samples were also collected approximately 30 meters downstream of the engine exit to study plume characteristics, particularly PM evolution; however, this summary will focus mostly the engine exit plane emissions. The PM sample stream at the engine exit (mostly non-volatile) was diluted with nitrogen near the probe tip to prevent water condensation, minimize particle losses in the sample lines and prevent saturation of the particle counting instruments. The PM sample line was at room temperature. PM measurements

were corrected for dilution, based on the raw and diluted CO_2 measurements. The PM emissions were characterized using conventional aerosol instruments. A TSI Model 3022A Condensation Particle Counter (CPC) was used to provide a count of particles per unit volume (particle number (PN)), a TSI Model 3936 Scanning Mobility Particle Sizer (SMPS) with a nano-differential mobility analyzer (DMA) to obtain the particle size distribution from 5-150 nm, and a Rupprecht & Patashnick Series 1105 Tapered Element Oscillating Microbalance (TEOM) was used to obtain real-time particle mass emissions. The low particle mass for these engines was below the TEOM detection limits, and thus TEOM data will not be discussed herein. An in-house designed and built smoke machine was used to collect soot samples for determination of the engine Smoke Number per SAE ARP 1179.[4] Gaseous emissions were sampled with undiluted probes and transported through heated lines kept at 150°C per the SAE ARP 1256.[5] Major and minor gaseous species were quantified using an MKS Multi Gas 2030 Fourier Transform Infrared (FTIR) based analyzer and total unburned hydrocarbons were quantified using a CAI 600 Heated Flame Ionization Detector. A non-disperse infrared analyzer measured the CO_2 for the diluted samples from the particle instruments.

Gaseous and PM emissions were sampled using probes located at the engine exit plane. A diagram of the probes that were set up is shown in Figure 1. Three undiluted probes (Gas) were used for smoke number and gaseous emissions measurements. The sample lines were individually connected to a valve box, which directed the sample from a particular probe to the smoke sampler, gas analyzer or to a vent tube. The PM sample was captured with two probes and was diluted at the probe tip (PM) to minimize particle loss and reduced the particle concentration to allowable levels for the CPC.

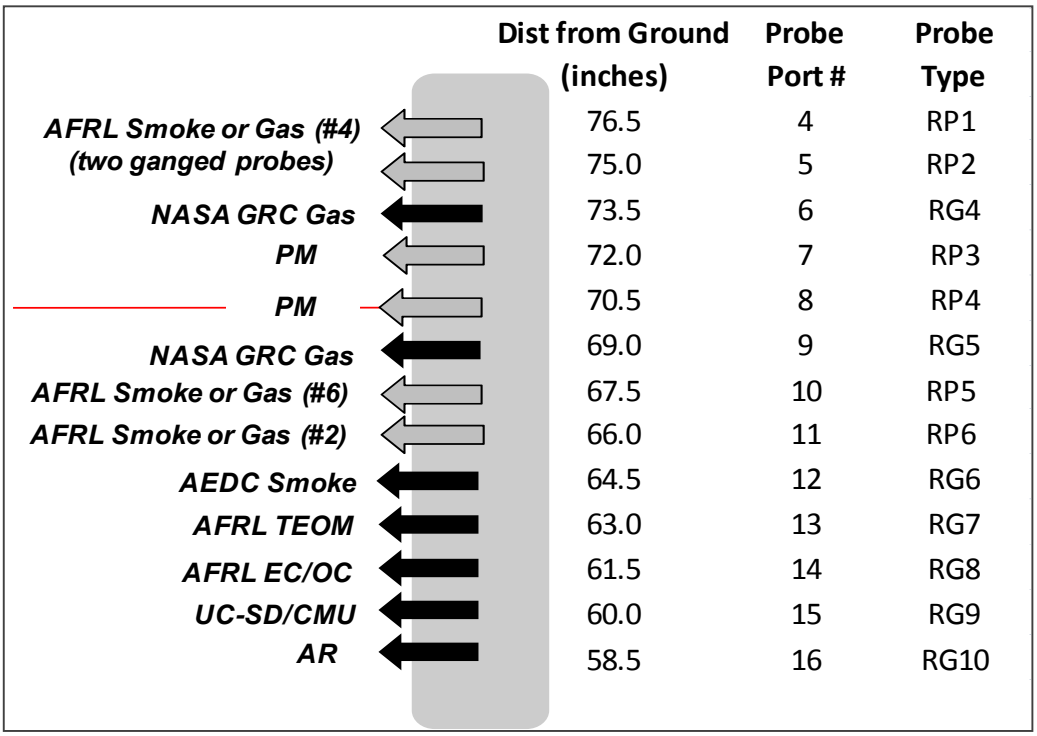

Figure 1. Setup of gas and particle probes. Red line shows engine centerline.

Test Data And Discussion

Chemical And Physical Analysis Of Fuels

Fischer-Tropsch Fuels

The Sasol (FT2 coal-derived) and Shell (FT1 natural gas-derived) fuels were produced via indirect liquefaction using FT synthesis. During indirect liquefaction, the feedstock is partially oxidized either via gasification or steam reforming to produce synthesis gas (carbon monoxide and hydrogen). The synthesis gas (syngas) is fed to an FT reactor where it is converted into higher molecular weight hydrocarbons. The Sasol SPK (also referred to as *Iso*-Paraffinic Kerosene (IPK)) is produced via polymerization of C_3 and C_4 olefins followed by hydrotreating and fractionation to produce a fuel with the desired boiling range.[6] This process results in an SPK with a very high degree of branching. The Sasol fuel was the first synthetic fuel to be approved as a blend feedstock (DEF STAN 91-91 fuel specification).[7] The Shell SPK was produced via the Shell Middle Distillate Synthesis (SMDS) process.[8] The SMDS process produces long-chain paraffins from syngas in multi-tubular fixed bed reactors, followed by hydrocracking, isomerization and fractionation. The Shell SPK fuel is a very narrow-cut kerosene compared to a typical JP-8.

Various physical and chemical properties of the alternative fuels and 50% by vol. blends were evaluated and compared to a specification JP-8. The fuels were sampled from the aircraft wing tank before and after the test series. Selected fuel specification properties for the post-test samples are shown in Table 1. In general, all SPKs evaluated had zero to very low aromatic content, negligible sulfur, lower density and higher hydrogen content compared to conventional JP-8.

Gas chromatograms of JP-8 and the neat FT fuels with the *n*-paraffin peaks identified are shown in Figure 2. As shown in Figure 2 and Table 1, the Shell and Sasol fuels are much narrower than conventional JP-8. Results of the hydrocarbon type analyses, performed using ASTM D6379 and D2425, are shown in Tables 2 and 3 and a comparison of the *n*-paraffin content of the fuels is shown in Table 4. As noted previously, the alternative fuels are primarily comprised of normal and branched paraffins with low or negligible aromatic content. Based on knowledge of the processing techniques employed for the FT-derived fuels, it was expected that these fuels would be solely comprised of paraffinic compounds and free of aromatics. It appears that aromatic compounds found in the Sasol FT fuel was produced during the upgrading steps of the FT products. Improved control of the fuel upgrading process parameters will likely eliminate the production of aromatic compounds in these fuels if deemed necessary. As shown in Table 1, properties of FT/JP-8 blends exhibit a mostly linear dependence with volume percent for all properties except the freeze point for the Shell FT. This non-ideal behavior for the freeze point has been observed with the Shell FT fuel in previous studies.[8]

Table 1. ASTM Specification Tests of Fuels Evaluated

TEST	JP-8	FT Shell (FT1)	FT1 Blend	FT Sasol (FT2)	FT2 Blend
Sulfur (ppm)	1148	19	699	22	658
Aromatics (%vol)	18.6	0	8	0.6	9.1
Distillation					
IBP (deg C)	158	157	156	160	158
10%	176	162	166	167	170
20%	184	164	170	170	175
50%	207	170	183	180	190
90%	248	186	232	208	233
EP	273	206	264	231	263
Residue (%vol)	0.8	0.9	1	1	0.8
Loss (%vol)	0.8	0.9	1	0.9	0.9
Flash Point deg C	46	41	43	42	46
Specific Gravity	0.82	0.74	0.78	0.76	0.79
Freezing Point deg C	-50	-54	-60	<-80	-60
Viscosity	4.7	2.6	3.3	3.6	4.1
Cetane Index	41	58	46	51	45
Hydrogen Content (%mass)	13.6	15.5	14.5	15.1	14.3
Naphtalenes (%vol)	1.6	0	0.8	0	0.8
Heat of combustion (MJ/kg)	43.3	44.4	43.8	44.1	43.8
Olefins (%vol)	0.9	0	0.6	3.8	3.3
Fuel H/C ratio	1.88	2.19	2.02	2.12	1.99

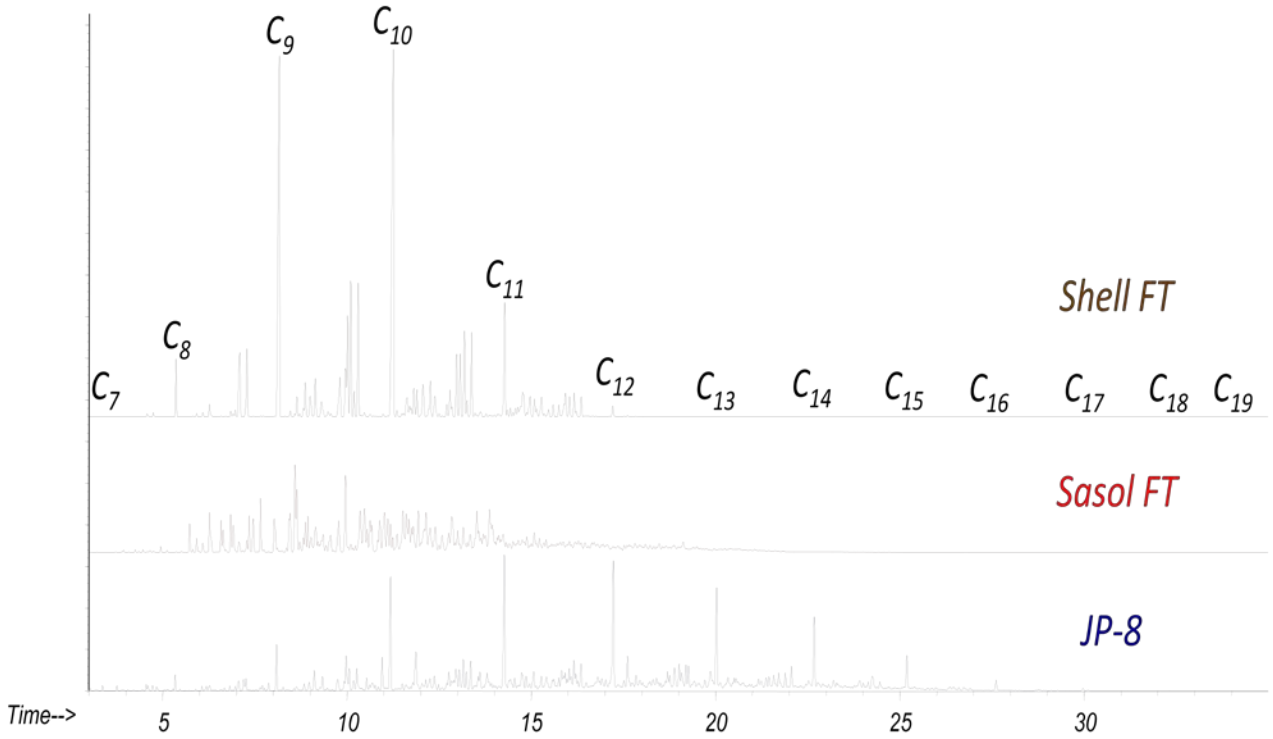

Figure 2. Gas Chromatograms of Alternative Fuels

Table 2. Aromatic Species Analysis by ASTM D6379 for Alternative Fuels

Aromatics (vol.%)	JP-8	Shell FT	Sasol FT
Mono-aromatics	17.6	<0.2	0.4
Di-aromatics	1.1	<0.1	<0.1
Total Aromatics	**18.7**	**<0.2**	**0.4**
Total Saturates	**81.3**	**>99.8**	**99.6**

The Shell FT fuel showed a mild degree of branching and was comprised of a much higher *n*-paraffin concentration than found in typical petroleum-derived jet fuels. High concentrations of long *n*-paraffins can result in poor low-temperature properties; however, the narrow distillation range with relative low carbon numbers (< C_{13}) produces a fuel with a sufficient freeze point.[8] On the contrary, the Sasol fuel had no detectable *n*-paraffins with a sufficiently high degree of branching (e.g., tri- and tetra-methylparaffins). The absence of *n*-paraffins results in an extremely low freeze point for the Sasol SPK.

Table 3. Hydrocarbon Type Analysis by ASTM D2425 for Alternative Fuels

Hydrocarbon Type (vol.%)	JP-8	Shell FT	Sasol FT
Paraffins (normal + iso)	50	> 99	88
Cycloparaffins	31	<1	12*
Alkylbenzenes	12	<0.4	0.4
Indans and Tetralins	5	<0.4	<0.4
Indenes and C_nH_{2n-10}	0.6	<0.4	<0.4
Naphthalene	<0.4	<0.4	<0.4
Naphthalenes	1	<0.4	<0.4
Acenaphthenes	<0.4	<0.4	<0.4
Acenaphthylenes	<0.4	<0.4	<0.4
Tricyclic Aromatics	<0.4	<0.4	<0.4
Total	100	100	100

*D2425 may over predict cycloparaffins for highly branched SPKs

The USAF approved the use of blends of SPK produced via FT-synthesis with conventional JP-8 provided that the required SPK and final blend properties are satisfied as detailed in MIL-DTL-83133F. In addition, ASTM also recently approved the use of FT-derived SPK in commercial Jet A and Jet A-1 as detailed in ASTM D7566-09. Both specifications allow a maximum of 50% by volume of SPK to be blended with conventional jet fuel. Selected properties for both the neat SPKs and the resulting fuel blend for each specification are shown in Table 5.

Table 4. Weight Percent of *n*-Paraffins for Alternative Fuels

n-Paraffins (wt.%)	Carbon No.	JP-8	Shell FT	Sasol FT
n-Heptane	C_7	0.10	0.012	<0.001
n-Octane	C_8	0.34	1.63	<0.01
n-Nonane	C_9	1.21	22.4	<0.05
n-Decane	C_{10}	3.48	25.1	<0.03
n-Undecane	C_{11}	4.24	3.78	<0.02
n-Dodecane	C_{12}	3.71	0.29	<0.01
n-Tridecane	C_{13}	2.84	0.003	<0.01
n-Tetradecane	C_{14}	1.79	0.001	<0.01
n-Pentadecane	C_{15}	0.87	<0.001	<0.005
n-Hexadecane	C_{16}	0.27	<0.001	<0.003
n-Heptadecane	C_{17}	0.089	<0.001	<0.001
n-Octadecane	C_{18}	0.024	<0.001	<0.001
n-Nonadecane	C_{19}	0.008	<0.001	<0.001
Total n-Paraffins		**19.0**	**53.3**	**<0.2**
C_7-C_9		1.7	**24.1**	**<0.06**
C_{10}-C_{13}		14.3	**29.2**	**<0.1**
C_{14}-C_{16}		2.9	**<0.003**	**<0.02**
C_{17}-C_{19}		0.12	**<0.003**	**<0.003**

Table 5. Comparison of Selected Neat SPK and Blend Properties in US Military and Commercial Fuel Specifications

	MIL-DTL-83133F		ASTM D7566-09	
	Min	Max	Min	Max
Requirements for Neat SPK				
Aromatic (vol %)	—	1.0	—	0.5
Density @ 15°C (kg/L)	0.751	0.840	0.730	0.770
Flash Point (°C)	38	68	38	—
Freezing Point (°C)	—	-47	—	-40
Cycloparaffin (mass %)	—	—	—	15
Distillation Temp (°C)				
10% recovered	157	205	—	205
50% recovered	168	229	—	Report
90% recovered	183	262	—	Report
Final	—	300	—	300
T90-T10 (°C)	—	—	22	—
Requirements for Petroleum and SPK Blend				
Aromatic	8.0	25.0	8.0	—
T50-T10 (°C)	15	—	15	—
T90-T10 (°C)	40	—	40	—

The general properties for the neat SPKs are similar for both specifications as each limit the maximum aromatic content while ensuring a minimum volatility range. The major difference between the SPK specifications is the allowable fuel density range, where the military minimum limit is 0.751 kg/L while the commercial is 0.730 kg/L. It should be noted that the Shell FT fuel did not satisfy the minimum military SPK density limit and barely satisfied the minimum volatility distribution. These properties will need to be addressed in subsequent formulations to meet the required fuel specifications. Both blend specifications require a minimum aromatic content of 8.0% by volume. This limit is specified to ensure that required "Fit-for-Purpose" (FFP) properties are maintained for the blends. Research is on-going to better define this lower limit.

Engine Emissions

CFM56 Particle Number Emission Index

JP-8 Fuel

The average particle number emission indices (EI_n) (number of particles per kg-fuel) for each engine burning JP-8 for the 1 m sampling location are shown in Figure 3. EI_n values (uncorrected for line losses) ranged between 3.0e14 – 1.1e15 particles/kg-fuel (95% confidence level). The EI_n for both engines are observed to follow the same trends as a function of engine power setting, with statistically significant higher values for the left engine at 40 and 60% power. EI_n data for emissions collected at 30 m are shown in Figure 4. As observed, the trends as a function of power setting are significantly different than for the 1 m sampling as the EI_n are relatively constant at engine powers above 7%, while for the 1 m measurements EI_n increased as a function of power for engine power above 45%.

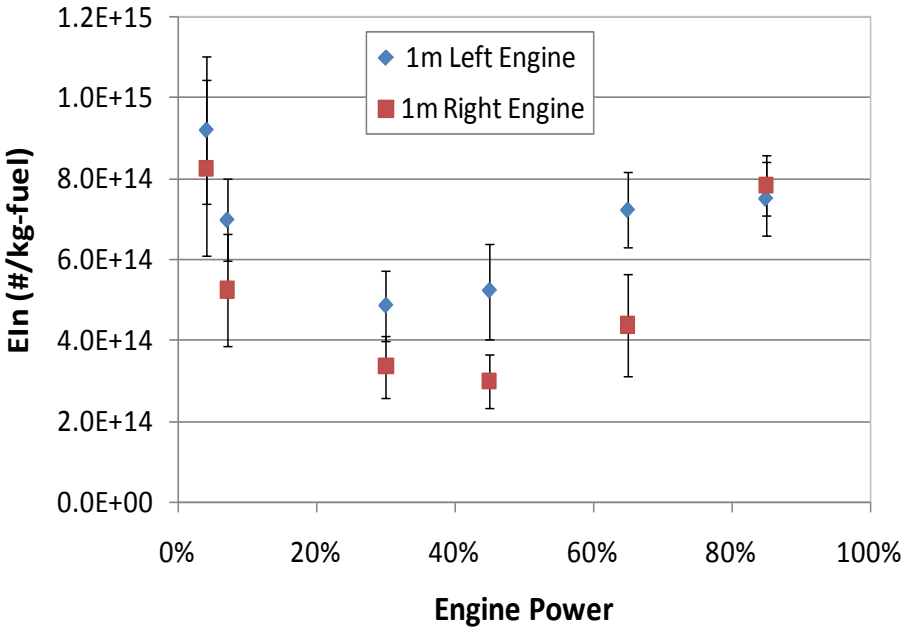

Figure 3. Particle number EI (not corrected for line losses) measured at 1 m from engine exit plane for CFM56 engines operated with JP-8

Although the actual particle number was lower at the 30 m location because of the natural sample dilution, the EI_n were 5-15X higher than at 1 m due to the transformation of volatile compounds (i.e., hydrocarbons and sulfur species) into particles as the plume cooled with surrounding air. This difference in EI_n between PM at 1 m and 30 m was significantly higher at low-engine power because of the higher concentration of volatile species.

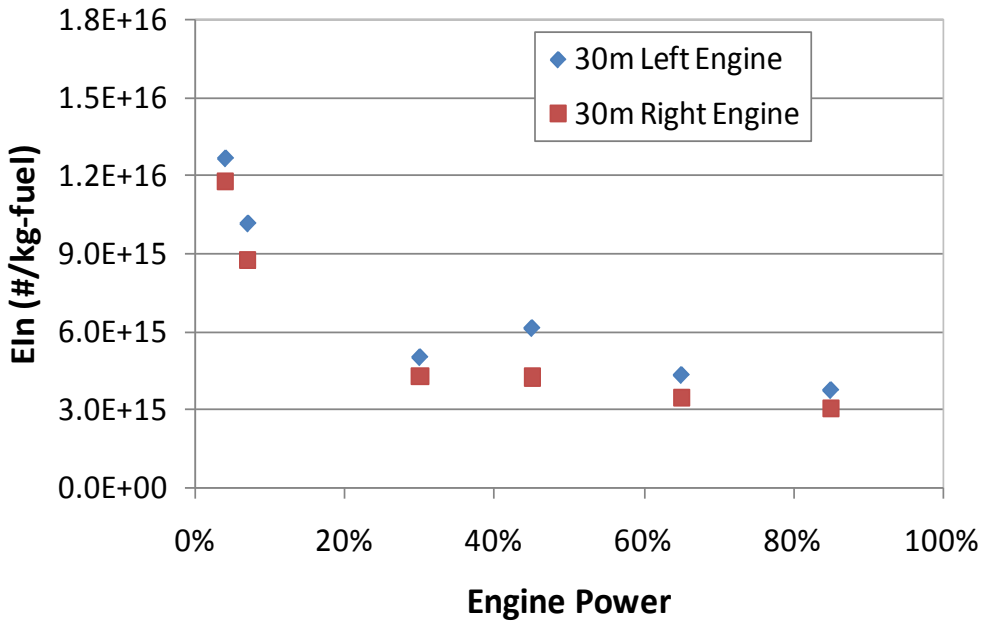

Figure 4. Particle number EI (not corrected for line losses) measured at 30 m from engine exit plane for CFM56 engines operated with JP-8

FT Fuels

EI_n data at the 1 m probe for the engine burning the Sasol (FT2), Shell (FT1) and baseline JP-8 fuels are shown in Figure 5. Significantly lower particulate emissions are observed with the FT fuels compared to JP-8. Nearly two orders of magnitude lower EI_n were observed at 4-45% engine power for both fuels. Smaller relative differences were observed at higher power. These results are consistent with previous measurements on T63, T701C and research combustors operated on neat FT fuels.[9-11] Lower EI_n are observed for most cases with the Shell FT compared to the Sasol FT, however, the differences are significantly lower between the FT fuels than between JP-8 and the FT fuels. Similar to test results on JP-8, EI_n measurements at 30 m relative to 1 m were significantly higher (up to 80X) at low engine power. This is noteworthy considering the FT fuels were free of sulfur compounds, which are considered a major contributor to volatile PM. This suggests that volatile hydrocarbons may have as much or higher contribution to volatile PM formation as sulfur species. Further research in this area is warranted.

Average EI_n data for all engine settings for the three neat fuels as a function of fuel end point (EP) are shown in Figure 6. The fuel EP is the defined as the temperature at which all distilled fuel is recovered (see Table 1). No clear trend of EI_n at each power setting as

a function of fuel EP is observed. However, it is clear that the higher fuel EP (JP-8) shows a more condensed range of EI_n than the two FT fuels, which show a wider range of EI_n values. This is a limited set of data; therefore, additional research with other non-aromatic alternative jet fuels with different EP is warranted to verify the impact and trends of fuel EP on engine EI_n and soot production propensity.

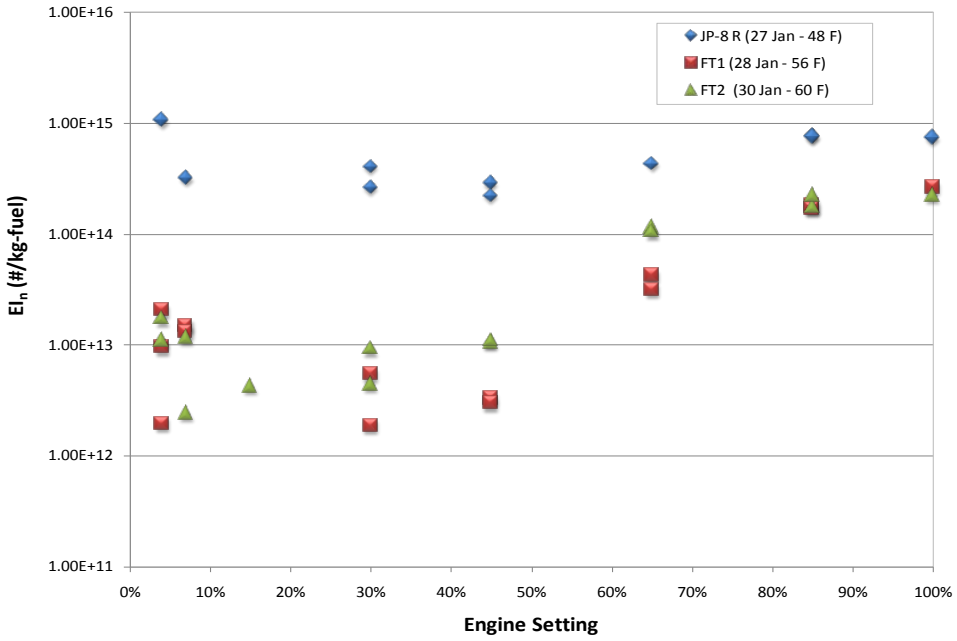

Figure 5. Particle number EI (not corrected for line losses) measured at 1 m from engine exit plane for CFM56 engines as a function of engine power and fuel type

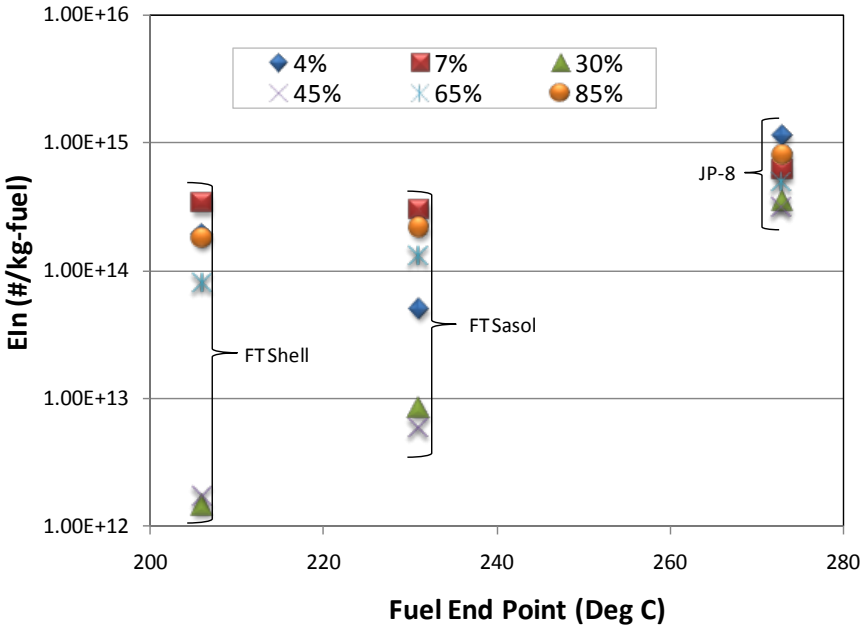

Figure 6. Particle number EI (not corrected for line losses) measured at 1 m from engine exit plane for CFM56 engines as a function of engine power and fuel end point

Particle size distribution data (acquired with the SMPS) show single mode lognormal distribution trends for all fuels and conditions considered when sampling at the 1 m probe position. Shown in Figure 7, are the size distribution curves for the 65% engine setting for JP-8 operation at both 1 m and 30 m locations. Dual mode distributions are evident in the 30 m samples with the original 1 m peak, at approximately 34 nm, and a new nucleation peak, at approximately 13 nm. The particles formed due to nucleation chemistry in the exhaust plume result in the significantly higher total EI_n as discussed previously. The average particle diameter for the 1 m data for each fuel as a function of engine setting are displayed in Figure 8. Larger mean particle diameters are observed for the neat FT fuels at the 4 and 7% settings, while smaller particles were produced with the FT fuels at the higher power settings. No clear trend was observed for engine conditions between 30-65%. These results disagree with previous research, which has shown consistently smaller particles for all engine powers with FT fuels relative to JP-8.[9-11] Sampling differences (e.g. heated vs. unheated sampling lines) may explain the discrepancies of these observations.

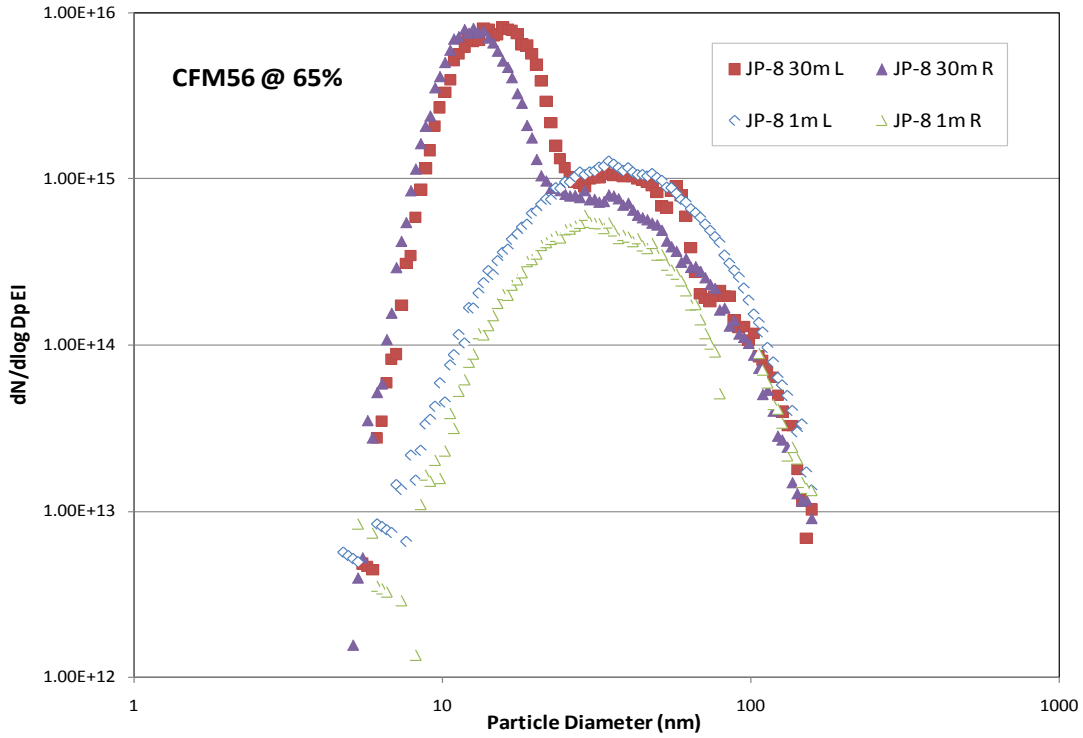

Figure 7. Particle size distribution sampling at 1 m and 30 m

Engine tests conducted at different ambient temperatures (e.g. 30°F morning 60°F afternoon) show significantly higher EI_n at lower ambient temperatures. This behavior was consistent with all fuels tested and was mostly prevalent at lower engine power. Poorer fuel vaporization and/or condensation of volatile species may explain the higher concentration of particles. Average CFM56 engine smoke numbers for settings of 85% and 100% power for the three neat fuels are shown in Figure 9. Smoke numbers at lower

engine settings with the FT fuels were below the measurable detection limit and not reported here. Average reductions of ~75% are observed at 85% and ~ 60% for 100% power for the FT fuels compared to JP-8. Consistent with EI_n data, the Shell FT produced slightly lower SN than the Sasol FT.

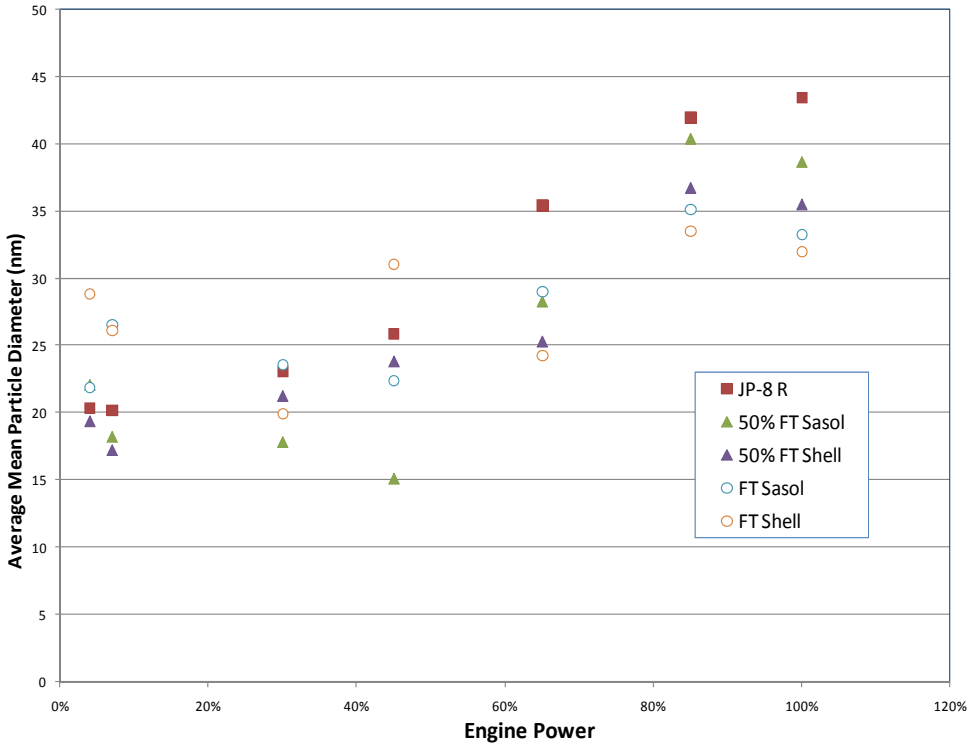

Figure 8. Average mean particle diameter for JP-8 and alternative fuels

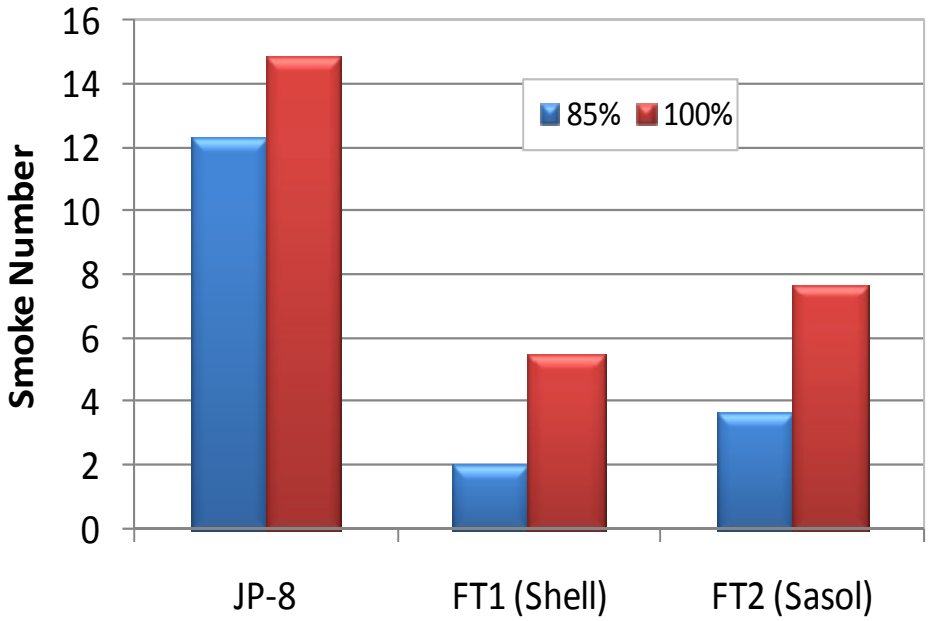

Figure 9. CFM56 engine smoke numbers at 85% and 100% power for neat fuels

Elemental and organic carbon (EC and OC) mass were estimated by performing off-line programmed temperature oxidation of collected soot samples using a LECO Multiphase Carbon Analyzer. Elemental carbon mass EI (oxidizes at temperatures > 350°C) for the 85% engine setting for the engine operating with the neat fuels and blends are shown in Figure 10. As shown, the EC mass EI was significantly lower (up to 70%) with the FT fuels (both neat and blended). Negligible differences in EC mass EI were observed between the FT fuels. The total mass EI and relative volatile fraction for the fuels are shown in Table 6. Significantly lower total (~65%) and organic (volatile) carbon mass were generated with FT fuels. The lower volatile fraction of JP-8 relative to the FT and FT blends is mainly due to the significantly higher EC production with JP-8. It was observed that at 100% power, OC/EC fractions of the fuels are similar to the 85% power; however, the difference in total carbon between JP-8 and the FT fuels is substantially lower (only 20% compared to 65% lower at 85% power).

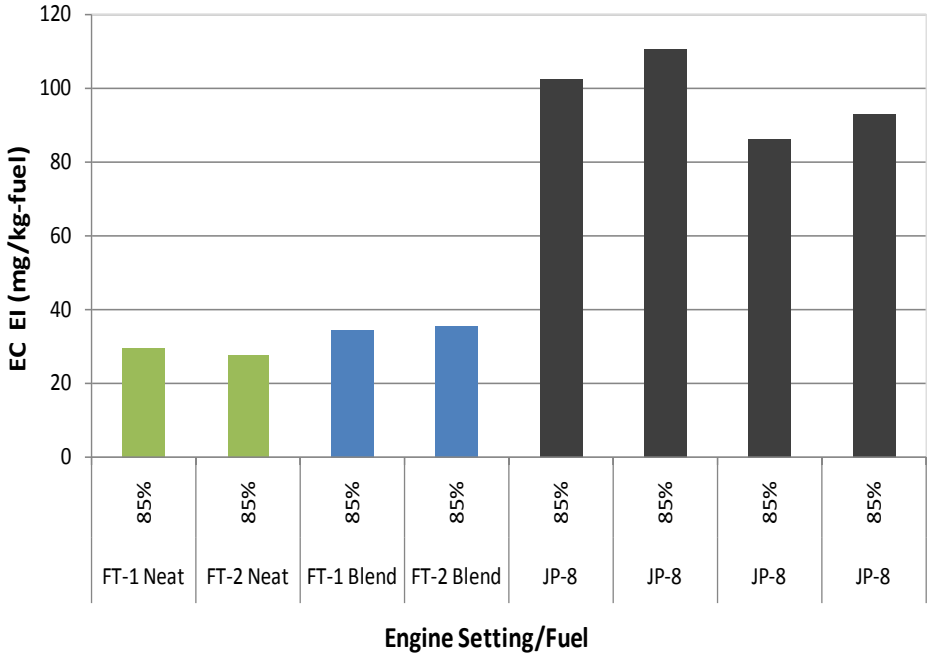

Figure 10. Elemental Carbon Emission Index for CFM56 Engine at 85% Power

Table 6. PM Mass via Carbon Burn-off Methods – CFM56 at 85% Power

Fuel	Total PM Mass (mg/kg-fuel)	EC Mass (mg/kg-fuel)	Volatile Fraction
JP-8	152	98	35%
FT Blends	60	35	41%
FT Neat	52	29	44%

Gaseous Emissions

The average impact of the FT fuels on CO and NO_x EI are shown in Figures 11 and 12. The error bars represent one standard deviation of an average of seven measurements for

the FT fuels and 20 for JP-8. It is observed that the CO EI for all engine conditions were very similar between the FT fuels and JP-8. Slightly lower NO_x EI were observed with the Shell FT at the 100% power condition, while minimum differences are shown between fuels for most conditions. As anticipated, lower sulfur emissions (not shown) were produced with the FT fuels relative to JP-8 which is attributed directly to the total sulfur content in the fuels.

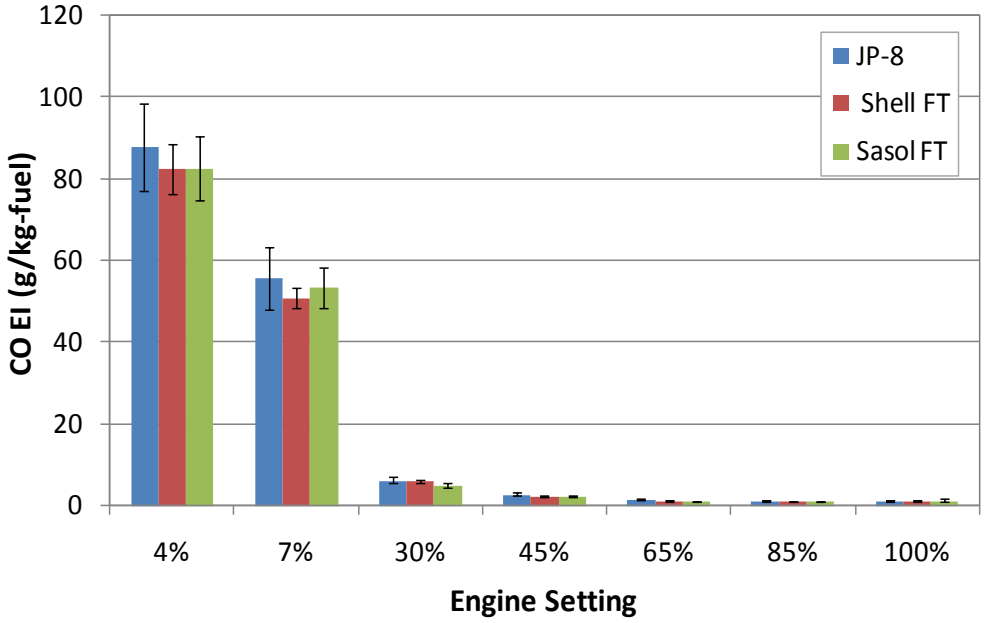

Figure 11. CO EI for CFM 56 Engine operated with JP-8 and two FT fuels

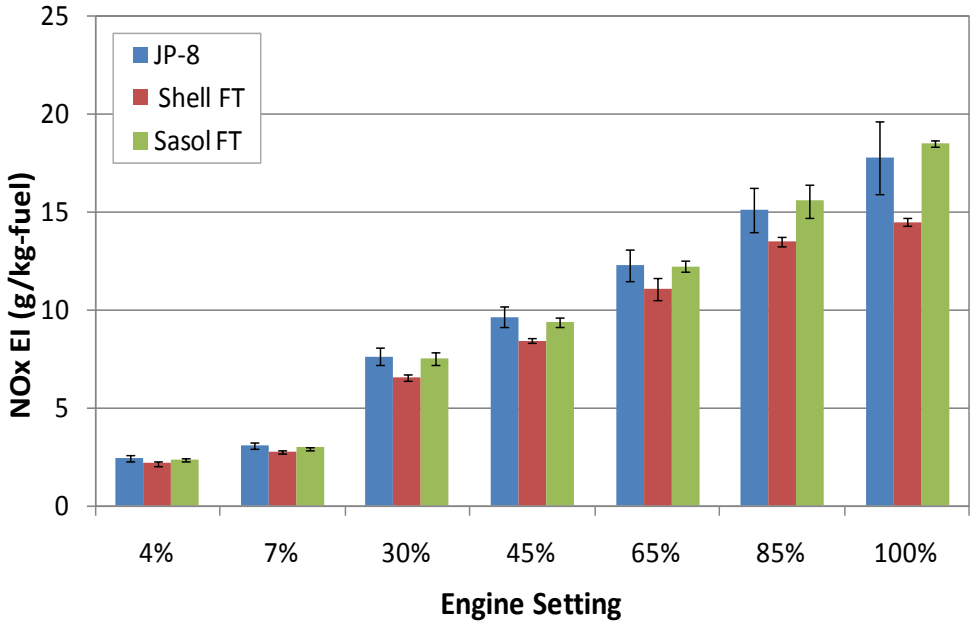

Figure 11. NO_x EI for CFM 56 Engine operated with JP-8 and two FT fuels

Summary
The gaseous and particulate matter emissions from a CFM56 engine operating with two FT fuels and JP-8 were evaluated. Detailed chemical analysis of the alternative fuels show that they are mainly composed of paraffins with negligible or no aromatic or sulfur species. Emissions data demonstrate that the two FT fuels produced significantly lower soot emissions, which is consistent with results from previous testing on research combustors and turbine engines. Negligible differences in gaseous emissions between the FT and JP-8 fuels were observed. Significant volatile particle nucleation occurred in the plume with both FT fuels and JP-8, which highlights the importance of the organic fraction on volatile particle emissions. In general, the impacts of these fuels on PM emissions agree with previous measurements on vastly different engine types, which increases confidence that similar results/trends will be observed in other turbine engines.

Acknowledgements

The authors gratefully acknowledge the assistance of Joe Mantz from UDRI and Tom Greene of Taitech Inc. during the engine tests. Appreciation is also extended to Linda Shafer, Rhonda Cook, and David Brooks of UDRI for the analysis of fuel and soot samples. The efforts of UDRI were supported by the USAF under contract F33615-03-2-2347.

References

1. Intergovernmental Panel on Climate Change Special Report, "Summary for Policymakers – Aviation and the Global Atmosphere," 1999.
2. MIL-DTL-83133F, "Detailed Specification, Turbine Fuel, Aviation, Kerosene Type, JP-8 (NATO F-34), NATO F-35, and JP-8+100 (NATO F-37)," released 11 April 2008.
3. ASTM D7566-09, "Standard Specification for Aviation Turbine Fuel Containing Synthesized Hydrocarbons," approved 1 Sept 2009.
4. SAE 1970, "Aircraft Gas Turbine Exhaust Smoke Measurement," SAE Aerospace Recommended Practice ARP 1179, SAE, Warrendale, PA USA, 1970.
5. SAE 1971, "Procedure for the Continuous Sampling and Measurement of Gaseous Emissions from Aircraft Turbine Engines," SAE Aerospace Recommended Practice ARP 1256, SAE, Warrendale, PA USA, 1971.
6. Moses, C.A., Stavinoha, L.L. and P. Roets, "Qualification of SASOL Semi-Synthetic Jet A-1 as Commercial Jet Fuel," *Report No. SwRI 8531*, Southwest Research Institute, San Antonio, TX, 1997.
7. Defense Standard 91-91, Turbine Fuel, Aviation Kerosene Type, Jet A-1 NATO Code: F-35
   Joint Service Designation: AVTUR, released 8 April 2008.
8. Bauldreay, J.M., Heins, R.J. and J. Smith, "Synthetic Jet Fuels and Their Role in the Future," *Proceedings of the 8th International Conference on Stability and Handling of Liquid Fuels*, Steamboat Springs, CO, 2003.
9. Corporan, E., DeWitt, M., Klingshirn, C., Striebich, R, S., Cheng, M.D., "Emissions Characteristics of Military Helicopter Engines Fueled with JP-8 and a Fischer-Tropsch Fuel," Accepted in Journal of Propulsion and Power, 2010.

10. Kahandawala, M., DeWitt M., Corporan, E., Sidhu, S., "Ignition and Emission Characteristics of Surrogate and Practical Jet Fuels", Energy & Fuels, 2008, 22 (6), 3673-3679
11. Corporan, E., Edwards, T., Shafer, L., DeWitt, M.J., Klingshirn, C., Zabarnick, S., West, Z., Striebich, R., Graham, J., Klein, J., "Chemical, Thermal Stability, Seal Swell and Emissions Characteristics of Jet Fuels from Alternative Sources," *Proceeding of the 11th International Conference on Stability and Handling of Liquid Fuels,* Prague, Czech Republic, 2009.

APPENDIX H: Concentrations and Physical Properties of Exhaust Particles from Aircraft Engines Burning Standard and Synthetic Fuels: AAFEX Results

Luke D. Ziemba, Andreas J. Beyersdorf, Charles Hudgins, David Liscinsky, K. Lee Thornhill, Edward L. Winstead, and Bruce E. Anderson

NASA Langley Research Center
Hampton VA 23662

1.0 Summary

The NASA Alternative Aviation Fuel Experiment (AAFEX) was conducted in January 2009 at the Dryden Aircraft Operations Facility (DAOF) in Palmdale, California to assess the impact of alternative jet fuels on aircraft engine and auxiliary power unit (APU) emissions. For the engines, five different fuels were tested under variable atmospheric conditions. The fuels included two synthetic kerosenes manufactured from natural gas (FT-1) and coal (FT-2) feedstocks using the Fischer-Tropsch process. This report examines the particle emissions from the NASA DC-8's two inboard, CFM-56 engines and establishes how exhaust particle number, size, mass and composition change as a function of fuel composition, plume age and ambient temperature. We also contrast particle emission parameters measured in exhaust from the APU as it burned pure FT-2 and standard JP-8 fuel. For the aircraft and APU, both black carbon and volatile aerosol emissions were substantially reduced from synthetic fuels compared to standard jet fuel.

2.0 Background

Alternative sources of aviation fuel are being investigated as a means of increasing domestic production, increasing fuel security, and stabilizing prices. Research efforts have primarily focused on developing "drop-in" replacement fuels that meet ICAO (International Civilian Aviation Organization) specifications and can be burned in aircraft with little or no modification to the propulsion or fuel storage and delivery systems. Although several viable fuels have been produced, very few studies have been conducted to evaluate the effects of the fuels on gas turbine engine performance and emissions. The few studies that have been conducted used military engines and evaluated fuel blends (Corporan et al., 2007; Cheng et al., 2009). Additionally, absolute emissions factors from engine manufacturer-sponsored testing are not publically available (Timko et al., 2010). Thus, additional testing is required to fully characterize alternative-fuel emissions from aircraft in various environmental conditions for incorporation into future air quality and climate models.

AAFEX was designed to help fill this information gap. A multi-agency, NASA-sponsored project, AAFEX was conducted at the DAOF in January 2009 and used the agency's DC-8, which is equipped with four CFM-56-2C engines, to evaluate alternative fuel impacts on aircraft operation and emissions. AAFEX also sought to examine dynamic plume chemistry and volatile aerosol formation as a function of fuel composition and ambient conditions. A total of five fuels were tested: standard JP-8, two synthetic fuels produced from natural gas (FT-1) and coal (FT-2) using the Fischer-Tropsch reformulation process, and two blends formed by mixing equal volumes the FT fuels and JP-8. The pure Fischer Tropsch (FT) fuels were essentially free of aromatic

hydrocarbons and sulfur impurities (Cheng et al., 2009) and were thus expected to produce much lower soot and sulfate aerosol emissions. The overall test involved characterizing the trace-gas and aerosol components in exhaust samples collected at three distances (1 m, 30 m, and 145 m) behind the NASA DC-8 aircraft as its CFM-56 engines burned each of the fuels and operated at power levels ranging from ground idle to full takeoff thrust. For each pure fuel (JP-8, FT-1 and FT-2), duplicate tests were conducted in early morning and afternoon to observe changes in emission characteristics as a function of ambient temperature. The tests also included examining JP-8 and FT-2 emissions from the aircraft's Auxiliary Power Unit (APU) operating under varying loads. In all, 13 engine and 3 APU tests were conducted, encompassing a total of 34 and 3 hours of engine and APU run-time, respectively.

The NASA Langley Research Center Aerosol Research Group (LARGE) participated in AAFEX by providing both project leadership and by conducting particle characterization studies. Our group operated an extensive suite of instruments in the NASA truck and in a community sampling trailer. This report describes the LARGE experiment and examines the characteristics of particulate matter (PM) emissions from the DC-8 as a function of fuel type and ambient conditions. A detailed description of the LARGE instrument suite and sampling system is included, and emission indices and calculated particle parameters are discussed. Results from a control test comparing JP-8 emissions from the DC-8's two inboard engines are reported and are discussed with respect to results from the previous APEX-1 (Aircraft Particle Emissions Experiment) campaign. Effects of fuel type on the non-volatile particle emissions are examined. Lastly, the formation and growth of volatile particles in engine exhaust as a function of fuel type and ambient temperature is discussed and APU emission tests results are presented.

3.0 Experimental Methods

3.1 Testing Protocol

DC-8 emissions testing was performed on the two inboard engines. A schematic of the test setup is shown in Figure 1. The left inboard engine (#2) was supplied JP-8 fuel and was used as a standard for direct comparison with emissions results from alternative fuels and will be referred to as the "control engine." The right inboard engine (#3) was supplied alternative fuels and will be termed the "test engine." The rationale for this approach was to use emission data from the control engine for evaluating fuel-related

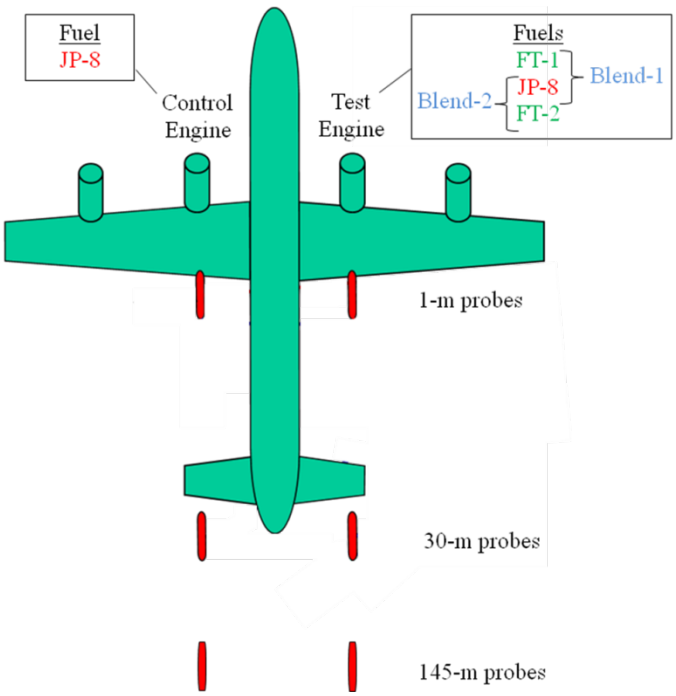

Figure 1. Diagram of DC-8 testing setup. Samples were taken from 1-, 30-, and 145-m probes mounted behind both the control engine (left, inboard), which burned only JP-8 fuel, and the test engine (right, inboard), which burned JP-8 and alternative fuels. Probe distances are not drawn to scale.

changes in the test engine emissions, as well as to collect a large data set for evaluating the role of ambient conditions on both gas- and particle-phase emissions. The "test engine" also was operated with JP-8 fuel in order to determine emission differences between the two engines. Test conditions for each sampling test are presented in Table 1. Included are the test objectives, fuel-type for each engine, engine start and stop times, and the engine power settings at which data were taken.

Samples were transported from each of the probe tips shown in Figure 1 to analytic instrumentation designed specifically for characterization of aerosol physical and chemical properties. Details regarding the sample distribution system are found in the AAFEX overview document (Anderson et al., 2010). Briefly, a "community" sampling manifold was connected through valves to each of the 1- and 30-m inlet probes and was used to deliver samples to each of the participating groups. A separate line was installed to deliver samples to the test engine 30-m inlet so that the instrumentation could make continuous PM measurements to compare with similar measurements being logged in a ruggedized enclosure (known as the "death box") mounted directly behind the inlet in order to assess sampling line particle loss (see Appendix P for more details on line loss experiments).

Table 1. AAFEX Tests

Test No.	Test Date	Test Objective	Aircraft Engine	Engine Fuel	Engine Start[1]	Engine Shutdown[1]	Sampled Thrust Levels (%)
1	26-Jan	Equipment Shakedown	control	JP-8	14:01	15:00	4, 45
			test	JP-8	14:03		4, 7, 30, 45, 65, 85, 100
2	26-Jan	Sampling-probe Mapping	control	JP-8	16:02	19:20	4, 7, 30, 45, 65, 85
			test	JP-8	16:04		4, 7, 30, 45, 65, 85, 100
3	27-Jan	JP-8, warm conditions	control	JP-8	12:38	15:46	4, 7, 30, 45, 65, 85
			test	JP-8	12:43		4, 7, 30, 45, 65, 85, 100
4	28-Jan	JP-8, cold conditions	control	JP-8	5:59	9:28	4, 7, 30, 45, 65, 85
			test	JP-8	6:03		4, 7, 30, 45, 65, 85, 100
5	28-Jan	FT-1, warm conditions	control	JP-8	12:35	15:54	4, 7, 30, 45, 65, 85
			test	FT-1	12:39		4, 7, 15, 30, 45, 65, 85, 100
6	29-Jan	FT-1, cold conditions	control	JP-8	5:41	8:36	4, 7, 30, 45, 65, 85
			test	FT-1	5:45		4, 7, 15, 30, 45, 65, 85, 100
7	29-Jan	JP-8 Fuel	APU	JP-8	12:34	13:57	EGT = 350, 610 °C
8	30-Jan	FT-1/JP-8 Blend	control	JP-8	6:14	9:38	4, 7, 30, 45, 65, 85
			test	Blend-1	6:19		4, 7, 15, 30, 45, 65, 85, 100
9	30-Jan	FT-2, warm conditions	control	JP-8	10:48	13:41	4, 7, 30, 45, 65, 85
			test	FT-2	10:51		4, 7, 15, 30, 45, 65, 85, 100
10	31-Jan	FT-2, cold conditions	control	JP-8	5:57	7:03	4, 7, 30, 45, 65, 85
			test	FT-2	5:42		4, 7, 15, 30, 45, 65, 85, 100
11	31-Jan	FT-2/JP-8 Blend	control	JP-8	8:28	10:59	4, 7, 30, 45, 65, 85
			test	Blend-2	8:31		4, 7, 15, 30, 45, 65, 85, 100
12	31-Jan	JP-8, warm conditions	control	JP-8	12:49	15:18	4, 7, 30, 45, 65, 85
			test	JP-8	12:52		4, 7, 15, 30, 45, 65, 85, 100
13	2-Feb	JP-8, cold conditions	control	JP-8	7:12	8:38	4, 7, 30, 45, 65, 85
			test	JP-8	7:14		4, 7, 15, 30, 45, 65, 85, 100
14	2-Feb	Line-loss testing	control	JP-8	9:37	12:07	4, 7, 30, 45, 65, 85
			test	JP-8	9:40		4, 7, 15, 30, 45, 65, 85, 100
15	2-Feb	APU, JP-8	APU	JP-8	14:12	15:23	EGT = 345, 365, 475, 550, 555, 610 °C
16	2-Feb	APU, FT2	APU	FT-2	15:40	16:37	EGT = 360, 475, 550, 555, 620 °C

[1]Local, Pacific Standard Time

For the 145-m probe, the velocity of the engine exhaust plume was insufficient to keep the sampling probe in the plume as cross winds would shift the plume away from the probe. In order to have sufficient sampling times, sampling was performed from a lagged aerosol grab (LAG) chamber that captured air samples at two to three minute intervals for subsequent sampling. The LAG chamber was installed directly behind the test engine at the 30-m probe. Three-way solenoid valves isolated the LAG chamber from the continuous flow line during instrument sampling. When a plume was detected from the 145-m probe (determined by a spike in particle number concentration), the chamber was

flushed with sample air and then isolated for analysis. When not in use, bypass flow maintained a constant flow through the LAG sampling system.

The initial test (1) was conducted to determine whether the sampling system was properly installed and to evaluate sample dilution and delivery procedures (Table 1). Data from this test were not finalized and hence are not presented in the sections below; all other Langley data were quality assured, finalized and submitted to the AAFEX project archive. Test 2 included sampling from multiple inlet probes on each of the 1-m rakes to map the distribution of emissions across the control- and test-engine exit planes to establish which of the six possible probes on the rakes were positioned in the core exhaust flow to provide the most representative particle emission factors. Engine tests 3 through 6 and 8 through13 were performed to examine fuel and ambient temperature effects on emission parameters. Tests 7, 15, and 16 were performed to specifically address emissions from the APU. Test 14 focused on sampling issues, and the primary focus was on particle loss to the walls of the inlet tubing. Results from this test are discussed in Appendix P of this document.

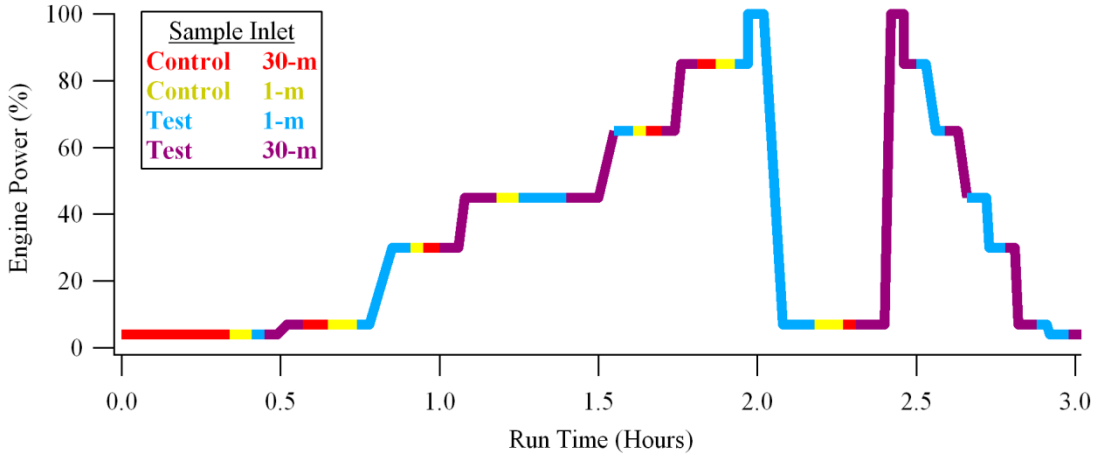

Figure 2. Example experiment matrix for the AAFEX emission characterization tests

A typical sampling procedure for AAFEX emissions testing is provided below and is presented in Figure 2. At engine start, the community sampling system was typically connected (via a valving system that is described in the AAFEX overview report) to the control-engine 30-m inlet probe for characterization until the engine was spun-up and had stabilized at ground idle (4%). The sampling system was then connected to the test-engine 30-m inlet to characterize the emissions through its start-up sequence. Once both engines were stable at 4% power, the valving box for the community manifold (located in the Missouri University for Science and Technology trailer) was again set to draw air from the control engine, 30-m probe and the beginning of the initial test point was recorded. After approximately three minutes, the valves were set to draw sample from the control-engine, 1-m inlet probe and, after emissions had stabilized (based on CO_2 mixing ratio), three minutes of data collection ensued. After this pattern was completed for the test engine at 1 m and 30 m, the next power setting was requested and the sampling process repeated. Data were typically acquired for both engines at 4, 7, 30, 45,

65, and 85% of maximum revolutions per minute (RPM) and additionally at 15 and 100% thrust for the test engine. To obtain better sampling statistics for the test-engine emissions and after a brief intermission at 7% thrust, the power sequence was repeated in reverse order, starting at 100% thrust and stepping downward through the power points until ground idle was reached.

3.2 Instrumentation

A robust suite of instrumentation was deployed for AAFEX to characterize aerosol chemical and physical properties. The specific parameters measured by these instruments along with their precisions and accuracies are listed in Table 2; brief descriptions are provided below. For completeness, the full instrument suite is introduced, but only a subset of measurements are analyzed and discussed in this report. AAFEX provided a helpful test setting for the development of instrumentation not considered in this report. Figure 3 shows a diagram of the Langley Research Center (LaRC) aerosol instrument suite that was used to characterize PM in samples drawn from the community-sampling manifold. Figure 4 shows a diagram of the LaRC aerosol instruments that sampled from the test engine 30-m inlet probe. Figure 5 shows a plumbing diagram for the LaRC aerosol instruments installed in the 145-m trailer.

Table 2. In Situ Aerosol Instrumentation

Measured Parameter	Instrument	Measurement Range	Response (seconds)	Precision
Nonvolatile CN Particle Number	TSI 3022A	$D_p > 0.01$ µm	1	20%
Total CN Particle Number	TSI 3775	$D_p > 0.004$ µm	1	20%
Aerosol Size Distribution	DMA w/TSI 3776	D_p: 0.009 - 0.310 µm	60	5% size, 25% conc.
Nonvolatile Aerosol Size Distribution	DMA w/TSI 3025	D_p: 0.009 - 0.310 µm	60	5% size, 25% conc.
Aerosol Size Distribution	TSI EEPS	D_p: 0.006 – 0.295 µm	1	20%
Cloud Condensation Nuclei	CCN	D_p: 0.02 – 1.0 µm	1	10%
Aerosol Size Distribution	UHSAS	D_p: 0.06 – 1 µm	1	5% size, 20% conc.
Aerosol Size Distribution	MetOne OPC	D_p: 0.3 – 10 µm	1	20% size, 25% conc.
Soluble Aerosols	PILS w/IC	> 10 ng m^{-3}	180	20%
Soluble Organic Aerosols	PILS w/TOC	0.03 ppb (liquid)	4	20%
Black Carbon Mass	MAAP	>100 ng m^{-3}	1	12%
Black Carbon Mass	SP2	> 1 µg m^{-3}	1	20%
Black Carbon Mass	PASS-3	40 ng m^{-3}	1	20%
NDIR CO_2 mixing ratio	LI-COR	0 – 10000 ppm	1	0.5%
Total Particle-Bound PAH	PAS 2000	~ 0.3 – 1 g m^{-3}	10	20%
Particulate SO_4^{2-}	Thermo SPA	> 0.50 μ g m^{-3} sulfate	1	10%
Total Aerosol Length	TSI EAD	0.01 – 2500 mm cm^{-3}	1	10%

Instruments highlighted in bold are the focus of this report. An explanation of issues associated with unhighlighted instrumentation is given in Section 3.6.

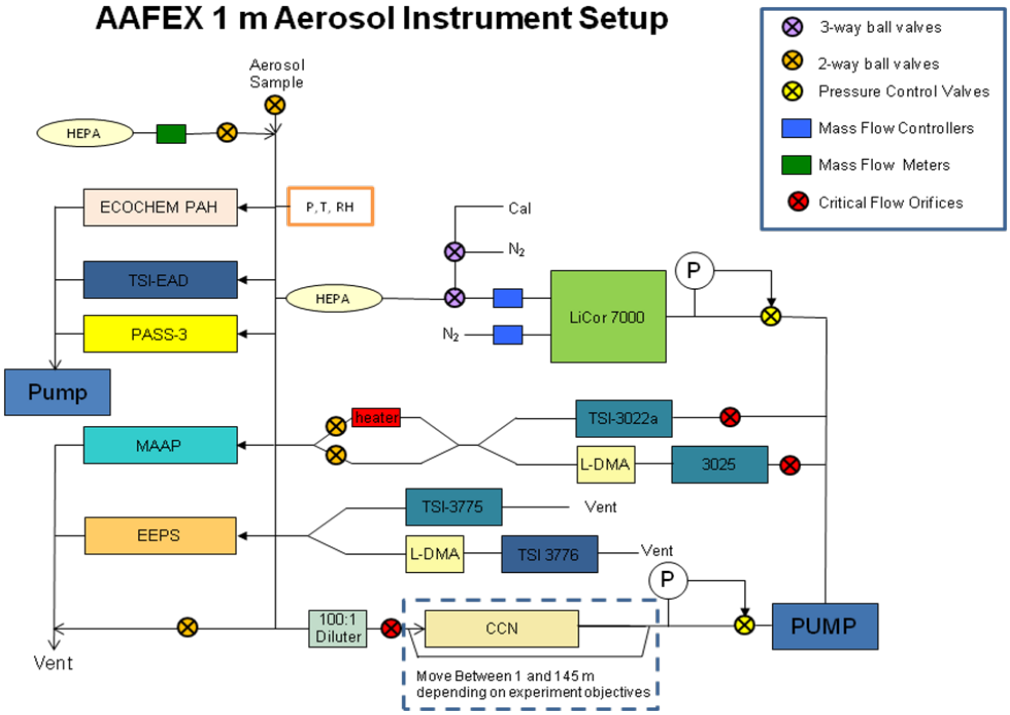

Figure 3. Plumbing diagram for instruments on the common aerosol inlet line at 1 m

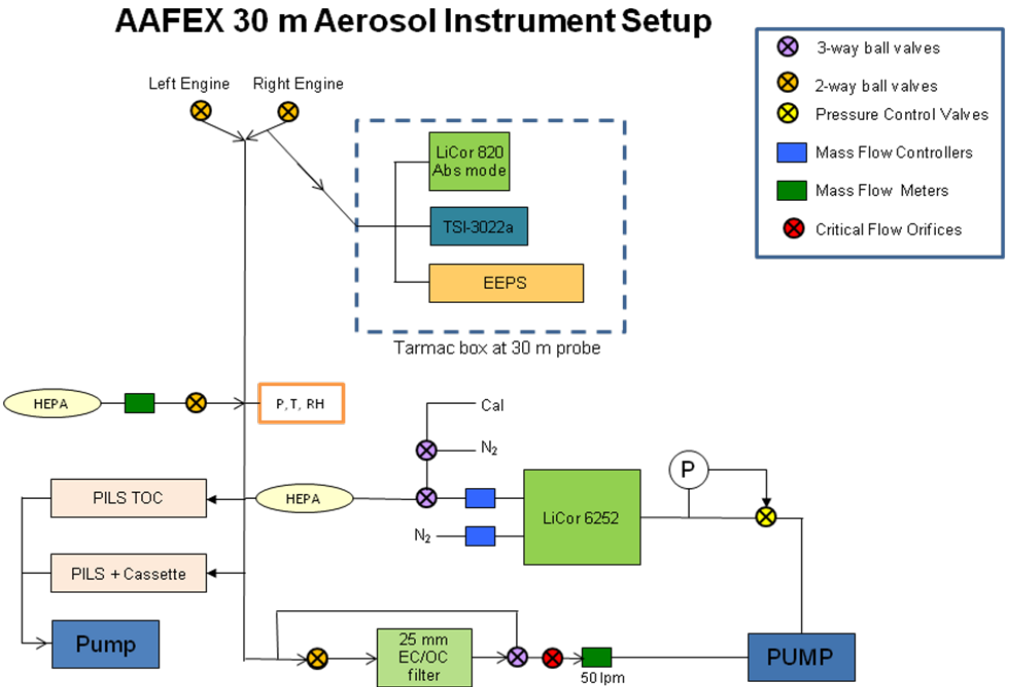

Figure 4. Plumbing diagram for instruments on the aerosol inlet line at 30 m behind the test engine

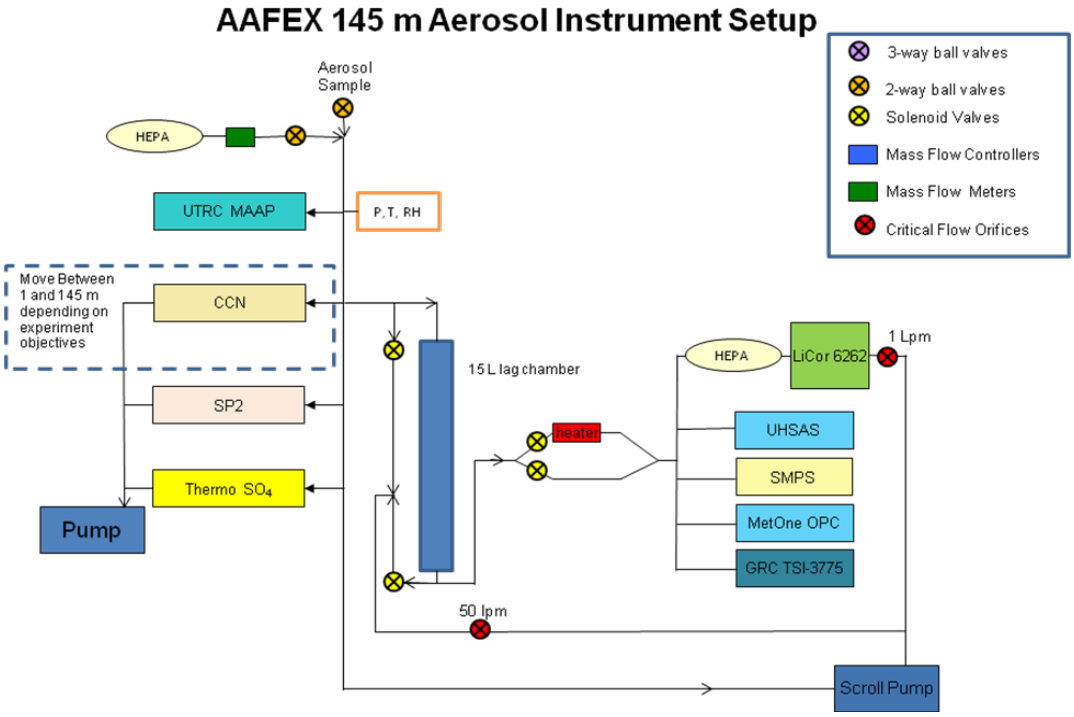

Figure 5. Plumbing diagram for instruments on the aerosol inlet line at 145 m behind the test engine.

3.2.1. Particle Number Concentration

Total aerosol concentrations were monitored with a TSI 3775 CPC. At low concentrations (0 to 5×10^4 cm^{-3}), an optical detector counts individual pulses produced as each particle passes through the sensing zone. For very high particle concentrations, 5×10^4 to 1×10^7 cm^{-3}, the model 3775 transitions from the single-count mode to a photometric mode where the total light scattered from the particles is used to determine concentration. This transition is particularly important because the exhaust samples often had particle number concentrations exceeding 1×10^6 cm^{-3}, even after a ten-fold dilution. This CPC has a 50% cut size of approximately 4 nm and a response time of 5 seconds.

The fraction of particles with diameter greater than 7 nm that are volatile at temperatures below 350□C were monitored with a TSI 3022A CPC, which has a photometric, ensemble sampling mode that extends its dynamic range up to $1x10^7$ cm^{-3}. This CPC has a 50% cut size of approximately 7 nm and a response time of 5 seconds.

3.2.2. Particle Size Distribution

The scanning mobility particle sizer (SMPS) measures the size distribution of particles using an electrical mobility detection technique that couples a differential mobility analyzer (DMA) and condensation particle counter (CPC). The SMPS uses a bipolar charger (^{210}Po) in the electrostatic classifier to give the particle population a known

charge distribution. The particles are then classified according to their ability to traverse an electrical field as the voltage is monotonically increased. One SMPS consisting of a long electrostatic classifier column with a TSI model 3776 CPC detector measured particle size distributions from 0.003 to 0.310 μm mobility diameter. A second SMPS consisting of a long electrostatic classifier column with a TSI model 3025 CPC detector measured non-volatile particle size distributions for the same size range by heating the sample to 350° C prior to DMA classification. Both SMPSs were operated at 60-second resolution with a sheath:aerosol flow rate ratio of 10:1.

The Engine Exhaust Particle Sizer (EEPS) is a fast-response, high-resolution instrument that measures size distribution and number concentration of engine exhaust particle emissions in the range from 0.006 to 0.560 μm at 1-sec time resolution. Particles enter the instrument through a 1-μm cyclone. The particles are given a known positive charge distribution using a corona charger. The charged particles enter the measurement region near the center of a high-voltage electrode column and are transported between two concentric columns surrounded by HEPA-filtered sheath air. A positive voltage is applied to the electrode with increasing voltage towards the bottom of the electrode. This creates an electric field that repels the positively charged particles outward according to their electrical mobility. The outer cylinder consists of a stack of detector electrode rings electrically insulated from each other and connected to highly sensitive electrometers. A particle with higher electrical mobility strikes an electrometer closer to the inlet where it transfers its charge and is detected. A particle with lower electrical mobility strikes an electrometer lower in the stack. This multiple detector arrangement allows for simultaneous concentration measurements of multiple particle sizes.

The DMT Ultra High Sensitivity Aerosol Spectrometer (UHSAS) is an optical-scattering, laser-based aerosol particle spectrometer system for sizing particles in the range from 0.055 μm to 1.0 μm diameter with size binning of 100 channels. The size of the particle is determined by measuring the light scattering intensity and using Mie scattering theory to relate this intensity to the particle size. The design of the scattering optics and the high intensity of the illuminating laser permit the detection of particles at 1-second time resolution.

The MetOne Optical Particle Counter (OPC) is an optical-scattering, laser-based aerosol particle spectrometer system for sizing particles in the range from 0.3 μm to 10 μm diameter into 8 channels. Particle size is determined by measuring light-scattering intensity and using the Mie scattering theory to relate this intensity to the particle size by a similar method as that used for the UHSAS. Sampling has a fast response at 1-second resolution.

3.2.3. Cloud Condensation Nuclei

The DMT CCN counter measures the concentration of particles that form cloud droplets at a specified temperature and water supersaturation, referred to as cloud condensation nuclei (CCN). The instrument design consists of a cylindrical, continuous-flow, thermal-gradient diffusion chamber employing a novel technique of generating a supersaturation by establishing a constant, streamwise temperature gradient so that the difference in

water vapor and thermal diffusivity yield a quasi-uniform centerline supersaturation. Ambient sample is introduced into the instrument, split into sheath and aerosol flows (typically with a sheath-to-aerosol flow ratio of 10:1). The sheath flow is filtered, humidified and heated, and surrounds the sample with particle-free air that constrains the particles to the centerline of the flow chamber within the CCN column. A positive temperature gradient is applied to the CCN column in the streamwise direction. Water vapor supersaturation is generated within the CCN column, where the particles grow by condensation. The supersaturation is varied between 0.1% and 2%. Particles are considered droplets when they are large enough for detection by an OPC at the exit of the CCN column. The OPC has been specially designed for the CCN and utilizes side scattering technology for the particle sizing. A diode laser is used as the light source with a wavelength of 660 nm. The particle sizing range is from 0.75 to 10 microns in 20 bins and sampling frequency is 1 second.

3.2.4. Aerosol Absorption and Black Carbon Concentration

A Multi-Angle Absorption Photometer (MAAP) measures black carbon (BC; here used interchangably with elemental carbon, EC) by determining the aerosol light absorption at 670 nm from the simultaneous measurement of light passing through and scattered back from particle-loaded glass fiber material. Additional detectors placed at defined scattering angles enable the determination of the proportion of the decrease in transmitted light attributed to absorbance rather than scattering by the particle sample and filter media. The data inversion algorithm is based on a radiation transfer method and therefore takes into account multiple scattering from the deposited aerosol and between the aerosol layer and the filter matrix. The absorption by aerosols is empirically related to black carbon content. The uncertainty of the absorbance is ± 12% at 1-second resolution.

As an instrument calibration check, black carbon concentrations measured with the MAAP were compared to filter-based black carbon determined by an OC/EC aerosol analyzer (Sunset Laboratory Inc., Tigard, OR). A linear regression of the two methods (Figure 6) showed that the EI_{bc} measured using the MAAP were typically greater by 15%. This is likely the result of interference in the filter based measurement by organic carbon. Processing error in the OC/EC split point increases with high loadings of organic carbon (as observed in engine exhaust).

The DMT Photoacoustic Soot Spectrometer (PASS-3) is a sensitive, high-resolution, fast-response instrument for measuring the absorption coefficient of aerosol particles. It provides a real-time, in-situ measurement of black carbon. It uses three wavelengths (red, green, and blue) to enhance measurement capabilities. The PASS-3 instrument measures light absorption by aerosols using the photoacoustic method, quantifying the sound pressure produced in an acoustic resonator caused by light absorption. The lower detection limit for light absorption is 0.4 Mm^{-1}, which corresponds to an elemental carbon mass density of ~40 ng m^{-3} assuming efficiency for light absorption of 10 m^2 g^{-1}.

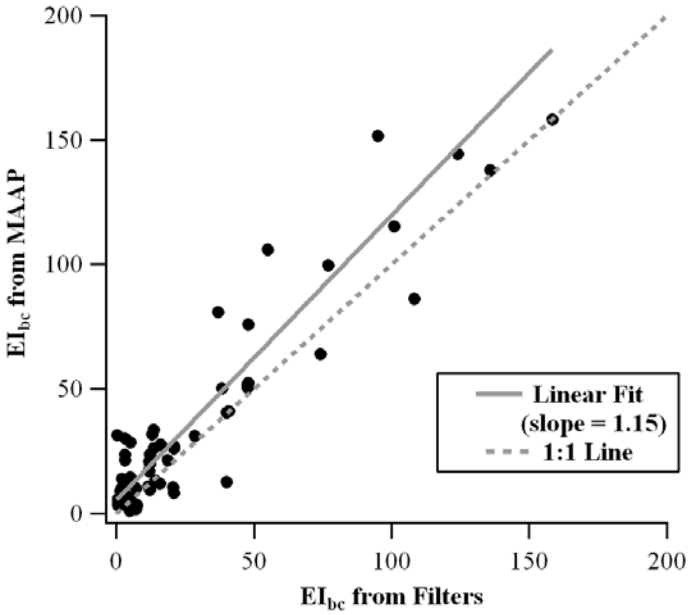

Figure 6. Black carbon mass emission indices (EI_{bc}, mg kg^{-1}) found by the MAAP and filter analysis. Calculation of emission indices is discussed in detail below.

The DMT Single Particle Soot Photometer (SP2) is designed to measure the mass and mixing state of individual black carbon particles based on the laser-induced incandescence (LII) technique. Particles enter the sample cavity of the SP2 and pass through the beam of a diode-pumped Nd:YAG laser (1.06 μm wavelength) where they scatter or absorb light. Particles that contain light absorbing material, at the wavelength of the laser, are heated as they pass through the beam and reach a temperature at which they incandesce and emit light at a wavelength that is proportional to the incandescence temperature. Four optical detectors are used. One detector is optically filtered to pass only the 1064 nm radiation to measure the scattering signal from all particles. Two photomultiplier tube (PMT) detectors measure the incandescence signal in the visible region. These channels are optically filtered to pass broadband light nominally from 400 to 800 nm and narrow band light nominally from 600 to 800 nm in wavelength. The ratio of the signals from these two detectors allows the color temperature of the incandescing particles to be calculated, providing assurance that the measured particles are elemental carbon. A fourth detector allows measurement of the leading edge of the scattering signal. This can be used to analyze the mixing state of the incandescing particle.

3.2.5. Total Particle-bound PAH

The Photoelectric Aerosol Sensor (PAS 2000) works on the principle of photo-ionization of particle-bound PAH. Using an Excimer lamp, the aerosol flow is exposed to UV radiation. The Excimer lamp offers a high intensity, narrow band source of UV radiation. The wavelength of the light is chosen such that only the PAH coated aerosols are ionized, while gas molecules and inorganic aerosols remain neutral. The particles that have

surface-adsorbed PAH molecules emit electrons that are subsequently removed when an electric field is applied. The remaining positively charged particles are collected on a filter inside an electrometer where the charge is measured. The resulting electric current establishes a signal which is proportional to the concentration of total particle-bound PAH.

3.2.6. Aerosol Length

The TSI model 3070A Electrical Aerosol Detector (EAD) measures a unique aerosol parameter called total aerosol length. Reported in units of mm cm^{-3}, aerosol length is the product of the particle number concentration and average geometric diameter. Theoretically, this aerosol length falls between number concentration and surface area. The operating principle of the EAD is based on diffusion charging of sampled particles, followed by detection of the aerosol using an electrometer.

3.2.7. Water-soluble Aerosol Chemical Composition

The Particle-Into-Liquid Sampler (PILS) collects airborne particles by impaction and concentration into a small stream of high purity water, producing a solution representative of the water-soluble aerosol composition. This is accomplished by mixing the sample flow with a smaller turbulent flow of steam. Rapid, adiabatic cooling of the warmer turbulent stream by the cooler sample flow gives a high supersaturation of water vapor. The aerosol particles grow into droplets large enough to be collected by an impactor. Two identical PILS samplers were deployed. With one PILS, the droplets are collected to produce a continuous liquid flow for online analysis of soluble organic carbon using the Total Organic Carbon (TOC) Analyzer as a detector. The Seivers TOC Analyzer utilizes a gas permeable membrane that selectively passes only the CO_2 produced from the UV/persulfate oxidation of organics in the liquid sample stream. TOC sampling frequency has 4-second resolution. With the other PILS, the droplets are collected for each sampling period (nominally 180 seconds) in vials, which are later analyzed in the laboratory for selected anions, cations and water soluble organics by ion chromatography (IC).

The Model 5020*i* Sulfate Particulate Analyzer (SPA) combines a continuous sulfate (SO_4^{2-}) to sulfur dioxide (SO_2) converter and a trace-level pulsed fluorescence SO_2 analyzer to provide real-time, 1-second resolution, measurements of sulfate aerosol. The measurement is based on the conversion of sulfate particles to gas phase SO_2 in a high-temperature converter module. The SO_2 formed in the converter module is directed to an analyzer module where it is continuously measured using a pulsed fluorescence technique. The pulsed fluorescence measurement operates on the principle that SO_2 molecules become excited by absorbing ultraviolet (UV) light at one wavelength and then emit UV light at a different wavelength when decaying back to a lower energy state. The SPA quantifies sulfate by comparing the signal produced when aerosol loaded sample air is drawn directly into the converter to a background signal that is produced when the sample stream is run through a high-efficiency particulate aerosol filter that removes the sulfate before conversion. The difference in signal between the filtered and unfiltered

sample is attributed to sulfate particles in the unfiltered sample stream. By routinely switching between the filtered and unfiltered sample streams, the instrument readings can be continuously adjusted or corrected for changes in background signal that would be produced by SO_2 or other interfering gases.

3.2.8. Carbon Dioxide

Carbon dioxide is measured using a LiCor differential, non-dispersive, infrared (NDIR) gas analyzer. The CO_2 measurements are based on the difference in absorption of infrared (IR) radiation passing through two gas-sampling cells. The reference cell is used for nitrogen containing no CO_2, and the sample cell is used for the sample of unknown CO_2 concentration. Infrared radiation is transmitted through both cell paths, and the output of the analyzer is proportional to the difference in absorption between the two.

3.3 Calculated Parameters

Data acquired from the LaRC instruments were corrected for sampling pressure and dilution in order to calculate the secondary variables listed in Table 3. Values for aerosol mass were found by integrating volume-size distributions (calculated from measured number concentrations assuming spherical particles) provided by the EEPS or SMPS instruments over a specific size range and then multiplying the resulting volumes by an appropriate aerosol mass density. Because the particles sampled during AAFEX were often a superposition of soot and condensed sulfates and hydrocarbons with poorly-defined morphologies, we assumed a mass density of 1 g cm^{-3}. Absorption coefficients measured by the MAAP were processed using Aerodyne Research Inc. algorithms (Onasch et al., 2009) and converted into a mass of black carbon using a mass absorption coefficient of 6.6 m^2g^{-1} (Petzold et al., 1998).

Table 3. List of parameters derived from experimental measurements

Parameter	Symbol	Units	Temporal Resolution	Estimated Precision
Aerosol Volume	V	μm^3 cm^{-3}	1 or 60 s	25%
Total Aerosol Mass	M	mg m^{-3}	1 or 60 s	50%
Geometric Mean Diameter	GMD or D_g	nm	1 or 60 s	< 2 nm
Volume Mean Diameter	VMD	nm	1 or 60 s	< 2 nm
Geometric Standard Deviation	σ_g	--	60 s	--
Number Emission Index	EI_n	kg^{-1}	1 s	20%
Total Mass Emission Index	EI_m	mg kg^{-1}	1 or 60 s	30%
Black Carbon Mass Emission Index	EI_{bc}	mg kg^{-1}	>10 s	20%

Aerosol size statistics were derived from the measured size distributions using formulas discussed by Hinds (1999). The number "mode" corresponds to the peak in the size distribution when plotted as a function of dN/dLogDp vs. Dp. The geometric mean diameter (GMD) is found using the following formula:

$$GMD = \exp\left[\frac{\sum_{i=D_{min}}^{i=D_{max}}\left[(dn_i/d\log D_i)\cdot\log(D_i)\right]}{\sum_{i=D_{min}}^{i=D_{max}}(dn_i/d\log D_i)}\right] \quad \text{Eq. 1}$$

where dn_i, D_i, and $d\log(D_i)$ are the number density, mean diameter, and normalized width of the i^{th} size channel. Similarly, the volume mean diameter (VMD) is calculated using the formula

$$VMD = \exp\left[\frac{\sum_{i=D_{min}}^{i=D_{max}}\left[(dv_i/d\log D_i)\cdot\log(D_i)\right]}{\sum_{i=D_{min}}^{i=D_{max}}(dv_i/d\log D_i)}\right] \quad \text{Eq. 2}$$

where v_i is the total volume calculated for the i^{th} channel as given by $v_i = n_i \cdot \cdot d_i^3 / 6$. Assuming the aerosols are log normally distributed in a single mode, i.e., unimodal, the geometric standard deviation (σ_g) of the size distribution is given by

$$\sigma_g = \exp\left[\frac{\sum_{i=D_{min}}^{i=D_{max}}\left[n_i\cdot\left(\log(D_i)-\log(GMD)\right)^2\right]}{(N-1)}\right]^{0.5} \quad \text{Eq. 3}$$

In conjunction with the GMD, the geometric standard deviation is useful for modeling aerosol emissions and represents the broadness or spread of the log normal function in that 95% of the particles within a log normal distribution fall within the size range defined by the following expression:

$$\exp\left(\log(GMD) \pm \left(2\log(\sigma_g)\right)\right)$$

Emission indices (EIs) are fundamental parameters used to describe the amount of pollutants emitted by a combustion source per unit of fuel consumed. Values were calculated for aerosol number density, mass and black carbon as follows:

$$EI_X\ (kg^{-1}\,fuel\,burned) = \left(\frac{\Delta X}{\Delta CO_2}\right)\cdot EI[CO_2]\cdot\left(\frac{M_{air}}{\rho\cdot M_{CO_2}}\right) \quad \text{Eq. 4}$$

Where ΔX (in number- or mass-based units) and ΔCO_2 (in ppmv) are the enhancements above background concentration for parameter X and CO_2, M_{air} and M_{CO2} are the molar masses of air and CO_2, respectively, and ρ is the density of air. For our calculations, we either used the measured carbon fractions or assumed the fuel contained ~86% carbon by mass, which yields an EI[CO_2] of approximately 3160 (g CO_2) (kg fuel burned) $^{-1}$.

As discussed in the AAFEX overview document, low-pressure fan speed (N1) was the parameter used throughout the experiment for setting engine power levels. GE Commercial Engines provided a table of nominal N1 values for each of the desired power levels. The aircraft operators subsequently used these data to adjust fuel flow rates to obtain the proper N1 power settings. Figure 7 shows the relationship between fuel flow and engine power setting, and highlights the variability as a function of ambient temperature. Power or thrust is a linear function of fuel flow, but the fuel flows vary (by more than 1200 lbs. hr^{-1} at 85 % thrust and as little as 600 lbs. hr^{-1} at 15 % thrust). Results from previous experiments (APEX, Aircraft Particle Emissions Experiment) indicate that engine emissions vary more closely with fuel flow rather than with percentage power. Some comparisons discussed in later sections used engine power setting for ease of calculations, but where possible, emission parameters are presented as a function of fuel flow. Hence, both parameters are included with the archived data sets.

3.4 Instrument Calibration

Instrument calibration was carried out frequently to ensure accurate and robust instrument performance. Two types of gas-phase instruments were deployed by Langley during AAFEX: an SO_2-based sulfate aerosol monitor and several nondispersive-infrared CO_2 analyzers. The flow and pressure sensors associated with these instruments were calibrated in the laboratory before deployment and checked periodically during the mission by comparison with a dry cell flow calibrator and ambient pressure monitor, respectively. The pulsed fluorescence SO_2 instrument was calibrated periodically using dry nitrogen to establish zero response and a NIST-traceable SO_2 standard was used to set the instrument gain over the expected range of concentrations.

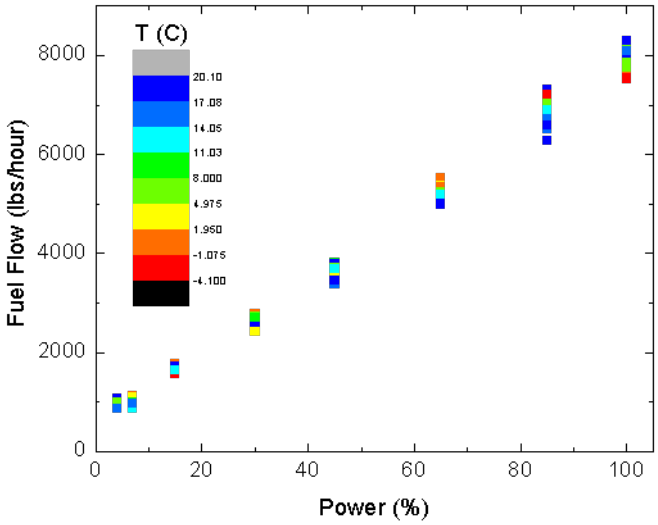

Figure 7. Plot of fuel flow versus power in terms of percentage of maximum RPM for the control engine for all the test points conducted during AAFEX. Points are colored according to ambient temperature.

The CO_2 instruments were calibrated on a daily basis using dry nitrogen as a zero reference and a pair of calibration gases with nominal 5000 and 1000 ppm mixing ratios for span. A CO_2 instrument comparison between NASA, ARI, EPA and MST was conducted during AAFEX, which revealed that the primary CO_2 instrument was somewhat nonlinear over the broad response range. A polynomial correction equation was derived and applied to the LARGE data before calculation of emission factors discussed below.

Because absolute standards are lacking, aerosol-instrument calibration efforts focused primarily on ensuring that the instruments were operating at the proper flows and pressures and were exhibiting the proper size registration for particles of a known size. This effort involved checking all instrument flows with a dry-cell calibrator prior to the mission and conducting checks on a daily basis throughout the experiment. For pressure, instruments were delivered a constant calibration aerosol and their response was monitored as a function of pressure to ensure the indicated concentrations changed as expected and the instrument plumbing was free of leaks. In addition, once the sampling systems in Figures 3 through 5 were installed, they were frequently operated at sub-ambient pressure while sampling cabin air through a high-efficiency particle filter to ensure that system and instrument plumbing was completely leak-free. For the size calibration, NIST-standard latex spheres were mobilized with an aspiration generator, size-selected with a TSI DMA, then assayed by the SMPS, EEPS, UHSAS and OPC instruments. During the mission, SMPS, EEPS and CPC data were examined on a continual basis to determine continuity in number and size response.

3.5 Data Processing

The aerosol data recorded during AAFEX were influenced by a variety of noise and artifact sources including rapid pressure or dilution changes and instrument saturation. To reduce these effects, the data were carefully screened to remove time periods when sampling system pressure was unstable or when species concentrations were changing rapidly (based on variations in CO_2 mixing ratio). In addition, for particle volume and size statistics calculations, integration of SMPS and EEPS size distributions excluded particles larger than 150 nm diameter at lower engine powers to reduce the contribution of background aerosols. Individual SMPS size distributions, because of the longer time response of the instrument, were discarded if particle concentrations (from a CPC) changed more than 10% during the time period of the scan. Number concentration data greater than 9×10^6 cm^{-3} and 5×10^6 cm^{-3} for the TSI-3775 and TSI-3022A instruments, respectively, were excluded to eliminate the effects of instrument saturation. Similarly, data associated with individual electrometers exceeding their range of sensitivity on the EEPS were removed.

Prior to the mission and in order to miniaturize the systems, the power supplies on the two DMAs in the SMPS systems used to derive total and non-volatile aerosol mass were replaced in favor of much smaller, programmable units. Unfortunately, these supplies had non-zero offsets (approximately 15 VDC) that caused the SMPS scans to exhibit artificially high particle counts at sizes below 10 nm when the particle populations were affected by nucleation-mode aerosol. These artifacts had very little impact on volume-based size distributions or calculated integrated volume but caused the number-based size distributions to exhibit a nucleation-mode artifact (potentially where none were present) and the SMPS integrated number concentration to exceed that measured using CPC instruments. Thus, particle size statistics (GMD, VMD) were only calculated for sizes greater than 11 nm.

The MAAP data was reprocessed after the mission using the ARI algorithm (Onasch et al., 2009), which yields 1-second resolution black carbon concentrations and extends the instrument range to accurately detect much higher mass loadings. However, the Langley MAAP instrument failed to record data at exactly 1-second intervals, which caused the ARI software to introduce brief periods of diverging concentrations into the output data set. These fluctuations were removed by hand-editing the black carbon data in view of simultaneous CO_2 and pressure records.

3.6 Instrumental Difficulties

Much of the instrumentation suite deployed during AAFEX was in early stages of laboratory characterization; subsequently, the performance of a variety of the Langley instruments was not ideal. These instruments are not highlighted in Table 2 and will not be the focus of this report but will be more efficiently utilized for future field deployments based on the valuable experience gained during AAFEX. A summary of the problems, solutions, and effects on data interpretation and analysis for these instruments is included here.

AAFEX was the first deployment of the LARGE PASS-3. This instrument is designed to measure aerosol absorption coefficients in the background atmosphere, where concentrations of interfering gas-phase species are typically quite low. Initial data processing used a mass absorption efficiency of 6.6 $m^2 g^{-1}$ to convert absorption coefficients to black carbon mass. For the red detection channel, this yielded BC emission indices that were a factor of two lower than those from the MAAP; for the blue and green detection channels, the values were several orders of magnitude too high. An examination of the PASS-3 data set with simultaneous certification-gas measurements suggested that the instrument's shorter wavelength channels are highly sensitive to interference from NO_x and potentially organic species. Although less severely, the red channel was also subject to interference, as absorption coefficient variability was observed independent of MAAP variability. The PASS-3 data for the propane-burner tests were highly correlated with black carbon mass from the MAAP over a broad range of concentrations, suggesting that in the absence of NO_X and gas-phase organic contamination, the PASS-3 performance was satisfactory. Still, because of these problems the PASS-3 data were not used to establish the engine emission characteristics for this report.

AAFEX was also the first field deployment for the SP2 instrument, with the goal of single particle measurements of soot size from 100 nm to 500 nm diameter and determination of coating thicknesses of aged exhaust particles. However, because of instrumental complexities, the data quality was unsatisfactory and will not be presented here. SP2 characterization, calibration, and intercomparison will be a focus of future laboratory and field deployments to best utilize its robust capability.

The LARGE instrument suite also included a photoelectric sensor to provide a measure of surface-bound PAH. Data from this instrument tended to correlate with black carbon observations over short time scales, but was also apparently influenced by relative humidity. For this reason, the PAH sensor data, although available on request, is not presented in the following discussions. The PILS instrument was set up to measure TOC and collect aerosol samples at a 4-minute integration time for subsequent IC analysis. In most cases, species concentrations in these samples were at or near the detection limit. Similarly, quartz-fiber filter samples collected from the 30-m, test engine inlet probe yielded potentially meaningful EC/OC measurements only at high engine powers or when JP-8 fuel was burned.

3.7 Line Losses and Impact of Background Aerosols

As discussed in Appendix X of the AAFEX report, particle losses to sampling system components profoundly influenced the observed particle concentrations and characteristics. Tests conducted after the mission indicated that up to 50% of the particles collected using the control engine 30-m inlet probe were lost during transport to the community sample distribution manifold. This was approximately 20% more than from the test engine 30-m inlet and approximately 50% more than from the control engine 1-m inlet. There was also evidence that the losses increased over time, as debris

and coatings built up within the long sampling lines. These time-varying, differential losses make it difficult to compare emissions from the two engines and to evaluate the evolution of particles between the 1- and 30-m sampling locations. However, for a variety of reasons not least of which was to avoid confusion, the AAFEX science team agreed to archive data without corrections for transmission losses. Where appropriate, the discussions below point out and take into consideration the potential impacts of line losses. Please refer to Appendix X for a robust treatment of particle line loss.

Another factor that potentially influenced aerosol emission indices and size statistics were contributions from background aerosol. Particle number EIs were typically less susceptible than mass EIs, since the engine generated high numbers of particles regardless of the fuel supply. For the JP-8 fuel tests, background particle number and mass concentrations at both 1 m and 30 m were several orders of magnitude lower than in the exhaust plume and were hence not a significant interference. However, for the FT fuel tests, background and exhaust aerosol loadings were often of the same order of magnitude, particularly at low engine powers. It was not possible to completely remove the effects of background aerosols because, even if the concentrations and characteristics of particles in the engine inlet were measured, they would undoubtedly undergo radical changes when passing through the engine's hot section. For this reason, we did not subtract background from the measured aerosol concentrations, but were careful to restrict SMPS volume integrations to the appropriate size ranges and to remove data that appeared to be heavily impacted by external sources.

Table 4. Fuel Properties

	JP-8	FT-1	Blend-1	FT-2	Blend-2
Sulfur (ppm)	1148	19	699	22	658
Aromatics (% vol)	18.6	0	8	0.6	9.1
Hydrogen Content (% mass)	13.6	15.5	14.5	15.1	14.3
Naphtalenes (% vol)	1.6	0	0.8	0	0.8
Olefins (% vol)	0.9	0	0.6	3.8	3.3
Fuel H/C ratio	1.88	2.19	2.02	2.12	1.99

3.8 Fuel Properties

Table 4 presents selected results from the post-mission analyses of fuel samples collected from the test engine supply line that were conducted by AFRL at Wright Patterson Air Force Base (AFB). Complete results are presented in Table 2 of the AAFEX overview document (Anderson et al., 2010). Blend-1 and Blend-2 were made prior to the campaign by mixing equal parts (by volume) of JP-8 and FT-1 and FT-2, respectively. The first column lists the pertinent characteristics of the JP-8 fuel purchased from Edwards AFB. Note that the JP-8 contained 1148 ppm sulfur, 18.6% aromatics, and 1.6% naphthalene compounds. In contrast, the FT fuels contained less than 25 ppm sulfur (probably introduced during handling or mixing with residual fuel in the aircraft), less than 1% aromatic compounds, and 0 % naphthalenes. The hydrogen contents of the fuels are also significantly different, reflecting the much higher aromatic and PAH content of the JP-8 and the predominance of n-alkanes in the FT fuels. These differences were

predicted to have substantial effects on both soot emissions and formation of volatile aerosols in the engine exhaust plume.

4.0 Results and Discussion

A complete set of the Langley particle emissions data from the 418 engine and 18 APU test points conducted during AAFEX is available on the project web site. Included are ambient temperature, ambient humidity, exhaust plume CO_2 enhancement, and a variety of emission indices for aerosol number, volume, and mass. Size distributions and size statistics (i.e., GMD, VMD) obtained with SMPS-type systems are also archived. Note that none of the archived data has been corrected for line losses or background aerosol interference. The following section summarizes these results regarding fuel and temperature effects on emission parameters.

4.1 Inboard Engine Emission Comparison

Because engine particle and gas emissions are known to vary considerably with temperature, AAFEX took the approach of using simultaneous measurements of PM emission from a test engine burning JP-8 fuel to evaluate fuel-related changes in the control engine PM emissions, the assumption being that the emission characteristics of the two engines would be identical and that these characteristics would exhibit the same ambient temperature dependence. To validate this assumption, tests 3 and 4 were conducted to measure emissions from the two engines both burning standard JP-8. During all the emission characterization tests, samples were drawn from the 1-m and 30-m inlets at power settings of 4, 30, 45, 65, and 85% of maximum RPM.

Results from these tests are shown in Figures 8 and 9 and Tables 5 and 6. Nonvolatile EI_n from the two engines (Figure 8, first two columns of Table 5) were highly variable, primarily because of ambient temperature effects, but it appeared that on average, the control engine exhibited slightly higher values at most power settings than the test engine. An examination of particle size distributions revealed that increased numbers of particles in the 10 to 20 nm size range accounted for the observed enhancements. This point is reinforced by the GMD and VMD versus fuel flow plots of Figure 7, which indicate that nonvolatile particles emitted from the test engine were on average smaller on both a number and volume basis than those from the control engine. Still, EI_n values compared well between both engines considering potential differences in line loss and general measurement uncertainty.

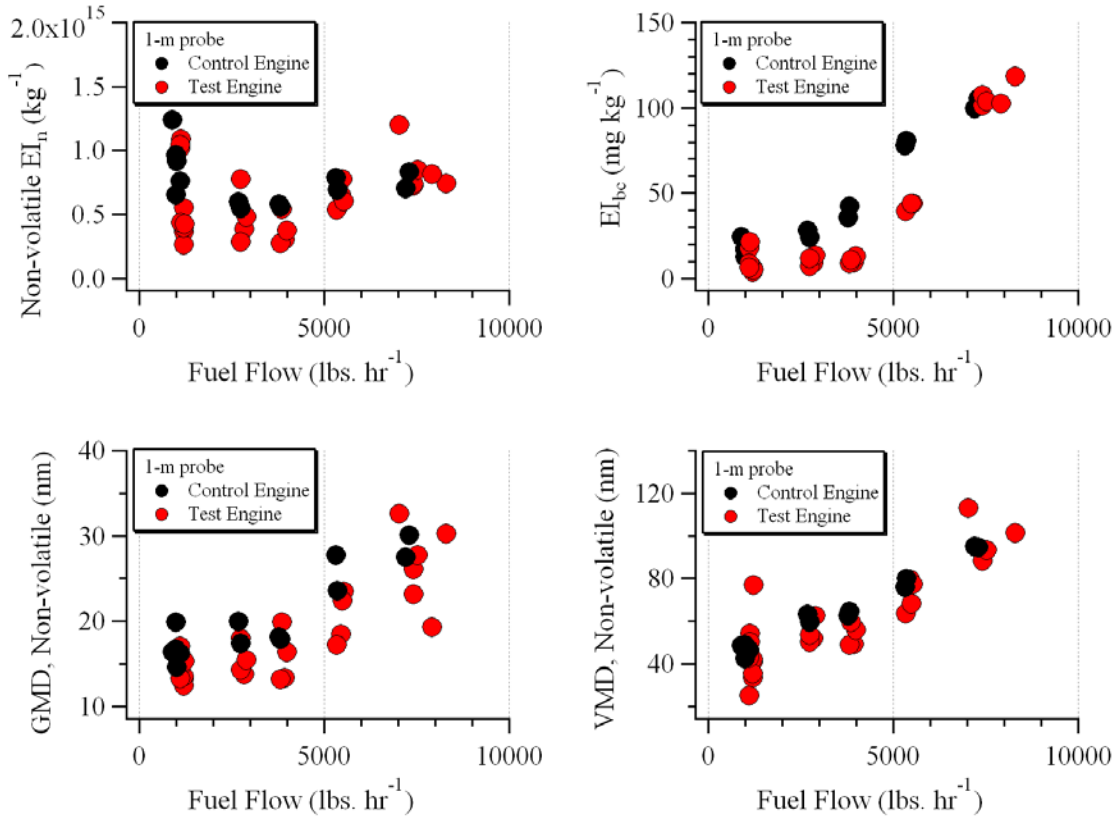

Figure 8. Comparison of emission parameters for control and test engines on 1-m probes on the afternoon of 27 January and morning of 28 January. Both engines burned JP-8 during this test.

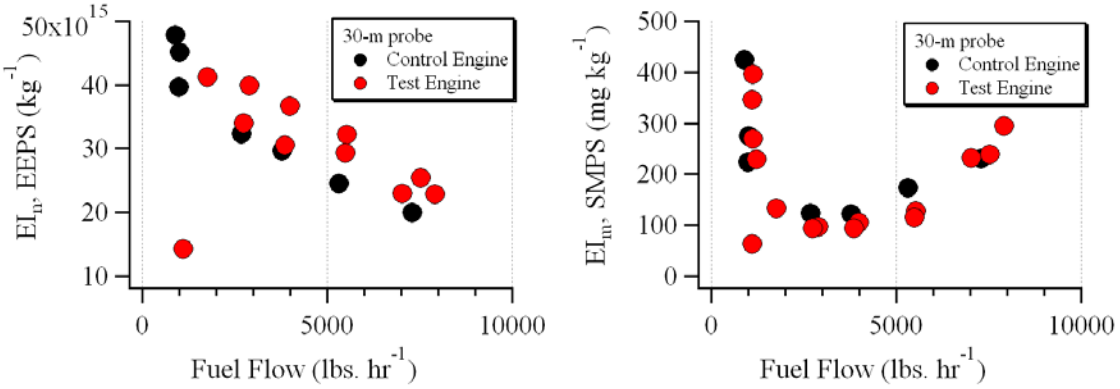

Figure 9. Comparison of emission parameters for control and test engines on 30-m probes on the afternoon of January 27 and morning of January 28. Both engines burned JP-8 during this test.

While the EI_n are in relatively good agreement, EI_{bc} for the control engine was two to four times greater at mid-power settings (30, 45, 65%) than those for the test engine. It is possible that the differences are an artifact caused by placement of the inlet rakes at non-

representative positions in the engine exhaust planes. Note that very little variation in EI_{bc} was observed between samples drawn from the six inlet tips on the control-engine rake during the exhaust mapping test (Test #2 in Table 1). On the other hand, EI_{bc} varied by a factor of two as a function of sampling position behind the test engine, but even the largest values at mid-power settings were still a factor of two lower than the control engine average. Thus it appears that, even though the two engines are of approximately same age and received the same maintenance and servicing, the control engine simply produced more soot at the mid-power settings.

Table 5. Comparison of non-volatile particle emission indices (EI_n) measured from 1-m probes.

Engine	Non-volatile Particle Number EI ($\times 10^{14}$ kg^{-1})					
	JP-8	JP-8	FT-1	Blend-1	FT-2	Blend-2
Power (%)	Control Engine	Test Engine				
4	9.9	8.8	0.05	3.7	0.45	3.8
7	7.7	4.3	0.05	1.2	0.25	2.2
15	--		0.16	0.56	0.08	0.66
30	5.3	3.6	0.05	0.73	0.12	0.69
45	5.4	2.9	0.08	0.58	0.12	0.43
65	7.3	4.4	0.76	2.2	1.2	2.7
85	7.3	7.1	2.0	4.0	2.1	4.8
100	--	6.9	2.8	4.8	2.5	5.5

All values are averages and have been divided by 1×10^{14} for presentation.

Table 6. Comparison of black carbon mass emission indices (EI_{bc}) measured from 1-m probles.

Engine	Black Carbon EI (mg kg^{-1})					
	JP-8	JP-8	FT-1	Blend-1	FT-2	Blend-2
Power (%)	Control Engine	Test Engine				
4	18.9	13.1	0.9	3.8	0.7	3.4
7	6.3	7.9	1.0	3.2	1.1	4.2
15			0.4	0.9	0.4	1.2
30	25.0	9.1	1.1	2.2	1.2	1.8
45	36.1	8.1	1.2	1.4	2.0	1.3
65	79.9	27.7	2.4	10.5	3.5	14.1
85	95.8	82.7	10.7	34.1	14.8	48.8
100		102.7	24.1	50.5	22.7	66.9

All values are averages.

Figure 9 provides plots of 30-m number and mass emission indices for the two engines during the comparison tests (Tests 3 and 4), again with both the control and test engines

burning JP-8. At this sampling distance the number emissions are dominated by nucleation mode aerosols formed from the condensation of sulfuric acid and low volatility organics. The variability in the data at any particular engine power is caused by changes in ambient temperature, and will be discussed in depth in Section 4.7. Note that the total aerosol mass emissions from the two engines are comparable at low and high thrust settings, but differ at mid-power settings by approximately the same levels as seen in the EI_{bc} plot of Figure 8 (approximately 30-50 mg kg^{-1}). EI_n appears to be greater for the test engine, but this difference is presumed to be caused by enhanced nucleation mode aerosol losses in the longer (46 m length compared to 38 m, respectively) sampling line connecting the control engine 30-m inlet with the common aerosol sample distribution manifold. Overall it appears that the test engine produces less nonvolatile particle mass emissions at middle-power settings, but that condensation processes occurring in the two plumes are of comparable magnitude.

4.2 JP-8 Emissions Comparison: AAFEX versus APEX-1

The emission characteristics of the DC-8's #3 engine (used as the test engine during AAFEX) was extensively documented during the Aircraft Particle Emission Experiment (APEX-1), which was conducted at NASA Dryden during May 2005 (Wey et al., 2007; Wey et al., 2008; Onasch et al., 2009). Similar to AAFEX, APEX-1 sought to establish particle emission profiles for the aircraft's CFM56 engine as a function of fuel composition, but in this case, the fuel variables were sulfur and aromatic hydrocarbon content. APEX-1 employed sampling rakes, inlet probes and sample transport lines that were similar to those used during AAFEX. Langley took part in this study, deploying many of the same instruments used during AAFEX to determine particle size distributions and number and mass EIs. Figure 10 shows a comparison of results from the two studies, where the APEX-1 data are an ensemble average of all measurements acquired from the 1-m sampling rake, regardless of fuel type, and the AAFEX data include only results from the JP-8 fuel tests**.**

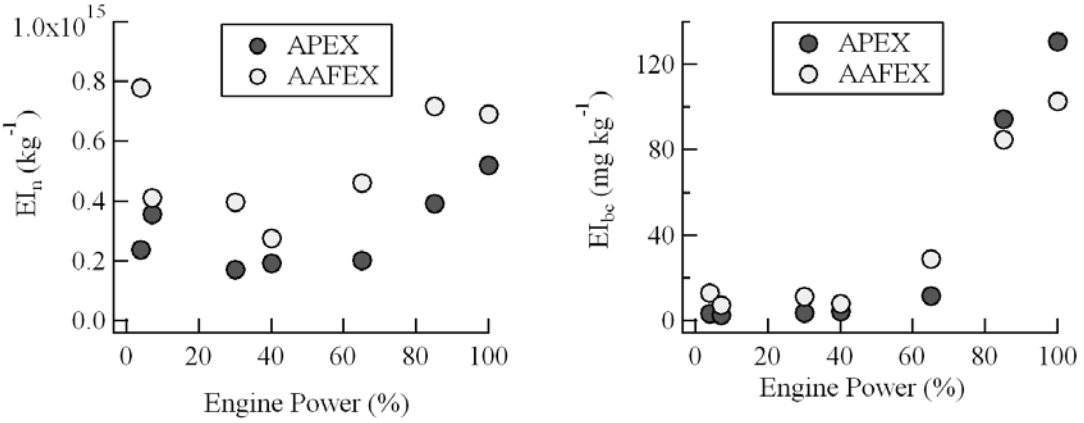

Figure 10. Comparison of non-volatile particle emission parameters for DC-8's #3 engine burning JP-8 fuel as measured during APEX-1 and AAFEX.

Note that all parameters show similar trends but differ to varying degrees in magnitude. Instrumental differences can account for some of these discrepancies. The CPCs

deployed during AAFEX had slightly smaller 50% cut-sizes than the CPCs used in APEX-1 (7 vs. 10 nm, respectively). We estimate that this can account for about 20% of the difference in EI_n at low-power settings where the GMD values are around 15 to 20 nm. Similarly, black carbon concentrations were measured with a MAAP instrument during AAFEX, as opposed to a Particle Soot Absorption Photometer (PSAP) during APEX-1. The PSAP deployed by ARI during APEX-1 tends to overestimate black carbon emissions compared to the MAAP (deployed during AAFEX), which can explain why the apparent APEX-1 EI_{bc} are higher at takeoff thrust. Differences in ambient temperature could have contributed to the differences in EIs between the two studies (APEX-1 was conducted during May when the average daily temperature in the Palmdale/Edwards AFB region is about 10°C warmer than during the January time frame of AAFEX). An engine oil leak and engine aging may also have contributed to slightly higher particle number and mass emissions at most power settings during AAFEX than observed during APEX-1. Still, the comparison of EI_n and EI_{bc} during AAFEX and APEX yields strong similarity in the trend and magnitude of emissions and thus the engine performance did not change significantly between sampling campaigns.

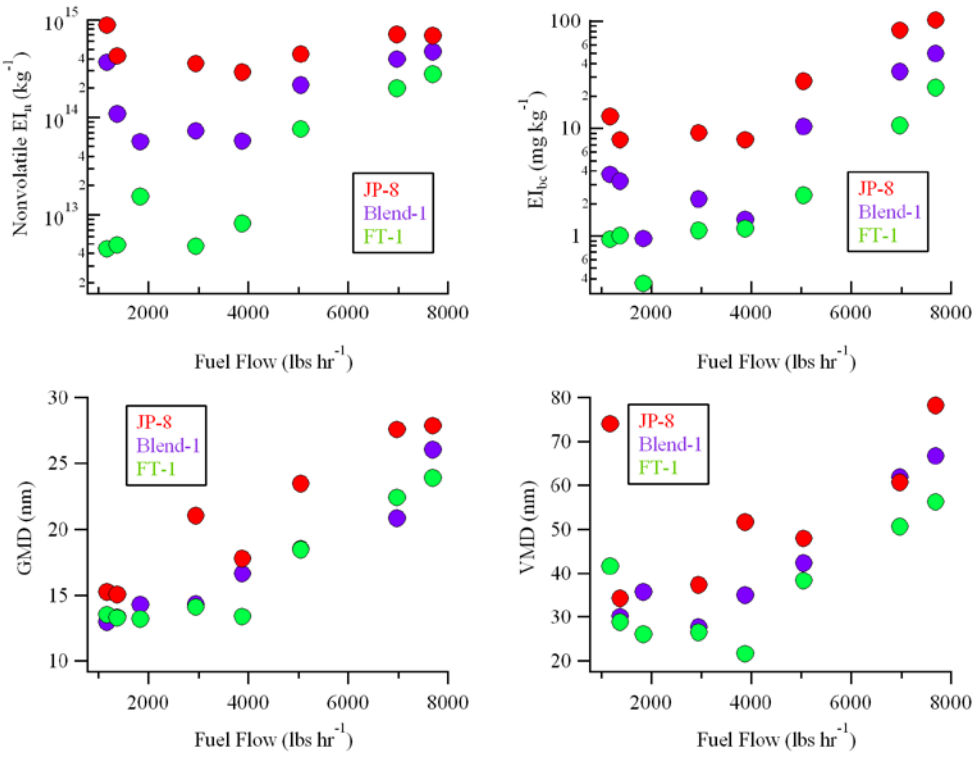

Figure 11. Particle emission characteristics for JP-8, FT-1, and Blend-1 at 1-m probe.

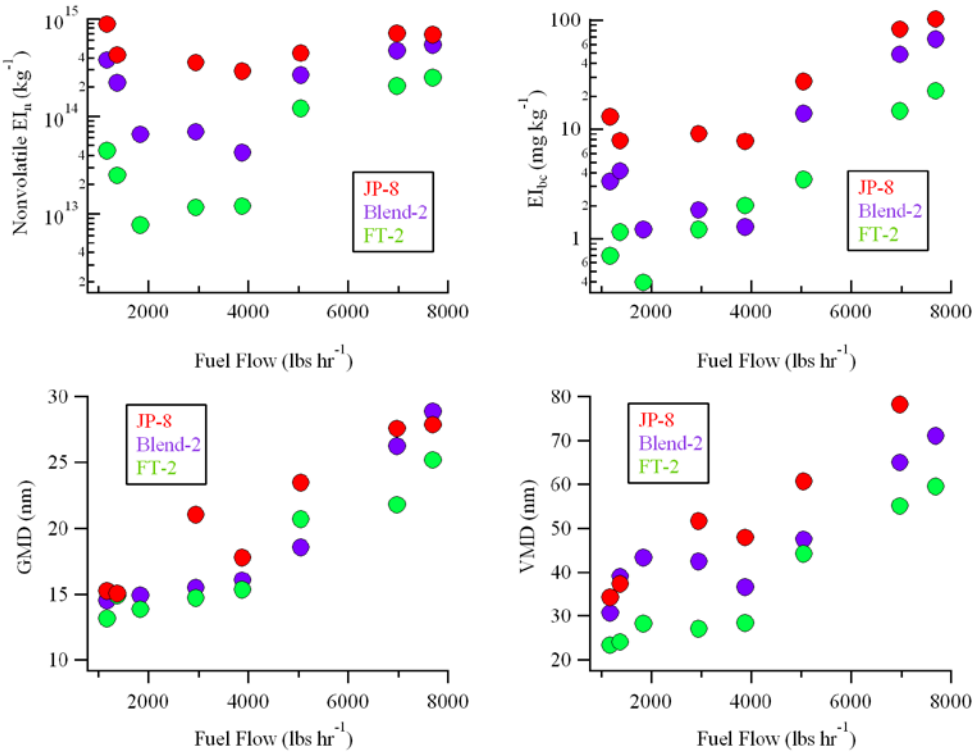

Figure 12. Particle emission characteristics for JP-8, FT-2, and Blend-2 at 1-m probe.

4.3 Alternative Fuel Effects on Particle Emissions: 1-m Probe

The analysis presented in Section 4.1 suggests that although there were differences in PM emissions between the control and test engines, the overall trends and characteristics of the emissions were similar. Section 4.2 showed that the emissions have not changed considerably from the APEX campaign (2005) to the current AAFEX campaign. This allows the use of #3 engine emissions data as a test engine for decoupling ambient temperature and fuel-related changes compared to the control engine emissions. This section examines results from tests 5 to 6 and 8 to 11, wherein the composition of exhaust from the two inboard engines was characterized as the right engine burned the various test fuels and the left engine was supplied the standard JP-8 baseline fuel.

Tables 5 and 6 compare non-volatile particle number and mass emission indices, respectively, for the different fuels and engines. Figure 11 and Figure 12 show fuel flow-dependent plots of average EIs and particle size statistics for each of the fuels in comparison to simultaneous measurements from 1-m probes of the same parameters from the control engine burning JP-8. PM emissions from the test engine, burning FT fuels, were substantially reduced compared to emissions from the control engine burning JP-8. This finding is consistent with previous studies (Corporan et al., 2007; Dewitt et al., 2008; Timko et al., 2010) and can be attributed to the higher hydrogen content, lack of aromatics, and lack of sulfur in the synthetic fuels.

A major goal of AAFEX was to examine the benefits of replacing current fuels (JP-8) used in commercial aircraft with pure or blended alternative fuels. To quantify the emissions characteristics of such a switch, an emissions benefit was defined as

$$\text{emissions benefit} = \frac{EI_{Y,JP-8}}{EI_{Y,X}} \qquad \text{Eq. 5}$$

where X denotes the alternative fuel (FT-1 or FT-2) or blend (Blend-1 or Blend-2). Y denotes an emissions parameter, and for this report, only particle number concentration emissions indices (EI_n) and black carbon mass emissions indices (EI_{bc}) are considered. Here, increased emissions benefit indicates a larger gap between the EI for JP-8 and the EI for the alternative fuel. Emissions benefit was calculated for both EI_n and EI_{bc} as a function of engine power and is shown in Figure 13 and Figure 14. For example, a particle number emissions benefit value of 100 for FT-1 fuel at 30 % engine power represents a JP-8 EI_n that is 100-fold- greater than FT-1 EI_n. Likewise, this emissions benefit corresponds to a 99 % reduction in EI_n emissions when switching from JP-8 to FT-1. Note that all particle number and black carbon emissions-benefit values are greater than unity, indicating that at all engine power settings JP-8 emissions exceeded those from FT fuels and blends.

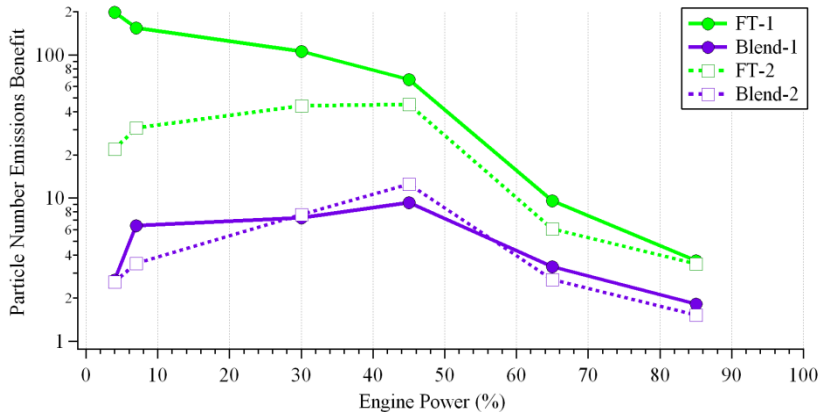

Figure 13. Particle number emissions benefit as a function of engine power for each alternative fuel and mixture. Note the logarithmic y-axis scale. Measurements taken from 1-m probe.

The greatest emissions benefit was associated with burning the FT-1 fuel, which had the highest hydrogen, lowest aromatic hydrocarbon, and lowest sulfur contents of all the fuels tested (Table 4). At low engine powers, nonvolatile EI_n values for FT-1 were two orders of magnitude lower than for JP-8 and thus the emissions benefit was significant. The FT-1 emissions benefit for particle number decreased with engine power but was still 2-3 at climb and takeoff thrust levels (Figure 13). For FT-2, Blend-1, and Blend-2, the particle number emissions benefit was significant throughout but was greatest at 45 % thrust level and was slightly reduced at idle thrust and significantly reduced at takeoff thrust settings.

In terms of PM mass emissions, EI_{bc} values were similarly reduced. The black carbon emissions benefit (Equation 5) for FT-1 and FT-2 was greatest at the 65% thrust level (33 and 23, respectively and was minimized at 7 % and 85 % [figure 14]). The peak black carbon emissions benefit for Blend-1 and Blend-2 was shifted to the 45% thrust level. The black carbon emissions benefit at idle (4 % thrust) may be underestimated because the corresponding MAAP signals (black carbon mass) for the FT fuels were barely

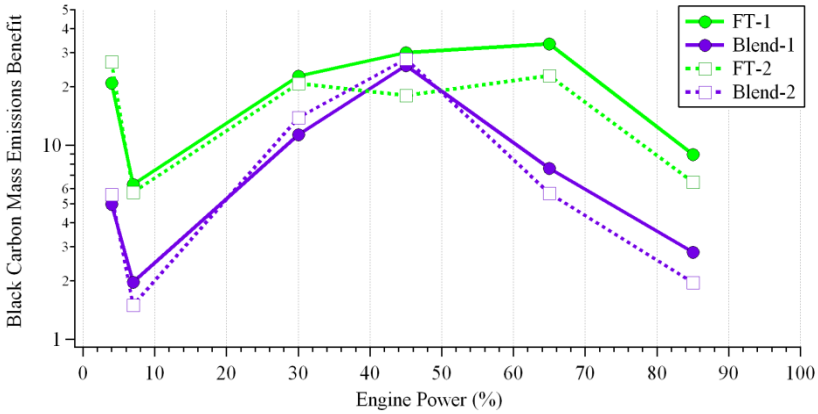

Figure 14. Black carbon emissions benefit as a function of engine power for each alternative fuel and mixture. Note the logarithmic y-axis scale. Measurements taken from 1-m probe.

detectible and were not corrected for background soot contributions. Number concentration enhancements in the FT fuel exhaust were much more robust but still somewhat variable (10-20%) due to contributions from background sources.

A diminishing emission benefit of the FT-1 fuel with engine power is consistent with previous observations (Corporan et al., 2007; Timko et al., 2010) and can be attributed to changes in the dominant soot formation mechanism with combustion flame temperature. At low combustion temperatures, condensation reactions involving aromatic hydrocarbons proceed at much faster rates than reactions involving n-alkanes. As the combustion temperature increases, the fragmentation and polymerization of both aromatic and alkane species compete with aromatic condensation, so the initial fuel composition has much less impact. This effect is clearly depicted in the low-power black carbon emissions benefit shown in Figure 14 for pure FT fuels and with their blends. But, the significant benefit observed at high power cannot be explained in this manner. Thus, fuel aromatic content is likely a key factor in regulating soot production, but additional work is necessary to understand soot formation from pure and blended alternative fuels more fully.

Differences in the primary particle size drive the differences in PM number and mass reduction ratios discussed above. The GMD and VMD plots shown in Figure 11 and

Figure 12 indicate that burning FT-1, and FT-2 fuels and respective blends produced smaller particles in comparison to JP-8 at all engine powers. Overall, for the 100% FT fuels, GMD differences were 5 to 10% at idle and 15 to 20% at takeoff thrust; VMDs were reduced 20 to 40% across the entire power range. The change in size with fuel composition is more clearly observed in the particle size distributions (PSDs) shown in Figure 15, which depict particle diameter-normalized EI_n as a function of diameter for each of the fuels at 7, 65 and 85% of maximum thrust. Note that the PSD modes shift to smaller sizes as the fraction of FT fuel is increased. For example, the particle emissions size distribution at 85 % thrust peaked in $dEI_n/dlogDp$ at 28.9 nm, 22.5 nm, and 19.5 nm for JP-8, Blend-1, and FT-1, respectively.

At idle, a large fraction of the particle population is smaller than the instrument detection limit, hence GMDs calculated from the PSDs are larger than the modal diameter; at 65 and 85% thrust, the effects of instrument sensitivity are reduced and the calculated GMDs and modal diameters correspond more closely. This explains why the relative difference in GMD between the fuels appears to increase with power, while the differences in VMD remain relatively constant. Regardless, a 20% reduction in particle size corresponds to a ~50% decrease in particle volume. Note that reduced particle size with fraction of FT fuel was observed in several recent studies (Corporan et al., 2007; Timko et al., 2010) and is related to the lack of the large aromatic hydrocarbon species that promote soot formation and growth in FT fuel.

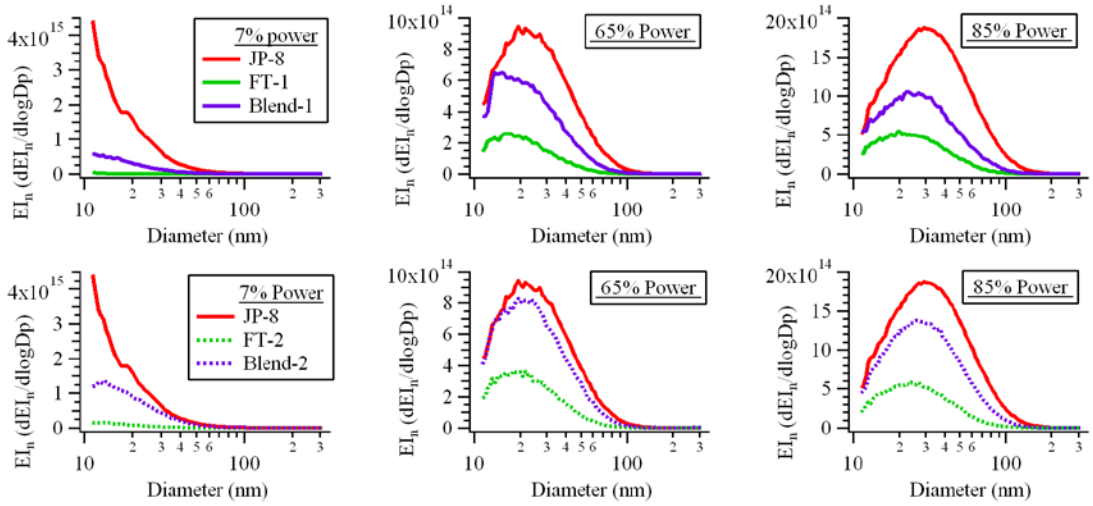

Figure 15. Number EI-based particle size distributions for the JP-8 fuel compared to particle size distributions for FT-1 and Blend-1 (top) and FT-2 and Blend-2 (bottom) fuels at 7, 65, and 85% power. All data are from 1-m probe.

Related to changes in particle size are changes in soot density. Timko et al. (2010) observed that FT fuel combustion in gas turbine engines produces less fractal and more dense soot particles. Effective density (ρ_{eff}), which takes into account both the chemical density and the particle shape for particulate fuel emissions, was calculated by

$$\text{particle effective density } (\rho_{eff}) = \frac{EI_{bc}}{EI_{v}} \quad (\text{g cm}^{-3}) \qquad \text{Eq. 6}$$

where EI_{bc} is from the MAAP and EI_v is from the SMPS. For AAFEX over the 65-100% power range ρ_{eff} values were 1.45±0.1 g cm^{-3} for FT-1, 1.2±0.15 g cm^{-3} for FT-2, 1.1±0.1 g cm^{-3} for Blend-1, 1.05±0.15 g cm^{-3} for Blend-2, and 0.92±0.08 g cm^{-3} for JP-8.

The alternative fuel blends also produced reductions in non-volatile PM number, mass and size when compared to combustion of standard JP-8 (Figure 11 and Figure 12). However, the reductions were typically different than would be predicted from averaging the emission parameters from the individual fuels, which would be expected since the blended fuels were produced by simple mixing of equal volumes of JP-8 and FT fuels. For example, at 30% engine power both PM number and mass were reduced by 75 to 80% when burning Blend-1 as opposed to JP-8. At takeoff thrust, EI_n and EI_m decreased 30 and 50%, respectively. It appears that soot emissions are nonlinear with fuel aromatic content and/or hydrogen content, particularly at low engine power. This is explored in more detail below.

The above discussion highlighted the impacts of burning FT-1 and the FT-1/JP-8 blend on engine PM emissions compared to traditional JP-8. Because of the similar composition of the two synthetic fuels, we found that FT-2 and its blend had qualitatively similar effects on reducing the number, mass and size of particle emissions. For example, the trends in emission parameters shown in Figure 10 for FT-1 are almost identical to those exhibited in Figure 11 for FT-2. Likewise, the size shifts in PSDs with fraction of FT fuel for FT-1 and FT-2 (see Figure 15) are quite similar.

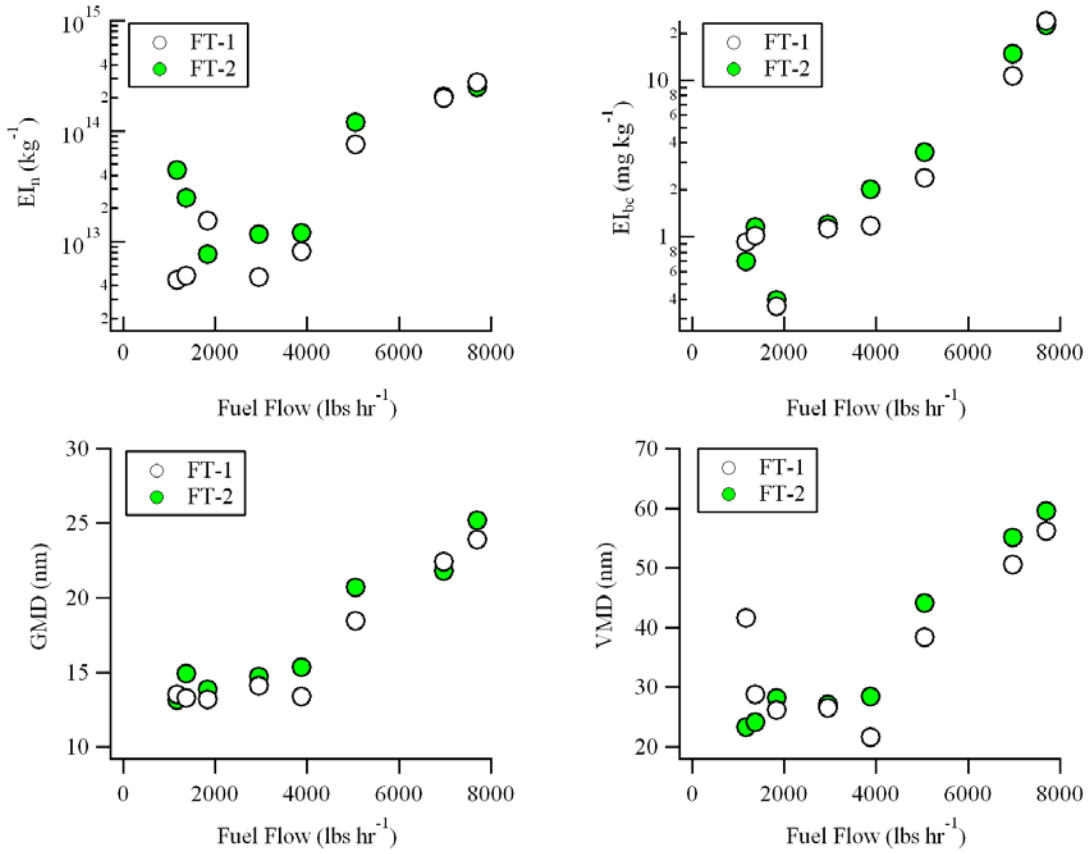

Figure 16. Comparison of FT-1 and FT-2 effects on engine PM emission characteristics at 1-m probe.

However, Figure 13 and Figure 14 highlighted significant differences in number- and black carbon-based emissions benefits between FT-1 and FT-2. The differences in pure alternative fuels are specifically compared in Figure 16. Both PM number and mass EIs were slightly higher for FT-2 at most power settings. This is especially evident at low engine power (and fuel flow) where the particle number emissions benefit (Figure 13) is an order of magnitude greater for FT-1 than for FT-2 and the EI_n for FT-2 is an order of magnitude greater than for FT-1 (Figure 16). This benefit diminishes with increasing engine power. The black carbon emissions benefit and FT-2/FT-1 EI_{bc} difference exhibits the opposite trend, increasing with increasing engine power when the total black carbon emissions (Figures 11 and 12) become most significant. This benefit is negligible at low engine power (Figure 14). Differences in the particle size for FT-1 and FT-2 emissions are less distinct. Nonvolatile particles associated with burning FT-2 tended to be slightly larger (with respect to both GMD and VMD) than those from FT-1 combustion (Figure 16).

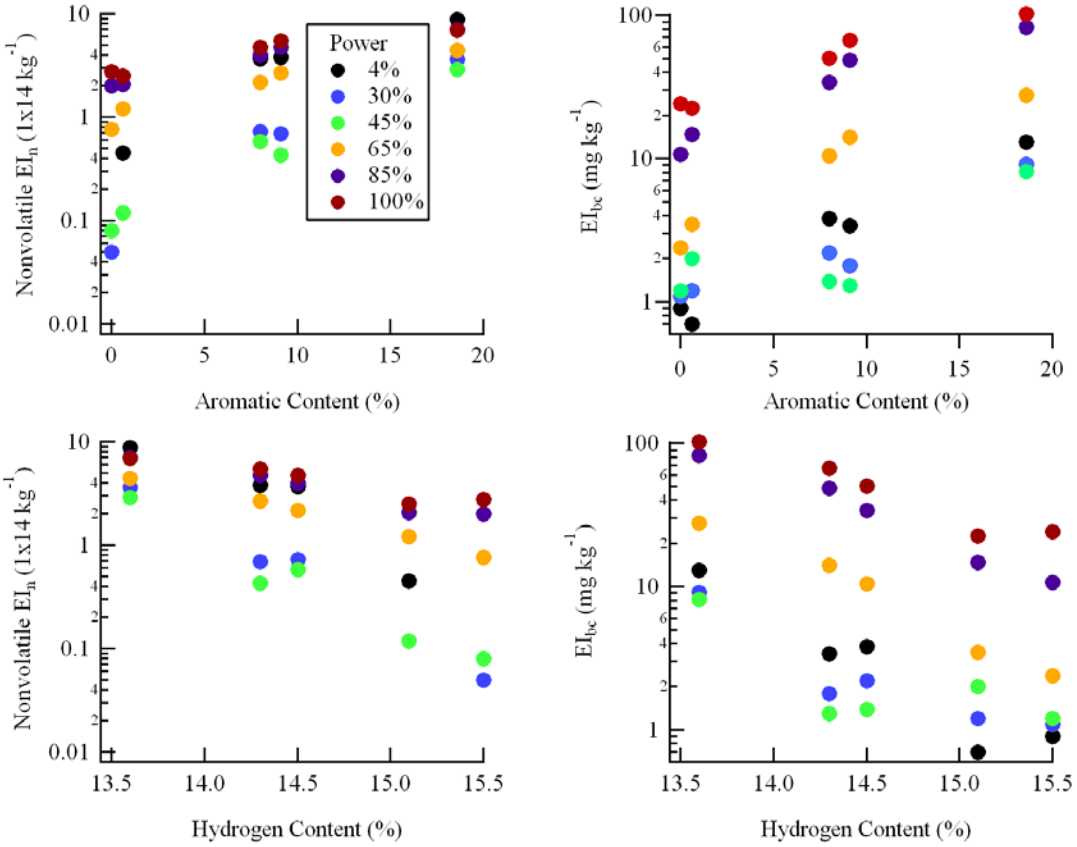

Figure 17. Particle EI_n and EI_{bc} as a function of fuel aromatic content (top) and fuel hydrogen content (bottom). All data are from the test engine 1-m probe.

The differences in PM emission characteristics observed between the two fuels are expected given with the current understanding of soot formation and growth in gas turbine engines. Several studies have shown that the soot production is inversely proportional fuel hydrogen content. For example, Sampath et al. (1986) successfully modeled the soot emissions from a PT6A-65 engine using hydrogen content as the sole fuel-related parameter. Rosfjord (1987) also found a linear relationship between hydrogen content and soot formation in the combustion zone of a high-pressure lab burner but found better correlations when a term for dicyclic aromatic content (DA, i.e., naphthalenes) was added to his empirical soot prediction equation. Chin and Lefebvre (1990a, 1990b) also developed an empirical expression for predicting gas turbine soot emissions, but they used smoke point (SP; the height above a laminar diffusion flame where visible smoke begins to form) along with DA as the principle variables. Other researchers note that fuel soot formation was negatively correlated to SP (i.e. Gulder et al., 1989), a parameter that tends to vary inversely with hydrogen content. However, by studying fuels with identical hydrogen contents but different SP values, Gulder et al. (1990) concluded that SP and H content are complimentary rather than interchangeable predictors of soot formation.

The fuel analysis conducted by AFRL on the AFFEX fuels included determination of hydrogen content, H/C ratio, olefins, total aromatics, and naphthalenes (see Table 4).

Taking the above discussion into consideration, we note that FT-2 had lower hydrogen (15.1 vs 15.5%), higher alkene (olefin, 3.8 vs. 0%) and higher aromatic (0.6 vs. 0%) content than FT-1, all of which suggests that it should exhibit the greater sooting tendency and thus greater EI_n and EI_{bc}.

To explore further the relationship between fuel composition and soot emissions, the power-dependent EI_n and EI_{bc} for the five fuels and fuel aromatic and hydrogen contents are presented in Figure 17. Additionally, a linear regression analysis was performed to explore the relationship between EI and fuel composition and the resulting statistics are presented in Table 5 and Table 6 for EI_n and EI_{bc}, respectively. Note the small sample size (N=5) for this analysis. The following results are suggested:

- EI_n and EI_{bc} at all power settings increased with aromatic content and decreased with hydrogen content.
- The variability in EI_n decreased with increasing aromatic content and decreasing hydrogen content. For example, EI_n for JP-8 (highest aromatics, lowest hydrogen) varied about 60% between idle and takeoff thrust whereas those for FT-1 (lowest aromatics, highest hydrogen) varied by almost two orders of magnitude. These findings are consistent with temperature dependence of soot formation, which is discussed in more detail below.
- EI_n and EI_{bc} were both well correlated with each fuel property. In general, correlation coefficients were greater for EI_n than for EI_{bc}, suggesting that the variability in EI_n was better captured by variability in fuel composition than was the variability in EI_{bc}.
- The best correlations were observed for idle (4%) and takeoff (100%) thrust settings for relationships between both EI_n and EI_{bc} with all fuel properties; correlation coefficients were minimized for 30% and 45% thrust settings.
- Slopes for EI_n linear regressions were greatest at the 4% thrust setting, suggesting that absolute EI_n values were most sensitive to variable fuel properties at aircraft idle.
- Slopes for EI_{bc} linear regressions were greatest at the 100 % thrust setting, suggesting that absolute EI_{bc} values were most sensitive to variable fuel properties at aircraft takeoff. Note that low black-carbon mass emissions at low engine thrust may have affected this result.
- Particle emissions appear to be better correlated with fuel aromatic than hydrogen content at all thrust settings for both EI_n and EI_{bc}. Note that fuel contents do not vary independently, so these results are only suggestive of observed relationships. Correlation coefficients for naphthalene were similar to those for total aromatics.

Table 7. Statistics for linear regression analysis for EI_n as a function of fuel chemical composition. Slopes and correlation coefficients are given for EI_n with aromatic content, hydrogen content, hydrogen-to-carbon ratio, and naphthalene content for each thrust power setting. The average values for each chemical property are also provided.

Aromatics	4 %	30 %	45 %	65 %	85 %	100 %	Average
slope	0.47	0.18	0.14	0.19	0.28	0.24	0.25
r^2	0.99	0.87	0.84	0.99	0.99	0.96	0.94

Hydrogen	4 %	30 %	45 %	65 %	85 %	100 %	Average
slope	-4.68	-1.75	-1.37	-1.94	-2.80	-2.44	-2.50
r^2	0.95	0.77	0.72	0.97	0.96	0.94	0.88

H/C ratio	4 %	30 %	45 %	65 %	85 %	100 %	Average
slope	-28.54	-10.59	-8.31	-11.84	-17.11	-14.92	-15.22
r^2	0.94	0.75	0.71	0.96	0.95	0.93	0.87

Naphthalene	4 %	30 %	45 %	65 %	85 %	100 %	Average
slope	5.24	1.99	1.58	2.12	3.11	2.73	2.79
r^2	0.98	0.83	0.79	0.96	0.98	0.97	0.92

Table 8. Statistics for linear regression analysis for EI_{bc} as a function of fuel chemical composition. Slopes and correlation coefficients are given for EI_{bc} with aromatic content, hydrogen content, hydrogen-to-carbon ratio, and naphthalene content for each thrust power setting. The average values for each chemical property are also provided.

Aromatics	4 %	30 %	45 %	65 %	85 %	100 %	Average
slope	0.64	0.40	0.32	1.34	3.82	4.35	1.81
r^2	0.91	0.80	0.66	0.99	0.98	0.98	0.89

Hydrogen	4 %	30 %	45 %	65 %	85 %	100 %	Average
slope	-6.18	-3.83	-3.03	-13.46	-38.76	-43.88	-18.19
r^2	0.80	0.69	0.56	0.94	0.95	0.94	0.81

H/C ratio	4 %	30 %	45 %	65 %	85 %	100 %	Average
slope	-37.47	-23.15	-18.28	-82.00	-236.32	-267.53	-110.79
r^2	0.78	0.67	0.54	0.93	0.94	0.93	0.80

Naphthalene	4 %	30 %	45 %	65 %	85 %	100 %	Average
slope	7.09	4.41	3.44	14.93	42.60	48.79	20.21
r^2	0.87	0.76	0.60	0.96	0.95	0.96	0.85

4.4. Volatile Aerosol Formation: 30-m and 145-m Probes

At the extreme temperatures of the exhaust plane, aerosols are composed completely of soot. These emissions are represented by the 1-m probe sampling documented in the Section 4.3. However as the plume ages, temperature decreases allow partitioning of gaseous compounds in the exhaust to the particulate phase forming volatile aerosols. This either occurs via the formation of nucleation-mode particles (typically with diameters less than 30 nm) or condensation onto soot-mode particles (with a diameter of between 50 and 200 nm). Samples taken from the 30-m and 145-m probes represent aged aircraft emissions and are discussed here.

4.4.1. Downwind JP-8 Sampling

In order to determine the effects of plume aging, sampling was performed at various distances downstream of the engine (with distance being used as a proxy for age). For the 1-m and 30-m probes, the same instruments were used with sample alternating between the two distances. However, differences in the inlets cause variation in particle transmission efficiency (Appendix P) with greater efficiency typically seen for the 30m inlet. Thus, care must be used when comparing the downwind and exhaust plane data.

Emission indices were calculated based on Equation 4. EI_n at 1 m were calculated from a CPC. At the 30-m probe, the particle number concentration was above the limits of the CPC, so the EEPS was used to determine EI_n. Size distributions and volume emission indices (EI_v) were calculated from the SMPS size distributions at 1 m and 30 m. EI_{bc} were measured continuously at 30 m by a MAAP and sporadically through the analysis of quartz filters by a OC/EC Aerosol Analyzer (Figure 6).

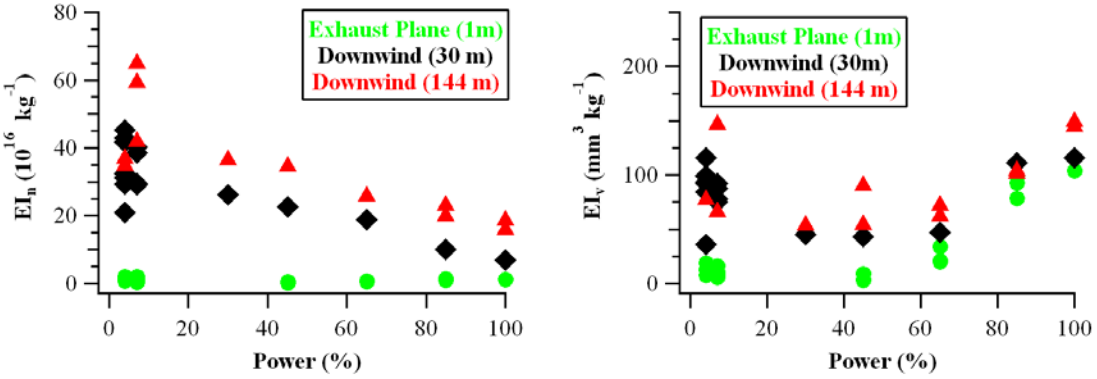

Figure 18. Results from test 12 showing EI_n (left) and EI_v (right) as a function of distance for JP-8 emissions.

Sampling was also performed 145 m behind the test engine. Due to the distance behind the engine, sampling of the engine exhaust was sporadic with interspersed periods of background and plume sampling. In order to find the emission indices, aerosol measurements during plume periods were plotted versus CO_2 to give the ratio of the emission indices. The emission index was then found based on the known emission index of CO_2. Because of uncertainties in the wind direction of the sampling, only data from

tests when JP-8 was burned in both engines is used at the 145 m probe. A CPC allowed for the determination of particle number concentration during tests 3, 4, 12, and 13, and a SMPS measured size distributions and was used for calculating EI_v during tests 12 and 13.

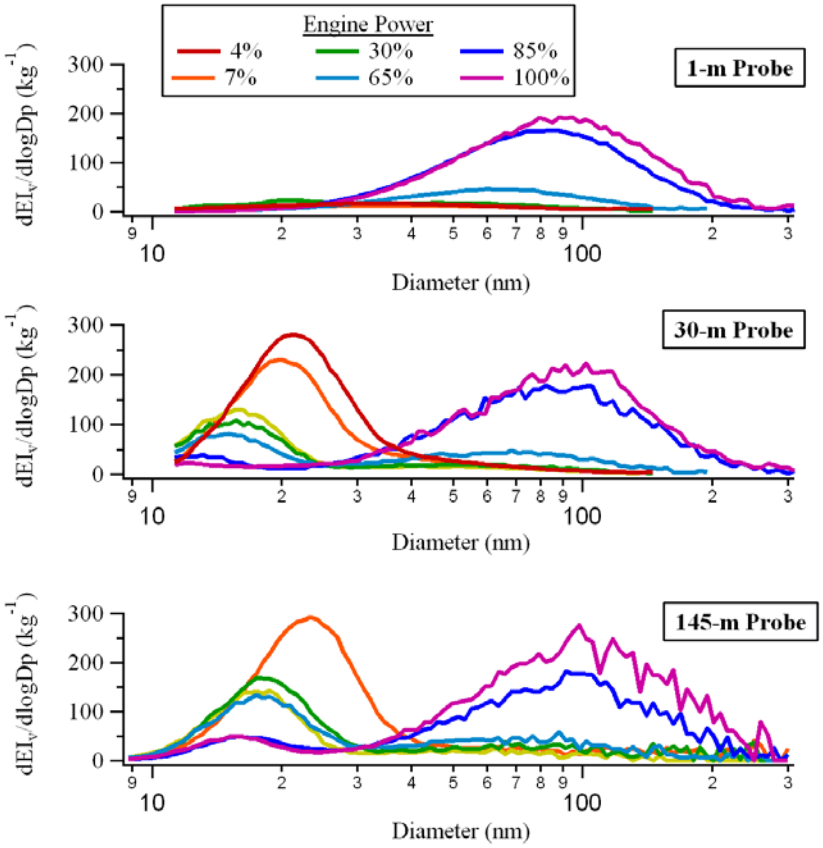

Figure 19. Size distributions ($dEI_v/dlogDp$, mg kg^{-1}) as a function of sampling probe and engine power setting for test #12 using JP-8 fuel. More uncertainty is observed with increasing probe distance because of increasing dilution correction factors.

A subset of results from the 145 m measurements are summarized in Figure 18; EI_n and EI_v as a function of engine power are shown and compared to values for 1-m and 30-m sampling. The downwind-increases in EI_n and EI_v are attributed to volatile aerosol formation and are the greatest at low power when emissions of gaseous precursors are greatest. Changes in particle size as a function of sampling probe are shown in Figure 19 as EI_v-weighted PSDs from test #12 on 27 January at 1, 30, and 145 m. At the exhaust plane the particles are comprised of a single soot mode (Figure 19, top panel), while an additional nucleation mode is only observed downwind. At low power, this nucleation mode dominates the PSD. As power increases the nucleation mode decreases and the soot mode increases with the soot mode dominating at high power. Very little variation is observed in the soot mode volume between each distance. Significant variability is observed for the nucleation-mode, as the peak-diameter and integrated volume each increase with increasing distance (from 30 m to 145 m, Figure 19), suggesting that gas-

to-particle conversion and particle growth is also occurring. This is also evident from Figure 18, as EI_v is greater at 145 m than at 30 m. Differences in EI_n are most significant between 1 m and 30 m, as the exhaust plume is cooling and particle nucleation is most prevalent. The difference between 30-m and 145-m EI_n is much less, suggesting that nucleation processes are still occurring but are less significant after 30 m.

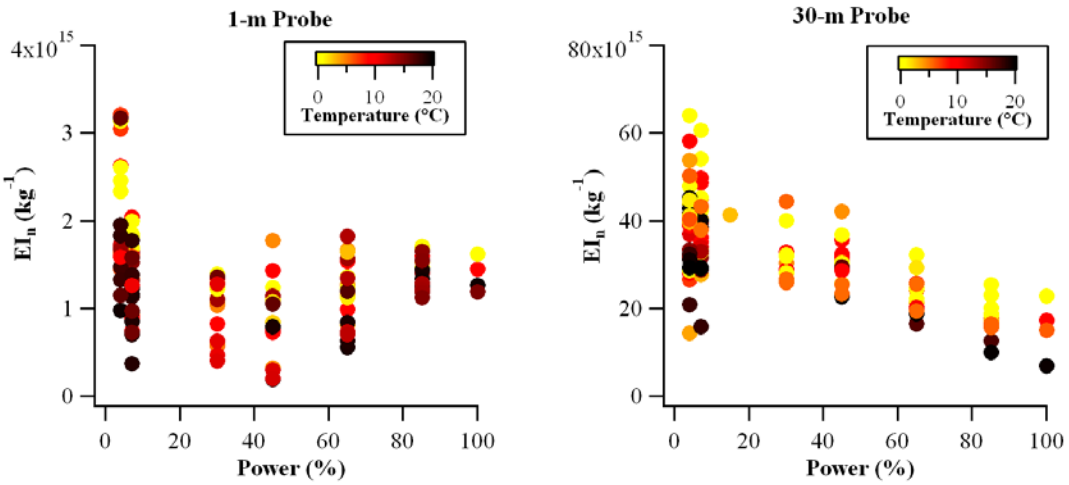

Figure 20. EI_n measured at 1 m (left) and 30 m (right) for all tests, colored by ambient temperature. Note the different y-axis scales for each plot.

4.4.2 *Temperature Dependence of JP-8 Emissions*

Analysis of EI_n at 30 m from all tests yielded large variability in values is observed. This is primarily the result of ambient temperature effects on combustion and plume aging. As ambient temperature decreases a clear increase in EI_n is observed at 30 m (Figure 20, right), which is likely the result of enhanced rate of new particle formation. As a comparison, the temperature dependence (denoted by the coloring in Figure 20) of EI_n measurements at 1-m are also provided in Figure 20 (left). Note that EI_n at 30 m are much greater than at 1 m, by more than an order of magnitude, because of particle nucleation downwind of the combustor. Additionally, the temperature dependence at 1 m is less distinct compared to 30 m measurements, suggesting that nucleation processes, and not changes in the soot formation mechanism, drive the observed temperature dependence at 30 m.

To focus on the change in number concentration at 30 m, a linear fit of EI_n versus temperature is performed for each power (for example, Figure 21, right). The y-intercept (and its error) gives the emission index at 0°C (and its error), while the slope (and its error) gives the temperature dependence (and its error) in kg^{-1} $°C^{-1}$. The EI_n at 10°C can then be calculated. 10°C is chosen as a reference because it is the midpoint of the ambient temperature range during AAFEX. The EI_n (10°C) at 30 m decreases with power (Figure 22, right) as a result of decreasing precursor hydrocarbon emission (which results in less new particle formation). The 30-m temperature dependence is greatest at low power (4 and 7 % thrust) and is relatively constant (but still negative) at higher powers.

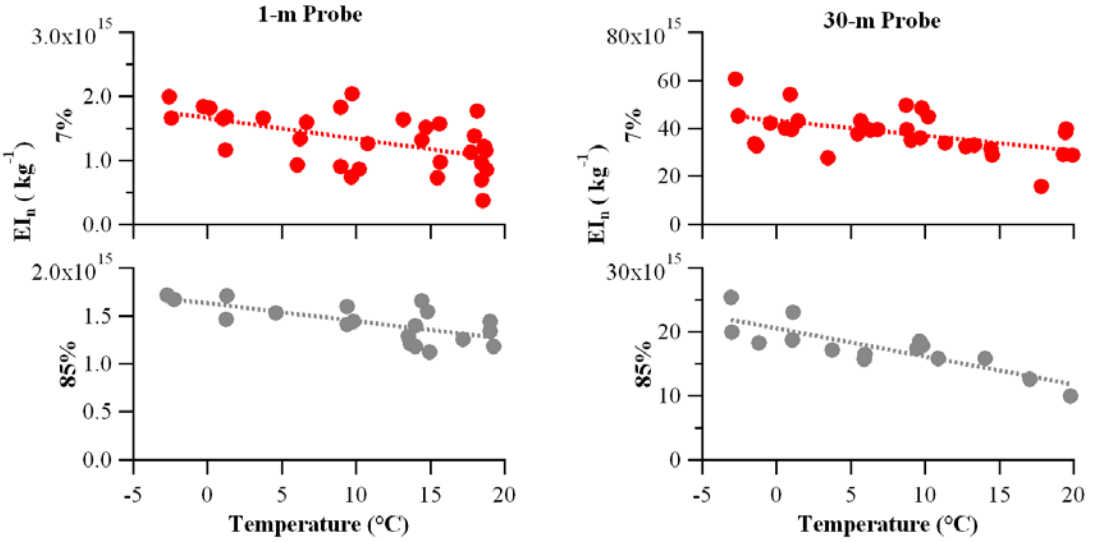

Figure 21. EI_n at 1 m (left) and 30 m (right) as a function of ambient temperature at 7% (top) and 85% (bottom) power. Note the different y-axis scales on each plot.

For comparison, the same analysis was performed for 1-m data. EI_n at 1 m are significantly lower than at 30 m, and the temperature dependence (for 7% and 85 % power settings) had more variability (Figure 21, left) compared to measurements at 30 m. Still, a negative correlation was obtained for all power settings, which is shown in Figure 23 (left). Note that the temperature dependence (linear regression slopes) are much smaller than at 30 m, but a similar trend was observed; the largest temperature dependence was observed at low power and fairly constant and slightly negative temperature dependence at higher engine power.

This temperature dependence analysis was also performed with respect to EI_{bc} at 30 m and at 1 m (for comparison). EI_{bc} at 10°C and the temperature dependence for both 1-m and 30-m probe measurements are shown in Figure 23. An increase in soot is observed as the engine-power increases with similar EI_{bc} values for both probes. Differences are attributed to increased line loss in the 1-m probe, as theoretically the EI_{bc} should not vary with probe distance or plume age. The trend in temperature dependence is less clear compared to the EI_n analysis but is similar for both probe distances. For both probes, a dependence of similar magnitude was observed at high engine power where concentrations are the largest. A negative temperature dependence was also observed at the lowest power setting for the 30-m probe and not the 1-m probe, and may be the result of erroneous interpretation of low concentration data at this power setting. The temperature and engine power dependence of black carbon measurements is likely the result of variable combustion conditions in the engine.

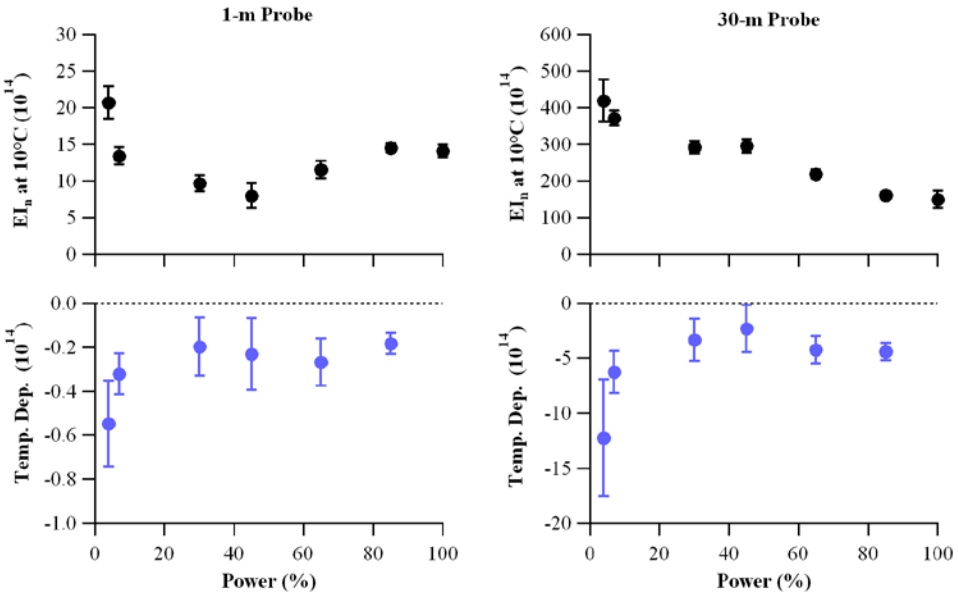

Figure 22. EI_n at 1 m (left) and 30 m (right) at 10°C (kg^{-1}, top) and its temperature dependence (kg^{-1} $°C^{-1}$, bottom) as a function of engine power. Error bars are the 1 sigma standard deviation of the linear fits. The temperature dependence for 100% power is not shown because there too few data points. Note the different y-axis scaling for the left and right panels.

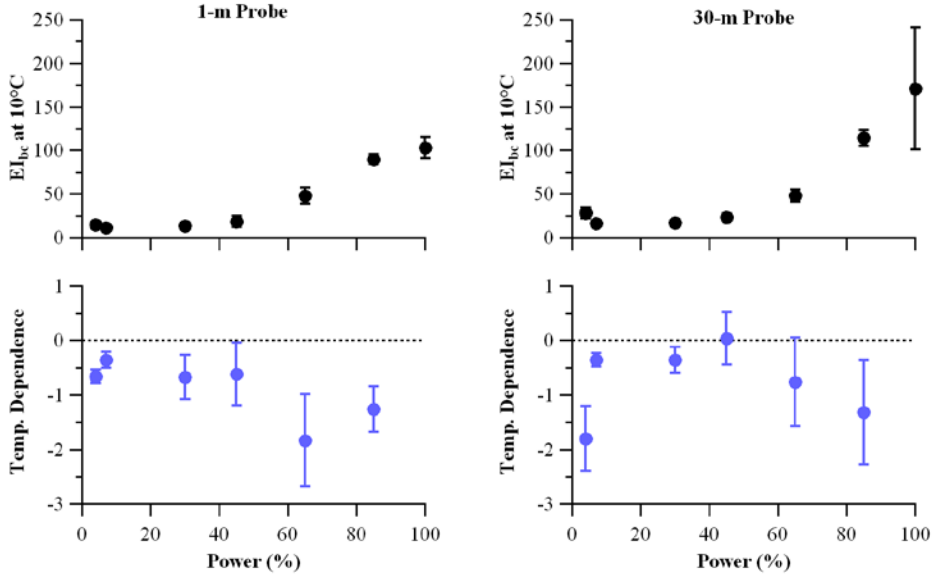

Figure 23. EI_{bc} at 1 m (left) and 30 m (right) at 10°C (mg kg^{-1}, top) and its temperature dependence (mg kg^{-1} $°C^{-1}$,bottom) as a function of engine power. Error bars are the 1-sigma standard deviation of the linear fits. The temperature dependence for 100% power is not shown because there are too few data points.

4.4.3 Temperature Dependence of Nucleation and Soot Modes; Soot Mode Coating

The aerosol measurements shown in Figure 19 clearly are a composite of both nucleation-mode particles and soot-mode. The soot mode is composed of black carbon with a potential coating of volatile organic compounds. In order to determine the importance of these components, the nucleation and soot modes are fitted (for example, Figure 24). The 30-m volatile aerosol volume corresponding to the soot mode is found by fitting the data between 50 and 200 nm. This is subtracted from the total size distribution to find the residual which is then fit to determine the volume corresponding to the nucleation mode. Because the 1-m PSDs did not exhibit the same bimodal trend, only the soot mode was fit. The EI_v and temperature dependence for the nucleation and soot modes is shown in Figure 25. Nucleation-mode mass is greatest at low power and fairly constant at higher powers, a trend similar to 30-m EI_n shown in Figure 22. Conversely, the soot mode particles increase as power increases, with a similar trend and magnitude as EI_{bc} in Figure 23, since black carbon makes up the majority of the soot mode volume. Temperature effects for the nucleation-mode and soot-mode EI_v are most significant at low and at high power, respectively, again analogous to EI_n and EI_{bc} at 30 m.

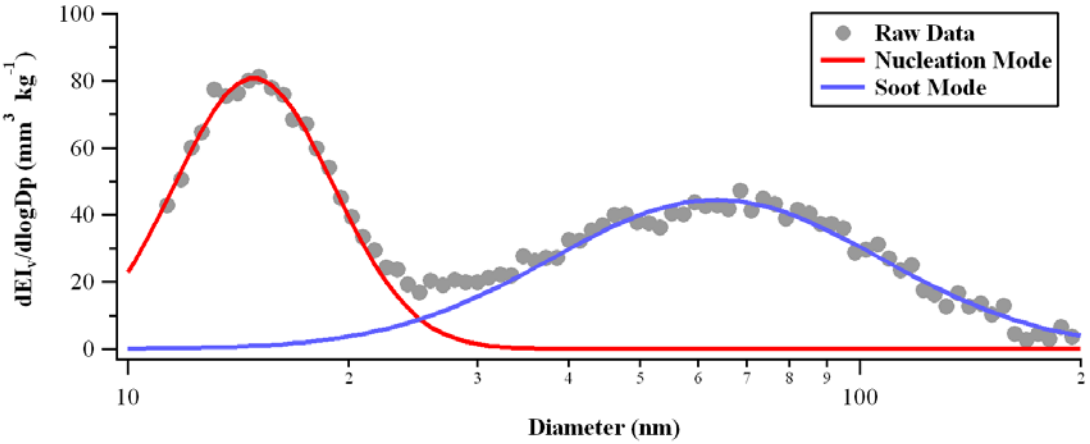

Figure 24. Representative size distribution at 65% power for the 30-m probe with fitting of the nucleation and soot modes.

The soot mode EI_v (Figure 24, right) is composed of black carbon and a possible volatile coating and exhibits a similar trend in EI_v as EI_{bc} found by the MAAP (Figure 22). However, in order to compare the soot EI_v and EI_{bc}, the density of the black carbon must be known. At the exhaust plane, the aerosol is composed entirely of soot. Using the 1-m SMPS and MAAP data, a black carbon effective density of 0.93 ± 0.02 g cm^{-3} for the JP-8 fuel was determined (see discussion above). Assuming this density is constant, black carbon volume for the 30-m MAAP samples is determined. These values agree with the total soot-mode aerosol volume (found by the SMPS) to within ±15 mm^3 kg^{-1} suggesting an upper limit of 15 mm^3 kg^{-1} for the volume of the soot-mode coating. This is consistent with data from the aerosol mass spectrometer which found soot-mode organic mass

emission indices on the order of 5 mg kg^{-1} (5.4 mm^3 kg^{-1} assuming a soot density of 0.93 g cm^{-3}).

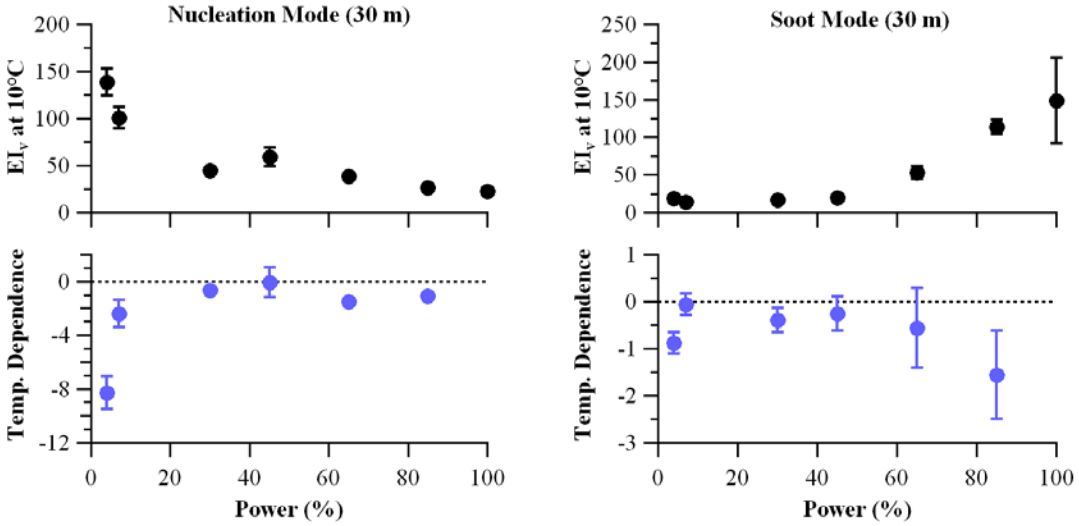

Figure 25. Nucleation mode (left) and soot mode (right) EI_v for the 30-m probe at 10°C (mm^3 kg^{-1}) and its temperature dependence (mm^3 kg^{-1} $°C^{-1}$) as a function of power. Error bars are the 1 sigma standard deviation of the linear fits.

4.4.4 Comparison of JP-8 and Alternative Fuel Emissions at 30-m Probe

Figure 26 compares total PM number and volume EIs measured in samples from the test engine 30-m inlet probe and illustrates the impact of fuel composition on volatile aerosol formation and growth in downstream engine exhaust. At low engine powers, total EI_n values for JP-8 were enhanced by a factor of 40 to 50 above corresponding 1-m values (comparing EI_n from Figure 26 to Figure 11 and Figure 12), which indicates that nucleation and growth of new particles occurred quite rapidly as the plume cooled and diluted with background air. EI_n decreased with power as more surface was available for condensation (for example, EI_m in Figure 26) and decreasing amounts of condensable organic gas were available for new particle formation. The JP-8 EI_m was significantly higher than 1-m values at all power settings regardless of ambient conditions.

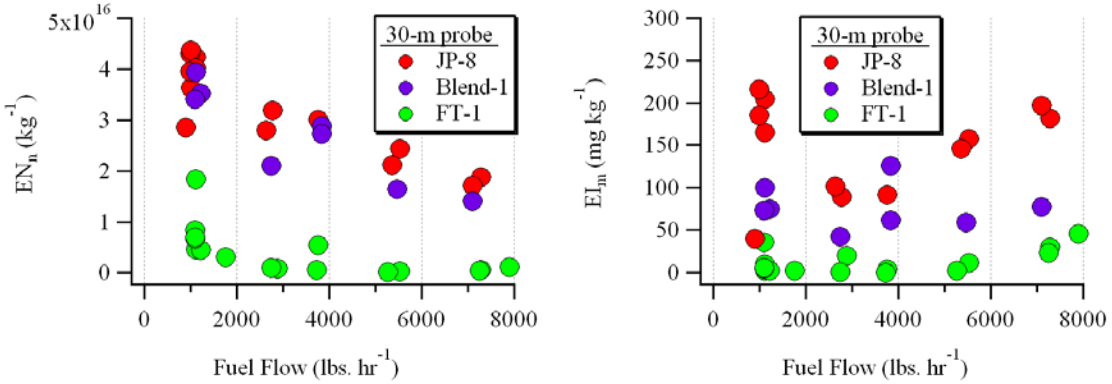

Figure 26. Number (left) and mass (right) emission indices at 30-m for JP-8, FT-1, and Blend-1. Data are only shown for ambient conditions where temperature was greater than -1°C and less than 7°C.

FT-1 total EI_n values were substantially lower than from JP-8, but still were enhanced above 1-m values. This difference is potentially due to the slight sulfur contamination or to nucleation of semi-volatile hydrocarbons at the relatively cold ambient temperatures. Blend-1 total EI_n values were similar to JP-8 values despite the factor of two difference in sulfur content between the fuels. This result is not unusual; Timko et al. (2010) observed higher relative EI_n in a plume generated by combustion of 50% synthetic fuel. From modeling analysis, they showed that the reduced availability of soot surface area in the blended fuel exhaust caused new particle formation to be favored over condensation of volatile material onto soot mode particles. Competition between the decreased condensation sink and decreased new particle formation potential (from reduced sulfur content) results in complex interpretation of the data that requires additional modeling effort. Here, we believe that volatile particle populations reached equilibrium between formation by nucleation and loss through coagulation that made the overall particle number densities vary independently from fuel sulfur content. This is supported by our observations that JP-8 nucleation-mode mean diameters were significantly larger than corresponding Blend-1 diameters in the 30-m samples at all power settings.

4.5 APU Emissions

The DC-8's APU is essentially a small turbo-jet engine (Honeywell Model GTCP85-98CK) that was manufactured in the 1960s and was expected to produce much greater EIs than the aircraft's CFM-56 engines. Tests 7, 15, and 16 were conducted to characterize emissions from the APU as it burned JP-8 and FT fuel under typical operational loads. For the tests, an inlet probe was positioned approximately 10 cm below the APU exhaust port, which is located on the starboard side of the aircraft, just ahead of the wing spar. Exhaust samples were diluted with dry nitrogen just inside the inlet tip and drawn into a community sample distribution manifold in the same manner implemented during the aircraft engine tests. APU load was varied by drawing power from the unit to drive aircraft electrical systems and air handlers and to start an engine. Exhaust gas temperature (EGT) was used to indicate APU load. EGT varied from

approximately 350°C at idle to greater than 610°C when bleed air was used to spin one of the aircraft's engines (for comparison, EGT for the DC-8's test engine varied from approximately 400°C at idle to 716°C at takeoff thrust). Typical samples contained 1000 to 2000 ppm CO_2 and particle number densities in the 10^{-5} to 10^{-6} cm^{-3} range, well within the concentration range of the diagnostic instruments. The individual set points were fairly reproducible and stable allowing representative data to be obtained with each of the fuels tested.

Figure 27 shows particle emission indices and size statistics for the APU as it burned JP-8 and FT-2. Corresponding volume-based PSDs are displayed in Figure 28. Note that data from test 7 are excluded from the plots because the operators were unable to access the full range of test loads on the APU on that day. Also, tests 15 and 16 were conducted back-to-back over a 2.5-hour period with ambient temperature remaining fairly constant; thus the trends in EI as a function of engine load (EGT) and fuel composition should not be influenced by changes in engine inlet temperature or pressure. These analyses demonstrate the significant reduction in EI_n and EI_{bc} observed by burning FT-2 compared to JP-8 at all engine loads and that the resulting aerosols are significantly smaller in diameter.

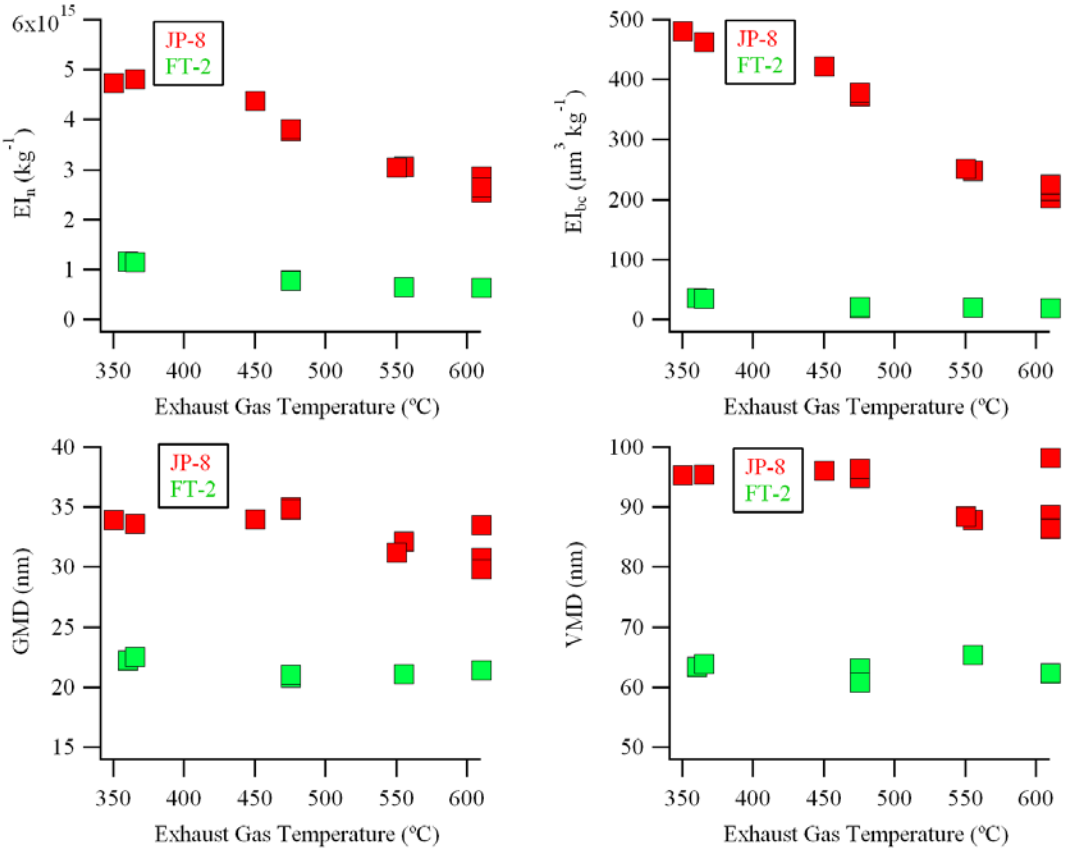

Figure 27. PM emission characteristics of the DC-8 APU as it burned standard JP-8 and FT-2 as a function of EGT (a proxy for engine load). Plots include data from tests 15 and 16 only.

Emissions indices are summarized in Figure 29 as average values for all DC-8 and APU sampling with JP-8 and FT-2 fuels. From a PM standpoint, the APU is much more polluting than the DC-8's CFM-56 engines. JP-8 APU emissions far exceeded those from the DC-8 for EI_n ($8.4x10^{15}$ and $7.2x10^{14}$ kg^{-1}, respectively) and for EI_{bc} (326 and 44 mg kg^{-1}, respectively). APU to DC-8 EIs varied with engine load. For example, when burning JP-8 at idle (350 EGT) the APU EI_n and EI_{bc} were about 6 and 35 times higher, respectively, than corresponding values for the DC-8. Moreover, the ratio between APU and engine EIs was greatest at idle and decreased significantly with power. Unlike for the high-pass engines on the DC-8, the normalized APU PM emissions decreased with increasing power (for example, the JP-8 EI_n and EI_{bc} trends in Figure 27). Indeed both EI_n and EI_{bc} values declined by more than a factor of two as the APU load was increased from minimum (cabin lights and avionics only) to maximum (air handler operation plus providing bleed air to spin the DC-8 control engine). Since the APU fuel-air-ratio increased with thrust (similar to the aircraft engine), the decreasing emissions can't be attributed to rich combustion conditions at idle. Improved combustion efficiency or increased combustor pressure with thrust are other factors that could influence the emission behavior of the APU.

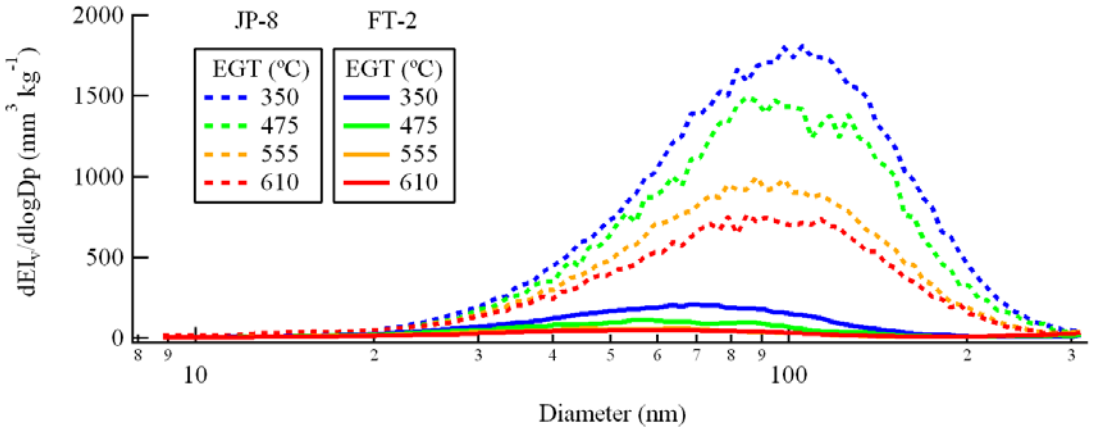

Figure 28. APU volume-based PSDs as a function of EGT for JP-8 (dashed lines) or FT-2 (solid lines).

Overall, PSDs for APU emissions resulted in larger diameter particles than from the DC-8 (Figure 29). For JP-8, GMDs were 32.9 and 21.2 nm for the APU and DC-8, respectively, and VMDs were 92.8 and 57.0 nm for the APU and DC-8, respectively. FT-2 particles were smaller compared to emissions from JP-8 but again were coincidentally comparable to the JP-8 GMD and VMD from the DC-8. Particle size also varied with engine load and APU GMD and VMD values decreased slightly with increasing load (Figure 28), which is opposite to the trends observed in DC-8 engine PM emissions (Figure 11). However, even at the highest load/thrust settings, APU particles were still 20-30% larger, on a volume-basis, than those emitted by the DC-8 engines.

The APU particles were also much more fractal and less dense than those emitted by the engines. For example, density values for JP-8 fuel combustion obtained by taking the ratio of EI_{bc} (from the MAAP) to EI_v (from an SMPS) averaged 0.51±0.02 g cm^{-3} for APU compared to 0.92±0.08 g cm^{-3} for the engines at thrust settings greater than 65 %.

APU PM emissions are likely more similar in size, density and fractal nature to soot emissions from older, low-pass aircraft engines.

However, the DC-8's APU and engines were similarly characterized by significnat PM emission-reduction benefits from burning FT fuel (Figure 27 and Figure 29). FT-2 average EI_n values were reduced compared to JP-8 for the APU ($8.4x10^{15}$ and $1.4x10^{15}$ kg^{-1}, respectively, a factor of six), but were still significant and comparable to JP-8 EI_n and EI_{bc} from the DC-8. A reduction by a factor of 13 was observed for average EI_{bc}. APU FT-2 combustion also produced significantly smaller particles compared to JP-8; GMD was 32.9 and 21.5 nm for JP-8 and FT-2, respectively and VMD was 92.8 and 63.2 nm, respectively. APU FT particles were more dense than APU JP-8 particles, with average density values of 0.60±0.06 g cm^{-3} as opposed to 0.51±0.02 g cm^{-3} for JP-8.

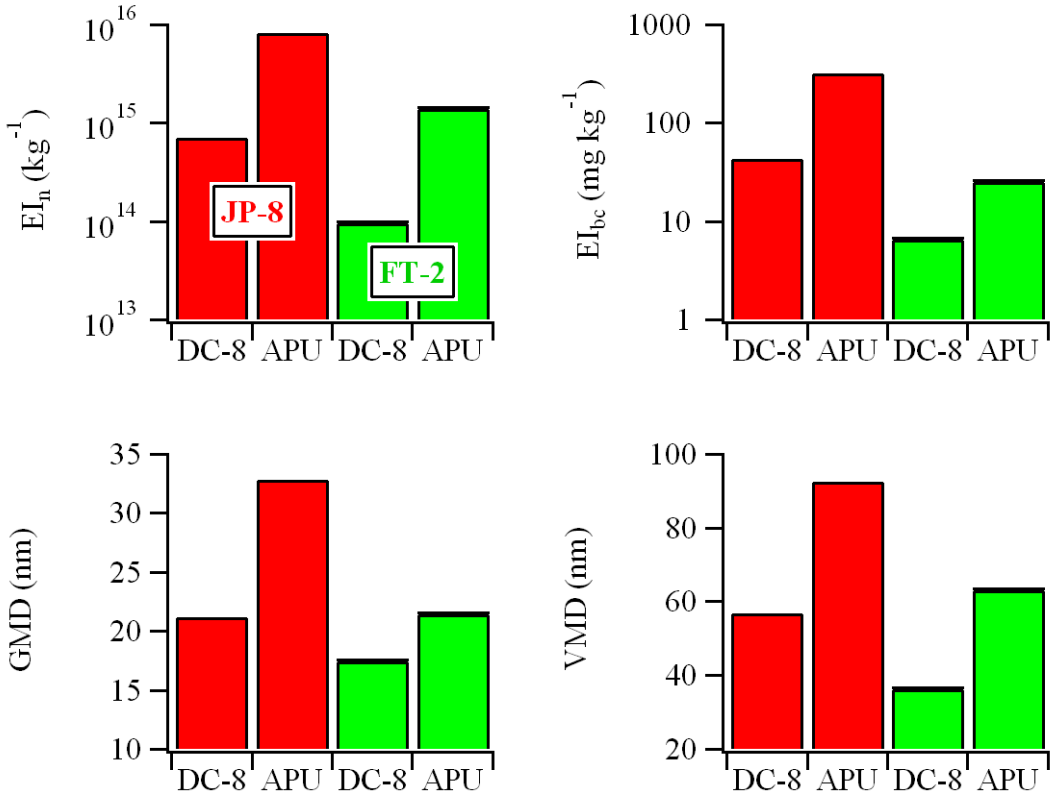

Figure 29. Comparison of average PM emissions from DC-8 and APU testing for JP-8 (red) and FT-2 (green) fuels.

5.0 Summary

Engine power dependent aerosol emissions were characterized using an extensive suite of instrumentation. Sampling protocol and inlet configuration was specifically designed to

focus on a robust comparison of emissions from standard JP-8 jet fuel and four alternative jet fuels and to assess dynamic aging processes as aircraft emissions are diluted and cooled to ambient atmospheric conditions. The alternative fuels selected were prepared by the Fischer-Tropsch (FT) process from natural gas and from coal feedstocks. The two inboard engines aboard the NASA DC-8 were used for testing and each produced a very similar emissions signature. Thus, one engine was used as a control and the other a test engine for assessing alternative fuel emissions.

Emissions from pure FT fuels were characterized by significantly reduced EI_n and EI_{bc} compared to emissions from JP-8, and emitted particles were smaller and more dense. The largest emissions benefit for EI_n is gained at low engine power. Consequently, a switch to FT fuels may be most beneficial to ground-level air quality improvement given the development of new air quality standards based on a shifting emphasis from particle mass to particle number concentration. The largest emissions benefit for EI_{bc} is gained in the middle range of engine power (65% thrust level) and thus the benefits of FT fuels, on a black carbon mass basis, may be greatest at cruise altitudes. Thus, the use of FT fuels may have significant climate effects as black carbon plays a critical role in atmospheric dynamics and cloud formation processes (Koch and Del Genio, 2010) by both absorbing light and acting as an ice nucleus.

By comparing emissions from JP-8, the two pure FT fuels, and the JP-8/FT blends, particle characteristics were found to vary directly with changes in fuel composition. EI_n and EI_{bc} both varied positively with fuel aromatic content and were inversely correlated with hydrogen content.

Downwind sampling resulted in emissions with very different properties at the engine exhaust plane compared to those sampled at two distances downwind. Initial emissions are characterized by a single soot mode comprised exclusively of black carbon. As the exhaust plume cools and dilutes, new particle formation occurs significantly increasing particle number concentrations as well as volatile aerosol volume. The majority of new particle formation occurs by 30 m downwind, and number concentration increases are considerably smaller between 30 m and 145 m. Still, aerosol sizes continue to increase after 30 m because of particle growth and further gas-to-particle conversion.

The new particle formation is highly temperature dependent as EI_n increases with decreasing temperature; this dependence is most sensitive at low engine power consistent with the largest concentration of organic gas-phase precursors (Anderson et al. 2006). Temperature dependence is also observed for EI_n and EI_{bc} at the engine exhaust plane, suggesting that soot formation inside the engine is also sensitive to ambient temperature changes. Aerosol emissions from the aircraft's APU were significantly greater compared to the DC-8 engine emissions. Use of FT fuels in the APU resulted in similar magnitude reductions in both for EI_n and EI_{bc} as were observed for the DC-8 engines.

6.0 References

Anderson, B. E., G. Chen, and D. R. Blake (2006), Hydrocarbon emissions from a modern commercial airliner, Atmospheric Environment 40, 3601-3612.

Cheng, M.-D., E. Corporan, M. J. DeWitt, and B. Landgraf (2009), Emissions of volatile particulate components from turboshaft engines operated with JP-8 and Fischer-Tropsch fuels, Aerosol and Air Quality Research 9, 237-256.

Chin, J. S., and A. H. Lefebvre (1990a), Influence of fuel composition on flame radiation in gas-turbine combustors, Journal of Propulsion and Power 6, 497-503.

Chin, J. S., and A. H. Lefebvre (1990b), Influence of fuel chemical-properties on soot emissions from gas-turbine combustors, Combustion Science and Technology 73, 479-486.

Corporan, E., M. J. DeWitt, V. Belovich, R. Pawlik, A. C. Lynch, J. R. Gord, and T. R. Meyer (2007), Emissions characteristics of a turbine engine and research combustor burning a Fischer-Tropsch jet fuel, Energy and Fuels 21, 2615-2626.

DeWitt, M. J., E. Corporan, J. Graham, and D. Minus (2008), Effects of aromatic type and concentration in Fischer-Tropsch fuel on emissions production and material compatibility, Energy and Fuels 22, 2411-2418

Gulder, O. L. (1989), Influence of hydrocarbon fuel structural constitution and flame temperature on soot formation in laminar diffusion flames, Combustion and Flame 78, 179-194.

Gulder, O. L., B. Glavincevski, and M. F. Baksh (1990), Fuel molecular-structure and flame temperature effects on soot formation in gas-turbine combustors, Journal of Engineering for Gas Turbines and Power-Transactions of the ASME 112, 52-59.

Koch, D. and A. D. Genio (2010), Black carbon absorption effects on cloud cover, review and synthesis, Atmospheric Chemistry and Physics Discussions 10, 7323-7346.

Petzold, A., and A. Dopelheuer (1998), Re-examination of black carbon mass emissions indices of a jet engine, Aerospace Science and Technology 29, 355-356.

Rosfjord, J. Role of fuel chemical-properties on combustor radiative heat load (1987), Journal of Propulsion and Power 3, 494-501.

Sampath, P., M. Gratton, D. Kretschmer, and J. Odgers (1986), Fuel property effects upon exhaust smoke and the weak extinction characteristics of the Pratt and Whitney PT6A-65 engine, Jouranl of Engineering for Gas Turbines and Power 108, 175-181.

Timko, M. T., Z. Yu, T. B. Onasch, H.-W. Wong, R. C. Miake-Lye, A. J. Beyersdorf, B. E. Anderson, K. L. Thornhill, E. L. Winstead, E. Corporan, M. J. DeWitt, C. D. Klingshirn, C. Wey, K. Tacina, D. S. Liscinsky, R. Howard, A. Bhargava, Particulate emissions of gas turbine engine combustion of a Fischer-Tropsch synthetic fuel, in preparation.

Wey. et al. (2006), An overview of the Aircraft Particle Emission Experiment, NASA Technical Manual.

Wey, C. C., B. E. Anderson, C. Wey, R. C. Miake-Lye, P. Whitefield, and R. Howard (2007), Overview on the aircraft particle emissions experiment, Journal of Propulsion and Power 23, 898-905.

APPENDIX I: Influence of Ambient Temperature on the PM Emissions at the Engine Exit

Donald E. Hagen, Prem Lobo, and Philip D. Whitefield

Center of Excellence for Aerospace Particulate Emissions Reduction Research
G-7 Norwood Hall, Missouri University of Science and Technology, Rolla, MO 65409

Introduction

Several studies have been carried out to characterize emissions from military engines (Corporan et al., 2005, 2007) and, more recently, commercial jet engines burning alternative aviation fuels (Lobo et al., 2010). NASA spearheaded a study called AAFEX: Alternative Aviation Fuels Emissions Experiment, to evaluate the impacts of synthetic fuels on commercial aircraft engine gaseous and Particulate Matter (PM) emissions. The Missouri University of Science and Technology Center of Excellence for Aerospace Particulate Emissions Reduction Research (Missouri S&T COE) was a team member for AAFEX.

The study was and was conducted in January 2009 in Palmdale, CA. The emissions tests were performed on the same CFM56-2C1 engine, mounted to a NASA DC-8 aircraft, which was studied during APEX-1 (Wey et al., 2007). The aircraft was parked on the runway, and emissions samples were extracted at the engine exit plane (1 m), in the near field (30 m), and in the advected plume (145m). The primary fuels used in this study were: JP-8, a Fischer-Tropsch fuel derived from natural gas (FT1), and a second Fischer-Tropsch fuel derived from gasified coal (FT2). In addition to these fuels, 50:50 blends of the Fischer-Tropsch fuels and JP-8 were also studied.

Instrumentation

The instrumentation onboard the Missouri S&T mobile laboratory to sample emissions at the engine exit plane consisted of the Cambustion DMS500, a state-of-the-art fast particulate spectrometer, to gather real-time size distribution information and total concentration of engine exhaust PM; a scanning differential mobility analyzer (SDMA) (TSI model 3071), to measure PM size distributions; a TSI condensation particle counter (CPC) (TSI model 3022) to measure total number concentration; a fast response carbon dioxide (CO_2) detector to monitor sample dilution and establish emission factors. The instruments have been extensively used in recent field campaigns to measure PM emissions from commercial aircraft engines burning conventional and as well as alternative aviation fuels (Lobo et al. 2007; 2010; Herndon et al., 2008).

Methodology

One of the main objectives of the AAFEX campaign was to investigate the effect of changing test condition variables such as engine power, ambient temperature, fuel type, probe position, etc. on emissions characteristics of the CFM56-2C1 engine. Normally the procedure to investigate such dependencies would be to hold all parameters constant

except for one, and measure the emissions as that parameter is varied. This procedure cannot be followed for ambient temperature. All the testing at AAFEX was conducted outdoors, and ambient temperature was dictated by nature. Large temperature variations were observed during the campaign, especially between early morning and late afternoon. This report summarizes and describes the results of AAFEX, in terms of the influence of ambient temperature on total PM emissions at the exit plane of a CFM56-2C1 engine.

In order to study the impact of temperature variation on PM emissions, two subsets of the entire AAFEX data set were selected, in which the fuel type and probe position were held constant while engine fuel flow (surrogate for power) and ambient temperature varied. The first data set chosen was for the reference fuel, JP-8, and the second data set was for the FT1 fuel. A third fuel, FT2, was also studied in the campaign. However during the time span for the FT2 measurements, the ambient temperature did not spread out over the temperature range as uniformly as was the case for JP8 and FT1 and hence this data was not incorporated into the following analysis.

These data sets were organized into the form $\{T_i, FF_i, ap_{ni}, \delta ap_{ni}\}$, where

FF_i denotes the fuel flow during the i-th measurement,

ap_{ni} denotes the measured value of the n-th aerosol parameter during the i-th measurement,

n = 1 refers to Dgn (number-based geometric mean diameter)
n = 2 refers to Dgm (mass-based geometric mean diameter)
n = 3 refers to EIn (number-based emissions index),
n = 4 refers to EIm (mass-based emissions index).

δap_{ni} denotes the uncertainty in the measurement of aerosol parameter ap_{ni}.

These aerosol parameters were derived from size distributions measured using a scanning differential mobility analyzer.

Consider the group of test points $\{T_i, FF_i, ap_{ni}, \delta ap_{ni}\}$ for a fixed sampling location and fuel, but which span a range of ambient temperatures and engine fuel flow rates. A set of temperatures $\{T_j, j=1,2,\ldots,J\}$ and fuel flow rates $\{FF_k, k=1,2,\ldots,K\}$ are selected which span the range of temperature and fuel flow rate represented in the data, and where possible fall near values where these parameters cluster. Two dimensional interpolation is employed to determine values for the aerosol parameter and uncertainty at these selected temperatures and fuel flow rates. A linear interpolation is accomplished with the software package Matlab, using Griddata and Meshgrid routines. Application of the interpolation method to the data set $\{T_i, FF_i, ap_{ni}, \delta ap_{ni}\}$ results in the interpolated data set $\{T_j, FF_k, ap_{njk}, \delta ap_{njk}\}$. ap_{njk} denotes the interpolated value for the n-th aerosol parameter at temperature T_j and fuel flow rate FF_k; δap_{njk} is its associated uncertainty. In summary, for a fixed fuel type and sampling location, the data from test point set $\{T_i, FF_i, ap_{ni}, \delta ap_{ni}\}$ is interpolated to give aerosol parameter values at prescribed temperatures and fuel flow rates $\{T_j, FF_k, ap_{njk}, \delta ap_{njk}\}$.

The range of temperatures encountered in the JP-8 data set (28–65°F) was larger than that for the FT1 fuel (34–58°F). In order to study the relationship between the temperature

dependencies for the different fuels, the JP-8 data was interpolated a second time using the same temperatures used for the FT1 analysis.

Results

Table 1 lists the interpolated emissions results for the FT1 fuel. The average aerosol parameters (Dgn, Dgm, EIn, and EIm) and their uncertainties are listed for the temperatures (°F): 34, 42, 47, 56, and 58, and fuel flow rates (lbs/hr): 1150, 2778, 3869, 5385, 6597, and 7685.

Table 1. PM emissions parameters for the FT1 fuel.

Dgn (nm)					
Fuel flow rate (lbs/hr)	**Temperature (°F)**				
	34	**42**	**47**	**56**	**58**
1150		11.46 ± 0.52	12.82 ± 0.73	15.70 ± 1.51	16.15 ± 1.89
2778	12.99 ± 0.94	13.53 ± 0.99	14.46 ± 0.96	16.09 ± 0.82	17.03 ± 1.82
3869	14.75 ± 1.84	13.93 ± 10.26	15.78 ± 7.77	19.10 ± 3.29	19.84 ± 2.30
5385	17.79 ± 0.42	17.27 ± 0.41	17.18 ± 0.37	17.01 ± 0.31	16.96 ± 0.32
6597	19.50 ± 0.35	20.09 ± 0.40	20.52 ± 0.42	21.25 ± 0.46	21.05 ± 0.38
7685		21.59 ± 0.46	22.59 ± 0.34	23.03 ± 0.37	

Dgm (nm)					
Fuel flow rate (lbs/hr)	**Temperature (°F)**				
	34	**42**	**47**	**56**	**58**
1150		142.53 ± 24.21	136.84 ± 29.37	126.60 ± 38.66	125.12 ± 38.56
2778	118.09 ± 19.16	112.30 ± 56.71	108.68 ± 80.19	144.73 ± 24.68	118.32 ± 87.06
3869	39.44 ± 344.86	30.54 ± 240.27	49.32 ± 181.26	83.13 ± 75.06	90.65 ± 51.46
5385	40.75 ± 47.77	47.86 ± 6.30	53.51 ± 6.28	63.56 ± 6.32	65.31 ± 6.62
6597	44.87 ± 1.28	46.18 ± 1.20	47.09 ± 1.17	49.09 ± 1.21	51.73 ± 1.67
7685		52.52 ± 0.74	54.86 ± 0.94	56.75 ± 0.85	

EIn (10^{14}/kg fuel)					
Fuel flow rate (lbs/hr)	**Temperature (°F)**				
	34	**42**	**47**	**56**	**58**
1150		0.173 ± 0.004	0.149 ± 0.003	0.107 ± 0.003	0.100 ± 0.003
2778	0.153 ± 0.007	0.115 ± 0.015	0.097 ± 0.010	0.066 ± 0.001	0.035 ± 0.001
3869	0.032 ± 0.001	0.066 ± 0.001	0.078 ± 0.002	0.100 ± 0.002	0.105 ± 0.003
5385	1.090 ± 0.010	0.777 ± 0.017	0.701 ± 0.015	0.564 ± 0.012	0.528 ± 0.012
6597	2.024 ± 0.018	2.028 ± 0.027	2.062 ± 0.032	2.109 ± 0.040	2.009 ± 0.033
7685		3.243 ± 0.029	3.477 ± 0.022	3.685 ± 0.030	

EIm (mg/kg fuel)					
Fuel flow rate (lbs/hr)	**Temperature (°F)**				
	34	**42**	**47**	**56**	**58**
1150		0.05 ± 0.10	0.06 ± 0.10	0.07 ± 0.10	0.07 ± 0.10
2778	1.59 ± 0.19	0.15 ± 0.11	0.18 ± 0.10	0.26 ± 0.09	0.13 ± 0.08
3869	0.02 ± 0.07	0.12 ± 0.21	0.14 ± 0.18	0.19 ± 0.12	0.20 ± 0.10
5385	1.07 ± 0.07	0.69 ± 0.08	0.67 ± 0.07	0.62 ± 0.06	0.63 ± 0.06
6597	3.10 ± 0.10	3.28 ± 0.11	3.51 ± 0.12	3.91 ± 0.14	3.81 ± 0.13
7685		7.46 ± 0.20	8.91 ± 0.26	10.15 ± 0.29	

APPENDIX I

Table 2a lists the interpolated emissions results for the JP8 fuel. The aerosol parameters (Dgn, Dgm, EIn, and EIm) are given for the temperatures (°F): 28, 38, 45, 52, and 65, and fuel flow rates (lbs/hr): 1150, 2778, 3869, 5385, 6597, and 7685.

Table 2a. PM emissions parameters for JP-8 the fuel

Dgn (nm)					
Fuel flow rate (lbs/hr)	Temperature (°F)				
	28	38	45	52	65
1150	14.78 ± 0.14	14.51 ± 0.20	14.54 ± 0.26		
2778	16.77 ± 0.54	17.51 ± 0.71	17.25 ± 0.59	16.04 ± 0.58	14.79 ± 0.42
3869	18.00 ± 0.79	17.85 ± 0.83	17.11 ± 0.63	16.09 ± 0.47	13.83 ± 0.54
5385	24.44 ± 0.32	24.25 ± 0.86	23.45 ± 1.08	23.96 ± 1.34	23.57 ± 0.37
6597	27.53 ± 0.55	27.89 ± 0.50	28.14 ± 0.46	28.39 ± 0.43	28.86 ± 0.36
7685		29.90 ± 0.41	30.14 ± 1.29	30.81 ± 1.42	

Dgm (nm)					
Fuel flow rate (lbs/hr)	Temperature (°F)				
	28	38	45	52	65
1150			34.61 ± 3.57		
2778		46.12 ± 13.76	47.47 ± 13.85	41.60 ± 7.10	38.56 ± 1.73
3869		49.70 ± 1.62	49.79 ± 2.51	47.80 ± 2.89	37.75 ± 1.41
5385	60.98 ± 0.61	59.49 ± 0.60	57.13 ± 0.61	58.07 ± 0.66	59.18 ± 0.91
6597	69.17 ± 0.71	70.17 ± 0.70	70.87 ± 0.70	71.57 ± 0.69	72.88 ± 0.68
7685		79.93 ± 0.84	81.14 ± 0.70	81.92 ± 0.64	

EIn (10^{14}/kg fuel)					
Fuel flow rate (lbs/hr)	Temperature (°F)				
	28	38	45	52	65
1150		6.321 ± 0.113			
2778		5.734 ± 0.058	6.339 ± 0.076	5.219 ± 0.038	5.088 ± 0.030
3869	3.204 ± 0.028	4.434 ± 0.100	5.217 ± 0.163	5.022 ± 0.077	4.621 ± 0.079
5385	5.870 ± 0.152	6.153 ± 0.143	6.485 ± 0.104	6.305 ± 0.130	4.861 ± 0.142
6597	7.307 ± 0.353	7.756 ± 0.298	8.070 ± 0.260	8.384 ± 0.222	8.968 ± 0.151
7685		13.650 ± 0.382	10.728 ± 0.245	8.957 ± 0.173	

EIm (mg/kg fuel)					
Fuel flow rate (lbs/hr)	Temperature (°F)				
	28	38	45	52	65
1150	26.80 ± 1.00	18.11 ± 0.69	11.28 ± 0.48		
2778	14.46 ± 0.64	6.36 ± 1.92	7.04 ± 2.01	4.32 ± 0.91	2.98 ± 0.13
3869	4.57 ± 0.23	5.69 ± 0.25	6.16 ± 0.37	6.65 ± 0.46	7.00 ± 0.39
5385	19.79 ± 0.68	19.28 ± 0.63	17.71 ± 0.50	19.11 ± 0.60	16.40 ± 0.69
6597	37.36 ± 2.22	41.06 ± 2.03	43.64 ± 1.90	46.23 ± 1.77	51.03 ± 1.52
7685		93.24 ± 4.34	76.09 ± 2.83	68.45 ± 1.98	

Table 2b lists another set of interpolated emissions results for the JP-8 fuel. The aerosol parameters (Dgn, Dgm, EIn, and EIm) are given here for the same temperatures used for

the FT1 interpolations, 34, 42, 47, 56, and 58°F, and fuel flow rates (lbs/hr): 1150, 2778, 3869, 5385, 6597, and 7685.

Table 2b. PM emissions parameters for the JP-8 fuel calculated at the FT1 interpolation temperatures.

Dgn (nm)					
Fuel flow rate (lbs/hr)	Temperature (°F)				
	34	42	47	56	58
1150	14.97 ± 0.13	14.53 ± 0.23	14.55 ± 0.28		
2778	17.22 ± 0.68	17.78 ± 0.60	16.89 ± 0.59	15.85 ± 0.65	15.76 ± 0.68
3869	18.02 ± 0.94	17.54 ± 0.70	16.82 ± 0.59	15.47 ± 0.39	15.11 ± 0.43
5385	24.33 ± 0.64	24.18 ± 1.07	23.66 ± 1.22	23.84 ± 1.04	23.78 ± 0.89
6597	27.75 ± 0.52	28.03 ± 0.48	28.21 ± 0.45	28.53 ± 0.41	28.61 ± 0.40
7685	29.61 ± 0.53	29.80 ± 1.05	30.36 ± 1.45		

Dgm (nm)					
Fuel flow rate (lbs/hr)	Temperature (°F)				
	34	42	47	56	58
1150		43.75 ± 9.93	34.71 ± 2.56		
2778	44.60 ± 7.13	50.06 ± 16.77	45.74 ± 11.91	41.17 ± 4.17	40.96 ± 2.71
3869	48.86 ± 1.30	50.20 ± 2.15	49.52 ± 2.76	45.57 ± 2.65	43.83 ± 2.38
5385	60.08 ± 0.60	58.89 ± 0.60	57.43 ± 0.62	58.41 ± 0.74	58.58 ± 0.78
6597	69.77 ± 0.71	70.57 ± 0.70	71.07 ± 0.70	71.98 ± 0.69	72.18 ± 0.69
7685	78.78 ± 0.88	80.63 ± 0.76	81.48 ± 0.67		

EIn (10^{14}/kg fuel)					
Fuel flow rate (lbs/hr)	Temperature (°F)				
	34	42	47	56	58
1150		5.730 ± 0.086			
2778	5.127 ± 0.064	6.834 ± 0.092	6.009 ± 0.064	5.161 ± 0.044	5.132 ± 0.047
3869	3.869 ± 0.047	4.950 ± 0.148	5.395 ± 0.174	4.899 ± 0.078	4.837 ± 0.078
5385	6.040 ± 0.147	6.266 ± 0.140	6.486 ± 0.113	5.861 ± 0.134	5.639 ± 0.136
6597	7.576 ± 0.320	7.935 ± 0.277	8.160 ± 0.249	8.564 ± 0.200	8.654 ± 0.189
7685	13.058 ± 0.448	12.184 ± 0.304	9.757 ± 0.205		

EIm (mg/kg fuel)					
Fuel flow rate (lbs/hr)	Temperature (°F)				
	34	42	47	56	58
1150	20.29 ± 1.00	14.21 ± 0.57	9.32 ± 0.42		
2778	8.46 ± 1.40	8.24 ± 2.49	6.24 ± 1.69	4.11 ± 0.51	4.01 ± 0.31
3869	4.99 ± 0.17	6.17 ± 0.33	6.15 ± 0.40	7.21 ± 0.48	7.16 ± 0.39
5385	19.48 ± 0.65	19.08 ± 0.61	18.36 ± 0.53	18.28 ± 0.63	17.86 ± 0.64
6597	39.58 ± 2.11	42.53 ± 1.96	44.38 ± 1.86	47.70 ± 1.69	48.44 ± 1.65
7685	87.09 ± 4.51	83.95 ± 3.53	70.85 ± 1.36		

Figure 1 shows the dependence of EIn on temperature for fixed fuel flow rates for JP-8 over its full ambient temperature range. EIn is observed to decrease with increasing temperature at the lower fuel flow rate (2778 lbs/hr) and highest fuel flow rate (7685

lbs/hr), whereas it increases modestly with increasing temperature at intermediate fuel flow rates 3869 lbs/hr and 6597 lbs/hr. It is independent of temperature at the mid fuel-flow rate, 5385 lbs/hr.

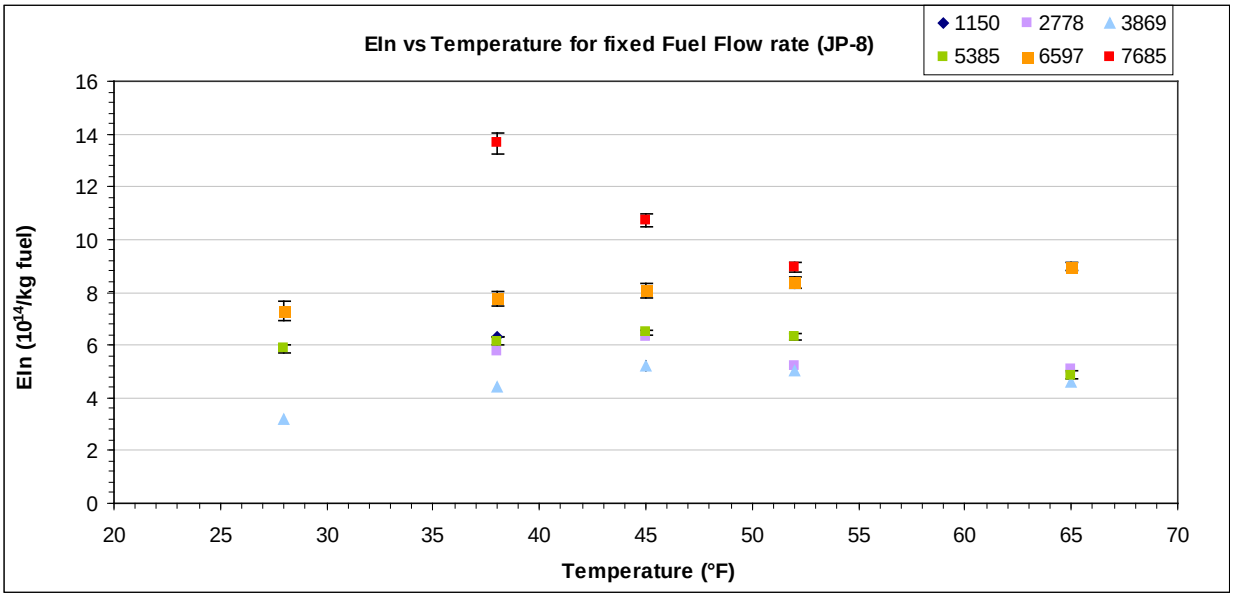

Figure 1. Number based emission index as function of temperature and fuel flow rate for JP-8

Figure 2 shows the dependence of EIm on temperature for fixed fuel flow rates for JP-8 over its full ambient temperature range. EIm shows temperature-fuel flow rate trends that are similar to those for EIn.

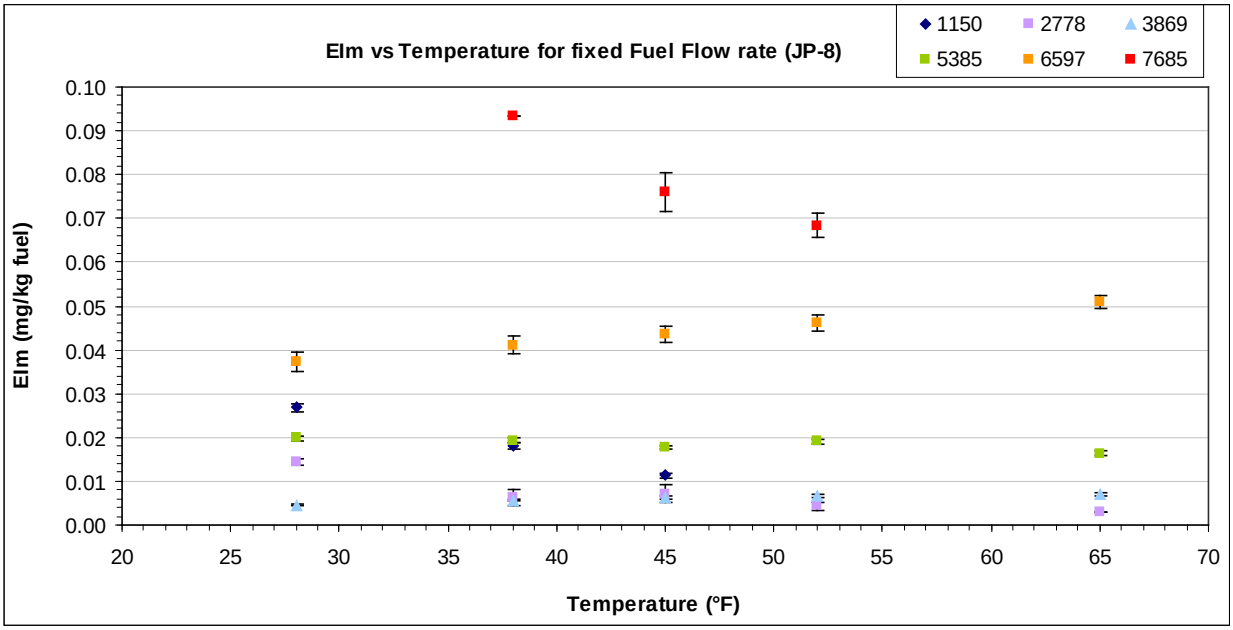

Figure 2. Mass based emission index as function of temperature and fuel flow rate for JP-8

Data from Tables 1 and 2a can be examined to determine the significance of ambient temperature as a variable that influences PM emissions. The two metrics that are useful to characterize the strength of temperature with regard to influencing PM emissions are:
Mcr = maximum change ratio, and $\Delta\%$ = maximum percent change.

For a fixed fuel type, fuel flow rate, and aerosol parameter, ap_n, Mcr_n is defined as
$Mcr_n = |ap_n(T_a) - ap_n(T_b)| / (\delta ap_n(T_a) + \delta ap_n(T_b))$,
where T_a and T_b are the temperatures which give the maximum value this ratio for fixed fuel flow rate.

When $Mcr_n \leq 1$ the error bars for the two temperatures overlap and the change in emissions between the two points is not statistically significant, i.e. there is no significant temperature effect for this case. When $Mcr_n \geq 1$ the error bars for the two temperatures do not overlap and there is a statistically meaningful change in emissions, i.e. there is a significant temperature effect for this case.

The parameter $\Delta\%$ gives the maximum percent change in aerosol parameter ap_n between two temperatures for the fixed fuel flow rate. Tables 3a and 3b present results for Mcr and $\Delta\%$. For JP-8 combustion (Table 3a) the aerosol parameter Dgn, does not show significant temperature change at the lowest and highest fuel flow rates (Mcr < 1), which yield percent changes of 2% and 3%. It does produce significant changes, up to 26%, at all other fuel flow rates. The mass based geometric mean, Dgm, likewise shows no significant temperature dependence at its lowest fuel flow rate, 2778 lbs/hr, but exhibits dependence at all higher fuel-flow rates. The emission index parameters, EIn and EIm, show significant change, exceeding 100% variation in one case, because of the temperature dependency. Hence the influence of temperature is significant and should be taken into account in the analysis of PM emissions data before influences of other operating conditions, e.g. fuel type, and be determined. For FT1 combustion (Table 3b) all aerosol parameters show significant temperature dependence (Mcr > 1), except for Dgm at the lower fuel flow rate conditions. Again, the aerosol parameters show large percentage changes because of temperature change, with several exceeding 100% change. The aerosol parameters for FT1 combustion exhibit a stronger temperature dependence than for JP-8 combustion; $\Delta\%$(FT1) exceeds $\Delta\%$(JP-8) 82% of the time, even though the JP-8 data spans a larger range of temperature change.

Table 3a. Change in emissions from JP-8 combustion due to temperature variation.

ap	Fuel Flow rate (lbs/hr)	Mcr	Δ%
Dgn	1150	0.8	2
	2778	2.4	17
	3869	3.1	26
	5385	1.3	4
	6597	1.4	5
	7685	0.5	3
Dgm	1150		
	2778	0.6	21
	3869	3.9	28
	5385	3.2	7
	6597	2.7	5
	7685	1.3	2
EIn	1150		
	2778	11.9	22
	3869	17.4	48
	5385	6.6	29
	6597	3.3	20
	7685	8.5	42
EIm	1150	10.5	82
	2778	14.9	132
	3869	3.9	42
	5385	2.5	19
	6597	3.7	31
	7685	3.9	31

Table 3b. Change in emissions from FT1 combustion due to temperature variation.

ap	Fuel Flow rate (lbs/hr)	Mcr	Δ%
Dgn	1150	2.1	34
	2778	1.8	27
	3869	1.2	35
	5385	1.1	5
	6597	2.2	9
	7685	1.8	6
Dgm	1150	0.5	19
	2778	0.6	28
	3869	0.2	99
	5385	1.4	46
	6597	2.3	14
	7685	2.6	8
EIn	1150	15.9	73
	2778	18.8	126
	3869	22.4	107
	5385	25.6	70
	6597	1.4	5
	7685	7.5	13
EIm	1150	1.2	141
	2778	5.4	171
	3869	1.02	165
	5385	3.4	52
	6597	3.4	23
	7685	5.5	31

An important question is whether PM emissions temperature dependency is fuel type dependent, i.e. can the temperature dependency be measured for one fuel type and then applied to other fuel types, or does the temperature dependency have to be measured separately for each fuel. This question can be studied by examining the correlations between the emissions for JP8 and FT1. Both of these fuels have data covering a common range of temperature and fuel flow rate. Emissions data for this comparison is restricted to cases where the aerosol parameters experienced statistically significant temperature change and had data available for at least three temperatures. Let CC denote

the correlation coefficient between the two sets of temperature dependent data, for fixed aerosol parameter and fuel flow rate. Table 4 presents the correlation results for the 15 cases that satisfied the above selection criteria.

Table 4. Correlation between the temperature dependence of JP8 and FT1 emissions.

ap	Fuel Flow rate (lbs/hr)	CC
Dgn	1150	1
	2778	-0.93
	3869	-0.97
Dgm	5385	-0.58
	6597	0.33
	7685	1
EIn	2778	0.29
	3869	0.67
	5385	0.36
	6597	0.33
EIm	1150	0.89
	2778	0.57
	3869	0.98
	5385	0.83
	6597	0.98

The results in Table 4 indicate a lack of consistent correlation between fuel types for the aerosol shape parameters, Dgn and Dgm. They exhibit both strong positive and negative correlations for various fuel flow rates. The emission index parameters, EIn and EIm, show consistently positive correlations. EIm exhibits the stronger correlation, with an average correlation coefficient of 0.85. Further study is needed on this issue.

Conclusions

PM emissions data was collected over an ambient temperature range of 28 to 65°F. Significant dependencies on temperature were observed, with Mcr's (maximum ratio of PM emission parameter change to experimental uncertainty) averaging 4.9 and 5.4, and ranging up to 17 and 26 for JP8 and FT1, respectively. The corresponding percentage changes in PM emission parameters due to temperature change, averaged 28 and 54 percent, and ranged up to 132 and 170 percent, for JP8 and FT1, respectively. The correlation between the temperature dependencies for JP8 and FT1 were investigated. Fifteen cases exhibited sufficient significant temperature dependence to consider. The aerosol shape parameters, Dgn and Dgm, showed no consistent correlation. The emission index parameters, EIn and EIm, showed consistently positive correlations, with EIm having the stronger correlation with an average correlation coefficient of 0.85.

Acknowledgements
This work was partly funded by the Federal Aviation Administration (FAA) through the Partnership for AiR Transportation for Noise and Emissions Reduction (PARTNER) – an FAA/NASA/Transport Canada-sponsored Center of Excellence under Grant No. 07-C-NE-UMR Amendments 006 and 007. The authors would like to acknowledge the AAFEX team, and NASA DC-8 personnel for substantial contributions to the successful execution of this study.

References

Corporan, E., Reich, R., Monroig, O., DeWitt, M., Larson, V., Aulich, T., Mann, M., and Seames, W., "Impact of Biodiesel on Pollutant Emissions of a JP-8-Fueled Turbine Engine", *J. Air & Waste Manage. Assoc.*, 2005, 55, 940-949

Corporan, E., DeWitt, M., Belovich, V., Pawlik, R., Lynch, A.C., Gord, J.R., and Meyer, T.R., "Emissions Characteristics of a Turbine Engine and Research Combustor Burning a Fischer-Tropsch Jet Fuel", *Energy & Fuels*, 2007, 21, 2615-2626

Lobo, P., Hagen, D.E. and Whitefield, P.D., "Comparison of PM emissions from a Commercial Jet Engine burning Conventional, Biomass, and Fischer-Tropsch Fuels", *manuscript in preparation* 2010.

Wey, C. C., Anderson, B. A., Wey, C., Miake-Lye, R. C., Whitefield, P., Howard, R., "Overview on the Aircraft Particle Emissions eXperiment (APEX)", *Journal of Propulsion and Power*, 2007, 23, 898-905

Lobo, P., Hagen, D.E., Whitefield, P.D., and Alofs, D.J., "Physical characterization of aerosol emissions from a Commercial Gas Turbine Engine", Journal of Propulsion and Power, 2007, 23, 919-929

Herndon, S.C., Jayne, J. T., Lobo, P., Onasch, T., Fleming, G., Hagen, D.E., Whitefield, P.D., and Miake-Lye, R.C., "Commercial Aircraft Engine Emissions Characterization of in-Use Aircraft at Hartsfield-Jackson Atlanta International Airport", *Environmental Science and Technology*, 2008, 42, 1877-18.

APPENDIX J: Aircraft Engine Particulate: Macro- Micro- and Nanostructure by HRTEM and Chemistry by XPS

R. L. Vander Wal
Pennsylvania State University

Abstract
Carbonaceous particulate emissions from jet engine aircraft are a significant source of emissions near urban areas. Available mass measurements and particle numbers are few. Absent is any electron microscopic or spectroscopic characterization of the physical nanostructure or surface chemistry though both are extremely relevant towards assessing impacts of combustion-produced soot upon the environment and assessing health impacts. In this report, high-resolution electron microscopy (HRTEM) and X-ray photoelectron (XPS) data are presented for particulate emissions from a CFM-56-3 engine aboard a DC-9 aircraft. Fuels studied included JP-8, Fischer-Tropsch and 50:50 blends. Power levels were varied from 4% to 100%. Soot aggregate macrostructure, microstructure and nanostructure are discussed with respect to combustion conditions. Ultrafine particle size distributions at idle and near full power conditions are highlighted and compare favorably to reported scanning mobility particle sizer (SMPS) measurements. Particle composition as inferred from the XPS ratio for sp2/sp3 carbon is compared to results from thermo-optical evaluation of organic and elemental carbon analysis at selected powers with excellent agreement.

The organization of this appendix is as follows:

I. Introduction - Levels of Soot Structure

Relevance to the Environment and Human Health

The effect of particulate emissions upon atmospheric processes has received increasing recognition of their multiple roles. Depending upon their surface chemistry they can contribute to cloud formation. Soot particles can contribute directly to radiative forcing both directly by strongly absorbing solar radiation and indirectly through water-uptake and cloud activation [1-3]. The can interact with gaseous chemical species, especially in

the near-field plume, and therein play a significant role in heterogeneous atmospheric chemistry [4].

Health effects associated with soot particles has received increasing recognition [5]. At airports emissions from aircraft idling, taxiing, taking-off and landing represent a significant source of particles into the surrounding (often urban) environment. [6]. Airport personnel and airline crews are exposed to varying degrees as well as the general flying public. As evidence, nearly everyone has "smelled" jet engine exhaust while outside the airplane. In this exhaust will be incidental combustion byproducts such as soot. Although soot aggregates' size is generally beyond nanoscale, small aggregates containing one to a few primary particles (subunits) are less than 100 nm in geometric dimension and can penetrate to the deepest regions of the lung, the aveoli. Such deep penetration generally precludes their exhalation and results in their entrapment. Thereafter the biological response will depend upon their composition and surface chemistry.

Jet aircraft are a unique source of such particles, contributing to both ground pollution in and around airports but also are the primary source of such particles in the upper trophosphere and lower stratosphere [7, 8]. Because of their transitory nature, the characteristics of aircraft particle emissions are one of the least quantified relative to those from other pollution sources such as power plants, industry and transportation.

Traditionally an emission inventory is the first step towards assessing a pollution source from which regional impacts are assessed by linking with transport models. To develop such emission inventories requires measurement of aircraft exhaust mass and particle numbers relative to fuel consumption. Concurrently emissions must be microscopically characterized to validate the suitability of traditional aerosol instruments given the variable nature of the particulate and that corresponding interpretations of mass and number distributions are accurate.

Nanostructure & Chemistry

There are three levels of structure describing the soot particles. The first is aggregate morphology, the second is the degree of connectivity between the primary particles within the aggregate, and the third is the nanostructure of the individual primary particles. These three descriptors provide complimentary measures over a set of hierarchical length scales to cover geometry, morphology and atomic layer plane coordination. These are the parameters by which conditions of power and fuel are compared.

Complimentary to high-resolution transmission electron microscopy (HRTEM) for physical nanostructure is X-ray photoelectron spectroscopy (XPS) analysis for carbon bonding. Moreover it can reveal surface chemistries such as oxygen functional groups and their bonding state as well. Nanostructure can be correlated to XPS data for carbon bonding leading to a comprehensive picture of particulate variations with engine power. HRTEM is particularly valuable given that it can reveal small particles that are difficult to observe using traditional aerosol measurement techniques. Both the particulate

nanostructure as extracted from the HRTEM data and composition as measured by XPS data change with engine power.

Specific trends were found for each of these measures in response to test conditions and are summarized in this appendix. These variations guide inferences regarding the combustion conditions and state of mixing as dependent upon the engine power level. Supportive background is extracted from the combustion literature of laboratory flames and basic aerosol mechanics.

2. Experimental Details

Table 1 summarizes the composition of the fuels in these tests. As detailed elsewhere in this report, engine powers were cycled in a staircase manner with the starboard engine running on the selected fuel with the port engine running on JP-8. As indicated, the FT fuels are essentially paraffinic in content, differing in their degree of branching (e.g. FT-Sasol would be characterized by a high degree of branching), whereas only JP-8 has a substantial aromatic component.

Table 1.

	n-Paraffins	Iso-parffins	Cycloparaffins	Aromatics
FT-Sasol		87.6	12.0	0.4
FT-Shell	46.7	53.3		
JP-8	19.0	31.3	31.0	18.7

Particulate Sampling

The sampling probe provided for direct collection of soot upon a TEM grid. The key advantage is the direct collection of the soot from the aerosol phase. This bypasses filter collection and therein the need for redispersal upon a TEM grid. Such processes are known to cause agglomeration of soot aggregates thereby obscuring individual aggregates. To permit HRTEM, lacey TEM grids were used. Further details of the TEM grid holder and its insertion into the sampling probe exhaust stream have been documented and will be published elsewhere [9].

XPS samples were collected using 400 stainless steel mesh coated with Ti/Au. These screens were held in 1.5-inch diameter HDPE filter holders along with a quartz tissue filter for added support. These units were inline with and downstream of the TEM sampling unit. For most conditions these screens did not appear overtly covered by soot with some metallic luster yet visible. The FT fuels did not yield sufficient particulate coverage to enable analysis.

A valve upstream of the TEM sample holders permitted isolation of these units until the exhaust stream for the test condition of interest had cleared the line. By this user-defined, manual operation, samples were collected for a time somewhat shorter than the nominal test duration. Sample holders were periodically cleaned by a combination of wiping and swabbing with commercial grade rubbing alcohol. Multiple units allowed for pre-loading of TEM grids and gold coated screens for rapid insertion between test points as the engine was ramped up and down in power.

With the primary emphasis being upon microscopy, partial or complete series sample sets as a function of engine power were obtained for JP-8 fuel. FT fuels yielded only sufficient particulate for these analyses at higher engine power levels as did the blends of JP-8 and FT fuels.

Electron Microsocpy and Spectroscopy

TEM images were taken using a Phillips CM200 having nominal resolution of 0.14 nm with Gatan Image Filter (GIF) for digital imaging featuring live Fourier transforms having nominal resolution of 0.14 nm. The instrument was operated at 200 keV using a LaB6 filament. Gatan image software v. 3.4 was used for microscope operation. Generally four to six widely separated regions were examined on each grid primarily to ensure representative images and secondarily to ensure even coverage (as an indicator of flow uniformity and sampling by deposition). For any given power level, a range of nanostructure (variability) was evident across imaged particles, though trends with power were visually evident. These image data sets will be summarized in a NASA database. Representative images were selected to illustrate the observed trends for this report.

Digital images were acquired and subsequently processed using custom algorithms interfacing with the Optimus software package from Media Cybernetics. Selected images were analyzed for fringe length, separation and tortuosity as nanostructure parameters. Results were generally exported to the program KaleidaGraph for subsequent plotting and data analyses. Further details have been reported elsewhere [10].

The PHI 500 Series XPS instrument uses a conventional dual anode X-ray source (Mg & Al) with a 200' hemispherical electron energy analyzer and a multi-channel detector. Analyzer electronics have an energy scan range of 0-4800 eV with a resolution of 0.025eV minimum step size; the lens is an Omni-Focus^{TM} III. The monochromatic Al X-ray source has a variable energy range of 4kV to 15 kV with 300 W power in continuous operation. The sample stage can be moved and focused in three dimensions.

High-resolution, multi-plex scans were run for carbon with a minimum of 10 sweeps and 7 cycles. The resultant high-resolution C1s peak was curve fit using Gauss-Lorenz peaks and a Shirley fit. Peak deconvolution was performed via a MATLAB® program after setting the background parameters. Peak assignments are indicated in the individual spectra, allowing for shifts due to sample charging. Further details on the deconvolution procedure will be reported elsewhere [11].

Reproducibility of the high-resolution scans was high with 2-3 scans were taken over different sections of the filters. Such data collection was repeated over 2 different sessions. Differences in deconvoluted peak intensities were quite small relative to those differences observed between each soot sample.

3. Survey of macro- micro and nanostructure with power – Comparisons across engine power levels by HRTEM

Figures 1-3 provide a side-by-side contrast of aggregate size, morphology and nanostructure. Details may be found in the captions for the corresponding figures. Figures 4-6 provide further comparisons across engine power levels of aggregate morphology, primary particle connectivity and nanostructure therein.

1. The soot aggregate morphology is a record of primary particle density and local concentration of growth species. As the (growing) aggregate evolves (traverses) over different regions of particle concentration and/or mixture fraction, variations in its compactness versus openness can occur. Aerosol clustering modes determine the morphology (e.g. reaction limited, ballistic or diffusion limited). These dynamics in turn depend upon the local concentration of constituent primary particles. High concentrations of primary particles result in reaction limited growth to produce a very compact aggregate whereas low concentrations lead to diffusion limited growth producing an open branched aggregate. In this manner morphology becomes a measure of the mixture fraction.

Of course, as fuel-rich pockets are encountered during the spatial trajectory of the aggregate, each with their own fuel-air stoichiometry and resulting primary particle density, clusters will reflect such time-varied additions by the radial variation in their morphology.

2. Soot microstructure refers to the connectivity of the primary particles. This topolological metric reflects the gaps or lack thereof between primary particles. This depends upon the occurrence of continued mass growth once primary particles coalesce. The degree of connectivity then reflects the time of coalescence relative to growth. Early coalescence followed by continued growth leads to virtually unrecognizable primary particles (and "dense" aggregates). They become highly merged and are fused together. Alternatively late (or delayed) coalescence leads to near-point contact between individual primary particles. This results in clear geometric demarcation between them and an open branched aggregate form. Clearly intermediate regimes exist as well. Figures 1-6 illustrate these two extremes.

4. Nanostructure Survey by lattice fringe analysis

Other aerosol instruments are designed for measurement of aggregate size and these results are contained elsewhere in this report. Therein our focus was upon aggregate substructure, namely primary particle size and in particular, soot nanostructure. Figure 7 conveys a HRTEM summary of primary particle nanostructure with engine power level. This data set came from an early test run and is observed to be consistent with data shown in Figures 1-6, demonstrating consistency of observations. Illustrative lattice fringe analyses for lamellae lengths results are summarized in Figure 7b.

3. Soot nanostructure of course reflects the species available for soot growth. A uniform species such as C2H2 will contribute to particle growth via the HACA mechanism. Polycyclic aromatic hydrocarbons (PAHs) will contribute by a similar free radical addition mechanism. The former species (C2H2) can produce a well-ordered structure referred to as graphitic nanostructure. The latter species class (PAHs) is unable to

produce contiguous graphene layers given their varied sizes and range of possible orientations reflecting several potential radical sites per molecule. This results in various types of irregular (disrupted) nanostructure. Variations may include tortuous, chaotic or even interwoven lamella. In any event, there is less long-range structure, larger separation distance between lamella and less stacking order.

A variation of nanostructure is the introduction of undulation in the form of curvature or tortuosity within lamella. Substantial local curvature in graphene layers arises by the incorporation of C5 (cyclopentadienyl) rings [12]. These species are not a fuel component. Instead they arise by gas phase chemistry involving oxygen. Partial oxidation of ethylene, a pyrolysis product, leads to acetaldehyde. Acetaldehyde is a well-known combustion intermediate. Such species can be incorporated into aromatics, e.g. phenoxy radicals [13]. Its decomposition yields cyclopentadienyl radicals that are then incorporated into growing PAHs. Alternatively oxygen can produce odd numbered carbon fragments that can build up to C5 rings, e.g. C2 + C3 species. Readily produced in radical form and stable at elevated temperatures, cyclopentadienyl radicals readily add to growing lamella [14]. Their introduction produces curvature, the well-known "macromolecular" example being fullerenes. For this reason, curvature in lamella is referred to as fullerenic nanostructure.

With the degree of fullerenic nanostructure dependent upon the concentration of C5 rings [12] whose concentration in turn depends upon partial oxidation intermediates, by transitive relationship, the degree of fullerenic nanostructure thus depends upon the level of partial premixing. Higher premixing will lead to more fullerenic nanostructure or primary particles containing more fullerenic nanostructure until the fuel-air ratio becomes to low.

5. Overview of aggregate populations with engine power

A particular advantage of TEM is the direct observation of particles. Differences in population size, morphology or microstructure are readily apparent. Traditional aerosol instruments are insensitive to particle micro- or nanostructure and generally possess cutoffs on the order of 10 nm. TEM examination of particles as deposited directly upon the grid revealed not only large aggregates but also a second size distribution composed of very small aggregates consisting of generally one to a few subunits, often highly fused together. Figure 8 are TEM images at two different magnifications of particulate collected from JP-8 using the 30-meter probe at a 4-7% power level. Figure 9 are corresponding TEM images at an 85% power level. In each case, the higher magnification image focuses upon one of the aggregates from the small-sized population.

The apparent high-particle number density observed on the TEM grid is consistent with data from Corporan, (See Appendix X) who, using the condensation particle counter (CPC), measured a 10-22:1 ratio of the emission number index (EI_n) for the 30-meter probe compared to the 1-meter probe. Such a large ratio suggests that the change (increase) in EI_n measured using the 30-meter probe is due to condensation of volatiles during the transit time in the sampling probe [15]. A much smaller ratio was observed at high power, likely reflecting fewer volatile precursors and a lower nucleation rate.

Lobo et al. speculate that low fuel flow rates correspond to relatively low linear velocities in the exhaust flow and hence longer residence times before the flow reaches the 30-m probe [16]. More time is then available for nucleation processes to boost the aerosol population the small size particle population. At high powers, high velocities and higher temperatures (and lower volatile concentrations) preclude nucleation via condensation, which is consistent with Corporan's data (Appendix X**)** who measured dilution ratios based on CO2 using a non-dispersive infrared reflectance (NDIR)**.** This explanation also accounts for the drastic decrease in number based emission with increasing engine power. [17].

6. Summary of microstructure measurements

Figure 10 presents a summary of the subunit sizes within these two very different aggregate distributions. Given a larger ultrafine particle population at the lowest power level, size measurements were performed on those samples. Cursory checks revealed no significant size difference between primary particles measured at the lowest and high-power levels (q.v. Figs. 8 & 9).

To address the particle size distribution, Corporan employed a scanning mobility particle sizer (SMPS). With the JP-8 fuel, at 4% power two size distributions were observed, one with a mean near 15 nm and the other near 60 nm. These two size ranges roughly agree with the average as measured directly from those collected upon the TEM grid. At 85% power, a second size distribution was also observed on the TEM grids but not observed using the SMPS (albeit with a lower deposition density). Given that the second particle size distribution was near the size cutoff limit and that this size fraction was not related to volatile condensation, its absence from the ELPI spectra suggests a significantly lower number density. That there is a change in ultrafine particle size and in overall particulate elemental carbon content between low and high power suggests a difference in composition and nanostructure, as examined next.

7. High Resolution analysis of nanostructure of aggregate subpopulations with engine power

To investigate the origins of the small sized aggregates, high-resolution TEM was performed. These results are shown in Figure 11 for both the low and high engine power levels. As evident, the particle nanostructure varies greatly between the two data sets. An admixture of these nanostructures was observed at intermediate power levels. These will be analyzed and reported subsequent to this report.

The particle structure as observed in the HRTEM images suggests particle composition that is largely organic carbon at the low power level. The short disconnected and randomly oriented lamellae (where recognizable) are of a size consistent with 6 to 10 ring PAHs. The high proportion of edge sites suggests termination under atmospheric exposure by H-atoms. In contrast, the particles produced at high power demonstrate graphitic structure with lamellae of extended length and order. Both features are hallmarks of a carbonaceous particle comprised mainly of elemental carbon, consistent with the bulk elemental analysis as reported by Corporan in Appendix X of this report.

8. Chemistry dependence upon power – XPS analyses

As reported for the APEX III campaign [9], XPS can provide a wealth of chemical information regarding both heteroatom content in addition to bonding configurations. For the single engine power studies in this campaign, changes in particle surface chemistry are of great interest for the aforementioned environmental and health considerations. Figure 12 shows the XPS data for three selected engine power levels. Deconvolution has been applied to the spectrum to resolve the carbon sp2, sp3 components and oxygen functional groups, as illustrated. A monotonic trend with power is observed for increasing sp2 content at the expense of sp3 bonded carbon.

To address composition, Corporan et al. used a LECO Carbon Analyzer to determine the relative carbon composition (volatile or non-volatile/refractory). The curves were integrated below or above 325C to differentiate the volatile fraction versus non-volatile (refractory) carbon fraction. Limited by the collected mass, the lowest power for which the volatile fraction was measured was 45%. Here the volatile content was ~ 58%. Our XPS data yielded an sp2/sp3 ratio of 1.4 at 65%. This translates into an organic (sp3) content of ~ 42%. With the assumption that organic content is synonomous with volatile fraction, the agreement between these two very different techniques is remarkable. At 85% power the LECO measured a volatile content of ~ 35%. Our corresponding XPS sp2/sp3 ratio of 2.3 for this same power level implies ~ 30% organic content, in excellent agreement. These different surface chemistries are mirrored by our HRTEM and XPS results.

9. Turbulent Gas Turbine Environments

Figure 13 illustrates the complicated sequence of overlapping chemical and physical processes underlying soot formation and growth. Figure 14 schematically shows varied mixing in the turbulent combustion environment of the jet engine. These figures form the basis for the interpretative discussion.

The long graphitic lamella point to continuity of growth conditions and species while irregular nanostructure, bordering upon amorphous suggests varied growth environments that are insufficient to form ordered graphene layers. While it should not be surprising that the two structures originate at different powers, the observation of varied soot nanostructure with engine power is a unique observation that has not been reported elsewhere. Such variation could be used to aid modeling results of gas phase chemistry as reflected by the very different nanostructures. In this manner soot nanostructure offers an archeological record of the gas phase chemistry.

10. Results

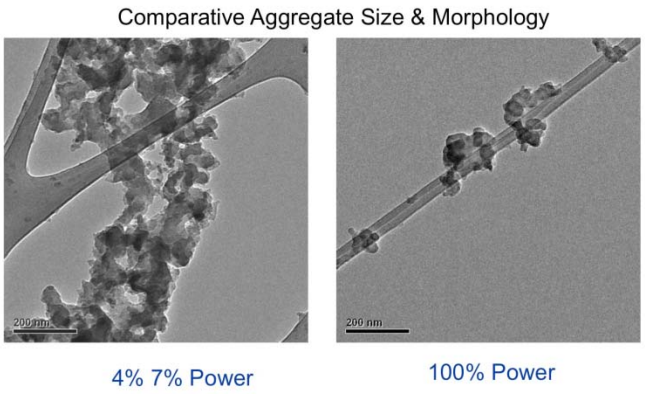

Figure 1. To establish the range of contrast of observed particulate emissions, shown above are images for the lowest (4-7% and highest (100%) engine power levels. At the lowest engine power, 4-7%, many particles, many sizes, were observed. Note the near single particles captured directly upon the lacey film. In contrast, at 100% power, the largest aggregates were generally less than 200 nm in equivalent diameter. At both powers, instead of highly branched morphologies, compact aggregates were prevalent in which the primary particles were highly fused.

That individual aggregates were clearly separate and distinct at the higher power levels provides an upper bound to their size. Given the potential for aggregate agglomeration upon the grid during collection, aggregate sizes are not presented for these conditions given this unknown bias at the lower power levels. Other aerosol instrumental measures presented elsewhere in the Appendices provide such data.

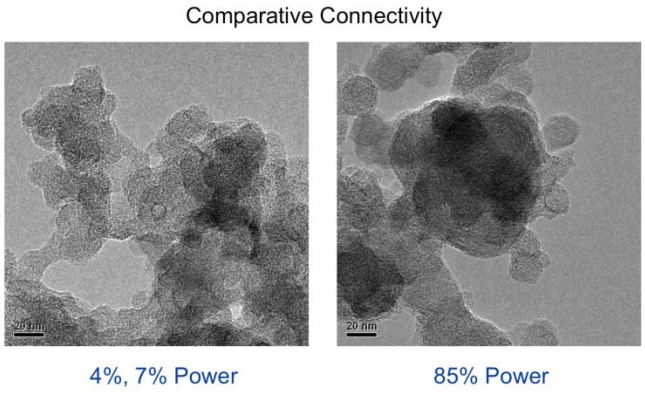

Figure 2. Generally highly fused aggregate structures were observed, but with increasing power, individual primary particles became increasingly recognizable.

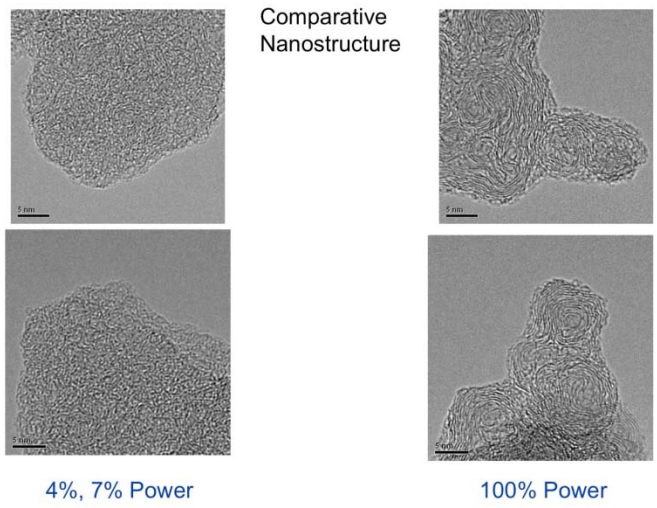

Figure 3. The comparative nanostructure between the two power settings is illustrated. At lower power nearly amorphous nanostructure was observed while at high power extended lamella organized into parallel stacks was found. The tortuous structure within the interior of the latter nanostructure is indicative of nonuniform growth reflecting primarily species and secondarily temperature. A variety of growth species would account for the irregular structure. In contrast very well defined ribbons around the particle perimeter suggests highly uniform growth conditions.

The perimeter of some primary particles (65% power) exhibits evidence of oxidation, not surprising given the exhaust conditions.

Difficult to say whether nanostructure is more well defined at 85% versus 65%, given variation. However the fact that internal nanostructure is recognizable is strong evidence for continued change in gas-phase chemistry.

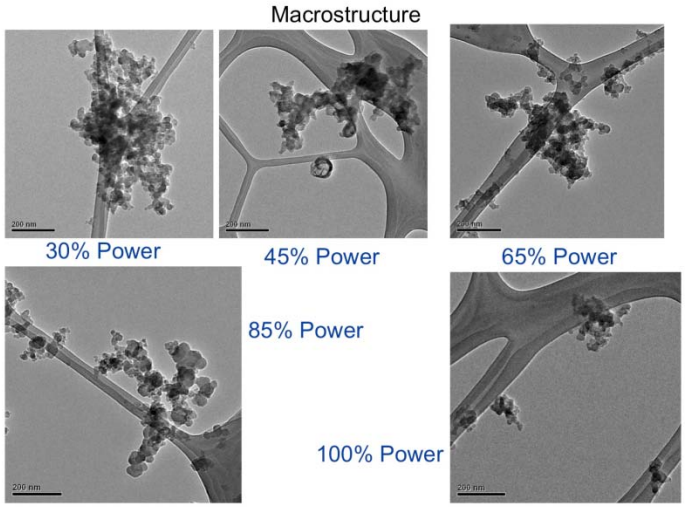

Figure 4. An illustration of changing aggregate size scale and morphology with increasing power level. The image at 65% power further illustrate aggregate size decrease (containing fewer primary particles) at higher power levels compared to lower powers. At 85% power the general trend of decreasing aggregate size is maintained in addition to decreasing primary particle. That individual aggregates were clearly separate and distinct at the 100% power level provides an upper bound to their size.

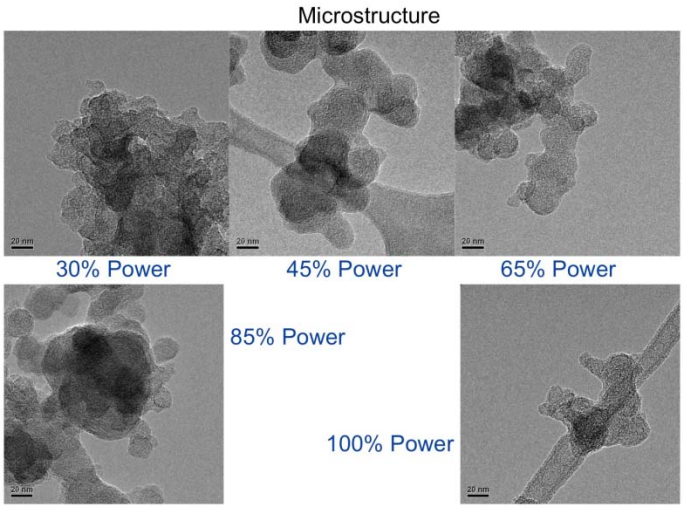

Figure 5. An illustration of the changing connectivity within the aggregate. While individual primary particles are largely undefined at low power, with increasing power primary particles become increasingly recognizable. Even at intermediate powers such as 65%, aggregate microstructure can consist of dense portions with notable lack of subunit definition. At 85% power, very distinct primary particles were observed, but generally along the aggregate perimeter. The variation in aggregate microstructure with radius (e.g. 100% power) suggests varying aerosol dynamics. Initial growth produced highly coalesced aggregates while individual primary particles formed at later times remained separate, only undergoing agglomeration at later times.

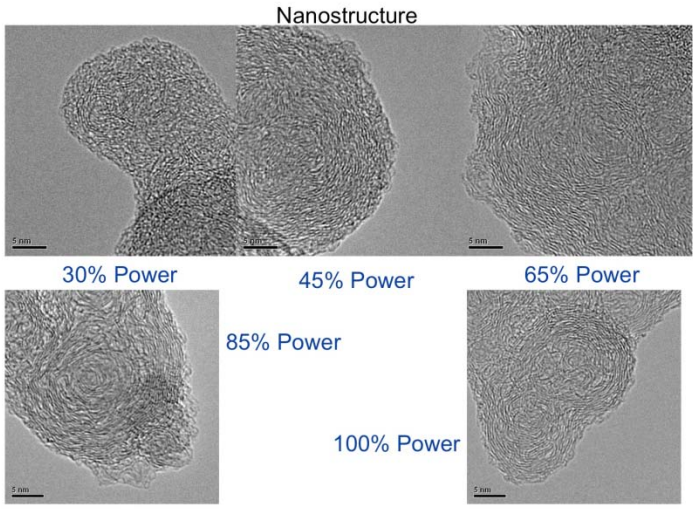

Figure 6. An illustration of the nanostructure evolution with increasing power level. At intermediate powers, recognizable lamella become increasingly recognizable within primary particles. In general they are not well ordered or highly stacked but clearly measurable. The tortuous structure of the nanostructure at intermediate power levels is indicative of non-uniform growth conditions reflecting varied species contributing to the particle growth. At higher powers, such as at 65%, very well defined ribbons around particle perimeters suggest highly uniform growth conditions. The perimeter of some primary particles (65% power) exhibits evidence of oxidation, not surprising given the high temperature exhaust conditions. It is difficult to judge whether nanostructure is better ordered at 85% versus 65% power, given observed variations at each condition. However the fact that internal nanostructure is recognizable is strong evidence for continued change in gas-phase chemistry relative to the lowest power level. At 100% power graphitic ribbons were common. Yet the overall nanostructure of the primary particle is not uniform but irregular, suggesting rather variable growth conditions in temperature and species.

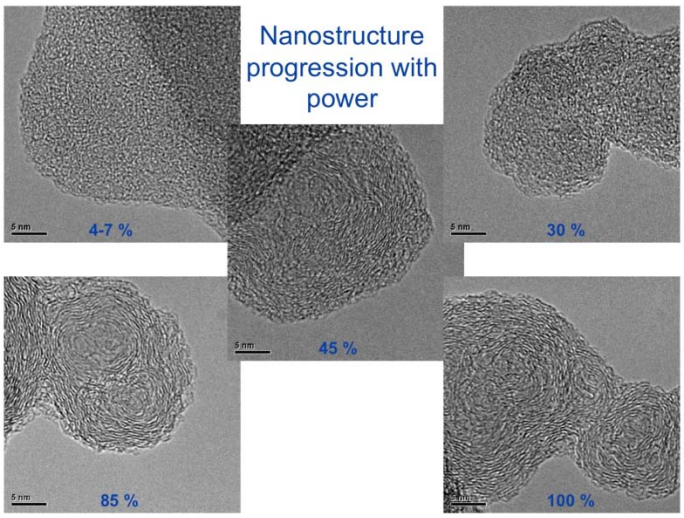

Figure 7. From early survey samples across engine powers, these were selected for image analysis, based on JP-8 fuel and a 1-meter sampling probe. Consistent with the aforedescribed data, there is a progressive increase in nanostructure order with increasing power. Going from amorphous at the lowest power, lamella become increasingly distinct and organized in stacks with increasing power. At the highest levels, extended lamella wrap the particle perimeter. These changes are quantified by the lattice fringe analyses shown in Fig. 6b for fringe (lamella) length.

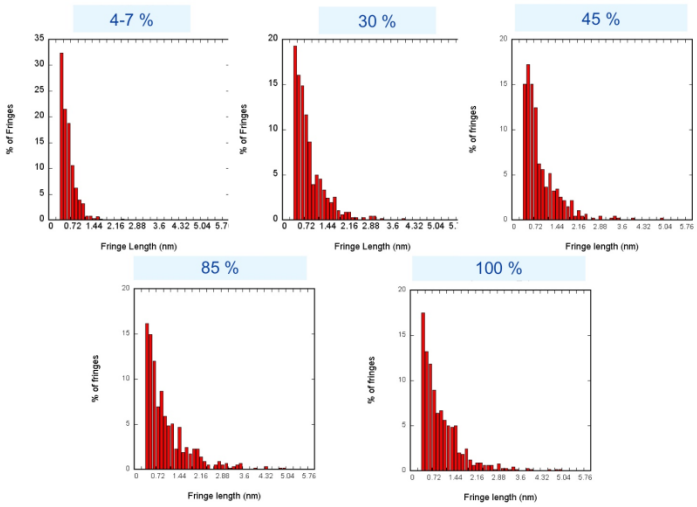

Figure 7b. Quantification of the HRTEM images can provide several statistical metrics describing the nanostructural order. Above are shown histograms of the lattice fringe length. There is a progressive change towards more graphitic structure with increasing power, but as shown, the level of graphitic nanostructure quickly asymptotes.

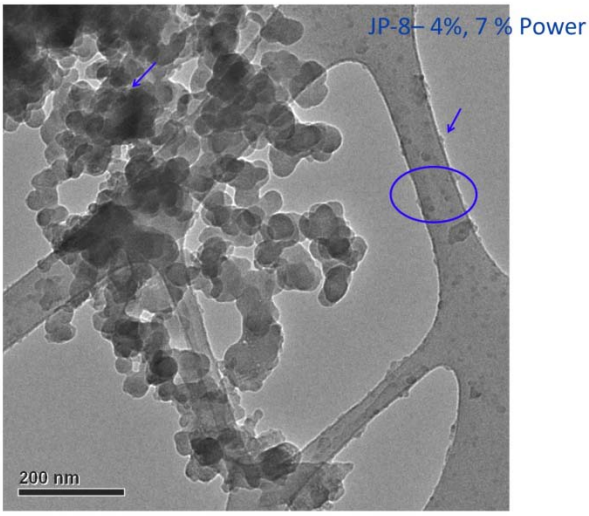

Figure 8a. The most notable find of this sample and those from other tests is the plethora of nanoparticles at the lowest power setting, 4-7%. They generally consist of only a few individual subunits (aka primary particles), often only one. Their high occurrence is evident on the lowest magnification image. These are clearly a health hazard and will not be filtered by normal airway mechanisms. The very fact that they survive the 30-meter sampling probe demonstrates that they appear remain separate and do not agglomerate.

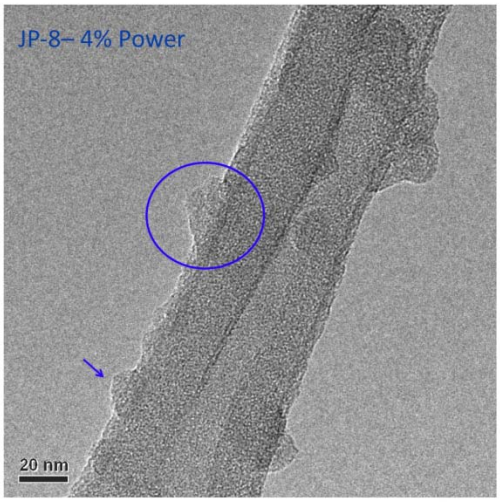

Figure 8b (continued). A higher magnification image of the (small) individual aggregates.

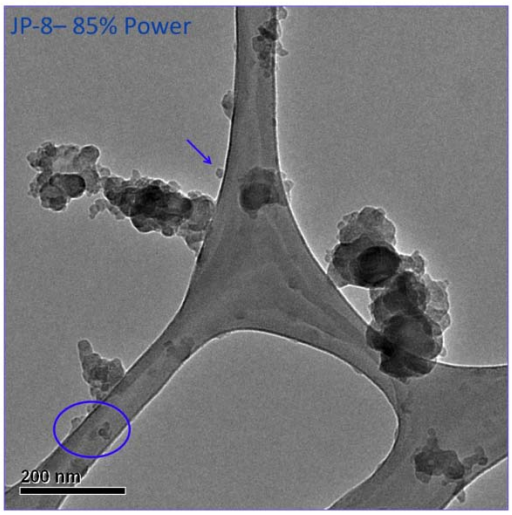

Figure 9a. Though small particles (< 50 nm diameter) were generally absent at mid-range power levels, but were again present at high power settings, though with an apparent lower number density, based on observed surface deposition upon the lacey grid.

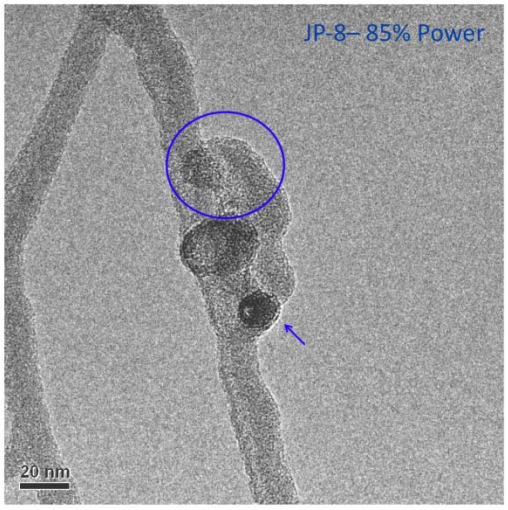

Figure 9b. As illustrated, the small particles at the high power were similar in size and number of primary particle subunits relative to those at the low "idle" power level of 4-7%.

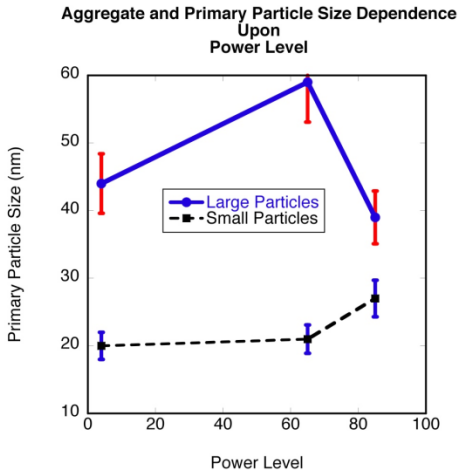

Figure 10. Variation in primary particle size with power level. There are two very different particle size populations based upon visual interpretation of the TEM grids, thereby accounting for the two plots.

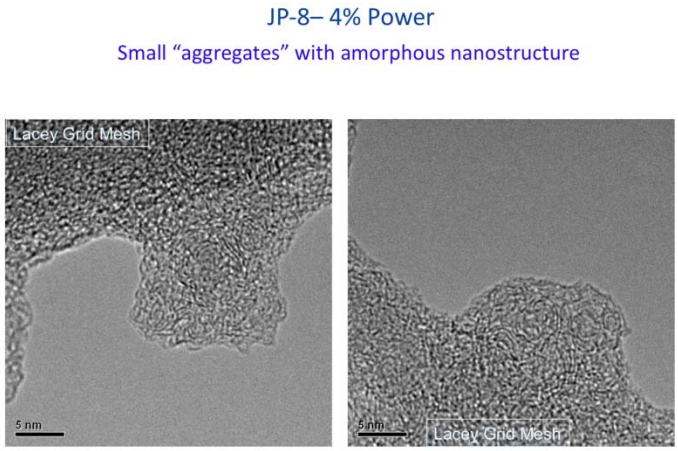

Figure 11a. Comparative nanostructure of the small aggregates as a function of power. The amorphous nanostructure of the particles is made clear by comparison to the adjacent lacey grid which is composed of an amorphous carbon film.

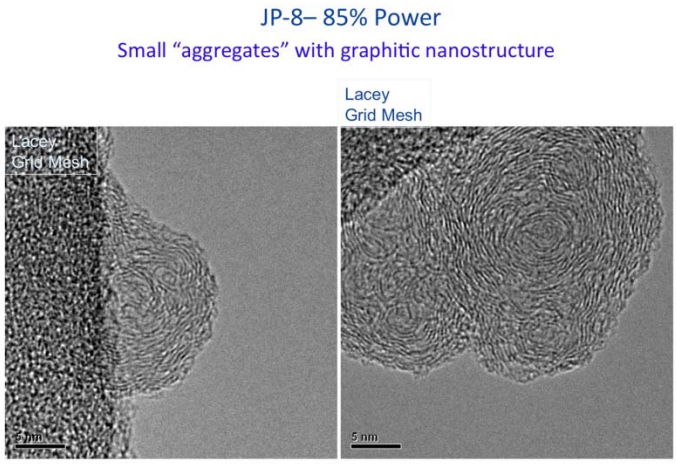

Figure 11b. Unlike the ultra-small particles observed at the low power, those at 85% (and 100%) power levels manifested a highly graphitic structure, quite similar to the large aggregates. Extended lamella often in stacks was were prevalent, again at the particle perimeter, suggesting similarity of growth environments or at least species continuity for these small aggregates and large aggregates at later particle growth stages.

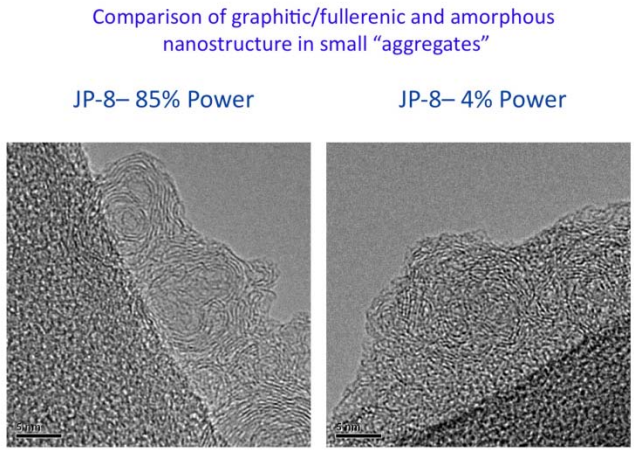

Figure 11c. A final image pair to contrast the nanostructure differences observed between the low and high power engine levels.

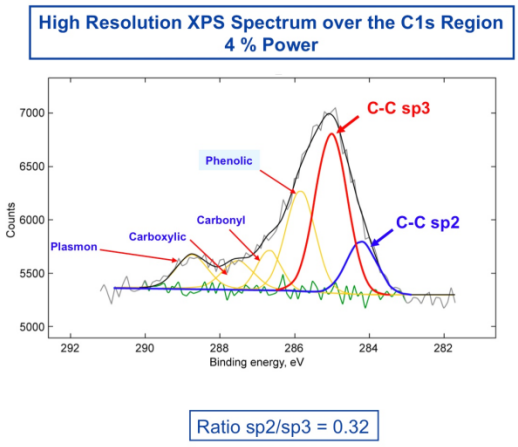

Figure 12a. Soot surface chemistry for jet engine produced soot using ultra low sulfur JP-8 fuel pertains mainly to oxygen functional groups. A high resolution scan over the C1s region illustrates the distribution of oxygen functional groups, phenolic, carbonyl and carboxylic in addition to differentiating between sp2 and sp3 carbon bonding. The ratio of sp2/sp3 can be considered as the ratio of organic to elemental carbon. For this low engine power, the carbonaceous particulate is mainly organic, reflecting considerably akyl-group (saturated hydrocarbon) content.

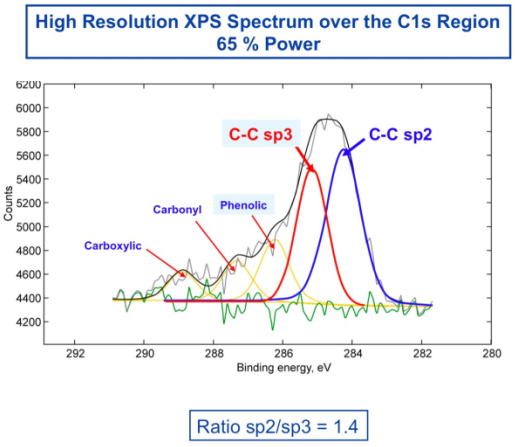

Figure 12b. With increasing engine power, the particulate bonding shifts from organic to elemental carbon as evidenced by the decrease in sp3 bonding and commensurate increase in sp2 carbon bond hybridization.

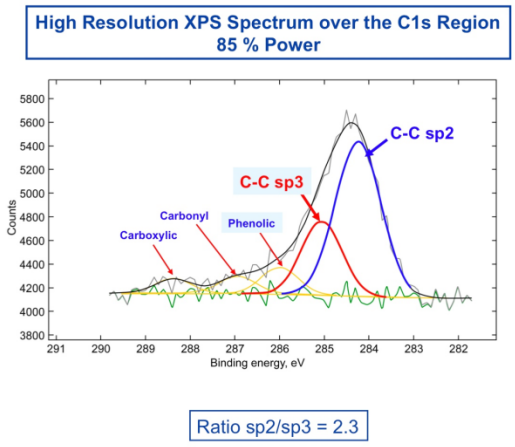

Figure 12c. At high engine powers, consistent with the graphitic physical (nano)structure revealed by HRTEM, the physical bonding mainly consists of C-C sp2, characteristic of graphitic carbon (or graphitic-like lamella). Notably the surface oxygen content is far less than at lower engine powers.

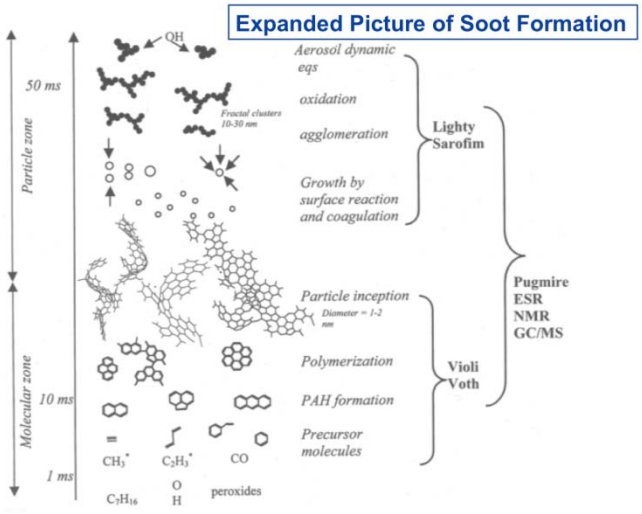

Figure 13. The soot formation process is quite complex consisting of several concerted processes of fuel pyrolysis, aromatic growth, particle inception, growth and oxidation.

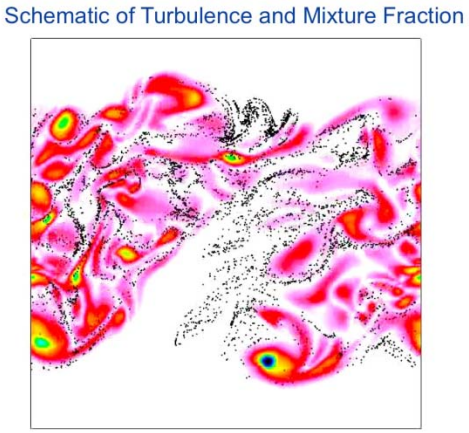

Figure 14. In reality the fuel-spray within the highly turbulent jet engine will consist of recirculation zones, fuel-rich pockets and varying levels of oxidation exposure. These spatial regions are conceptually illustrated above.

11. Conclusions

Regarding particulate (soot) macrostructure, in general, power level (fuel concentration and mixing) governs local fuel-air equivalence ratio. The implication as suggested by our observations is that soot aggregate morphology is a record of primary particle density and local concentration of growth species.

Regarding particulate (soot) microstructure, mixing controls timescale of coalescence relative to growth. The implication as borne out by our observations is that early coalescence followed by continued growth leads to virtually unrecognizable primary particles as they are highly merged and are fused together. This reflects a high hydrocarbon concentration, rapid particle nucleation and subsequent growth. Alternatively late coalescence leads to near point contact between primary particles. This reflects a lower hydrocarbon concentration, with delayed particle formation and coalescence.

Regarding particulate (soot) nanostructure, it reflects the species available for growth. Fuel-air mixing produces oxygenated intermediates that lead to C5 species introducing curvature in nanostructure. A single species such as C2H2 will contribute to uniform and ordered growth of carbon lamellae. Alternatively PAHs will contribute by a similar free radical addition mechanism but given their varied sizes, will not be able to orderly template upon the particle resulting in disrupted nanostructure that can give rise to a nanostructure that appears textured, (in which the graphene layers appear "woven"), chaotic (where the graphene layers have no orientational order) or amorphous (an absence of recognizable graphene segments).

Results presented here for low engine powers confirm the high relative concentration of ultrafine particles as secondary aerosols arising from the condensation of heavy hydrocarbons. With a nominal size of ~ 10 nm or less, these nucleation mode particles challenge traditional aerosol measurement instruments. In contrast HRTEM is ideally suited for their physical characterization. Though abundant in number, collectively this size mode contains very little mass. This challenges other traditional analytical chemistry techniques. X-ray photoelectron spectroscopy can decipher both elemental composition and carbon hybridization state. This latter ability is particularly useful for differentiating elemental and organic carbon, a key distinguishing characteristic of nucleation mode particles.

While a particle mode consistent with the nucleation size mode is observed at high engine powers, both HRTEM and XPS reveal these particles to be largely elemental carbon. The origin of these particles is clearly not secondary nucleation of volatile organics, though they are within the "nucleation" size range. These particles either arose by oxidative breakup of larger aggregates or perhaps by carbonization of small particles of condensed phase organics. Necessarily requiring elevated temperatures, this carbonization would have occurred inside the engine. These observations reveal the importance of combining electron microscopy and spectroscopy techniques with traditional aerosol measurements.

With regards to environmental implications, the presence of significant oxygen content upon the soot surfaces can potentially render them hydrophilic or at the very least aid condensation of polar emission species such as NOx and SOx. Both could potentially be converted to nitrate and sulfate species. In such a process the soot particles effectively heterogeneously catalyze formation of mixed nitrate and sulfate aerosols.

With regards to human health concerns, the ultra-fine particles (nanoparticles) at the 4-7% low power (idle) and high power (takeoff) engine levels are clearly a health hazard and will not be filtered by normal airway mechanisms. The very fact that they survive to the 30-meter probe illustrates that they do not to agglomerate nor deposit upon surfaces but remain separate and suspended. Thus the ambient air at and around airports is clearly hazardous during normal jet operations.

From these observations we conclude that engine specific conditions that control fuel-air mixing and the number and degree of fuel-rich pockets govern carbonaceous aerosol production. This does not discount fuel effects that could contribute, but in the absence of a sufficient number of reference samples from the FT1 and FT2 fuels, definitive conclusions for this report from the present limited data set cannot be reached.

12. Acknowledgements

The author gratefully acknowledges sample collection during the weeks of field campaign testing by Dr. Kathleen Tacina (NASA-Glenn) and overall project coordination and experimental assistance and support by Dr. Bruce Anderson (NASA-Langley). Vicky M. Bryg (USRA) is acknowledged for TEM and XPS work and fringe analyses and Mr. Chung-Hsuan Hunag (Penn State University) for sizing analyses and Dr. Corporan (WPAFB) for graciously sharing his experimental data prior to publication.

Support for this work was through the NASA Aeronautics Subsonic Fixed Wing (SSFW) Program, NASA Cooperative Agreement NNX09AD42A with The Pennsylvania State University, at University Park PA.

13. References

1. Haywood, J. M., and Shine, K. Pl, "Effect of anthropogenic sulfate and soot aerosol on the Clear-sky planetary radiation budget," Geophysical Research Letters 22, 60-30606 (1995).

2. Karcher, B., Peter, T., Biermann, U. M., and Schumann, U., Initial composition of jet condensation trails, Journal of the Atmospheric Sciences, 53, 3066-3083 (1996).

3. Schumann, U., Strom, J., Busen, R., Baumann, R.., Gierens, K., Krautstrunk, M., Schoder, F. P., and Sting, l, J., In Situ Observations of Particles in Jet Aircraft Exhaust and Contrails for Different Sulfur Containing Fuels, Journal of Geophysical Research, 101, 6853-6869 (1996).

4. Pueschel, R. F., Blake, D. F., Snetsinger, K. G., Hansen, A. D, A., Verma, S., and Dato, K., Black carbon (soot) aerosol in the lower stratosphere and upper troposphere, Geophysical Research Letters, 19, 1659-1662 (1992).

5. Armistead, G., R., and Brunekreef, B., A focus on particulate mater and health. Environ. Sci. and Technol. 43:4620-4625 (2009).

6. Samet, J., M., Dominici, F., Curriero, F. C., Coursac, I., and Zeger, A. L., Fine Particulate Air Pollution and Mortality in 20 U.S. Cities, 1987-1994, New England Journal of Medicine Medical Progress Series, 343, 1742-1749 (2000).

7. Hagen, D. E., and Whitefield, P. D., Particulate emissions in the exhaust plume form commercial jet aircraft under cruise conditions, *Journal of Geophysical Research, Atmospheres, 101, 19551-19557 (1996).*

8. Penner, J. E., Lister, D. H., Griggs, D.J. Dokken, D. GJ., and McFarland, M., (Eds.) *Aviation and the Global Atmosphere,* Intergovernmental Panel on Climate Change Rept., Cambridge Univ. Press, Cambridge, England, U.K. p. 373 (1999).

9. Vander Wal, R. L., Aircraft Engine Particulate: Macro- Micro- and Nanostructure by HRTEM and Chemistry by XPS (Atmospheric Environment, to be submitted).

10. Vander Wal, R. L., Tomasek, A. J., Pamphlet, M. I., Taylor, C. D., and Thompson, W. K., J. of Nanoparticle Research 6 (2004) 555-568.
See also, Vander Wal, R. L., Tomasek, A. J., Street, K. W., Hull, D. R., and Thompson, W. K., Applied Spectroscopy 58:230-237 (2004).

11. Vander Wal, R. L., Bryg, V. M., and Hays, M. D., XPS Analysis of Combustion Aerosols for Chemical Composition, Surface Chemistry and Carbon Chemical State (*Analytical Chemistry, submitted).*

12. P. J. F. Harris, S. C. Tsang, Philos. Mag. A 76:667-677 (1997).

13. Norton, T. S., The combustion chemistry of simple alcohol fuels, PhD thesis, Princeton Univ., Princeton, NJ, 1990. See also, Norton, T. S., and Dryer, F. L., Proc. Combust. Inst. 23 (1990), pp. 179–185.

14. McEnally, C. S., and Pfefferle, L. D., Experimental study of nonfuel hydrocarbons and soot in coflowing partially premixed ethylene/air flames, Combustion and Flame 121:575-592 (2000).

15. Wey, C. C., Anderson, B. E., Wey, C., Miake-Lye, R., Whitefield, P., and Howard, R., Overview on the Aircraft Particle Emissions Experiment. J. of Propulsion and Power, 23:898-905 (2007).

16. Lobo, P., Hagen, D. E., Whitefield, P. D., and Alofs, D. J., Physical Characterization of Aerosol Emissions form a Commercial Gas Turbine Engine. J. of Propulsion and Power 23:919-929 (2007).

17. Vander Wal, R. L., Soot Nanostructure: Physical and Chemical Characterization *Invited presentation*, APEX III, Cleveland, OH Nov. 29th – Dec. 1st, (2006)

APPENDIX K: Composition of Gas Turbine Engine Combustion Volatile Particle Material

M. T. Timko, Z. Yu, S. C. Herndon, E. C. Wood, R. C. Miake-Lye

Aerodyne Research Inc.
Billerica, MA 01821

Author's note: This Appendix summarizes results from laboratory studies, APEX-3, AAFEX, and the Midway Airport 2009 study. This report is based on a Final Report submitted previously to NASA describing activities under contract # NNC07CB57C. We acknowledge as outstanding issues of further inquiry: 1) the mass balance closure gap between integrated SMPS measurements and the AMS, 2) effective density and shape factor analysis of the non-volatile soot PM by comparison of SMPS (and/or EEPS) mobility diameter data, to AMS vacuum aerodynamic diameter data, to electron microscopy data.

Introduction

In this report, we summarize on-going efforts to analyze the composition of volatile PM emitted from gas turbine engines. The report describes some of the effects of engine technology and fuel composition on volatile PM composition. Specifically, the report contains the following

1) raw fuel aerosol mass spectrometer analysis;
2) aerosol mass spectrometer analysis of jet fuel combustion PM emitted from a laboratory diffusion flame burner;
3) mathematical analysis of the APEX-3 data set to identify the effects of engine technology on volatile PM composition;
4) detailed analysis of the AAFEX data set to identify the effects of fuel composition on volatile PM composition.

Raw Fuel Analysis

We used the aerosol mass spectrometer (AMS) to analyze a petroleum jet fuel and synthetic jet fuels manufactured using the Fischer-Tropsch (FT) process. For these tests, we acquired 2 FT fuels from AFRL, one produced by Syntroleum ("FT-Syntroleum" fuel), the other by a proprietary Company B ("FT-B" fuel). Figure 1 shows the diffusion flame spectra of the three fuels. All three spectra share characteristics common to fragmentation of compounds in a hydrocarbon matrix, chiefly the prominent peaks at m/z 27 and 29, 41 and 43, 55 and 57, 69 and 71, 83 and 85. Because the oxygen content of the fuels is negligible, we can confidently assign these peaks to the C_2-C_6 series. The ratio of nearby peaks to one another (e.g., 41 and 43) is a measure of the degree of unsaturation of the hydrocarbon fragments, and indirectly, of the parent hydrocarbon matrix. For example, m/z = 41 corresponds to the unsaturated molecular ion $C_3H_5^+$ whereas m/z = 43 corresponds to the saturated ion $C_3H_7^+$. The two

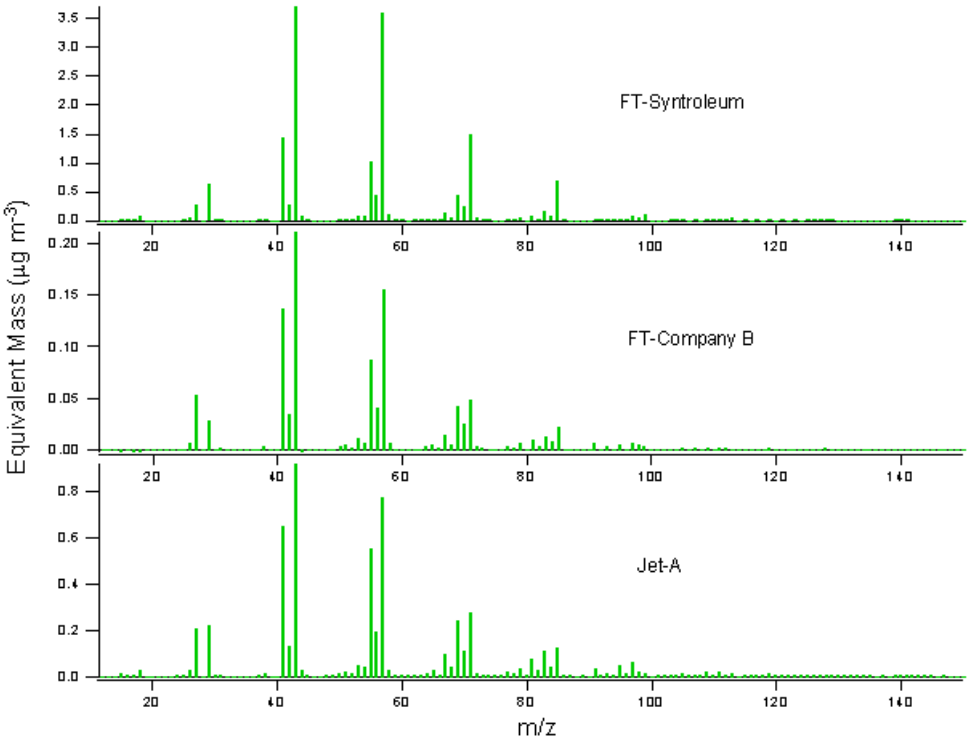

Figure 1. Raw Fuel Particle Mass Spectrometer Data. Aerosol mass spectra of FT-Syntroleum, FT-B, and Jet-A jet fuels.

series result from fragments with the formulas $C_nH_{2n-1}^+$ and $C_nH_{2n+1}^+$, respectively, and are sometimes referred to as the n = 0 and n = 2 series. The ratios $C_nH_{2n+1}^+$ (e.g., m/z 42) to $C_nH_{2n-1}^+$ (e.g., m/z 41) series are on the order of 1.5 for both the FT-B and Jet-A jet fuels. For the FT-Syntroleum fuel, the ratio is much higher, approximately 2.5. Another key difference in the three fuels is that the Jet-A spectrum contains more large ion fragments (defined here as m/z > 71) than either FT fuel. Likewise, the FT-Syntroleum spectrum contains more large fragments than the FT-B spectrum.

At this point, we attempted to extract molecular information from the differences in the two FT fuel mass spectra. As a starting point, we used the results of the AFRL chemical analyses of the jet fuels. Interestingly, the AFRL analysis for both the FT-Syntroleum and FT-B fuels indicate no difference in their content of olefinic, aromatic, or cyclic compounds – the three primary sources of unsaturated compounds in jet fuel mixtures. Instead of unsaturation, AFRL indicates that the primary differences between the two FT fuels are: 1) the carbon chain distribution of FT-B fuel is narrower than for the FT-Syntroleum fuel, with the FT-B fuel distribution centered at C_9, C_{10}, and C_{11}, and the FT-Syntroleum fuel containing substantial (~5%) components as large as C_{16}; 2) the percentage of linear paraffins in much higher in FT-B fuel (53.3 vol%) than FT-Syntroleum fuel (17.2 vol%). The increased prominence of large mass fragments (m/z > 71) in the FT-Syntroleum spectrum is consistent with the larger hydrocarbon chains present in the original fuel. The difference between the saturated/unsaturated mass

spectra of FT-B fuel and FT-Syntroleum fuel is likely due to differences in branching. According to McLafferty and Turacek (p 226 of *Interpretation of Mass Spectra*, 4th Ed., 1993), we expect that more branching would lead to an *increased* importance of the C_nH_{2n+1} series, consistent with the mass spectra data. Interestingly, the ratios of C_nH_{2n+1} to C_nH_{2n-1} peaks in Jet-A are comparable to FT-B, despite the fact that branching in Jet-A is comparable to FT-Syntroleum (roughly 18 vol%). The enhanced C_nH_{2n-1} series in Jet-A is likely due to the presence of aromatic (15 vol%), cyclic (20%), and olefinic (1%) compounds in the Jet-A fuel. Both olefinic and cyclic compounds have enhanced C_nH_{2n-1} signals relative to linear paraffins.

The extension of the Jet-A mass spectrum to larger masses than either FT fuel is consistent with its increased aromatic content. Aromatic compounds tend to be stable during ionization and yield a greater percentage of parent ions than olefinic or paraffinic compounds. Moreover, like FT-Syntroleum, Jet-A contains substantial mass in larger hydrocarbons (~5% in C16). Therefore, the extension of the Jet-A spectrum to mass larger than FT-B is likely due to the larger hydrocarbon molecules in the fuel matrix. The extension of the Jet-A spectrum beyond FT-Syntroleum may be due to the presence of aromatic compounds in Jet-A.

In summary:

1) the increased prominence of the C_nH_{2n+1} series in the FT-Syntroleum spectrum relative to FT-B is due to its increased branching ratio (only 17% of its content is in linear alkanes compared to 53% for FT-B);
2) the increased prominence of the C_nH_{2n-1} series in Jet-A relative to FT-Syntroleum is likely due to the presence of olefins and cyclic compounds in Jet-A;
3) the cyclic/olefinic compounds present in Jet-A balance its high degree of linear paraffins resulting in C_nH_{2n+1} series which are comparable to FT-B;
4) the FT-Syntroleum and Jet-A spectra extend to much higher m/z's than FT-B, consistent with the former to fuels containing more long-chain hydrocarbons than the former;
5) the Jet-A spectrum extends to slightly higher m/z's than FT-B, which may be consistent with either more long-chain hydrocarbons in the Jet-A fuel or more aromatic content in the Jet-A fuel.

Laboratory Combustion Particles

We performed tests using a laboratory diffusion flame burner and liquid jet fuels (JP-8, FT fuel, and a biofuel). Figure 2 provides representative results obtained while operating with a very fuel rich (orange) flame. The characteristic peaks of PAH ranging from $C_{16}H_{10}$ to $C_{34}H_{16}$ are present in the fuel-rich JP-8 diffusion flame spectrum. In contrast to HPLC analysis of filter samples during the PW308 tests, which found that fluorene ($C_{13}H_{10}$) and pyrene ($C_{16}H_{10}$), $C_{22}H_{12}$ is the dominant PAH formed in the fuel-rich JP-8 diffusion flame. We wanted to understand two aspects of the PAH data: 1) whether the differences between the PW308 data and the laboratory flame data could be attributed to differences in combustion conditions or sampling conditions and 2) what effects fuel composition might have on the diffusion flame particles.

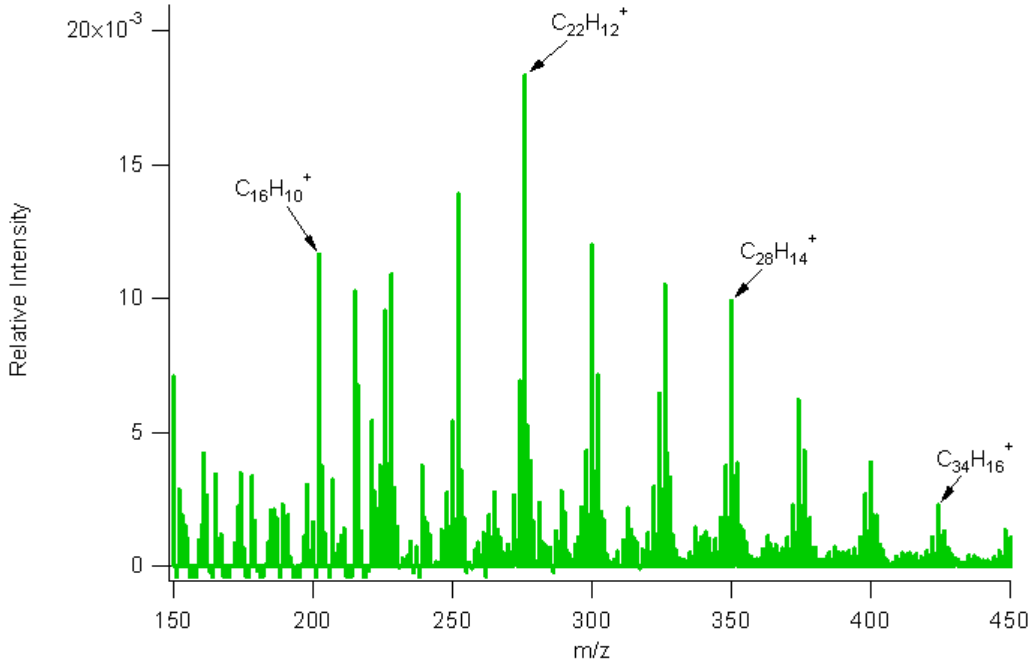

Figure 2. Particle-bound PAH Formed in Laboratory Burner**. M**ass spectrometer composition data obtained for JP-8 combustion in a laboratory diffusion flame burner.

We performed jet fuel diffusion flame tests for JP-8, three different FT fuels (Sasol, Syntroleum, and Shell), and a biofuel. NASA and AFRL technical staff helped us obtain the fuel samples for our tests. We performed the tests under fuel lean (blue flame) and fuel rich (orange flame) conditions. Figure 3 shows the PAH results for the various fuels tested. A drawback to our diffusion flame burner is that it lacks fuel flow and fuel/air ratio diagnostics. Qualitatively, the data in Figure 3 seem to have been collected during less fuel rich conditions than the data in Figure 2. Comparing the two PAH distributions, the very rich conditions tested for Figure 2 produced a broad range of PAH compounds whereas less rich conditions tested in Figure 3 produced only the $C_{16}H_{10}$ pyrene peak. The PAH product spectrum shift strongly suggests that combustion conditions play an important role in the PAH product spectrum.

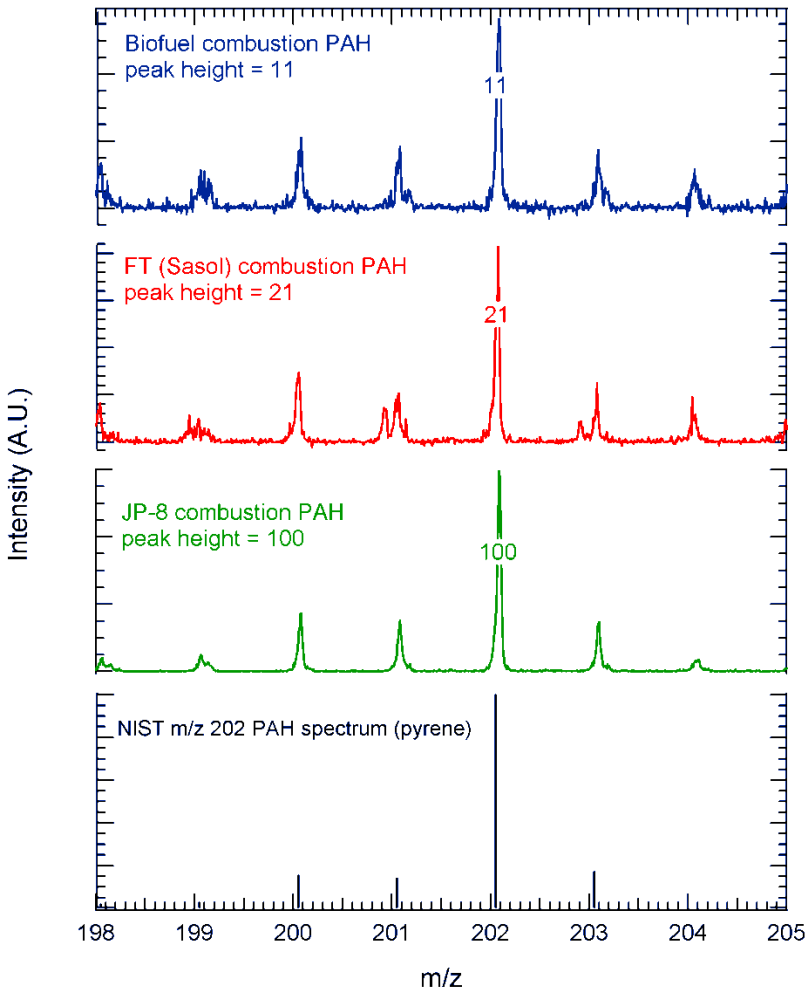

Figure 3. Particle-bound Pyrene Formed in Laboratory Burner**.** Laboratory diffusion flame results for combustion of various fuels highlighting production of the $C_{16}H_{10}$ PAH.

We analyzed the Figure 3 spectrum quantitatively to verify that it is likely pyrene and to compare the effects of fuel composition on PAH production as a function of fuel characteristics. The NIST mass spectrum for pyrene is showed in Figure 3; the close match in the isotopic pattern recorded by NIST and that measured in the laboratory confirms the identification of a $C_{16}H_{10}$ PAH. Figure 3 carries quantitative content that indicates a major difference in PAH production for combustion of the various fuels. The relative peak heights of the m/z 202 molecular fragment are labeled in Figure 3 and the order is clearly JP-8 >> FT (Sasol) > biofuel. The three FT fuels behaved similarly, and pyrene was always the primary PAH product formed for all 5 fuels. Thus, not only do we find that changing the fuel/air ratio changes the PAH product distribution, but we also find that varying fuel composition can change the quantity of PAH compounds formed. Consistent with previous studies, we speculate that the negligible aromatic content of the FT fuels leads to their reduced PAH production. The reduced PAH production of the biofuel is more confusing since the AFRL assay indicates that it contains 13.1 vol%

aromatic content. JP-8 typically contains between about 14-20 vol% aromatic so the biofuel is in a similar range to petroleum jet fuel. We speculate that the aromatic distribution in the biofuel may be different than in the JP-8 and that specific fuel aromatic compounds (e.g., multi-ring aromatic compounds) or other fuel hydrocarbon compounds (e.g., naphthenes) may play a disproportionately large role in PAH formation. PAH production for biofuel combustion is an interesting as of yet unresolved issue that bears further investigation.

We analyzed rich diffusion flame products using high resolution mass spectrometry for JP-8, FT Sasol, and biofuel. Figure 4 provides results of the diffusion flame tests. The m/z 41 peak is always dominated by $C_3H_5^+$ without even traces of the oxygenated $C_2H_3O^+$ fragment, a trend that is consistent with fragment stability patterns. The m/z 43 peak, however, shows a strong contribution for both $C_3H_7^+$ and the oxygenated fragment, $C_2H_3O^+$. The $C_2H_3O^+/C_3H_7^+$ integrated peak area ratios increase sharply from 0.44 for JP-8 combustion to more than 0.7 for both the biofuel and the FT fuel. The oxygen content therefore increases from 11% for the JP-8 combustion particles to 16% for the other two fuels.

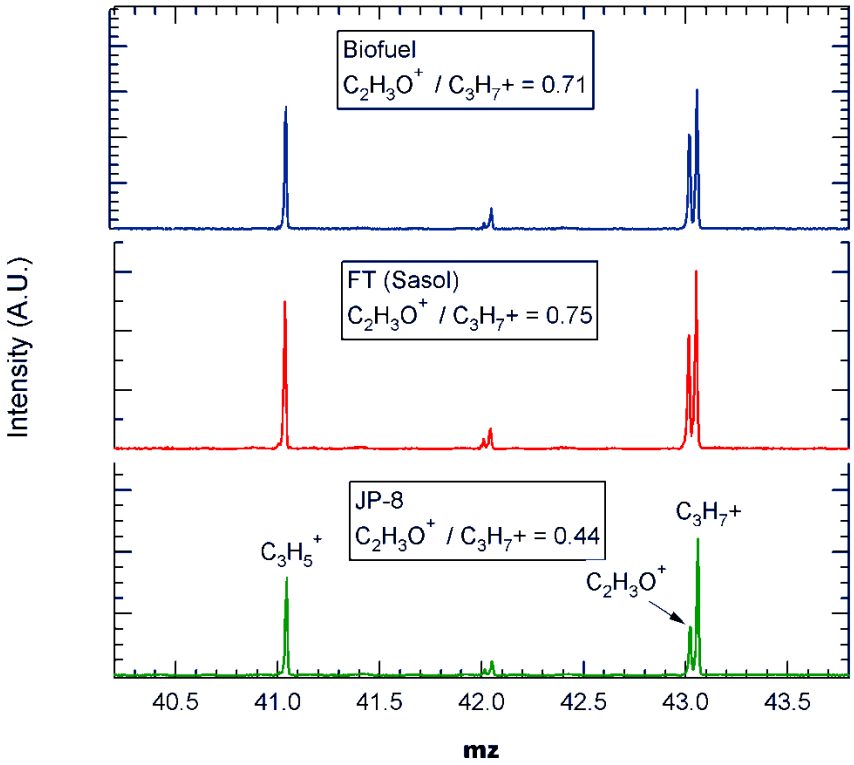

Figure 4. High Resolution Mass Spectra of Diffusion Flame Particles**. H**igh resolution mass spectrometer data for rich jet fuel diffusion flame data for JP-8, a FT fuel, and a biofuel.

In addition to fuel composition, fuel/air ratio also plays a role in the oxygen content. A very rich JP-8 diffusion flame produced PM with a $C_2H_3O^+/C_3H_7^+$ of about 10%, corresponding to an oxygen content of about 2.6%. Therefore, decreasing the fuel/air

ratio increases the oxygen content of the combustion PM. In terms of physical behavior, we anticipate that the biofuel/FT fuel combustion particles produced at lower fuel/air ratios would be more hygroscopic than the very rich-flame JP-8 particles. The hygroscopicity differences should in turn influence the environmental fate of the combustion PM. Extending the detailed high resolution mass spectrometer composition information to aircraft particles might prove useful.

Gas Turbine Engine Particle Emissions
Refined Analysis of APEX-3 Data.

We have analyzed our APEX-3 volatile PM composition data set using a pattern recognition tool termed positive matrix factorization (PMF). Although we originally presented preliminary results during the APEX-3 results workshop in November 2006, improvements in the PMF algorithm itself, the application of the PMF algorithm to volatile PM composition data, and our understanding of the APEX-3 results (largely due to our continuing efforts as part of this NRA) made re-analyzing the APEX-3 data set an important and productive activity. We include the results here as they provide important insight into the effects of combustor technology on volatile PM composition.

PMF is a powerful pattern recognition technique that has been applied to many AMS data sets to extract information and apportion a data set between various sources. As an input, PMF takes the mass spectrometer signals, the mass spectrometer uncertainties (based on statistical averaging), and the number of sources to be assigned. As an output, PMF identifies sets of mass spectra signals that tend to track one another. Each of these sets of signals potentially represents a separate source or component. We applied the PMF algorithm to the APEX-3 data set to identify individual components. Based on a preliminary APEX-3 analysis, we knew that PMF should identify siloxanes and lubrication oil in the APEX-3 volatile PM composition data. Our chief motivation was understanding better what we termed "residual" organic – that is organic PM that can neither be classified as lubrication oil nor siloxane. We performed PMF analyses with 3, 4, and 5 sources, and Figure 5 provides the results of our 5 source PMF analysis. As expected, siloxanes and lubrication oil were two of the sources. A source containing many features characteristic of aromatic compounds (m/z 77, 91, and 115) was identified as was a source that appears to be a typical hydrocarbon based on its m/z 55/57, 69/71, 81/83, 95/97 features. The final factor we label "unknown". When lubrication oil dominates the volatile PM composition (e.g. for RB211-535E4-B engines), the unknown source scales with lubrication oil. Otherwise, the unknown source does not contain sufficient features to make a strong identification. In some instances, the unknown may be a contribution from ambient particles.

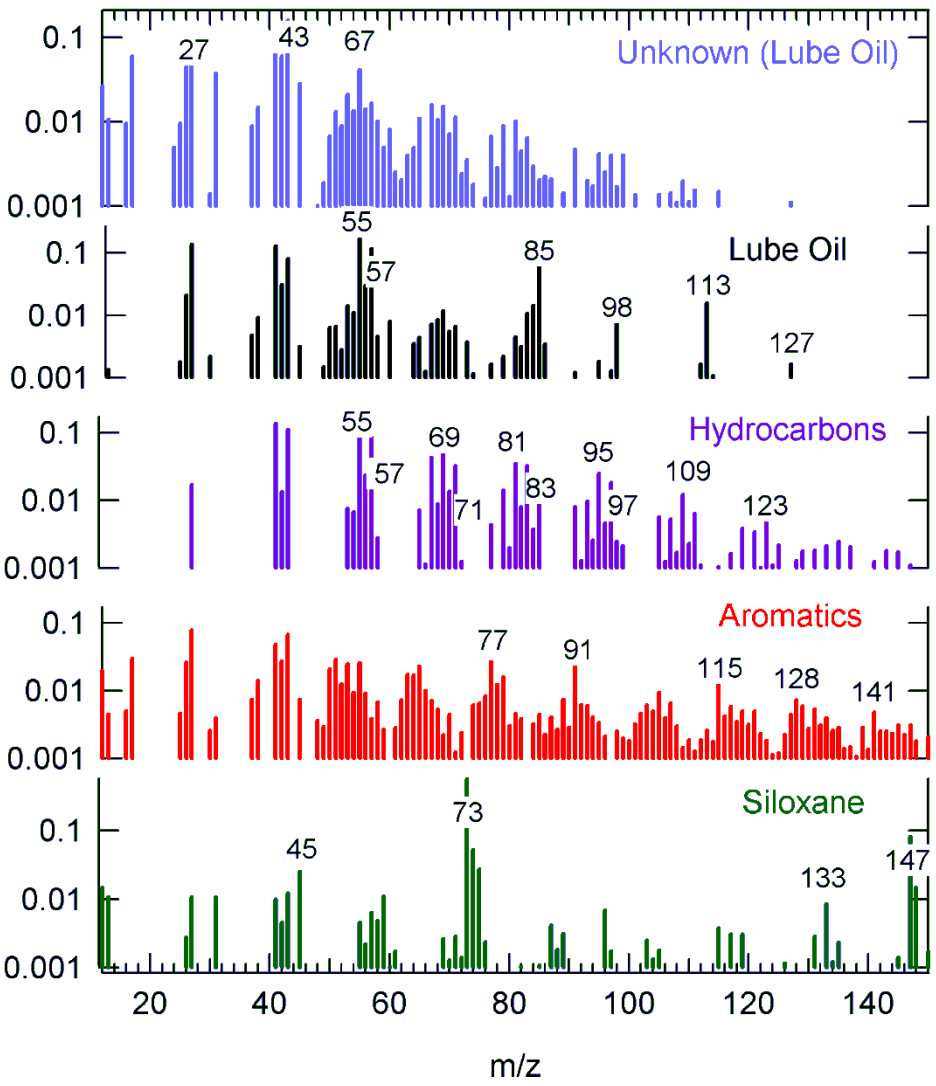

Figure 5. PMF Factors for APEX-3 Data**.** PMF analysis results for the APEX-3 data set.

The quality of the PMF analysis is reflected in the percentage of the actual EI_m-organic signal that it fits. In other words, a high quality PMF analysis fit is distinguished by a low residual. For 4 of the 9 APEX-3 engines, the residual was less than 10%: the CJ6108A on the NASA Learjet, the RB211-535E4-B engines on the Boeing 757 airframes (2 separate engines), and the CFM56-3B1 engine. The other engines (3 AE3007 engines and the PW4158) had residuals in excess of 10%. Therefore, we restrict our data presentation to the CJ6108A, CFM56-3C1, and RB211-535E4-B engines. We present results for the APEX-3 PMF analysis in Figure 6 after dividing engine operation into low (<15%), intermediate (>15% and <65%) and high power (>65%) operation. The results for the two RB211-535E4-B engines were nearly identical when plotted in the Figure 6 format, so we show data for only one of the engines as representative. Several features are immediately apparent in Figure 6: 1) as expected, lubrication oil accounts for over 90% of the volatile organic PM of the RB211-535E4-B emissions at all powers, the

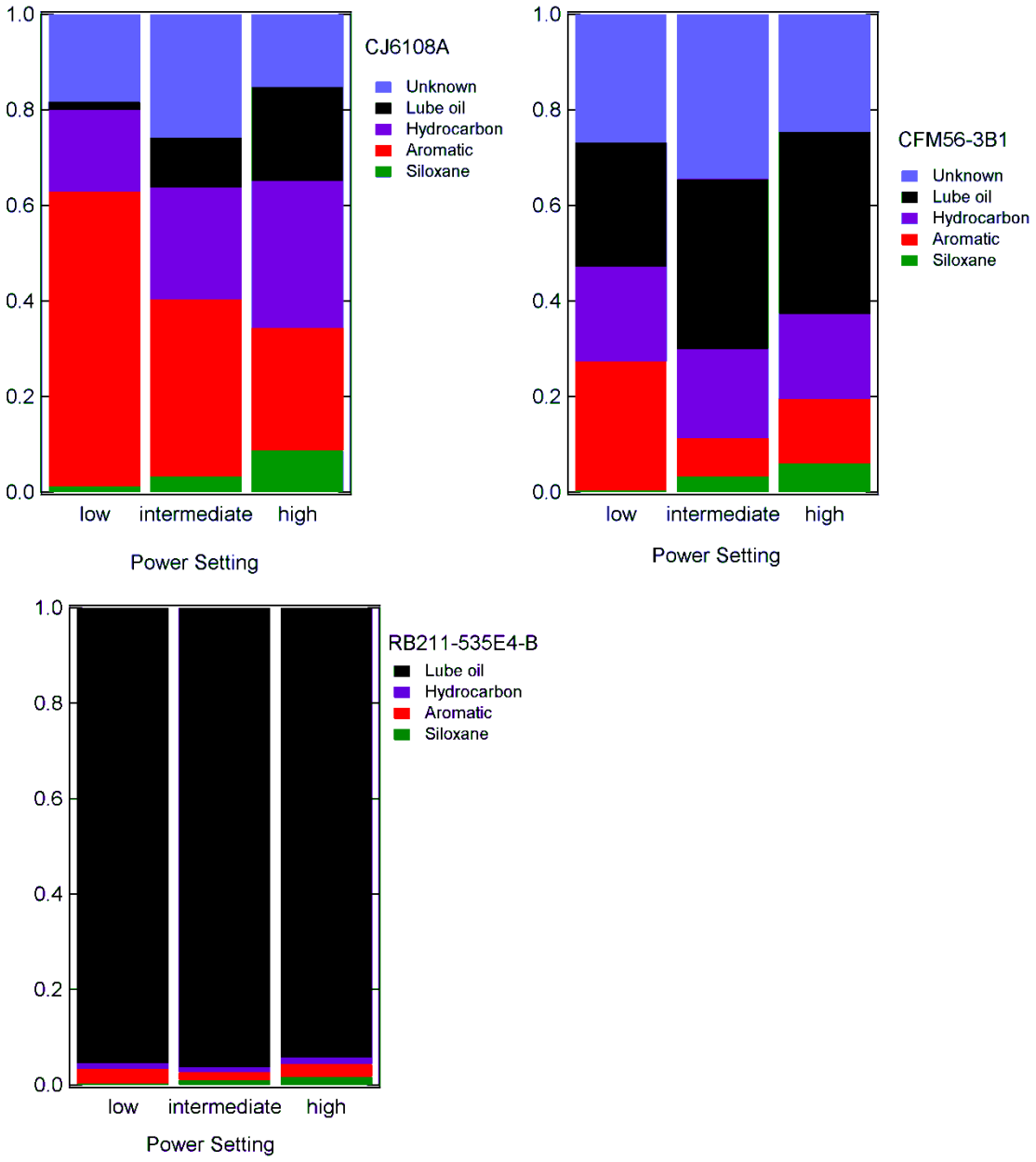

Figure 6. PMF Results for APEX-3 Data**.** PMF analysis results for three APEX-3 gas turbine engines.

fraction remaining is relatively steady with respect to power; 2) the products of incomplete combustion (specifically hydrocarbons and aromatics) dominate the CJ6108A volatile organic PM composition for all powers, and the fraction decreases with increasing power; 3) lubrication oil and products of incomplete combustion make similar contributions to the CFM56-3B1 volatile organic PM emissions. The dominance of incomplete combustion products in the CJ6108A is consistent with low efficiency combustor. The CJ6108A EI_m-HCHO was 2500 mg kg^{-1} at idle compared to 500 mg kg^{-1} for the CFM56-3B1 and 100 mg kg^{-1} for the RB211-535E4-B [Timko et al., 2009c]. The dominance of lubrication oil in the RB211-535E4-B volatile PM was expected; however,

our previous estimated placed the contribution at greater than 80%, rather than the 95% that we now calculate.

Having performed the PMF analysis to quantify the contributions of lubrication oil, siloxane, and un-identified components more accurately than had been done previously [Timko et al., 2009a], and having divided the "residual hydrocarbon" category into a hydrocarbon and an aromatic fingerprint, we were able to perform additional data analysis. Figure 7 contains plots of EI_m-organic/hydrocarbon and EI_m-organic/aromatic for the four APEX-3 engines that provided high-quality PMF data fits. After removing the

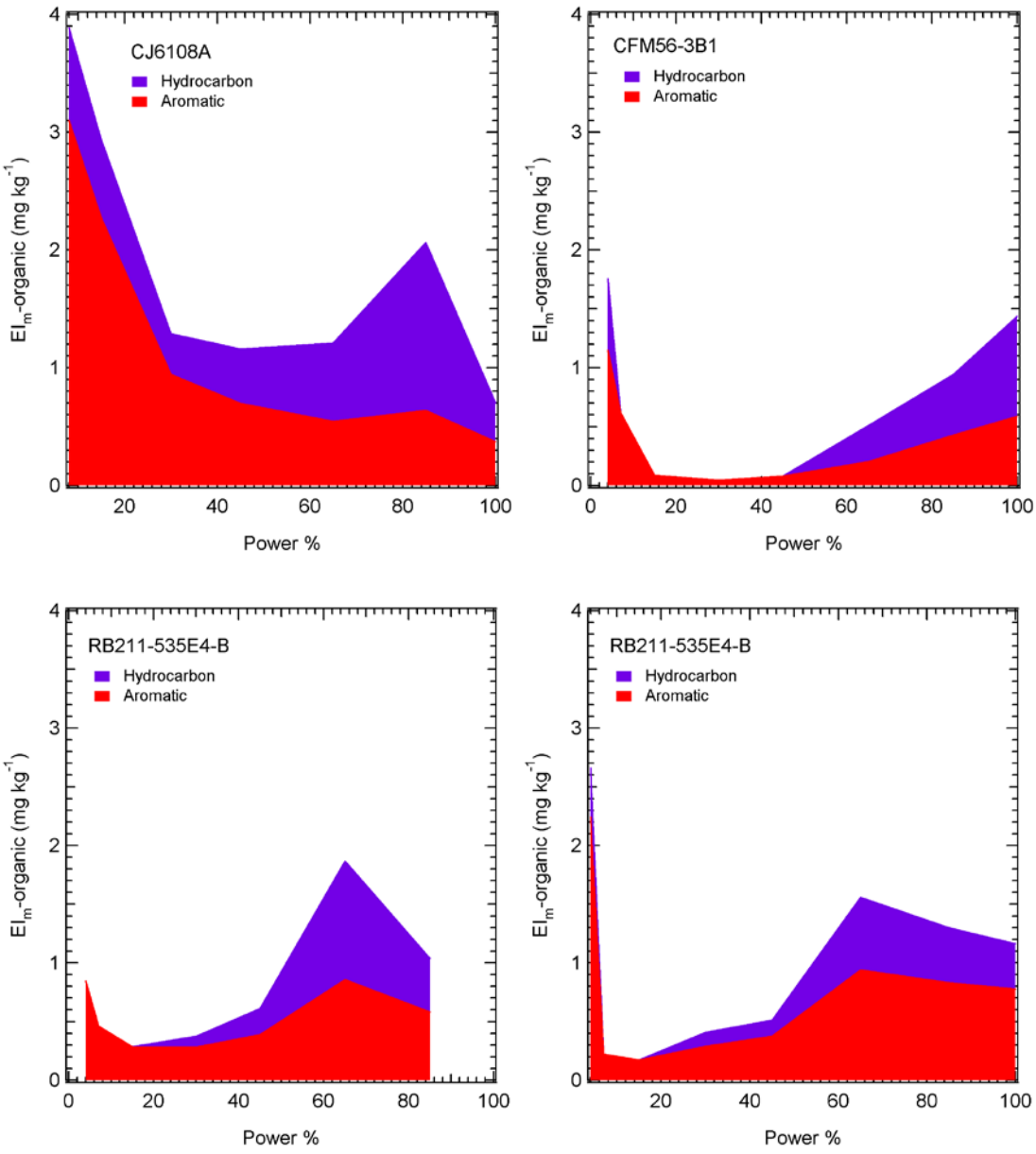

Figure 7. Hydrocarbon and Aromatic Contributions to Volatile PM Mass**. EI_m**-organic/hydrocarbon and EI_m-organic/aromatic for 4 APEX-3 engines.

lubrication oil contribution, organic PM for all four engines fall in the same range and are roughly ordered by EI_m-HCHO. In general, EI_m-organic/aromatic decreases from 0-15% and then increases from 65-100%. EI_m-organic/hydrocarbon generally increases with increasing thrust.

Figure 8 contains plots of the same data as shown in Figure 7, but now plotted as the sum of the two components (left panel) or their ratio (right panel). The overall trend in the organic PM signature is apparent in the left panel to Figure 8 - decreasing from 0-15%,

reaching a minimum at roughly 30-45%, and then increasing from 65-100%. The drop-off from 0-15% mirrors the decline in trace gas markers for combustor (in)efficiency, including EI_m-HCHO and EI_m-CO. The right panel to Figure 8 plots the ratio of EI_m-aromatic to the sum of the aromatic and hydrocarbon organic PM EIs. Interestingly, all four engines follow a similar trend as the fractional contribution of EI_m-aromatic decreases with increasing thrust from 0-65% and then levels off or increases slightly. Quantitatively, the fractional contribution of EI_m-aromatic is similar for all four engines, varying from 100% for the CFM56-3B1 engine at idle to 35% for the CJ6108A at 85%. Interestingly, the least efficient engine, the CJ6108A, generally has the lowest fractional contribution from EI_m-organic/aromatic of all three engine types.

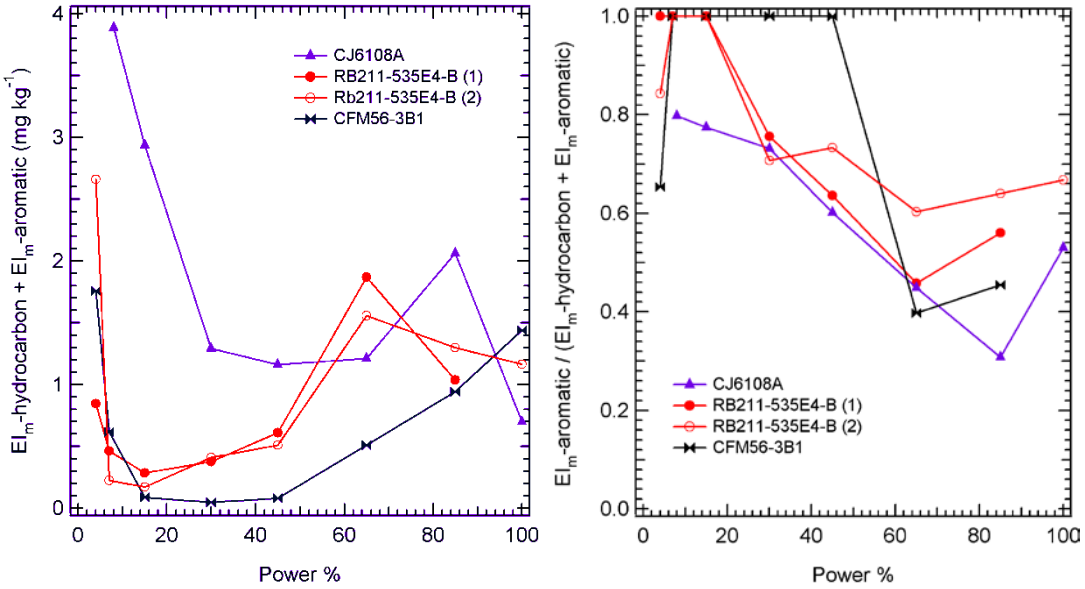

Figure 8. Comparison of Hydrocarbon and Aromatic Contributions to Volatile PM Mass**.** EI_m-organic/hydrocarbon and EI_m-organic/aromatic particle composition data from APEX-3 plotted as a sum (left panel) and a ratio (right panel).

We considered further the relative ordering of the fractional aromatic contribution to EI_m-organic, i.e., CFM56-3B1 ~ RB211-535E4-B > CJ6108A. In addition to engine technology differences (fuel/air ratio, pressure ratio, combustor temperature – all of which are proprietary data), fuel composition differences may be important. Fuel aromatic, naphthalene, and olefin content would seem to be the most important fuel composition differences that might plausibly explain the data in Figure 8. The fuel contents of the four fuels are provided in Table 1. Based on the data in Table 1, either fuel aromatic content or fuel naphthalene content may be important for the EI_m-aromatic/organic fractional contribution provided in Figure 8. Fuel aromatic content and fuel naphthalene content are roughly proportional to one another, so distinguishing between them is not possible. We can reject fuel olefinic content as an important variable for this analysis since its value is constant at roughly 0.7 vol%. For both aromatic content and naphthalene content, the CFM56-3B1 and RB211-535E4-B engines all have similar compositions (about 20 vol% and 1.8 vol%, respectively), but the CJ6108A has a

much different composition with lower aromatic (14 vol%) and naphthalene (0.6 vol%) contents.

Table 1. Fuel hydrocarbon properties for APEX-3 tests.

Engine	Aromatics vol%	Naphthalenes vol%	Olefin vol %
CJ6108A	14.2	0.57	0.77
CFM56-3B1	18	1.62	0.58
RB211-535E4-B (1)	21.8	1.84	0.76
RB211-535E4-B (2)	20.3	2.04	0.74

Engine technology differences and engine maintenance histories may play secondary roles in determining the fractional contributions of aromatic to the overall organic PM signature. For instance, the CFM56-3B1 aromatic contribution is greater than the RB211-535E4-B contribution at idle, even though the opposite order is predicted by their fuel compositions. Moreover, engine technology differences may play an important role in the upswing in the fractional aromatic contributions observed at powers greater than 65%. And, though the differences between the two RB211-535E4-B engines are minor, some of that variation may be attributable to poorly characterized differences in engine maintenance history – especially given that fuel composition alone would predict a stronger fractional aromatic contribution for RB211-535E4-B (1) than (2), and we observe the opposite behavior at power >45%.

Analysis of the AAFEX Data Set

The AAFEX campaign provided an opportunity to study organic PM composition and its potential fuel dependencies for a much wider range of fuel properties than APEX-3. Moreover, unlike APEX-3, a single engine was used, thus removing engine technology differences as a potential factor to be evaluated. Specifically during AAFEX, we performed trace gas and PM measurements for two CFM56-2C1 engines burning JP-8, a FT fuel manufactured from natural gas (Shell), a FT fuel manufactured from coal synthesis gas and coal liquids (Sasol), and 50/50 blends of the two FT fuels in JP-8. Tests were performed during "cold" ambient conditions (270-275K) and "warm" ambient conditions (285-290 K).

Before considering fuel properties and organic PM composition, we first introduce total PM mass data. Figure 9 provides AAFEX PM mass data when the engine was running JP-8 at cold conditions. Both integrated 30 m EEPS mass data (with an assumed particle density of 1 g cm^{-3}) and 1 m/30 m MAAP soot mass data are shown in figure 9. The 1 m and 30 m MAAP masses agree reasonably well for most of the power range, though the 1 m MAAP mass data are typically 10-25% lower than the 30 m MAAP mass data. We suspect that the difference is due to loss in the 1 m probe or sampling line. We have observed small discrepancies between 1 m and 30 m MAAP mass data previously; however, the AAFEX data set is more detailed than previous data sets and permits a cleaner distinction to be made. Interestingly, the port side CFM56-2C1 engine has a higher EI_m-soot than the starboard engine by as much as 25%. The difference between EI_m-soot for the two engines is most obvious at 65% power and is almost negligible at 85% power.

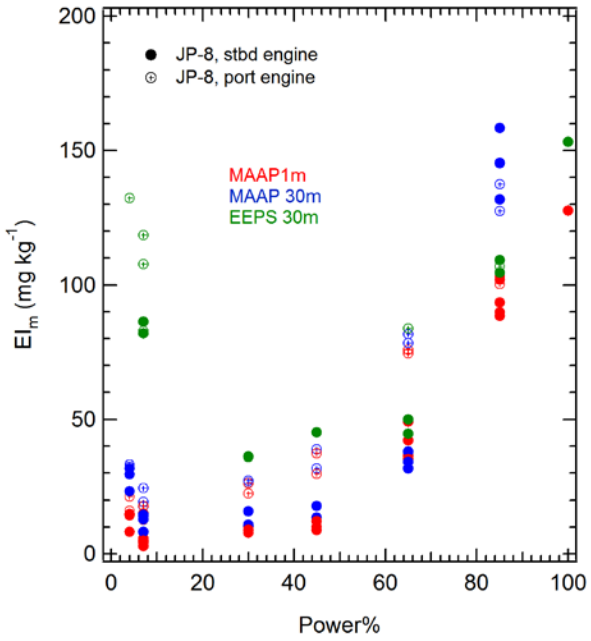

Figure 9. Total JP-8 PM Mass Emissions. PM mass data for a CFM56-2C1 engine burning JP-8 fuel as measured by an EEPS (EI_m-total) and a MAAP (EI_m-soot).

The EEPS data are a measurement of total PM mass. Under cold conditions, the total PM mass measured by EEPS is greater than 100 mg kg^{-1} at idle and falls to less than 50 mg kg^{-1} at 30%, before increasing to 150 mg kg^{-1} at 100% power. Agreement between EEPS and MAAP at powers greater than 30% is reasonably good and within the range of experimental scatter at powers greater than 65%. For 4 and 7% power, the EEPS PM EI_m-total measurement is much greater than the MAAP EI_m-soot measurement, indicative of a strong nucleation mode containing roughly 100 mg kg^{-1} of mass. EI_m-nucleation (or EI_m-volatile) of 100 mg kg^{-1} is large compared to that obtained in previous tests, and we attribute the high value to a) the high fuel sulfur content of the JP-8 fuel (1200 ppm mass) and b) the cold ambient conditions prevalent during this test (270 K). The remainder of this section is investigates the composition of the volatile PM, beginning with EI_m-sulfate.

Figure 10 plots EI_m-sulfate (at 30 m) as a function of engine power for the JP-8 and FT fuels for the CFM56-2C1 engine. First, the dependence on fuel composition is apparent. For JP-8, EI_m-sulfate varies from about 1 mg kg^{-1} at idle to nearly 4 mg kg^{-1} at take-off. EI_m-sulfate for both pure FT fuels is below detection limits (0.2 mg kg^{-1} for these tests) for all power conditions. EI_m-sulfate for the blended FT fuel was intermediate to the pure FT fuels and JP-8, though closer to the FT data. Power clearly played a role in EI_m-sulfate – consistent with previous work [Onasch et al., 2009; Timko et al., 2009a]. Increasing power increased EI_m-sulfate, most likely because of the power dependence of EI_m-soot and the better ability of the AMS to quantify soot sized particles (and/or their coatings) than nucleation/growth mode particles. Temperature was also important. As

temperature increased, so too did EI_m-sulfate. This counter-intuitive finding is likely due to the competition between nucleation (favored at low temperature) and soot coating (favored at high temperature) – and the relative sensitivity of the

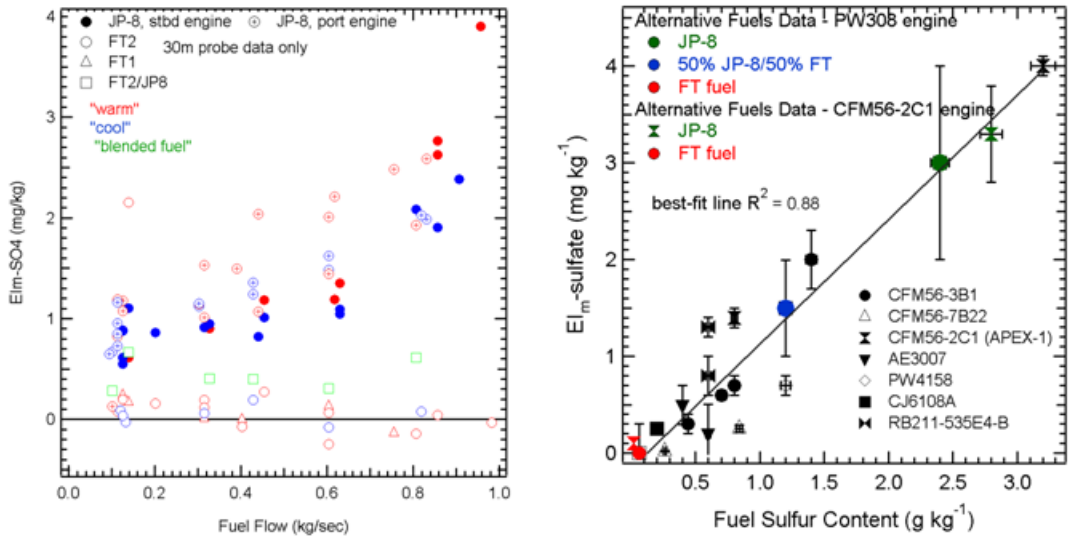

Figure 10. AAFEX Sulfate PM Mass Emissions**.** EI_m-sulfate data obtained during AAFEX (left panel) and a summary plot of EI_m-sulfate from AAFEX, APEX-1, 2, and 3, and the PW308 tests.

AMS to nucleation particles (low) and soot particles (high). Consistent with these observations, EI_m-sulfate for the port engine is greater than the starboard engine, just as EI_m-soot for the port engine is greater than for the starboard engine.

Because of the high sulfur content of the JP-8 (1200 ppm) and the negligible sulfur content of the FT fuels, AAFEX provides an opportunity to re-visit the fuel sulfur conversion analysis performed previously [Timko et al., 2009a]. As suggested in our description of the left panel of Figure 10, the AMS provides an incomplete measure of total sulfate PM because of its poor detection capability for particles smaller than 50 nm. For particle sizes typical of soot (>50 nm), AMS data is nearly quantitative. Therefore, we restrict our analysis to 85% and 100% power when EI_m-soot is maximized and the AMS data is closest to quantitative. Plotting EI_m-sulfate (85/100%) as a function of fuel sulfur content alongside archival data from APEX-1, 2, and 3, and the PW308 tests reveals EI_m-sulfate to be a reproducible measurement from campaign to campaign. The best fit line between EI_m-sulfate and fuel sulfur content is shown. The slope of the best fit line, which is also the S(IV) to S(VI) conversion efficiency - remains roughly 0.1%, as it was after considering only APEX data. Engine technology does not seem to play a role in the conversion efficiency. The 100% FT data and the 50/50 blend data fall on the curve for JP-8 and Jet-A, with the exception of the 50% FT (Sasol) blend from AAFEX which is low by a factor of about 2. The Sasol blend may be low due to a) the fact that it

was studied at a maximum power of 85%, whereas the other AAFEX fuels have 100% power data or b) an additional fuel related factor that distinguished Sasol blends from other FT fuel blends. Of these, the power difference seems more reasonable, but we cannot rule out fuel related differences based on our data alone.

Figure 11 contains a plot of EI_m-organic measured for the various fuels during the AAFEX campaign. As with EI_m-sulfate, EI_m-organic depends on the fuel, the power condition, and ambient conditions. The dependence of EI_m-organic on the engine (port or starboard) is weaker than for EI_m-sulfate. Taking the other three variables in turn: 1) fuel: EI_m-organic is greater at all power conditions for JP-8 than for the FT fuels or the blended fuel, 2) temperature: EI_m-organic increases with decreasing ambient temperature, 3) power: consistent with APEX results, EI_m-organic decreases from 0-15% (plotted as fuel flows ranging from 0 to 0.3 kg sec^{-1}) and then increases from 65-100% (0.6 to 1 kg sec^{-1}). Quantitatively, EI_m-organic at idle and low ambient temperature reaches a value of nearly 15 mg kg^{-1} – the highest ever measured during an aircraft test. The high idle value of EI_m-organic can be attributed to the low ambient temperature of the test and the relatively low efficiency of the CFM56-2C1 combustor when operated near idle.

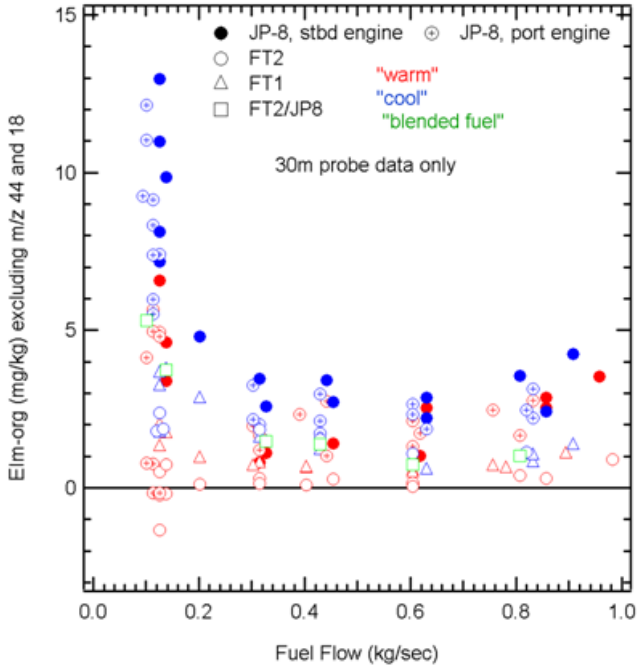

Figure 11. AAFEX Organic PM Mass Emissions**.** **EI_m**-organic measured during the AAFEX campaign.

The ratio of EI_m-sulfate to EI_m-organic is an interesting quantity, and we plot that ratio in Figure 12 for JP-8. For FT fuels, the ratio is not meaningful since EI_m-sulfate was below detection limits for these fuels. For JP-8, Figure 12 clearly shows that the ratio of EI_m-sulfate to EI_m-organic increases steadily with increasing power. At idle, the volatile PM material is dominated by organic material which contributes more than 90% of the total mass. At take-off, the ratio of organic to sulfate PM is nearly 1:1. Interestingly, the ratio of sulfate to organic depends on ambient temperature – at least for powers greater than 4%. Higher ambient temperatures favor EI_m-sulfate. We propose two explanations: 1)

lower ambient temperatures decrease combustion efficiency, thereby increasing the amount of organic precursors available to form organic PM or 2) decreasing temperature shifts sulfate material preferentially to the nucleation mode (and away from the soot mode) where it is not detected efficiently.

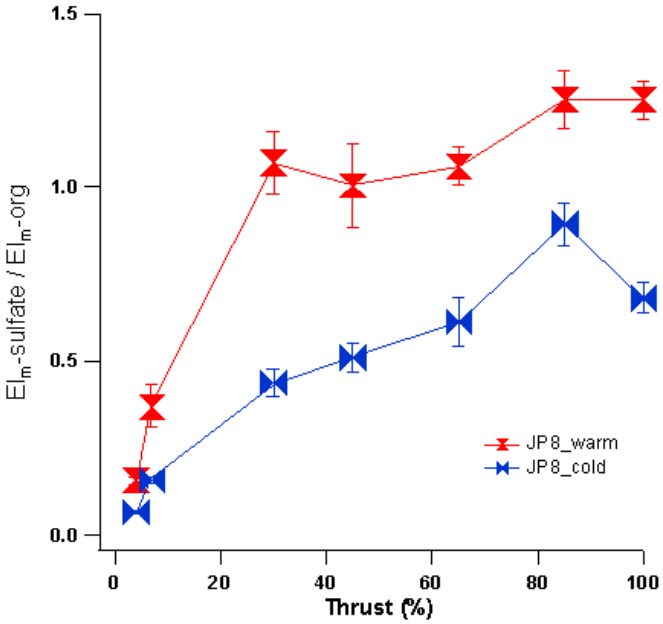

Figure 12. Comparison of Sulfate and Organic for JP-8**. Ratio** of EI_m-sulfate to EI_m-organic measured during AAFEX.

Particle size data provide an opportunity to test the two theories forwarded to explain Figure 12. Figure 13 provides particle size data for JP-8 obtained at idle (left) and take-off (right) conditions. Data for warm (top) and cold (bottom) ambient conditions is provided. As expected, the particle size distribution obtained at idle peaks at roughly 30 nm, consistent with a nucleation/growth mode truncated by the AMS sensitivity for small particles. Also as expected, the distribution favors organic materials at idle by a factor of about 10:1. At take-off, the ratio of sulfate to organic material in the soot mode is roughly 1:1. Interestingly, however, at cold conditions we detect a slight peak in the sulfate particle size distribution at take-off power that seems to fall in the nucleation/growth mode size range (bottom right of Figure 13). The sulfate peak is not present in the organic size distribution nor in either distribution at warm conditions. Therefore, the cold take-off power data presented in Figure 13 seems to indicate that decreasing ambient temperature preferentially drives sulfate material to the nucleation/growth mode. We tentatively conclude then that the temperature dependence of the EI_m-sulfate/EI_m-organic ratio at idle is determined by combustor efficiency and at higher power by the preference of sulfate material for the nucleation/growth mode at lower temperatures. Although the sulfate nucleation peak is not very strong in Figure 13, the SMPS data shown in Figure 14 support the observation of a nucleation mode under these conditions, though the SMPS shows that the mode peaks at less than 20 nm instead of almost 30 nm. The observation that the nucleation mode may have a different ratio of sulfate to organic material than the soot mode t is new and potentially important –

especially at cruise conditions at altitude. For that reason, we plan to continue to analyze the AAFEX data to understand better the EI_m-sulfate/EI_m-organic ratio and its dependence on power.

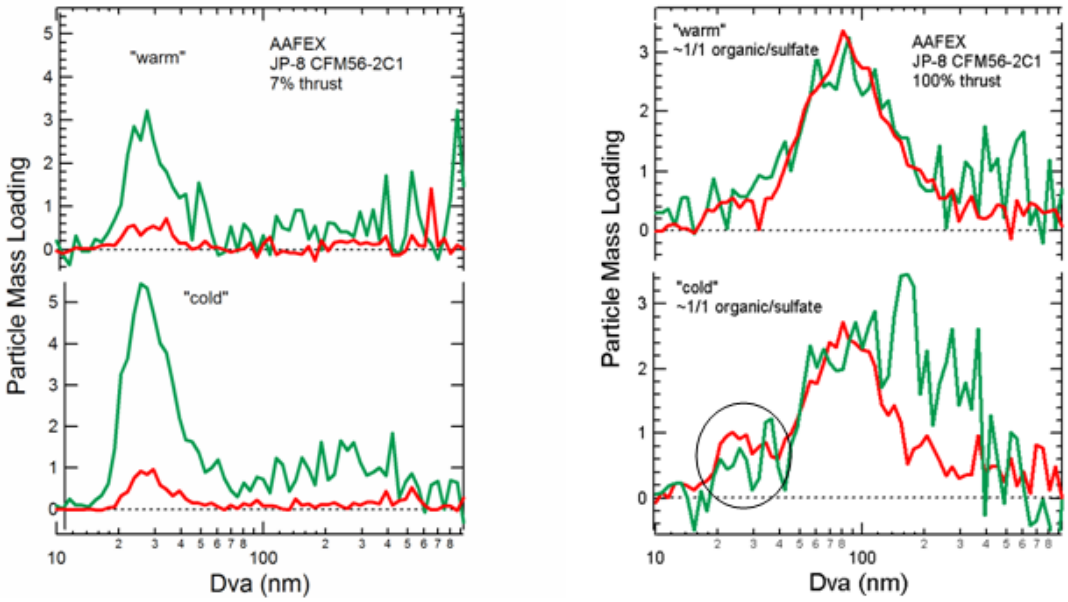

Figure 13. Particle Size Distributions for Volatile PM**.** Particle size data for volatile PM obtained during AAFEX: left, idle conditions, right, take-off; top: warm ambient temperature; bottom: cold ambient temperature.

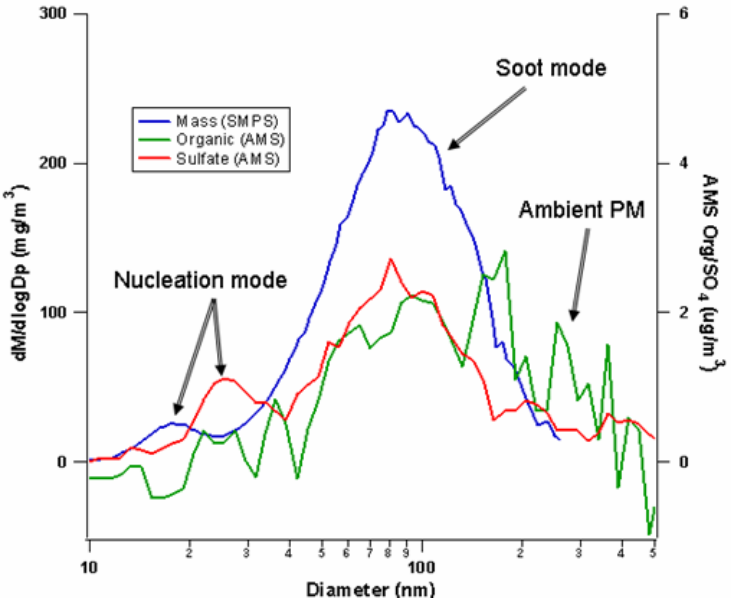

Figure 14. Comparison of SMPS and AMS Particle Size Data**.** Comparison of the 85% power AMS data shown in Figure 13 with the SMPS size distribution data.

We characterized the composition of the organic PM more carefully by analyzing the particle mass spectra we obtained during AAFEX. Figure 14 provides the mass spectra results. As in Figure 13 the left panel of Figure 15 contains idle data (4%) and the right panel contains high-power data (85%). Data for only cold ambient conditions are provided in Figure 14 except for the FT blended fuel which was performed only once at warm conditions. All of the spectra presented in Figure 14 contain features consistent with a hydrocarbon – apparent from the m/z 41/43, 55/57, 69/71 fragments. At low power, JP-8 contains evidence of the APEX-3 aromatic signature – m/z 77, 91, and 115. The aromatic signature is nearly absent from the FT fuel mass spectra and decreases strongly at high power for all the fuels. Lubrication oil, characterized by the m/z 85, 113 fragments, is present in all the spectra and dominates the high-power mass spectra. The AAFEX mass spectra seem to contain all of the components present in the APEX-3 spectra, and the aromatic signature is the only feature that seems to be fuel dependent.

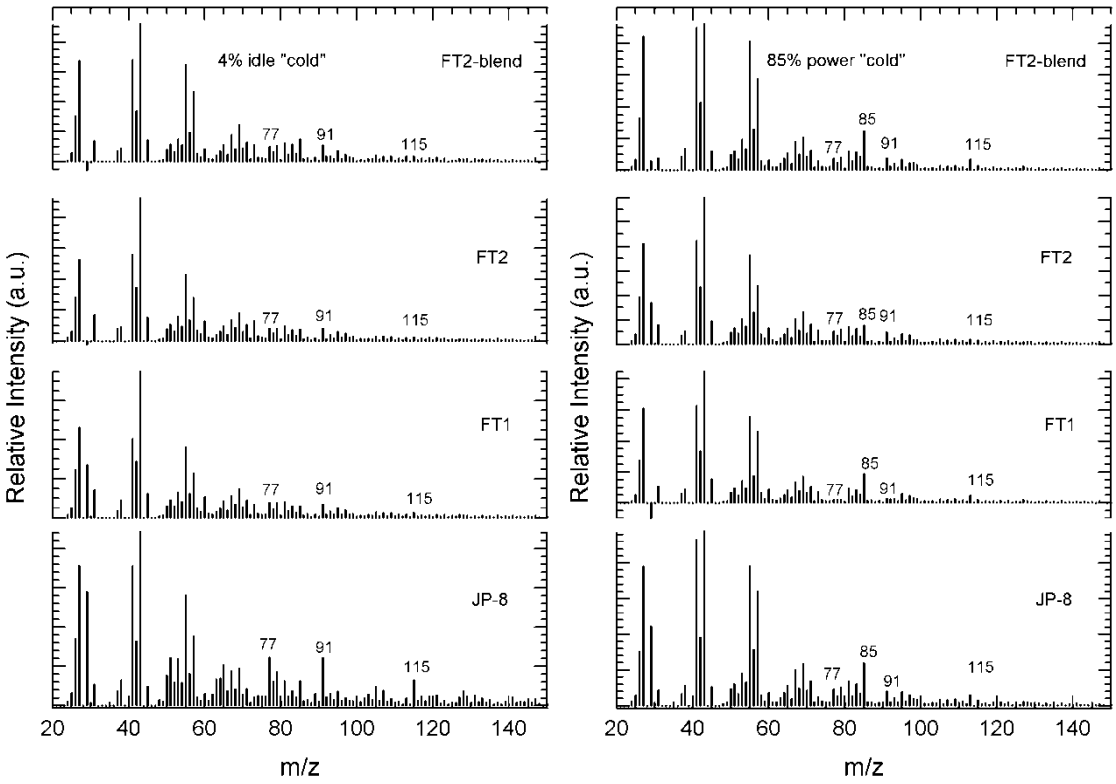

Figure 15. AAFEX Particle Mass Spectrometer Data**.** Mass spectra data obtained during AAFEX for idle (left panel) and climbout (right panel) conditions for the various fuels.

We have yet to perform a PMF analysis of the AAFEX data; however, we have performed a qualitative analysis of the aromatic signature as shown in Figure 16. On an absolute basis (left panel), the quantity of aromatic mass decreases sharply with increasing power and is nearly absent from the FT fuel particles. On a relative basis

(right panel), the aromatic contribution still decreases with increasing power. But unlike the APEX-3 data, all of the fuels seem to follow a similar trend. Clearly, we need to continue to analyze the AAFEX composition data to relate it to APEX-3.

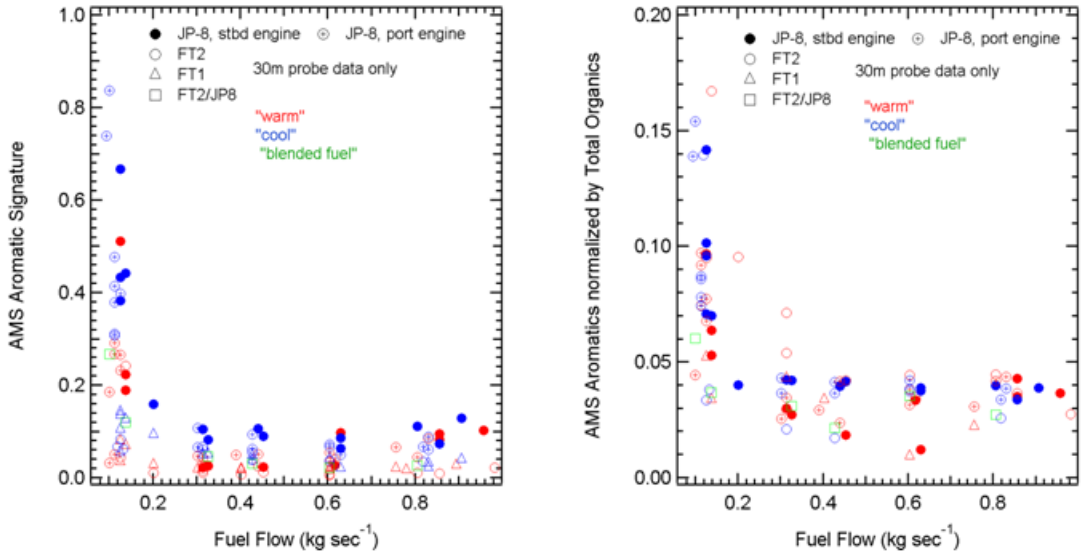

Figure 16. AAFEX Aromatic PM Content**.** Qualitative apportionment of the organic PM mass to the aromatic contribution.

APPENDIX L: Microphysical Evolution of Gas Turbine Engine Combustion Particles

M. T. Timko, Z. Yu, S. C. Herndon, E. C. Wood, R. C. Miake-Lye

Aerodyne Research Inc.
Billerica, MA 01821

Author's note: This Appendix summarizes results from AAFEX, and the Midway Airport 2009 study (MDW-09). This report is based on a Final Report submitted previously to NASA describing activities under contract # NNC07CB57C. We acknowledge as outstanding issues of further inquiry: 1) resolution between model estimates and experimental measurements of particle characteristics in evolving plumes, 2) mass balance closure gaps between SMPS and AMS data sets, 3) evaluation of the importance of ambient PM on exhaust PM evolution, 4) importance of sampling line effects (line loss, evolution in the line, etc.) to measured PM characteristics.

Introduction

One of the most challenging aspects of studying aircraft PM is that it continues to evolve on a 1-sec time scale as the exhaust plume cools and dilutes. We observe this behavior during standard dedicated engine tests; almost no volatile PM is detected at 1 m, and the detected volatile PM mass increases by a factor of 10 or more at 30 m. Some of the observed discrepancy between 1 m and 30 m may be due to the loss of volatile PM precursors or volatile PM itself on the sampling probes and transfer lines. Much of it, however, seems to be due to gas-to-particle conversion of volatile PM precursors that occurs on rapid (<10 sec) timescales. Figure 1 provides 30 m SMPS measurements of particle size obtained for JP-8 during AAFEX. The left panel shows number density data, while the right shows particle volume data measured at 30 m. At all conditions, a size mode peaking at approximately 10-20 nm and consistent with nucleation/growth mode particles dominates the number density data. In the volume plot, the contribution of nucleation/growth mode particles is still apparent at all powers; however, nucleation/growth mode volume dominates only for power <65%. At 1 m (data not shown), the nucleation/growth mode is absent. During AAFEX and MDW-09, we augmented dedicated engine test measurements with measurements made further downfield (>50 m) to understand better microphysical evolution of cooling exhaust plumes.

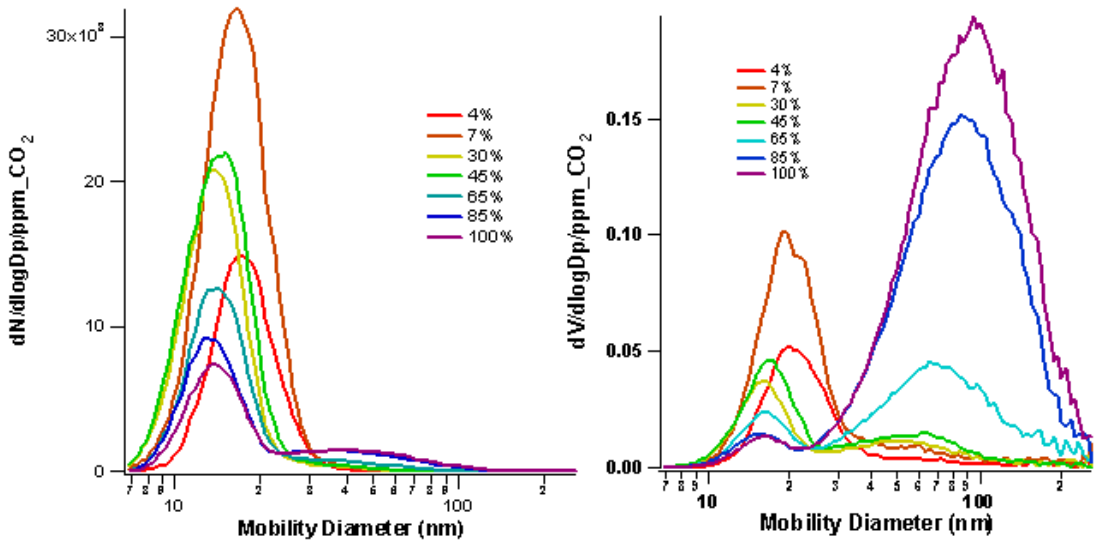

Figure 1. AAFEX SMPS Data**.** SMPS particle size data obtained at 30 m during AAFEX for JP-8 combustion.

Plume Results

Figure 2 plots EI_n-total as a function of engine power at 1 m, 30 m, and >50 m for the AAFEX data set with a JP-8 fuel. EI_n-total increases sharply between 1 m and 30 m, by a factor of 10 or more (the CPC particle counter saturated at 4/7% for the JP-8 tests at 30 m or else the increase between 1 m and 30 m at these conditions would likely be even more significant). Moving to >50m, EI_n-total increases by another factor of 10. This increase is likely due to continuing microphysical evolution of the plume which a) increases the size of nucleation/growth mode particles so that a larger fraction can be detected and b) increases the number density of nucleation/growth mode particles. Reduced line loss of nucleation/growth mode particles (samples extracted >50m required only a short, >5m, sample distribution system) may also play a role in the increase in EI_n-total observed between 30 m and >50m.

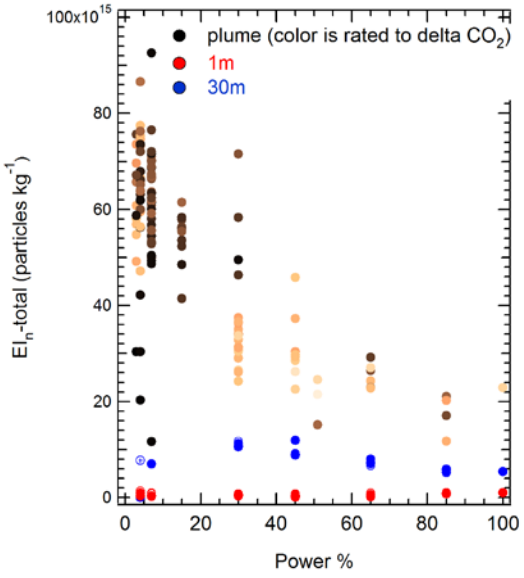

Figure 2. AAFEX Plume Particle Number Density**.** EI_n-total data obtained during AAFEX at 1 m, 30 m, and >50m.

Particle microphysical evolution clearly includes particle growth, as made clear in figures 3, and 4. In figure 3, we compare SMPS size data obtained during AAFEX for a fresh plume (sampled at roughly 60m form the engine) with an aged plume (sampled at roughly 150m from the engine). Ambient conditions and engine operation (4% ground idle) were similar for the two events. Clearly, the peak in the number density particle size distribution has shifted from about 15 nm (fresh plume) to about 25 nm (aged plume). Moreover, the relative ratio between the nucleation mode and the soot mode has changed with an increasing contribution because of nucleation/growth mode observed in the aged plume.

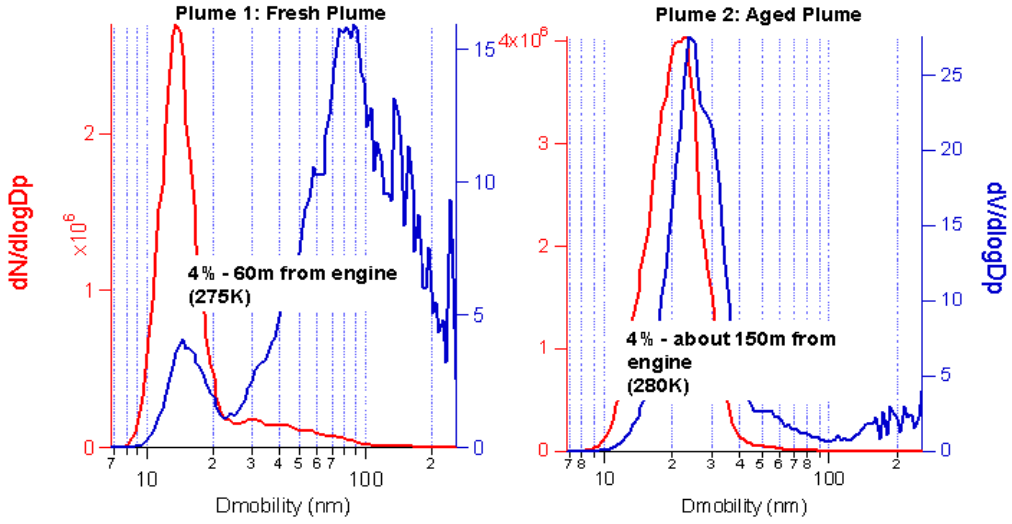

Figure 3. SMPS Plume Data**.** SMPS size data obtained during AAFEX for a fresh plume (left) and an aged plume (right).

Figure 4 shows EEPS particle size data, which support the conclusions drawn from Figure 3. In Figure 4, particle size data for downstream distances ranging from 50-200m is shown. At 50m, the peak in the number weighted particle number density size distribution is slightly greater than 20 nm. Particle size gradually increases with downstream distance, reaching a value of nearly 30 nm for a downstream distance of 160m. Consistent with an analysis of the PW308 data set, we assert that processing time – and not distance *per se* – is the critical variable for microphysical evolution. However, translating downstream distance reliably into process time (which depends on both engine excess momentum and prevailing winds) is not straightforward.

Figure 5 plots the peak diameters shown in Figure 4 as a function of distance traveled. The importance of downstream distance (or, more likely, aging time) is apparent. The data points in Figure 4 are color coded for temperature, revealing a secondary effect of ambient conditions; increasing ambient temperature decreases particle size when all other factors (aging time, engine power, fuel) are held constant. As with our previous observations, we cannot conclude whether this behavior is due to combustor efficiency (decreasing with decreasing ambient temperature) or microphysical differences. However, based on our previous analysis efforts, a combination of the two factors is likely at play.

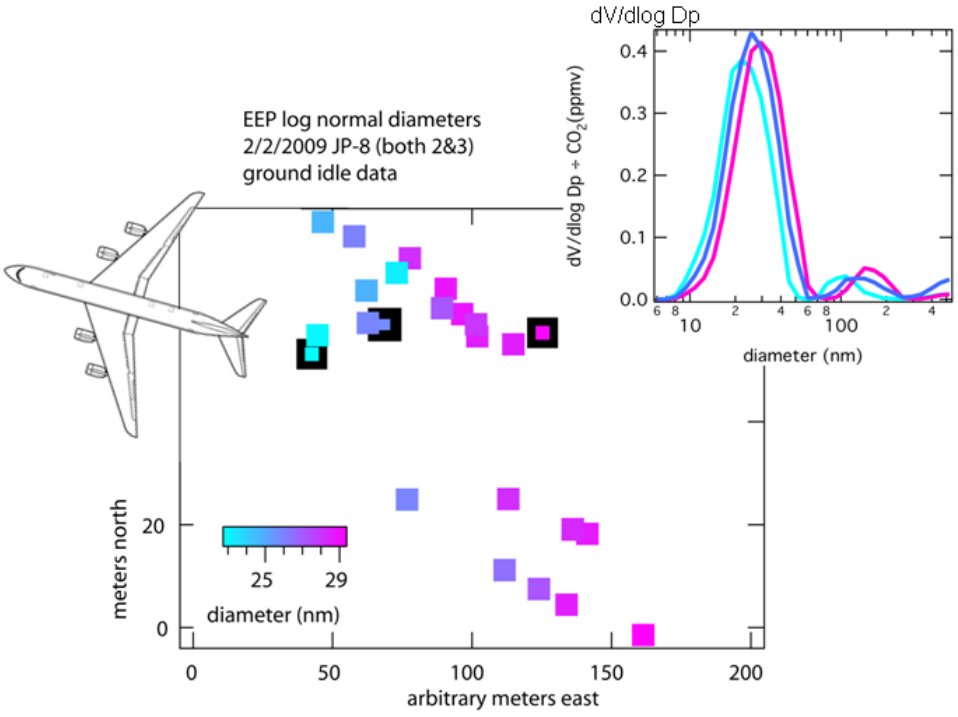

Figure 4. EEPS Plume Data**.** EEPS size data obtained during AAFEX for various sampling (>50m) locations.

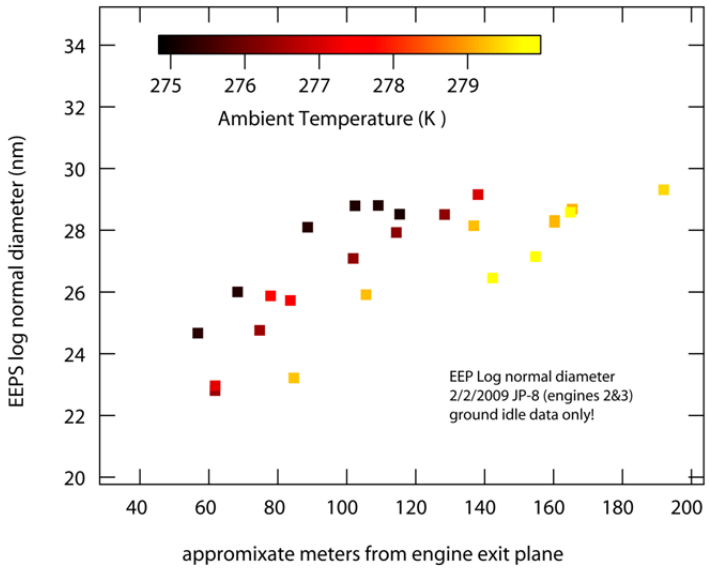

Figure 5. Particle Size in a Plume**.** Number density particle size distribution data obtained at >50m during AAFEX.

We were able to obtain volatile PM composition data for the first time in evolving plumes during AAFEX and later the MDW-09 Airport Study. We credit advances to our measurement capabilities made during Year 1 of this contract for the success we had during Year 2. Figure 6 provides our most convincing measurement of plume organic PM content made during the MDW-09 study. Figure 6 provides time-series plots of organic PM, CO_2, CO, NO_X, and soot. The high degree of correlation between the organic PM and CO_2 signals provides convincing evidence that we have obtained composition data. The low values of soot and NO_X and high value for CO during this time interval indicate an aircraft engine idle exhaust plume. We obtained idle plume data for 9 idle events during the MDW-09 study and several additional idle events during AAFEX. We obtained plume data for 6 events characterized as aircraft takeoff during MDW-09.

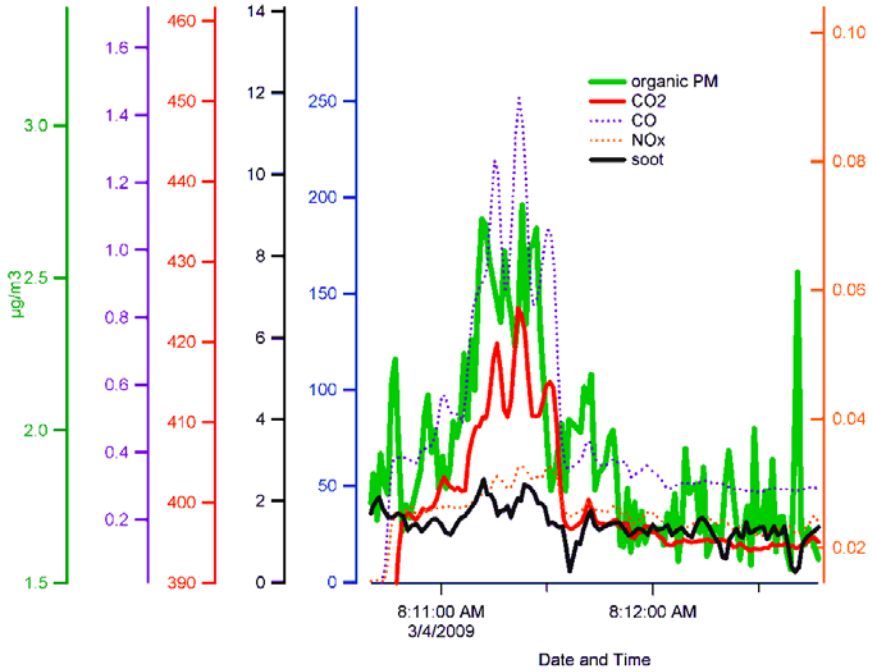

Figure 6. MDW-09 Plume Data**.** Time series data obtained during an idle plume event at Midway Airport.

Analysis of the plume data is on-going, but we have already made three important observations: 1) for aged plumes (>100 sec), EI_m-organic ranges from 50-150 mg kg^{-1} (idle conditions, 275 K), 2) the aromatic signature identified at 30 m perseveres or even grows at >50 m and 3) EI_m-organic scales with EI_m-CO. Measuring EI_m-organic > 50 mg kg^{-1} brings the volatile PM data into better agreement with the total PM data measured at idle during AAFEX and may go a long way in reconciling the data sets. We attributed the larger values of EI_m-organic obtained for the plume to the growth of nucleation mode particles during aging, which in turn leads to increased instrument sensitivity. Figure 7 provides plume mass spectrometer data obtained during an idling event at AAFEX. Not only does the m/z 77, 91, 115 series standout from the background with >10 signal to noise, additional members of the family (chiefly m/z 128, 141, and 165) are also apparent. We need to continue to analyze this data to understand whether aging plumes can become enriched in certain species – presumably those with the lowest vapor pressures and presumably due to preferential vaporization of more volatile species.

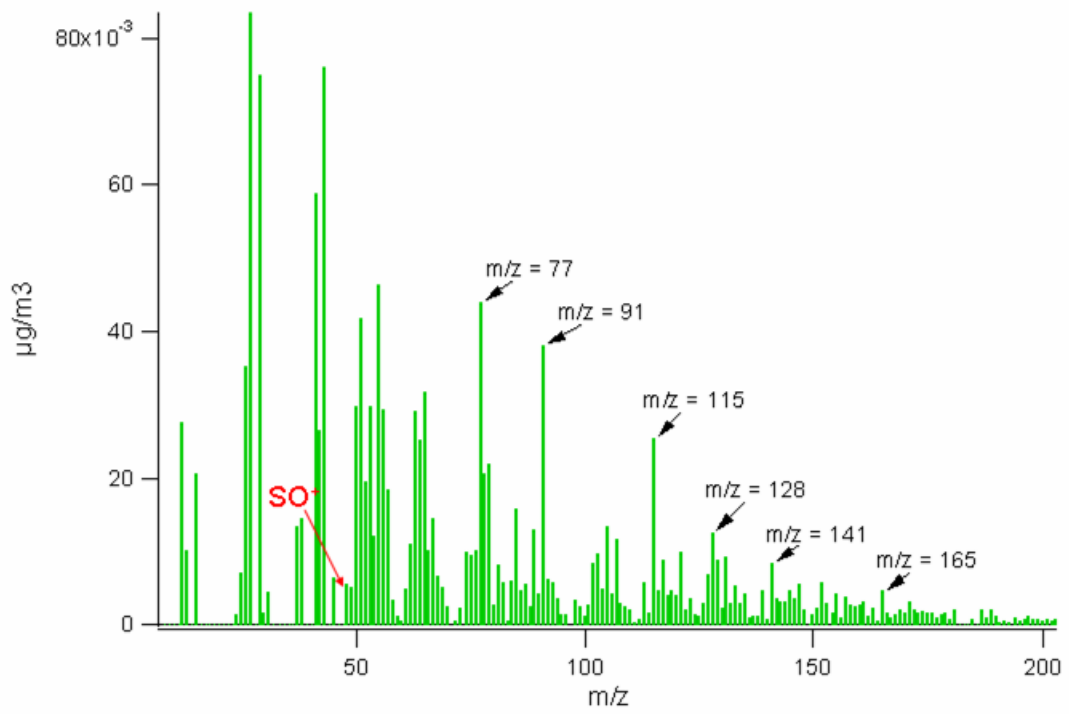

Figure 7. Composition of Plume Particles**.** Mass spectrometer data obtained during an idling plume event at AAFEX.

Based on the representative data shown in Figure 6 and 7, we performed a systematic analysis of the MDW-09 idle plume data. Figure 8 shows MDW-09 data in which EI_m-organic scales with EI_m-CO near idle power. Due to the scaling between EI_m-organic and EI_m-CO, we conclude that combustor (in) efficiency seems to play an important role in EI_m-organic, at least at idle power. We attempted to account for effects of plume mixing on gas-to-particle microphysics by rating the points in Figure 8 by above ambient CO_2 levels (delta CO_2). No trend between EI_m-organic and delta CO_2 is apparent in Figure 8, suggesting that plume dilution plays a secondary role in determining EI_m-organic – at least for the dilution range we have observed (1200-700 fold). Furthermore, two sampling distances were tested at MDW-09 (labeled "1" and "2" in Figure 8) and no sampling location influence is apparent in the EI_m-organic data, suggesting that processing time plays a secondary role in determining EIm-organic – at least for the limited, 2-location data set available from MDW-09. Physically, we expect both dilution level and processing time will influence EI_m-organic and additional studies are merited for evaluating these effects.

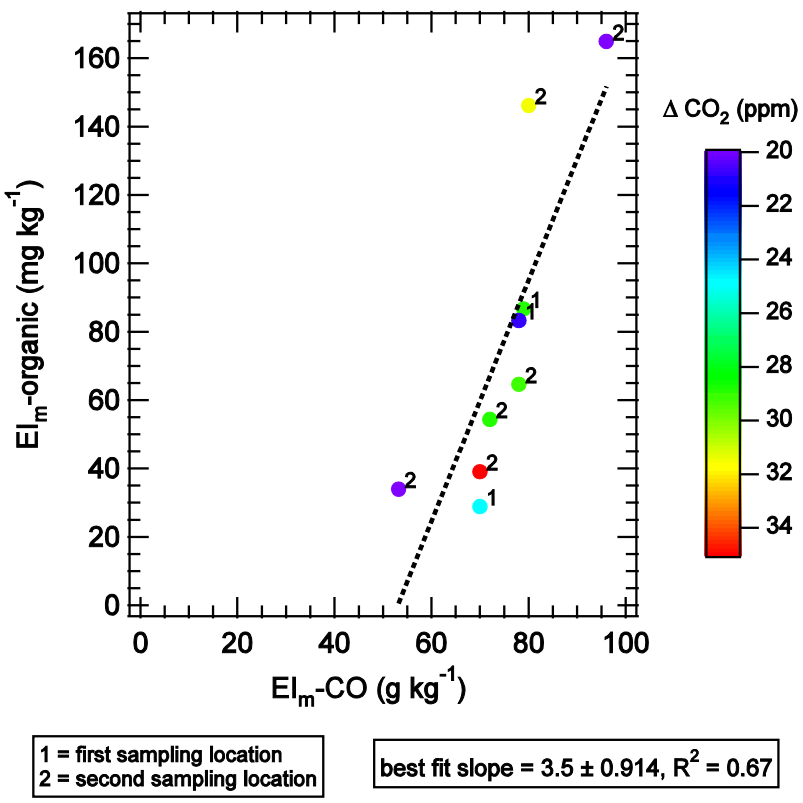

Figure 8. Comparison of Organic PM to CO in Plumes. EI_m-organic as a function of EI_m-CO for idle plume events observed during the MDW-09 Airport Study.

APPENDIX M: Determination of the Emissions from an Aircraft Auxiliary Power Unit (APU) during the Alternative Aviation Fuels EXperiment (AAFEX)

John S. Kinsey, U. S. Environmental Protection Agency, Office of Research and Development, National Risk Management Research Laboratory, Research Triangle Park, NC 27711

Michael T. Timko, Scott C. Herndon, Ezra C. Wood, Zhenhong Yu, Richard C. Miake-Lye, Aerodyne Research, Inc., 45 Manning Road, Billerica, MA 01821

Prem Lobo, Philip Whitefield, Donald Hagen, Center of Excellence for Aerospace Particulate Emissions Reduction Research, Missouri University of Science and Technology, Rolla, MO 65409

Changlie Wey, ASRC Aerospace Corporation, Cleveland, OH

Bruce Anderson, Andreas Beyersdorf, Charles Hudgins, Lee Thornhill, Eddie Winstead National Aeronautics and Space Administration, Langley Research Center, Hampton, VA.

Robert Howard, Aerospace Testing Alliance, U. S. Air Force Arnold Engineering Development Center, TN

Dan Bulzan, Kathleen Tacina, National Aeronautics and Space Administration, John Glenn Research Center, Cleveland, OH

Berk Knighton, Montana State University, Bozeman, MT

APPENDIX M

1. Introduction

The gas- and particle-phase emissions from the auxiliary power unit (APU) were also characterized by the research team as part of the Alternative Aviation Fuels Experiment (AAFEX) conducted in January/February 2009. This portion of the program was conducted on a time available basis and was organized by the U. S. Environmental Protection Agency's National Risk Management Research Laboratory (EPA) in Research Triangle Park, NC. Two tests were performed on the APU. The first test was conducted on January 29 with JP-8 fuel and the second test on February 2 using both JP-8 and Fisher-Tropsch fuel. The specific organizations participating in the APU tests and the lead individual for each organization is shown in Table 1.

Table 1. Participating Organizations

Organization	**Research Lead(s)**
U. S. Environmental Protection Agency-NRMRL, Research Triangle Park, NC (EPA)	John Kinsey
Aerodyne Research, Inc., Billerica, MA (ARI)	Richard Miake-Lye
Missouri University of Science and Technology, Rolla, MO (MST)	Phil Whitefield/Prem Lobo
National Aeronautics and Space Administration-Glenn Research Center, Cleveland, OH (NASA-Glenn)	Changlie Wey
National Aeronautics and Space Administration-Langley Research Center, Hampton, VA (NASA-Langley)	Bruce Anderson
Montana State University, Bozeman, MT (MSU)	Berk Knighton
U. S. Air Force, Arnold Engineering Development Center, TN (AEDC)	Robert Howard

The following sections describe the APU tested, fuel composition, experimental apparatus, test matrix, and the emissions data obtained during AAFEX.

2. Description of APU

The APU tested was a Honeywell (formerly Garrett) Model GTCP85-98CK (Figure 1) mounted cross-wise in a forward baggage compartment of the DC-8 (the DC-8 was not supplied with an APU as original equipment). This particular APU is an integral bleed type where part of the compressor flow is provided to the combustor with the remainder supplied as bleed air to the aircraft for use by the environmental control system (ECS), for engine start, etc. The APU tested was designed mainly for ground operation and is not certified for use at altitude for engine restart. The following are general specifications for the APU:

Two-stage centrifugal compressor

Single-stage radial inflow turbine

Shaft work output priority

Single can combustor

Bleed air flow: 58 kg/min @ 220 °C exhaust gas temperature (EGT) and 0 kW shaft work

Maximum shaft work: 149.2 kW

Maximum EGT: 621 °C

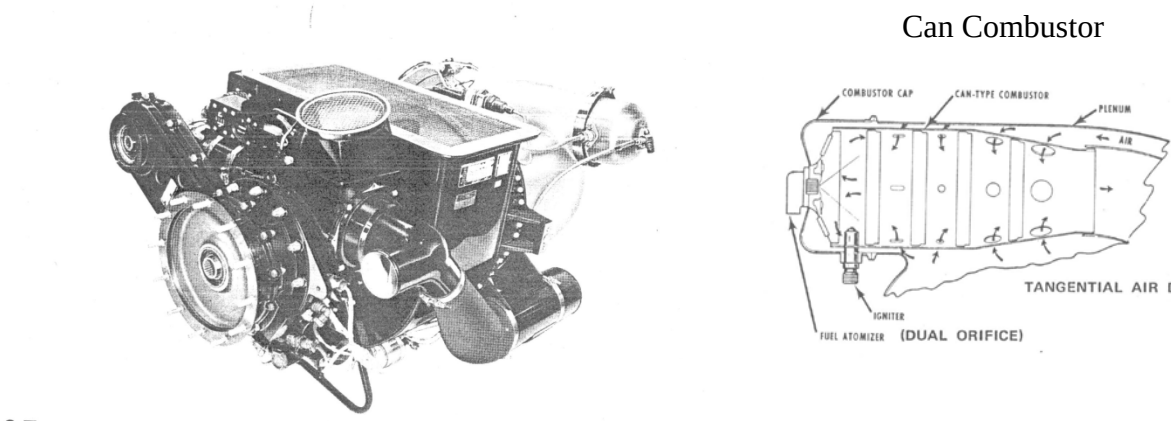

Figure 1. Garrett 85 Series APU and can combustor

In general, APUs are tested in three operating modes each representing a specific load on the turbine: (1) no-load (idle); (2) ECS (all air conditioning [A/C] packs operating); and main engine start (MES). During AAFEX, however, only Condition 3 could be easily identified along with several other lower operating points. Since the lack of engine instrumentation prevented an accurate determination of load on the APU or fuel flow, it was decided to present all of the emissions data in terms of EGT which was used as an indicator of total turbine output. In the future, if more detailed operational data could be made available, some of the scatter in the data might be reduced by using a better indicator of engine power such as fuel flow or equivalence ratio. The latter could not be reliably determined since the undiluted combustion gas concentrations were adversely effected by probe position as discussed in Section 4.1 below.

3. Fuel and Lube Oil Composition

During the APU tests, the emissions from two different fuel types were evaluated. These fuels included the base JP-8 fuel and Fischer-Tropsch fuel No. 2 (FT-2), which was produced from a coal feedstock and purchased from Sasol in South Africa. Nominal specifications of both fuels are shown in Table 2. The lubrication oil used in the APU is Mobile Jet II which is the same as used in the main engines.

Table 2. Nominal Fuel Composition[a]

Fuel	Symbol	C Fraction	H/C Ratio	Sulfur	Aromatics	Naphthalenes	Olefins
		wt/wt	mol/mol	ppm	vol%	vol%	vol%
Base fuel	JP-8	0.8619	1.88	1148	18.55	1.55	1.6
Coal-derived Fischer-Tropsch fuel[b]	FT-2	0.8486	2.12	22	0.6	0	3.8

a. All values are for samples collected earlier in the AAFEX campaign. Fuel samples were not collected during the APU tests. See Section 6.1 below.

4. Experimental Apparatus

4.1 Sampling System

Experiments to characterize the aircraft's APU emissions were performed by each group by drawing samples through a single probe and a 12.7- or 9.5-mm (outside diameter) stainless steel sampling line positioned approximately 0.5 m downstream of the unit's exhaust port (Figure 2). For particle sampling, the sample gas was diluted with dry nitrogen downstream of the probe and therefore should represent only the non-volatile PM emissions (Wey et al., 2007). The sampling lines then ran ~ 23 to 38 m from the probe stand to each trailer where instrumentation was located to make the necessary measurements. All sample lines were unheated except for AEDC/NASA-Glenn which was kept at a nominal temperature of 150 ^{o}C. Due to time and resource constraints, particle losses through the sample lines could not determined and thus all data presented here represent uncorrected results. It would be expected, however, that the particle losses would be similar to those determined in prior testing of this type (Kumar et al., 2008; Liscinsky and Hollick, 2010).

As can be seen in Figure 2, probes used by the various investigators were not exactly co-located. The AEDC probe position, coupled with the high cross winds present during testing, may have adversely affected the smoke number and raw combustion gas measurements as discussed below.

4.2 Instrumentation

A variety of different instrumentation was used by the various research organizations participating in the APU testing during AAFEX. This instrumentation and its operation are described in detail elsewhere in this report and other publications such as Kinsey (2010) and thus will not be repeated here. Table 3 is a summary of the parameters measured and instrumentation used by each group during the two APU tests conducted.

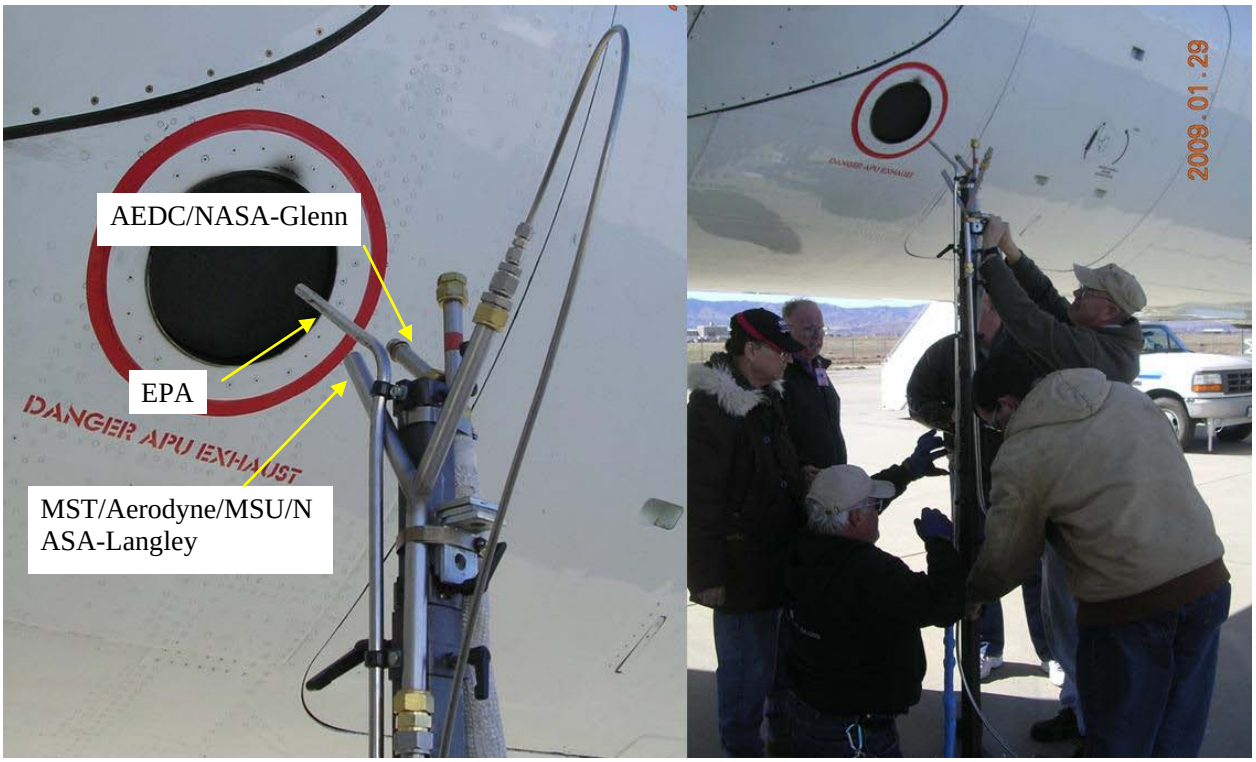

Figure 2. Probe arrangement at the APU exhaust port

Table 3. Experimental Parameters and Instrumentation.

Parameter Measured	Organization	Measurement Technique	Instrument(s)[a]
Sulfur dioxide	NASA-Glenn	UV fluorescence	Monitor Lab - ML9850
	EPA-NRMRL	Pulsed fluorescence analysis (diluted)	Thermo Scientific Model 43a
Total hydrocarbons	NASA-Glenn	Heated FID	Signal - 300HM
Carbon dioxide and carbon monoxide	NASA-Glenn	Non-dispersive infrared spectroscopy	Siemens Ultramat 23 (CO_2/CO/O_2) California Analytical Inc - 602P
Carbon dioxide	EPA-NRMRL	IInfrared absorption	Horiba Model VA-3000
	MST		Sable Systems Model CA-2A
	Aerodyne		LICOR 7000/LICOR 820
	NASA-Langley		LICOR 7000
Oxygen	NASA-Glenn	Para-magnetic analysis	Siemens Ultramat 23 California Analytical Inc - 602P
Nitrogen oxides/nitrogen oxide/nitrogen dioxide	NASA-Glenn	Chemiluminescence	Eco Physics - CLD 844 M hr
HCHO, NO_x, CO, and C_2H_4	Aerodyne	infrared absorption	Tunable Infrared Laser Diode Absorption Spectrometer (TILDAS)

Speciated gas phase organic compounds	MSU	Photon transfer reaction mass spectroscopy (PTR-MS)	Ionicon
PM number concentration	EPA-NRMRL	Differential mobility analyzer/condensation nuclei counter (electrical mobility diameter < 0.5 μm)	TSI Model 3936 SMPS (Model 3080 Classifier + Model 3081 long DMA + Model 3025a CPC)
	MST	Condensation nuclei counter	TSI Model 3025a CPC
	Aerodyne	Condensation nuclei counter	TSI Model 3025a CPC
	NASA-Langley	Condensation nuclei counter	TSI Model 3775 CPC
Particle size distribution	EPA-NRMRL	Differential mobility analyzer/condensation nuclei counter (electrical mobility diameter < 0.5 μm)	TSI Model 3936 SMPS (Model 3080 Classifier + Model 3081 long DMA + Model 3025a CPC)
	MST	Scanning differential mobility analyzer	TSI Model 3071
	NASA-Langley	Differential mobility analyzer/condensation nuclei counter (electrical mobility diameter < 0.5 μm)	TSI Model 3071SMPS (long DMA)
		Electrical mobility analysis	TSI Model 3090 EEPS
Smoke number	AEDC	Optical reflectance	Smoke meter
PM black carbon	EPA-NRMRL[b]	Reflectometer/radiative scattering	Thermo Scientific Model 5012 MAAP
	Aerodyne	Reflectometer/radiative scattering	Thermo Scientific Model 5012 MAAP
	NASA-Langley	Reflectometer/radiative scattering	Thermo Scientific Model 5012 MAAP
PM surface polycyclic aromatic hydrocarbons	EPA-NRMRL	Ultraviolet analysis	EcoChem PAS 2000
Aerosol chemical composition	Aerodyne	Aerodynamic lens, particle time of flight, and time-of-flight mass spectrometer	Aerodyne Aerosol Mass Spectrometer (AMS)

a. SMPS = scanning mobility particle sizer; CPC = condensation particle counter; DMA = differential mobility analyzer; EEPS = Engine Exhaust Particle Sizer; and MAAP = multi-angle absorption photometer.
b. The MAAP data collected by EPA are not reported here since it was found that the instrument substantially under-measured the emissions. This under-measurement was attributed to the fact that the data generated directly off the instrument was used for the calculations as discussed in Kinsey (2010).

5. Test Matrix

As discussed above, two tests were conducted during AAFEX to investigate the APU emissions. The first took place on January 29, 2009 and used the JP-8 base fuel only whereas the second was conducted on February 2, 2009 and was run with both JP-8 and FT-2 fuel. In these tests, the emissions were monitored with varying load conditions based on exhaust gas temperature (EGT). Table 4 presents the recorded EGT and corresponding operating modes for these two tests.

Table 4. Experimental Test Matrix

Test Date	Fuel Type	Engine Load Condition[a]	EGT (°C)
January 29	JP-8	Generator mode	345
		Motor Engine #2	610
		Generator mode	350
		Motor Engine #2	610
		Generator mode	345
February 2	JP-8	Generator mode	345
		Generator mode	365
		Minimum A/C pack	475
		Medium A/C pack	555
		Motor Engine #2	610
		Generator mode	365
		Minimum A/C pack	475
		Medium A/C pack	550
		Motor Engine #2	610
	FT-2	Generator mode	360
		Minimum A/C pack	475
		Medium A/C pack	555
		Motor Engine #2	610
		Generator mode	365
		Minimum A/C pack	475
		Medium A/C pack	550
		Motor Engine #2	620

[a] A/C = air conditioning. "Motor" indicates when APU bleed is used to spin the engine.

6. Experimental Results

The APU emission indices for sulfur dioxide (SO_2), total hydrocarbons (THC), carbon monoxide (CO), nitrogen oxides (NO_x), speciated gas phase emissions, PM mass and number, black carbon, and speciated PM were determined from the measurements. In addition, particle size distribution (PSD), number-based geometric mean particle diameter (GMD), geometric standard deviation (GSD), and smoke number were also determined from the data collected. The following sections provide the experimental results obtained by the research team for these parameters.

For each pollutant, the experimental results for each group are shown on the same graph along with error bars reflecting the standard deviation of the data collected at each power condition during the course of each test. Plotting the uncertainty as the standard deviation provides information on data reproducibility. Plotting results from various research groups side-by-side also provides reliable information on instrument-to-instrument reproducibility. We assert, therefore, that the precision of the data set is well defined. In a field measurement activity, a number of sources of systematic error, including particle line losses and chemical reactions occurring in the long sampling lines, cannot be quantified. Likewise, the various research groups used different instrumentation, probes, and sampling lines and uncertainty introduced by these differences is included in the data set. In the graphs presented below, we make general comparisons of data trends based on our estimated precision and provide additional information on data accuracy where possible.

6.1 SO_2 Emissions

Figure 3 shows the SO_2 EI results for the APU tests as determined by EPA and NASA-Glenn. It is seen that the EIs obtained from both JP-8 and FT-2 fuels remained approximately constant as the EGT increased. Also, the data obtained by the two groups agree very well. The SO_2 EI was about 1.5-1.8 g/kg-fuel for the JP-8 fuel and 0.13-0.15 g/kg-fuel for the FT-2 fuel. If these EIs are compared to a theoretical 100% conversion of sulfur in the fuel to SO_2 (e.g., 2.3 g SO_2/kg for JP-8), the JP-8 values would be lower than expected and the FT values would be higher. Note, however, that fuel samples were not collected during the APU tests and the actual fuel sulfur content is not known. Finally, according to the EPA data collected, the use of the alternative fuel reduced the SO_2 emissions by 92% on average for these tests.

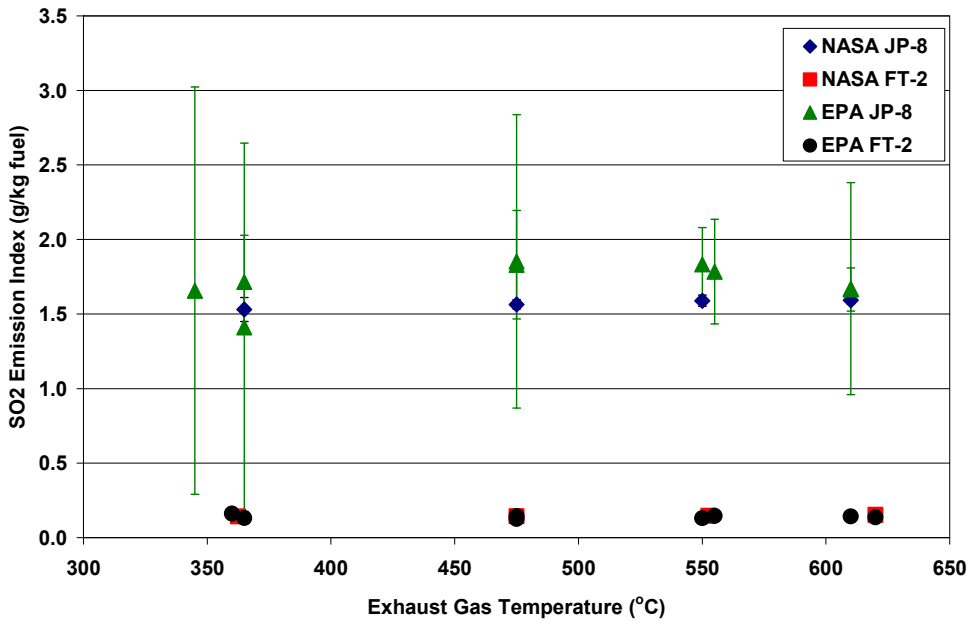

Figure 3. SO_2 emission indices determined by EPA and NASA-Glenn (2/2/09 only).

6.2 Total Hydrocarbon Emissions

Figure 4 provides the THC EIs as calculated from the data collected by NASA-Glenn for the APU tests. As shown, the THC EIs decreased rapidly with increasing EGT for both fuels with the values ranging from 0.27-1.4 g/kg for JP-8 and 0.14-1.3 g/kg for FT-2 fuel. The data also indicate an average reduction of about 37% over all operating conditions for the use of FT-2 fuel in this particular APU. Because THC contains contributions from a range of VOC sources, each with its own response factor, THC data can be prone to systematic error. However, the 37% reduction in THC reported in Figure 4 is a statistically significant difference between the fuels and the trend with respect to EGT is likewise statistically significant.

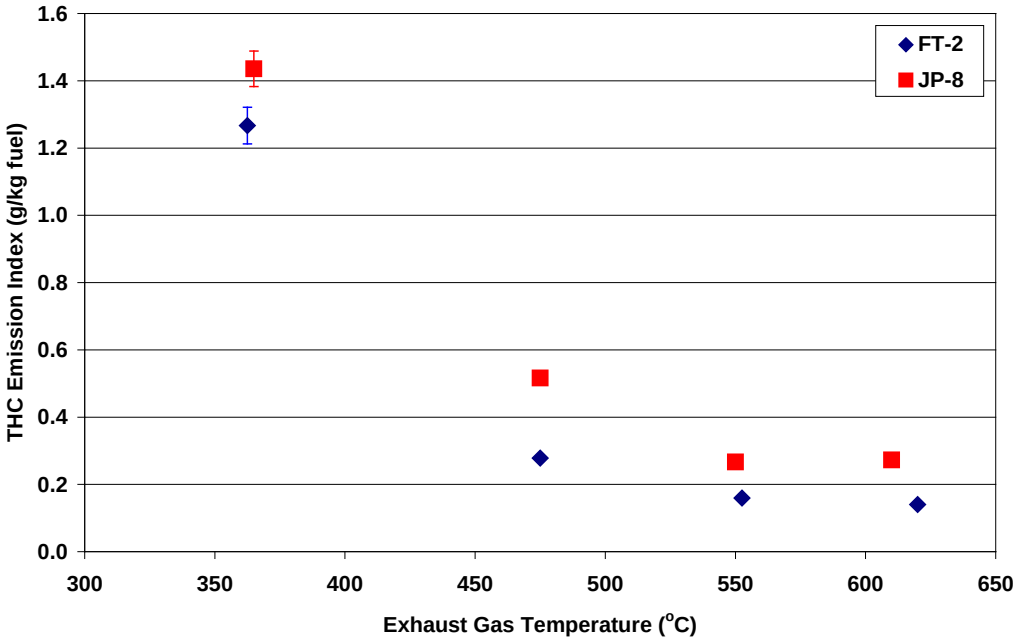

Figure 4. THC emission indices determined by NASA-Glenn (2/2/09 only).

6.3 Carbon Monoxide Emissions

The CO EIs determined by NASA-Glenn for the APU are shown in Figure 5. As indicated, the emissions decrease linearly with increasing EGT for both fuels with the EI ranging from ~12-30 g/kg depending on operating condition and fuel type. In addition, only a small reduction (~ 9%) in CO emissions was observed for the use of FT fuel during these tests. CO is generally considered to be a robust measurement. Therefore, a 10% reduction in CO, although modest, is statistically significant.

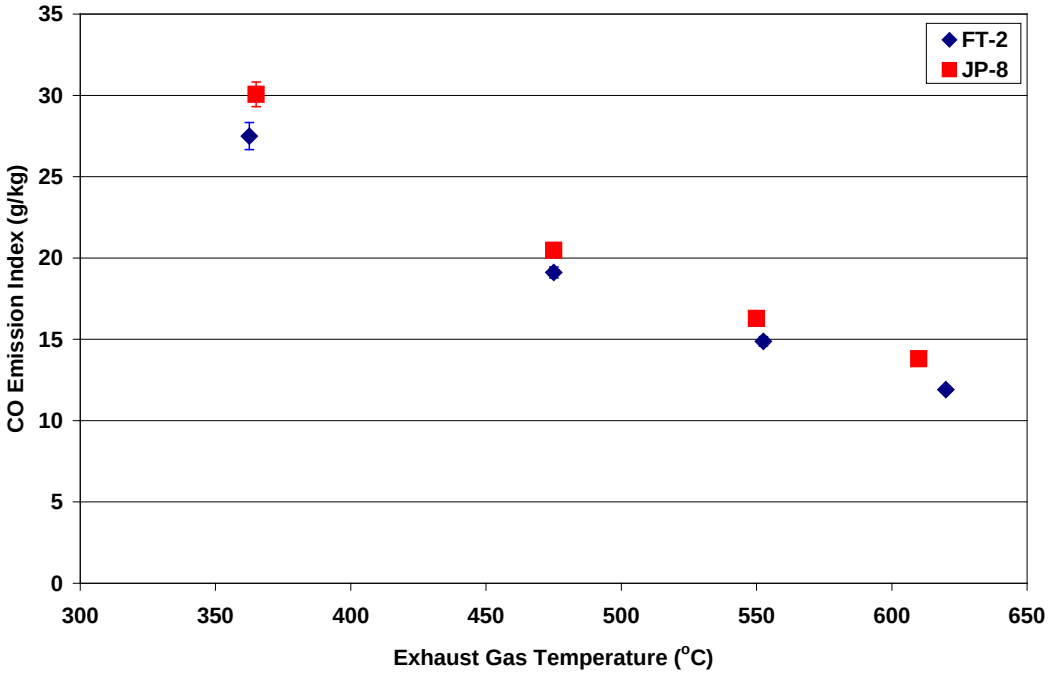

Figure 5. CO emission indices determined by NASA-Glenn (2/2/09 only).

6.4 Nitrogen Oxide Emissions

Figure 6 provides the NOx emission indices as derived from data collected by NASA-Glenn and ARI. Figure 6 shows that the NOx EIs obtained by each group agree well, were fairly consistent across all operating conditions (~ 4.5 g/kg fuel), and varied little by fuel type. An average reduction of only 1.9% for the FT fuel was determined from the NASA data set. While NO_X measurements can be considered robust and reproducible, the 1.9% decrease observed here for FT fuel is within the bounds of experimental uncertainty.

A distinct feature of aircraft exhaust NO_X is the high fraction of NO_2, especially under idle conditions (Wood et al., 2008). We examined the NO_2/NO_X ratio for APU exhaust and plot the data in Figure 7. For the APU, the ratio of NO_2 to NO_X varies from 0.65 at 350 °C to 0.25 at 620 °C. The NO_2/NO_X ratio is, therefore, significantly lower than the 0.9 measured for a CFM56 engine at idle (Wood et al, 2008). As with total NO_X, the NO_2/NO_x ratio data show no statistically significant dependence on fuel composition. The decreasing trend of NO_2/NO_x with respect to EGT is, however, statistically significant.

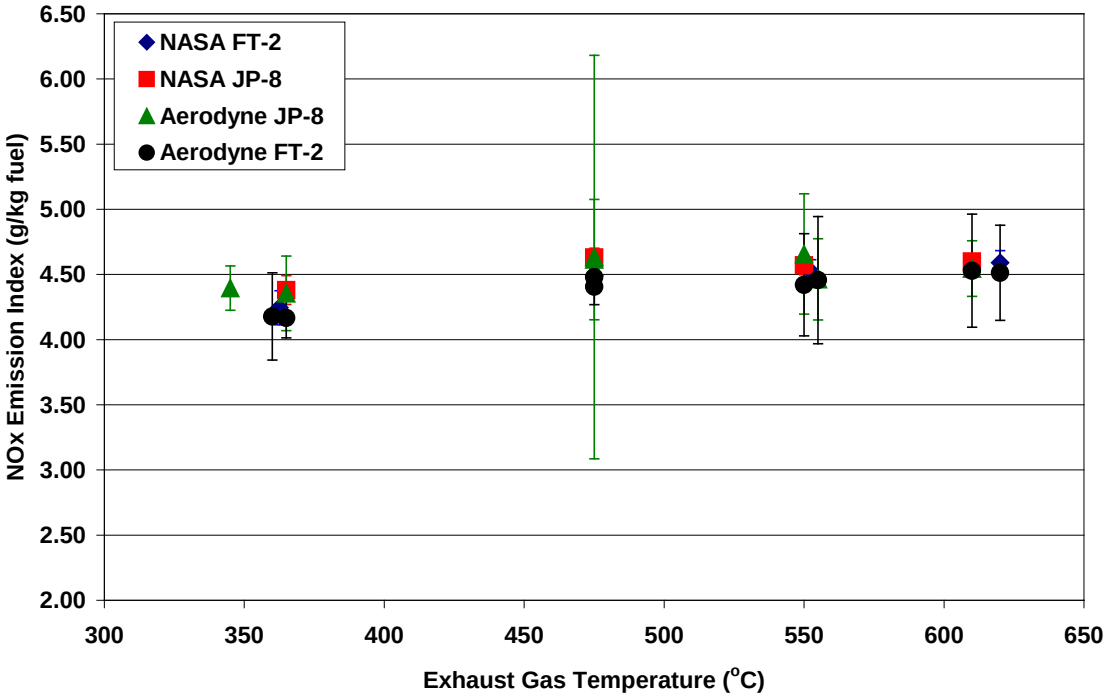

Figure 6. NO_x emission indices determined by NASA-Glenn and ARI (2/2/09 only).

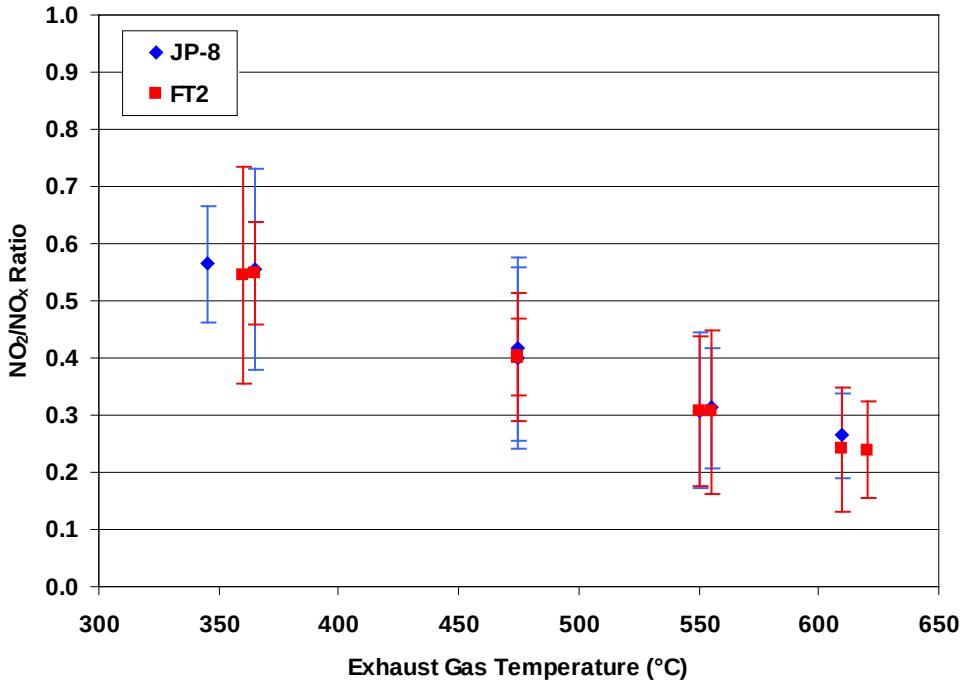

Figure 7. NO_2 to NO_x ratios for both test fuels.

6.5 Speciated Gas Phase Emissions

Speciated hydrocarbon emissions were monitored using the PTR/MS and QCL-TILDAS instruments. A range of oxygenates (formaldehyde, acetaldehyde, etc.), alkenes (ethylene, propene, etc.), and aromatic compounds (benzene, toluene etc.) were measured. Here, we present a subset of the full data set. Figure 8a is a plot of the HCHO EI as a function of exhaust gas temperature for JP-8 and FT-2 fuel combustion. The HCHO EIs for JP-8 are 10-20% higher than for FT-2 combustion. The reduction in the HCHO EI is, therefore, roughly in line with that observed for total hydrocarbons (see Figure 4). This is an interesting observation given that the total hydrocarbon flame ionization method does not detect HCHO emissions (Spicer et al., 1992). The reduction in HCHO emissions associated with FT fuel combustion is therefore consistent with the conclusion that the observed 37% decrease in THC emissions was statistically significant.

Figure 8b plots the benzene EI as a function of exhaust gas temperature. The effect of fuel composition on benzene emissions is much stronger than observed for HCHO as benzene is reduced by a factor of two when FT-2 fuel replaces JP-8. We attribute the large effect of fuel composition on the benzene EI to the fact that JP-8 contains 18.55 vol% aromatics (presumably dominated by single-ring alkyl chain substituted compounds), whereas FT-2 fuel contains 0.6 vol% aromatics. The 2-fold reduction in benzene emissions is consistent with previous measurements of benzene emissions for FT fuel combustion and with the hypothesis that benzene is formed both by decomposition of fuel aromatic compounds ("top down") and recombination of smaller products of incomplete combustion ("bottom up") chemical pathways. (Richter and Howard, 2001; Zhang et al., 2009; Hansen et al., 2009; Marchal et al., 2009; Tosatto et al., 2009).

In practice, we have found that VOC EIs can be very sensitive to modest changes in ambient temperature or aircraft engine fuel flow (Timko et al., 2010a, Yelvington et al., 2007, Knighton et al., 2007, Herndon et al., 2009). Therefore, the impressive decreases in the benzene EI shown in Figure 8b might plausibly be caused by something other than differences in fuel composition. More detailed analysis of the benzene to HCHO ratio confirms that the benzene reduction is almost certainly due to differences in fuel composition and not an experimental artifact. Since, for a given fuel, various hydrocarbon EIs tend to vary in scale with one another (Knighton et al., 2007), the ratio of one hydrocarbon EI to the next is much more reproducible than the absolute hydrocarbon EIs. Plotting individual VOC EIs as functions of HCHO (or C_2H_4) has been a useful tool for characterization of aircraft VOC emissions (Herndon et al., 2009). Figure 9 plots the benzene EI_m as a function of HCHO. As expected from prior aircraft emissions data, the benzene EI varies linearly with the HCHO EI. Interestingly, the slope of the best fit line depends on fuel. Specifically, the FT-2 fuel benzene/HCHO slope is noticeably less than the JP-8 best-fit slope. We take the data in Figure 9 as confirmation that combustion of FT-2 fuel has reduced benzene emissions relative to JP-8 combustion.

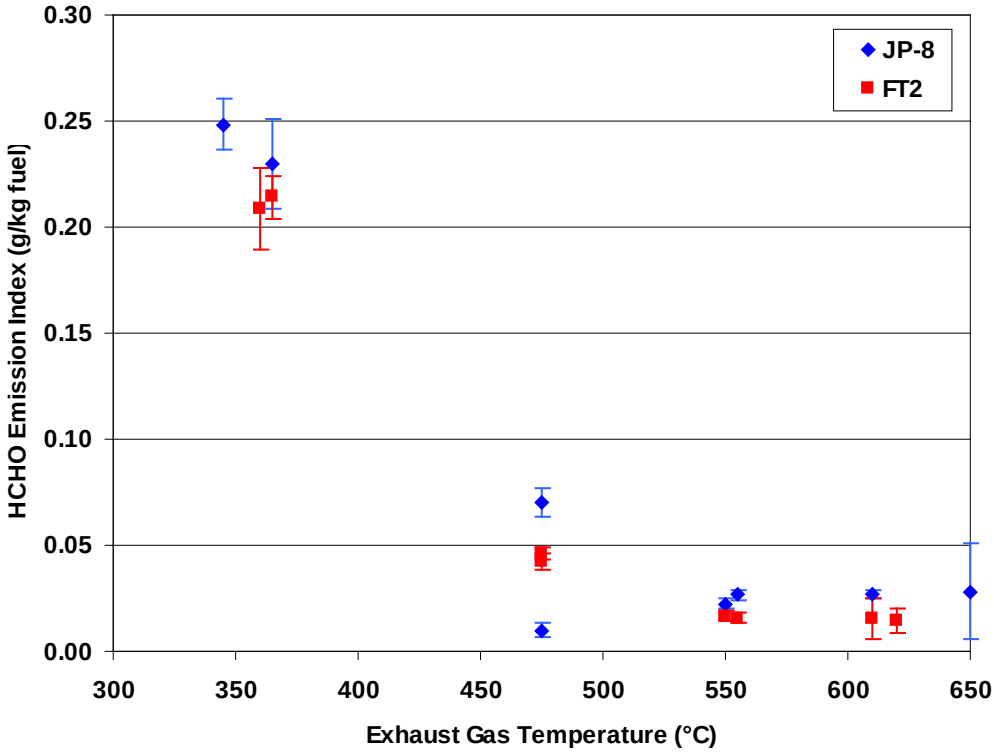

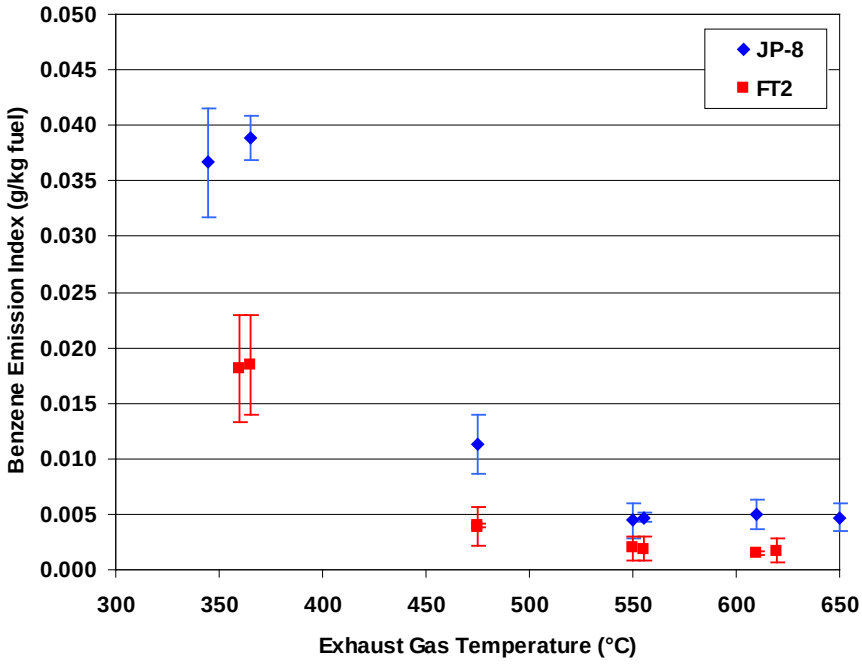

Figure 8. Emission indices for: (a) formaldehyde; and (b) benzene.

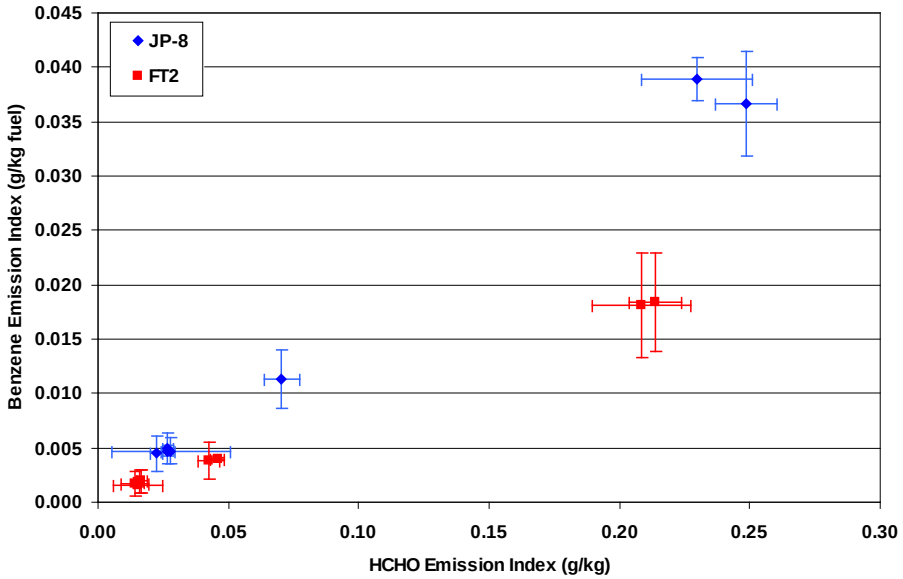

Figure 9. Benzene vs. formaldehyde emission indices.

6.6 PM Mass Emissions

The PM mass emission indices (EI_m) calculated from the experimental data obtained by MST, EPA, and NASA-Langley are shown in Figure 10a for JP-8 fuel and Figure 10b for FT-2. These values were derived from the SMPS PM number concentrations assuming unit particle density.

As shown by Figure 10a, the EIs for JP-8 obtained by the three groups decline linearly from about 700 mg/kg fuel to 200 mg/kg with increasing load on the turbine (EGT). In the case of the FT-2 fuel in Figure 10b, the mass EIs appear to decrease from approximately 80 to 20 mg/kg fuel with rising EGT. For FT-2 fuel combustion, however, the decrease in emissions with increasing EGT is more of an exponential function based on the data shown. Using the EPA data set, an overall average reduction in PM EI_m of 92% was obtained through the use of the FT fuel. Although EI_m measurements showed 50% variability between the various groups, the effect of fuel on EI_m was large enough to be statistically significant. If the analysis is restricted to data measured by the same instrument, which should remove biases introduced by sampling line losses and instrumental differences, the statistical significance of the EI_m reduction becomes even clearer.

The EPA mass EIs determined on February 2 are plotted in Figure 11 against EGT for both fuels along with comparable data collected by the U. S. Air Force for the same model APU as determined by Williams and Lee (1985). As shown in the figure, the Air Force JP-4 EI falls within the same range as the current EI_m values for JP-8 but that for JP-5R is over a factor of 2 higher. The latter results are probably due to variations in fuel composition between JP-8 and JP-5R.

(a)

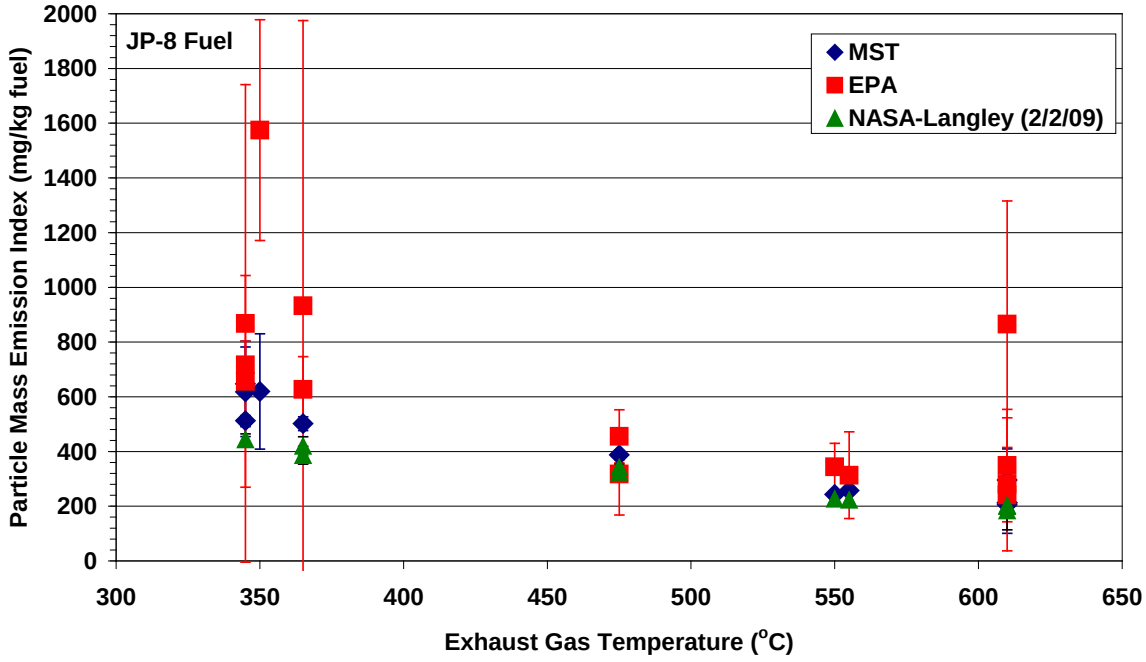

(b)

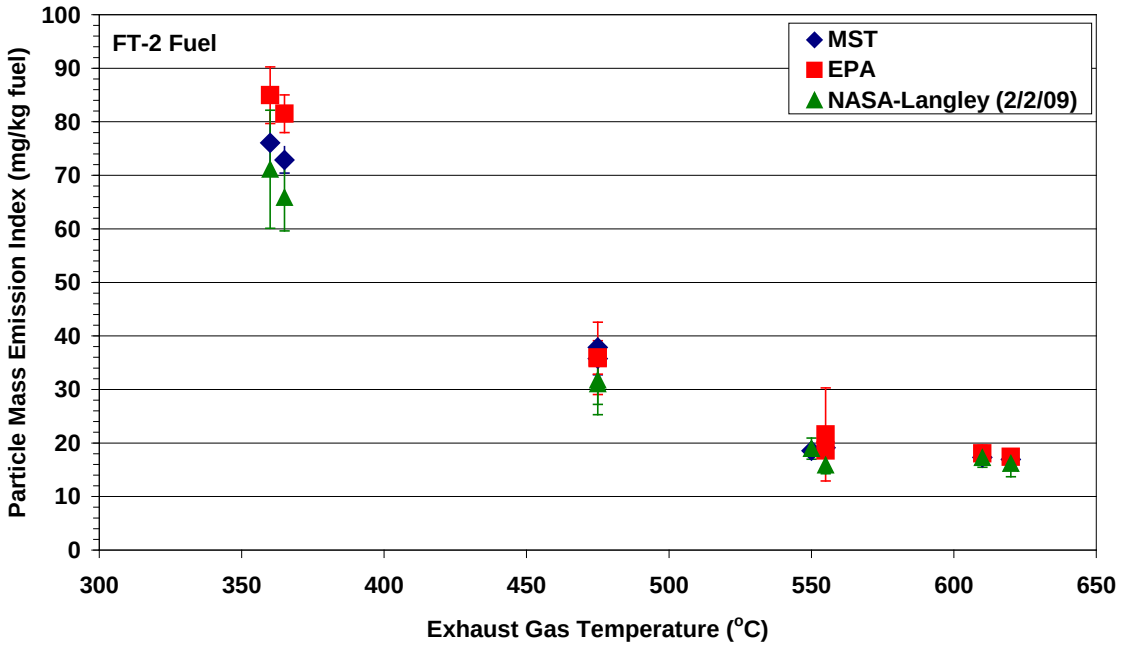

Figure 10. PM mass EIs (EI_m) determined by MST, EPA, and NASA-Langley for: (a) JP-8; and (b) FT-2 fuels.

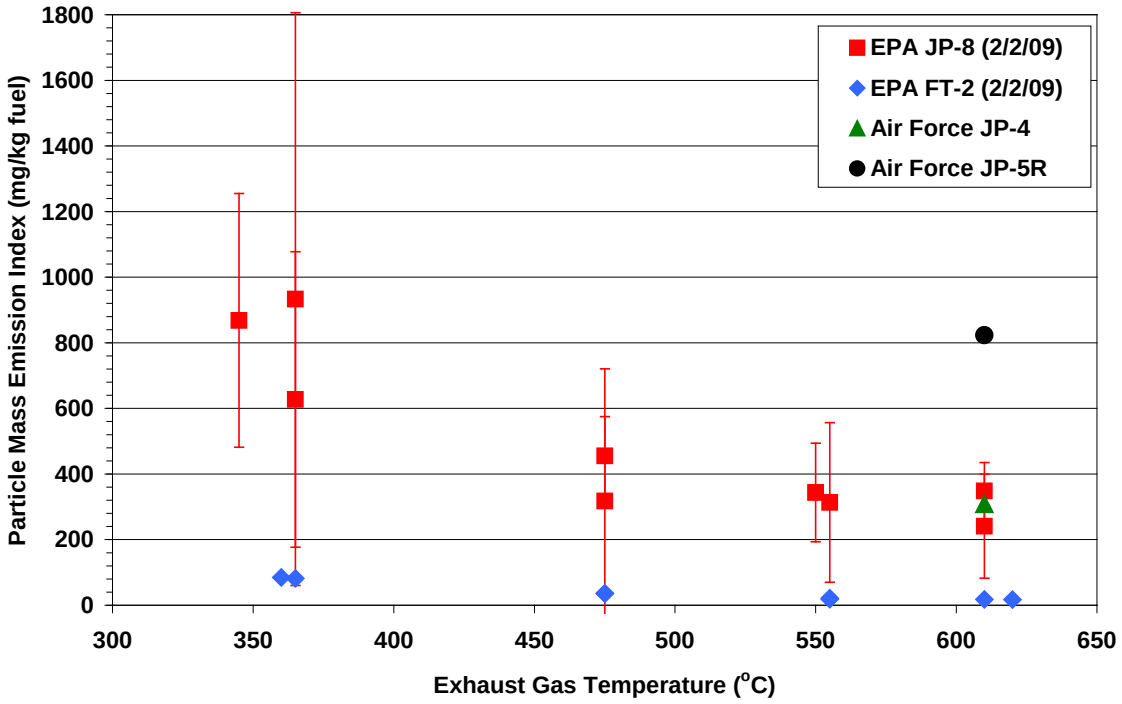

Figure 11. Comparison of mass EIs determined by EPA to other experimental results.

6.7 PM Number Emissions

Figure 12 provides the particle number emission indices (EI_n) collected by Aerodyne, MST, EPA, and NASA-Langley for both JP-8 and FT-2 fuel. For JP-8 in Figure 12a, the Aerodyne, MST, and EPA EIs fall within the same range with the NASA results being slightly higher. In the case of the FT-2 fuel, however, the data appear to be segregated into two groups, with the MST and NASA EIs being generally higher than the EPA and Aerodyne results. This is interesting in the fact that the mass EIs shown previously are very close to each other regardless of which group collected the data. Possible explanations would be different losses of small particles in the sampling system, which would affect the EI_n but not necessarily the EI_m, and differences in the lower size cut of the instruments used by NASA/MST and EPA/Aerodyne. In any event, switching from JP-8 to FT-2 fuel reduces EI_n – a statistically significant result. As with EI_m, if the analysis is restricted to data measured by a single group, the statistical significance of the EI_n reduction becomes even stronger.

Also shown by the data provided in Figure 12, the EI_n for JP-8 decreases linearly from about $5(10)^{15}$ at low EGT to $3(10)^{15}$ particles/kg fuel at high EGT. For FT-2, the EI_n also diminishes linearly with increasing EGT from a high of approximately $1.5 - 3(10)^{15}$ to a low of $0.5 – 1(10)^{15}$ particles/kg depending on which data set is used. Based on EPA data, an average 68% reduction in EI_n was determined by comparing the FT-2 EIs to the results when the JP-8 fuel was used in the same test on February 2.

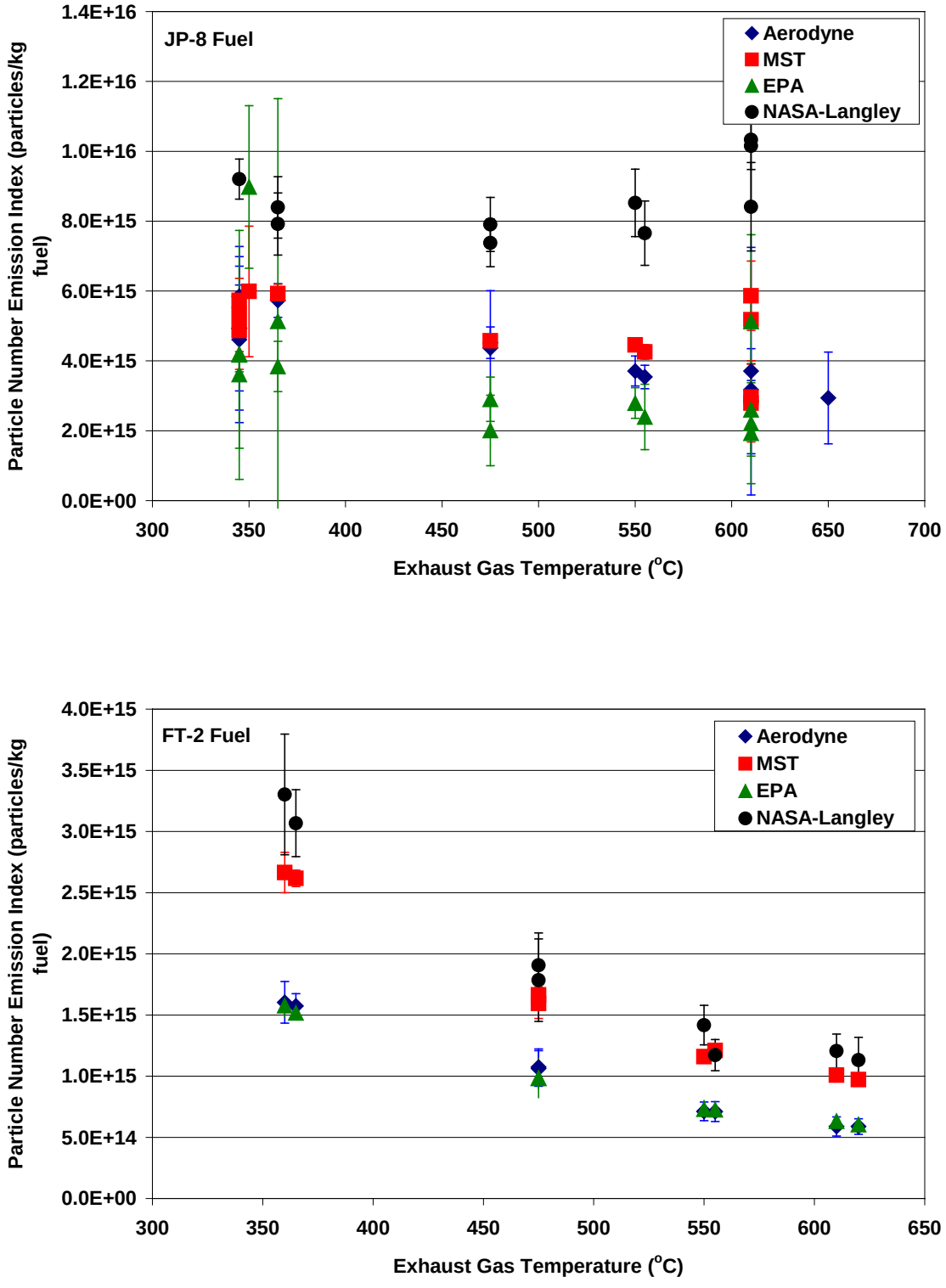

Figure 12. PM number EIs (EI_n) determined by ARI, MST, EPA, and NASA-Langley for: (a) JP-8; and (b) FT-2 fuels.

6.8 Particle Size Distribution (PSD)

The particle size distribution (PSD) of the PM emissions from the APU was determined by EPA, MST, and NASA-Langley using electrical mobility analysis (Yeh, 1993). For example, Figure 13 provides the EPA PSDs for the APU while burning both test fuels for the cold engine condition (increasing power from a cold start). As shown in Figure 13, the particle size is generally larger for JP-8 at the various power conditions as compared with the FT-2 fuel. A similar observation was also made for the main propulsion engine as discussed by Kinsey (2010).

There are also several interesting features of the PSDs shown in Figure 13 which are worthy of note. The distributions tend to broaden or have "shoulders" suggesting the presence of one or more minor modes in the range of 30-60 nm for JP-8 and 20-60 nm for the FT fuel. These features are mainly present at EGTs > 475 ºC for JP-8 and at all power levels for FT-2. Possible explanations for the observed features in the PSDs include particle microphysics in the long sampling line or ingestion of ambient particles, though ingestion of ambient particles seems unlikely given the sampling probe configuration (Figure 2).

Probably the best way to compare the PSDs developed from the data collected by the various research teams is by plotting the geometric number mean particle diameter (GMD) and standard deviation of the PSD against EGT. Figure 14 provides the GMDs developed by the three groups for the two fuels tested in the APU. As can be seen, the GMDs tend to decrease from about 50 to 20 nm with increasing EGT for JP-8 and approximately 30 to 20 nm for FT-2. The EPA values are also generally higher than those determined by MST or NASA for both fuels. The higher EPA GMDs observed could be the result of increased small particle losses in the sampling line which was considerably longer than that used by MST and NASA. When all of the PSD data are considered together, switching from JP-8 to FT-2 fuel has only a small effect on particle size. However consideration of PSD data within the same organization, as is more reliable given group-to-group differences, indicates a statistically significant reduction in particle size associated with FT-2 fuel combustion relative to JP-8.

With regard to the GSDs determined for the APU, the data from the three groups are shown in Figure 15 for both fuel types. As shown in Figure 15a for JP-8 fuel, the GSDs ranged from ~ 1.7 to 2 depending both on EGT and which group collected the data. For FT-2 (Figure 15b), the GSDs were substantially smaller ranging from about 1.6 to 1.8 depending on EGT. In addition, the EPA GSDs shown in Figure 15 are generally smaller than the other data collected for both fuel types which again may be due to differential small particle losses in the longer EPA sampling line.

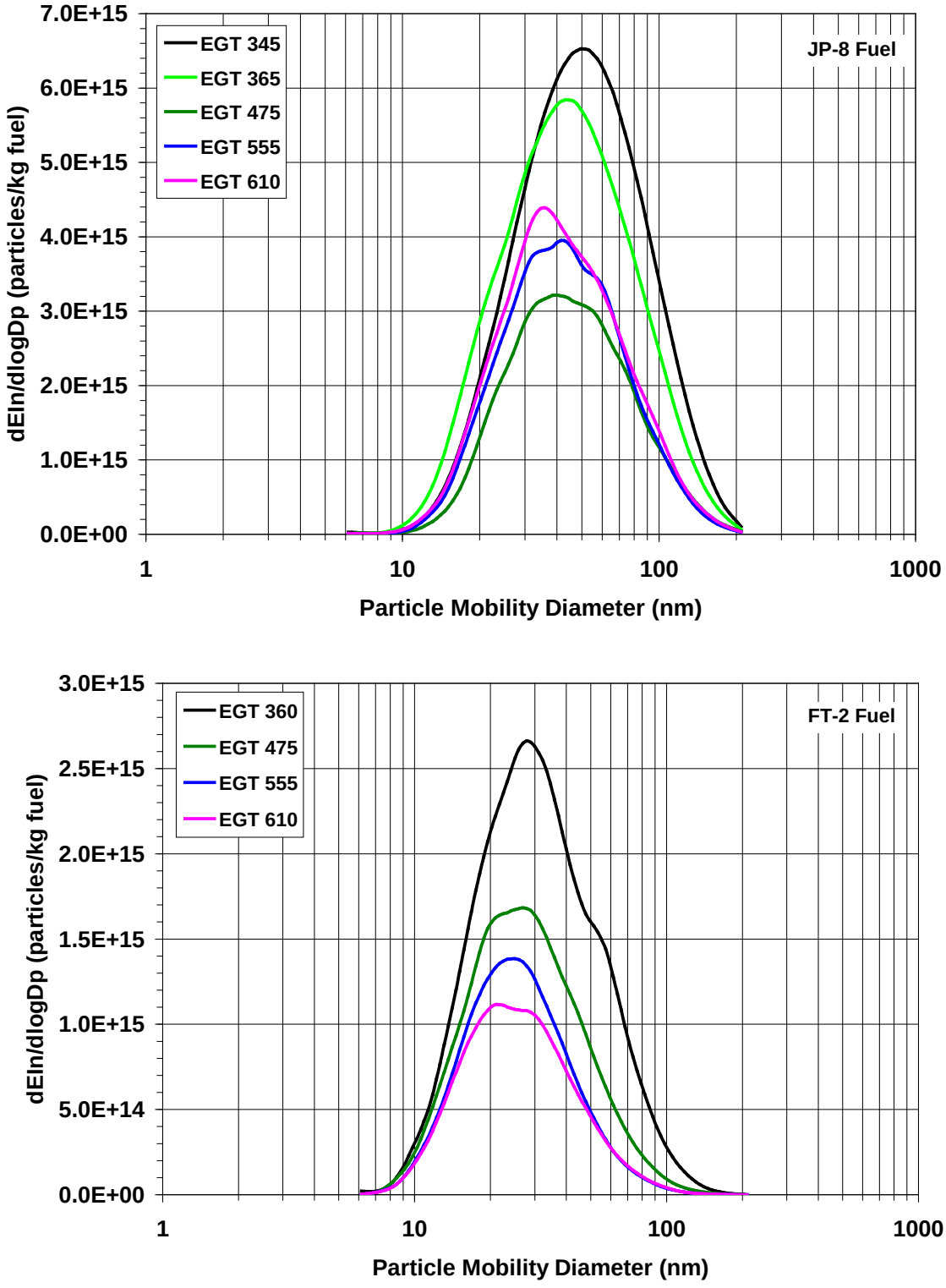

Figure 13. Example differential EI_n particle size distributions for APU burning: JP-8 fuel; and FT-2 fuel.

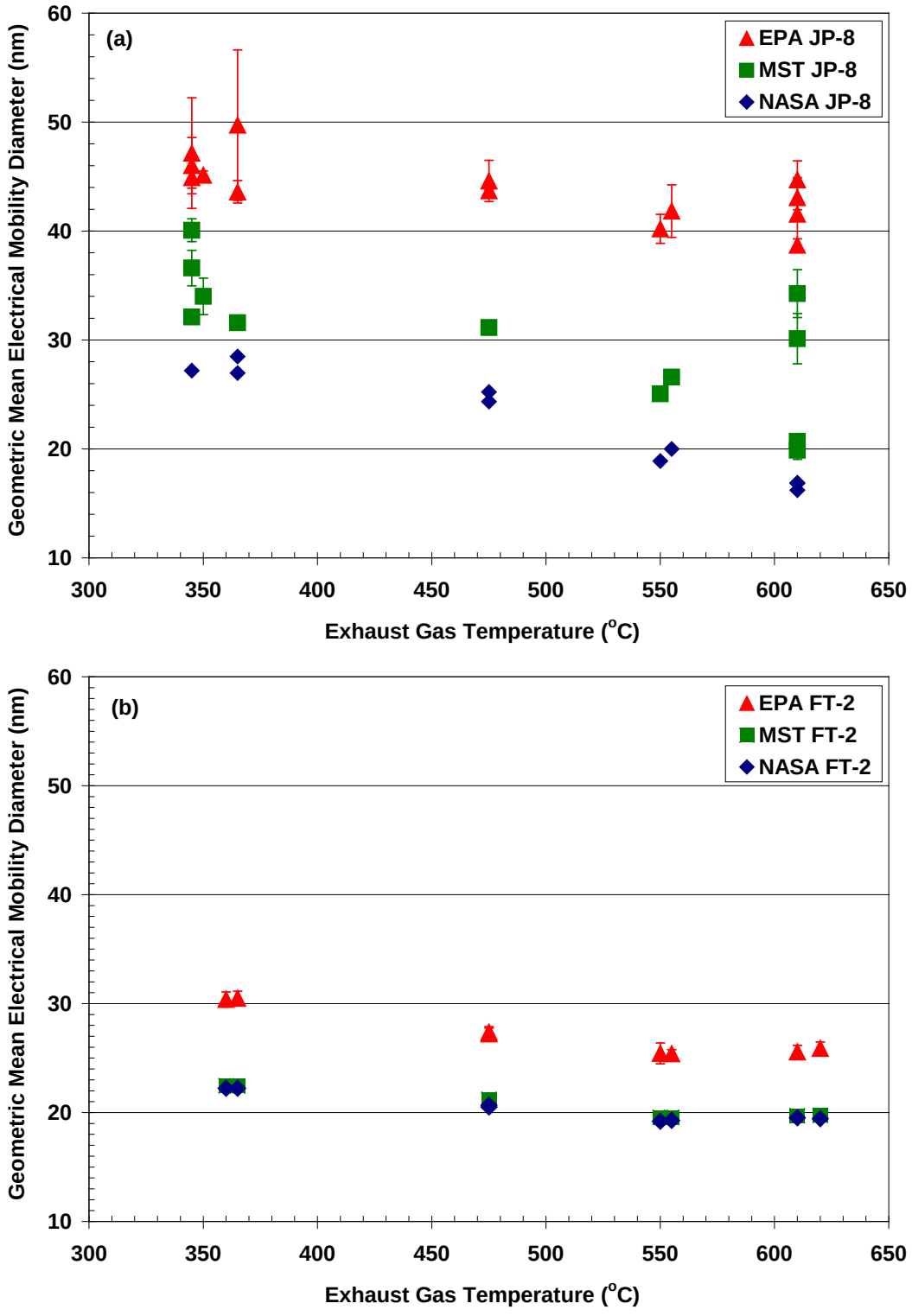

Figure 14. Geometric number mean particle diameter for: (a) JP-8; and (b) FT-2.

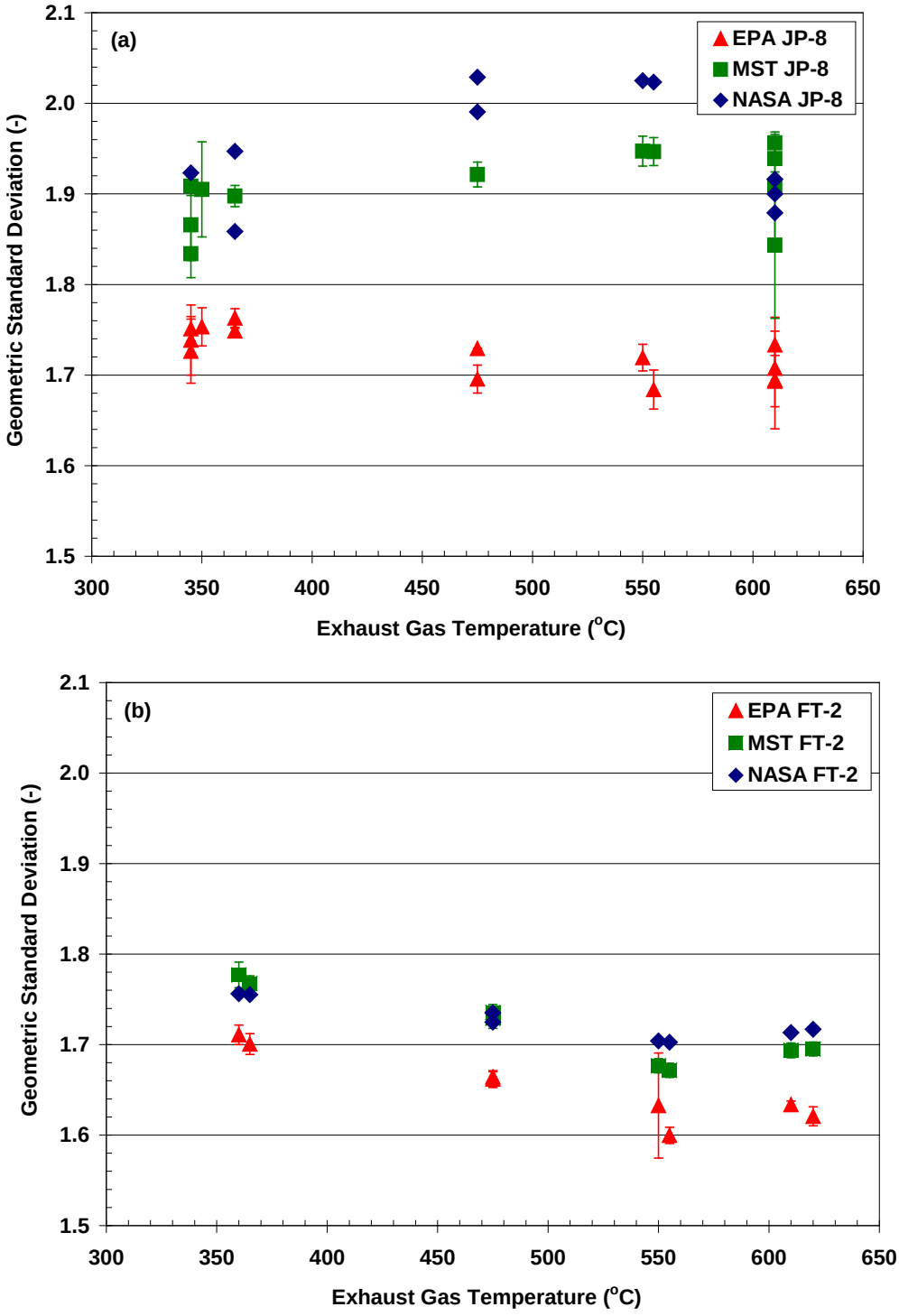

Figure 15. Geometric standard deviation of the PSD for: (a) JP-8; and (b) FT-2.

6.9 Smoke Number

Smoke Number (SN) measurements were acquired using the AEDC probe shown in Figure 2. The instrument was operated according to SAE ARP1179, except that measurements were acquired only at a small spatial region and not spatially integrated/averaged across the exit flow field. The SN data should be used with caution for comparisons or correlations to particle mass since CO_2 measurements were not performed on the SN sample line to verify that the sample consisted primarily of APU core exhaust. The AEDC probe was also not strictly co-located with other probes and there were moderate cross winds during the measurement. Other particle and gas measurements are pseudo corrected for by a conversion to emission index which essentially ratios the measured data to the CO_2 concentration, but not for the smoke number measurements.

Figure 16 shows the SN data versus EGT measured by AEDC. According to SAE ARP1179, the smoke number measurement is accurate to ±3.0, even though measurements for a given smoke meter are usually repeatable to ±1.5 for a constant combustion source. As seen in Figure 16, the APU SN measurements were approximately constant (within ±2.0) over the range of EGT for each fuel, respectively.

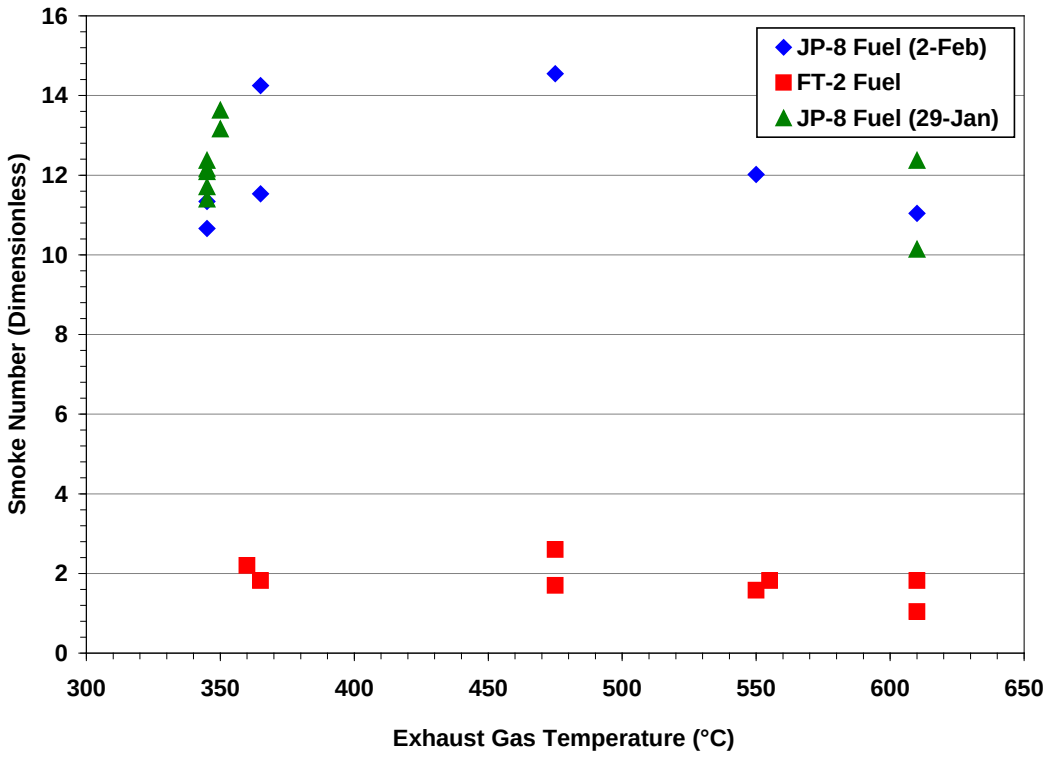

Figure 16. Smoke Number measurements measured for JP-8 and FT-2 fuel.

6.9 PM Chemical Characterization

6.9.1 Black Carbon Emissions

Figure 17 presents the BC mass EIs as determined by Aerodyne and NASA-Langley for both fuels tested as determined using the multi-angle absorption photometer (MAAP) developed by Petzold and Schonlinner (2004). As shown, the BC emissions tend to decrease linearly for both fuels, with the decline most apparent for JP-8. For JP-8, the EIs declined from approximately 450 to 200 mg/kg fuel with increasing EGT with the FT-2 EIs decreasing from a high of 80 mg/kg to a low of 20 mg/kg over the same operating range. Also note that the BC EIs are very similar to those shown previously for the PM EI_m which would be expected since the sample was collected at the engine exit and thus should represent only non-volatile soot. The data shown in Figure 17 indicate a clear and statistically significant reduction in black carbon EI across the entire EGT range studied here.

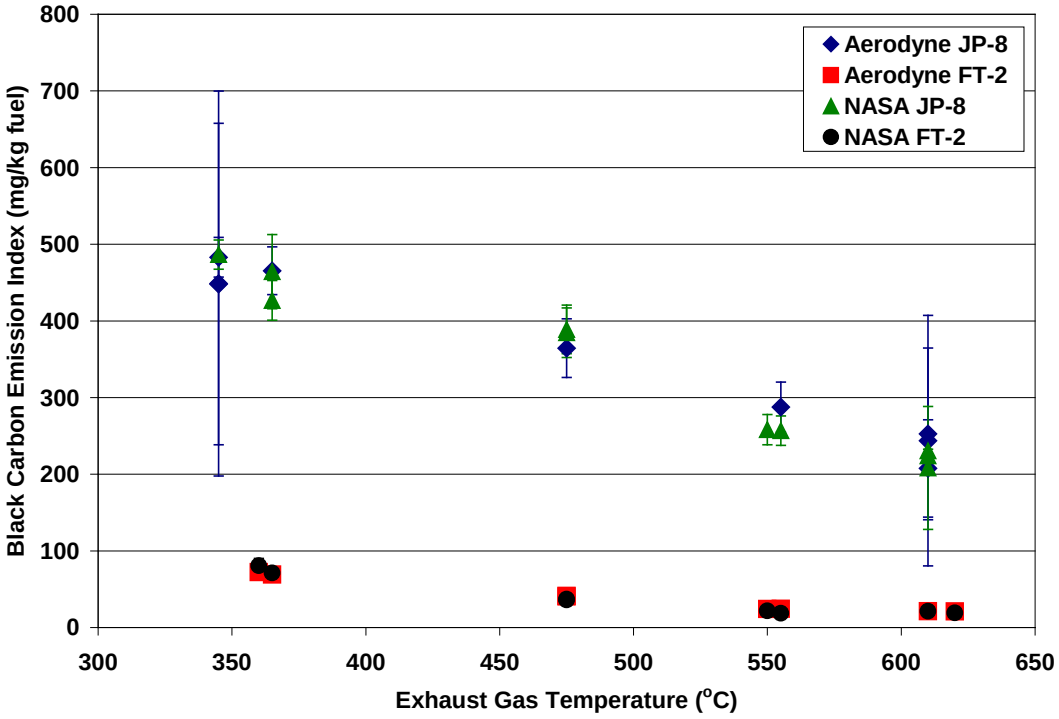

Figure 17. BC emission indices as determined by ARI and NASA-Langley.

The PM BC data reported in Figure 17 are roughly half that reported for the SMPS data in Figure 10. The differences between the BC EIs (Figure 17) and the EI_m (Figure 10) are probably due to a systematic departure from unit density that was assumed to estimate EI_m from the SMPS data. The reductions in BC emissions from the use of the FT fuel were also similar to those determined for the PM EI_m which was in the range of about 90% over all operating conditions.

6.9.2 Surface Polycyclic Aromatic Hydrocarbons

During the APU testing, a number of specialized instruments were employed to determine the chemical composition of the PM emissions and their resulting emission indices. Figure 18 provides EIs for particle surface polycyclic aromatic hydrocarbons (PAHs) as determined by EPA using the PAS 2000 instrument. As can be seen from the figure, the PAH EIs generally decrease with increasing EGT with the EIs for the FT fuel being somewhat lower than those for JP-8 for all engine operating conditions. The PAH EIs range from a low of about 30 to almost 2000 µg/kg fuel depending on EGT and fuel type. A number of reliability problems have been found with the PAS instrument in other studies of this type (Kinsey, 2009) and thus the data shown in Figure 18 should only be used to assess trends and not considered as absolute values.

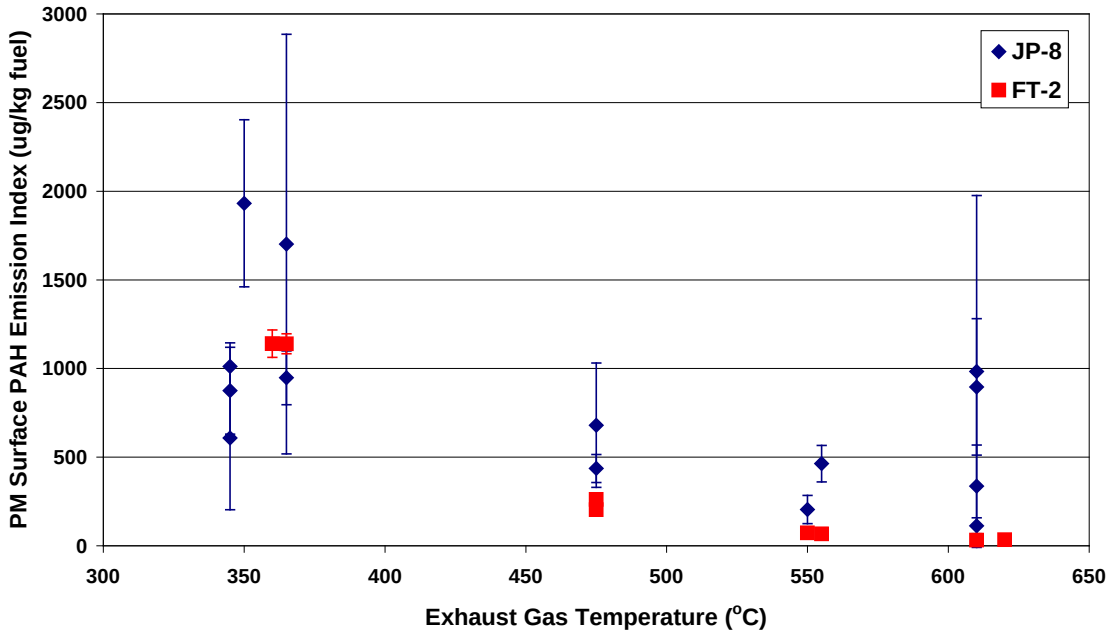

Figure 18. PM surface PAH emission indices as determined by EPA.

6.9.3 Speciated Emissions

The Aerosol Mass Spectrometer (Jayne et al., 2000; Canagaratna et al., 2007; Timko et al., 2010b) was also used to chemically characterize the PM emissions from the APU. Figure 19 presents the organic and sulfate volatile PM mass EIs for the APU. Several features are obvious in Figure 19: (1) the organic EI decreases with increasing EGT; (2) the sulfate EI is reasonably constant with respect to EGT, at a value of approximately of 1.2 mg/kg for JP-8; (3) both the organic and sulfate EI decrease substantially when JP-8 fuel is replaced with FT fuel with the organic EI being reduced by a factor of 5; and (5) the sulfate EI for FT fuel combustion is less than instrument detection limits (here, roughly 0.1 mg/kg). The reductions in organic and sulfate PM mass emissions are statistically significant with the decrease in the sulfate EI directly related to the

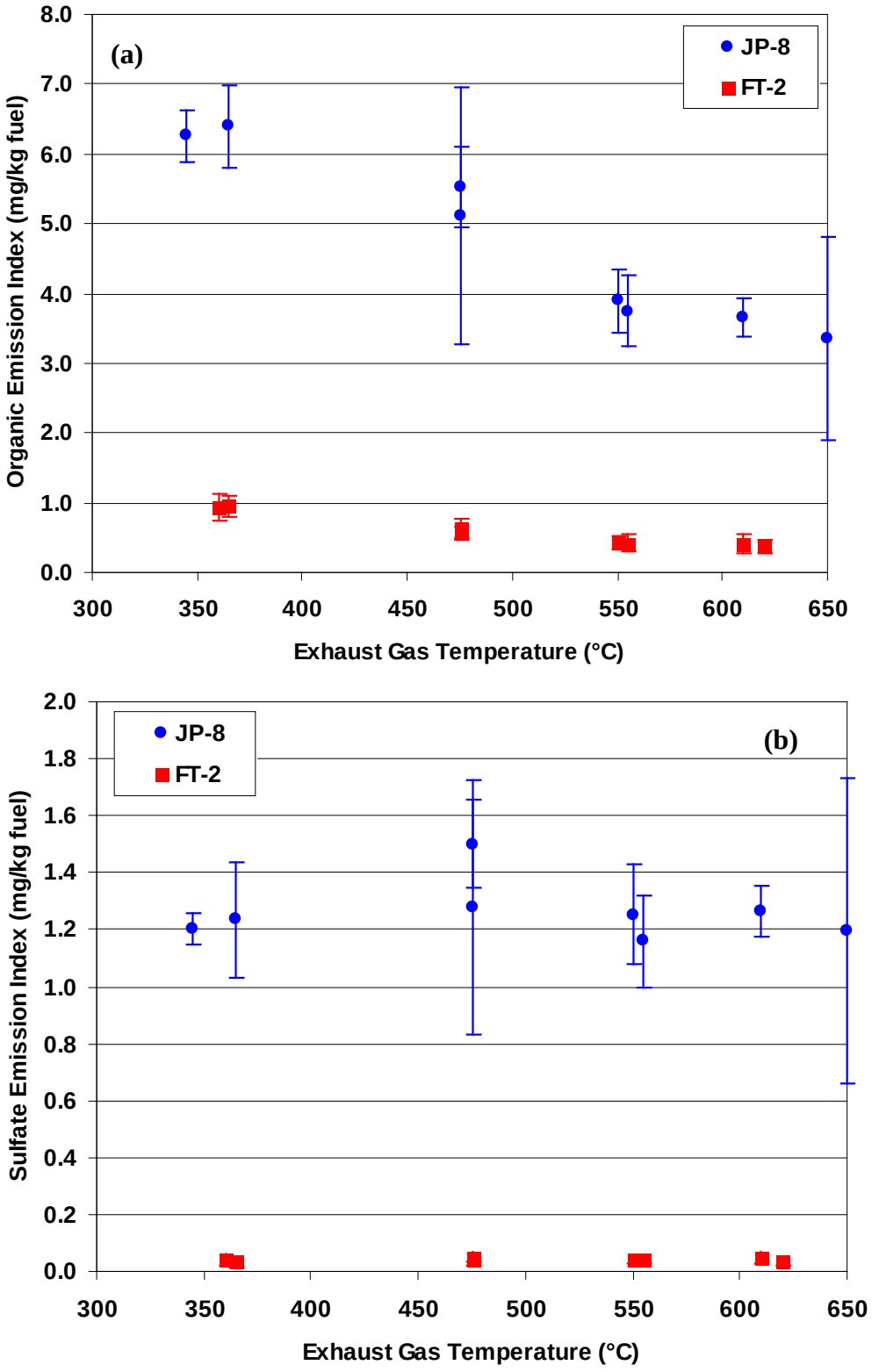

Figure 19. Mass emission indices vs. EGT for: (a) PM organics; and (b) PM sulfate.

negligible fuel sulfur content of the FT fuel. For JP-8, the sulfate EI that we measure corresponds to roughly 0.03% conversion of fuel sulfur to condensable sulfate. We regard this estimate of sulfur conversion to be a lower limit and suspect that sulfur may be lost due to condensation onto the sampling line walls either as particle sulfate or gas phase sulfuric acid. Particle size distributions (see below) indicate that the majority of the PM was likely in a size mode that is well sampled by the AMS; however, PM residing in particles smaller than 50 nm will only be partially sampled, and this may contribute to the low SO_2 to sulfate conversion efficiency that we have measured.

The AMS provides information on the composition of the organic PM emissions. Figure 20 contains mass spectrometer plots of the APU exhaust particles obtained for JP-8 and FT-2 fuel combustion. Focusing first on the comparison of FT-2 fuel and JP-8 (at a consistent exhaust gas temperature of roughly 350 °C), both types of PM emissions contain m/z 41/43, 55/57, 69/71 features that are consistent with aliphatic hydrocarbons. The ratio of the important mass peaks, m/z 55 and 57, is approximately the same for both types of combustion particles, consistent with similar branching and/or bond saturation for JP-8 and FT-2 fuel combustion PM. The primary difference in the JP-8 and FT-2 fuel PM mass spectra is that JP-8 contains the m/z 77, 91, 115 series, whereas FT-2 fuel PM does not. The m/z 77, 91, 115 series is typically attributed to aromatic fragments. Therefore, the contribution of the m/z 77 series to JP-8 PM and its absence from FT-2 fuel PM is consistent with the trace gas benzene data shown previously. Comparing JP-8 PM composition data at the two exhaust gas temperatures (i.e., 345 °C and 650 °C) indicates that the aliphatic signature remains while the aromatic signature decreases. Interestingly, a new mass indicator, m/z 87, appears in the JP-8 APU PM mass spectrum at an exhaust gas temperature of 650 °C. The m/z 87 fragment is not typically attributed to either aliphatic or aromatic compounds (McLafferty and Turacek, 1993) and may instead be an oxidized hydrocarbon, although that assignment is speculative at this time. In previous aircraft measurement campaigns (Timko et al., 2010b), we have frequently found evidence of lubrication oil in aircraft PM exhaust. Lubrication oil is readily identified by its unusual fragmentation pattern, consisting of m/z 85, 113, 127, and sometimes several other masses. Therefore, when an unusual mass spectrum is obtained, lubrication oil should be considered as a potential source. However, the APU engine used the same lubrication oil as the CFM56-2C1 engine (Mobile II) and the m/z 87 fragment is not consistent with the aircraft lubrication oil fragmentation pattern (Timko et al., 2010b). Therefore, we conclude that the m/z 87 mass fragment observed in the APU exhaust is not attributable to lubrication oil – unless the lubrication oil had previously undergone substantial oxidation and/or pyrolysis conversion.

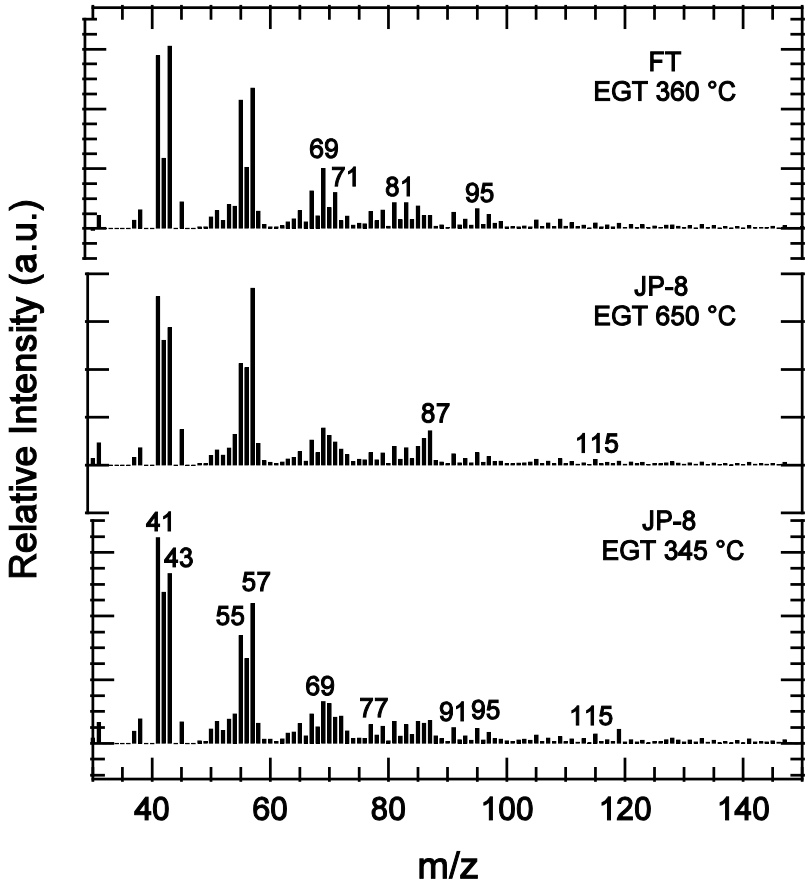

Figure 20. Representative particle mass spectra for APU exhaust PM**.**

6.9.4 Speciated Emissions by Particle Size

The AMS measures vacuum aerodynamic diameter size distributions that complement the electric mobility diameter size distributions discussed above. Figure 21 provides AMS size distribution data collected for JP-8 and FT-2 fuel combustion at an exhaust gas temperature of 345 °C. The AMS size distribution data for JP-8 combustion exhibits clear bimodal behavior. The peak at approximately 60 nm corresponds to soot. The peak at 220 nm may correspond to the shoulder observed in the electrical mobility diameter data. The 220 nm mode may be from an engine source, or it may be ambient aerosol that was ingested into the sample extraction probe. Given the high ratio of organic to sulfate present in the 220 nm mode and the positioning of the sampling inlet relative to the exhaust outlet, the 220 nm mode is unlikely to be ambient particles. The FT-2 fuel combustion data show an apparent peak at approximately 40-50 nm; however, the signal/noise ratio is insufficient to be more quantitative. Interestingly, the 220 nm peak is absent from the FT-2 combustion data, suggesting either that ingestion of ambient air is a random phenomenon or that the 220 nm peak has a combustion origin.

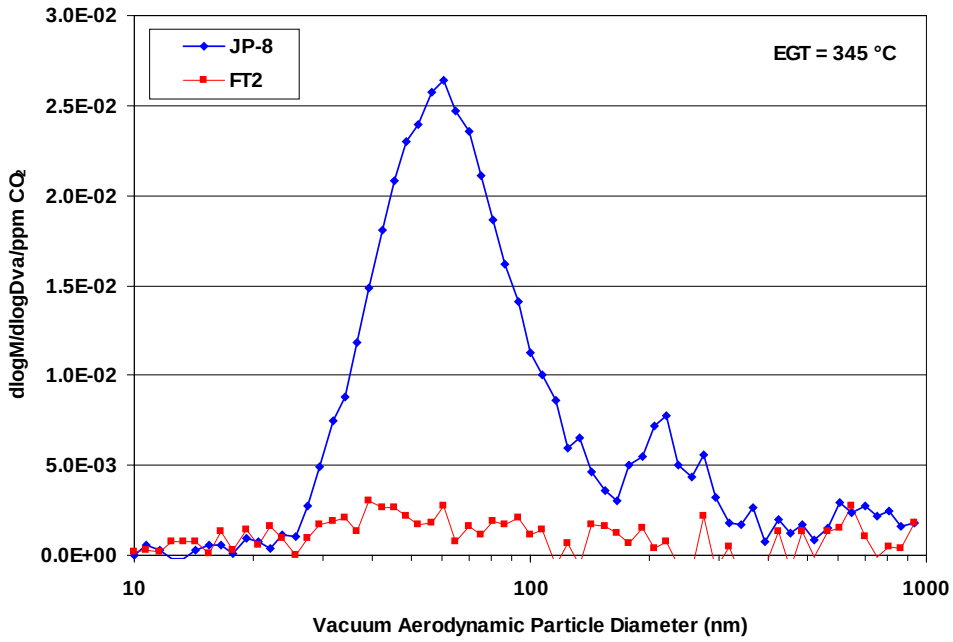

Figure 21. Vacuum aerodynamic diameter size distribution collected by the AMS for JP-8 and FT-2 fuel combustion.

Given the low signal-to-noise of the FT-2 vacuum aerodynamic diameter data, we continued our analysis of the AMS size distributions by focusing strictly on JP-8 combustion data. Figure 22a contains chemically resolved AMS size distribution data collected at 345 °C exhaust gas temperature for JP-8 combustion. Both organic and sulfate data are shown. The distribution that peaks at 60 nm appears to consist of approximately 20% sulfate material and 80% organic material, consistent with the data presented in Figure 13, and to be internally mixed. The portion of the size distribution that peaks at 220 nm also contain well mixed organic and sulfate components and may contain a larger percentage of organic material than the 60 nm peak.

Figure 22b contains vacuum aerodynamic diameter data for JP-8 combustion as a function of exhaust gas temperature. Two modes are apparent in the JP-8 AMS particle size data: a primary mode centered at 60 nm; and, consistent with the electrical mobility diameter data, a secondary distribution centered at 220 nm. The peak in the primary AMS size distribution trends to smaller sizes as exhaust gas temperature increases. The primary peak only shifts approximately 10 nm as exhaust gas temperature increases from 345 °C to 610 °C but the trend is consistent as exhaust gas temperature is incrementally increased. Instead of shifting in response to changes in exhaust gas temperature, the 220 nm secondary peak disappears entirely at an EGT of 610 ºC.

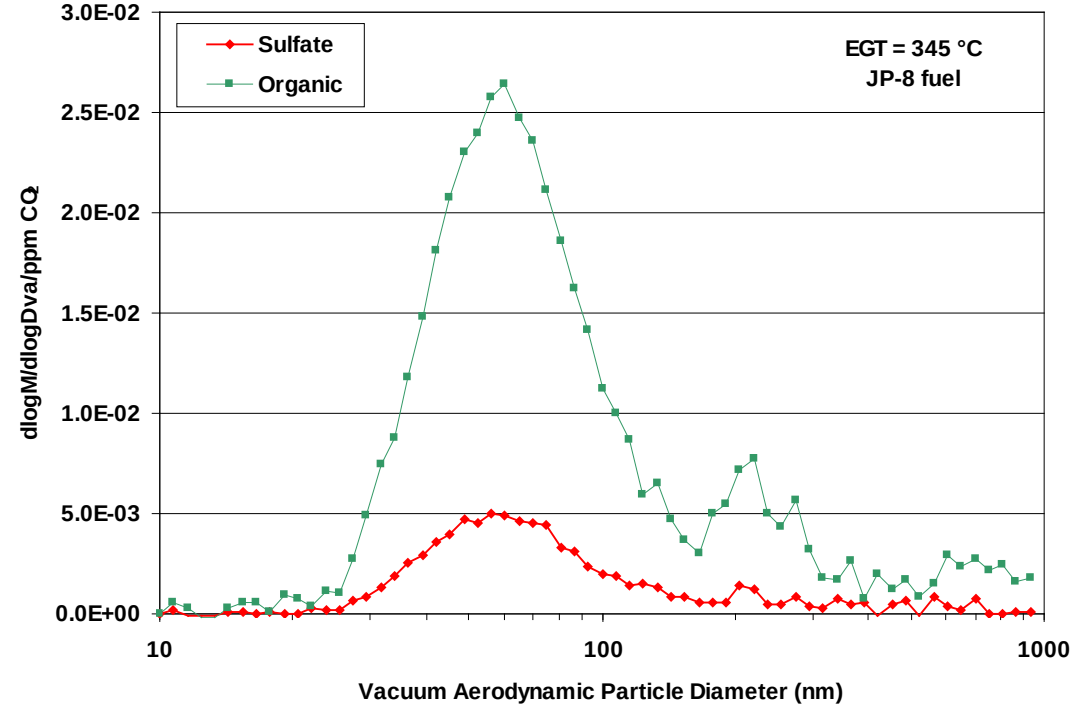

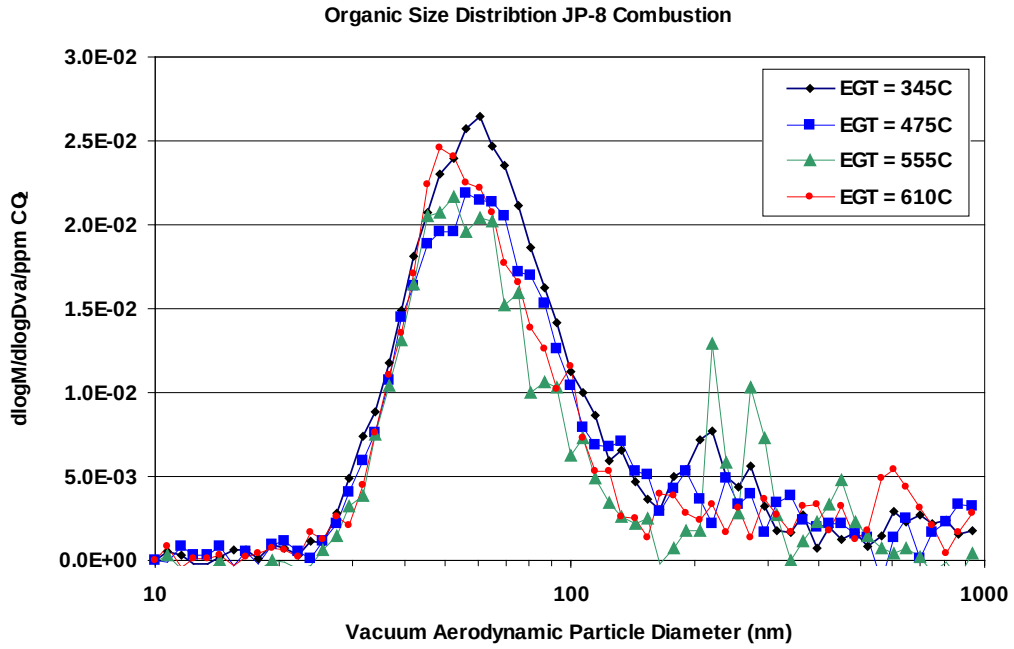

Figure 22. Vacuum aerodynamic diameter size distribution data for JP-8 combustion presented as: (a) chemically resolved organic and sulfate material; and (b) organics as a function of exhaust gas temperature.

7. Conclusions

The following conclusions were reached from the data presented above comparing emissions characteristics of the APU burning JP-8 and FT-2 fuels:

- Major reductions in the SO_2 emissions were determined for the FT-2 fuel due to the lack of sulfur in the fuel. Only small differences were found in the THC, CO and NOx emissions, however, between the two fuels tested.

- Significant reductions in both the EI_m and EI_n were observed for the use of FT-2 fuel in the APU. These reductions were on the order of > 90% for the EI_m and 68% for EI_n, respectively. Differences were found in the EI_n data for the four research teams participating in the study, with the NASA-Langley results being generally higher.

- The sizes of the particles generated by the APU for JP-8 are substantially larger than those emitted by the APU burning FT-2 with the GMDs ranging from 20 to 50 nm depending on EGT and fuel type. Also, the particle size of the APU emissions are considerably larger than that observed for main propulsion Engine 3 burning the same fuel.

- Similar to that found for the EI_m, the BC EIs decrease with increasing EGT indicating that non-volatile particles were being sampled. However, the BC data reported are roughly half of that reported for the SMPS. These differences are probably due to a systematic departure from unit density that was assumed to estimate EI_m from the SMPS data.

- Particle-bound sulfate and organics were both reduced during combustion of the FT-2 fuel. Consistent with the reduction in SO_2 emissions, particle-bound sulfate emissions were reduced by nearly 100%. Particle-bound organics were reduced by a factor of 5 as compared to JP-8.

8. References

Canagaratna, M. R., Jayne, J. T., Jimenez, J. L., Allan, J. D., Alfarra, M. R., Zhang, Q., Onasch, T. B., Drewnick, F., Coe, H., Middlebrook, A., Delia, A., Williams, L. R., Trimborn, A. M., Northway, M. J., DeCarlo, P. F., Kolb, C. E., Davidovits, P., Worsnop, D. R. (2007). Chemical and microphysical characterization of ambient aerosols with the aerodyne aerosol mass spectrometer. Mass Spectrometry Reviews**,** 26, 185-222.

Hansen, N., Miller, J. A., Kasper, T., Kohse-Hoinghaus, K., Westmoreland, P. R., Wang, J., and Cool, T. A. (2009). Benzene formation in premixed fuel-rich 1,3-butadiene flames. Proceedings of the Combustion Institute, 32, 623.

Herndon, S. C., Wood, E. C., Northway, M. J., Miake-Lye, R., Thornhill, L., Beyersdorf, A., Anderson, B. E., Dowlin, R., Dodds, W., Knighton, W. B. (2009). Aircraft hydrocarbon emissions at Oakland International Airport. Environmental Science & Technology, 43, 1730-1736.

Jayne, J. T., Leard, D. C., Zhang, X. F., Davidovits, P., Smith, K. A., Kolb, C. E., Worsnop, D. R. (2000). Development of an aerosol mass spectrometer for size and composition analysis of submicron particles. Aerosol Science and Technology**,** 33, 49-70.

Kinsey, J. S. (2010). Characterization of the fine particle emissions from alternative aviation fuels. Draft Final Report, U. S. Environmental Protection Agency, Research Triangle Park, NC, January.

Kinsey, J. S. (2009). Characterization of emissions from commercial aircraft engines during the aircraft particle emissions experiment (APEX) 1 to 3. EPA Publication EPA/600/R-09/130, U. S. Environmental Protection Agency, Research Triangle Park, NC, October.

Knighton, W. B., Rogers, T. M., Anderson, B. E., Herndon, S. C., Yelvington, P. E., Miake-Lye, R. C. (2007). Quantification of aircraft engine hydrocarbon emissions using proton transfer reaction mass Spectrometry. Journal of Propulsion and Power**,** 23, 949-958.

Kumar, P., Fennell, P., Symonds, J., Britter, R. (2008). Treatment of losses of ultrafine aerosol particles in long sampling tubes during ambient measurements. Atmospheric Environment, 42, 8819-8826.

Liscinsky, D. S., Hollick, H. H. (2010). Effect of particle sampling technique and transport on particle penetration at the high temperature & pressure conditions found in gas turbine combustors and engines. Report No. NASA/CR-2010-NNC07CB03C, National Aeronautics and Space Administration, Glenn Research Center, Cleveland, OH, March.

Marchal, C., Delfau, J. L., Vovelle, C., Moreac, G., Mounaim-Rousselle, C., and Mauss, F. (2009). Modelling of aromatics and soot formation from large fuel molecules. Proceedings of the Combustion Institute, 32, 753.

McLafferty, F. W., Turacek, F. (1993) Interpretation of Mass Spectra. University Science Books, Sausalito, CA.

Petzold, A., Schonlinner, M. (2004). Multi-angle absorption photometry - a new method for the measurement of aerosol light absorption and atmospheric black carbon. Journal of Aerosol Science, 35, 421-441.

Richter, H., and Howard, J. B. (2001). Formation and consumption of single-ring aromatic hydrocarbons and their precursors in premixed acetylene, ethylene and benzene

flames." 77th International Bunsen Discussion Meeting of the Deutsche-Bunsengesellschaft-fur-Physikalische-Chemie, Bad Herrenalb, Germany, 2038.

Schneider, J., Weimer, S., Drewnick, F., Borrmann, S., Helas, G., Gwaze, P., Schmid, O., Andreae, M. O., and Kirchner, U. (2006). Mass spectrometric analysis and aerodynamic properties of various types of combustion-related aerosol particles. International Journal of Mass Spectrometry, 258, 37.

Slowik, J. G., Stainken, K., Davidovits, P., Williams, L. R., Jayne, J. T., Kolb, C. E., Worsnop, D. R., Rudich, Y., DeCarlo, P. F., and Jimenez, J. L. (2004). Particle morphology and density characterization by combined mobility and aerodynamic diameter measurements. Part 2: Application to combustion-generated soot aerosols as a function of fuel equivalence ratio. Aerosol Science and Technology, 38, 1206.

Spicer, C. W., Holdren, M. W., Smith, D. L., Hughes, D. P., Smith, M. D. (1992). Chemical composition of exhaust from aircraft turbine engines. Journal of Engineering for Gas Turbines and Power-Transactions of the ASME, 114, 111-117.

Timko, M. T., Herndon, S. C., Wood, E. C., Onasch, T. B., Northway, M. J., Jayne, J. T., Canagaratna, M. R., Miake-Lye, R. C., Knighton, W. B. (2010a). Gas turbine engine emissions - Part I: volatile organic compounds and nitrogen oxides. Journal of Engineering for Gas Turbines and Power-Transactions of the ASME, 132, 061504-1 to 061504-14.

Timko, M. T., Onasch, T. B., Northway M. J., Jayne, J. T., Canagaratna, M. R., Herndon, S. C., Wood, E. C., Miake-Lye, R. C., Knighton, W. B. (2010b). Gas turbine engine emissions - Part II: chemical properties of particulate matter. Journal of Engineering for Gas Turbines and Power-Transactions of the ASME, 132, 061505-1 to 061505-15.

Tosatto, L., La Mantia, B., Bufferand, H., Duchaine, P., and Gomez, A. (2009). Chemical structure of a methane counterflow diffusion flame perturbed with the addition of either JP-8 or a jet fuel surrogate. Proceedings of the Combustion Institute, 32, 1319.

Wey, C. C., Anderson, B. E., Wey, C., Miake-Lye, R. C., Whitefield, P., Howard, R. (2007). Overview on the aircraft particle emissions experiment. Journal of Propulsion and Power, 23, 898-905.

Williams, R. C. and J. B. Lee (1985). Effects of alternate fuels on APUs. Report No. AFWAL-TR-85-2083, U. S. Air Force Wright Aeronautical Laboratories, Air Force Systems Command, Wright-Patterson AFB, OH.

Wood, E. C., Herndon, S. C., Timko, M. T., Yelvington, P. E., Miake-Lye, R. C. (2008). Speciation and chemical evolution of nitrogen oxides in aircraft exhaust near airports. Environmental Science & Technology**,** 42, 1884-1891.

Yeh, H-C (1993). Electrical Techniques. Chapter 18 in *Aerosol Measurement: Principles, Techniques, and Applications*, K. Willeke and P. A. Baron eds., Van Nostrand Reinhold, New York.

Yelvington, P. E., Herndon, S. C., Wormhoudt, J. C., Jayne, J. T., Miake-Lye, R. C., Knighton, W. B., Wey, C. (2007). Chemical speciation of hydrocarbon emissions from a commercial aircraft engine. Journal of Propulsion and Power, 23, 912-918.

Zhang, H. R., Eddings, E. G., Sarofim, A. F., and Westbrook, C. K. (2009). Fuel dependence of benzene pathways. Proceedings of the Combustion Institute, 32, 377.

9. Acknowledgements

Missouri S&T and ARI were funded by the Federal Aviation Administration (FAA) through the Partnership for AiR Transportation for Noise and Emissions Reduction (PARTNER) – an FAA/NASA/Transport Canada-sponsored Center of Excellence under Grant No. 07-C-NE-UMR Amendments 006 and 007 (Carl Ma, Project Manager). Any opinions, findings, and conclusions or recommendations expressed in this paper are those of the authors and do not necessarily reflect the views of the FAA.

APPENDIX N: Insights Into The Combustion Chemistry Within a Gas-Turbine Driven Auxiliary Power Unit as a Function of Fuel Type and Power Level Using Soot Nanostructure as a Tracer

R. L. Vander Wal
Pennsylvania State University

Abstract

Particulate emissions were collected from an Auxiliary Power Unit (APU) directly upon transmission electron microscope (TEM) grids for particle characterization by high-resolution transmission electron microscopy (HRTEM). Carbonaceous emissions from two fuels, a coal-based Fischer-Tropsch and standard JP-8, were compared at three power levels each. Differences in soot nanostructure, specifically fullerenic content, illustrate changes in the combustion chemistry with engine power level, as do differences in aggregate size between the two fuels. As inferred from the soot nanostructure, comparison between fuels demonstrates the impact of fuel structure upon combustion chemistry.

Introduction

A vast, ground-based infrastructure that is largely unrecognized supports aircraft operations. One of the most prevalent, whether as a stand-alone, independent unit for smaller aircraft or as built-in units on many jets, is auxiliary power units, APUs. As the name implies, these units supply power for lighting, air conditioning, engine starts and other electrical needs until the jet engines are operative. With respect to exposure, these units pose the greatest particulate emissions hazard to which baggage and freight handlers, food service caterers, ground crews, etc. are exposed as these ground support personnel work in and around the parked aircraft during operation of the APUs, in contrast to having departed prior to aircraft engine operation and jet roll-back.

Soot archeology

Archeology is uncovering details of the past by examination of relics and artifacts. Classification and characterization of objects may be grouped into the generic categories of shape, structure and composition. Such details can both date the item as well as permit its history to be traced. Archeologists use both large and small tools to pick apart the objects and a variety of analytical techniques to characterize structure and composition. Significant insights may be gained by combining knowledge gained from archeology with that from other fields to obtain a more complete picture of the local environment, temporal continuity, or lack thereof, and evolution as affected by external factors.

Traditionally soot has been viewed as a pollutant or an incidental byproduct of incomplete combustion [1]. Recently soot nanostructure has been recognized as a valuable characterization goal for its relevance to soot reactivity, e.g. oxidation [2-5]. In this proposal, we propose soot archeology as an alternative paradigm to obtain insights into the combustion dynamics. Unlike gas phase species, soot nanostructure provides an integrated history of the combustion environment. Its radial nanostructure provides a timeline reflective of the gas phase chemistry during particle inception, growth and

oxidation. Therein soot nanostructure serves as a tracer of the local combustion environment. This history is inclusive of chemical origin, growth and partial oxidation.

Sampling and quenching chemical species within a gas turbine engine is enormously challenging as well as implementing non-intrusive optical diagnostics. To date, the approach followed is to use exhaust species as a benchmark by which to infer all reaction chemistry that ultimately led to their formation. This end-product approach possesses extreme sensitivity to extrapolated upstream chemistry, both spatially and temporally. In general, single concentration values of end products are non-unique. Other supplementary data, however obtained, whether chemical or physical in nature, can help to anchor numerical codes and their trajectories [6]. Here we suggest that soot nanostructure is one such data type that offers a temporal trace of the combustion environment from the fuel nozzle to the exhaust. Presently our results are qualitative and quantitative analyses of the HRTEM image data via image analysis algorithms will be presented elsewhere. Nevertheless, this non-traditional approach has the potential to provide breakthrough insights into both chemistry and fluid dynamics within the gas-turbine engine environment as a function of both fuel type and engine power. An example of this archeological concept is applied here to the APU emissions as a function of power.

Experimental

For reader convenience, pertinent experimental details are repeated here. The sampling probe details may be found in the Appendix entitled, "**XX**", as will the nominal fuel compositions. The FT fuel (designated elsewhere in this report as FT2) is a Fischer-Tropsch fuel derived from coal. It contains linear, branched and cycloparaffins the JP-8 contains these in addition to ~ 18% aromatic content with a very low sulfur content of ~ 0.8 wt.%.

The APU is located in the forward baggage compartment and is essentially a small, low-technology, gas-turbine engine known as a Honeywell Model GTCP85-98CK. When powered, its exhaust is mixed with bleed air and blown out through a shuttered port on the starboard side of the aircraft, just ahead of the wing spar. This particular APU is designed mainly for ground operation and is not certified for use at altitude for engine restart. The following are general specifications for the APU: Two-stage centrifugal compressor, single-stage radial inflow turbine and single can combustor. Further details may be found elsewhere in this report [Overview]. Sampled exhaust was diluted with dry N2 to reduce condensable gas concentrations and prevent particle coagulation with the TEM grid, directly capturing particulate emissions by impaction.

For HRTEM imaging at NASA Glenn, soot was deposited on a lacey C/Cu grid by depositing a drop of the soot suspension created by ultrasonication in ethanol. TEM images were taken using a Phillips CM200 having nominal resolution of 0.14 nm with Gatan Image Filter (GIF) for digital imaging, featuring live Fourier transforms having nominal resolution of 0.14 nm. The instrument was operated at 200 keV using a LaB6 filament. Gatan image software v. 3.4 was used for microscope operation.

In general, APUs are tested in three operating modes, each representing a specific load on the turbine: (1) no-load (idle); (2) ECS (all air-conditioning [A/C] packs operating); and main engine start (MES). During the NASA Alternative Aviation Fuel Experiment (AAFEX), however, only condition 3 could be identified along with several other lower load points. Since the lack of engine instrumentation prevented an accurate determination of load on the APU, it was decided to present all of the emissions data in terms of exhaust gas temperature (EGT) that was used as an indicator of total load on the turbine.

Results

Images are divided into three groups, one for each power level of the APU. Within each group is a comparison between data for the two different fuels. This data consists of HRTEM images at a series of magnifications to illustrate the different size scales of the particulate emissions. Each scale is related to the combustion chemistry differences between the fuels.

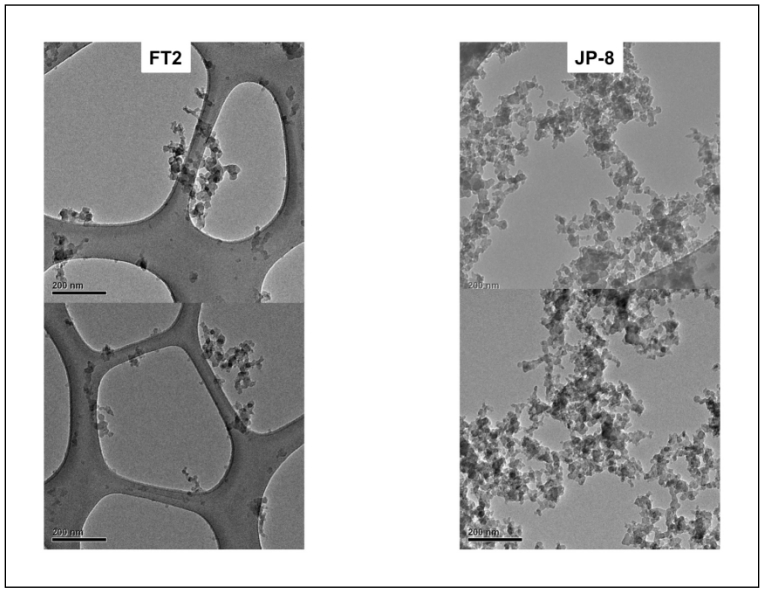

Figure 1a. Comparison between particulate matter produced at low (generator mode) by the APU running on JP-8 or FT2 fuel, as indicated. A vast size and morphology difference was observed depending upon which fuel was used. As outlined in the text, particles were captured directly upon the TEM grid. Notably very small (ultrafine particles) were produced by the FT2 fuel. These aggregates consisting of few primary particles were frequent in occurrence, qualitatively comprising ~ 50% of observed aggregates.

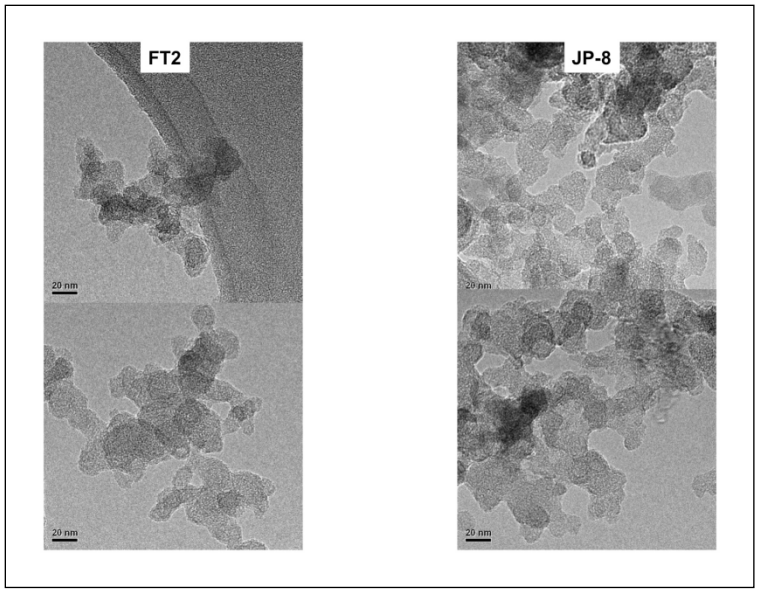

Figure 1b. Higher magnification images illustrating the connectivity (microstructure) between subunits, i.e. primary particles. That high similarity of particle fusion observed suggests that aerosol dynamics governs this structural parameter.

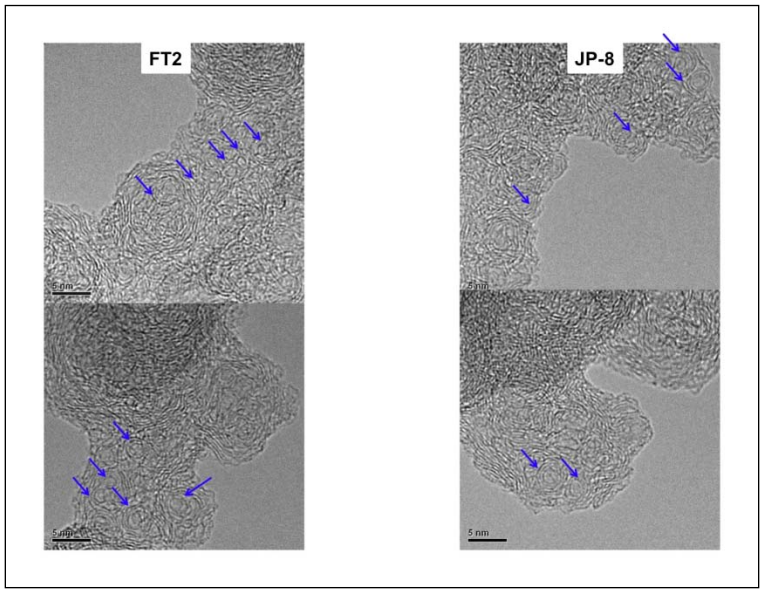

Figure 1c. HRTEM images illustrating the prevalent fullerenic nanostructure in particulate derived from both fuels. Curved lamella, in stacks of 2-3 form near spherical objects that are often closed or nearly so. Notably their interiors appear to be voids. Sizes range from ~ 2 nm to 5 nm which would nominally correspond to C96 and C512 fullerenes.

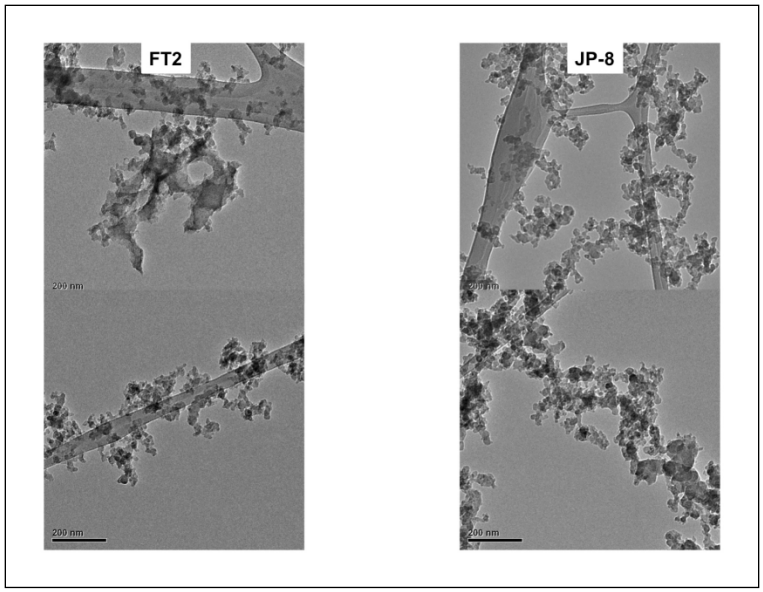

Figure 2a. Comparison between aggregates as captured, produced at the intermediate power setting of the APU, "park mode". Images are shown for FT2 and JP-8 derived particulate. For these conditions it is more difficult to discern whether significant differences in aggregate size or morphology exist between fuels.

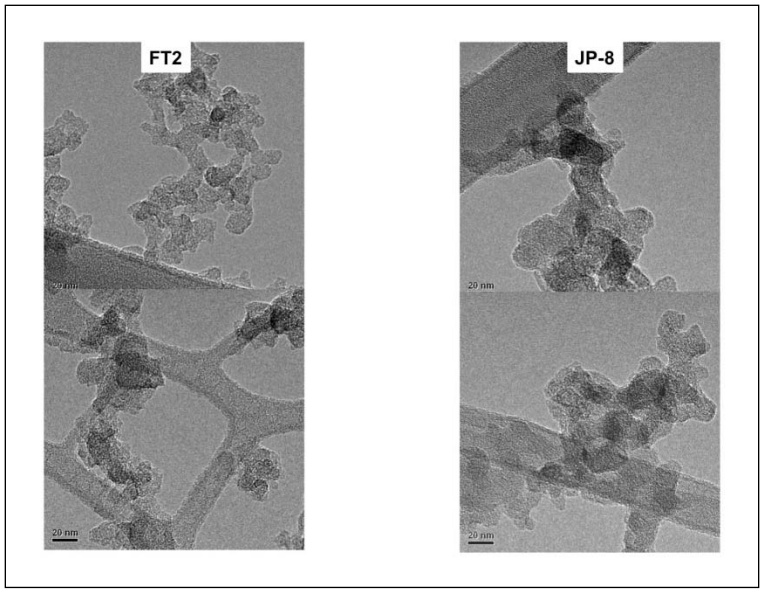

Figure 2b. Higher magnification images of aggregate microstructure for the corresponding fuels as indicated, at the intermediate power level "park mode". Characteristic of particulate from gas turbine engines is the compact, highly fused morphology, reflecting reaction limited particle cluster growth.

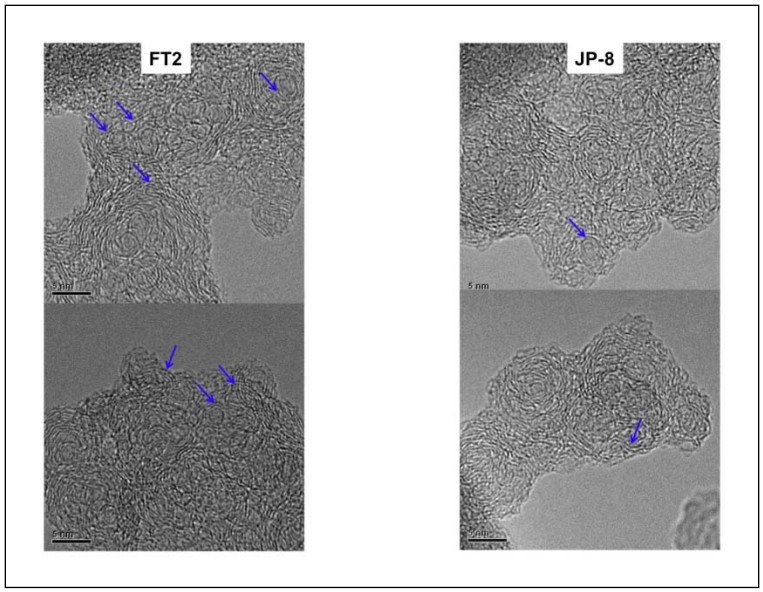

Figure 2c. A further illustration of the fullerenic nanostructure evident in particulate from the two fuels. Qualitatively there appeared to be lesser degree of curvature or tortuosity in the fringes for the JP-8 fuel. Lattice fringe analysis is expected to quantify the differences and will be reported elsewhere.

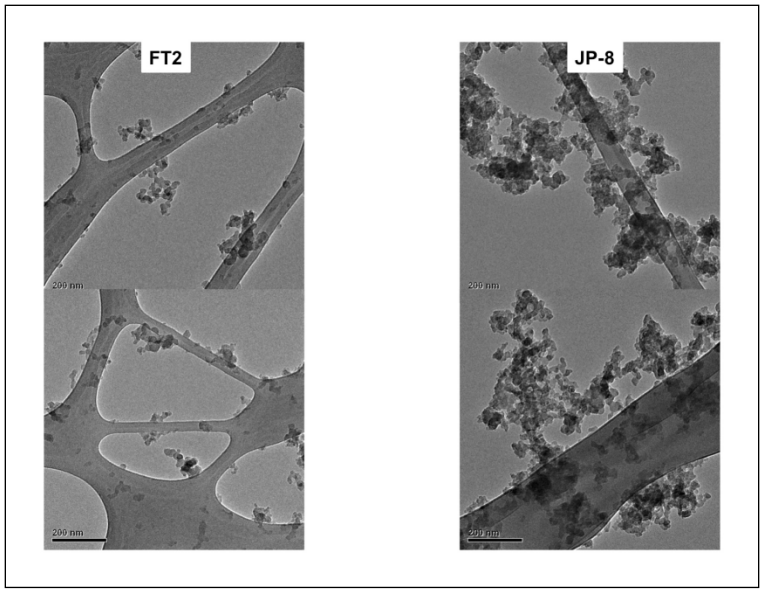

Figure 3a. Overview of differences in aggregate size and morphology in particulate between the two fuels from the APU at high power, "motor mode". Notably very small (ultrafine) particles, even some single primary particles are evident for the FT2 fuel. The highly compact nature of the aggregates, particularly their central portions is not consistent with simple physical agglomeration of aggregates which would be expected to result in more open structures with greater interior voids and pockets. Therein it is unlikely that the clustering observed for the JP-8 fuel is solely due to agglomeration, though our sampling technique does not disallow that possibility. For this reason we do not quantify size, but rather couch our observations in terms of morphology.

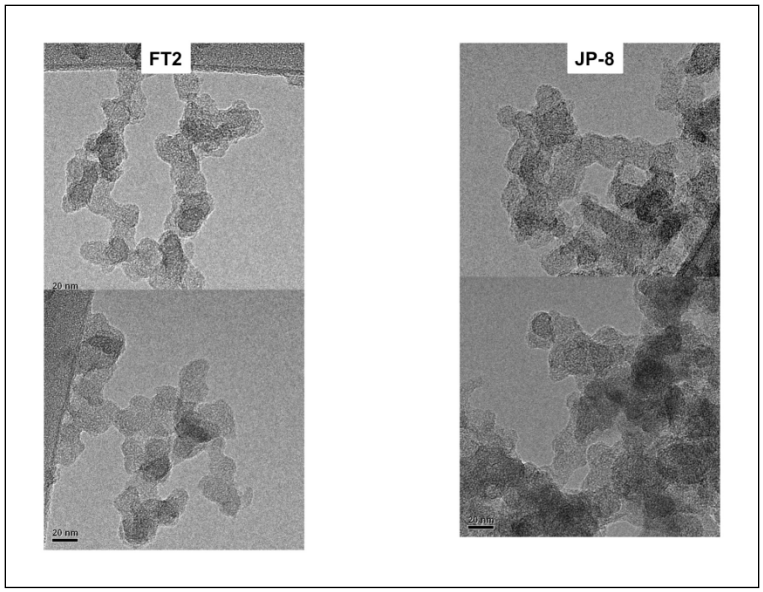

Figure 3b. The degree of fusion between primary particle subunits was observed to be similar for both aggregates. Apparent differences reflect the primary particles appearing to be in a 2-d plane for small aggregates versus being surrounded by other primary particles in large aggregates. Therein primary particle number density is the more relevant metric and reflects the aggregation dynamics. This is turn will reflect the gas-phase density of precursor species and corresponding concentration of primary particles.

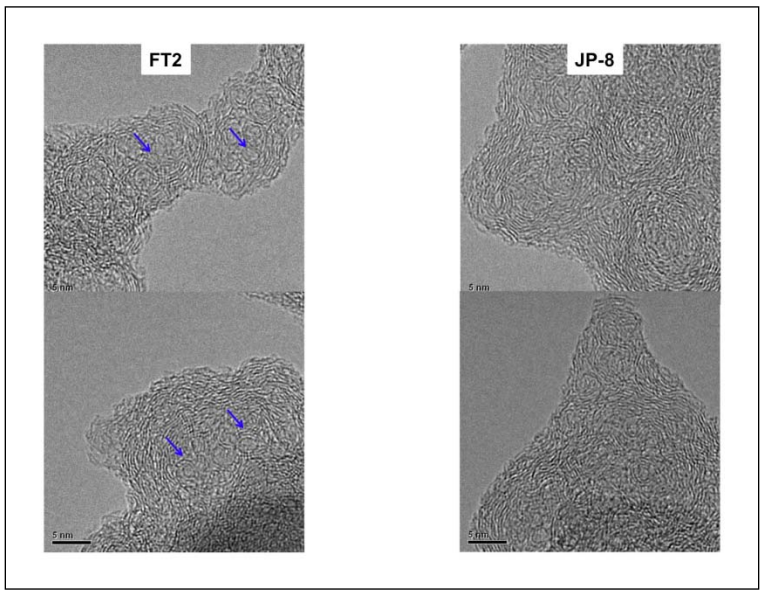

Figure 3c. HRTEM images of primary particles from the indicated FT2 and JP-8 fuels. Notably the FT2 fuel produces yet fullerenic nanostructure and a higher overall degree of tortuosity (or curvature) in the lamellae overall. The loss of fullerenic nanostructure is evident in the JP-8 derived fuel that shows few curved lamellae and these with generally a low degree of curvature. Smaller curvature may be observed but only lamellae appearing as small "arcs", not closed shells or substantial portions thereof.

Discussion

The APU unit is a miniature gas turbine engine operating with continuous rather than cyclic combustion as in a diesel engine (the later imposing combined temporal and spatial variations per cycle). Common to both engine types is that additional fuel is injected to realize increased power. By design, this leads to an overall increase in the fuel-air equivalence ratio. However, as modeling studies have shown, this measure is not a good predictor for soot emission levels [7]. Soot necessarily forms in fuel-rich regions with a non-linear dependence upon temperature [8]. Aerodynamics will also change as power levels increase [9]. This can change the size and relative spatial locations of fuel-rich recirculation zones that help to stabilize the flame. As temperature changes oxidizing rates necessarily will change. Nevertheless, such intertwined fluid mixing dynamics and temperature fields would be expected to be rather similar for both fuels as a continuous fuel spray is used. Different fluid dynamics with changing power levels does explain the overall trend of declining fullerenic content as discussed below. To the extent that the different fuels produce not only different soot yields at each power level but also soots with different nanostructures suggests that the chemistry differences between the fuels is responsible for the observed differences in both regards.

PAH and soot formation sequence

Soot formation begins with the formation of unsaturated hydrocarbons and aromatic compounds that form soot precursor particles [10]. Continued growth and carbonization leads to recognizable primary particles that undergo further mass growth and aggregates through their coalescence, as outlined in Figure 1. Dehydrogenation to form acetylene and aromatics followed by radical addition processes are two key pyrolysis reactions for paraffinic (saturated) hydrocarbons [11]. By jumpstarting the result of thermal and oxidative pyrolysis processes, unsaturated hydrocarbons and aromatics can produce soot more readily than paraffinic compounds [12]. Therein the starting fuel has profound consequences on the combustion emissions.

While thermal pyrolysis leads to dehydrogenation, oxygen also accelerates soot production by increasing the concentration of precursors, as named above [13]. During initial oxidation, oxygen extracts H-atoms during oxidation yielding unsaturated hydrocarbons. However oxygen will also open new pathways to aromatic formation from paraffins by the formation of odd numbered carbon species [14]. Examples include allylic and propenyl radicals that can react with C2 to yield C5 rings by direct molecular recombination. Finally, some oxygenates such as acetaldehyde, even though appearing to be on a chemical path opposite dehydrogenation can react to form oxygenated aromatics (e.g. phenoxy radicals) with subsequent elimination to yield C5 membered rings [15, 16]. In summary, oxygen alters the concentration and identity of species acting as soot precursors and those contributing to additional mass growth.

Rationale to hydrocarbons

Synthetic fuels such as FT derived fuels are composed of paraffins and cycloparaffins. Generally they contain no aromatics. Aromatics and acetylene formation occurs only through pyrolysis processes which necessarily take time. The lack of initial precursor and growth species delays soot nucleation and growth [17]. Additionally, the higher H

content slows oxygen-assisted dehydrogenation that produces unsaturated compounds such as poly aromatic hydrocarbons (PAHs). Premixing occurs for an increased time relative to soot formation and growth processes. Yields of partially oxygenated intermediates and odd numbered carbon species increase [18].

Both effects will increase the concentration of cyclopentadienyl radicals and aromatics containing C5 membered rings, e.g. naphthalene [19]. C5 membered rings have been shown to be integral to fullerene formation by enabling curvature of carbon lamella [20]. Therein it is the thermal and oxidative stability of the parent fuel that drives the fullerenic nanostructure of soot from a paraffinic fuel.

In contrast, the JP-8 fuel contains a significant fraction of unsaturated hydrocarbons and aromatics [Summary]. These species are significantly progressed, chemically, towards soot precursors and can directly serve as growth species without further (initial) dehydrogenation or oxidative pyrolysis reactions [21]. Soot formation begins upon formation of free radicals and H-atoms that continue radical chain propagation processes [12, 14, 15, 17, 21, 22]. Concurrently the other pyrolysis processes associated with paraffinic species as a component of JP-8 can occur as discussed above but a) the presence of unsaturated compounds will compete for oxygen, these species being more susceptible to electrophilic species in general [22], and b) the unsaturated compounds can directly react with the paraffins to form alkyl substituted aromatics [23]. Through inhibition of oxidative pyrolysis and oxygenate formation, (by oxygen scavenging and direct reaction with paraffins), the aromatic content of JP-8 fuel causes fullenenic precursor concentrations to be lower than for the FT fuel, at least as aided by oxygen [24]. Therein the degree of fullerenic nanostructure in the soot decreases. It also declines for another reason; with unsaturated hydrocarbons and aromatics initially present in the parent fuel, the timescale for soot formation is dramatically cut relative to the pure paraffinic fuel. Consequently the degree of partial premixing prior to the onset of soot formation is much less. Therein the relative contribution of oxygen assisted soot formation (via oxidative pyrolysis reactions) is less and associated fullerenic nanostructure is diminished.

That the FT derived (paraffin-derived) soot yet retains fullerenes and fullerenic nanostructure at the intermediate power while the JP-8 does not reflect the combustion chemistry dependence upon the nascent fuel. The fact that such structures are present attests to the delayed pyrolysis, lack of unsaturated hydrocarbons and aromatics, resulting time for increased fuel-air mixing with formation of oxygenated intermediates and odd numbered carbon species leading to cyclopentadienyl rings and C5 containing species. Notably this occurs at the molecular level prior to soot formation. Conversely, fullerenic structure for JP-8 derived soot is largely absent, reflecting its advanced pyrolysis state by virtue of high aromatic content in the nascent fuel. At high power, the higher initial fuel concentration for both fuels likely impedes the oxygen-assisted pathway towards fullerene formation, as witnessed by the reduced fullerenic nanostructure for each fuel, but just not at equal rates.

The inferred offset chemistries are also consistent with the overall lower soot production of the paraffinic fuel. This is perhaps the most significant find for green technologies for alternative or renewable fuels, e.g. biodiesel etc. or FT. These processes, based upon natural gas or coal, naturally produce paraffinic fuels. Their aromatic and naphthenic content is negligible. At any given power level emission indices by particle number or total particle mass (EI_n) and EI_m respectively) were lower for the FT fuel than for the JP-8 fuel (q.v. Appendix X). As discussed, for a given fuel amount and power level (meaning similar aerodynamics and fuel-air mixing levels and temperature environments), the lower soot yield and particle number for the FT derived soot can be interpreted as reflecting a combination of a lowered rate of soot production and a higher rate of soot oxidation for the paraffinic fuel. Fullerenic nanostructure consists of highly strained carbon framework [25]. Alternatively, it may be considered as possessing a mixture of sp2 and sp3 bonds [26]. By either interpretation, it is more reactive towards oxidation as found experimentally and theoretically [2]. Therein the synthetic FT fuel is not only greener in their production but also from an emissions perspective.

Necessarily the combustion temperature will vary, as dependent upon both the fuel-to-air ratio [27]. Numerous combustion studies have sought to elucidate the relative effects of oxygen addition to the fuel stream. Competing factors are dilution that lowers the average temperature and premixing, which raises the average temperature [28-30]. Changes in the fuel-air ratio and as inferred here, changes in pre-mixing, impose both effects. However, changes in combustion temperature have been studied for purposeful production of fullerenes by combustion using partial premixing [31]. Not until temperatures exceed 2000 K do fullerenes arise by temperature effects [32]. Therein the chemical path is notably different as well, with PAHs no longer being thermodynamically stable but actually undergoing decomposition [33]. The combustion conditions within the turbine are entirely outside this parameter space. Even if temperature was playing some role in the production of fullerenic nanostructure, this would only arise by partial premixing which is inherent to the rationale set forth here as a necessary condition by which to explain the changes in chemistry reflected in the soot nanostructure.

Aggregate Size

The variation of fullerenic content is also consistent with the change in aggregate size. Differences in aggregate dimensions are clear from the side-by-side images of deposits upon the TEM grid. Given an unknown degree of aggregate-aggregate overlap, only a lower bound can be placed upon those derived from the JP-8 fuel, ~ 200 nm. By comparison, cursory inspection of aggregates from the FT fuel suggests two vastly different aggregate size classes, i.e. a bimodal size distribution. The averages are < 50 nm and ~ 200 nm for both the low and high power tests based on over two dozen measurements. This former class is traditionally referred to as the "nucleation mode." These particles are composed of only one to a few primary particles. This bimodal distribution is unique to the FT fuel. Interestingly no such ultrasmall size class was observed at the intermediate power. The primary particles comprising these two aggregates are also significantly different. As summarized in Table 1, the mean size for mature aggregates is ~ 20 nm or larger, depending upon power level whereas the primary particles within the ultrafine mode aggregates is ~ 15 nm (as no ultrasmall aggregates

were observed at the intermediate power, no primary particle sizes could be measured). The smaller number of primary particles within aggregates for the FT fuel compared to the JP-8 fuel suggests a lowered primary particle concentration, indicative of a lower concentration of nucleating species. The smaller primary particle size at the low power operation suggests a lower concentration of nucleation and growth species, i.e. PAHs and acetylene. This finding is consistent with both the FT fuel composition being devoid of aromatics and other unsaturated organics and the delayed onset of soot formation from paraffinic fuels compared to those with significant aromatic content.

Table 1. Primary Particle Size Results

Power Level	Size, nm (within mature agg.)*	Size, nm (in ultrasmall agg.)*
Low	24 +/- 3	15 +/- 3
Intermediate	17 +/- 2	
High	19 +/- 2	21 +/- 3

* Size given in nanometers with uncertainty estimated by one Std. deviation.

Similar observations were found for the main engine tests (**q.v. Appendix XX**). For both low and high engine powers, a distinct smaller size class of aggregates was found. Their composition (and hence origin) differed, however, as inferred from HRTEM and x-ray photoelectron spectroscopic (XPS) analyses.

Conclusions

Synthetic fuels composed of paraffinic species delay the onset of particle formation and growth by absence of dehydrogenated species and aromatics. This permits increased fuel-air mixing, increased formation of oxygenated intermediates and production of alkyl intermediates containing an odd number of carbon atoms, in addition to dehydrogenated molecules and aromatics. These species will increase the concentration of cyclopentadienyl radicals and aromatics incorporating them, such as naphthalene. Such compounds incorporated into graphene segments give rise to curvature and result in fullerenic nanostructure. The degree or content of fullerenic structure is here postulated to correlate with level of partial premixing. Nanostructure comparisons as a function of engine power supports this postulate as increased fuel concentration with increased (required) power decreases the level of partial premixing, both local and global. The result is a lesser content of fullerenic nanostructure, as observed by HRTEM. Comparisons between the FT and JP-8 fuels provides further support in that for the same power level, soot from the JP-8 fuel contains less fullerenic nanostructure, reflecting its substantial aromatic content, that accelerates soot formation which minimizes the impact of partial premixing. Differences in aggregate size between the two fuels at each power level are consistent with this interpretation. Therein soot nanostructure preserves a record of the gas phase species contributing to its formation and growth and can be used as an in situ tracer of the early combustion chemistry within the engine.

Acknowledgements
The author gratefully acknowledges sample collection during the weeks of field campaign testing by Dr. Kathleen Tacina (NASA Glenn) and overall project coordination and steadfast experimental aid and technical input by Dr. Bruce Anderson (NASA Langley). Vicky M. Bryg is acknowledged for TEM work and Mr. Chung-Hsuan Hunag (Penn State) for sizing analyses and Dr. John Kinsey (U.S. EPA) for graciously sharing his experimental data prior to publication. Support for this work was through the NASA Aeronautics Subsonic Fixed Wing (SSFW) Program, NASA Cooperative Agreement NNX09AD42A with The Pennsylvania State University, at University Park PA.

References

1. Glassman, I., Soot formation in combustion processes. Symposium (International) on Combustion 22:295-311 (1989). (fuel str, tmp,

2. Vander Wal, R. L., and Tomasek, A. J., Soot Nanostructure: Dependence Upon Synthesis Conditions. Combustion and Flame 136:129-140 (2003).

3. Vander Wal, R. L., and Tomasek, A. J., Soot Oxidation: Dependence Upon Initial Nanostructure. Combustion and Flame 134:1-9 (2003).

4. Boehman, A. L., Song, J., and Alam, M., Biodiesel blending on diesel soot and the regeneration of particulate filters. *Energy Fuels,* 19:1857–1864 (2005).

5. Al-Qurashi, K., and Boehman, A. L., Impact of exhaust gas recirculation (EGR) on the oxidative reactivity of diesel engine soot. Combustion and Flame 155:675-695 (2008).

6. Reilly, P. T. A., Gieray, R. A., Whitten, W. B., and Ramsey, J. M., Fullerene evolution in flame generated soot. J. Am. Chem. Soc. 122:11596-11601 (2000).

7. a) Vander Wal, R. L., LIF-LII measurements in a turbulent gas-jet flame. Experiments in Fluids 23:281-287 (1997).

b) Pitsch, H., Riesmeir, E., and Peters, N., Unsteady flamelet modeling of soot formation in turbulent diffusion flames. Combustion Science and Technology 158:389-406 (2000).

8. Wang, R., and Cadman, P., Soot and PAH production from spray combustion of hydrocarbons behind reflected shock waves. Combustion and Flame 112:359-370 (1998).

9. Subsonic Fixed Wing (SFW) and Supersonics (SUP) NRA Annual Review of the Combustion Awards, on January 26th and 27th respectively, at the Ohio Aerospace Institute (OAI) in Cleveland, OH.
a) Menon, S., Subgrid combustion models for the next generation national combustion code.
b) Pitsch, H., Emissions Modeling and Prediction of Supersonic Vehicle Combustion Systems.

c) Pitsch, H., Integrated Large Eddy Simulation of Multi-Phase Turbulent Reacting Flows for Realistic Gas-Turbine Combustors.
d) Modest, M., LES Modeling of Spectral Multiphase Radiation and Turbulence/Chemistry/Radiation Interactions in Reacting Turbulent Flow.

10. Dobbins, R. A., Fletcher, R. A., and Chang, H.-C., Evolution of soot precursor particles in a diffusion flame, Combustion and Flame 115:285-298 (1998).

11. Kazakov, A., Wang, H., and Frenklach, M., Detailed modeling of soot formation in laminar-ethylene flames at pressure of 10 bar. Combustion and Flame 100:111-120 (1995).

12. Frenklach, M., Taki, S., and Matula, R. A., A conceptual model for soot formation in pyrolysis of aromatic hydrocarbons. Combustion and Flame 49:275-282 (1983).

13. McEnally, C. S., and Pfefferle, L. D., Experimental study of non-fuel hydrocarbons in coflowing partially premixed ethylene/air flames. Combustion and Flame 121:575-592 (2000).

14. Frenklach, M., Reaction mechanisms of soot formation in flames. Phys. Chem. Phys. Chem. 4:2028-2037 (2002).

15. D'Anna, A., and Violi, A., Detailed modeling of the molecular growth process in aromatic and aliphatic premixed flames. Energy and Fuels 19:79-86 (2005).

16. Marinov, N. M., Pitz, W. J., Westbrook C. K., Castaldi, M. J., and Senkan, S. M., Modeling of aromatic and polycyclic aromatic hydrocarbon formation in premixed methane and ethane flames. Combustion Science and Technology 116:211-287 (1996).

17. D'Anna, A., and Violi, A., Detailed modeling of the molecular growth processes in aliphatic premixed flames. Energy and Fuels 19:79-86 (2005).

18. a) Zhang, H. R., Eddings, E. G., and Sarofim, A. F., A Journey from n-heptane to liquid transportation fuels of the allylic radical and its related species in aromatic chemistry. Energy and Fuels 22:945-953 (2008).

b) McEnally, C. S., and Pfefferle, L. D., Species and soot concentration measurements in a methane/air nonpremixed flame doped with C4 hydrocarbons. Combustion and Flame 115:81-92 (1998).

19. a) Bachmann, Griesheimer, J., and Homann, K. –H., The formation of C60 and its precursors in naphthalene flames. Chemical Physics Letters 223:506-510 (1994).

b) 19. Silvestrini, M., Merchan-Merchan, W., Richter, H., Saveliev, A., and Kennedy, L. A., Fullerene formation in atmospheric pressure opposed flow oxy-flames. Symposium (International) on Combustion 30:2545-2552 (2005).

20. a) Goel, A., Hebgen, P., Vander Sande, J. B., and Howard, J. B., Combustion synthesis of fullerenes and fullerenic nanostructures. Carbon 40:177-182 (2002).

b) Grieco, W. J., Howard, J. B., Rainey, L. C., and Vander Sande, J. B., Fullerenic carbon in combustion generated soot. Carbon 38:597-614 (2000).

21. a) Richter, H., and Howard, H. B., Formation of polycyclic aromatic hydrocarbon growth to soot – a review of chemical reactivity. Progress in Energy and Combustion Science 26:565-608 (2000).

b) Wen, Z., Yun, S., Thomson, M. J., and Lightstone, M. F., Modeling soot formation in turbulent kerosene jet diffusion flames. Combustion and Flame 135:323-340 (2003).

22. Violi, A., D'Anna, A., and D'Alessio, A., Modeling of particulate formation in combustion pyrolysis. Chemical Engineering Science 54:3433-3442 (1999).

23. Ciajolo, A., D'Anna, A., Barbella, R., PAH and high molecular weight species formed in a premixed methane flame. Combustion Science and Technology 100:271-281. (1994).

24. Simmie, J. M., Detailed chemical kinetic models for the corresponding hydrocarbon fuels. Progress in Energy and Combustion Science 6:599-6334 (2003).

25. Barnard, A. S., Russo, S. P., and Snook, I. K., Size dependent phase stability of carbon nanoparticles: Nanodiamond versus fullerenes. J. Chem. Phys. 118:5094-5098 (2003).

26. Saito, R., Fujita, M., Dresselhaus, G., and Dresselhaus, M. S., Electronic structure of graphene tubules based on C60. Phys. Rev. B 46:1804-1811 (1992).

27. Mansurov, Z. A., Soot formation in combustion processes (Review) Combustion, Explosion and Shock Waves 41:727-744 (2005).

28. Glassman, I., Sooting laminar diffusion flames: Effect of dilution, additives, pressure and microgravity. Twenty-Seventh Symposium (International) on Combustion/The Combustion Institute 1589-1596 (1998).

29. Gulder, O., Effects of oxygen on soot formation in methane, propane, and *n*-Butane diffusion flames. Combustion and Flame 101:302-310 (1995).

30. Sidebotham, G. W. and Glassman, I., Flame temperature, fuel structure, and fuel concentration effects on soot formation in inverse diffusion flames. Combustion and Flame 90:269-272 (1992).

31. Ozawa, M., Deota, P., and Osawa, E., Production of fullerenes by combustion. Fullerene Science and Technology 7:387-409 (1999).

32. Hammida, M., Fonseca, A., Doome, R., De Hoffman, E., and Nagy, B., C60, C60O, C70 and C70O fullerene formation in benzene-oxygen flames. Symposium (International) on Combustion. 27:1663-1668 (1998).

33. Graham, S. C., Homer, J. B., and Rosenfeld, J. L. J., The formation and coagulation of soot aerosols generated by the pyrolysis of aromatic hydrocarbons. Proc. R. Soc. Lond. A 344:259-285 (1975).

APPENDIX O: Spatial Variation of PM Emissions at the Engine Exit

Donald E. Hagen, Prem Lobo, and Philip D. Whitefield

Center of Excellence for Aerospace Particulate Emissions Reduction Research
G-7 Norwood Hall, Missouri University of Science and Technology, Rolla, MO 65409

Introduction

Several studies have been carried out to characterize emissions from military engines and, more recently, commercial jet engines burning alternative aviation fuels. NASA sponsored a study called AAFEX: Alternative Aviation Fuels Emissions Experiment, to evaluate the impacts of synthetic fuels on commercial aircraft gaseous and particle emissions. The Missouri University of Science and Technology Center of Excellence for Aerospace Particulate Emissions Reduction Research (Missouri S&T COE) was a team member for AAFEX. The study was and was conducted in January 2009 in Palmdale, CA. The tests were performed on the same CFM56-2C1 engine studied during APEX-1

The characteristics of the PM exhaust emissions can be spatially non-uniform over the engine exit plane. In this section of the report a methodology to characterize this spatial non-uniformity is described, a suitable metric is developed, and results are calculated for AAFEX PM emissions data. The analysis uses the derived parameters calculated from size distributions measured using a scanning differential mobility analyzer.

Instrumentation

The instrumentation onboard the Missouri S&T mobile laboratory to sample emissions at the engine exit plane consisted of the Cambustion DMS500, a state-of-the-art, fast-particulate spectrometer, to gather real-time, size-distribution information and total concentration of engine exhaust particulates. Also onboard was a scanning differential mobility analyzer (SDMA) (TSI model 3071), a traditional and slower instrument to measure aerosol size distributions, a TSI condensation particle counter (CPC) (TSI model 3022) to measure total number concentration, and a fast response carbon dioxide (CO2) detector to monitor sample dilution and establish emission factors. The instruments have been extensively used in recent field campaigns to measure PM emissions from commercial aircraft engines burning conventional and as well as alternative aviation fuels (Lobo et al. 2007; 2010).

Methodology

Here the data reduction methodology is given to compute a metric, $\sigma_{k,var}$, to characterize exhaust spatial non-uniformity from the data collected from the engine mapping run. The measurement data set is represented by $\{ap_{nij}, \delta ap_{nij}, A_{ij}\}$.
ap_n denotes an aerosol parameter of type n.

ap_1 = number-based geometric mean diameter (Dgn),
ap_2 = mass-based geometric mean diameter (Dgm),
ap_3 = Geometric standard deviation in the size distribution (Sigma),
ap_4 = Number-based emissions index (EIn), and
ap_5 = Mass-based emissions index (EIm).

A grid is used to define sampling locations (x_i,y_j) in the engine exit plane; i denotes a horizontal position index, and j denotes sampling tip, i.e. vertical position. Grid locations relative to the center of the engine exit plane are given in Table 1.

Table 1. Sampling locations in engine exit plane

i	x_i(inches)	j	y_j(inches)
3	3.5	3	5
2	2.0	2	3.5
1	0.5	1	2
0	-1.0	0	0.5
-1	-2.5	-1	-1
-2	-4.0	-2	-2.5
-3	-5.5	-3	-4

Let A_{ij} denote the fractional area associated with each probe location; $\Sigma_{ij}A_{ij} = 1$. An area and uncertainty weighted average value is calculated for ap_n. This is our best estimate for what the whole engine will produce (engine average) regarding parameter n.

$$\overline{ap}_n = (\Sigma_{ij} ap_{nij} A_{ij} / \delta ap_{nij}^2) / (\Sigma_{ij} A_{ij} / \delta ap_{nij}^2)$$

A normalized (fractional) value is computed for this parameter

$$bp_{nij} = ap_{nij} / \overline{ap}_n$$

The normalization allows different types of parameters, e.g. Dgn and EIn, to be coupled on an equal basis. Now consider a weighted average normalized global aerosol parameter, $\overline{bp}$, to represent the collection of aerosol parameters. An uncertainty and area weighted weight function is used:

$w_{nij} = w_n A_{ij} (ap_n / \delta ap_{nij})^2$.

w_n is chosen by the user to give a desired relative weight to each aerosol parameter, e.g. w_1(Dgn)=1, w_2(Dgm)=1, w_3(σ)=1, w_4(EIn)=2, w_5(EIm)=2.

$$\overline{bp} = (\Sigma_{nij} w_{nij} bp_{nij}) / (\Sigma_{nij} w_{nij}) = 1$$

We are not interested in $\overline{bp}$ itself, but rather its variance. The unbiased variance in $\overline{bp}$ is given by

$$\text{Variance} = (\Sigma_{nij} w'_{nij} (bp_{nij} - \overline{bp})^2) / (1 - \Sigma_{nij} w'^2_{nij})$$

$w'_{nij} = w_{nij} / \Sigma_{nij} w_{nij}$ (normalized weight function).

This can be rewritten as:
Variance $= [(\Sigma_{nij} w_{nij})(\Sigma_{nij} w_{nij} bp_{nij}^2) - (\Sigma_{nij} w_{nij} bp_{nij})^2] / [(\Sigma_{nij} w_{nij})^2 - (\Sigma_{nij} w_{nij}^2)]$
The standard deviation is taken as the usual square root of the variance.
$\sigma_{var} = (\text{variance})^{1/2}$.
σ_{var} represents the variability (standard deviation) of PM emissions across the engine exit plane at the given engine power condition.

$$\sigma_{var} = \{[(\Sigma_{nij} w_{nij})(\Sigma_{nij} w_{nij} bp_{nij}^2) - (\Sigma_{nij} w_{nij} bp_{nij})^2] / [(\Sigma_{nij} w_{nij})^2 - (\Sigma_{nij} w_{nij}^2)]\}^{1/2}$$

Results
During the mapping phase of Project AAFEX, 12 grid points were selected for sampling at 4% power, 9 points at 65%, and 5 points at 85%. The locations in the engine exit plane are depicted in Table 2; the numbers in the grid cells indicate the power settings for which measurements were made at the indicated locations.

Table 2. Sampling locations in engine exit plane for mapping.

j \ i	**-3**	**-2**	**-1**	**0**	**1**	**2**	**3**
-3				4%			
-2					4%		
-1		4%,65%,85%	65%,85%	65%,85%	4%,65%	65%,85%	
0		4%,65%,85%	4%	4%	4%	4%,65%	
1					4%,65%		
2					4%		
3					4%,65%		

Measurement data for Dgn, Dgm, Sigma, EIn, and EIm taken at the locations and engine powers given in Table 2 were extracted from the master spreadsheet and are given in Appendix A. Measurements were taken on different days under different ambient temperature conditions, which can influence emissions. To suppress the differences associated with day-changes, the data for a given day were normalized to a reference day, i.e. the aerosol parameters, averaged over sampling locations were normalized to have the same daily average. The following normalization procedure was used:

Let $\{ap_{n,pwr,day,loc}\}$ denote the data set for aerosol parameter ap_n for a given engine power (pwr), on a given day (day), and sampling location (loc). January 26 was selected as the reference day (rday); data from the other days was normalized to its data.

Let $Nap_{n,pwr,day,loc}$ denote the normalized data.
$Nap_{n,pwr,day,loc} = ap_{n,pwr,day,loc} *< ap_{n,pwr,rday,loc} >/< ap_{n,pwr,day,loc} >$,
where < > indicates an average taken over different sampling locations.

The spatially dependent PM emissions data for engine powers 4%, 65%, and 85% from Appendix A were processed using the following sets of parameter weight functions (1 refers to Dgn, 2 – Dgm, 3-Sigma, 4 - EIn, 5 – EIm): (w1 w2 w3 w4 w5) = (0 0 0 1 1), (2 2 1 5 5), and (1 1 1 1 1). For weighting (0 0 0 1 1), the size-distribution shape parameters are excluded and only emission indices are included, EIn and EIm, with equal weight. For (2 2 1 5 5) the size distribution shape parameters are brought into the analysis, with the geometric means having twice the weight as the width parameter, and the emission indices having the greatest weights. For (1 1 1 1 1) all, the aerosol parameters are included with equal weights. Since the data taken was relatively sparse, no attempt was made to define unique areas (A_{ij}'s) to the sampling locations. All the areas were set to unity. The results for σ_{var} (representing the variability of PM emissions across the engine exit plane at the given engine power condition) vary with different weight function choices. The results are given in Table 3. The variability is lowest at high power and maximum at the 65% power condition.

Table 3. PM emissions variability (standard deviation) in percent across engine exit plane.

Power	σvar (0 0 0 1 1)	σvar (2 2 1 5 5)	σvar (1 1 1 1 1)
4%	47.0	10.4	6.2
65%	68.9	21.6	14.9
85%	15.3	7.9	5.9

The emission indices have larger variabilities than the size distribution shape parameters. The PM emissions variability calculations were repeated at power conditions 4% and 65% using un-normalized data. These results are shown in Table 4. Here the variability is always greater, by an average of 61%.

Table 4. PM emissions variability across engine exit plane using unnormalized data.

Power	σvar (0 0 0 1 1)	σvar (2 2 1 5 5)	σvar (1 1 1 1 1)
4%	74.8	12.9	7.3
65%	156.2	40.3	22.6

Conclusions

Spatially resolved PM emissions data was acquired at engine power settings of 4%, 65%, and 85%, during Project AAFEX. Most data was taken at low power, 4%. There was a good spread in the horizontal and vertical directions, but the sampling points were not well distributed; they were primarily taken near the horizontal and vertical centerlines. Data was taken on multiple days, introducing ambient temperature dependence into the data. A normalization of the data to a reference day temperature was done to suppress the effect of ambient temperature changes. The observed variability was power dependent – minimum variability at the highest power and max variability at mid power. A dependence of the variability on how the PM emissions parameters were weighted in the analysis was observed. The emission indices showed more variability than the size distribution shape parameters. The observed variability in emissions ranged from 6% to 70%.

Acknowledgements

This work was partly funded by the Federal Aviation Administration (FAA) through the Partnership for AiR Transportation for Noise and Emissions Reduction (PARTNER) – a FAA- NASA-Transport Canada- sponsored Center of Excellence under GrantNo.07-C-NE-UMR Amendments 006 and 007. The authors would like to acknowledge the AAFEX team, and NASA DC-8 personnel for substantial contributions to the successful execution of this study.

References

Lobo, P., Hagen, D.E., Whitefield, P.D., and Alofs, D.J., "Physical characterization of aerosol emissions from a Commercial Gas Turbine Engine", Journal of Propulsion and Power, 2007, 23, 919-929.

Lobo, P., Hagen, D.E. and Whitefield, P.D., "Comparison of PM emissions from a Commercial Jet Engine burning Conventional, Biomass, and Fischer-Tropsch Fuels", *manuscript in preparation* 2010.

APPENDIX O

Appendix L-A

Table A1. Normalized aerosol parameters and their associated uncertainties at locations in Table 2 and engine power 4%.

Dgn

j/i	-3	-2	-1	0	1	2	3
-3				**15.9**			
-2					**16.0**		
-1		**16.4**			**14.9**		
0		**15.1**	**16.3**	**15.6**	**14.6**	**14.4**	
1					**14.8**		
2					**14.7**		
3					**16.2**		

Dgm

j/i	-3	-2	-1	0	1	2	3
-3				**40.1**			
-2					**35.3**		
-1		**38.9**			**29.2**		
0		**34.4**	**29.0**	**36.9**	**29.6**	**28.9**	
1					**25.2**		
2					**24.3**		
3					**45.8**		

Sigma

j/i	-3	-2	-1	0	1	2	3
-3				**1.46**			
-2					**1.48**		
-1		**1.48**			**1.40**		
0		**1.42**	**1.41**	**1.43**	**1.39**	**1.39**	
1					**1.36**		
2					**1.34**		
3					**1.47**		

EIn

j/i	-3	-2	-1	0	1	2	3
-3				**2.41E+15**			
-2					**2.12E+15**		
-1		**8.50E+14**			**3.31E+15**		
0		**1.83E+15**	**4.08E+15**	**3.45E+15**	**4.43E+15**	**4.74E+15**	
1					**6.15E+15**		
2					**6.96E+15**		
3					**2.37E+15**		

EIm

j/i	-3	-2	-1	0	1	2	3
-3				**0.0139**			
-2					**0.0121**		
-1		**0.0063**			**0.0124**		
0		**0.0092**	**0.0095**	**0.0155**	**0.0131**	**0.0132**	
1					**0.0193**		
2					**0.0205**		
3					**0.0157**		

δDgn

j/i	-3	-2	-1	0	1	2	3
-3				**0.30**			
-2					**0.52**		
-1		**0.30**			**0.51**		
0		**0.50**	**0.30**	**0.30**	**0.55**	**0.30**	
1					**0.61**		
2					**0.30**		
3					**0.30**		

δDgm

j/i	-3	-2	-1	0	1	2	3
-3				**7.89**			
-2					**4.30**		
-1		**9.80**			**4.30**		
0		**4.30**	**4.30**	**5.61**	**4.30**	**4.30**	
1					**4.30**		
2					**4.30**		
3					**9.44**		

δSigma

j/i	-3	-2	-1	0	1	2	3
-3				**0.016**			
-2					**0.022**		
-1		**0.016**			**0.028**		
0		**0.025**	**0.016**	**0.016**	**0.016**	**0.016**	
1					**0.034**		
2					**0.016**		
3					**0.016**		

δEIn

j/i	-3	-2	-1	0	1	2	3
-3				**3.84E+14**			
-2					**6.85E+14**		
-1		**3.84E+14**			**6.34E+14**		
0		**3.84E+14**	**3.84E+14**	**3.84E+14**	**8.37E+14**	**3.98E+14**	
1					**9.93E+14**		
2					**3.84E+14**		
3					**3.84E+14**		

δEIm

j/i	-3	-2	-1	0	1	2	3
-3				**0.0021**			
-2					**0.0039**		
-1		**0.0021**			**0.0024**		
0		**0.0021**	**0.0021**	**0.0025**	**0.0021**	**0.0021**	
1					**0.0044**		
2					**0.0021**		
3					**0.0025**		

Table A2. Normalized aerosol parameters and their associated uncertainties at locations in Table 2 and engine power 65%.

Dgn

j/i	-3	-2	-1	0	1	2	3
-3							
-2							
-1		**23.5**	**22.3**	**20.8**	**25.2**	**20.8**	
0		**21.5**				**14.1**	
1					**21.9**		
2							
3					**16.8**		

Dgm

j/i	-3	-2	-1	0	1	2	3
-3							
-2							
-1		**75.2**	**70.1**	**75.4**	**83.9**	**69.0**	
0		**65.2**				**32.0**	
1					**74.1**		
2							
3					**56.5**		

Sigma

j/i	-3	-2	-1	0	1	2	3
-3							
-2							
-1		1.69	1.64	1.61	1.70	1.64	
0		1.68				1.33	
1					1.69		
2							
3					1.50		

EIn

j/i	-3	-2	-1	0	1	2	3
-3							
-2							
-1		7.26E+14	5.71E+15	3.80E+15	1.07E+15	4.40E+15	
0		1.28E+15				1.96E+16	
1					1.45E+15		
2							
3					1.14E+16		

EIm

j/i	-3	-2	-1	0	1	2	3
-3							
-2							
-1		0.0203	0.0500	0.0292	0.0246	0.0326	
0		0.0306				0.0629	
1					0.0230		
2							
3					0.0643		

δDgn

j/i	-3	-2	-1	0	1	2	3
-3							
-2							
-1		0.21	0.21	0.21	0.21	0.55	
0		0.32				0.21	
1					0.21		
2							
3					0.29		

δDgm

j/i	-3	-2	-1	0	1	2	3
-3							
-2							
-1		1.47	1.47	3.07	1.47	1.47	
0		1.47				1.47	
1					1.58		
2							
3					2.13		

δSigma

j/i	-3	-2	-1	0	1	2	3
-3							
-2							
-1		0.009	0.009	0.009	0.009	0.022	
0		0.012				0.009	
1					0.009		
2							
3					0.019		

δEIn

j/i	-3	-2	-1	0	1	2	3
-3							
-2							
-1		1.78E+14	1.78E+14	1.78E+14	1.78E+14	3.03E+14	
0		1.78E+14				6.29E+14	
1					1.78E+14		
2							
3					4.38E+14		

δEIm

j/i	-3	-2	-1	0	1	2	3
-3							
-2							
-1		0.0014	0.0016	0.0021	0.0014	0.0014	
0		0.0014				0.0018	
1					0.0014		
2							
3					0.0041		

Table A3. Normalized aerosol parameters and their associated uncertainties at locations in Table 2 and engine power 85%.

Dgn

j/i	-3	-2	-1	0	1	2	3
-3							
-2							
-1		**27.9**	**25.9**	**26.2**		**26.4**	
0		**16.3**					
1							
2							
3							

Dgm

j/i	-3	-2	-1	0	1	2	3
-3							
-2							
-1		**71.8**	**71.2**	**75.4**		**71.3**	
0		**65.4**					
1							
2							
3							

Sigma

j/i	-3	-2	-1	0	1	2	3
-3							
-2							
-1		**1.78**	**1.77**	**1.78**		**1.77**	
0		**1.73**					
1							
2							
3							

EIn

j/i	-3	-2	-1	0	1	2	3
-3							
-2							
-1		**8.08E+14**	**1.43E+15**	**1.63E+15**		**8.43E+14**	
0		**4.13E+15**					
1							
2							
3							

EIm

j/i	-3	-2	-1	0	1	2	3
-3							
-2							
-1		**0.0578**	**0.0525**	**0.0660**		**0.0617**	
0		**0.0709**					
1							
2							
3							

δDgn

j/i	-3	-2	-1	0	1	2	3
-3							
-2							
-1		**0.44**	**0.44**	**1.01**		**0.44**	
0		**1.00**					
1							
2							
3							

δDgm

j/i	-3	-2	-1	0	1	2	3
-3							
-2							
-1		**0.93**	**0.93**	**2.70**		**0.93**	
0		**1.34**					
1							
2							
3							

δSigma

j/i	-3	-2	-1	0	1	2	3
-3							
-2							
-1		**0.018**	**0.018**	**0.041**		**0.018**	
0		**0.042**					
1							
2							
3							

APPENDIX O

δEIn

j/i	-3	-2	-1	0	1	2	3
-3							
-2							
-1		**2.04E+14**	**2.04E+14**	**3.07E+14**		**2.04E+14**	
0		**6.52E+14**					
1							
2							
3							

δEIm

j/i	-3	-2	-1	0	1	2	3
-3							
-2							
-1		**0.0018**	**0.0018**	**0.0059**		**0.0018**	
0		**0.0018**					
1							
2							
3							

APPENDIX P: Sampling System Effects On Particle Emission Measurements

B. E. Anderson, D. S. Liscinsky, A.J. Beyersdorf, C.H. Hudgins, K.L. Thornhill, M. Trueblood, E.L. Winstead, and L.D. Ziemba

1.0 ABSTRACT

To observe PM emissions in both the near- and far-field exhaust regimes, AAFEX deployed paired sample inlets at 1 and 30 m behind both DC-8 inboard engines and used long, unheated sampling lines to transport diluted sample from the inlets to diagnostic instruments housed in trailers or trucks parked just off the aircraft's right wing. To characterize sampling system impacts on the downstream measurements, experiments and analyses were conducted to 1) determine size-dependent sampling line transport efficiencies; 2) examine particle formation and growth within the 30-m sampling lines; 3) determine PM spatial variability across the engine exhaust plane; 4) assess inlet collection efficiency as a function of flow velocity; 5) evaluate particle losses in the 1-m inlet probes; and 6) examine whether samples collected with modified gas inlet probes yield representative PM emission measurements. Important findings include the following.

- After 35 hours of engine testing, up to 50% of particles of all sizes were lost in the long sample transport lines. Apparently the losses were modest initially, but increased in time as soot and other contamination accumulated on tubing walls. Indeed in the longest sampling line, transmission efficiency dropped ~5%/day over the course of the experiment.
- Under relatively cold conditions (~0^{o}C), volatile particle nucleation typically reached an equilibrium between formation and coagulation before reaching the 30-m inlet probe. However, volatile particle mass continued to form during the subsequent 16-second transport time within sampling lines, potentially increasing calculated mass emission indices by 50 to 75% at high engine powers.
- Nonvolatile PM mass and number EIs were fairly stable and equivalent within 4" of centerline, suggesting that single point sampling in that region would yield emission parameters broadly representative (within 20%) of the entire engine.
- At high engine thrust, PM emissions generally increased with freestream-to-sample inlet velocity ratio, Uo/U, suggesting that particle populations were being enhanced by virtual impaction. However, the enrichment trends did not faithfully follow sub-isokinetic flow predictions, and were thus possibly caused by other mechanisms.
- Nonvolatile PM emission indices measured from 30-m samples were systematically higher than measured at 1-m, indicating possible particle loss in the 1-m inlets or transport tubes; thermophoretic deposition and turbulent eddy impaction possibly account for these losses.
- PM emission measurements made on samples collected with a special particle probe and a gas probe with dilution gas introduced 1.5 m downstream typically agreed to within 10%, suggesting that existing gas certification sampling probes used by engine manufacturers may be modified to yield representative particle number, mass and PSD measurements.

APPENDIX P

The sections below describe each of the sampling experiments and include comprehensive discussions of results and possible physical explanations for the observed PM measurements. The last section discusses lessons learned and provides a list of recommendations for future tests and improved sampling strategies.

2.0 INTRODUCTION

The methods used to extract and transport PM samples from gas turbine engine exhaust to remotely located diagnostic instruments can have profound impacts on measured emission parameters. Losses in number and mass can occur through a variety of processes occurring on or within the sampling system including: catalytic oxidation on hot metal surfaces; turbulent impaction on the inlet probe, bends in tubing or abrupt changes in tubing diameter within valves or fittings; turbulent diffusion and inertial impaction to tubing walls; thermophoretic diffusion related to temperature gradients; particle coagulation or agglomeration; electrophoretic diffusion; and sedimentation. PM mass and numbers can also increase from condensation of low volatility gas-phase species onto the surface of existing particles; through homogeneous nucleation to form new ultra-fine-mode particles; or from inertial enrichment linked to sub-isokinetic sampling. Although some of these mechanisms have negligible effects on the submicron particles typically emitted by aircraft or can be avoided by using conductive tubing and valves and by diluting the samples soon after collection, the effects of others can only be dealt with by designing the system to maximize transport efficiency and then conducting careful characterization studies of each implementation to quantify the sampling losses and develop empirical equations for correcting important emission parameters such as number and mass EI.

NASA has sponsored a number of experiments to characterize sampling system effects on aircraft emission measurements. For example, the Aerosol Measurement Workshop (AMW) conducted in 1999 at Langley included sampling of PM emissions from the NASA Langley T-38 to evaluate the efficiency of two aerosol inlets probes of vastly different design (Cofer et al., 2000). Results showed that nanometer-sized particles are easily lost to inlet surfaces if dilution air and wall cooling were not implemented in a careful fashion and that samples should be diluted soon after collection to prevent number losses due to coagulation.

Using lessons learned during AMW and tests conducted in the propulsion test cell at NASA GRC, engineers from Arnold Engineering Development Center (AEDC, Robert Howard, POC) designed an inlet probe that introduced a concentric flow of dilution gas just downstream of the inlet tip; this probe was evaluated in laboratory tests conducted at the University of Minnesota and found to efficiently collect and transport particles in the 20 to 200 nm size range (Anderson et al., 2005, Appendix A). The probe was deployed during the 2002, Experiment to Characterize Aircraft Volatile Aerosol and Trace Species Emissions (EXCAVATE, Anderson et al., 2005), where it was found to produce soot mass EIs that were comparable to those from samples collected 25-m behind the aircraft where flow velocities, temperatures and sample concentrations are much less a problem. Sampling line transmission efficiency tests conducted during EXCAVATE suggested that

particle losses within the sampling system were consistent with predictions of empirical models.

Miniaturized versions of the AEDC "dilution probes" mounted in a muli-tipped rake were used during the Aircraft Particle Emissions Experiment (APEX-1) and were found to collect exhaust particles with reasonable efficiency. However, sample line efficiency tests conducted at the conclusion of the experiment suggested that more than half of the exhaust particles collected from 1-m inlet probes were lost during transport to diagnostic instruments (Wey et al., 2006, Appendix I). Later tests conducted on a similar sampling system deployed during APEX-3 indicated that the losses were modest and well-correlated with empirical model predictions (Anderson et al., 2010).

These conflicting findings motivated NASA to sponsor a series of experiments to investigate sampling system issues. The tests included: 1) an aircraft "start-cart" experiment in April 2006 at LaRC to evaluate probe design and efficiency; 2) a comprehensive line-loss test to assess the transmission efficiency of sampling systems used in APEX-1, APEX-3 and the Joint-Strike Fighter (JSF) emissions test; and 3) a week-long field deployment at NASA GRC to assess probe collection efficiency, sample line transport efficiency and aerosol instrument performance using a Learjet as the particle source. Results of these experiments were summarized and presented at the 2007, American Association for Aerosol Research annual meeting in Reno, Nevada and are available in presentation form from the author of this report. Important conclusions drawn from these experiments include the following.

- Sample transport lines should be as short in length as possible and constructed of conductive tubing with relatively large ID to minimize pressure drop and diffusive losses.
- Sample line bends and connections should be minimized.
- Line losses are best determined by flowing monodisperse test particles down the lines and measuring particle concentrations on the up- and downstream ends of the line with a single, pressure-corrected condensation particle counter. The use of polydisperse particles with a single set of diagnostic instruments is only acceptable for quick integrity checks.
- Actively heating sample lines appears to lower transport efficiency by 10 to 20%—the explanation for this is not obvious, but may relate to thermophoretic losses caused by temperature gradients in the lines.
- For most practical sampling systems, loss of < 20 nm diameter particles is severe, but loss of 20 – 300 nm particles is modest and can generally be predicted using empirical models.
- Losses inside the specially-designed "dilution-probes" are modest at low to mid power settings; losses are negligable at high power.
- Immediate dilution of exhaust sample at the inlet tip with ten-fold dilution with dry N_2 is the best approach for preserving particle size distributions and avoiding condensation of volatile aerosol precursors within the sampling lines.
- It may be possible to use gas probes if inlet diameters are reduced to eliminate probe tip stagnation and dilution gas is introduced within 1 second after the sample collection to prevent particle coagulation.

- Water cooling requirements are unclear, but only appear to be necessary for sampling low-bypass and military-type engines which exhibit extremely high exhaust gas temperatures.
- The optimum inlet probe design is still an open question. However, for purely research venues, use of AEDC dilution probes is recommended to maintain consistency with previous data sets.

These recommendations were taken into consideration in designing and implementing the PM sampling system used in the NASA-sponsored Alternative Aviation Fuel Experiment (AAFEX). This mission was conducted at the Dryden Aircraft Operations Facility in Palmdale, California during January 2009 and sought to assess the impact of synthetic fuels on the NASA DC-8 aircraft's operations and emission performance and to examine the effect of ambient temperature, fuel composition and plume age on volatile aerosol formation in downwind exhaust. To address project objectives, a rather complex set of rakes, inlet probes and corresponding sampling lines were installed 1 and 30 m behind each inboard engine. The left and right 1-m rake bodies supported multiple "gas" and "particle" sample inlet probes mounted on 1.25-inch centers and were cooled using high pressure water flow. Sufficient dry N_2 gas was delivered to the 1-m particle probes to maintain sample CO_2 concentrations around 2000 ppm, which is a factor of 10 or more less than typical values measured in core flow at the exhaust plane. Sampling inlets were connected to a central sample distribution manifold using tubing of varying diameters, lengths, and surface composition.

This report presents results from a number of tests or analyses that were conducted to characterize and assess the collection and transmission efficiency of the AAFEX exhaust sampling systems. We begin in section 3.0 by discussing results from a comprehensive "line-loss" experiment that was conducted on February 2, at the conclusion of the experiment when the sampling lines had already been used in over 35 hours of engine testing. We show size-dependent line penetration curves and compare them to empirical model predictions and examine how observed emission parameters changed in time as tubing walls became coated with soot and other condensed material. In section 4, we compare PM measurements made in an enclosure mounted behind the right 30-m inlet with an identical set of measurements made on samples collected from the standard 30-m probe and transported through over 30-m of tubing. We continue by examining the variation of emission parameters across the #3 engine exhaust plane (section 5) and by assessing the impact of flow velocity changes on measured PM emission profiles (section 6). Section 7 includes a comparison of nonvolatile PM measurements made using the 1 and 30-m inlet probes. We conclude by assessing efficacy of using gas probes, as opposed to dilution probes, to collect exhaust at the 1-m sampling position.

3.0 ASSESSMENT OF SAMPLING LINE EFFECTS

Figure 1 shows an aerial photograph of the AAFEX experiment site with red lines representing the sampling lines that connected the right and left 1- and 30-m (R1, L1, R30 and L30) inlet probes to the common sample distribution manifold located in the MST trailer. Table 1 lists the tubing diameters, lengths, volumes and calculated

residence times for each sampling line; corresponding Reynolds numbers are not given, but were calculated to exceed 4000 in all tube sections under typical sampling conditions. The list includes the dimensions of all elements within the flow path. For example, for L1, sample first passed through a 0.04 inch inside diameter (ID) inlet probe for a distance of 2 cm, then into a 1.53 m, 0.25 inch ID transport line to the base of the sampling stand. From there it was carried through a 1.94 m length of 0.31 inch ID tubing to a 0.56 inch ID, 0.03-m long fitting then through a 1.33-m long stretch of 0.31 inch ID tubing as it arrived and passed through the 6-port aerosol sample selection box. Output from the left 1-m valve box then passed through 35.45 m of 0.62 inch ID stainless tubing before reaching the sample selection box in the MST trailer. Overall, the L1 sampling line was 40 m long and had a 8.4 liter volume that, assuming piston flow, took 6.75 seconds to flush at a flow rate of 75 L min^{-1} (lpm). From Table 1, we see that the overall line lengths varied from 24 to 46 m with corresponding calculated sample residence times that varied from 3.8 and 7.2 s. Overall residence times measured between inlet tips and diagnostic instruments located in the equipment trailers were about a factor of two longer at typical flow rates, most likely due to the added tubing lengths required to transport sample from the MST trailer to the individual experiment stations.

Figure 1. DC-8 with red lines superimposed showing the four sampling lines used to transport exhaust from the 1- and 30-m inlets to the sample distribution manifold located in the MST trailer.

The sample lines used during AAFEX were primarily constructed from electro-polished, seamless stainless steel tubing. However, several 20-foot lengths of ¾-inch OD conductive PTFE tubing were used in the 30-m sampling lines and in the 1-m trunk lines between the left and right 1-m, 6-port valve boxes and the MST trailer; laboratory tests conducted prior to the field deployment indicated that clean, carbon-impregnated PTFE and stainless steel have equivalent particle transport characteristics. All tubes, regardless of composition, were cleaned and blown free of particle contamination before installation. Tests were conducted before and during the engine runs to verify that the sampling lines were leak-tight and yielded low particle counts when transporting filtered air.

Table 1. Characteristics of aerosol sampling lines.

Left 1 M Line				
Line Inner Diameter (in)	Line Length (m)	Tube Volume (L)	Residence (s) 75 lpm	Residence (s) 125 lpm
0.04	0.02	0	0	0
0.25	1.53	0.05	0.04	0.02
0.31	1.94	0.09	0.07	0.04
0.56	0.03	0	0	0
0.31	1.33	0.06	0.05	0.03
0.62	35.45	6.9	6.58	3.95
Totals	40 meters	6.9 liters	6.75	4.05

Right 1 M Line				
Line Diameter (in)	Line Length (in)	Tube Volume (L)	Residence (s) 75 lpm	Residence (s) 125 lpm
0.04	0.02	0	0	0
0.25	1.55	0.05	0.04	0.02
0.31	1.84	0.09	0.07	0.04
0.56	0.03	0	0	0
0.31	0.54	0.03	0.02	0.01
0.62	19.92	4.8	3.7	2.22
Totals	24 meters	4.8 liters	3.8 seconds	2.3 seconds

Left 30 M Line				
Line Diameter (in)	Line Length (in)	Tube Volume (L)	Residence (s) 75 lpm	Residence (s) 125 lpm
0.62	46	9.03	7.23	4.34
Totals	46 meters	9.0 liters	7.2 seconds	4.3 seconds

Right 30 M Line				
Line Diameter (in)	Line Length (m)	Tube Volume (L)	Residence (s) 75 lpm	Residence (s) 125 lpm
0.62	38.2	7.44	5.95	3.57
Totals	38.2 meters	7.4 liters	6 seconds	3.6 seconds

Sampling line transmission efficiencies were calculated using the UTRC empirical aerosol transport model, which includes terms for thermophoretic, diffusional, electrostatic, and inertial losses; results spanning the particle size range for aircraft

emissions are shown in Figure 2. Turbulent diffusion is obviously the most important loss mechanism, particularly for aerosols smaller than 100 nm in diameter, and is the reason the line transport efficiencies drop to ~50% at around 10 nm. Thermophoretic and electrostatic losses are negligible in the unheated, electrically conductive sampling lines. Inertial losses are small, but more important in the 1-m lines which have significantly more bends and abrupt diameter changes. The overall model results suggest that transmission losses should be relatively small and comparable for each of the four sampling lines.

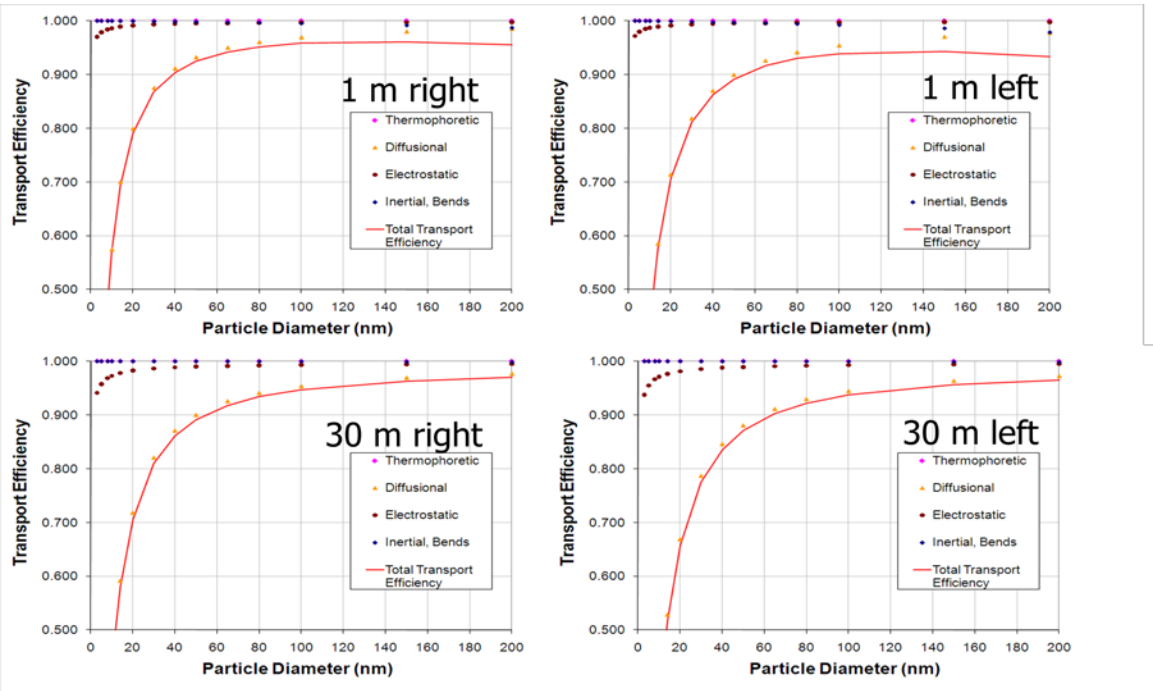

Figure 2. Penetration efficiencies of AAFEX aerosol sampling lines calculated using the UTRC aerosol transport model (Liscinsky et al., 2010).

Experimental assessments of sample line transport efficiency were conducted on the day following the last engine run (February 2, 2009). Our approach was to generate a series of mono-disperse particles and use identical sets of diagnostic instruments to measure their concentrations on the up- and downstream ends of each sample lines; the ratio of the two measurements at each size diameter yielded the particle penetration function. Figure 3 shows the experimental apparatus used to perform this task. Its primary components were: a tube furnace to generate NaCl particles; a differential mobility analyzer (DMA) to select a narrow size range of the NaCl particles; an ejector to draw constant sample flow through the DMA then dilute and inject it into the sampling line; and identical sets of pressure transducers and particle counters to measure pressure and particle number density on the up- and downstream ends of the sample line. Particles were generated by passing filtered air over a small ceramic boat filled with NaCl crystals that was inserted into the mid-section of the tubular furnace. The furnace temperature was adjusted between 590 and 800 ^{o}C to produce NaCl PSDs that best fit the size range of interest. The DMA was a custom-made, high flow (up to 40 lpm sheath flow) unit constructed by MST and operated with a sample-to-sheath flow ratio of 8. Total flow

through the ejector (Fox Valve, Mini Eductor) was monitored with a mass flow meter and set using a two-stage pressure regulator on the high-pressure N_2 gas supply. A small needle valve installed on the vacuum input of the ejector was used to adjust the monodisperse sample flow from the DMA. Ejector output was plumbed into the aerosol sample distribution manifold located in the MST, then sample inlet selection valves were alternately opened to force test aerosols through each of the sampling lines. Total test particle flow rate was set to around 70 lpm to match typical flow rates encountered during the engine tests. The CPCs (TSI model 3010) and pressure transducers were teed into the common sample distribution manifold (i.e., the input end of the sample lines) and into the downstream end of the line under test. In bench tests the pressure transducers agreed to within 0.5 mb and CNC units to within 3% across their full dynamic range of concentrations.

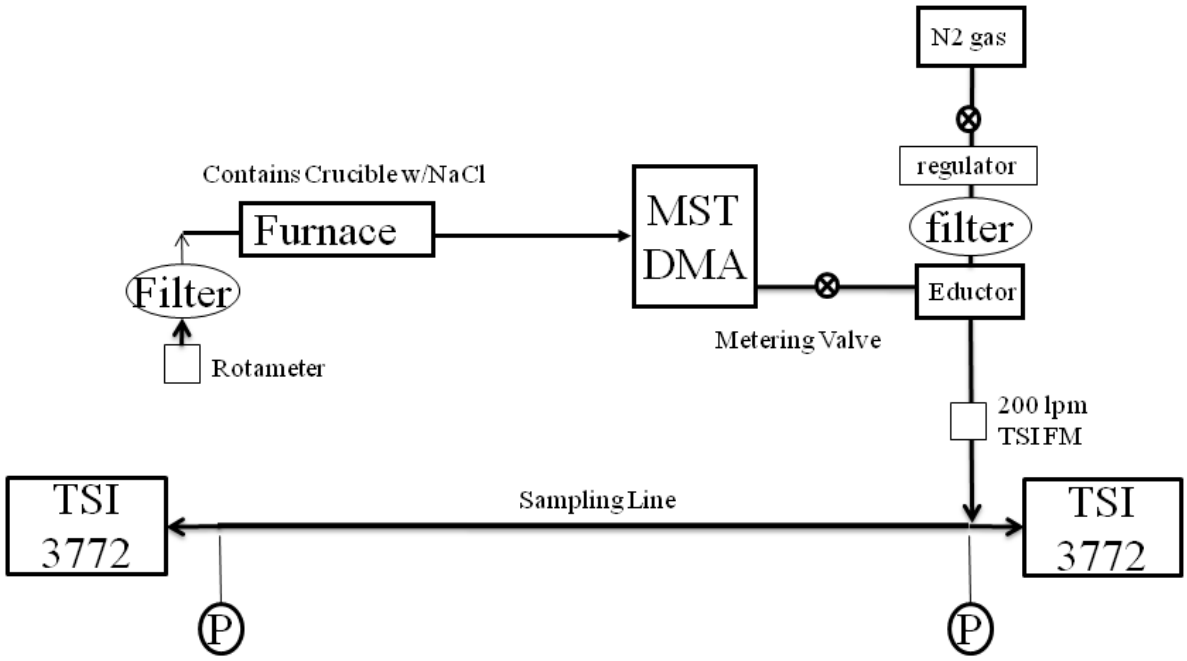

Figure 3. Instrument setup used to assess sampling line transport efficiency.

A team of three researchers performed the line penetration measurements, with one operating the particle generation system and the other two stationed at either end of the selected sampling line to read and record particle concentration and sample pressure measurements. Digital output from the CNCs were also fed through 100-foot long RS232 cables and recorded on a central computer. The procedure involved selecting a particle size and then recording about 2-minutes of data once particle concentrations had stabilized. Duplicate sets of measurements for particle sizes of 10, 15, 20, 30, 50, 75, 100, 150, and 200 nm were recorded on each sampling line. Particle counts were subsequently corrected for pressure and the downstream:upstream ratios were plotted versus particle diameter to reveal the penetration functions.

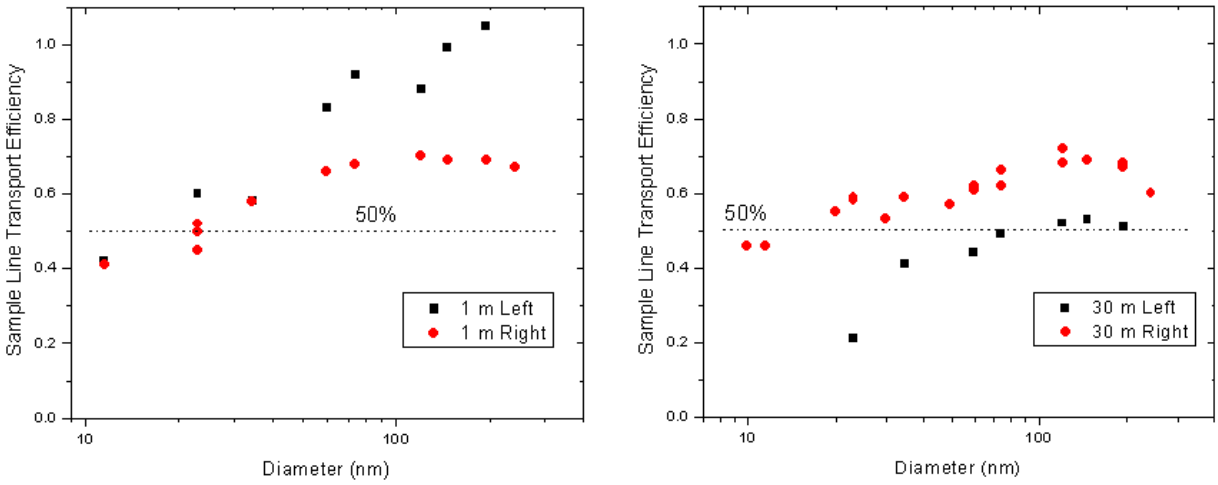

Figure 4. Sample line transport efficiency as a function of particle diameter measured using the apparatus shown in Figure 3 for each of the 4 primary aerosol sampling lines.

Test results for the 1- and 30-m sampling lines are shown in the respective left- and right-hand plots in Figure 4. Error bars are not shown but are on the order of ±10% and ±5% for particles in the 10-20 and 30-200 nm size ranges, respectively. Note that, except perhaps for L1, each of the lines exhibit much lower transport efficiencies at all sizes than calculated with the UTRC model (Figure 2). L30 exhibited particularly severe losses and the penetration of 100-200 nm particles through 3 of the 4 lines were extremely low, which cannot be explained by loses due to inertial deposition. Overall these results were unexpected and conflicted with our careful assessments of particle penetration through the APEX-3 sampling lines, which fit model predictions within experimental error. However, the APEX-3 lines were all stainless steel and had been cleaned just prior to the transport efficiency evaluations. As we note above, the AAFEX line-loss tests were conducted after the 35 hours of engine emission tests had been completed.

Indeed, there is evidence that sampling line efficiency decreased over the course of the experiment as low volatility gases and aerosols accumulated on tubing surfaces. Figure 5 shows normalized BC EI as measured on L30 plotted as a function of experiment day, with day 0 corresponding to the mapping test that was conducted on January 26. The BC values were obtained by dividing the 65 and 85% EI_{bc} data by corresponding data obtained during the first set of experiments. The plot has a slope of -0.05, which suggests that the sampling line transport efficiency decreased 5% per day. The data also suggest that after 7 consecutive days of use, the line was removing about half the material being transported through it, which is consistent with the efficiency assessment shown in Figure 4. Interestingly, the biggest drop in transmission occurred between day 5 and 7. Based on a general realization that the 30-m lines were becoming dirty, we flushed both out with tap water for approximately 15 minutes on the afternoon of Saturday, Jan 31 (day 5) and then used a vacuum pump to draw approximately 25 lpm ambient air through them until testing resumed on Monday, February 2. Apparently this "cleaning" led to further loss of transmission efficiency.

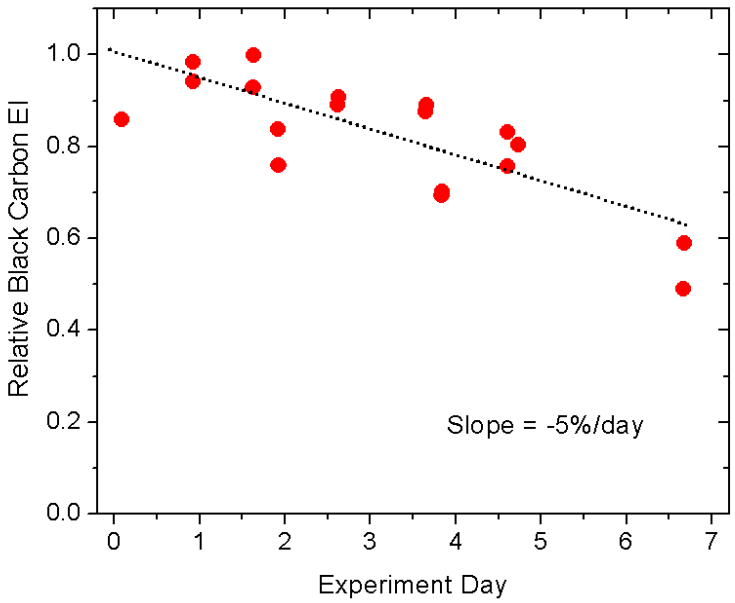

Figure 5. Apparent change in black carbon EI of the #2 engine over the course of the experiment.

Re-examining Figure 4, we see that the efficiency trends for the lines are L1 > R1 ~ R30 > L30. Interestingly, the total "official" sampling times for the lines were: L1=2.0 hrs; R1=9.2 hrs; L30=4.2 hrs; R30=6.2 hrs, which suggests that if the losses were caused by increasingly dirty tubing, the order should be L1 > L30 > R30 > R1. However, the left engine always burned JP-8 (35 hrs), whereas the right burned JP-8 (~24 hrs) and some combination of alternative fuel for the remainder of the time. Another complication is that, to prevent sample stagnation and reduce the time needed to establish stable constituent concentrations, the sample selection box located in the MST trailer was designed to draw a low flow of diluted exhaust air through each unused sampling line at all times during the tests. To accomplish the task, R30 and L30 were coupled to a vacuum pump through critical flow orifices such that ~25 lpm of inlet air was drawn through each line throughout the day, regardless of whether the engines were running or if the lines were selected for sampling. Thus, if background aerosols contributed significantly to the line degradation, we would expect that the ratio of the transport efficiencies for L30 and R30 should roughly equal the inverse ratio of their lengths. The actual L30:R30 efficiency ratio for the 75-250 nm diameter range is ~1.25 and the inverse length ratio is 1.2, a little bit smaller but in the right range. It is likely that the added hours of drawing JP-8 emissions through L30 can account for the difference.

Regarding the efficiency differences in R1 and L1, during engine runs equal amounts of dilution air (enough to satisfy the 70 lpm combined demand of AAFEX participants) was delivered to the 1-m dilution probe tips at all times, again to prevent stagnation and reduce response time. Diluted sample air was then drawn through the transport lines back to the sample selection box, either by the combined vacuum produced by participants' diagnostic instruments, or, for the unselected line, by a small vacuum pump located in the MST trailer. At engine powers >30% the required dilution gas flow rates

were so high that the "selected" sampling line had to be vented to the atmosphere to prevent over-pressurizing sensitive diagnostic instruments. The unselected 1-m sampling line was not vented, so it is likely that dilution gas was being blown out the inlet tip (i.e., the lines were being more or less purged) in high thrust conditions. Other factors may have contributed L1's higher relative transmission efficiency: the left engine was never sampled at 100% power and the right engine was "officially" sampled at 85% power and above for 141 minutes as opposed to 13 minutes for the left engine. R1 was probably a lot dirtier by the end of the mission than L1 and hence should have exhibited much lower transmission efficiencies, which indeed was the case.

The above discussion establishes that accumulation of particles and perhaps low volatility gases on the inside surfaces of the sampling lines produced corresponding reductions in particle transport efficiency. A number of questions now arise including: just how dirty were the lines and by what mechanism did this "dirt" influence transport efficiency?

Consider L30: if we assume an average mass transmission efficiency of 75%, an average exhaust-plume soot mass loading of 50 mg m^{-3}, and an average sample flow rate of 40 lpm over the 35 hour testing, we calculate that approximately 4.2 g black carbon accumulated in the tube over the course the experiment. The deposited mass of volatile aerosols and gases and dust may have been several times higher, but is difficult to quantify. This BC coating amounts to ~184 σg cm^{-2} if evenly distributed over the surface of the 46-m long, 1.6-cm diameter line. If we assume an aerosol mass density of 1 g cm^{-3}, the depth of the deposited material would be 0.184 mm, which would reduce the inside tubing diameter by ~0.02%. Let us examine how this might affect particle transmission efficiency.

The UTRC transport model predictions presented in Figure 3 are valid for clean, conductive smooth-bore tubing at operated at 70 lpm flow rates at 293 K and 1 atm. Losses due to turbulent diffusion, turbulent inertial deposition, thermophoretic effects and electrostatic interactions are taken into consideration. Deposition of dirt on the tubing walls increases surface roughness and reduces tubing diameter and surface conductivity, which can potentially influence all but the thermophoretic effect loss process included in the model.

First examining diffusion, Hinds (1982) gives the following equation for fractional particle loss (η_d) in turbulent pipe flow:

$$\eta_d = \exp\left[-4 \cdot V_d \cdot L/_{d \cdot v}\right] \qquad (1)$$

where v is flow velocity, L and d are the respective pipe length and diameter, and V_d is the deposition velocity given by:

$$V_d = 0.04 \cdot \left[{}^{\nu}/_{Re^{1/4}} \right] \cdot \left[{}^{\rho \cdot D}/_{\nu} \right]^{2/3} \quad (2)$$

where ρ and ν are respectively air density and viscosity, Re is the tube Reynolds number and D is particle diffusion coefficient. These equations predict a 6.5% loss of 100 nm particles during transport through a clean L30. Dirty walls could change these results by increasing ν and Re and reducing d. We note however, these parameters cannot be changed independently: a 10% decrease in d produces 10 and 23% increases in Re and ν, respectively. But even these rather drastic changes only produce an additional 0.5% reduction in 100-nm particle transport efficiency. Indeed it would take a 10-fold increase in V_d to decrease L30, 100-nm particle transport efficiency to the level seen in Figure 4; such a change would completely remove particles < 60 nm in diameter from the flow, but would only increase 200-nm particle deposition from 3 to 29%. Thus it appears that the enhanced losses cannot be explained by this mechanism.

Another possibility is that the surface contamination altered the electrical characteristics of the sampling lines and led to increased losses through electrostatic deposition. Gas turbine engine soot emissions can be highly charged and the test aerosols used in the above line-loss assessments were singly-charged NaCl particles. The UTRC model includes terms for particle image charge and space charge effects and the predicted losses for the AFFEX sampling lines are quite small. For example, under typical operating conditions only 1 in 1×10^8, singly-charged, 100-nm particles are lost to L30 tubing walls due image and space effects. The model equations don't consider surface resistance, however. Noting that particle penetration through plastic tubing was often quite poor, Liu et al. (1985) developed an expression for sampling line transmission efficiency (P) that included electric field effects:

$$P = 1 - {}^{A \cdot Z \cdot E}/_{Q} \quad (3)$$

where A is tubing surface area, Z is particle electrical mobility, E is the induced electric field, and Q is sample flow rate. Figure 6 shows results for singly charged particles being drawn through a 46-m long, 1.6 cm diameter line at a 70 lpm flow rate (i.e., typical operating conditions for L30). Note that a relatively small electric field can effectively remove 50% of the100 nm particles in the flow, but at the same time, it completely remove particles smaller than 60 nm. Thus these results do not replicate the size dependent transmission efficiency of L30 depicted in Figure 4. It is also difficult, if not impossible, to induce a constant electric field in even a completely non-conductive tube. Liu et al. (1985) were able to charge Teflon tubing by bending it multiple times before use, but they also noted that the charge gradually bled off within a couple of hours. For AAFEX, it is possible that the PTFE tubing used in some of the lines acquired a charge from vibration during high power engine runs, but this would quickly dissipate through the conductive outer covering when the stimulus was removed. We thus conclude that electrostatic effects cannot satisfactorily explain the reduced transmission efficiencies of the dirty AAFEX aerosol sampling lines.

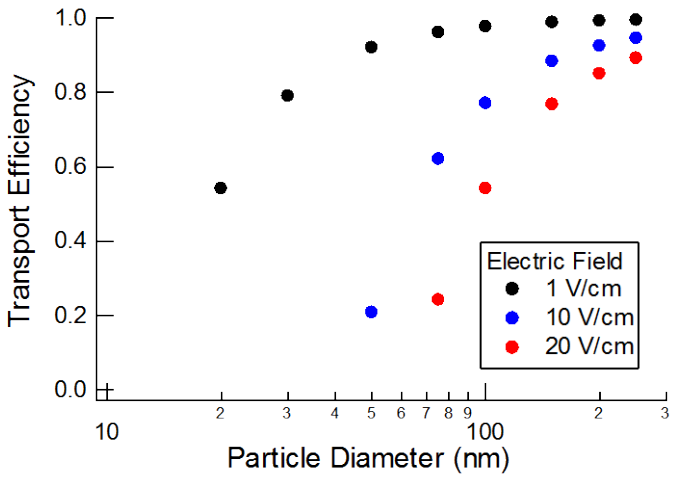

Figure 6. Modeled L30 transport efficiency as a function of particle size for induced electric fields of 1, 10, and 20 V/cm.

Inertial deposition or turbulent eddy impaction is another possible mechanism for removing 100-300 nm particles. Baron and Willeke (2005) give the following expression for particle loss in turbulent flow:

$$\eta_{id} = \exp\left[-4 \cdot V_t \cdot {}^{L}/_{d \cdot v}\right] \quad (4)$$

where the turbulent inertial deposition velocity, V_t, is dependent on the Reynold's number and Stokes number (Stk):

$$V_t = Stk \cdot Re^{3/4} \quad (5)$$

$$Stk = {}^{\rho_p \cdot {d_p}^2 \cdot C_c \cdot v}/_{1.8 \times 10^9 \cdot \nu \cdot d} \quad (6)$$

where ρ_p and d_p are particle mass density and diameter, and C_c is the particle Cunningham Slip Correction Factor, which is a constant for a given particle size and working gas. These equations predict that 1 out of every $1{\times}10^7$ 100-nm particles would be lost during transport through a clean L30. From examining equation 4, we see that the only way to increase η_{id} to 0.5 (i.e., 50% losses) is to increase V_t by 6 orders of magnitude. Working with clean tubing assumptions, this change can only be affected by increasing sample flow velocity to mach 1, particle diameter to 5000 nm, or particle density to a black-hole-like 1200 g cm^{-3}. The alternative is to assume that dirty walls increase surface roughness, effectively increasing V_t by changing the thickness of the viscous sublayer adjacent to the tube wall. Im and Ahluwalia (1989) developed a dimensionless model for turbulent eddy impaction that took into consideration surface roughness induced by accumulation of particles on pipe surface. They indeed showed that V_t increases several orders of magnitude and becomes somewhat independent of

particle size when roughness element heights begin to represent a measureable fraction of the pipe diameter. Application of this model is well beyond the scope of the present study however.

Another way to characterize the impact of surface roughness is to treat the accumulated material on the tubing walls as a highly porous filter. It is possible that the soot was not evenly deposited on the tubing walls, but rather agglomerated to form more sparsely distributed, chain aggregates that would extend through the viscous sublayer near the wall, into the core sample flow. These dendritic structures would then capture additional particles through interception, turbulent eddy impaction, etc., and collectively become an increasingly efficient filter over time (i.e., Kanaoka, 1989). To evaluate the feasibility of this mechanism, let us examine the equation for fibrous filter collection efficiency (E) given by Baron and Willeke (2005):

$$E = 1 - \exp\left[{-4 \cdot \eta \cdot \alpha \cdot L} \Big/ {\pi \cdot d_f \cdot (1x10^{-4}) \cdot (1 - \alpha)} \right] \quad (7)$$

where η is the single fiber collection efficiency, α is filter packing density, L is filter depth, and d_f is the fiber diameter. If we solve equation 7 for $\eta = 0.01$, $d_f = 1$ μm, L = 4600 cm, and $\alpha = 1\times10^{-6}$ we obtain an overall filter collection efficiency of about 50%, which is roughly equivalent to the particle losses through L30. Except for the tubing length, the input values are crude estimates, but the result does show that even slight accumulation of fiber-like materials on tubing walls can significantly reduce transmission efficiency.

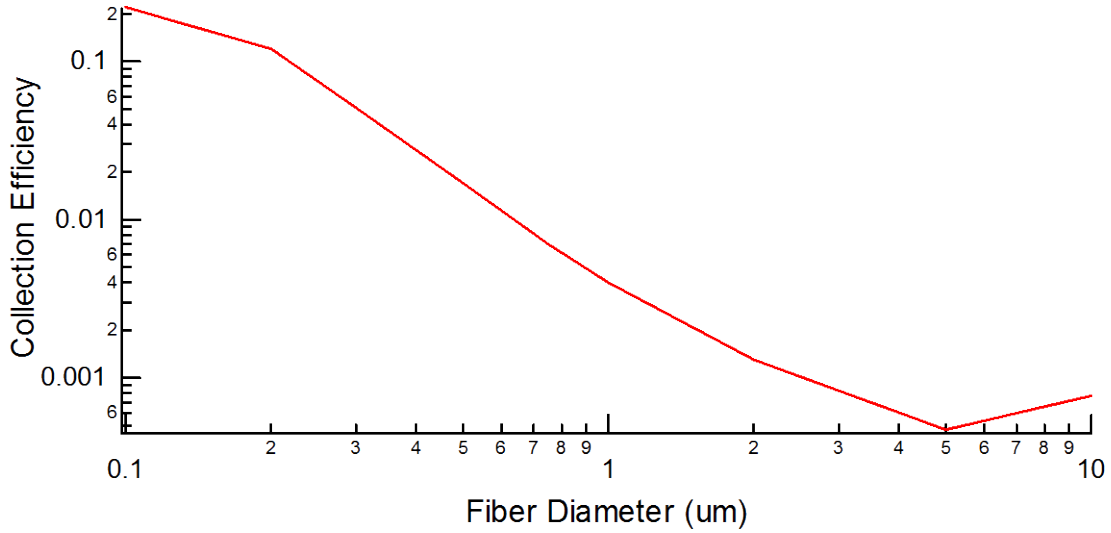

Figure 7. Single fiber efficiency for collecting 100-nm spherical particles.

Equation 7 reveals that overall filter efficiency is highly dependent on individual fiber diameter and collection efficiency. It turns out these two parameters are coupled and also dependent on particle size. Figure 7 shows a plot of collection efficiency versus fiber

diameter as calculated for 100-nm particles, 600 cm s^{-1} flow velocity and constant packing density using empirical equations developed in Baron and Willeke (2005), which include terms for particle loss through diffusion, interception, impaction and gravitational settling. Note that 100-nm diameter fibers such as might be envisioned to form from soot agglomeration are highly efficient at removing 100 nm particles. Figure 8 shows results of additional calculations that were performed to further explore the particle-size-dependent collection efficiencies of individual fibers. Here we varied packing densities and filter thicknesses to obtain efficiencies less than 1 for all cases. It is interesting to note that the smaller the fiber, the more effectively it removes particles in the 100 – 200 nm size range. A close inspection of the filter efficiency equations indicates that this is caused by increased efficiency for particle removal by interception and impaction. The smaller fibers are also less efficient at removing ultrafine aerosols, which is also consistent with the observations presented in Figure 4. It thus appears that filtration by small dendritic structures growing in time on the tubing walls has the potential of explaining the loss of 75 – 250 nm particles in dirty sampling lines. However, more laboratory and theoretical work is needed to better understand the deposition of soot to sampling lines and to develop strategies to minimize its effects on particle transport.

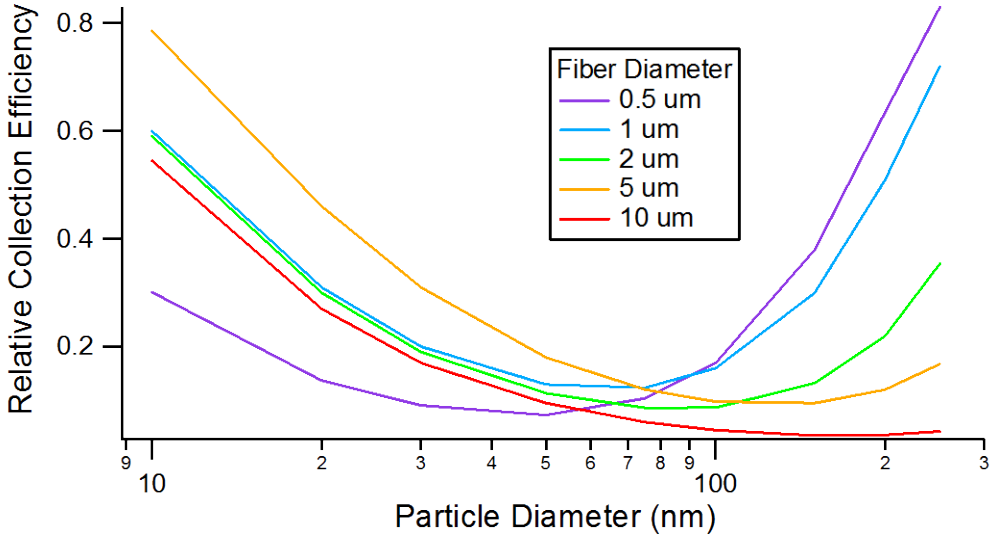

Figure 8. Relative collection efficiency as a function of particle size for 0.5, 1, 2, 5, and 10 µm diameter fibers.

5.0 AN INVESTIGATION OF PARTICLE FORMATION IN SAMPLING LINES

Early investigations conducted to measure aircraft particle emissions at altitude often found that volatile particle number concentrations were greather than soot number concentrations by at least a factor 20 in aged engine exhaust plumes (i.e., Anderson et al., 19978). Modeling studies suggested these nucleation-mode particles are composed of sulfuric acid and perhaps organic species and that they form very rapidly as the exhaust cooled and mixed with background air at cold temperatures. Volatile particles were first

observed in ground-based engine emission studies during the 1999 Aerosol Workshop conducted at NASA LaRC (Cofer et al., 2000); there, samples collected 25 m behind the exhaust of an idling J85-GE engine were found to contain a large numbers of <20-nm aerosols that were not present in samples drawn from a 1-m inlet. Measurements conducted during the EXCAVATE experiment confirmed the rapid formation of volatile aerosols in aging aircraft exhaust plumes and tied both the mass and number of such particles to fuel sulfur content (Anderson et al., 2005). APEX-1 measurements provided more details on exhaust plume sulfate nucleation and revealed that low-volatility organic species and background aerosols were also involved in the condensation process (Wey et al., 2007). Efforts to model volatile aerosol microphysics in ground-based exhaust plumes have exposed a conundrum, however: do the volatile particles form and grow primarily within the engine exhaust plume during its rapid transport (<< 1 sec) from the engine exit to the 30 m sampling probe or during the subsequent 10 to 20 seconds it takes to transport the samples through sampling lines to remotely located diagnostic instruments.

To address this question, AAFEX participants designed a relatively simple experiment that involved placing sensitive aerosol instruments in a sturdy enclosure positioned directly in the plume and subsequently comparing the resulting measurements with data recorded by a similar set of instruments sampling off a long sampling line connected to the R30 inlet. Nicknamed the "death box" because of its precarious position within the engine exhaust plume, the enclosure (Figure 10) was designed and constructed by AEDC and consisted of a 2 inch aluminum angle framework with ¼ inch aluminum sides and top. Death box instruments included a CPC, EEPS and CO_2 analyzer that drew samples through a 1-m long 3/8 inch diameter stainless tube that faced forward and was affixed to the side of R30. Power cables and RS232 signal wires were run out to the box from the NASA truck; data from the instruments were monitored and recorded by an operator sitting in this location. Measurements recorded in the death box were compared with output from a similar set of instruments located in the NASA truck that drew samples from R30 through ~38 m of 0.62-inch ID stainless tubing and 5 m of 0.41-inch ID conductive PTFE. We estimate sample residence times were <0.5 sec and 15-20 sec for the death box (DB) and NASA trailer (NT) sampling lines, respectively. The two EEPS generally agreed to within 10% in number density when sampling from the same aerosol source. The CO2 analyzers were calibrated on a daily basis using the same reference and span gases.

Although simultaneous DB and NT measurements were recorded during many of the 13 engine runs conducted during AAFEX, the results from the morning of Jan 28 shown in Figure 11 serves to illustrate the general findings. During the test which extended from 5:53 to 9:25 local time, ambient temperature increased from -4 to 4^{o}C, winds were steady from the west (i.e., aligned with the longitudinal axis of the aircraft) at 1 to 4 m/s and relative humidity decreased from 70 to 62%. These conditions are known to promote rapid formation of volatile aerosols and as can be seen in Figure 11, this was indeed the case. The two plots show total number and mass EIs versus engine power as measured from the DB and NT; nonvolatile PM number and mass EIs as measured from R1 samples using NT instrument suite are also included. The 1-m data were corrected for

line losses using correction factors derived from Figure 4, R1 data. The NT R30 data set were also corrected, but two cases were examined, one each assuming that 50% (solid blue squares) and 100% (open blue squares) of the transmission line inefficiencies shown in Figure 4 had been incurred by the Jan 28 test date. Assuming that aerosols were neither lost nor formed in the short DB sampling line, several characteristics are apparent from the Figure 11 plots:

- Death box EIn and EIm are larger than the 1 m probe, showing that a large amount of volatile aerosol particles formed in the plume at all engine powers.This indicates that sulfuric acid condensation must proceed on millisecond time scales once the plume temperature decreases below the species boiling point.
- At all power settings, DB number EIs are about the same as corrected NT EIs, indicating that most of the core nuclei are formed before reaching the 30-m aerosol inlet and no new particle formation occurs after this point.
- Mass EIs are larger for the corrected NT than the death box suggesting increasing particle mass in the sample line. This suggests that condensation of material onto existing particles is favored over nucleation. An increasing fraction of volatile aerosol mass is formed in the sampling line as power was increased.

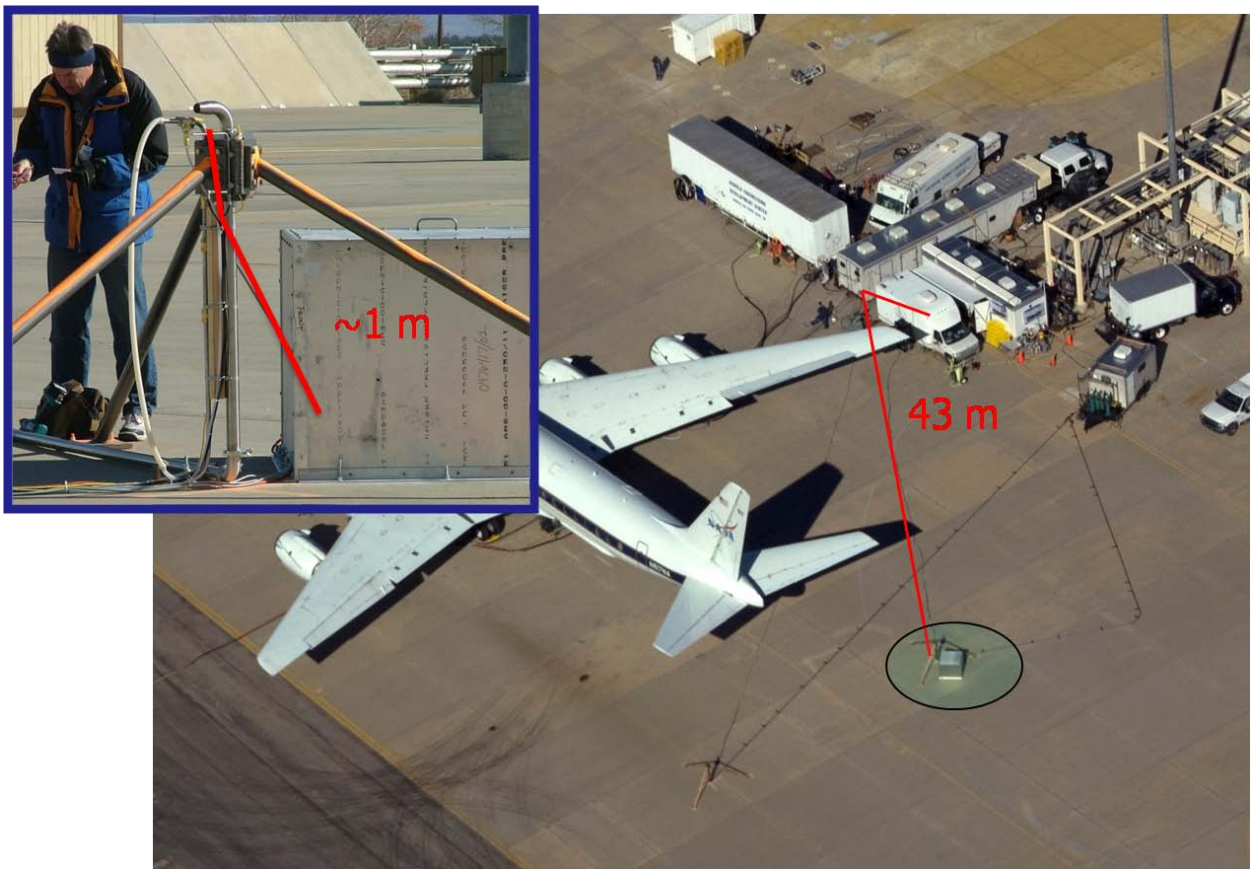

Figure 10. Photographs showing the relative lengths of sampling line used for the aerosol instruments located in the deathbox and NASA truck.

Detailed particle size distributions provide additional insight into the microphysical processes occurring within the plume and sampling line. Figure 11 presents DB and NT particle size distributions (PSDs) plotted in mass EI space to accentuate the modal structure of the emissions. Three versions of the NT data are shown: one with no line loss corrections (solid blue line), a second with 50% of the Figure 4 corrections applied (dashed blue line) and the third with 100% corrections applied (dotted blue line). NT 1-m PSDs are also shown and were corrected for 100% of the Figure 4 R1 losses. In the PSDs, the small-diameter mode represents freshly nucleated volatile aerosols and the larger mode is composed of soot with volatile aerosol coatings. From examining these plots we can make the following observations:

- At idle, nucleation mode particles completely dominate total aerosol number and mass.
- The nucleation mode decreases in total mass and shifts to smaller diameters as power is increased. This may be due to the reduced availability of volatile material, shorter transport times from the engine to the inlet probe, preferential deposition of the volatiles on soot rather than in the nucleation mode, or some combination of these factors.
- Particle mass in the 6-10 nm size range appears to be lost in the sampling lines, either due to turbulent diffusional deposition or coagulation.
- The nucleation mode peak generally shifts to larger sizes and becomes broader during transport through the sampling line. For example, at 65% power the peak shifts from 12 to 15 nm and the total mass at 20-nm increases by a factor of 2 to 4.
- The soot-mode peak in the 30-m total aerosol PSDs always appears at larger diameters than in the 1-m samples. For example, at 30 and 45% power, the 1-m soot mode peaks at 35 nm whereas the 30-m soot mode peaks at ~60 nm in both the DB and NT spectra. Although this may be caused by differential losses between the 1 and 30 m sampling lines, it could be a result of the soot particles becoming coated with volatile material.
- The amount of volatile material condensing in the soot mode appears to increase with power, probably as condensation onto existing particle surface becomes energetically more favorable than forming new aerosols.
- At idle power settings, a volatile mode is present at ~100 nm that does not correspond to the soot mode, but may rather be caused by condensation onto background particles.
- Additional volatile aerosol condenses in both the nucleation and soot modes within the sampling lines.

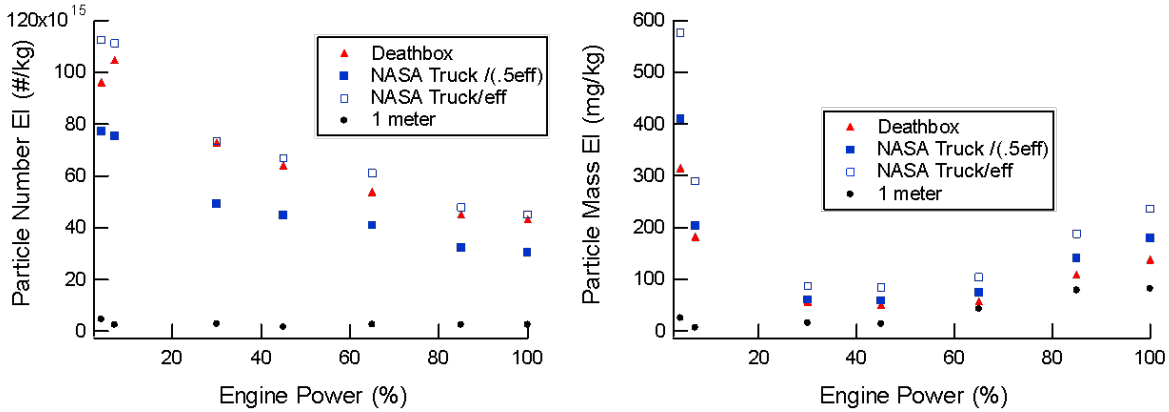

Figure 11. Comparison of death box and NASA Truck particle number and mass EI measurements for the #3 engine as it burned JP-8 fuel under cold ambient conditions. Values from 1-m probe were corrected for line losses using a polynomial fit to data shown if Figure 4. Results from the NT 30-m inlet were corrected for 50% (solid blue squares) and 100% (open blue squares).

Small aerosols are lost to tubing surfaces or undergo coagulation as described in the sample line loss section of this report and those losses somewhat explain why the number concentration at the outlet is less that the measured particle number at the inlet. But significantly there is a large number of small particles present at the inlet. In fact the number of particles at the probe inlet is typically 10 to 20 times higher than the number of particles measured at close to the engine exit (1m) due to nucleation of volatile aerosols in the exhaust plume. In addition the volatile aerosol mass has been reported to be greater than BC mass at the 30m location in some cases. The bottomline is that volatile material is significant at 30m.

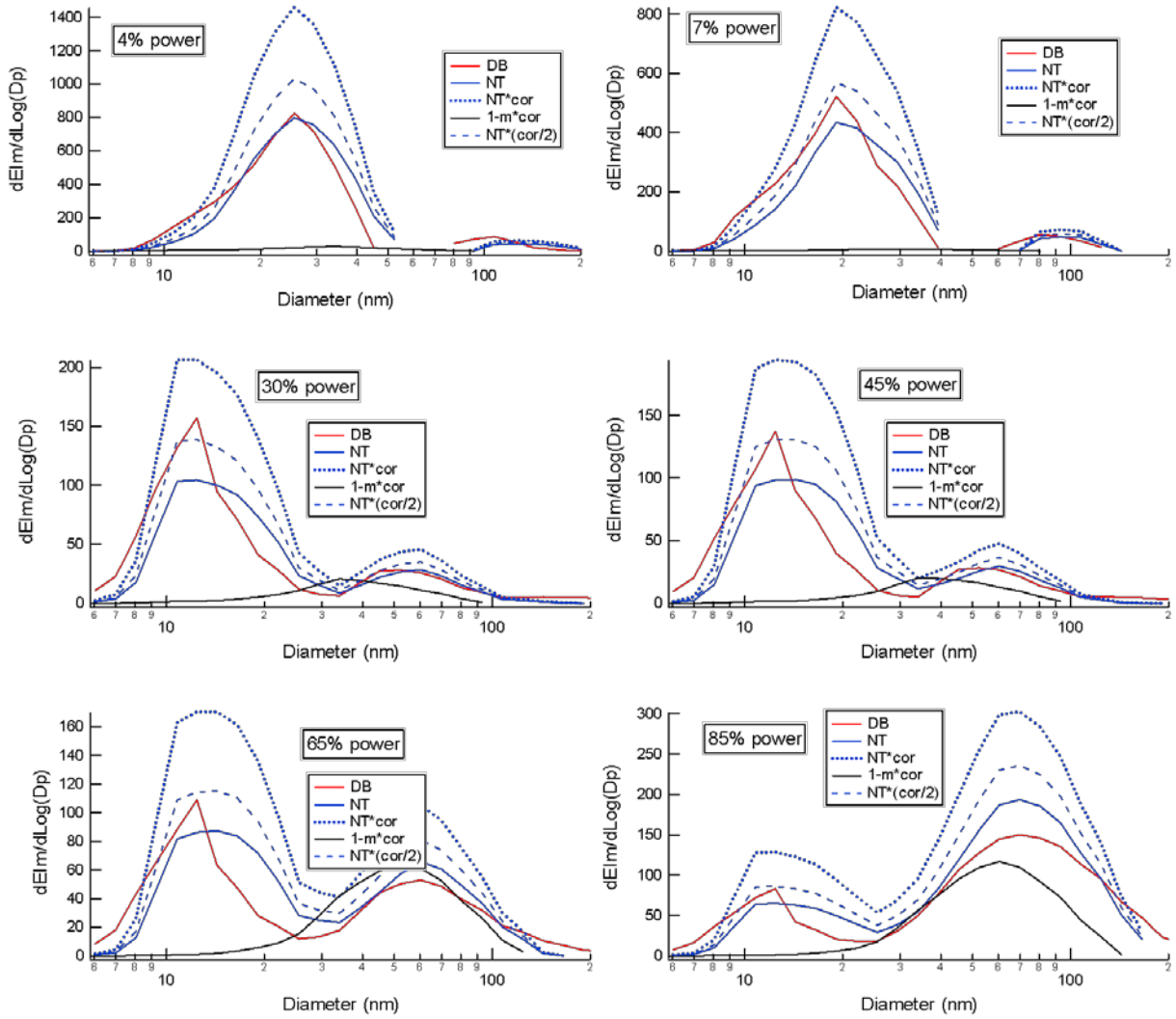

Figure 12. Comparison of mass-EI-based size distributions measured behind the #2 engine on the morning of January 28th as the engine burned JP-8 fuel with 1200 ppm S content. The black lines respresent1-m NT EEPS measurements corrected for particle losses using data shown in Figure 4. Deathbox values (red lines) are presented without any correction. The NT 30-m data are shown without correction (blue line) and with 50 (dashed blue line) and 100% (dotted blue line) of the Figure 4 corrections applied.

The data in Figures 11 and 12 provide evidence that particle number EIs were mostly dictated by processes occurring within the exhaust plume while mass EIs were influenced by condensation occurring within the sample lines. Figure 13 examines these issues in more detail. The plots were generated by correcting the DB and NT EIs for nonvolatile contributions (with 100% R1 line loss corrections) to obtain volatile EIs and then allowing DB values to represent the EIs at the 30-m inlet tip. The points are essentially given by 100* (DB/(NT*line-loss correction)). With no corrections applied, we see that ~180 to 200% and 80 to 120% of the aerosol number and mass emissions, respectively were present at the 30-m inlet tip. Conversely, if we apply 100% of the Figure 4 line-loss corrections we estimate that 90-100 and 20-60% of the respective volatile aerosol number and mass formed in the plume. If we assume the 50% R30 line loss correction

is more representative of particle mass transmission half-way through the mission, we conclude that, depending on power (which is inversely related to plume residence time), from 10 to 60% of the volatile mass formed in the sampling line. Thus sampling line effects clearly have to be taken into consideration if a standard is ever established for aircraft volatile aerosol emissions.

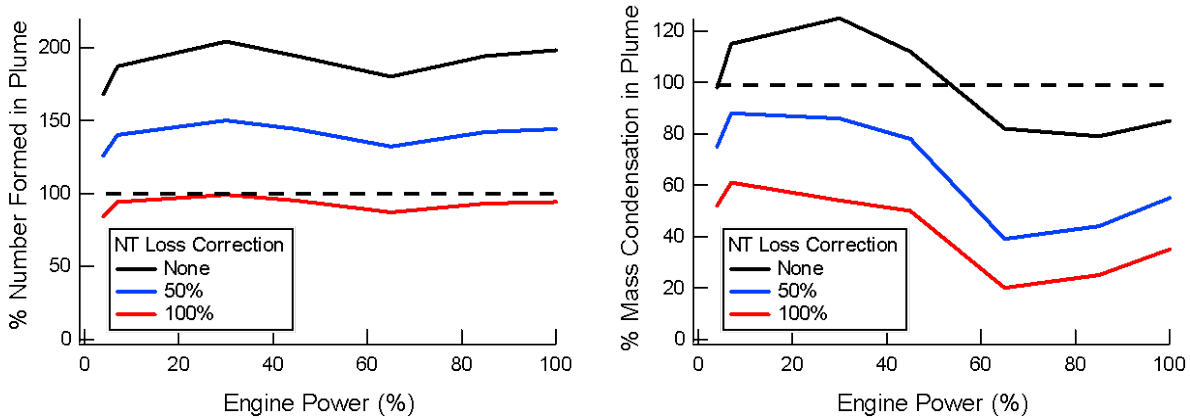

Figure 13. Percentage of volatile particle number and mass formed in exhaust plume as a function of power calculated by correcting for nonvolatile particle number and mass emissions and applying 0 (black line), 50 (blue) and 100% of the R30 line loss corrections derived from Figure 4 data.

5. DISTRIBUTION OF EMISSIONS ACROSS THE ENGINE EXHAUST PLANE

Current procedures for certifying gas turbine engine emissions require that emission factors be area-weighted averages of measurements made at multiple points across the engine exhaust plane. These measurements are often obtained using multi-tipped sampling rakes mounted on translation stages, which allow complete mapping of exhaust composition at 2-inch vertical and infinite horizontal resolution. Another approach is to use cruciform rakes with arms that span the entire exhaust plane and have inlet tips spaced to draw area-weighted flow into a converging manifold that delivers a single continuous gas stream to diagnostic instruments. In either case, it is very difficult to adapt the existing sampling probes and inlets to introduce clean, filtered gas near the inlet tips to reduce particle concentrations to prevent coagulation and gas-to-particle conversion in sampling lines. A possible alternative is to obtain certification species measurements at multiple points to evaluate the spatial distribution of the emissions, then to make detailed particle measurements at only a single point selected from the gas-phase measurements to represent the entire exhaust plane.

AAFEX evaluated the single-point measurement approach by conducting tests to observe the variability of particle emission parameters as a function of distance from engine centerline. The experiment was performed on the afternoon of January 31 as the engines burned JP-8 fuel in relatively warm and stable conditions. It involved recording 2-3 minutes of data from particle probe #3 with the rake R1 at 8, 4, 2 and 0 inches to the left of the #3 engine centerline. Sample dilution was maintained at a constant rate (when possible) so measured CO_2 mixing ratios could be used to assess gas-phase homogeneity

across the exit plane. Emission indices were calculated using the coincident CO_2 measurements. Measurements were made at 4, 7, 30, 45, 65, and 85% of maximum rated engine thrust to examine spatial variations in exhaust composition as a function of power.

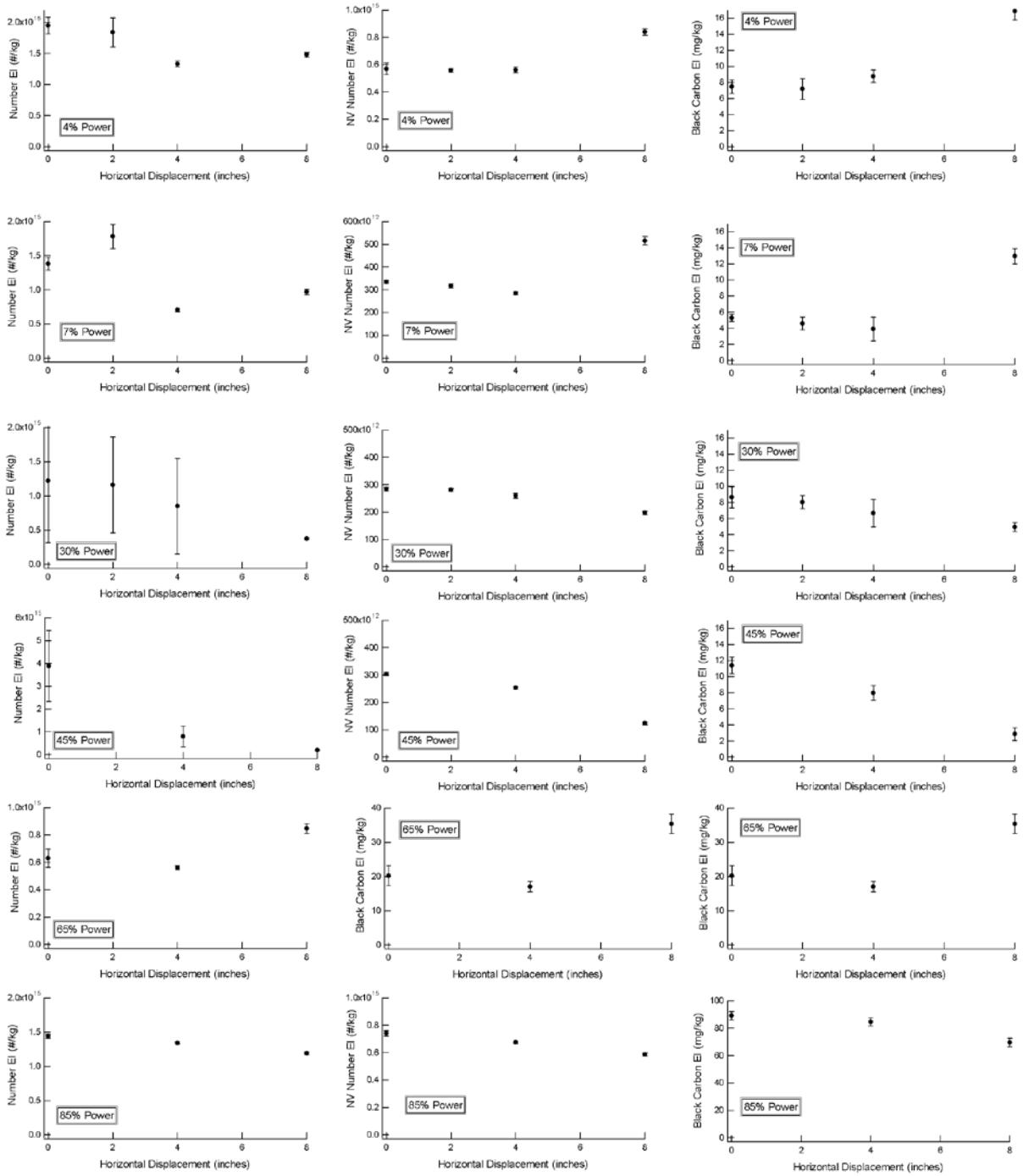

Figure 14. Emission indices for total number density (left column), nonvolatile number density (middle) and black carbon mass (right) at various power settings as a function of

horizontal distance from the #3 engine centerline. Data are averages of time series such as those shown in Figure 15. Error bars represent ±1 standard deviation.

Results are summarized in Figure 14, which shows plots of PM EIs versus horizontal rake offset for the indicated power settings. Measurements of black carbon EI (EI_{bc}), total aerosol number EI (EI_n) and nonvolatile aerosol EI (EI_{nv}) are included. Table 2 provides the relative percentage deviations of these plots; results for simultaneous CO_2 measurement are also included to allow for an assessment of gas-phase species variations across the exhaust plane. PM emissions were much more variable across the exit plane at all power settings than CO_2. For example, discounting the 30% power point where sample dilution was changed during the engine transect, CO_2 deviated 2.1 to 7.9% across the power range whereas EI_{bc}, EI_n and EI_{nv} varied by 13 to 63%, 10 to 122% and 12 to 41%, respectively. For EI_{bc} and EI_{nv} changes that occurred between the two outermost sampling locations were in general responsible for these large deviations. For example, at 65% power, both these parameters increased by a factor of two when the rake was moved outward from 4 to 8"; a similar trend was observed for 4 and 7% thrust. At 30, 45 and 85% power, the nonvolatile parameters decreased slightly when the rake was repositioned from 4 to 8". The source of these variations is not clear.

Table 2. Percentage deviation of emission parameters as a function of engine power and horizontal distance from the engine centerline.

Engine Power	Carbon Dioxide		Black Carbon		Total Number		Nonvolatile Number	
	0 - 8"	0 - 4"	0 - 8"	0 - 4"	0 - 8"	0 - 4"	0 - 8"	0 - 4"
4	5.4	1.4	45	11	18	19	22	1
7	5.1	0.7	63	15	39	42	29	8
30	*	0.9	23	13	43	18	16	5
45	4.1	0.9	58	25	122	93	41	13
65	7.9	0.5	41	12	22	8	19	5
85	2.1	1.3	13	4	10	5	12	6

*Dilution flow changed during horizontal scan.

Note that EI_n exhibited the most overall variability, particularly near the engine center line. The cause for this is revealed in Figure 15, which shows a time series of total (cold CN) and nonvolatile (hot CN) aerosol number densities recorded at 30% engine power as the rake was moved inward, pausing at each of the 4 sampling locations. Beginning at 4", high frequency spikes were imposed on the cold CN baseline; these increased in frequency at the 2" and 0" sampling locations to the point that the signal never returned to the baseline value. In contrast, the hot CN measurements were steady throughout the time period, indicating that the cold CN fluctuations were driven by nucleation of volatile material either in the exhaust plume or within the long sample transport lines. The source of this material was most likely an engine oil leak known to the aircraft maintenance crew. However, it is also possible the oil mist emanated from the engine's central vent tube, which is used to vent the turbomachinery to the atmosphere. In any case, these emissions caused EI_n to be a poor proxy for black carbon number emissions, particularly near the engine centerline and at medium power settings.

The PM emissions were more uniformly distributed across the exhaust plane at higher engine powers. For example, all emission parameters varied less than 15% across the entire transect at 85% power. Conversely variability maximized at 45% thrust, where EI_{nv} exhibited the least horizontal deviation at 41%. For EI_n, this spatial variability was caused by the aforementioned oil leak; the source of the variation in EIbc and EInv is not known, but may be due to fuel-to-air ratio variations within the combustor.
Reviewing the Figure 14 and Table 2 data, we can draw these conclusions regarding the representativeness of single point PM emission sampling:

- Nonvolatile emissions are relatively well mixed within a 4" radius of engine centerline. For example, deviations in EI_{bc} and EI_{nv} measurements made within this exhaust region respectively ranged from 4 to 25 and 1 to 13% over the entire power range, which should be acceptable for most purposes.
- Collected samples should be thermally treated to remove volatile material before particle number and size distribution measurements are recorded. Condensation of oil and other precursors within the sampling stream can cause aerosol parameters to be quite variable and significantly elevated above measurements provided by instruments operating with thermal denuders.

We caution, however that these observations are valid for the NASA DC-8's #3, CFM-56 engine as it was operating on the afternoon of January 31, 2009. Additional measurements recorded across the exhaust planes of a variety of commercial aircraft engines are required to further establish the viability of this measurement approach.

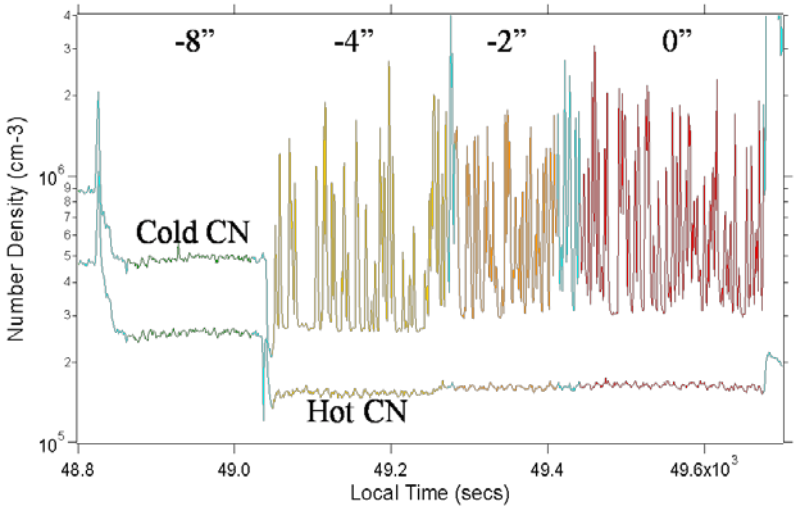

Figure 15. Time series of hot and cold particle number densities measured from particle probe 3 on R1 at 30% engine power as the rake was translated in 2" increments from 8 inches to the left of center to engine center. The apparent decrease in CN number density at 49030 seconds was caused by an increase in sample dilution. The factor of 2 difference in cold and hot CN values at -8" are mostly caused by particle losses in the thermal denuder and differences in the lower size sensitivities (5 versus 8 nm) of the two particle counters for used for the measurements.

APPENDIX P

7.0 EFFECTS OF SUB-ISOKINETIC SAMPLING

Previous studies have shown the importance of matching aerosol inlet velocity with free stream velocity (known as isokinetic sampling) to avoid inertial enrichment or depletion of large aerosol particles in the collected sample flow. This is particularly true when sampling from aircraft where inlet and free-stream velocities can be mismatched by more than 100 m s^{-1}. Some researchers capitalize on this effect by operating aerosol inlets at very high ratios of free-stream velocity (U_0) to tip velocity (U) to enrich large particles in the collected sample stream; enhancement ratios of 10 are easily obtained for particles larger than 5 μm in aircraft sampling applications. These virtual impactors (VI) can also be operated with filtered gas blowing gently out the inlet tip to prevent penetration of background air and small particles, while allowing particles with significant inertia to be collected. Known as counter-flow virtual impactors (CVI), these inlets are primarily used for sampling cloud droplets and ice particles from airborne platforms, but are also available for coarse-mode particle sampling in ground-based applications.

Essentially all the studies examining isokinetic inlet effects have focused on super-micron sized particles while few if any have examined inlet velocity effects on submicron aerosol collection. However, theoretical studies suggest that these are subject to anisokinetic sampling errors under some conditions. For example, Hangal and Willeke (1990) derived the following expression for inlet aspiration efficiency (η_{asp}) based on laboratory studies:

$$\eta_{asp} = 1 + \left[\left({}^{U_0}/_{U}\right) \cdot \cos\phi - 1\right] \cdot \left[3 \cdot \mathrm{Stk}^{\left({}^{U}/_{U_0}\right)^{-1/2}}\right] \qquad (8)$$

Where ϕ is the angle between the inlet longitudinal axis and the free stream flow direction, and Stk is Stokes number as defined in equation 5. The expression was validated for Stk values between 0.01 and 100 and for U_0/U ratios between 0.01 and 10. Figure 16 shows η_{asp} values calculated from equation 8 for spherical particles with mass densities of 1.5 g cm^{-3} assuming parameters representative of AAFEX sampling at high engine thrust (a 1 mm inlet diameter, free-stream velocity of 400 m s^{-1} and temperature of 350^{o}C).

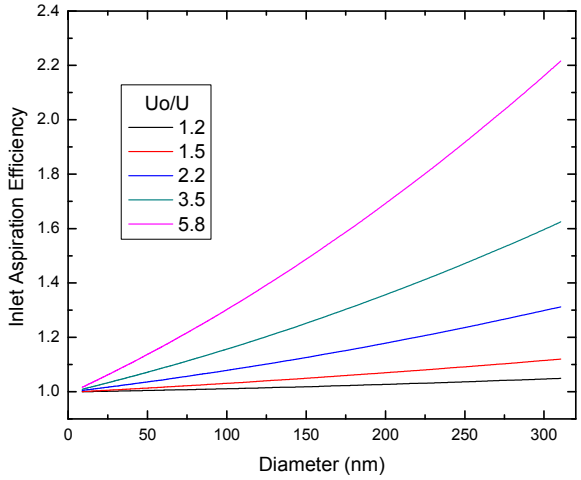

Figure 16. Results of calculations showing the potential enrichment or depletion of particles in samples collected using inlet velocities that are significantly mismatched with the exhaust stream velocity.

From reviewing Figure 16, we infer that particles in the size range of those emitted by aircraft engine can be substantially enriched if inlet and exhaust stream velocities aren't controlled to within a factor of two under high power sampling conditions. The effect, however, should be most noticeable in particle mass, since the enrichment increases exponentially with particle size.

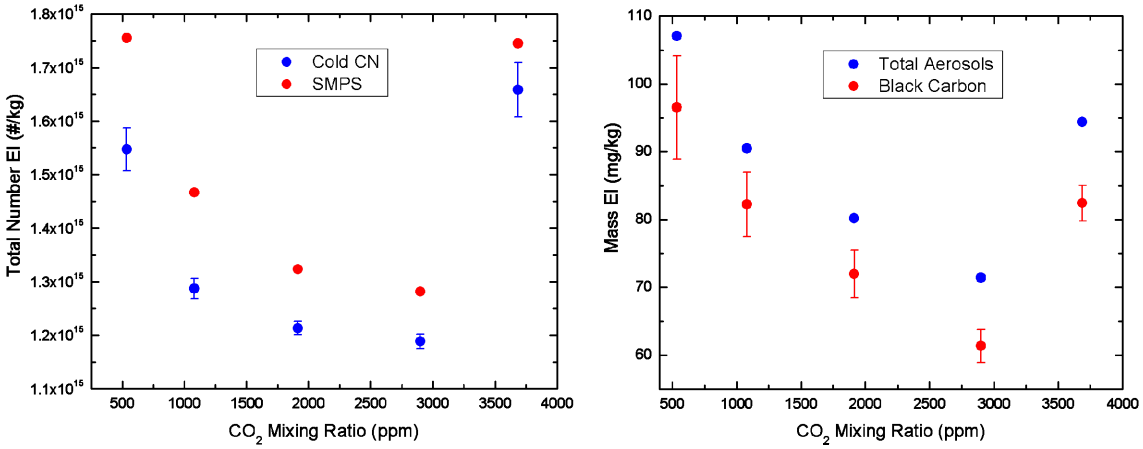

Figure 17. Particle number (left) and mass (right) EIs measured on R1 as inlet tip velocity was varied by changing dilution gas flow.

A short experiment was conducted during AAFEX to investigate anisokinetic sampling effects. It involved varying sample dilution ratio while sampling from a single probe at constant engine power, the logic being that because of flow restrictions in the probe outlet, increased diluent flow would raise pressure inside the inlet thereby decreasing the

inlet tip velocity. Indeed, increased dilution gas flow is often used to purge the sampling lines during engine starts or to obtain "zero" gas samples for verifying instrument calibrations. The test was conducted over a 30-minute period on the morning of February 2, when background conditions were stable and the #3 engine was burning JP-8 fuel at 85% of maximum thrust. As shown in Table 3, five different dilution settings were examined with nominal CO_2 mixing ratios of 535, 1080, 1913, 2900, and 3700 ppm; from an undiluted exhaust CO_2 mixing ratio of 34000 ppm, dilution ratios of approximately 64, 31, 18, 12 and 9 were calculated. Sample flow rates were calculated from the dilution ratios and measured dilution flow rates. An inlet isokinetic flow rate (Q_{iso}) of 5.7 standard lpm was estimated assuming: 1) an impact pressure of 20 PSI (Robert Howard, personal communication), 2) an exhaust temperature of 350^{o}C, 3) a tip diameter of 0.106 cm, and 4) a discharge coefficient of 0.61. Free-stream-to-inlet-tip velocity ratios, U_0/U, were then calculated from the ratio of Q_{iso}/Q_{sample}. Values varied from 1.4 to 5.2, and when compared to Figure 16 results, suggest that anisokinetic sampling effects could have affected the corresponding particle measurements.

Table 3. Measured and estimated flow and particle emission parameters from the dilution tests.

CO_2	Dilution	Est. Flow Rates (lpm)			Total Number EI		Total Aerosol		Nonvol. Aerosol		Black Carbon EI	
ppm	Ratio	Diluent	Sample	U_0/ U	avg.	stdev	EI_m	VMD	Eim	VMD	average	stdev
535	64	70	1.1	5.2	1.55E+15	3.99E+13	107.1	79.6	104.6	111.2	96.5	7.7
1080	31	57	1.8	3.2	1.29E+15	1.84E+13	90.5	78.8	73.1	96.4	82.3	4.7
1913	18	45	2.7	2.1	1.21E+15	1.23E+13	80.2	78.2	59.1	89.5	72.0	3.5
2899	12	39	3.6	1.6	1.19E+15	1.36E+13	71.5	76.0	45.7	83.7	61.4	2.4
3686	9	33	4.0	1.4	1.66E+15	5.10E+13	94.4	75.6	59.5	83.9	82.5	2.6

Indeed data shown in Figure 17 and Table 3 do provide some evidence that the mismatched inlet /exhaust steam flow velocities impacted the measured particle emission parameters in a way that was mostly consistent with the Figure 16 predictions. Note that, except for the anomalous points at 3700 ppm CO_2, both the mass and number EIs increase steadily with velocity ratio, which suggests that reduced inlet velocity potentially enriches the sample flow with larger diameter particles. The lowest dilution point doesn't follow the number and mass trends: it was recorded between the 2900 and 534 CO2 mixing ratio points, so it is unlikely that a change in engine power was the cause. Other possibilities include changes in sampling line transmission characteristics at lower total flow rates, nonlinear changes in flow dynamics within the inlet tip, and so forth.

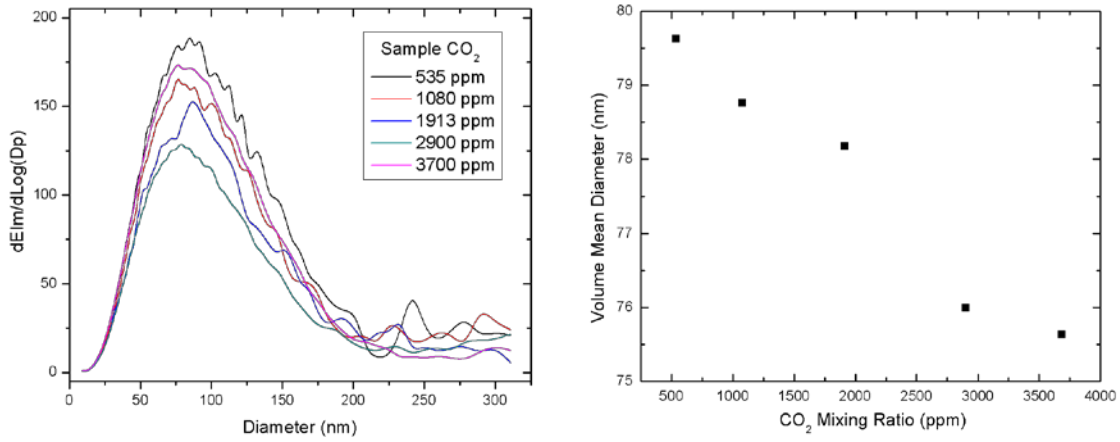

Figure 18. Change in total mass EI-based size distributions (left) and volume mean diameters (right) with change in dilution flow. Data are from the cold SMPS.

The data presented in Figure 18 provides further evidence that sub-isokinetic sampling influenced measured emission parameters. The left-hand plot shows PSDs measured by the unheated SMPS for each dilution setting and the right-hand plot shows the corresponding volume mean diameter of the size distributions as a function of CO_2. Note that the PSDs increase in integrated area and shift to slightly larger diameters as sample dilution and U_0/U are increased; corresponding VMDs increase from ~75 to 80 nm in going from minimum to maximum sample dilution. Interestingly, both the PSD and VMD point for the 3700 ppm CO2 dilution fit the expected trends.

To further explore the possible effects of anisokinetic sampling, we multiplied the 3700 ppm PSD of Figure 18 by the aspiration efficiencies shown in Figure 16 (we selected this particular PSD to represent the base case because it exhibited the smallest VMD and standard deviation). Figure 19 shows the resultant number and mass EIs, where the data have been normalized to the respective values for the 2900 ppm dilution case (Table 3). Figure 20 presents PSDs and VMDs without additional normalization. Parameters in both figures are plotted on roughly the same scales as in Figures 17 and 18 to better facilitate comparisons.

Figures 19 and 20 with 17 and 18, show similar trends in the modeled and observed parameters, but, except for VMD, the changes in the calculated parameters are more damped. Although the calculated PSDs replicate the observed dilution related enhancements in the 200-300 nm size range, the do not exhibit the same progressive increases in the peak diameter region.

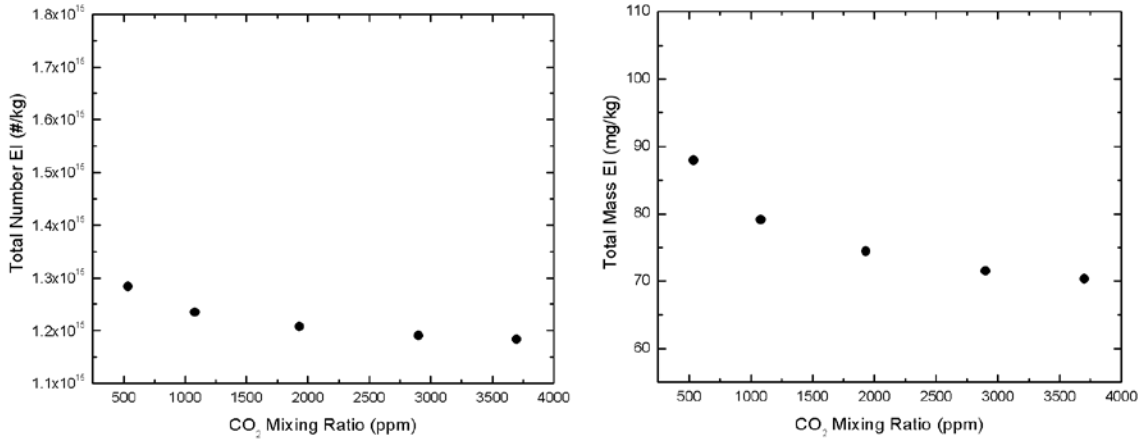

Figure 19. Particle number (left) and mass (right) EIs calculated from product of inlet aspiration efficiency vectors and 3700 ppm PSD. Values are normalized to 2900 ppm total number and mass values presented in Table 3.

To better quantify the differences between the observed and calculated values, we can calculate the following ratio for each parameter:

$$dX = (X_{535} - X_{2900})_{observed} \; / \; (X_{535} - X_{2900})_{calculated} \qquad (8)$$

where X is any particular emission parameter and the numerical subscripts denote the respective dilution settings. This expression yields values of 3.8, 2.2, and 0.9 for number, total mass, and VMD, respectively. The large ratio for EIn is not surprising, because sub-isokinetic sampling primarily enriches the larger particle population which contributes little to the integrated number density; even doubling U_0/U would not significantly reduce the dEIn ratio. We suspect the disproportionate increase in observed EIn with dilution is caused by decreased line losses at the correspondingly higher sample flow rates. For example, using equation 3 we calculate that a 50% flow increase results in a 10% reduction in 8 nm particle diffusion losses within R1. Although inertial losses increase with flow, losses due to the "filtration" mechanism discussed in section 3 also decrease inversely with flow rate. For example, the collection efficiency of a single, 0.1 µm fiber drops by 25% when flow velocity is increased by 50%. Sample line filtration effects may also explain the enhanced dEIm ratio and might explain all the dilution related changes seen in the tests. Independent line loss assessments at a variety of sample flow velocities are needed to resolve this issue.

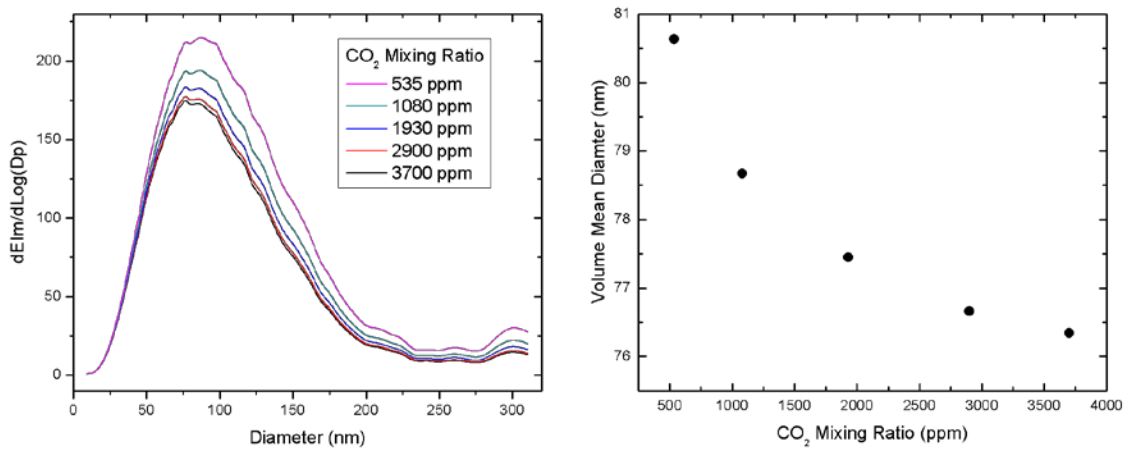

Figure 20. Mass EI based size distributions (left) and volume mean diameters (right) calculated from the product of the aspiration efficiency vectors in Figure 16 and the 3700 ppm PSD.

In summary, the AAFEX sampling tests produced data that suggest sub-isokinetic sampling can influence observed emission parameters at high thrust conductions. The experiment results are not conclusive however, as the changes in inlet velocity were convoluted with changes in total sample flow, making it difficult to resolve inertial enrichment effects from flow velocity related variations in sample line transport efficiency. To better resolve the two effects, a more careful experiment is needed in which the inlet tip velocity is changed while downstream sample line flow velocity is held constant. Since this is difficult to achieve, another approach is to use clean sample lines throughout the experiment and determine their size-dependent transmission efficiency over the range of experiment flow rates to establish accurate sample line correction factors. In either case, it is important to record inlet probe pressure, diluents flow rate, total sample flow rate, and exhaust stream temperature, velocity and CO_2 concentration. It would also be interesting to repeat the experiment with a variety of probes with different tip diameters, as equation 9 predicts that inlet aspiration efficiency at any particular velocity ratio is a strong function of inlet diameter. For example, using equation 8 we calculate that the inertial enrichment of 300 nm particles at $U_0/U = 5.2$ drops by ~23% if the inlet tip diameter is increased from 0.1 to 0.2 cm. Moreover, the isokinetic sampling issue is a tractable problem, but is not easily addressed in laboratory investigations as it requires replication of the free-stream temperatures and velocities that are only available at the exit plane of gas turbine engines operating at near takeoff thrust.

8.0 PARTICLE LOSSES TO SAMPLING PROBES

The above discussion highlighted some of the difficulties inherent in collecting particle samples from the exit plane of an engine operating at high thrust. For some engines, exhaust velocities reach or exceed mach 1 and this high velocity coupled with high temperatures can cause dynamically heated inlet probes to glow cherry red. Indeed, high-pressure water cooling is needed simply to ensure the survival of inlet probes/rake stands used to sample low-bypass military engines. Exhaust air undergoes dramatic changes in velocity, pressure, and temperature as it is drawn into narrow diameter, water-

cooled inlet probes, which can lead to equally dramatic changes in particle concentrations and microphysical properties. For example, tests conducted in the exhaust of a J85-GE engine operating at full military power during the AWEX-99 experiment showed that an inlet probe with non-optimum dilution and cooling flow introduction could reduce PM number EIs by more than an order of magnitude (Cofer et al. 2000) and double the diameter at which the PSD peak appeared. However, there is no guarantee that properly designed probes operating with minimal cooling and optimal dilution co-flow will preserve PM number densities and size distributions. Indeed, the visually-evident blackening of the R1 rake and inlet probes over the course of AAFEX (Figure 21) raised concerns that internal probe surfaces were acting as a similar particle sink.

Figure 21. Photographs of the #3 engine sampling rake before (left) and after (right) the 35 hours of engine runs conducted during AAFEX.

To assess potential inlet losses, we compared back-to-back 30- and 1-m emission parameter measurements, assuming that by virtue of the much lower plume velocities and temperatures, the 30-m data were less subject to inlet probe effects. Ratios of individual mass and nonvolatile particle number EI data pairs, plotted as functions of engine thrust for are presented in Figure 22, where the top and bottom panels show results for the right (#3) and left (#2) engines, respectively. The data are not corrected for sample line transmission efficiency, so horizontal lines representing average transmission line transport efficiency ratios are included to provide a reference for evaluating probe transmission effects. For example, ratios of twice the reference value indicate that 50% of the particle number or mass is removed in the 1-m inlet probe. Inclusion of very low-valued data from the synthetic fuel run accounts for the wide variability in the #2 engine plots. Nonvolatile number EI ratios at low engine powers ($\leq$45%) are also falsely

elevated due to reformation of volatile aerosol downstream of the thermal denuder in the 30-m samples; there is no evidence that this occurred at higher engine powers. Similarly, the #2 engine black carbon EI ratios are somewhat enhanced at low engine powers because of background contributions to the 30-m synthetic fuel measurements; ambient particles had a negligible impact on the JP-8 and high thrust data points.

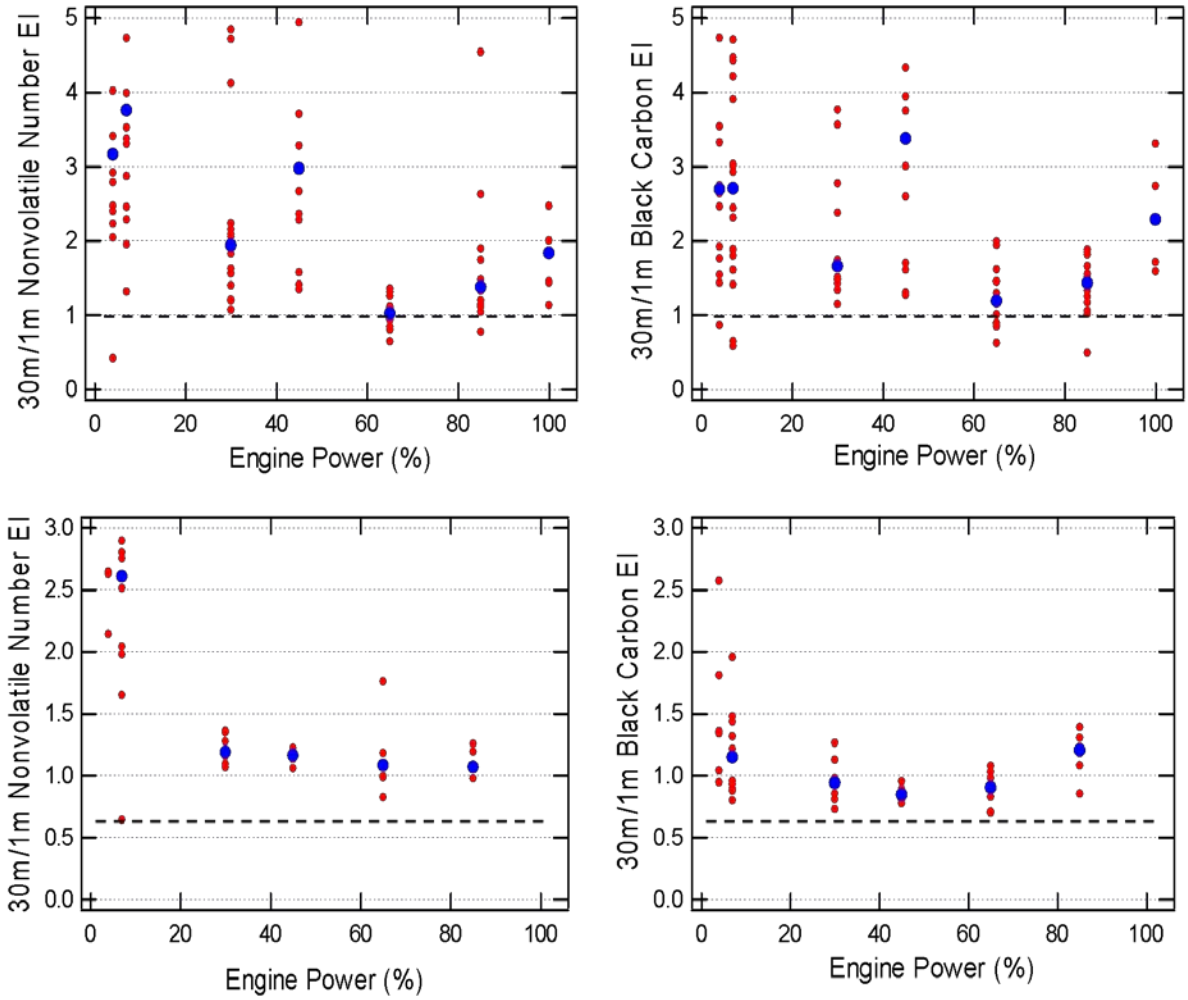

Figure 22. Ratios of emission parameters measured at 30- and 1-m behind the right (top) and left (bottom) engines, where the red and blue points represent the individual and median values, respectively. The top panels (#2 engine) include all data pairs regardless of fuel type; the bottom panels for the #2 engine are for JP-8 fuel only. The dashed horizontal lines represent the average 30-m/1-m sample line transmission efficiency ratios calculated from Figure 3 data.

Figure 22 shows that over 95% of individual EI ratios reside above the reference lines, which indicates that the 1-m inlet probes were much less efficient at collecting/transmitting both particle mass and number than their respective 30-m counterparts. Many of the points are two to three times their respective reference values, suggesting that the 1-m inlet probes were only 33 to 50% efficient under some conditions. Discounting the #2 engine 45% data points which were possibly

contaminated with engine oil, the losses were apparently more severe at high and low engine thrust settings. As noted above, contributions from volatile and light-absorbing background aerosols may account for a portion of the apparent 1-m inlet probe losses at low power settings. The high thrust losses are real, however, and appear to be in the 30 to 50% range for both the left and right inlet probes at 85-100% power.

Probe losses are further exemplified in Figure 23, a series of nonvolatile particle volume-EI-based PSD plots recorded behind the left engine at 85% power on various days throughout the experiment. The data are not corrected for line losses, so differences between the 30 and 1-m spectra are possibly much greater than depicted. In any case, the downstream PSDs invariably exhibit more volume in the 100 to 200 nm size range than the 1-m spectra. Particle loss in this size range is usually incurred through either turbulent deposition or thermophoresis; the filtration mechanism discussed in section 3 could also be a factor. Turbulent diffusion is not a good candidate as changes large enough to effect 100 nm particles would completely eliminate particles < 60 nm in diameter.

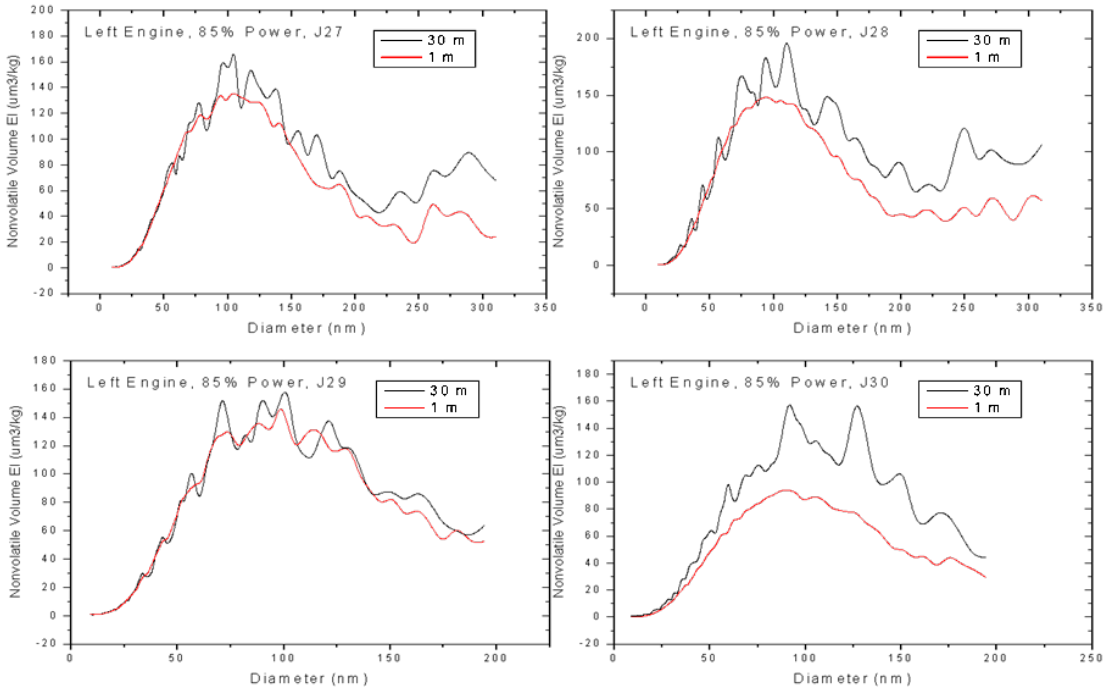

Figure 23. Volume EI size distributions from the 1- (red curves) and 30-m (black) inlet probes behind engine #2 as it was burning JP-8 fuel. Data are from 85% power runs recorded on consecutive days, starting on January 27 (upper right-hand plot).

Based on arguments presented in Section 3 above, simple turbulent inertial deposition also seems like an unlikely explanation. For example, assuming an inlet diameter and length of 0.1 and 1 cm respectively, a sample line diameter and length of 0.5 and 500 cm, respectively, a tip flow of 7 lpm, and an exhaust temperature of 350^{o}C, equation 3 predicts less than a 0.3% loss of 100 nm particles through the inlet up to the sample-selection valve box. If we use a slightly more complicated formula that considers non-

isoaxial sampling (reference), we still calculate less than 1% losses even if the probe is oriented parallel to the engine exhaust plane.

Thermophoretic deposition is a more likely explanation for some if not all the observed probe losses. For example, line-loss experiments conducted during engine tests performed at Tinker Air Force Base in 2007 (referred to as the Tinker engine tests) showed that heated sampling lines removed 20-30% of particles with diameters larger than 75 nm without significantly affecting smaller (<40 nm) particle transmission. Both AAFEX 1-m rakes and probes were actively cooled with high-pressure water flow so that hot particles entering the inlet experienced large temperature gradients during the first few meters of transport. Indeed, the AAFEX 1-m rake plumbing and temperature gradients are somewhat similar to those of an apparatus used by Romay et al. (1998) to characterize thermophoretic transport losses in turbulent pipe flow. In that experiment, particles embedded within gas flow of various temperatures were introduced into a 1-m length of 0.5 cm I.D., water-cooled copper tubing. At 35 lpm flow, the investigators observed largely size-independent thermophoretic losses of about 0.1% per degree temperature difference between the hot gas and cooled tubing. If we extrapolate this finding to the AAFEX situation where ΔT was 300 - 400^{o}C, we predict losses on the order of 30 to 40% for the 1-m probes. These values are probably an upper limit however, as although tube diameters were about the same, flow rates were typically higher (50 – 70 lpm) and the temperature gradients less steep in AAFEX compared to the Romay et al. (1998) experiment. However, these authors also observed measureable (3-10%) losses of 100 to 300 nm particles in cases where $\Delta T = 0$ and $Re=1\times10^{4}$, which they attributed to turbulent eddy impaction. The authors also indicate losses due to this process as well as themophoresis are exacerbated by having particle concentration gradients, which is potentially the case for the particle dilution probes which initially sheath the collected exhaust stream with a concentric flow of dry filtered nitrogen gas. At high thrust conditions, turbulence levels are also higher in the AAFEX 1-m rakes, with Re approaching 20,000 in the 0.55 cm tubing that connects the probes with the valve box.

Moreover, it appears that significant losses of both particle mass and number occurred within the AAFEX particle probes, particular at high engine power settings. Circumstantial evidence suggests that the losses are caused by thermophoretic deposition and perhaps turbulent eddy impaction, possibly enhanced by concentration gradients present just downstream of the inlet tip. Further confirmation and characterization of these losses require additional experiments wherein temperatures, flow rates, and size-dependent particle transport efficiency are carefully measured. A systematic laboratory study using a replica of the engine probe heated to reproduce engine sampling conditions could identify and establish the range of sensitivity of the parameters (i.e., temperature gradients, particle size, sample velocity) that control both thermophoretic and turbulent eddy impaction losses. Subsequent engine exhaust tests should employ thermocouples and pressure ports at various points to carefully measure temperature and pressure gradients in the flow path. Both the laboratory and engine exhaust test would benefit greatly if coupled with a theoretical component.

9.0 COMPARISON OF DOWNSTREAM WITH PROBE-TIP DILUTION

Aircraft engines are recognized as being significant sources of ultrafine particles, thus regulatory agencies are moving in the direction of imposing limits on their number and mass emissions to mitigate possible human health and climate impacts. Sampling the emissions is not a trivial endeavor, however, as the exhaust contains very high concentrations of not only black carbon particles, but of aerosol precursor gases as well. Thus to accurately measure these emissions, exhaust samples must be diluted very quickly to prevent coagulation and formation of new aerosols through condensation of low volatility species. To achieve this task, Arnold Engineering Development Center (AEDC) has developed special "particle" probes that introduce a concentric flow of filtered gas just downstream of the inlet tip, effectively diluting samples within milliseconds of collection. Indeed, all of the detailed aircraft particle emission studies to date (EXCAVATE, APEX-1-3, UNA-UNA, AAFEX) have used some variation of these probes to collect samples for particle measurements. There are several disadvantages to using the particle probes, however: they are expensive to construct; they must be mounted in specially designed (and expensive) sampling rakes; the rakes are difficult and time consuming to install; and the amount of plumbing required leads to bulky, difficult to operate and maintain leak-free, rake installations. Because of the high cost and inconvenience, engine manufacturer are understandably reluctant to endorse standard exhaust particle sampling procedures that require modifying their existing rakes to accommodate the special dilution probes. They have challenged the measurement community to evaluate whether the dilution probes are absolutely necessary for accurately sampling gas turbine engine particle number and mass emission or if modified gas probes can yield adequate results.

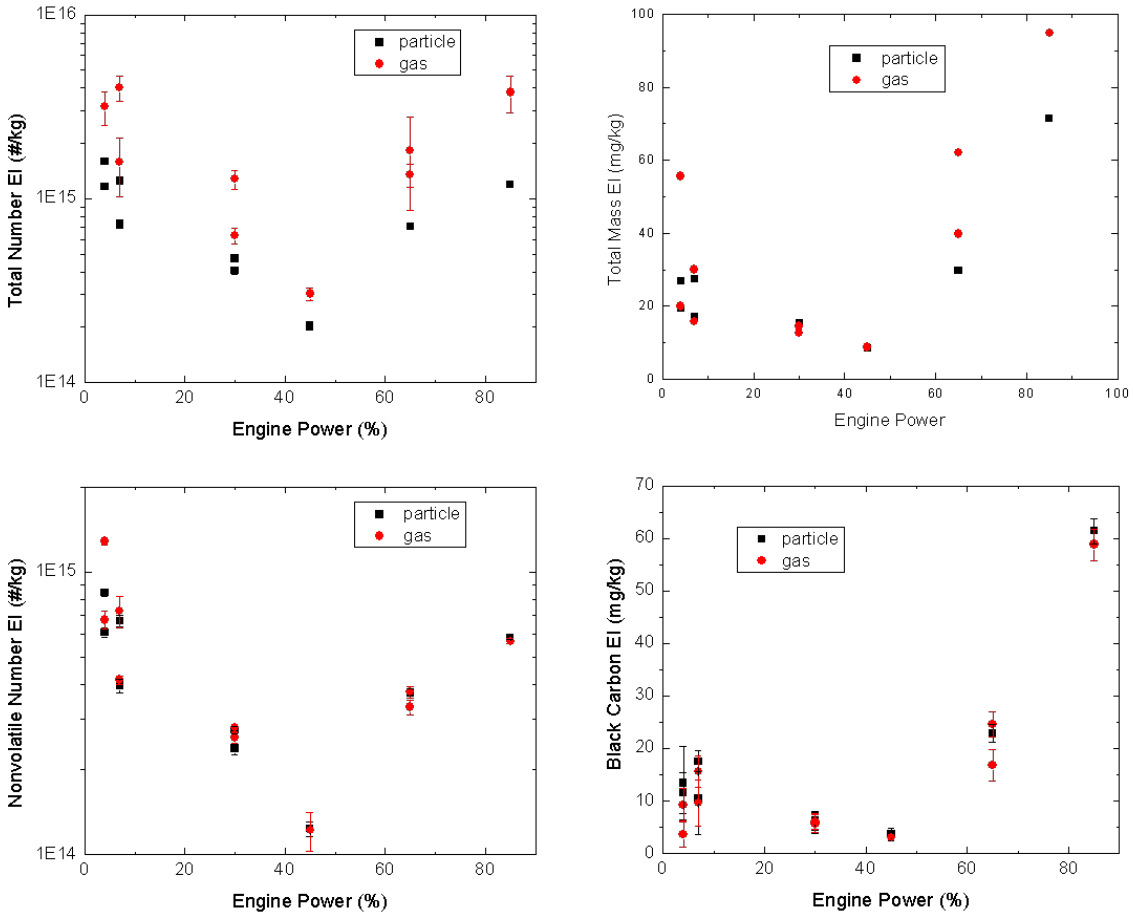

Figure 24. Comparison of total (top) and nonvolatile particle emission indices measured downstream of the gas (red points) and particle (black) inlet probes on R1.

To address this challenge, AAFEX conducted an experiment to compare particle number and mass EIs as measured in samples collected by an adjacent pair of particle and gas probes located on the 1-m right engine sampling rake. These water-cooled probes were separated by 1.25 inches and mounted very near the engine centerline where particulate emissions were uniformly distributed across the engine exit plane (see section 6). For the particle probe, exhaust sample was diluted just downstream of the inlet tip with a concentric flow of filtered N_2 gas and was transported through approximately 3 m of 3/8" OD tubing to a 6-port valve box. For the gas probe, undiluted sample was collected and transported through 1.5 m of ¼" OD stainless tubing to a Swagelok, ¼" to 3/8" reducing tee located at the rake-stand base. The ¼" side of the tee was bored out to ¼" and the transport tube was inserted though the tee and about 1" into the 3/8" thin-walled stainless outlet tube attached to the opposing side; filtered dilution gas was piped into the tee's 90^o connector and was mixed with sample as a concentric flow at end of the inserted ¼" transport tube. The resulting diluted sample was transported ~1.5 m through the 3/8" tube to the 6-port valve box. The diluted particle and gas probe samples shared a common flow path from the valve box back to the sample distribution manifold in the MST trailer. The lines and valve boxes were unheated.

Table 4. Comparison of emission measurements made on the Particle and Gas inlet probes.

Engine	Total Number EI (1e14/kg)				Novolatile Number EI (1e14/kg)				Total Aerosol		Nonvolatile Aerosol		Black Carbon EI (mg/kg)			
Power	Particle		Gas		Particle		Gas		Mass EI (mg/kg)		Mass EI (mg/kg)		Particle		Gas	
norm %	avg	std	avg	std	avg	std	avg	std	Part	Gas	Part	Gas	avg	std	avg	std
4	13.7	0.4	71.4	9.2	7.3	0.2	9.8	0.4	23.1	37.8	13.8	11.6	12.5	5.5	6.4	2.9
7	10.0	0.5	25.0	3.4	5.3	0.3	5.9	0.7	22.1	23.7	11.8	11.6	14.0	4.4	11.8	3.5
30	4.4	0.1	9.6	1.1	2.6	0.1	2.7	0.1	15.1	13.5	8.5	8.4	6.0	1.9	5.9	1.6
45	2.0	0.1	3.0	0.2	1.2	0.1	1.2	0.2	8.5	8.7	4.5	4.9	3.6	1.2	3.0	0.5
65	7.2	0.4	15.9	5.8	3.7	0.1	3.5	0.2	30.7	50.9	27.8	25.3	24.6	2.1	20.7	2.7
85	11.9	0.1	37.8	8.6	5.8	0.1	5.7	0.1	71.5	95.0	45.7	51.7	61.4	2.4	58.8	3.0

The probe comparison test was conducted on Monday, February 2, 2009 between 10:15 and 12:00, local time. Winds were calm, but ambient temperature increased from ~10 to ~16^{o}C between the start and end of the experiment. The aircraft was burning sulfur-rich (1200 ppm) JP-8 fuel in the test engine (#3) to enhance volatile aerosol formation in undiluted samples. The test matrix involved collecting comparative data at 4, 7, 30, 45, 65, and 85% engine thrust. Standard procedure was to establish stable engine power, then alternately draw sample from the two probes by switching valves in the 6-port. Sample dilution in each case was adjusted to maintain a nominal 10:1 dilution ratio as estimated from measured CO_2 mixing ratios. About three minutes of data were recorded on each probe before the next condition was requested.

Results of the study are presented in Figure 24 and Table 4. The data include "nonvolatile" and "total" EIs, which refer to measurements made respectively with and without thermal-denuders placed in the flow paths leading to the CN counters and SMPS systems used to determine particle number and volume concentrations. The total and nonvolatile mass EIs were calculated from SMPS integrated volumes assuming a density of 1 g cm^{-3} for both the soot and volatile aerosol particles. A number of points in the table represent the average of several individual data points (4, 7, and 65%). At the 85% power setting, gas probe measurements were only recorded over a single 3-min interval, while particle probe data was collected during 6, 3-minute intervals at different dilution ratios to evaluate sub-isokinetic sampling effects on particle concentration and size; the particle probe data included in Table 4 and Figure 24 are from the sampling interval with a dilution ratio that most closely matched that of the gas probe run.

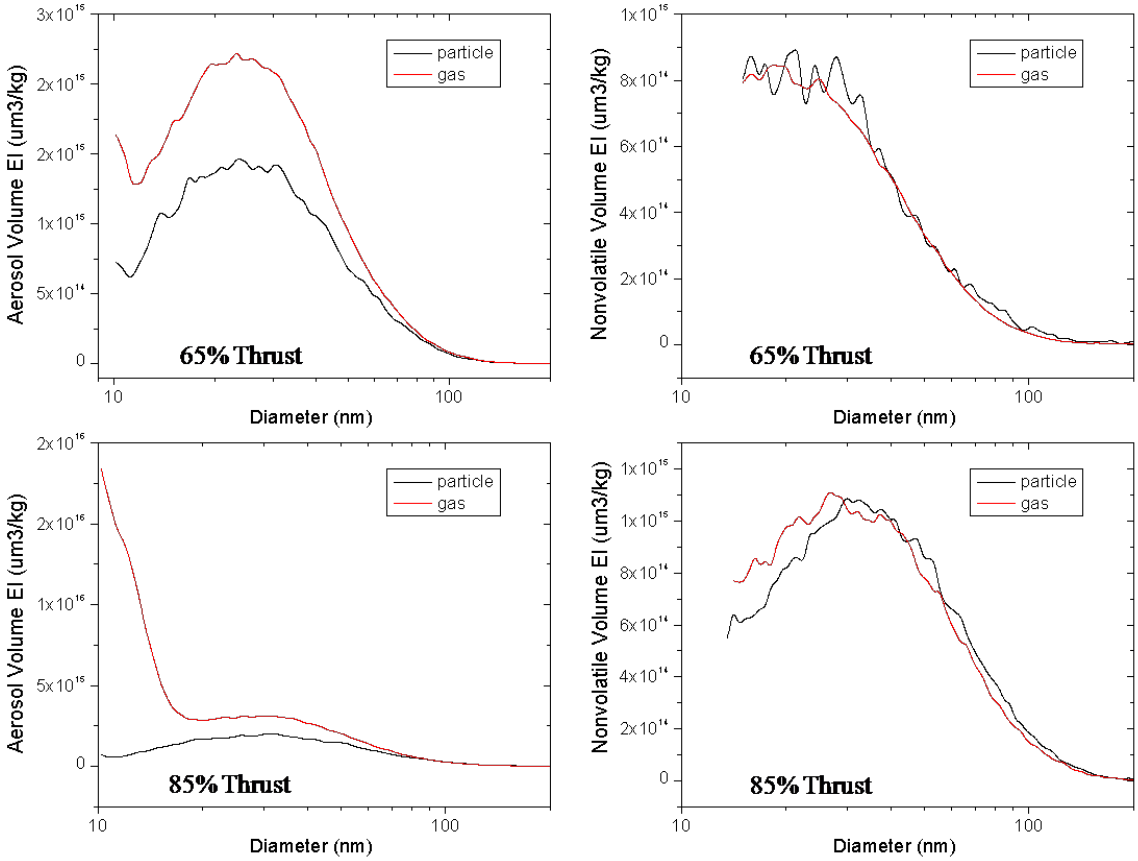

Figure 25. Comparison of volume based size distributions measured downstream of the gas (red curves) and particle probes (black) as the #3 engine was operated at 65 (top) and 85% (bottom) of maximum rated thrust. Plots on the left represent the total (nonvolatile + volatile) emissions, whereas those on the right are for nonvolatile particles only.

From reviewing Figure 24 and Table 4, we see that total aerosol number (EI_n-tot) and mass (EI_m-tot) EIs were significantly higher in the gas probe samples indicating that aerosol nucleation and growth was occurring vary rapidly in the 1.5-m, ¼" tube that transported undiluted exhaust from the inlet tip to the dilution point. For example, at idle, gas probe EI_n-tot and EI_m-tot values were respectively ~5 and ~1.5 times higher than values measured using the particle probe. This pattern was particularly evident at low and high power settings and was likely caused by the overwhelming availability of condensable material at idle and the propensity of sample to stagnate in the line at higher thrust settings.

In contrast to the total aerosol emission parameters, the EI_n-nv, EI_m-nv and EI_{bc} for the gas and aerosol probes were in remarkably good agreement. Figure 25, which shows PSDs recorded at 65 and 85% power, provides additional insight into the differences between the gas and particle probe measurements. The left-hand plots were recorded on unconditioned samples, whereas the righthand plots were obtained on samples that had

first passed through a 350^{o}C tube heater. The unconditioned gas probe samples clearly exhibit nucleation mode aerosols and substantial coatings on soot mode particles. The thermal denuder evaporates the volatile particles and coatings and as a result, the gas and particle probe PSDs are almost indistinguishable in peak position and shape. Indeed the average percent differences between the gas and aerosol probes EI_n-nv, EI_m-nv, and EI_{bc} across all power settings was respectively 3, -1 and -10%, where negative values indicate that particle probe measurements are on average greater. The EI_n-nv values were incredibly close, with only the 4% and 7% idle point differing by more than |3%|; the higher gas probe values at lower power settings are caused by reformation of volatile particles downstream of the thermal denuder.

EI_{bc} values differed by a factor of two (12.5$\pm$5.5 versus 6.4$\pm$2.9 mg kg^{-1} for the particle and gas probes respectively) at ground idle, but the error bars overlapped significantly. However, particle probe EI_{bc} values were slightly higher than gas probe values at all power settings. Possible causes for this include: enhanced turbulent losses inside the gas probe inlet; greater wall losses in the gas lines due to soot build up in the undiluted sample line; slight differences in emissions at the two probe locations; or greater line losses in the trunk lines leading back to the community sampling manifold. The gas probe inlet tip gradually expands from 0.06" to 0.20" ID diameter and flow is undoubtedly very turbulent in this region; indeed one can envision turbulent eddies forming just inside the inlet tip, which might lead to losses via the eddy impaction process described in the section above. In contrast, within the particle probe, the exhaust stream is initial confined to within a 0.04" ID capillary before being dumped into the center of a sheathing flow of dilution gas; this approach possibly isolates the sample from wall contact until the flow is well-established and somewhat stable. Of course, a modeling analysis is required to verify whether this is the case or not. As for dirt buildup, the transport efficiencies of the individual gas and aerosol lines were not measured, but this experiment was conducted at the end of AAFEX when the lines were their dirtiest and it is safe to say that particle concentrations were at least a factor of 10 higher in the gas lines, when in use, than in the particle sampling lines; we thus cannot rule this out as a possible explanation. As for differences in probe location, our section 5 analysis indicates that, discounting the 45% power point, black carbon values varied by up to 42% within 4" of the engine centerline; the variations were less at high engine power, which is also the case with the Table 4 data. Again excluding the 45% data point, EI_n-nv only varied by 1-8% within 4" of the engine centerline, which is also consistent with the good agreement seen between measurements made of this parameter using the gas and aerosol probes spaced 1.25" apart. Thus spatial variations may have at least contributed to the slightly higher EI_{bc} observed in the particle probe samples. Particle transport losses may also account for a fraction of the difference. Particle probe total diluted sample flows (i.e., sample + diluent gas) were up to 50% higher than for the gas probe, which should have reduced wall losses due to the lower residence times. This possible mechanism should have had a greater impact on particle number than mass, which, in view of the almost perfect agreement in gas and particle probe EI_n-nv, was not the case. However, it's possible that volatile coatings reduced the mean gas probe particle mobility and hence reduced their susceptibility to turbulent diffusive loss, more or less canceling out the increased number losses due to lengthier residence times. In

turn, this decreased mobility may have increased the loss of larger particles through the "filter" effect discussed in Section 3 above.

Moreover, it is somewhat surprising that the gas and particle EI_n-nv values agreed so well as particle coagulation was expected to occur in the undiluted section of gas probe line. From measured dilution flows (approximately 35 lpm) and sample and exhaust CO_2 concentrations (1300-2300 and 22000-36000 ppm, respectively), a calculated approximately 28 cm^{-3} pre-dilution line volume, and an assumed .0013 g cm-3 sample density, we calculate that sample remained undiluted for between 0.6 and 0.9 seconds. Exhaust nonvolatile particle number densities ranged from 0.2 - 2 x 10^7 cm^{-3} at standard pressure and temperature conditions. Assuming a polydisperse size distribution with a respective mode and standard deviation of 20 nm and 1.6 and using equations developed by Baron and Willeke (2005), we calculate coagulative particle losses that range from 1 to 6.2%, where the worst case is at idle and the best at 45% thrust. Apparently the coagulative losses are in the range of particle sizes (3-10 nm) that are almost completely removed by turbulent diffusion during sample transport, so their absence cannot be detected by downstream instruments.

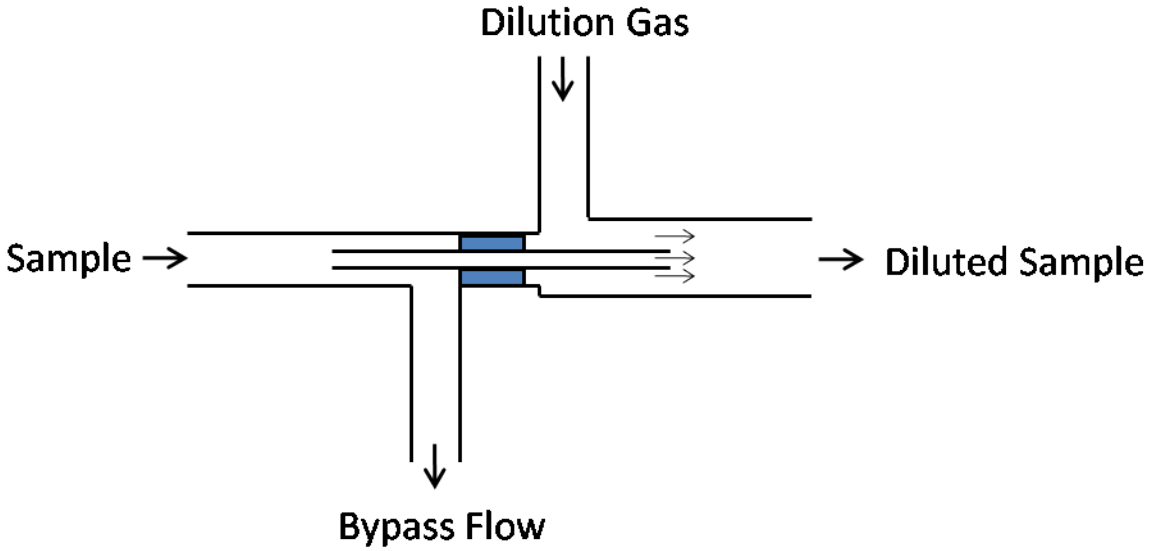

Figure 24. Rough schematic of an improved gas-line dilution system.

It is also surprising that for the gas probe, acceptable dilution ratios (14-19 as calculated from exhaust and sample CO_2 mixing ratios) were obtained across the entire engine power envelope using a constant, 35 lpm dilution flow rate; dilution flow requirements for the particle probe were much more variable (30-50 lpm). For the gas probe, calculated tip flow rates varied from 1.9 to 2.5 lpm (substantially below the 8 lpm critical flow calculated for a 0.15 cm orifice at standard temperature and pressure). Inlet flow should have increased in proportion to impact pressure, which typically doubles in going from idle to takeoff thrust. Clearly, additional modeling and measurement work is needed to understand flow dynamics within both the gas and particle probes.

We finally note that freestream to gas probe inlet velocity ratios, U_0/U, varied from ~2 to 6, depending on power, suggesting that particle mass may have been artificially enhanced in some cases from sub-isokinetic sampling effects.

In summary, we conclude that standard gas probes can yield representative gas turbine engine number and mass EIs and size distribution measurements, provided that the exhaust samples are diluted within a couple of meters of the inlet tip and that the diluted samples pass through a thermal-denuder immediately upstream of the diagnostic instruments to remove volatile material formed during initial transport through the undiluted gas line. The introduction of dilution gas must be carefully implemented, however, to avoid additional particle loss through turbulent inertial or eddy impaction processes at the dilution point or creating a pressure restriction that leads to exhaust sample stagnation within the upstream portion of transport tube. Indeed, there is considerable room for improvement in the AAFEX gas probe sampling scheme. A more optimum design would include dilution system that allows for gas-line bypass flow to reduce sample residence time. An example is shown in Figure 24. Here, the bypass line is attached to a pump to draw a continuous flow through the gas line to reduce aerosol nucleation and coagulation. The bypass line is also pressure controlled at ~1 atmosphere so that the dilution gas and diluted sample flows remain constant regardless of engine power. This will simplify line loss assessments and eliminate the need to constantly monitor and change dilution gas flows, line pressures and vent valve settings. The sample line leading into the dilution box should also be heated to prevent water vapor condensation and volatile aerosol formation within the undiluted gas sample.

The question remains as to how long the exhaust samples can remain undiluted before coagulation and agglomeration processes significantly change nonvolatile number EIs and PSDs. In AAFEX, particle losses due to coagulation were calculated to be minor and mostly in the size range that is effectively filtered out during sample transport through the long sampling lines. DC-8 exhaust particle concentrations were also relatively low, peaking at 2×10^7 cm^{-3} at idle and coagulative losses were calculated to be 6% for a 1-second, pre-dilution lifetime. Assuming a nominal PSD mean diameter of 20 nm and standard deviation of 1.6, if we increase the particle concentrations to 1×10^8 cm^{-3} (corresponds to an EI_n-nv of around 5×10^{15} kg^{-1}, which is common for older engines) and residence time to 5 seconds, we calculate that number densities will drop 65% and the mean diameter will shift to 28 nm before dilution air is introduced.

10. SUMMARY AND RECOMMENDATIONS

AAFEX collected a great deal of information regarding the characteristics and performance of the particle sampling installation. Important observations include the following.

- Accumulation of soot and volatile materials on sampling line walls can significantly reduce particle transport efficiencies, leading to underestimates of both number and mass emissions. Continuously drawing sample flow through unused lines contributes to the dirt build-up.

- Particles in the 100-300 nm size range are readily lost to dirty tubing walls, which defies explanation by the standard smooth-bore tubing loss mechanisms included in the UTRC model. Since easily applied theoretical treatments incorporating surface roughness elements are lacking, we postulate that soot deposits to tubing walls to form dendritric, fiber-like structures, then invoke filter theory which easily accounts for particle loss in this "inert" size range.
- Under relatively cold conditions (~0^{o}C) and lower power settings, volatile particle nucleation typically reaches equilibrium between formation and coagulation before reaching the 30-m inlet probe. However, volatile particle mass continues to increase during sample-line transport, potentially increasing by 50 to 75% at high engine powers, depending on how line-loss corrections are applied.
- PM emissions were surprising variabile across an 8 inch span to the left of DC-8's #2 engine centerline. For total PM emissions, the fluctuations were linked to oil fumes emanating from a leak in the engine nacelle. Nonvolatile PM mass and number EIs were fairly stable within 4 inches of the centerline, suggesting that single point sampling in that region would yield emission parameters broadly representative (within 20%) of the entire engine.
- At high engine thrust where the plume velocity approached Mach 1, PM emissions generally increased with freestream to sample inlet velocity ratio, U_0/U, indicating particle populations were being enhanced by the inertial effects associated with sub-isokinetic sampling. However, the enrichment trends did not faithfully follow predictions, and were possibly caused by other mechanisms such as improved sample line transport efficiency at the higher flow rates needed to produce large U_0/U ratios.
- Nonvolatile PM emission indices measured from 30-m samples were systematically higher than measured at 1-m, indicating possible particle loss in the 1-m inlets or transport tubes. Because the 1-m inlet probes are cooled, thermophoretic effects must be considered and by similarity to previous work, we estimate they could account for a large fraction of the observe difference in the 1 and 30-m measurements. Turbulent eddy impaction is another possibility, but cannot be evaluated without additional testing under appropriate conditions.
- PM emission measurements made on samples collected with a special particle probe and a gas probe with dilution gas introduced 1.5 m downstream typically agreed to within 10%, suggesting that existing gas certification sampling probes used by engine manufacturers may be modified to yield representative particle number, mass and PSD measurements. However, the success of this approach is contingent on diluting exhaust samples within a few meters of the gas probe tip and placing an efficient thermal denuder just upstream of diagnostic instruments to evaporate and absorb volatile aerosol components. Sampling from the gas probes may other advantages in addition to the obvious lower cost and easier implementation. Optimally-designed gas-probe dilution systems will deliver a constant ratio of dilution gas to sample flow, greatly simplifying sample system operation and monitoring requirements. This approach will also enable use of laminar flow rates in sample lines as only a fraction of the exhaust gas passing through the inlet tip need be diluted and transported back to the diagnostic instruments; particle diffusive and inertial losses are substantially lower in laminar, as opposed to turbulent, pipe flow.

AAFEX also provided a valuable learning experience and suggested changes or activities that could be implemented to improve future experiments.

- The loss in sampling line transport efficiency due to increasing wall roughness over the course of AAFEX was particularly troublesome. For long term experiments, this can be avoided by making daily sampling line efficiency assessments based on the fraction of ambient aerosols that penetrate the subject sampling line. This type of experiment is easily implemented by drawing representive flows through the lines and measuring total particle concentrations on the up- and downstream ends with identical particle counters as was done during the end-of-mission line loss evaluation discussed in section 3.0 above. Dips in efficiency below a certain threshold value, say 80%, would mandate line cleaning or replacement.
- The 1-m sampling probe losses were probably exacerbated by accumulation of soot on the inside surfaces of the probe and transport tube leading to the 6-port valve box. The box was designed to deliver dilution gas and draw a small flow through each unused probe, which unnecessarily added to the wall contamination. A more optimum valve-box design would blow purge gas out each unused particle probe inlet tip.
- For unknown reasons, PM emissions are sensitive to sample dilution at high engine powers. A comprehensive sample probe experiment is needed to investigate the source(s) of this variability. This requires generating a high pressure particle stream and measuring the concentration up and downstream of dilution probe. The dilution characteristics of a modified gas probe is also of interest and can be established at the same time.
- Particle losses in the 1-m inlet probe were fairly substantial under some conditions, possibly from thermophoretic deposition or turbulent eddy impaction, which are difficult to distinguish under actual engine test conditions. Thus, the above probe dilution test should also investigate the effect of sample-probe temperature differences and include several points at $\Delta T=0$ to investigate impaction losses as a function of total probe flow. Again, these tests should be conducted on both the particle and modified gas probes. Future engine tests should include temperature and pressure measurements at various points in the 1-m sample flow path so that the lab results can be extrapolated to actual sampling conditions.
- AAFEX results suggest that gas probes can be used to collect representative PM emission samples. To more firmly establish the viability of this approach, future research-style engine tests (i.e., AAFEX-II) should deploy an optimally designed gas probe dilution system and perform a more comprehensive comparison of gas and particle probe measurements over a broad range of dilution ratios and engine conditions.

References

Anderson, B.E. et al., 1998: Airborne observations of aircraft aerosol emissions II: Factors controlling volatile particle production. GEOPHYS. RES. LETT.25 (10): 1693-1696.

Anderson, B.E., 2005: An overview of the NASA Experiment to Characterize Aircraft Volatile Aerosol and Trace-Species Emissions (EXCAVATE), NASA/TM-2005-19019.

Anderson, B.E., et al., 2010: Aircraft Exhaust Sampling Strategies, NASA TM in preparation.

Cofer, W.R., et al., 2001: Results of the August 1999 Aerosol MeasurementIntercomparison Workshop, T-38 Aircraft Sampling Phase, NASA/TM-2001-211226.

Hangal and Willeke, 1990: Overall efficiency of tubular inlets sampling at 0-90 degrees from horizontal aerosol flows, Atmos. Environ., 24A, 2379-2386.

Hinds, W.C., 1999: Aerosol Technology, 2nd Edition, New York, John Wiley and Sons.

Im, K., and R. Ahluwalia, 1989: Turbulent eddy deposition of particles on smooth and rough surfaces, J. Aerosol Sci. 20, 431-436.

Otani, Y. et al., 1989: Experimental study of aerosol filtration by the granular bed over a wide range of Reynolds Numbers, Aerosol Science and Technology, 10(3), 463-474.

Romay, F. et al., 1998: Thermophoretic deposition of aerosol particles in turbulent pipe flow, J. Aerosol Sci., 29, 943-959.

Wey, C.C., et al., 2006: Aircraft Particle Emissions Experiment (APEX), NASA/TM-2006-2143822007

Willeke, K. and P. Barron, 2005: Aerosol Measurement, 2nd Edition, New York, John Wiley and Sons.

APPENDIX Q: Instrument Inter-Comparison

D.S. Liscinsky, B.E. Anderson, Changlie Wey, Anuj Bhargava, Rick Miake-Lye, Edward Winstead, Phil Whitefield, Don Hagen and Prem Lobo

ABSTRACT

Requirements and limits for PM metrics demand reliable instrumentation and a suitable particle calibration source. Intra-instrument comparisons of the MAAP for the measurement of black carbon mass showed that as expected the same instrument analyzing the same sample produces the same result. Inter-instrument comparison illustrated that particle properties and instrument factors can influence the results. The removal of volatile particles is a key to compare mass and number datasets. Instrument efficacy can be obtained, however without established instrument calibration methods, traceability is lacking and measurement uncertainty remains. A commercially available, portable particle generator based on a well-controlled propane diffusion flame, produced results which encourage further assessment of this generator as a source for field measurement of line loss and instrument calibration.

DISCUSSION AND RESULTS

A collaborative study was performed at AAFEX on Feb 3, 2009 using a portable soot generator as an engine surrogate. The objectives of the study were to compare instruments and take a first look at this soot generator as a calibration source for field measurements. The soot source was distributed to a number of different instruments so that simultaneous measurements could be performed. Although the suite of instruments provided the capability of measuring particle concentration, size distribution, and mass, the focus of the experiment was to compare instruments that measure BC mass because line loss measurements were not performed and mean particle sizes ranged from 50 to 110 nm (typically larger than engine particles). The instruments consisted of: (1) ThermoElectron Multi Angle Absorption Spectrometer (MAAP) model 5012, (2) Artium LII-200 Laser Induced Incandescence instrument, (3) Droplet Measurement Technologies Photo-Acoustic Soot Spectrometer (PASS-3), (4) standard Smoke Number instrument, (5) Scanning Mobility Particle Sizer (SMPS), (6) Condensation Particle Counter (CPC).

In AAFEX and several previous studies, intra-instrument comparisons have been performed. Since the ThermoElectron Multi Angle Absorption Spectrometer (MAAP) model 5012 provides an inexpensive, real-time measurement of BC mass, it has received much attention. Recent efforts yieded direct comparisons where the same sample was delivered to different instruments with different operators. The results of two direct comparisons are shown in Figure 1 where the measurements of BC mass from two different instruments are plotted against one another. On the left-hand side measurements made at AAFEX are compared and, except for one point the agreement, is well within +/- 10% (the outlier is a high-power point where the sampling system was not well-stabilized during the measurement period). On the right-hand side are

measurements taken at AFRL while sampling a T-63 gas turbine. Again, excellent agreement is shown. Additional examples of intra-instrument further confirm that the same instrument, given the same sample can produce the same result which is the definition of instrument efficacy. Although instrument efficacy is only shown for the MAAP, similar results have been shown for practically all standard PM instruments.

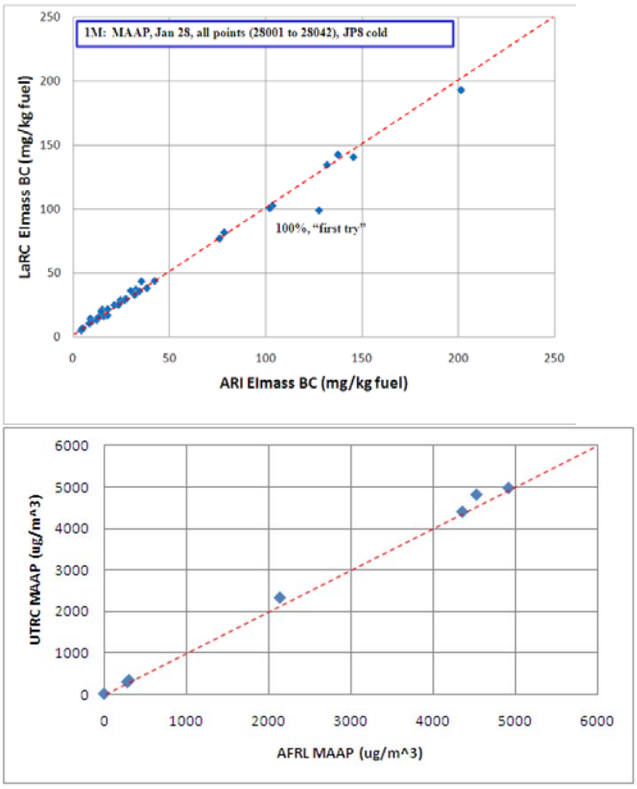

Figure 1: Intra-Instrument Comparison of MAAP Measurements of BC mass

Inter-instrument comparisons were performed at AAFEX using a soot generator from Jing AG Limited, Switzerland: Model 5202 RSG mini-CAST (Real Soot Generator mini Combustion Aerosol Standard). More details can be obtained at www.sootgenerator.com. The miniCAST was developed following deployment of the CAST (Combustion Aerosol Standard) in 1999 by the Swiss Federal Office of Metrology and Accreditation. The CAST has been widely used in Europe, most notably in the ongoing UNECE GRPE Particle Measurement Programme (PMP), which is focused on the characterization of emissions from diesel engines. Whereas the CAST is quite heavy (40kg), the miniCAST is 5 kg and therefore appropriate for field use. Furthermore, the output from a combustion source is somewhat more representative of aircraft emissions than other calibration aerosols such as salt, polystyrene latex spheres and the like, which are typically used in laboratory settings.

A photo of the Model 5202 RSG mini-CAST and its external flow control system is shown in the upper left of Figure 2 along with a simplified schematic of the flow paths to illustrate the control features of the miniature co-flow propane diffusion flame (inside the

purple dashed lines). A key to the performance of this unit is accurate flow metering. This is handled by 5 independent precise mass flow controllers which are set and monitored by computer software. The propane/air diffusion flame generates soot particles which are subsequently quenched and diluted inside the unit to avoid soot buildup. By controlling the metered fuel to air ratio and quenching rate a range of particle size distribution and total particle number can be delivered. However, note that this is not a premixed flame, so the metered air to fuel ratio defines a global equivalence ratio. The operating condition of the burner is better described by using the fuel to N2 ratio since introduction of N2 into the fuel flow is used to modify (lower) the flame temperature and change the level and rate of soot production.

The utility of the miniCAST is evident due to portability, dynamic range of soot output and ease of use. However, it was found that over much of the design space of the device the number concentration of generated particles exceeds 1E8/cm^3 (and mass loading typically exceeds 10mg/m^3). At this high number density, particle size/mass distributions rapidly evolve because of particle-to-particle collisions. Therefore a secondary dilution system is required for this device to be used as a calibration source. A dilution system consisting of an off-the-shelf Fox Valve Mini-Eductor was used in the initial evaluation of this device. The eductor operates by setting the pressure of the motive air eliminating the need to meter a dilution flowrate and discharges a rapidly mixed diluted sample stream at a positive working pressure. However it was found that the eductor is so efficient (by design) that the dilution ratio could not be varied sufficiently in all cases by just changing the motive flowrate, i.e. pressure. A simple solution was to insert a flow-limiting orifice on the suction side of the eductor as shown in Figure 2. Commercial diluters such as the Dekati DI-1000 would be logical replacements for the system used in the laboratory evaluation described in the following.

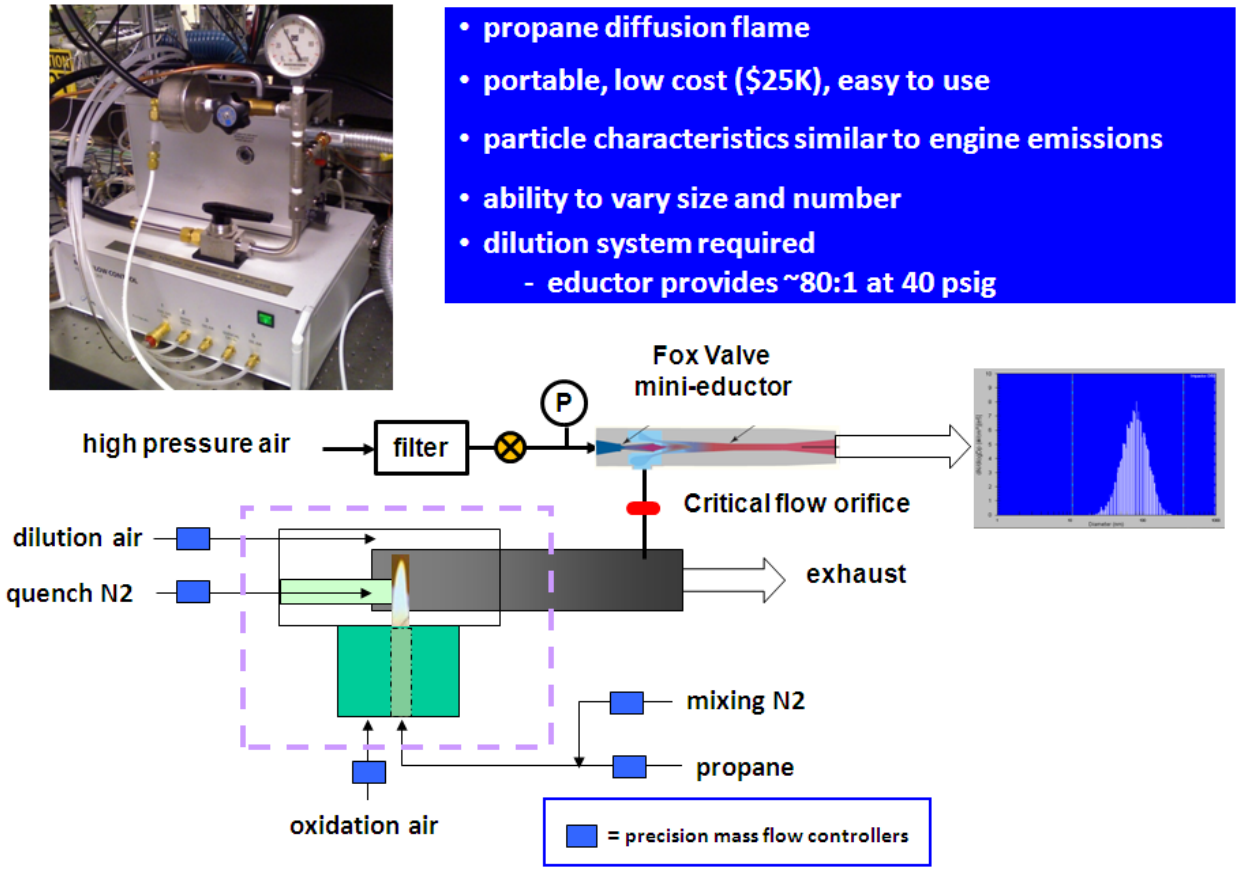

Figure 2. Schematic description of the Flow Streams of the Model 5202 miniCAST

Results obtained after AAFEX are shown in Fig. 3 to illustrate typical miniCAST reproducibility over time where the left-hand plot is UTRC data and the right-hand plot from LaRC data. Over 2.5 hrs the system was found to output a size distribution with a GMD that was within 1nm and a variation of concentration within 2%, however the output did appear to have a trend which was changing over time possibly because of the dilution system. Typical source size distributions used on Feb 3 along with some stability info shown in Fig. 4.

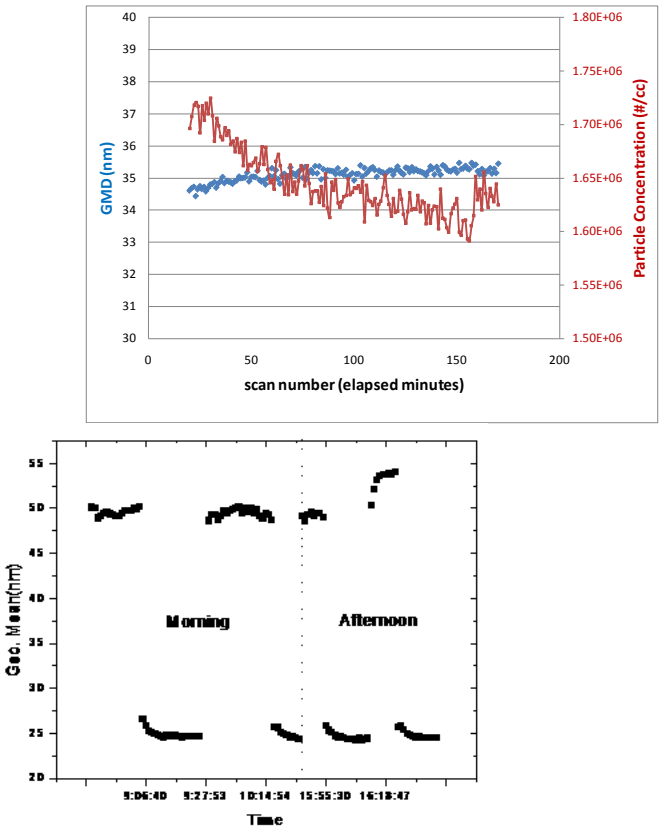

Figure 3. Short-term Stability and Longer-term Reproducibility of the miniCAST

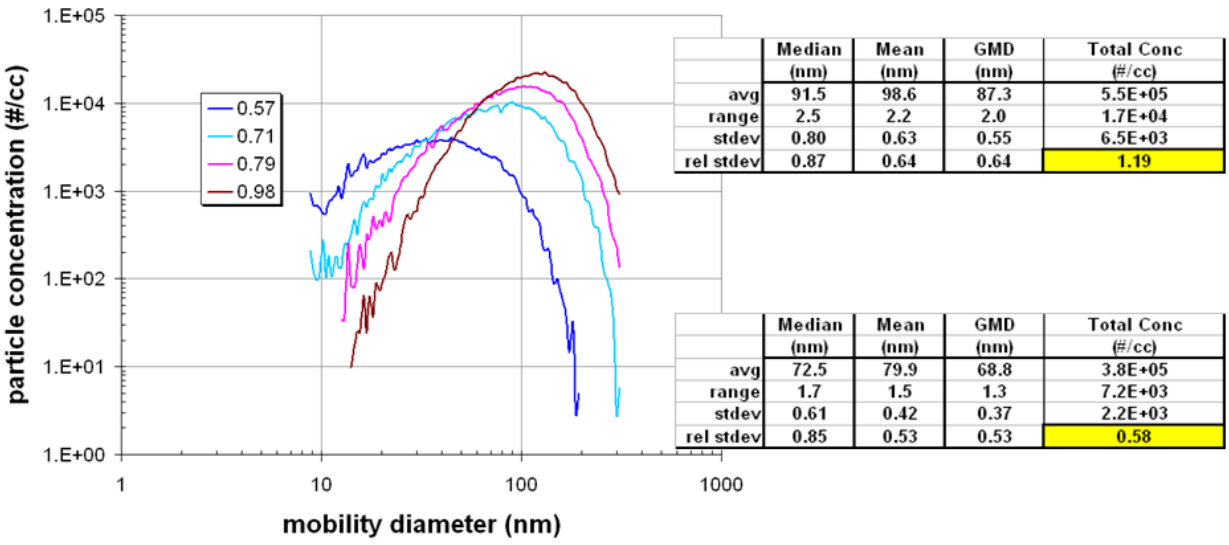

	Median (nm)	Mean (nm)	GMD (nm)	Total Conc (#/cc)
avg	91.5	98.6	87.3	5.5E+05
range	2.5	2.2	2.0	1.7E+04
stdev	0.80	0.63	0.55	6.5E+03
rel stdev	0.87	0.64	0.64	1.19

	Median (nm)	Mean (nm)	GMD (nm)	Total Conc (#/cc)
avg	72.5	79.9	68.8	3.8E+05
range	1.7	1.5	1.3	7.2E+03
stdev	0.61	0.42	0.37	2.2E+03
rel stdev	0.85	0.53	0.53	0.58

Figure 4. Size distributions used for the AAFEX instrument comparison experiment

Measurements of BC mass are compared in Figure 5. A series of measurements were made as the miniCAST combustion air was changed in discrete steps to provide a wide

range of BC concentration. The plotted points are averages over the time on point which was 10min. Measurements reported by the LII and PASS instruments are compared to MAAP and show similar trends although differences in value reported by LII are ~30% to ~50% over much of the data with the PASS in better agreement.

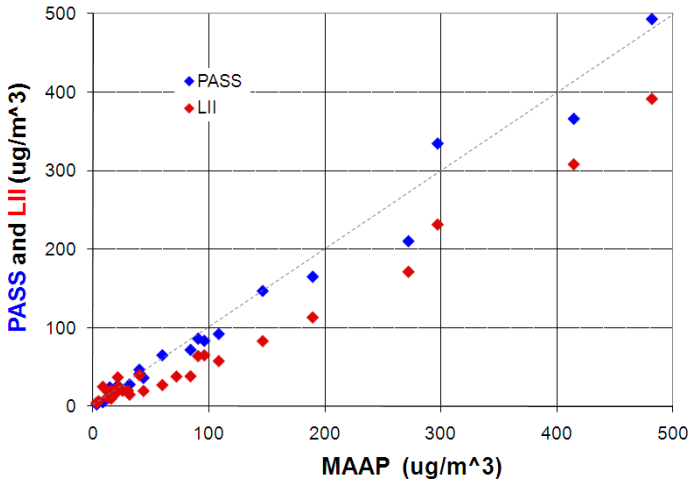

Figure 5. Comparison of MAAP to LII and PASS measurements of Black Carbon mass

Measurements of BC mass are plotted vs. SN in Figure 6**.** The green line predicts soot mass from a correlating expression developed by Med Colket at UTRC which represents the best fit to a wide number of reported data sets that infer soot mass from measured SNs. The x symbols represent the concentration index calculated from FOA 3.0. The measured values tend to be higher than the correlations would predict and the deviation is seen to increase as soot loading increases.

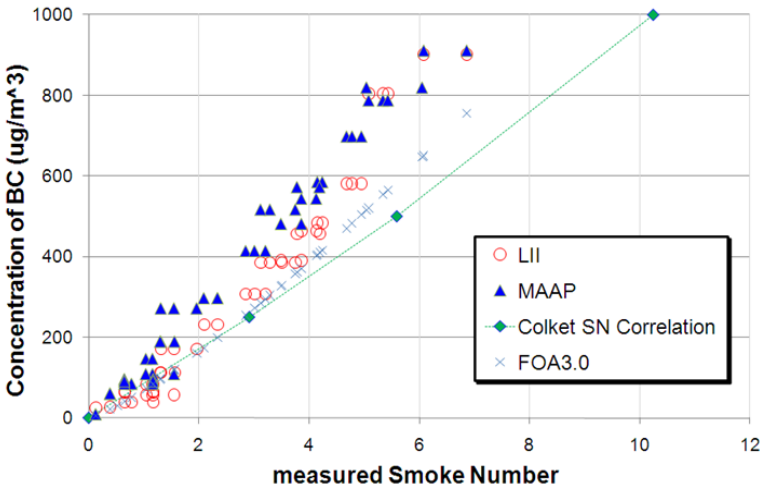

Figure 6. Comparison of SN to measured Black Carbon mass

The presented measurements of BC mass under steady conditions highlight the difficulty of correlating measurements using different instruments. As expected, variation between identical instruments was small, however comparison of the results obtained by different measurement techniques showed greater variation often on the order of 50%. Some of the disagreement maybe attributed to volatile coating of the soot particles produced by the miniCAST since both LII and PASS are less sensitive to organic content than MAAP.

Additional instrument comparisons were performed using the engine data acquired during AAFEX. Efficacy was found between sizing instruments although the level of agreement was not as good as with the MAAP. In Figure 7 the results of a large number of SMPS measurements collected by MS&T and LaRC at AAFEX are compared on a point-to-point basis, i.e. the same sample analyzed by different instruments/operators. Although the trend in total number of particles is clearly the same for each instrument and the average of all measurements appears to be 1:1, sizable deviations are noted. No line-loss corrections have been applied to the data, which may explain some of the deviation (different length sample lines, etc.). In addition a comparison of operating conditions may uncover slightly different size cut offs. So although the plot illustrates efficacy, rigorous comparison of absolute value would be aided by a calibration procedure.

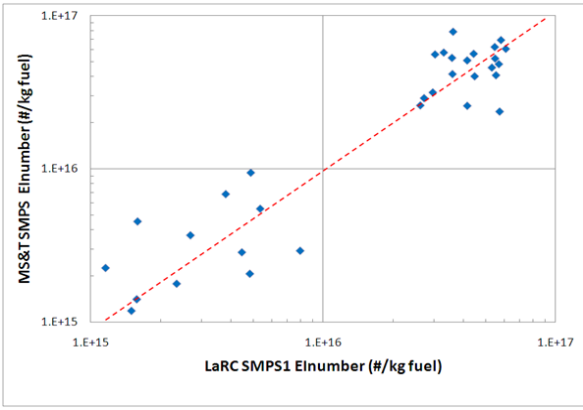

Figure 7. Comparison of Total particle number measured by SMPS

In the left-hand plot in Figure 8 measurements of EImass calculated from thermally denuded size distributions obtained using an SMPS and an EEPS from the 1 m sample probe at AAFEX are compared to MAAP measurements. The SMPS measurements provide the better correlation of EImass with the EEPS correlation indicating a lower size distribution, i.e. undersizing compared to SMPS. Slightly different size cut offs may have been set for the instruments, which would explain the different trends; however in the right-hand plot a comparison of the size distributions confirms that the EEPS consistently undersizes. Comparisons such as these illustrate the difficulty in comparing results if calibration methods are not established and used.

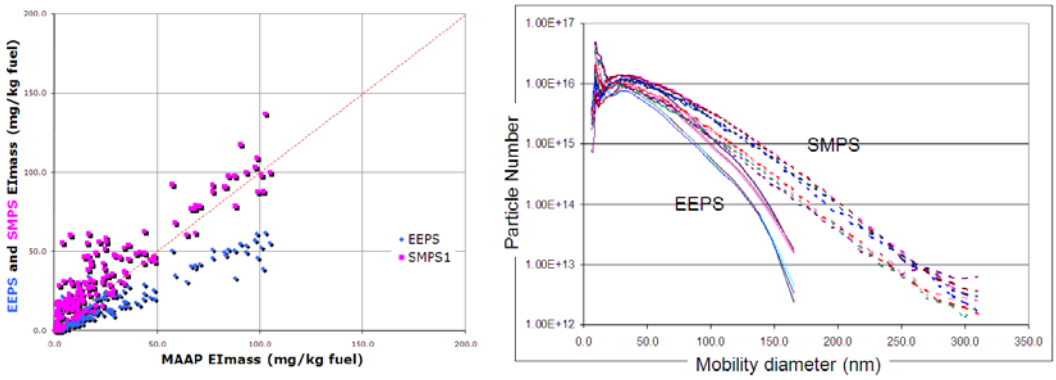

Figure 8. Comparisons of SMPS and EEPS

SUMMARY

As the collection science for PM becomes increasingly more sophisticated, tolerance for error and uncertainty is getting smaller. Traceable calibration methodology is required if the data collected by the different instruments are to be used in a quantitative analysis for setting standards and regulations. One weakness of PM instrumentation (and also in evaluation of the sampling system) is the lack of a suitable calibration technique that can be easily performed in the field, similar to calibration of gas speciation instruments. A calibration methodology would not only help in identifying issues with different instruments but would also be useful in resolving other problems, like sample line and probe losses, encountered while making particle measurements.

REPORT DOCUMENTATION PAGE

Form Approved
OMB No. 0704-0188

1. REPORT DATE *(DD-MM-YYYY)*	2. REPORT TYPE	3. DATES COVERED *(From - To)*
01- 02 - 2011	Technical Memorandum	

4. TITLE AND SUBTITLE
Alternative Aviation Fuel Experiment (AAFEX)

5a. CONTRACT NUMBER

5b. GRANT NUMBER

5c. PROGRAM ELEMENT NUMBER

6. AUTHOR(S)
Anderson, B. E.; Beyersdorf, A. J.; Hudgins, C. H.; Plant, J. V.; Thornhill, K. L.; Winstead, E. L.; Ziemba, L. D.; Howard, R.; Corporan, E.; Miake-Lye, R. C.; Herndon, S. C.; Timko, M.; Woods, E.; Dodds, W.; Lee, B.; Santoni, G.; Whitefield, P.; Hagen, D.; Lobo, P.; Knighton, W. B.; Bulzan, D.; Tacina, K.; Wey, C.; Vander Wal, R.; Bhargava, A.; Kinsey, J.; Liscinsky, D. S.

5d. PROJECT NUMBER

5e. TASK NUMBER

5f. WORK UNIT NUMBER
561581.02.08.07.16.02

7. PERFORMING ORGANIZATION NAME(S) AND ADDRESS(ES)
NASA Langley Research Center
Hampton, VA 23681-2199

8. PERFORMING ORGANIZATION REPORT NUMBER
L-19989

9. SPONSORING/MONITORING AGENCY NAME(S) AND ADDRESS(ES)
National Aeronautics and Space Administration
Washington, DC 20546-0001

10. SPONSOR/MONITOR'S ACRONYM(S)
NASA

11. SPONSOR/MONITOR'S REPORT NUMBER(S)
NASA/TM-2011-217059

12. DISTRIBUTION/AVAILABILITY STATEMENT
Unclassified - Unlimited
Subject Category 45
Availability: NASA CASI (443) 757-5802

13. SUPPLEMENTARY NOTES

14. ABSTRACT

The rising cost of oil coupled with the need to reduce pollution and dependence on foreign suppliers has spurred great interest and activity in developing alternative aviation fuels. Although a variety of fuels have been produced that have similar properties to standard Jet A, detailed studies are required to ascertain the exact impacts of the fuels on engine operation and exhaust composition. In response to this need, NASA acquired and burned a variety of alternative aviation fuel mixtures in the Dryden Flight Research Center DC-8 to assess changes in the aircraft's CFM-56 engine performance and emission parameters relative to operation with standard JP-8. This Alternative Aviation Fuel Experiment, or AAFEX, was conducted at NASA Dryden's Aircraft Operations Facility (DAOF) in Palmdale, California, from January 19 to February 3, 2009 and specifically sought to establish fuel matrix effects on: 1) engine and exhaust gas temperatures and compressor speeds; 2) engine and auxiliary power unit (APU) gas phase and particle emissions and characteristics; and 3) volatile aerosol formation in aging exhaust plumes.

15. SUBJECT TERMS
Aircraft fuels; Exhaust gases; Aerosol emissions; Alternative fuels; Aviation

16. SECURITY CLASSIFICATION OF:			17. LIMITATION OF ABSTRACT	18. NUMBER OF PAGES	19a. NAME OF RESPONSIBLE PERSON
a. REPORT	b. ABSTRACT	c. THIS PAGE			STI Help Desk (email: help@sti.nasa.gov)
					19b. TELEPHONE NUMBER *(Include area code)*
U	U	U	UU	408	(443) 757-5802